AD/A115 370

RAMJETS AND RAMROCKETS FOR MILITARY APPLICATIONS

Advisory Group for Aerospace Research and Development
France

March 1982

AD A115370

AGARD-CP-307

AGARD-CP-307

AGARD

ADVISORY GROUP FOR AEROSPACE RESEARCH & DEVELOPMENT

7 RUE ANCELLE 92200 NEUILLY SUR SEINE FRANCE

AGARD CONFERENCE PROCEEDINGS No.307

Ramjets and Ramrockets for Military Applications

A

NORTH ATLANTIC TREATY ORGANIZATION

REPRODUCED BY
NATIONAL TECHNICAL
INFORMATION SERVICE
U.S. DEPARTMENT OF COMMERCE
SPRINGFIELD, VA. 22161

DTIC FILE COPY

DISTRIBUTION AND AVAILABILITY
ON BACK COVER

This documen a approved
for public rel sale; it
distribution is

82 06 09 093

THE MISSION OF AGARD

The mission of AGARD is to bring together the leading personalities of the NATO nations in the fields of science and technology relating to aerospace for the following purposes:

- Exchanging of scientific and technical information;
- Continuously stimulating advances in the aerospace sciences relevant to strengthening the common defence posture;
- Improving the co-operation among member nations in aerospace research and development;
- Providing scientific and technical advice and assistance to the North Atlantic Military Committee in the field of aerospace research and development;
- Rendering scientific and technical assistance, as requested, to other NATO bodies and to member nations in connection with research and development problems in the aerospace field;
- Providing assistance to member nations for the purpose of increasing their scientific and technical potential:
- Recommending effective ways for the member nations to use their research and development capabilities for the common benefit of the NATO community.

The highest authority within AGARD is the National Delegates Board consisting of officially appointed senior representatives from each member nation. The mission of AGARD is carried out through the Panels which are composed of experts appointed by the National Delegates, the Consultant and Exchange Programme and the Aerospace Applications Studies Programme. The results of AGARD work are reported to the member nations and the NATO Authorities through the AGARD series of publications of which this is one.

Participation in AGARD activities is by invitation only and is normally limited to citizens of the NATO nations.

The content of this publication has been reproduced
directly from material supplied by AGARD or the authors.

Published March 1982

Copyright © AGARD 1982
All Rights Reserved

ISBN 92-835-0312-X

Printed by Technical Editing and Reproduction Ltd
Harford House, 7–9 Charlotte St, London W1P 1HD

AGARD-CP-307

AD/A 115 390

NORTH ATLANTIC TREATY ORGANIZATION

ADVISORY GROUP FOR AEROSPACE RESEARCH AND DEVELOPMENT

(ORGANISATION DU TRAITE DE L'ATLANTIQUE NORD)

AGARD Conference Proceedings No.307

RAMJETS AND RAMROCKETS FOR MILITARY APPLICATIONS

REPRODUCED BY
NATIONAL TECHNICAL
INFORMATION SERVICE
U.S. DEPARTMENT OF COMMERCE
SPRINGFIELD, VA. 22151

Papers presented at the Propulsion and Energetics 58th Symposium, held at Church House,
London, United Kingdom, on 26–29 October 1981.

REPORT DOCUMENTATION PAGE

1. Recipient's Reference	2. Originator's Reference	3. Further Reference	4. Security Classification of Document
	AGARD-CP-307	ISBN 92-835-0312-X	UNCLASSIFIED

5. Originator
Advisory Group for Aerospace Research and Development
North Atlantic Treaty Organization
7 rue Ancelle, 92200 Neuilly sur Seine, France

6. Title

RAMJETS AND RAMROCKETS FOR MILITARY APPLICATIONS

7. Presented at

8. Author(s)/Editor(s)	9. Date
Various	March 1982

10. Author's/Editor's Address	11. Pages
Various	274

12. Distribution Statement
This document is distributed in accordance with AGARD policies and regulations, which are outlined on the Outside Back Cover of all AGARD publications.

13. Keywords/Descriptors

Ramjet engines
Rocket engines
Ducted rocket engines
Missile propulsion

14. Abstract

The Conference Proceedings contain 32 papers presented at the AGARD Propulsion and Energetics Panel 58th Symposium on Ramjets and Ramrockets for Military Applications which was held in London, United Kingdom, on 26–29 October 1981.

The Technical Evaluation Report is included at the beginning of the Proceedings. Questions and answers of the discussions follow each paper.

The Symposium was arranged into six sessions: Survey Papers (3); Propulsion Systems (6); Inlet Diffusers (5); Interference and Drag Reduction, Engine Testing (5): Combustion, Fuels, Propellants (11); and Integral Booster and Transition (2). A Round Table Discussion followed the sessions.

The aim of the Symposium was to provide a forum for discussions to research scientists and development engineers and to furnish a comprehensive survey on modern ramjet and ramrocket technology and their possibilities in missile propulsion to application experts in government and military staffs.

This volume contains the Unclassified papers, the Classified papers are published in CP 307 Supplement.

NOTICE

THIS DOCUMENT HAS BEEN REPRODUCED FROM THE BEST COPY FURNISHED US BY THE SPONSORING AGENCY. ALTHOUGH IT IS RECOGNIZED THAT CERTAIN PORTIONS ARE ILLEGIBLE, IT IS BEING RELEASED IN THE INTEREST OF MAKING AVAILABLE AS MUCH INFORMATION AS POSSIBLE.

PROPULSION AND ENERGETICS PANEL

CHAIRMAN: Professor E.E.Covert
Department of Aeronautics and Astronautics
Massachusetts Institute of Technology
Cambridge, Massachusetts 02139, USA

DEPUTY CHAIRMAN: M. le Professeur Ch.Hirsch
Vrije Universiteit Brussel
Dienst Stromingsmechanica
Pleinlaan 2 – 1050 Brussel
Belgium

PROGRAMME COMMITTEE

Dipl.-Ing. B.Crispin (Chairman)
Messerschmitt-Bölkow-Blohm GmbH
Unternehmensbereich Raumfahrt – Abt RT 31
Postfach 80 11 69 – 8000 München 80, Germany

Professor F.E.C.Culick
Professor of Engineering & Applied Physics
California Institute of Technology
Pasadena, California 91125, USA

Dr J.Dunham
National Gas Turbine Establishment
Pyestock, Farnborough, Hants GU14 OLS, UK

Professor R.Monti
Istituto di Aerodinamica, Università degli Studi
Piazzale Tecchio 80 – 80125 Napoli, Italy

M. l'Ingénieur en Chef M.Pianko
Coordinateur des Recherches en Turbomachines,
ONERA
29 Avenue de la Division Leclerc
92320 Châtillon-sous-Bagneux, France

Professor Ir. H.Wittenberg
Delft University of Technology
Department of Aerospace Engineering
Kluyverweg 1 – 2629 HS Delft, Netherlands

HOST NATION COORDINATOR

Group Captain R.D.Hillary (Rtd)
Ministry of Defence (Room 2115)
Main Building, Whitehall
London SW1A 2HB, UK

PANEL COORDINATOR

Dr J.Dunham
National Gas Turbine Establishment
Pyestock
Farnborough, Hants GU14 OLS, UK

PANEL EXECUTIVE

Dr-Ing. E.Riester
AGARD-NATO
7 rue Ancelle
92200 Neuilly sur Seine
France

ACKNOWLEDGEMENT

The Propulsion and Energetics Panel wishes to express its thanks to the UK National Delegates to AGARD for the invitation to hold its 58th Symposium in London, and for the personnel and facilities made available for this meeting.

Avail and/or
Dist Special
A

CONTENTS

Page

PANEL OFFICERS AND PROGRAMME COMMITTEE iii

TECHNICAL EVALUATION REPORT
by F.D.Stull vii

Reference

SESSION I – SURVEY PAPERS

ADVANCES IN US AIR-BREATHING PROPULSION: 1960s THROUGH 1980s*
by J.L.Fields, C.R.Limage and R.H.W.Waesche 1

INTERET DE LA PROPULSION PAR STATOREACTEUR A COMBUSTIBLE SOLIDE POUR LES PETITS MISSILES*
par J.P.Counil et A.Ravier 2

Paper is cancelled

THE OUTLOOK FOR RAMJETS AND RAMJET DERIVATIVES FOR MILITARY APPLICATIONS IN THE UNITED STATES*
by A.N.Thomas, Jr 4

SESSION II – PROPULSION SYSTEMS

CONCEPTION D'UN STATOREACTEUR A ACCELERATEUR INTEGRE*
par M.Ravel 5

CONCEPTIONS NOUVELLES POUR STATO-FUSEES DE FAIBLE COUT*
par B.Petit et L.Nadaud 6

LOW-COST COMBUSTOR FOR A SUPERSONIC TACTICAL MISSILE
by T.D.Myers and A.P.Peters 7

ENGINE SIZING AND INTEGRATION REQUIREMENTS FOR HYPERSONIC AIRBREATHING MISSILE APPLICATIONS
by P.J.Waltrup, F.S.Billig and R.D.Stockbridge 8

DESIGN CONSIDERATION AND ANALYTICAL COMPARISON OF DIFFERENT TYPES OF RAMJETS AND RAMROCKETS
by P.Benkmann and P.A.Kramer 9

VALVELESS PULSEJETS AND ALLIED DEVICES FOR LOW THRUST, SUBSONIC PROPULSION APPLICATIONS
by J.A.C.Kentfield 10

SESSION III – INLET DIFFUSORS

COMPARAISON DE DIFFERENTES CONFIGURATIONS D'ENTREE D'AIR DE MISSILES SUPERSONIQUES*
par G.Laruelle 11

MULTIPLE INTAKES FOR RAMROCKETS
by E.-O.Krohn and K.Triesch 12

ONE-DIMENSIONAL NON LINEAR CONSIDERATIONS ON SUPERSONIC DIFFUSER BUZZ
by H.-L.Weinreich 13

THE INTERNAL PERFORMANCE AND EXTERNAL DRAG OF SOME WEAPON INTAKES*
by E.L.Goldsmith, R.W.Jeffery and M.Cameron 14

---

*Papers published in CP 307 Supplement (Classified)

Reference

RANGE MAXIMIZATION METHOD FOR RAMJET POWERED MISSILES WITH FLIGHT PATH CONSTRAINTS
by U.M.Schöttle 15

SESSION IV – INTERFERENCE AND DRAG REDUCTION, ENGINE TESTING

JET-AFTERBODY INTERFERENCE ON MISSILES IN SUPERSONIC FLOW
by B.Wagner 16

BASE AND EXTERNAL BURNING FOR PROPULSION
by W.C.Strahle and J.E.Hubbartt 17

A SMALL SCALE TESTING FACILITY FOR RAMROCKET PROPELLANTS*
by P.J.Boszko 18

METHODES ET MOYENS D'ESSAI DES STATOREACTEURS ET STATOFUSEES. COMPARAISON DES RESULTATS OBTENUS AU SOL ET EN VOL*
par P.Cazin et P.Berton 19

SERVICE EXPERIENCE WITH THREE GENERATIONS OF RAMJETS
by C.F.Fletcher and D.R.Lane 20

SESSION V – COMBUSTION, FUELS, PROPELLANTS

EXPERIMENTAL INVESTIGATION OF A HYDROCARBON SOLID FUEL RAMJET
by D.Meinköhn and J.W.Bergmann 21

BORON COMBUSTION IN DUCTED ROCKETS
by K.C.Schadow 22

INVESTIGATION OF BORON SOLID PROPELLANTS COMBUSTION IN DUCTED ROCKETS*
by H.L.Besser 23

RECHERCHE ET MISE AU POINT D'UN PROPERGOL SOLIDE POUR STATO-FUSEE
par JD.Bérard, G.Doriath et C.Perut 24

THE DEVELOPMENT OF FUEL-RICH CAST DOUBLE BASE PROPELLANTS FOR RAMROCKET APPLICATIONS*
by P.J.Boszko 25

DESIGN OF HYDROGEN FUELED RAMJETS AND RAMROCKETS
by D.Dini 26

THE ROLE OF LIQUID PHASE DROPLET DECOMPOSITION IN AN ADVANCED AIRBREATHING PROPULSION SYSTEM
by M.Gerstein and P.R.Choudhury 27

PRACTICAL SWIRLERS FOR RAMJET DUMP COMBUSTORS*
by F.D.Stull, R.R.Craig and P.L.Buckley 28

COMBUSTOR MODELING FOR RAMJET DEVELOPMENT PROGRAMS
by P.T.Harsha, R.B.Edelman, S.N.Schmotolocha and R.J.Pederson 29

THE MATHEMATICAL MODELLING OF AIR-AUGMENTED ROCKET COMBUSTORS: A PROGRESS REPORT
by J.C.P.Birchley, L.T.Glasspoole and A.S.Wilson 30

COMBUSTOR MODELLING STUDIES FOR RAMJETS
by P.Roy, A.F.Schlader and J.Odgers 31

---

*Papers published in CP 307 Supplement (Classified) √

Reference

SESSION VI – INTEGRAL BOOSTER AND TRANSITION

DEVELOPMENT OF AN INTEGRAL ROCKET RAMJET BOOSTER FOR PROPULSION TECHNOLOGY FLIGHT TEST DEMONSTRATION PROGRAM*
by W.G.Haymes, K.F.Miller, J.E.Tobin and T.D.Burnette 32

MULTIPLE INLET AND TRANSITION DEVELOPMENT FOR AN INTEGRAL ROCKET-RAMJET*
by J.F.Doherty 33

---

*Papers published in CP 307 Supplement (Classified)

TECHNICAL EVALUATION REPORT

by

Dr F.D.Stull
Air Force Wright Aeronautical Laboratories/
Aero Propulsion Laboratory/PORT
Wright-Patterson AFB, Ohio 45433
US

1. INTRODUCTION

The 58th meeting of the Propulsion and Energetics Panel was held at the Church House, Great Smith Street, London, England on 26–29 October 1981. The purpose of the meeting was to hold a symposium on "Ramjets and Ramrockets for Military Applications." The meeting theme was to provide a forum for discussion to research scientists and development engineers and to furnish a comprehensive survey on modern ramjet and ramrocket technology and their possibilities in missile propulsion to application experts in government and military staffs. The topics were to include:

I Survey Papers
II Propulsion Systems
III Inlet Diffusers
IV Interference and Drag Reduction, Engine Testing
V Combustion, Fuels, Propellants
VI Integral Booster and Transition

2. SUMMARY AND COMMENTARY

The goals of the basic purpose, theme and individual topics were, for the most part, achieved in the presentation of 32 papers in 6 sessions, plus a round table discussion. The availability of published preprints of papers presented and the excellent support provided by the language interpreters helped to make the symposium run smoothly. The arrangements were particularly well suited for encouraging active informal technical interchanges between the attendees. Opening remarks by the Propulsion and Energetics Panel's Chairman, Prof. Eugene E.Covert, followed by an address from the Chief Scientist of the RAF, Mr Don Harper, started the symposium off to a good start.

Session chairmen did a good job in keeping the presentations on schedule and in encouraging an active question and answer period. The papers, for the most part, were well prepared with good visual material. The subject material reflected the meeting theme covering a broad number of topics from basic component research to an extensive survey of service experience with three generations of liquid fueled ramjets. Some of the specific topics of interest to the researchers and development engineers dealt with inlet buzz, multiple inlet interactive effects, prediction of axisymmetric base flows, use of swirl in combustors, boron combustion, combustion modelling, inlet integration requirements for hypersonic missiles, pulsejets and range optimization techniques. Above all, through several comprehensive surveys, the papers demonstrated the maturity of modern ramjet and ramrocket propulsion technology and discussed applications where it offers distinct advantages in range, weight, volume, average velocity, and terminal velocity for maneuverability over existing missile systems. What the papers did not cover in detail, which was beyond the scope of this meeting, was the overall aspects of a missile system, such as guidance and control, observables and cost effectiveness studies. Some of these issues were raised and discussed briefly during the question and answer periods and during the round table discussion.

3. DISCUSSION

The symposium consisted of 32 papers (one paper had been cancelled from the meeting announcement) presented in 6 sessions. There were 9 papers which dealt with overall ramjet (including ducted rocket and solid fuel ramjet) state-of-the-art summaries, propulsion systems and application studies, several of which dealt with such critical items as cost considerations and ramjet service experience. In addition to ramjets, there were individual papers covering such related propulsion systems as Scramjets, H_2 fuel turboramjets, external/base burning projectiles and pulsejets, thereby extending the Mach number capability of the conventional ramjet in both directions to very high Mach numbers and to subsonic speeds, respectively. The inlet area was well covered in 6 detailed papers which included the stability effects of multiple inlets and inlet buzz. The combustion area was also well represented by 7 papers presenting experimental results for liquid fuel ramjets, ducted rockets (ramrockets) and solid fuel ramjets, plus 3 other combustor modelling papers encompassing a hierarchy of models from a modular semi-global kinetics model to the more elegant finite difference techniques. Engine testing and IRR booster/transition filled out this well balanced program. Figure 1 summarizes the content of the meeting. Two excellent movies were also shown of recent ramjet flight tests.

Sessions I and II

The theme of Sessions I and II was to furnish a comprehensive survey on modern ramjet and ramrocket propulsion technology and their possibilities in missile propulsion. Papers 1 and 4 gave a historical overview of US ramjet propulsion programs emphasizing the solid and liquid fuels area, respectively, as well as discussing the merits of ramjet type propulsion systems for the next generation missile systems. Paper 4 concluded with an excellent movie showing results of a recent liquid fuel ramjet flight test program. Paper 2 described French propulsion programs in the solid fuel area using either self-pyrolysing or ablative fuels for relatively small tactical missiles. Advantages of such ramjet systems over solid propellant rocket engines were discussed. Paper 3 was cancelled.

Paper 5 presented a detailed discussion on the design and development of integral booster ramjets for large flight envelope missiles. The requirements imposed on the various components, including the inlet, by the high performance of the liquid fuel ramjet and the transition process from integral rocket boost to ramjet operation were addressed. Papers 6 and 7 considered the importance of cost in developing tactical missiles. Paper 6 considered several relatively small ramrocket configurations using an integral, nozzleless, solid propellant booster, whereas Paper 7 discussed how cost reductions were made on a liquid fuel integral rocket/ramjet with essentially no loss in propulsion system performance. Later during the symposium, an impressive movie was shown of the flight test for this program. Paper 8 was unique in that it dealt with engine sizing and integration requirements of scramjet engines for hypersonic air-breathing missile applications. Results of a comprehensive study on various inlet configurations were included. Paper 9 presented an analytical study of ramjets and ramrockets and discussed design considerations with respect to performance impacts. Results showed that in addition to specific impulse, Thrust per unit cross-section is an equally important parameter in making such comparisons. Paper 10 was a comprehensive review of valveless pulsejets and concluded that current technology valveless pulsejets are best suited to low thrust (less than 600 Newtons or 130 lb_f), short-range subsonic applications where low initial cost, simplicity and reliability are of dominant importance.

Session III

Four out of the five papers presented pertained to detailed inlet diffuser investigations. Paper 11 discussed parametric studies of various inlet configurations (including circular, semi-circular and two-dimensional), number of inlets, position of inlet relative to missile body, and height of external boundary layer bleeds. Paper 12 discussed in detail the phenomena of flow instability and flow reversal which can occur when multiple inlets are used in conjunction with a common combustion chamber. A computer program was developed which calculates the overall performance of the inlet system from single-intake data. Paper 13 was a comprehensive review and discussion on the fundamental aspects of supersonic intake buzz with 69 references listed. A non-linear theoretical model and comparison of theoretical trends with experimental work was presented. Paper 14 discussed the performance of a variety of inlet configurations and the effect of the intake's location in regards to the rest of the missile body. Paper 15 was not an inlet paper, but dealt with trajectory optimization for ramjet powered missiles. It was shown that by employing parametric optimization methods using the continuous throttle capabilities of the ramjet propulsion system, range improvements of from 5 to 11%, depending on mission requirements, can result when compared to more conventional fuel control.

Session IV

This session dealt with a variety of diverse topics. Paper 16 was a theoretical treatment of the base flow problem with respect to missiles. Using the method of characteristics for the inviscid flow regions and Korst's treatment for turbulent shear layers, an approach was introduced which accounts for the influence of the approaching boundary layers and leads to reasonable predictions of base pressures for small angles of attack. Paper 17 presented the results of experimental studies concerning base and external burning behind an axisymmetric bluff base body in a Mach 3 airstream. Pure hydrogen and hydrogen diluted with CO_2, He and N_2 were used as the fuels. It was found that the major determinant of I_{sp} performance was the total heat release rate into the wake. Paper 18 described a small scale direct connect test facility for use in the development of ramrocket propellants. Paper 19 was an extensive review of the various test facilities in France along with detailed discussions of testing techniques. Special facilities were described which can test full scale ramjet missiles with solid propellant boosters. Paper 20 was a comprehensive survey paper dealing with three generations of ramjets for operational surface-to-air missiles with the RAF and Royal Navy. It was shown that the liquid fuel ramjet has a comparable in-service reliability to that of the simple solid rocket, in spite of its greater complexity, while offering a much wider operational capability. Such experience gained from the Bloodhound and Sea Dart propulsion systems has led to the establishment of "wooden round" or "sealed for life" status for the liquid fuel ramjet with simple maintenance checks currently performed at only 5 year intervals.

Session V and VI

These two sessions addressed combustors, fuels and fuel-rich propellants along with combustion modelling. Of the fuel-rich grains discussed, two were hydrocarbon fuels and two were boron fuels. Paper 21 discussed direct connect combustion tests of a solid fuel ramjet consisting of a rearward facing step as its flameholding device, an ignitor, a combustion chamber containing the hydrocarbon solid fuel grain, and an afterburner for enhancement and completion of the combustion. Regression rates and combustion efficiency results were obtained over a range of flight conditions for several hydrocarbon fuels, including polyethylene, and for different port geometries. Paper 22 described the results of water tunnel tests and two-dimensional windowed combustor tests with two opposing 45° side air inlets. These were used to provide qualitative insight into the effects of important combustor parameters on the overall performance of boron propellant gas generator ramjets (ducted rockets). It was found that the highest combustion efficiencies were achieved at the lowest fuel injection momentum and at the lowest air injection momentum. Reasons were postulated for these results. Paper 23 provided a comprehensive review of the boron combustor investigations conducted at MBB for ducted rockets. These included boron reactions during the primary combustion (burning of the fuel-rich propellant grain), as well as the behavior of boron during ram-combustion. Also discussed were special experimental techniques applied during these investigations. Paper 24 described the development and characterization of a class of hydrocarbon propellants for ducted rockets. A third generation fuel bearing the reference number 1603 was shown to have a relatively high heating value (8020 cal/g), excellent mechanical properties and a low exhaust signature. Paper 25 discussed the development of fuel-rich cast double propellants for ramrocket applications. Paper 26 was not a combustion paper, but rather discussed the use of high energy fuels, particularly hydrogen, in advanced mixed cycle airbreathing configurations for military applications.

Paper 27 described a research effort involving the coupled effects of decomposition and evaporation of a typical liquid fuel spray. Results indicated that liquid phase droplet decomposition at higher pressures may cause a significant reduction of combustion efficiency in advanced airbreathing propulsion systems. Paper 28 discussed the use of swirl in ramjet combustors and showed that a properly designed contoured swirler can achieve higher combustion efficiencies, along with significantly lower pressure losses, than a typical frameholder configuration. These same swirlers have also been applied with success to the solid fuel ramjet. Paper 29 presented a detailed discussion of a modular model for the analysis of sudden-expansion ramjet combustors. This model is based on a concept in which the recirculation zone, treated as a stirred reactor, is coupled to a parabolic boundary layer formulation for the flow outside the recirculation zone. Hydrocarbon oxidation kinetics and turbulent kinetic energy turbulence models are included. Paper 30 described the theoretical approach for the calculation of axisymmetric and three-dimensional ducted flows suitable for ducted rockets. A numerical computer code employing finite difference forms was developed from existing free-flow computation techniques to calculate axisymmetric, non-recirculatory ducted flows. Future work would develop a computer code to calculate three-dimensional ducted flows with due allowance for flow asymmetry and recirculation. Paper 31 described a simple three-step model, empirically derived from a premixed propane-air baffle-stabilized ceramic lined combustor, which can predict composition and temperature profiles in ramjet like combustors including the effects of vitiated preheat and heat loss.

Session VI

The two papers which were presented in this session dealt with details associated with the transition process from integral rocket boost to ramjet combustor operation. Paper 32 gave a historical accounting of the development of an Integral Rocket-Ramjet booster for a propulsion technology flight demonstration program. Paper 33 discussed multiple-inlet and transition development for another integral rocket-ramjet program.

Round Table Discussion

Following Session VI, a round table discussion chaired by B.Crispin (Germany) was held. Other members of this panel were E.L.Goldsmith (UK), R.Marguet (France), F.D.Stull (US) and A.N.Thomas, Jr (US). The primary issues addressed during this round table discussion were (1) the state-of-the-art of ramjet technology and (2) reasons for the retardation in making the new generation of ramjets operational in military projects.

4. CONCLUSIONS AND RECOMMENDATIONS

The large participation (over 60 authors and 75 observers for "Ramjets and Ramrockets for Military Applications") shows the importance and timely nature of the subject chosen by the AGARD Propulsion and Energetics Panel for its 58th Symposium. Comprehensive surveys presented on modern ramjet and ramrocket propulsion technology have shown that neither the lack of technical progress nor the lack of attractive missions are the reasons for the hesitation in applying new generation ramjets to operational military projects. Rather it was sugggested, that ramjets need to improve their "image" with military planners and missile designers.

A *future AGARD meeting might be held,* perhaps in conjunction with another panel, to address the overall missile systems aspect and cost effectiveness of using ramjet technology. Propulsion related technology areas to be discussed should include:

- Missile guidance and control and its effect on inlets and propulsion performance: skid-to-turn vs. bank-to-turn
- Propulsion system observables: i.e., IR, RADAR signature and visible smoke

- Missile effectiveness
- Life cycle costs

In addition, an update on inlet performance and combustor modelling, including the combustion of boron at low pressures, would be appropriate.

Paper No.	Authors	Survey	Application Studies	Theoretical	Experimental	Testing/Techniques	Intakes	Combustion	Integral Booster/ Transition	Base Flow	Liquid Ramjet	Ducted Rocket	Solid Fuel Ramjet	Other Cycles	Cost Considerations	Service Experience
1	Fields, Limage, Waesche	*	*								*	*	*	*		
2	Counil, Ravier		*										*			
3	Cancelled															
4	Thomas	*	*								*	*	*	*	*	
5	Ravel	*									*					
6	Petit, Nadaud		*									*				
7	Myers, Peters					*					*				*	
8	Waltrup, Billig, Stockbridge		*				*							*		
9	Kramer, Benkmann		*								*	*				
10	Kentfield	*			*									*	*	
11	Laruelle				*		*									
12	Krohn, Triesch			*	*		*									
13	Weinreich			*			*									
14	Goldsmith, Jeffery, Cameron				*		*									
15	Schöttle		*	*												
16	Wagner			*						*						
17	Strahle, Hubbartt				*					*				*		
18	Boszko					*						*				
19	Cazin, Berton					*										
20	Fletcher, Lane	*									*					*
21	Meinköln, Bergmann		*		*			*					*			
22	Schadow				*			*				*				
23	Besser				*	*		*				*				
24	Berard, Doriath, Perut				*			*				*				
25	Boszko				*			*				*				
26	Dini		*											*		
27	Gerstein, Choudhury			*				*			*					
28	Stull, Craig, Buckley				*			*			*		*			
29	Harsha, Edelman, Schmotolocha, Pederson			*				*			*					
30	Birchley, Glasspoole, Wilson			*				*				*				
31	Roy, Schlader, Odgers			*	*			*			*					
32	Haymes, Miller, Tobin, Burnette					*			*		*					
33	Doherty					*	*		*		*					

Figure 1

LOW-COST COMBUSTOR FOR A SUPERSONIC TACTICAL MISSILE

T. D. Myers and A. P. Peters
Chemical Systems Division/United Technologies Corporation
P.O. Box 358
Sunnyvale, California 94086 U.S.A.

INTRODUCTION

In April 1979, a low-cost liquid fuel integral rocket ramjet (LFRJ/IRR) was successfully flown at the Navy Pacific Missile Range at Point Mugu, California. The low-cost LFRJ/IRR propulsion system was a derivative of the earlier flight-demonstrated advanced low volume ramjet (ALVRJ). The ALVRJ baseline propulsion system seen in Figure 1 had performed perfectly in a series of five flight tests in which typical missile boost, sustain, and flight maneuvers were commanded. A summary of the ALVRJ flight test results is seen in Figure 2. These five flight tests were made over a two-year period, starting with the first flight in November 1974. The propulsion system ground test development program began in 1968 and continued for the next six years up until 1974.

After the key technical aspects of the LFRJ/IRR propulsion system had been demonstrated, studies were conducted to identify the best mission application for the ALVRJ propulsion system. One of the most promising mission applications for the ALVRJ was for the Supersonic Tactical Missile (STM) shown in Figure 3. When compared to an equivalent weight- and volume-constrained rocket motor, the ALVRJ propulsion system could provide over twice the range with a higher terminal velocity. Moreover, when compared to a comparable weight- and volume-constrained turbine engine, the ALVRJ could provide higher velocity and a multiple shot capability, increasing the mission hit probability.

Cost studies revealed, however, that the ALVRJ unit cost production was approximately five times higher than desired for the STM. Therefore a design study was conducted to determine where production cost savings could be made for the ALVRJ propulsion system without a significant sacrifice in performance. The cost reduction design study was conducted by the Vought Missile Systems Division and was supported by both Chemical Systems Division (CSD) and the Naval Weapons Center (NWC). Vought was responsible for designing the vehicle and integrating the propulsion system components; CSD was responsible for developing the low-cost ramburner technology; and NWC was responsible for fabricating the integral booster motor and providing inlet and combustor test facilities. The specific cost goal was to reduce the cost of the experimental configuration from $200,000 by a factor of 4 to 5 with no performance penalty.

The approach for developing the low-cost ALVRJ propulsion system for the STM and other tactical mission applications is summarized as follows. First, a series of propulsion system performance/cost vehicle systems trades were conducted. Key propulsion system requirements that most strongly influenced cost were: (1) fuel flow rate accuracy, (2) inlet pressure recovery, and (3) required combustor operational life. From these trade studies specific low-cost ramjet component designs were selected, including: (1) inlet, (2) fuel controller, (3) rocket booster motor nozzle release mechanism, and (4) combustor/thermal protection system (TPS). The low-cost combustor/TPS development effort is the primary subject of this paper. The low-cost inlet technology developed by Vought and the low-cost fuel controller developed jointly by Vought and NWC are subjects for separate papers. Although the basic low-cost combustor development was primarily an in-house research and development effort by CSD/Vought, some of the key component ground tests and the flight test were conducted by NWC.

SUPERSONIC TACTICAL MISSILE (STM) LOW-COST RAMJET COMBUSTOR DEVELOPMENT

The ALVRJ ramjet combustor case was rolled and welded from Inconel 718. The inlet entry ports and nozzle shell actuator mounts were machined from forgings. Thermal protection was provided by a refractory zirconia layer and local hot spots protected either by regenerative fuel cooling or air cooling. The high cost of Inconel 718 combined with the extensive machining required for the local fuel and air cooling resulted in a very expensive design. In addition, the fuel/air ratio was required to be held very lean to avoid combustion temperatures in excess of 1,922°K, which limited the maximum thrust capability of the engine.

The ALVRJ TPS design was selected in 1968 and reflected the best state-of-the-art technology available at that time. By 1977, however, separate industry development programs had produced a new ablative thermal protection system that proved to be a very effective insulator for ramjet combustors. This carbon-filled elastomer material, designated as DC 93-104, has excellent low thermal conductivity and is also resistant to the oxidizer-rich ramjet combustor gases. By using DC 93-104, CSD could select the less costly case material, 17-4 ph, and also eliminate the expensive machinery operations associated with local fuel and air cooling. DC 93-104 has lower fabrication costs than the zirconia liner. In addition, the combustion temperature limit needed for the zirconia-protected ALVRJ combustor case could be removed with DC 93-104 and the full thrust potential of the engine could be realized.

An illustration of the low-cost combustor is shown in Figure 4. Together with the primary cost reductions associated with the use of 17-4 ph steel and DC 93-104, several supplementary cost savings were realized by using castings in place of forgings for the

7-2 inlet entry sections. The tensile strength of the castings was increased by hot isostatic pressing (HIP) to a level normally attained only by using a more expensive forging. These key cost reduction design features, which permitted the 4-5:1 production unit cost projection, are summarized in Figure 5.

LOW-COST COMBUSTOR DESIGN AND FABRICATION

The low-cost combustor assembly is shown in Figure 6. The combustor assembly consists of two major subassemblies, the forward combustor case and the nozzle, which are married in the final assembly by a circumferential EB weld.

Critical airframe interfaces are machined after final assembly by means of Vought-supplied locators and templates. Machining interfacing surfaces after assembly ensures accurate alignment of the booster motor nozzle. The forward end of the combustor is a dome formed to a shape approximating a 2:1 ellipsoidal dished section with an 0.24/0.22-cm wall thickness. A boss, butt-welded to the center of the dome, serves multiple functions: it acts as a centering hole for the TPS casting mandrel, a casting port for the DC 93-104 insulation, a centering hole for the booster grain mandrel, and a pressure port for combustor pressure measurement. After the dome has been joined to the inlet actuator mounting pad/nozzle support ring, the subassembly is aged to the H-775 condition before the nozzle skin is installed to facilitate nondestructive testing (NDT) inspection of the critical fin support pad welds. Following qualilty control (QC) acceptance of the aged subassembly, the nonstructural nozzle skin is welded in place. Subsequent heat treatment is not required.

The nozzle liner is molded from chopped squares of U.S. Polymeric FM 5020. The material is bonded to the nozzle support structure with American Cyanamid HT-924 adhesive. A silicone O-ring between the liner and the support ring ensures that gas does not leak across the nozzle bond line. Additional sealing is provided by the DC 93-104 nozzle entrance fillet, which is installed at final combustor assembly, and a soft silastic material that is installed between the aft-radial surface of the liner and the support rings.

Alignment surfaces of the snap-ring interface and the ramjet throat are machined after combustor assembly to ensure that the required alignment tolerances are met.

Acceptance of the completed combustors was in accord with CSD Acceptance Specification TP-2630-003. Weld efficiencies meeting or exceeding design requirements were demonstrated for all weld types. A weld qualification program to ensure sound welds was conducted for the 13 weld or weld-type joints used in the fabrication of the low-cost combustor. Weld procedures were developed for each of these joints in accordance with the standard CSD weld qualification specification.

An extensive materials evaluation program was conducted in support of the low-cost combustor design. Vehicle weight restrictions required qualification of a material meeting high strength requirements while still maintaining sufficient toughness and stress corrosion resistance.

Material for the low-cost combustor was initially specified by CSD as a 17-4 ph aged to the H-811 condition; however, in response to Vought's weight reduction requirement, CSD determined the best compromise between material strength and toughness. The selected combustor design, based on 17-4 ph and aged to 775°K condition, has an ultimate strength of $1,275 \times 10^6$ N/m^2 for sheet, $1,241 \times 10^6$ N/m^2 for forged materials, and $1,172 \times 10^6$ N/m^2 for case material. Since resistance to stress corrosion cracking was very important, stringent NDT and acceptance test procedures were used to ensure that components and fabricated assemblies were free from defects.

Preliminary design values were based on review of available literature or data from previous Vought programs. These values were revised as CSD material test data became available. As a result of the materials evaluation program and selective procurement, design stress values approximately 20% above MIL-HBK-5 design allowables were approved for use in the low-cost combustor design.

To achieve CSD cost objectives, the complex air inlets (Figure 7) were cast instead of machined. The cast inlets reduced the inlet cost per combustor by approximately 75% of the cost of machined inlets, representing a savings of about $12,000 per combustor. This is the first time CSD had used castings at high stress levels as an integral part of a combustor case pressure shell. In a continuing effort to reduce fabrication costs, the technology gains from the inlet casting effort were expanded to investigate the casting of the entire forward inlet section. This design, though not completed in time for this initial program, would reduce combustor costs further by eliminating the complex jigging and welding required to form the forward assembly. Designs were prepared and a contract released for casting a single inlet section, formerly comprised of the four inlet castings, the four roll-formed interconnecting sheet segments, and the forged forward dome/forward attach "y" ring section. This integral inlet section, shown in Figure 8, met all inspection requirements established for the single inlet castings used in the low-cost combustor development program (LCCDP) combustors. The integral inlet section was subjected to the same HIP process as the single inlet castings. No defects due to the HIP process were detected, and a posttest dimensional inspection showed the casting to be dimensionally stable during HIP.

An extensive insulation processing study was conducted to develop procedures for installing the TPS in the LCCDP.

Personnel in CSD's Research and Advanced Technology Department installed the Dow-Corning DC 93-104 insulation into the prototype combustors using procedures developed through literature research and prior experience. Requirements and procedures for receiving/inspection, storage, mixing, and casting of the DC 93-104 material were developed and used throughout the program.

The successful casting of the STM combustor liners provided a significant increase in CSD's understanding of the handling and processing of the Dow-Corning DC 93-104 material.

VALIDATION TESTS

Ground test activities in support of the STM program successfully demonstrated the adequacy of the design for defined STM flight trajectories. These activities are summarized in Table 1 and discussed below.

CASE STRUCTURAL/HYDROTEST

This test demonstrated the structural adequacy of the low-cost combustor. These tests, conducted at CSD, subjected the finished combustor to full combustor design conditions.

The low-cost combustor was subjected to two hydrotests. The first test was designed to demonstrate the adequacy of the combustor to withstand the design internal pressure (1.25 times maximum expected operating pressure (MEOP), 12×10^6 N/m^2); the second test was designed to demonstrate the adequacy of the combustor to withstand actual flight internal and external loads. For each test, the analytically determined stresses in the inlet area were higher than the experimentally derived stresses.

The first low-cost combustor booster test was successfully accomplished, with support from CSD, at the NWC Skytop test facility. Posttest inspection of the combustor indicated that little degradation of the TPS had occurred. A decision was made to lightly sand the DC 93-104 surface and cast a second booster grain into the combustor. The second booster test was successfully conducted in early 1979. All test objectives were met, including the ejection of the port covers and booster nozzle.

CSD supported the NWC investigation into the cause of a propellant-to-TPS unbond which occurred in the second motor. The cause of the unbond was traced to a procedural error in propellant casting. The Dow-Corning DC 93-104 insulation had not been "baked" before casting of the solid propellant, and volatiles evolving from the DC 93-104 during the propellant cure cycle had caused the unbonds between the TPS and the propellant. In the first motor, insulation repair at CSD before delivery to NWC had exposed the TPS to elevated temperature for an extended period of time. This exposure drove off most of the volatiles in the DC 93-104, allowing a normal bond with the propellant. NWC procedures were revised to include a post-cure "baking" of the DC 93-104 before the propellant casting operation. All following booster motor grains were cast without additional problems.

The low-cost combustor thermal endurance test, supported by CSD, was conducted at the NWC T-range facility on March 30, 1979. The same combustor, previously used for the two booster qualification tests, was used for this test. Because of the limitations of the T-range test facility, the endurance test was conducted at a single condition (approximately 10.7-km altitude chamber pressure conditions).

The goal of the thermal endurance test was to demonstrate the ability of the TPS to withstand long-duration cruise conditions. The results of the test were then used to update the thermal math model and to define more accurately the high heat fluxes that occur in a local hot zone around each inlet pad. Movie cameras positioned to look into the combustor during ramjet operation produced photos showing two things of interest. One good view of the inlet area showed edge burning of the DC 93-104 pyrolysis gases around the inlet window frame. From demonstration combustor tests, it had been speculated that a larger combustion zone aft of each inlet had formed, and the math model was modified accordingly. The second interesting observation from the movies was that charred lines on the sides of the inlets had been blown off after ramjet shutdown. Thermocouple data did indicate, however, that some top layers of char may have also been lost on the inlet sides during ramjet operation (Figure 9). Since temperatures were not excessive, it was obvious that good insulation remained on the case. On the basis of the thermocouple data, thermal paint indications, and movies, the heating around the inlets is believed to be driven by edge burning effects around the inlets in the recirculation zone created by the aft facing step. The model hypothesis is illustrated in Figure 10.

The internal boundary conditions were revised to model this phenomenon by first making the source temperature for the window frame, Zone C (Figure 11), equal to 1,944°K, the approximate combustion temperature of pyrolysis gases, and then systematically reducing the heat transfer to a coefficient until a good match with test data was obtained. In addition, the source temperature downstream of the inlets, Zone B, was reduced from 1,939°K to 1,700°K, which is consistent with the ALVRJ data base. As Figure 9 shows, the pretest overprediction is corrected by the model update. The same internal boundary conditions were successfully used to predict the final ground test results and STM flight test results.

Maximum temperatures measured on the combustor hot zone were only 978°K, including a 255°K preheat during 60 sec of facility inlet air flow stabilization prior to ramjet ignition. This is well below the 1,200°K design allowable established by a structural creep analysis.

The last ground test to qualify the low-cost combustor for flight was the integrated system test conducted on April 16, 1979, in the CSD ramjet test facility (Figure 12). This test was designed to simulate fully the conditions and sequences of events to be encountered in the STM-flight test.

The STM, IRR test was the first connected-pipe, rocket-to-ramjet transition, full trajectory simulation test conducted by CSD and is thought to be the first in the United States for a full-size flight combustor. All test sequences and test parameters were designed to simulate actual STM flight conditions. Extensive planning, system checks, and flow calibrations were carried out prior to the final authorization for conducting the test. On April 6, 1979, with representatives from the Naval Weapons Center and Vought Systems Division in attendance, the test was successfully conducted. All systems performed within specified limits and all test objectives were met.

Figure 13 presents test data showing the thrust and combustion pressure history of the low-cost combustor during the IRR test. Both parameters were exactly as predicted from the ground tests. For this test, aerodynamic heating was applied to one quadrant of the combustor only. Since the external surface of the combustor is exposed to aerodynamic heating in only four zones approximately 12.7 cm wide, between the inlet fairings, it was felt that each zone would react independently of the other zones in actual flight; therefore, simulation of one zone was sufficient. The heat transfer coefficients expected to be encountered during the STM flight were supplied to CSD by Vought. These coefficients were correlated to backside shroud air flow and temperature for this test by calibration tests conducted on the bare wall fit check combustor. The temperature response at critical locations around the combustor (Figure 14) clearly show the excellent thermal protection provided by the DC 93-104 TPS.

Upon completion of the fully successful integrated systems ground test, a flight demonstration was scheduled. The specially modified A-7 aircraft took off from NWC at Ridgecrest, California, and flew out over the Navy Pacific Missile Center. The STM vehicle was dropped at high altitude and allowed to free fall approximately 5 sec to clear the launch plane. The booster motor was ignited in a diving attitude, accelerating the missile to greater than Mach 3 at booster burnout. The dive was continued for 30 sec, whereupon a climb was initiated. The desired cruise speed and altitude were reached and a sustained cruise was maintained to a range greater than 100 km, whereupon a terminal dive to sea level was initiated. The vehicle was allowed to impact into the Pacific Ocean at 151 sec, under full power. All aspects of the actual flight were achieved in a perfect flight test demonstration of this low-cost IRR propulsion system for application to an STM. The STM vehicle and flight trajectory are shown in Figure 15. A comparison between the predicted downstream range vs time and the actual radar flight test data (Figure 15) showed a perfect flight was realized.

CONCLUSIONS

The low-cost combustor for the STM propulsion system has been successfully demonstrated through a series of ground tests and in a totally successful flight test. The 5:1 combustor cost reduction for the STM propulsion system compared to the ALVRJ propulsion system was achieved with no performance penalty.

TABLE 1. STM VALIDATION PROGRAM

Item	Test Description	Location/ Agency	Objective	Status
1	Booster test; test plan Vought 2-53390/6R-51359	NWC	Demonstrate adequacy of booster/ablative insulation interface	Completed; successful
2	Ramjet test; test plan Vought 2-53390/6R-51359	NWC	Demonstrate structural/ thermal adequacy of TPS (cruise condition)	Completed; successful
3	Ramjet test; test plan JAT-24-77-B	CSD	Demonstrate structural/ thermal adequacy of TPS for STV-P trajectory (cruise/dive)	Completed; successful
4	Case structural/hydroburst test; test plan DTP-2630-001	CSD	Demonstrate structural adequacy of low-cost combustor case	Completed; successful
5	Booster nozzle retention tests; test plan JAT-19-77-B	CSD	Demonstrate structural adequacy of ring/reliable ejection of booster nozzle	Completed; successful
6	Booster nozzle retention tests	NWC	Demonstrate structural adequacy of snapring/ reliable ejection of booster nozzle	Completed; successful
7	Port cover tests	VSD	Demonstrate structural adequacy of port covers	Completed; successful
8	Booster test (two tests planned)	NWC	Demonstrate structural adequacy of low-cost combuster case/booster nozzle ejection	Completed; successful
9	Ramjet durability test (two tests planned)	NWC	Demonstrate ramjet TPS adequacy	Completed; successful
10	Booster/ramjet transition test; test plan DTP-2630-004	CSD	Demonstrate structural adequacy of low-cost combustor case/booster (ramjet transition/ ramjet durability/FMS test)	Completed; successful
11	STV-P flight test	CSD/NWC/ VSD	Demonstrate STM flight test	Completed; successful

7-6

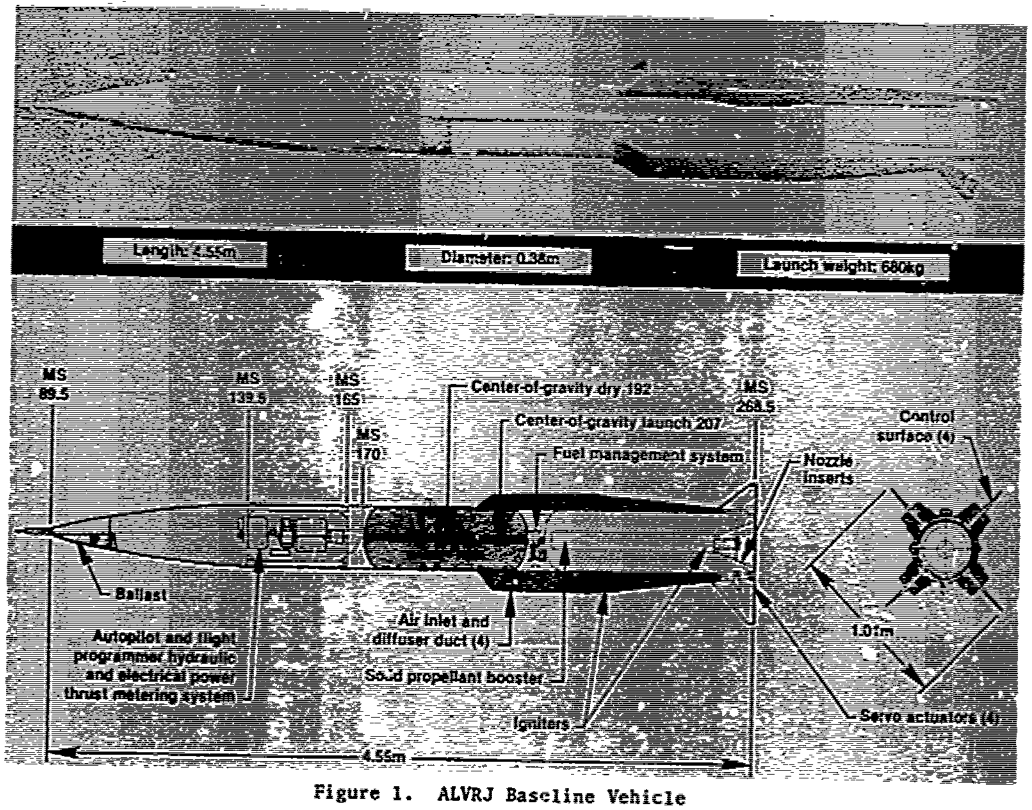
Length: 4.55m
Diameter: 0.38m
Launch weight: 680kg
MS 89.5
MS 139.5
MS 165
MS 170
Center-of-gravity dry 192
Center-of-gravity launch 207
Fuel management system
MS 268.5
Nozzle inserts
Control surface (4)
Ballast
Autopilot and flight programmer hydraulic and electrical power thrust metering system
Air inlet and diffuser duct (4)
Solid propellant booster
Igniters
1.01m
Servo actuators (4)
4.55m

Figure 1. ALVRJ Baseline Vehicle

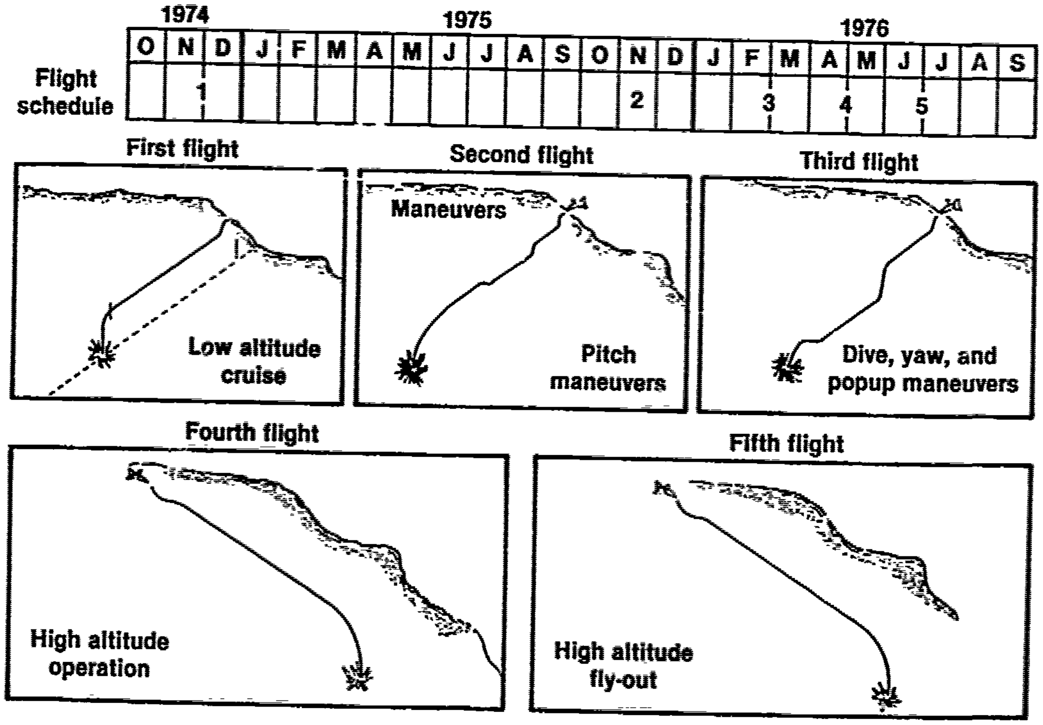
1974
1975
1976
O N D J F M A M J J A S O N D J F M A M J J A S
Flight schedule
1
2
3
4
5
First flight
Low altitude cruise
Second flight
Maneuvers
Pitch maneuvers
Third flight
Dive, yaw, and popup maneuvers
Fourth flight
High altitude operation
Fifth flight
High altitude fly-out

Figure 2. ALVRJ Test Flight Results

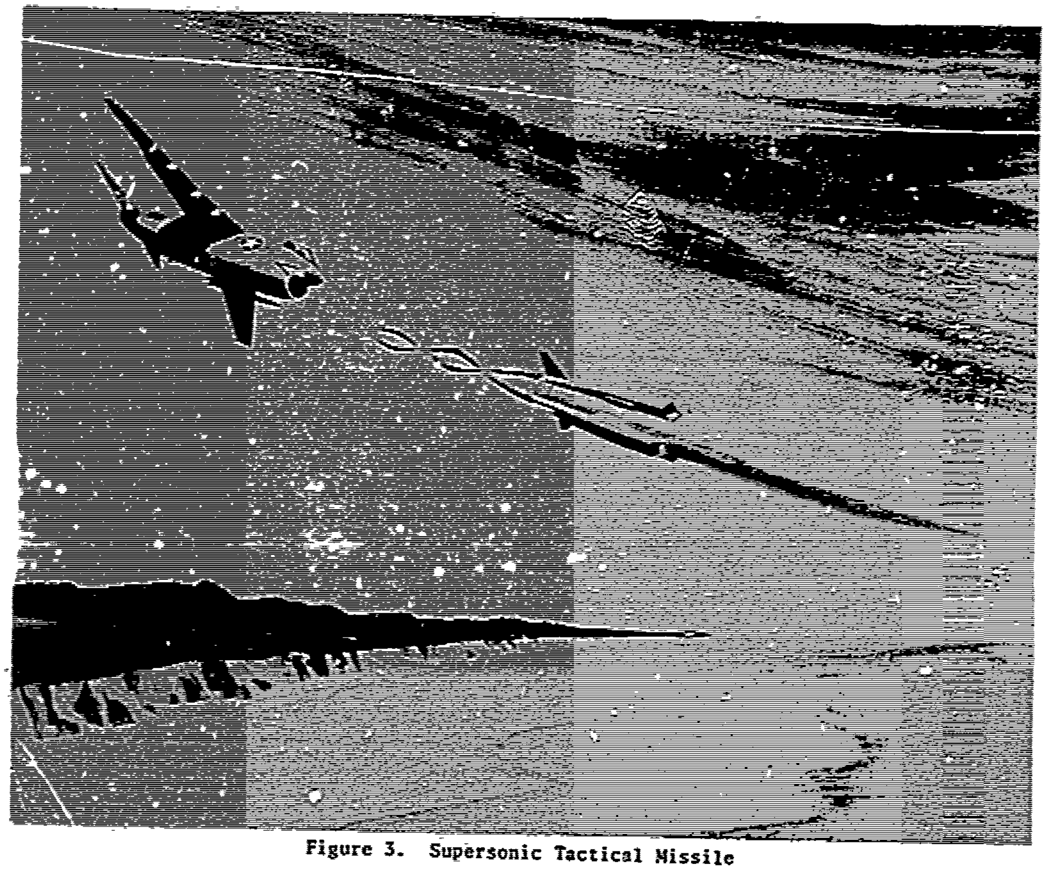

Figure 3. Supersonic Tactical Missile

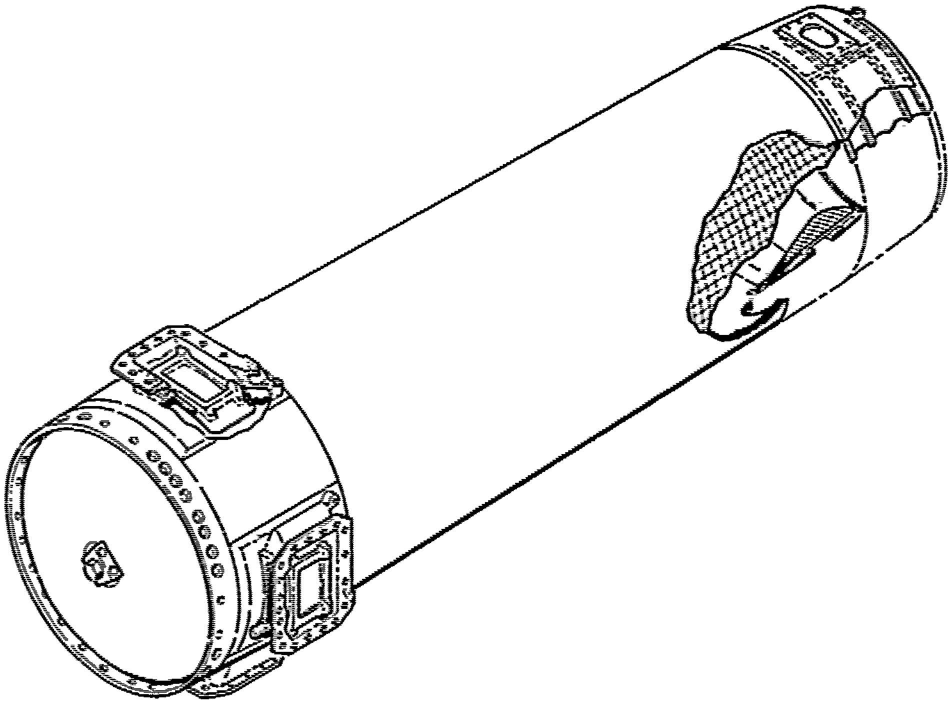

Figure 4. Low-Cost Combustor

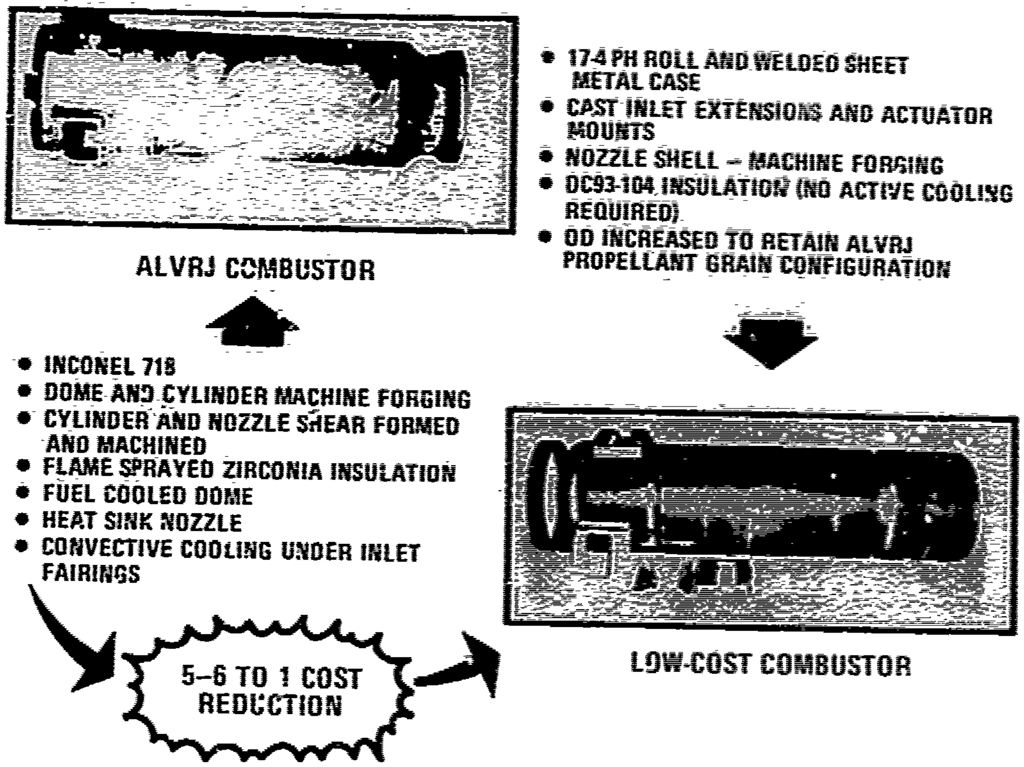
ALVRJ COMBUSTOR
• 17-4 PH ROLL AND WELDED SHEET METAL CASE
• CAST INLET EXTENSIONS AND ACTUATOR MOUNTS
• NOZZLE SHELL – MACHINE FORGING
• DC93-104 INSULATION (NO ACTIVE COOLING REQUIRED)
• OD INCREASED TO RETAIN ALVRJ PROPELLANT GRAIN CONFIGURATION
• INCONEL 718
• DOME AND CYLINDER MACHINE FORGING
• CYLINDER AND NOZZLE SHEAR FORMED AND MACHINED
• FLAME SPRAYED ZIRCONIA INSULATION
• FUEL COOLED DOME
• HEAT SINK NOZZLE
• CONVECTIVE COOLING UNDER INLET FAIRINGS
5–6 TO 1 COST REDUCTION
LOW-COST COMBUSTOR

Figure 5. Comparison of ALVRJ and Low-Cost Combustors

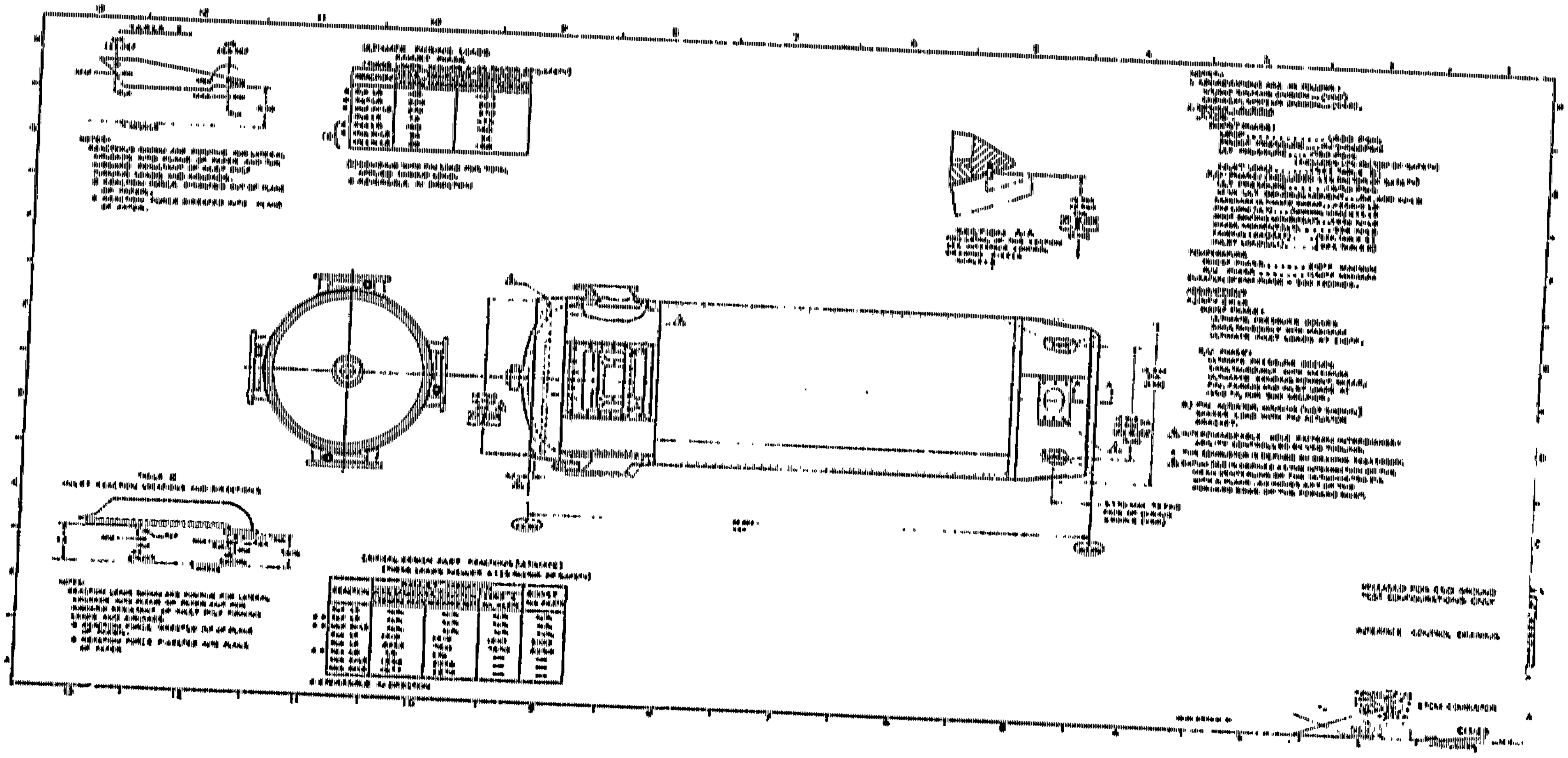

Figure 6. Combustor Assembly

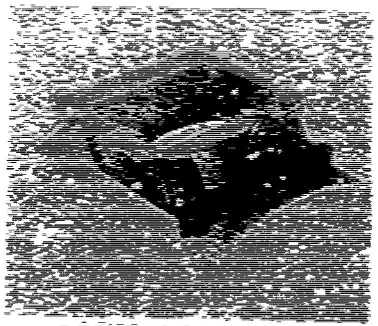

LCCDP air inlet casting

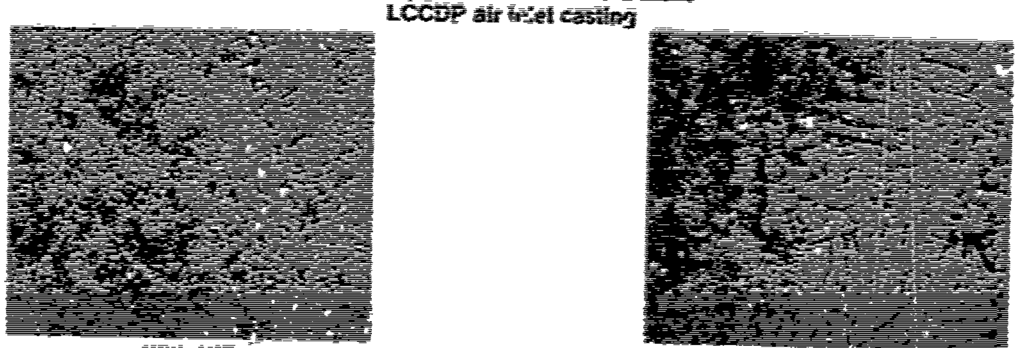

With HIP

Without HIP

Figure 7. LCCDP Air Inlet HIP Casting

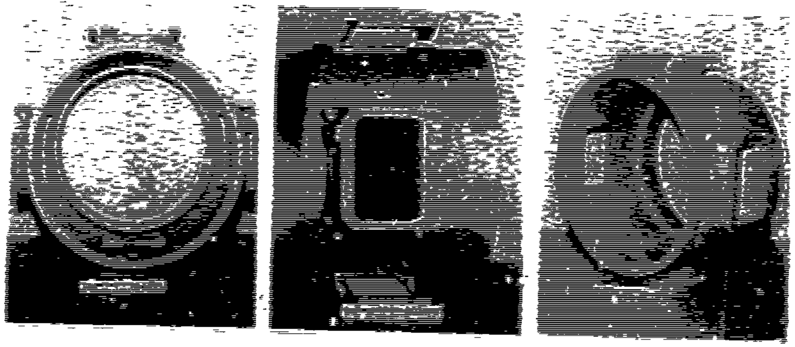

Figure 8. STM Combustor/Inlet Ramp Section Casting

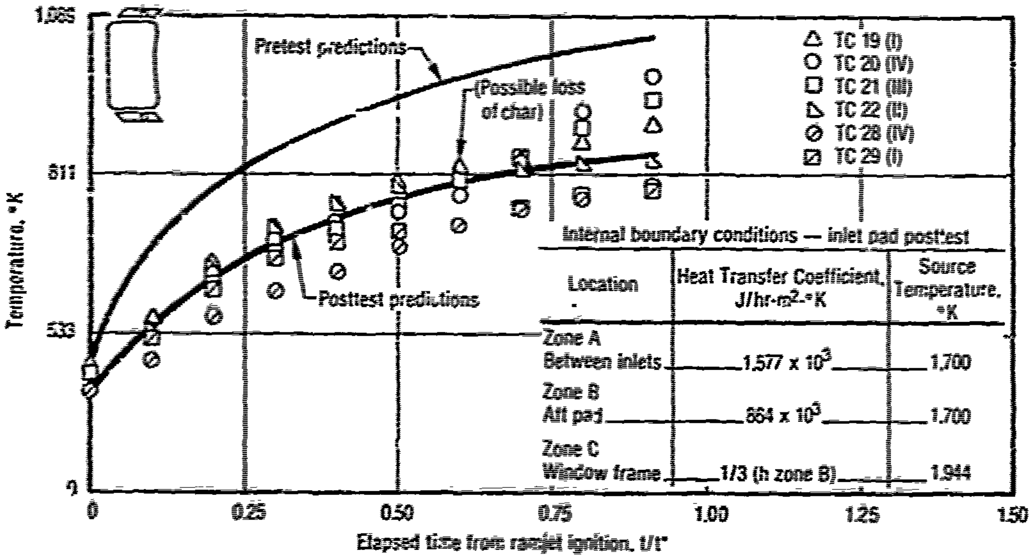

Internal boundary conditions — inlet pad posttest

Location	Heat Transfer Coefficient, J/hr-m²-°K	Source Temperature, °K
Zone A Between inlets	1,577 x 10³	1,700
Zone B Aft pad	864 x 10³	1,700
Zone C Window frame	1/3 (h zone B)	1,944

Figure 9. NWC Connected-Pipe Test - Thermal Endurance

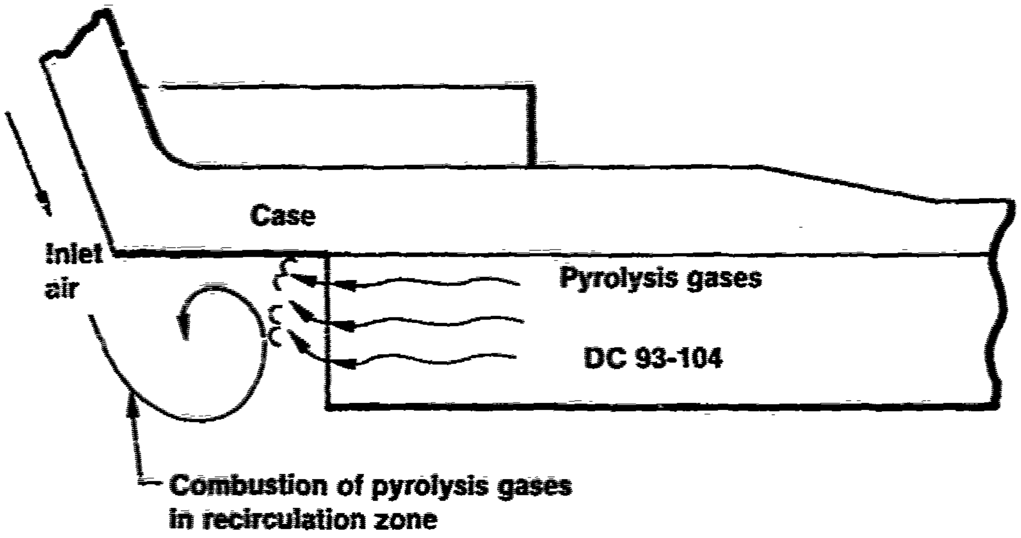
Case
Inlet air
Pyrolysis gases
DC 93-104
Combustion of pyrolysis gases in recirculation zone

Figure 10. Basic Math Model Hypothesis - Edge Burning of DC 93-104 Around the Inlets

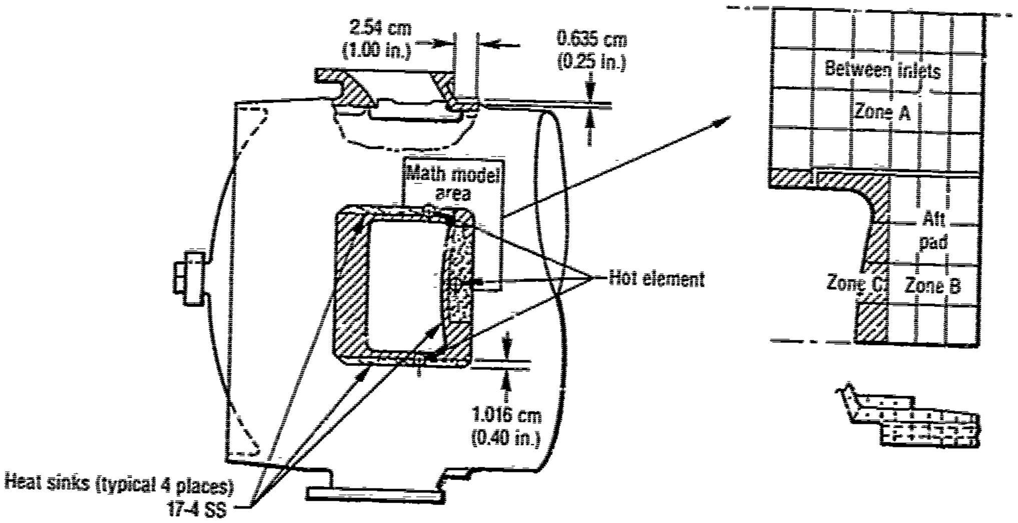
2.54 cm
(1.00 in.)
0.635 cm
(0.25 in.)
Math model
area
Hot element
1.016 cm
(0.40 in.)
Heat sinks (typical 4 places)
17-4 SS
Between inlets
Zone A
Aft
pad
Zone C
Zone B

Figure 11. STM Combustor with Added Heat Sinks

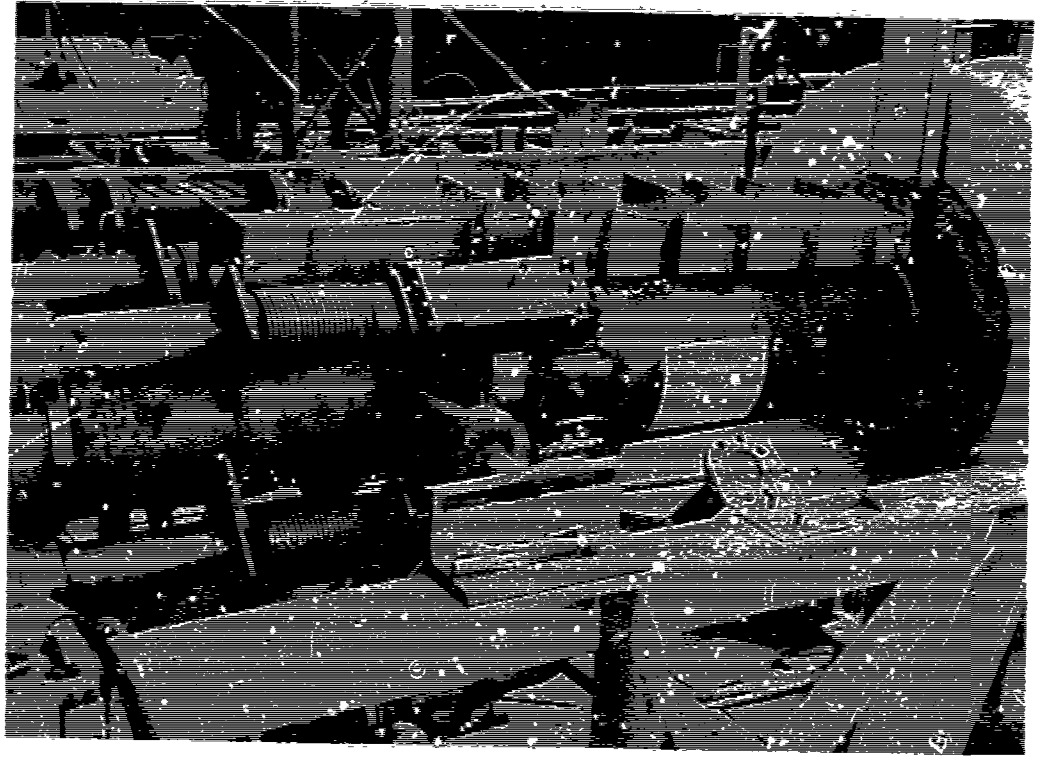

Figure 12. Combustor, Aeroshroud, and Inlet Test Hardware

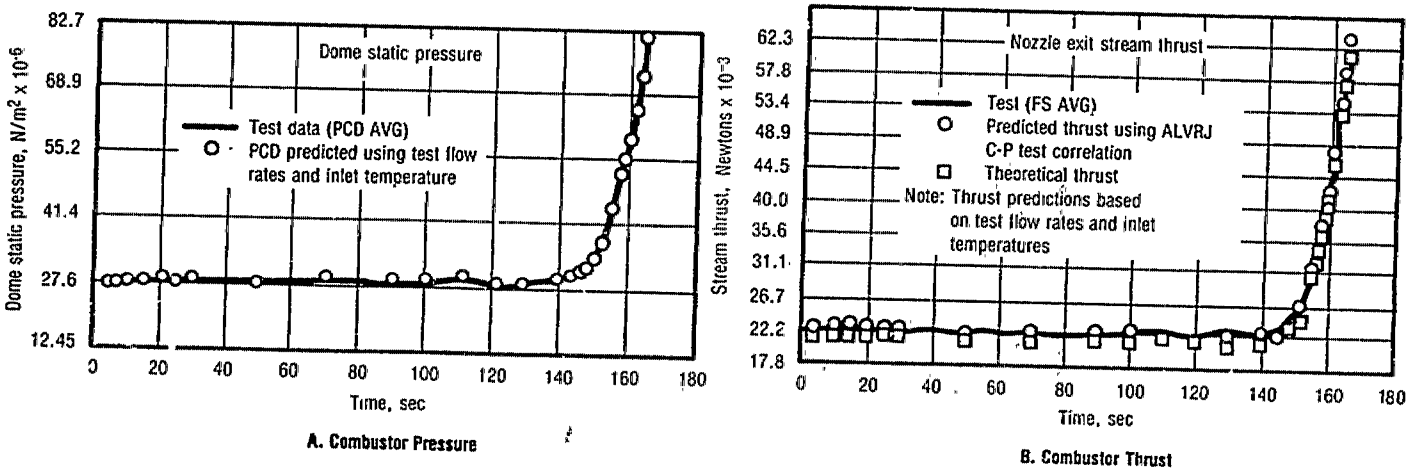

A. Combustor Pressure

B. Combustor Thrust

Figure 13. Ramjet Ground Test Performance

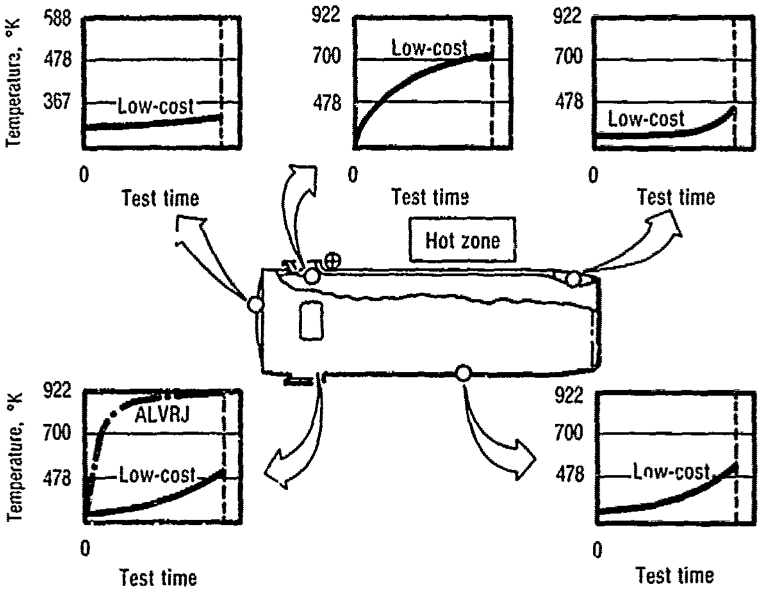

Figure 14. Low-Cost Combustor TPS Performance

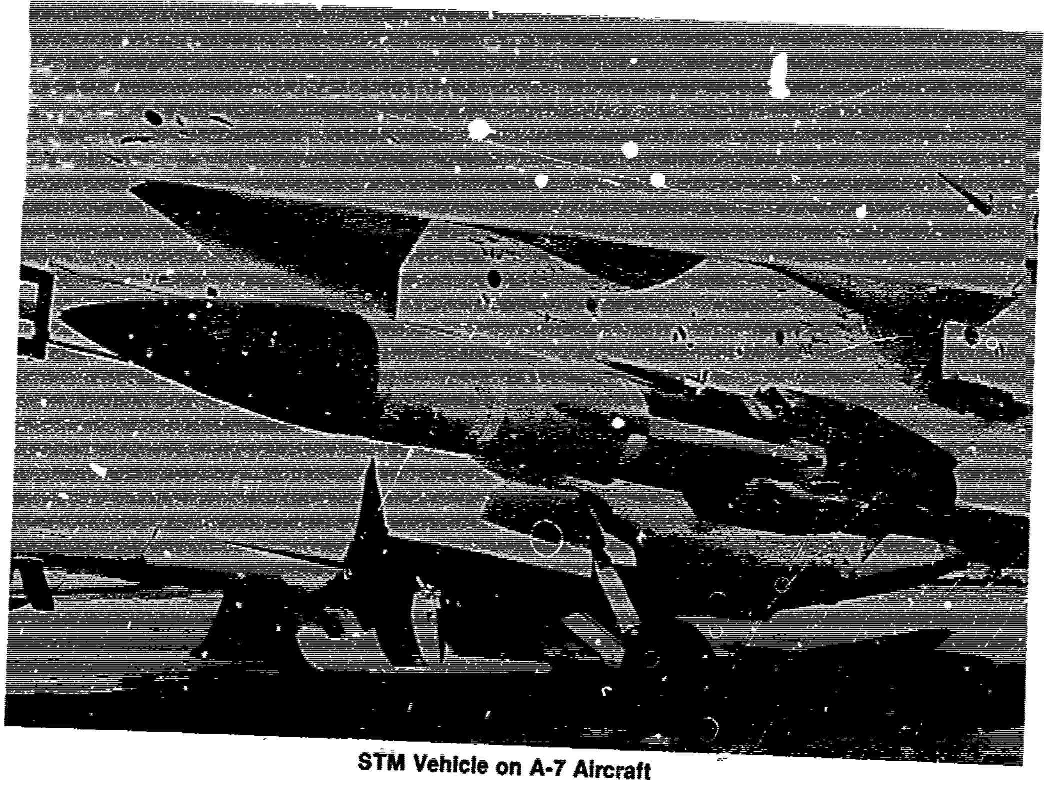

STM Vehicle on A-7 Aircraft

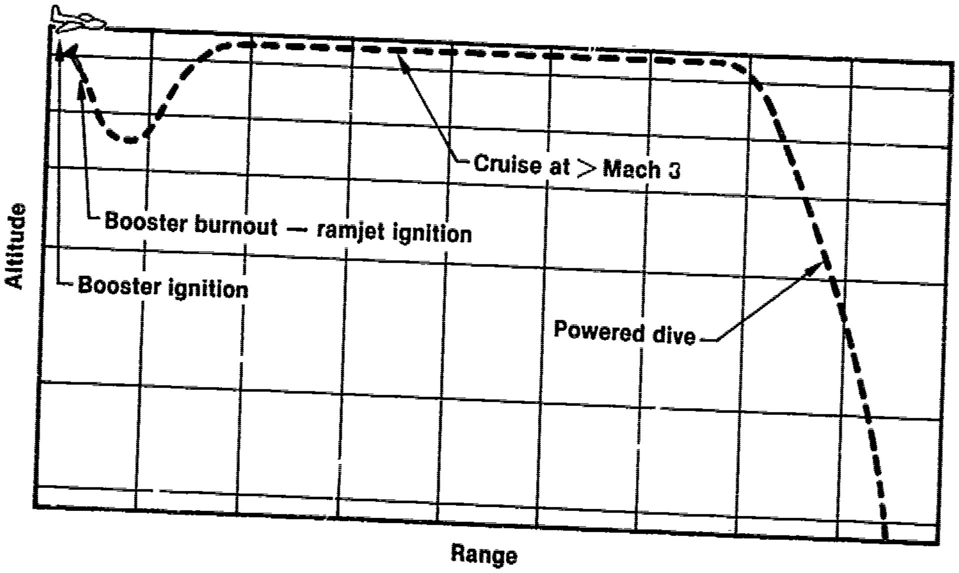

STM Flight Trajectory
21 April 1979, Pt. Mugu Test Range

Figure 15. Supersonic Tactical Missile

ENGINE SIZING AND INTEGRATION REQUIREMENTS FOR HYPERSONIC AIRBREATHING MISSILE APPLICATIONS

by

Paul J. Waltrup, Frederick S. Billig and Richard D. Stockbridge
The Johns Hopkins University
Applied Physics Laboratory
Johns Hopkins Road
Laurel, Maryland 20707
U.S.A.

SUMMARY

A procedure that provides a rational means for selecting an inlet/combustor configuration for a hypersonic airbreathing missile is presented. The particular problem that is addressed is the design of the sustained engine of a two-stage missile that is constrained to be launched from a stowage volume that is either square or circular in cross-section. The sustainer engine accelerates from a low altitude separation at Mach 4 and climbs to high altitude for cruise at Mach 8. The results show that a missile with an axisymmetric nose inlet provides a somewhat higher thrust capability and slightly better fuel efficiency than a chin type inlet. Aft entry inlets are shown to have a substantially lower thrust potential and lower engine efficiency. A criterion for determining the maximum contraction ratio of a fixed geometry inlet is established and applied to the exemplary missile designs. Combustor area ratio is examined and found to have a relatively small effect on engine performance for area ratios equal to or larger than that required to obtain maximum thrust at the take-over Mach number.

NOMENCLATURE

A = area
C_D = total vehicle drag coefficient
$C_{D_{n,le,cw,add,f,tw,tf}}$ = nose, leading edge, cowl wave additive, body friction, and tail drag coefficients
C_N = normal force coefficient
C_{T_g} = gross engine thrust coefficient [Eq. (A-1)]
C_{T_N} = net vehicle thrust coefficient = $C_{T_g} - C_D$
D = diameter
ER = fuel-air equivalence ratio
F = stream thrust
f_s = stoichiometric fuel-air ratio
L = length
M = Mach number
P = pressure
$\dot{Q}$ = heat transfer
q_o = free stream dynamic pressure
r, R = radius
T = thrust, temperature
U = velocity
$\dot{w}_f$ = fuel flow rate
W_B = box width (Fig. 1)
x = distance
Z = altitude
α = angle-of-attack
β = $(\phi-90)/2$
γ = ratio of specific heats
ϕ = inlet smile angle
ψ = $90-\phi/2$
$\eta_{KE,n,c}$ = inlet kinetic energy, exit nozzle and combustion efficiency

subscripts

0 - 5 = station numbers (Fig. A-1)
a = body
c = cruise
∞ = maximum circle in box
i, s = inlet cowl
max = maximum
n = nose
ref = reference
t = total
w = wall

Approved for presentation and publication at the NATO/AGARD/PEP 58th Symposium. Additional distribution limited to U. S. Government agencies only. Other requests for this document must be referred to the Johns Hopkins University/Applied Physics Lab, Johns Hopkins Road, Laurel, Md. 20707.

INTRODUCTION

8-2

The design of a missile involves the consideration of numerous factors that include both the mission requirements and the constraints that are imposed due to weight and volume limitations. It is the purpose of this paper to present a rational procedure for guiding the design of a supersonic combustion ramjet (scramjet)-powered missile constrained to a particular cross-sectional area. The scramjet has been chosen because it is the most efficient propulsion cycle for hypersonic flight within the atmosphere (Ref. 1). To explain the technique it is necessary to select a particular mission requirement, but the approach is not dependent on this selection.

The problem is posed as follows:

1) The missile is to be designed into a launcher that has a fixed cross-sectional area, either square or round, but, as will be explained below, the detailed analysis will be directed to the square cross-section;

2) The missile is a rocket-boosted fixed geometry scramjet that has an end-of-boost Mach number of 4 and a cruise Mach number of 8.

3) The scramjet is of the dual mode type, i.e., at high flight Mach numbers and low fuel/air equivalence ratios, the flow in the combustor is supersonic, whereas at low Mach number and high equivalence ratio, a normal shock precedes the combustion (see Ref. 2 for a detailed discussion); and

4) The inlet capture area is either circular or a sector of a circle which is commonly referred to as a "chin" inlet and, by permitting the inlet cowl lip to be located downstream of a forebody, an aft entry inlet is also represented.

The objective is to develop a rational procedure for selecting the geometry of the inlet capture area, the design Mach number, M_{DES}, the inlet contraction ratio, the combustor area ratio and the nozzle-to-inlet area ratio.

INLET CONSTRAINTS

The problem begins as an exercise in geometry to determine the range of "smile" angle, ϕ, of chin and aft entry type inlets that can be considered. Initially the criteria for selection will be based on the maximum projected frontal area of the inlet, later the effects of reduced inlet area will be discussed. Figure 1 depicts the packaging of a chin type inlet constrained to fit within either a square or circular cross-section. In each sketch the axis of the inlet is located to give the maximum inlet area for a given ϕ. For the square, or box, constraint (Ref.3) the axis is concentric with the box axis for $360° \geq \phi \geq 270°$. For $270° > \phi \geq 90°$ the axis moves along the diagonal and reaches the corner at $\phi = 90°$. For $\phi \leq 90°$ the axis is in the corner. Each sketch also shows the outline of the circular body, concentric with the inlet axis having the maximum radius, $r_{a_{MAX}}$. For $360° \geq \phi \geq 270°$, $r_{a_{MAX}}/W_B = 2$, where W_B is the length of the box side. For $\phi \leq 270°$, $r_{a_{MAX}}/W_B$ decreases monotonically to 0 at $\phi = 90°$. It would be permissible to have a radius $r_a < r_{a_{MAX}}$ and still have the maximum inlet area. Moreover, r_a can be greater than $r_{a_{MAX}}$ but only by decreasing the inlet area.

For a circular constraint and $360° \geq \phi \geq 180°$, maximum inlet area is obtained with the chin inlet axis concentric with the axis of the circular "container." For $\phi < 180°$ the inlet axis moves progressively outward, reaching the periphery at $\phi = 90°$. For $\phi < 90°$ the axis is on the periphery.

The ratio of the inlet area A_i to the area of the circumscribed circle A_e, i.e., $\pi W_B^2/4$ or πr_B^2 for $r_a = r_{a_{MAX}}$ is:

BOX

$360° \geq \phi \geq 270°$

$$\frac{A_i}{A_e} = \frac{\phi}{360} \qquad (1)$$

$270° > \phi > 90°$

$$\frac{A_i}{A_e} = \frac{\phi}{90\,(1+\sin\beta)^2} \qquad (2)$$

where $\beta = \frac{\phi-90}{2}$

$90 \geq \phi \geq 0$

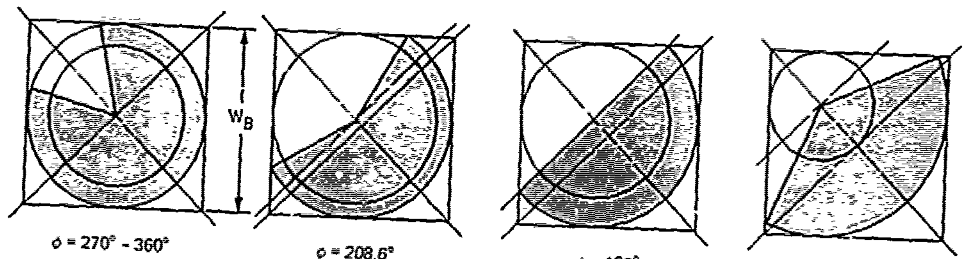

$\phi = 270° - 360°$ $\phi = 208.6°$ $\phi = 180°$ $\phi = 135°$

(a) Box launcher

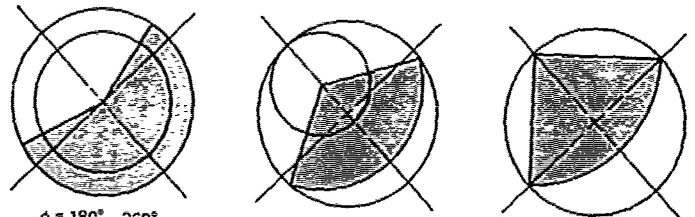

$\phi = 180° - 360°$ $\phi = 133.6°$ $\phi = 90°$

(b) Circular launcher

Fig. 1 Schematic of inlet area as a function of launcher constraints and inlet smile angle.

$$\frac{A_i}{A_e} = \frac{\phi}{90 \cos^2\beta} \tag{3}$$

CIRCLE

$360° \geq \phi \geq 180°$

$$\frac{A_i}{A_e} = \frac{\phi}{360} \tag{4}$$

$180° > \phi \geq 90°$

$$\frac{A_i}{A_e} = \frac{\phi}{360 \cos^2\psi} \tag{5}$$

where $\psi = 90° - \frac{\phi}{2}$ (6)

$90° \geq \phi \geq 0$

$$\frac{A_i}{A_e} = \frac{\phi}{90 \cos^2\left(\frac{90-\phi}{2}\right)} \tag{7}$$

Figure 2 is a plot of the A_i/A_e versus ϕ for the circle and box. Note that there is a minimum in the mid portion of each curve. For the box the minimum occurs at

$$\phi_{MB} = \frac{180}{\pi}\left(\frac{1 + \sin\beta_M}{\cos\beta_M}\right) \tag{8}$$

or at $\phi = 208.56°$ and $A_i/A_e = 0.670$. For the circle

$$\phi_{MC} = \frac{180}{\pi} \tan\left(\frac{\phi_{MC}}{2}\right) \tag{9}$$

or at $\phi = 133.56°$ and $\frac{A_i}{A_e} = 0.4393$.

Even though A_1/A_e values are shown for the entire range of ϕ, some designs would not be reasonable in that it would be impractical to fair the asymmetric inlet into a circular or near circular cross-section that would be typical of a missile. A reasonable limit would be $r_a/W_B \simeq 0.3$, which corresponds to $\phi = 140°$ for the box constraint. Thus, for $\phi < 140°$, smaller values of A_1/A_e would result. In this study this limit was not enforced but as it turns out, it is a moot point because for other reasons the chin inlets of interest have $\phi > 140°$. Moreover, to limit the scope of the analysis only the box constraint was studied in depth, which, as shown in Fig. 2, gives the chin (or aft entry) inlet a more favorable inlet capture area relative to a circular inlet for $\phi < 270°$ than would result with the circular constraint.

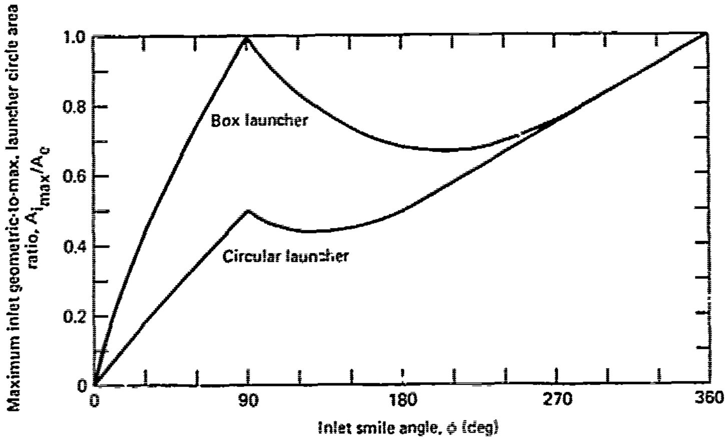

Fig. 2 Maximum inlet air capture area as a function of inlet smile angle and launcher type.

INLET PERFORMANCE

The next step in the analysis is the determination of the inlet air capture ratio, additive drag and cowl drag as a function of inlet design Mach number M_{DES}, flight Mach number M_0, and angle-of-attack. Here, to limit the study, it is necessary to be somewhat arbitrary in defining the geometry of the compression surface. Previous experience has shown that a surface having an initial compression angle of 12.5° yields a good compromise between length and pressure loss. Consequently, as shown in Figure 3, 12.5° was used throughout. All of the additional compression in the inlet was assumed to take place downstream of the last characteristic passing through the cowl lip in this conical flow, i.e., the compression waves would fall inside the cowl lip regardless of the Mach number and angle-of-attack. For the aft inlet, a 2.6:1, 3/4 power forebody shape was selected and was joined to a circular cylinder. Here again, it was necessary to be somewhat arbitrary in selecting 0.6 as the ratio of the radius of the nose cylinder to the radius of the cowl r_a/r_s. A smaller value would not permit sufficient packaging in the forebody, whereas a larger value would decrease the amount of capture area. Even if the cross-section of the aft inlet is circular, i.e., $\phi = 360°$, the maximum air capture ratio is less than one because the cowl lip lies inside the bow shock generated on the forebody. For example, if the aft inlet was placed in the most forward position, as shown dotted in Fig. 3, the shock generated by the 12.5° surface intersects the bow shock at values of $\frac{r_a}{r_s} = 0.386$; 0.442 and 0.488 for zero angle-of-attack, $\alpha = 0°$, at $M_0 = 6$, 7, and 8, respectively. To a lesser degree the inlet air capture depends on the downstream location of the cowl lip. This was examined parametrically at the most upstream location, at a point $x/r_a = 10$ from the nose, and midway between the two extremes. As it turned out, the results were not strongly dependent on x/r_a so to limit the scope of the study the subsequent performance numbers were generated only for $x/r_a = 10$.

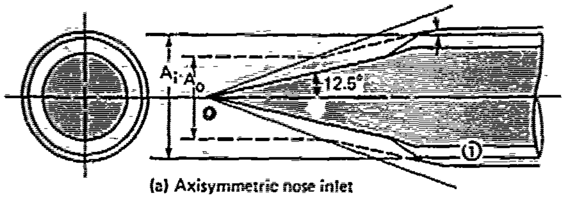

(a) Axisymmetric nose inlet

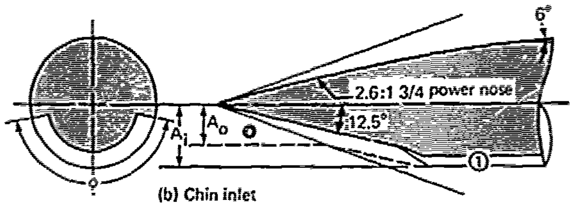

(b) Chin inlet

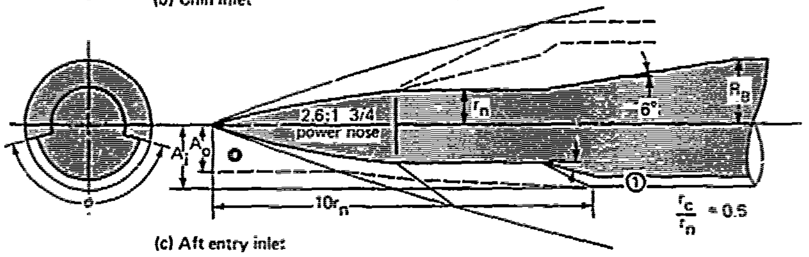

(c) Aft entry inlet

Fig. 3 Schematic illustrations of inlet types considered.

The air capture ratio and additive drag were obtained by means of a finite difference solution of the hyperbolic equations of motion for a steady inviscid flow (Ref. 4). This code utilizes a standard MacCormack predictor-corrector algorithm for the solution of the governing equations in cylindrical coordinates in conservation form. A non-orthogonal shock-layer transformation is used to normalize the mesh between the body and the peripheral bow shock. The bow shock is fitted to the free stream, whereas internal shocks are captured.

After the flowfield solution is obtained, the data are processed to yield the various parameters of interest in inlet design. For example, streamlines are traced from the bow shock to their intersection with the inlet cowl lip. The area of the resulting stream tube at the bow shock is obtained by numerical integration, and the ratio of this area to the inlet cowl area gives the air capture ratio, A_o/A_i. Similarly, integration of the pressure along this stream tube gives the additive drag.

The air capture and additive drag data so obtained have been compared to the analytical results available for a cone at zero angle-of-attack. Excellent agreement has been found, with errors on the order of 1% or less. Verification of the angle-of-attack behavior has not been established due to the paucity of suitable experimental results or analyses with which to compare. Side plates were not considered in the computation of A_o/A_i and $C_{D_{add}}$ for the chin and aft entry inlet designs, nor were inlets with noncircular cross-section.

Figures 4 and 5 typify the results of these calculations summarized in the appendix. Hereinafter the $\phi = 360°$ inlet will be referred to as the "nose" inlet. Figure 4 shows the air capture ratio for $M_{DES} = 6$ nose/chin inlets operated at $M_0 = 4$ and 6. Curves are shown for $\alpha = -10°$, $-5°$, $0°$, $5°$ and $10°$ for $0° \leq \phi \leq 360°$. For $\alpha = 0°$ the air captured is independent of ϕ; for α negative, air capture decreases with decreasing ϕ, but for positive α there is an optimum $\phi < 360°$ for each α and M_0. This favorable air capture characteristic of chin inlets at positive α is the principal reason for considering their use in missile applications, especially when bank-to-turn steering can be used and thus eliminate the need to operate at α negative. Figure 5 compares the nose/chin inlet with the aft entry inlet for inlets with $M_{DES} = 6$ and 8 operating at $M_0 = 4$ and 6, all for $\alpha = +5°$. This figure rather dramatically shows the adverse effect on air capture that results when the inlet is positioned downstream of the forebody.

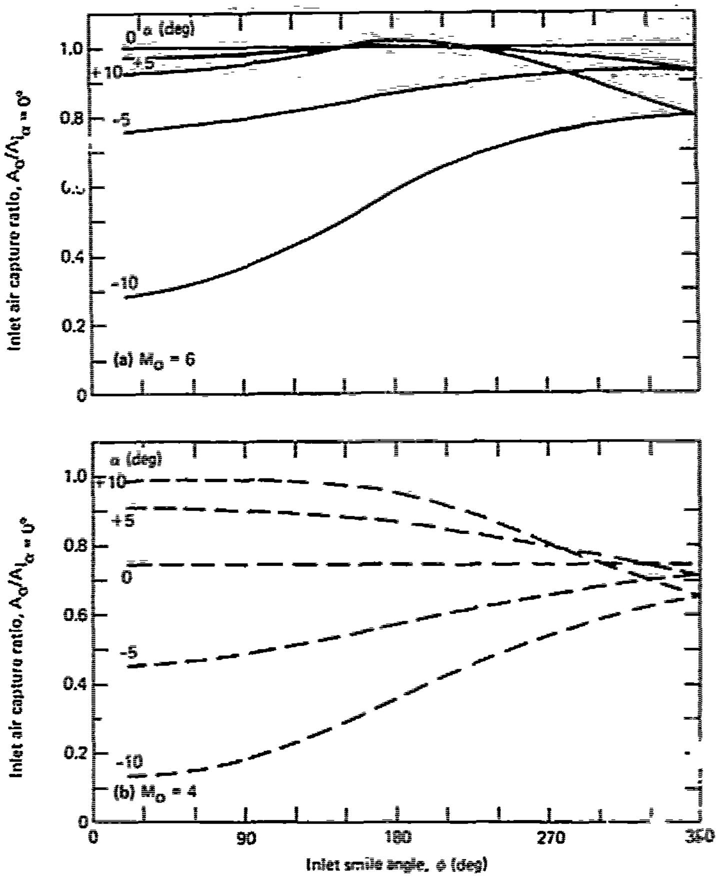

Fig. 4 Air capture characteristics of M_{DES} = 6, nose/chin inlets at M_0 = 6 and 4.

With air capture so defined, it is necessary to determine inlet efficiency in order to develop a rationale for selecting inlet contraction ratio and overall engine performance. In Ref. 5, an argument with considerable merit, viz. that inlet efficiency should decrease monotonically with inlet contraction ratio was given. Results of calculations for inviscid flow for a series of optimized oblique compressions were presented and simple expressions were developed for η_{KE}, the inlet kinetic energy efficiency in terms of M_0 and the Mach number at the end of compression, M_1. (For inlets compressing to subsonic flow, M_1 would be the Mach number ahead of the normal shock.) This relationship is shown as the dashed line in Fig. 6. Also shown in Fig. 6 are available data from tests of high-speed inlets (Refs. 1 and 6-8) which, of course, have losses due to both shocks and viscous effects. Following the argument of Ref. 5 the relationship

$$\eta_{KE} = 1 - 0.4(1 - M_1/M_0)^4 \qquad (10)$$

has been taken to represent the data and is used herein to generate inlet performance. The data are not sufficiently extensive to deduce an angle-of-attack dependency, therefore it was tacitly assumed that $\eta_{KE} \neq f(\alpha)$.

8-7

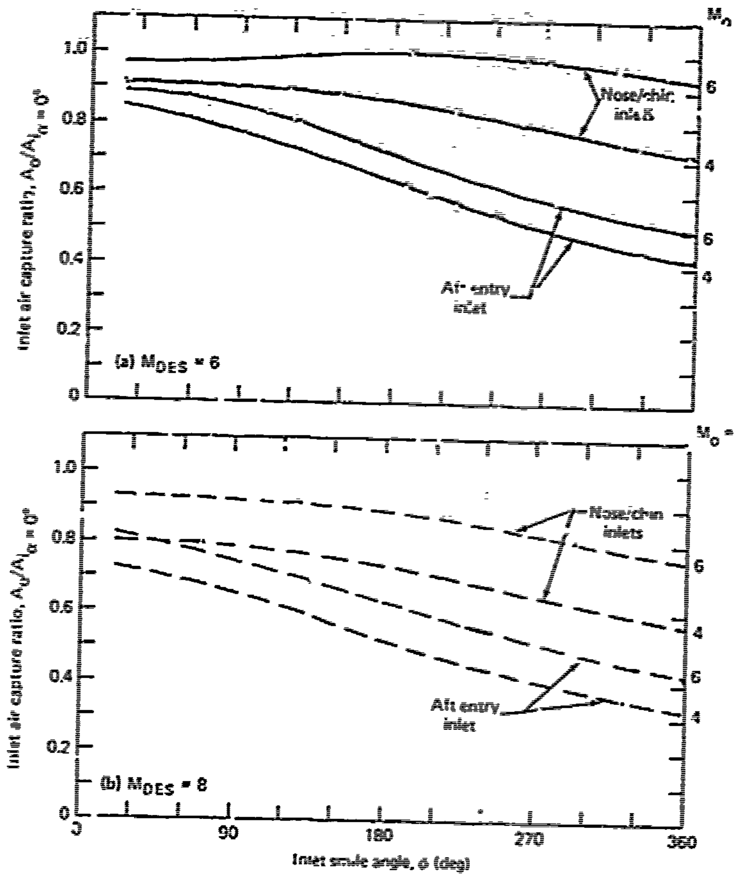

Fig. 5 Comparison of inlet air capture at α = +5° of nose/chin and aft entry inlet designs.

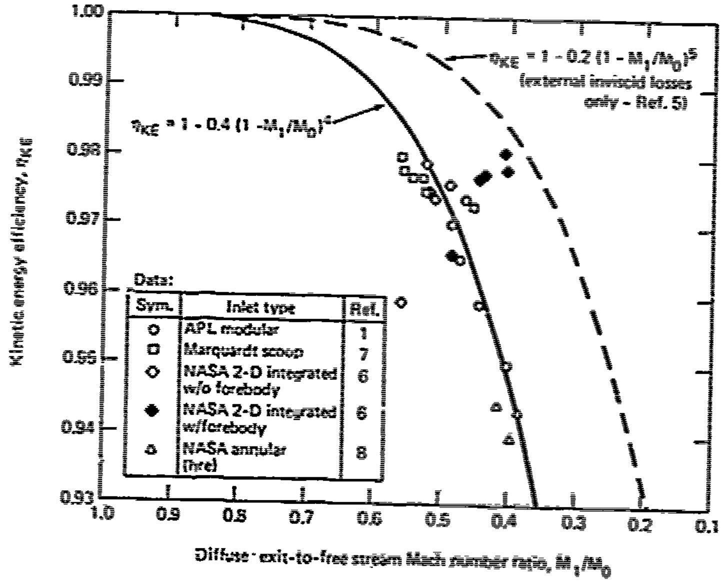

Fig. 6 Kinetic energy efficiency as a function of diffuser exit-to-free stream Mach number ratio.

8-9

With η_{KE} so defined, the inlet total pressure recovery can be found as a function of the inlet contraction ratio A_0/A_1, where A_1 is the area following compression. For approximations, the relationship

$$\text{TOTAL PRESSURE RECOVERY} = \frac{P_{t_1}}{P_{t_0}} = \left[\frac{(1-\eta_{KE})(\gamma-1)M_0^2+1}{2}\right]^{\frac{\gamma}{\gamma-1}} \qquad (11)$$

can be used; for this study real gas calculations for flight within the tropopause, i.e., Z = 15.24 km (50K ft), T_0 = 217°K (390°R), P_0 = 11.7 kPa (1.69 psia) were made. The results of these calculations are shown in Fig. 7. For each M_0, P_{t_1}/P_{t_0} decreases with increasing A_0/A_1 until a maximum value of A_0/A_1 is reached; further increases in A_0/A_1 are not possible. Moreover, there exists an overall maximum value of A_0/A_1 = 8.5 at M_0 = 7. This is an extremely important point, which in many parametric studies has been overlooked and should be given considerable attention when designing an inlet for a particular application.

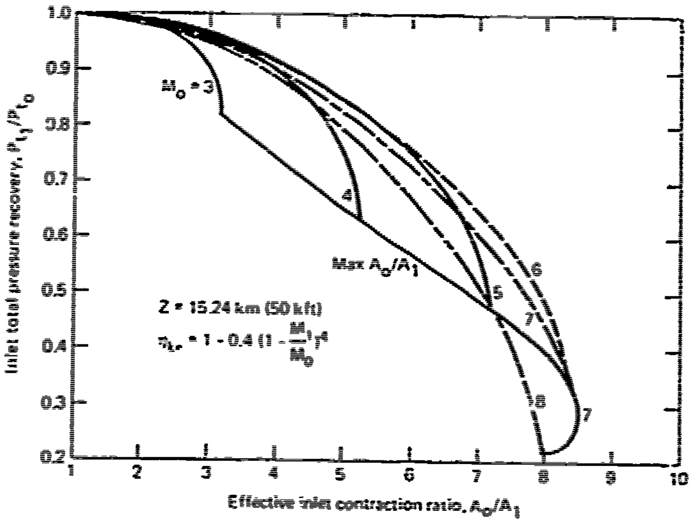

Fig. 7 Inlet total pressure recovery as a function of effective contraction ratio.

Up to this point in the discussion no consideration needed to be given to whether the compression was occurring externally or internally. Later, it will be assumed that the maximum internal contraction is 20%, which implies for cases with large A_0/A_1 that the external compression surface will require more than 12.5° of turning as shown schematically in Fig. 3. Additionally, since the maximum contraction ratio is based on the captured streamtube, not the inlet area which is less than or equal to the cowl area, it is necessary to combine the effects shown in Figs. 4 and 5 with those shown in Fig. 7 to determine the inlet size that does not exceed the maximum contraction ratio. This is depicted in Fig. 8 where the limit curve from Fig. 7 is redrawn. For an inlet operating below its design Mach number, air is spilled, therefore it is not known apriori which flight condition will determine the maximum contraction. For example, for a nose inlet (Fig. 8a) with M_{DES} = 8 that was to be operated over $4 \le M_0 \le 8$ and $0° \le \alpha \le 5°$ the maximum contraction ratio is set by the M_0 = 8, α = 0 condition, i.e., $(A_i/A_1)_{MAX}$ = 7.9. However, for $M_{DES} \le 7$, it is the M_0 = 4, α = 0 condition that sets $(A_i/A_1)_{MAX}$. If the range of operating M_0 is changed, then another minimum on the respective M_{DES} curves would define $(A_i/A_1)_{MAX}$. For chin and aft entries the air capture at $\alpha \neq 0$ is a function of ϕ, so for each ϕ and M_{DES} the $(A_i/A_1)_{MAX}$ is found for the desired M_0, a range of interest. Figure 8b shows curves for ϕ = 160° and M_{DES} = 6. For this case the conditions corresponding to M_0 = 4 are always limiting. More contraction is permitted with an aft entry than with a chin inlet because the capture is lower. For the aft entry α = 5° determines the limit, whereas for the chin, α = 10° is limiting. The limits so established define the effective inlet contraction ratio that are used to compute engine performance. It can be shown that the use of a lower contraction ratio will degrade performance.

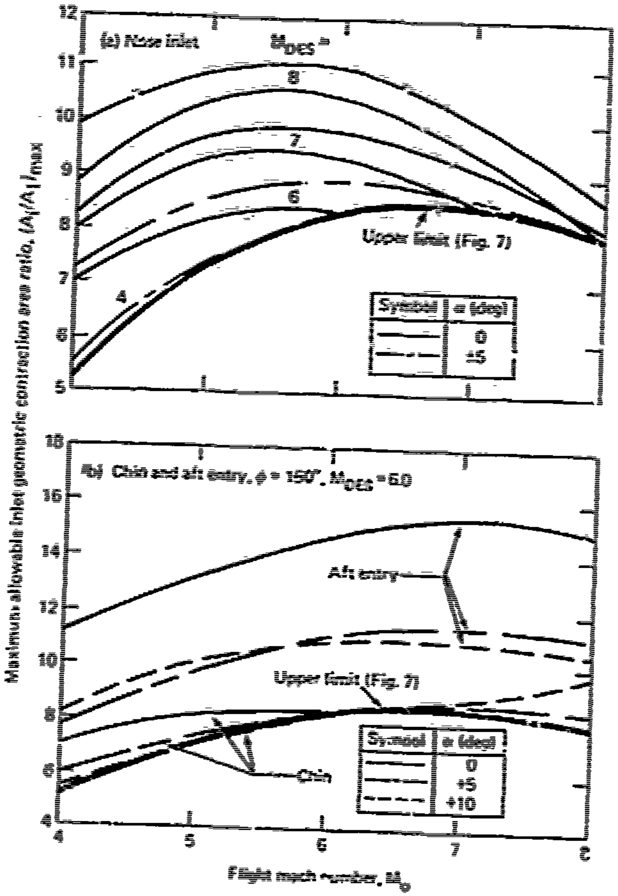

Fig. 8 Maximum inlet geometric contraction area ratio as a function of M_0, M_{DES} and α.

COMBUSTOR PERFORMANCE

Before imposing the $(A_1/A_1)_{MAX}$ constraint, more general arguments can be developed regarding the range of interest of the ratio of areas of the combustor exit to combustor inlet A_4/A_2 (= A_4/A_1 in this study). This can be done by examining gross engine thrust coefficients C_{T_G} based on capture area at a single value of $A_5/A_0 = 1$, where A_5 is the area of the engine exhaust nozzle exit. Generally, $A_5/A_0 > 1$ which increases C_{T_G} but does not alter the arguments.

Figure 9 shows C_{T_G} as a function of ER, the fuel/air equivalence ratio. For these and all other thrust calculations, RJ-5 fuel is assumed. The definition of C_{T_F}, the assumptions made regarding deviations from equilibrium flow and the properties of RJ-5 are given in the appendix. For this figure the inlet contraction ratio is the so-called "upper limit" from Fig. 7. Two important effects are shown. At high M_0, the thrust is nearly independent of A_4/A_2. At low M_0, increasing combustor area ratio decreases engine efficiency; that is, to produce a given C_{T_G} ER, hence fuel flow must increase. However, the far more important effect is that the maximum C_{T_G} increases markedly with increasing A_4/A_2 as shown by the boundary curves for A_4/A_2 values of 2, 3 and 4. As the problem was originally posed, high acceleration at $M_0 = 4$ was required; from the figure at $M_0 = 3$ $C_{T_{GMAX}} = 0.700$ for $A_4/A_2 = 2$, 1.18 at $A_4/A_2 = 3$, and about the same at $A_4/A_2 = 4$. Thus, $A_4/A_2 = 2$ was not considered further and the selection between 3 and 4 was left to a more complete examination which entailed addressing the effects of air capture ratio.

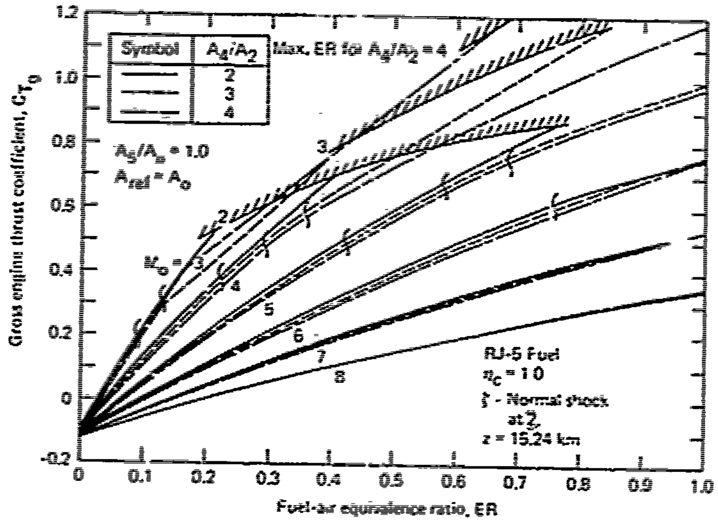

Fig. 9 Engine gross internal thrust coefficient as a function of fuel-air equivalence ratio for maximum inlet geometric contraction ratio. (Fig. 7)

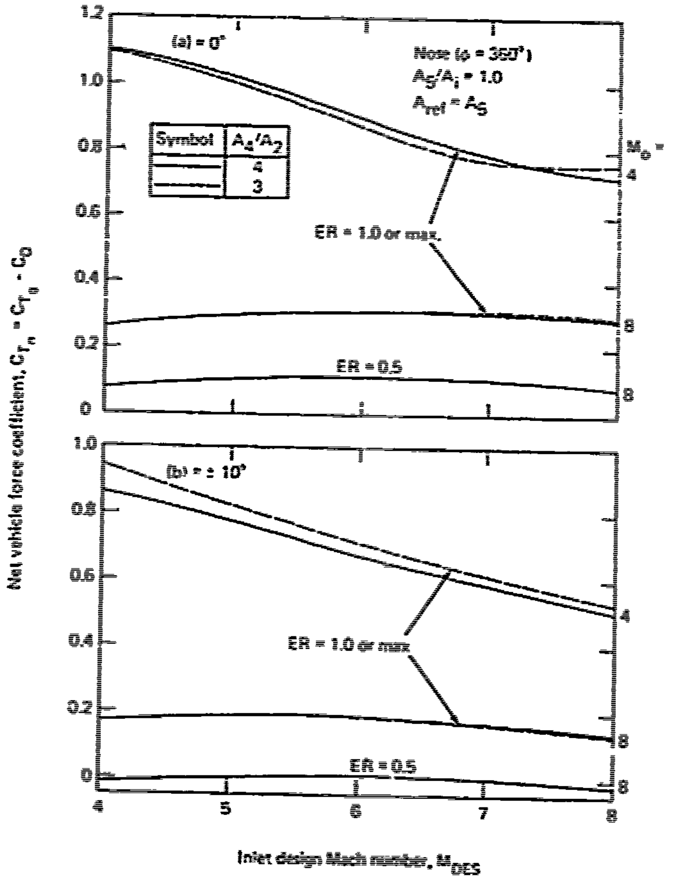

Fig. 10 Net vehicle thrust coefficient for nose inlet (φ = 360°) as a function of inlet design Mach number for 0 and ±10° angles of attack.

VEHICLE PERFORMANCE

To make the final judgment on A_4/A_2 and select M_{DES} and the preferred inlet geometry, it is necessary to consider the net force on the engine, since any change in the inlet size relative to the nozzle, the air capture ratio, ϕ and inlet type affects both the internal thrust and the external drag. The procedures for calculating additive, leading edge, cowl wave, control surface friction drag and lift drag are given in the appendix together with typical results. To correctly estimate friction drag introduces a defined vehicle size into what has heretofore been a dimensionless problem. For this study, the vehicle is assumed to have a 50-cm (19.7-in) exit diameter and a length-to-exit diameter ratio of 8. As it turns out, however, the effect of missile size is only second order.

Figures 10 and 11 show net force coefficients, which are based on the net force normalized by the maximum engine area (i.e., the nozzle exit area, $A_5 = A_e$). Thus, engines having different inlet geometries and air capture characteristics can be compared on an absolute basis without ambiguity. Figure 10 is for the nose inlet ($\phi = 360°$) at $\alpha = 0°$ and 10°. Inlet contraction ratios are consistent with those shown in Fig. 7 by the method discussed previously. Curves are shown for ER = 1 at $M_0 = 4$ and 8, which correspond to maximum acceleration that could be representative of climb-out-to-cruise. The ER = 0.5 at $M_0 = 8$ curve is an approximate representation of cruise conditions, where interpolation (or extrapolation) between the two curves shows that constant velocity ($C_{T_N} = 0$) would be near $\alpha = 10°$ for all M_{DES}. For a particular cruise altitude, α and ER for lift equal weight would have to be determined and for a specific missile design one set of conditions would result in maximum cruise range. Nonetheless, these curves can be used to explain the particular selections of $M_{DES} = 6$ and $A_4/A_2 = 4$. The maximum in the C_{T_g} curves occur at $M_{DES} = 6$ for $M_0 = 8$ and at $M_{DES} = 4$ at $M_0 = 4$. If there were no other considerations,

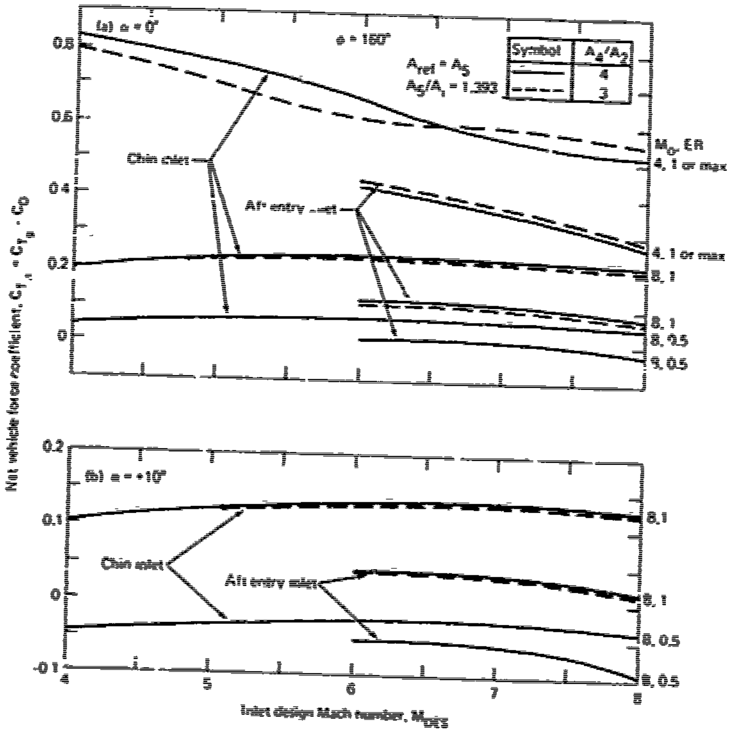

Fig. 11 Net vehicle force coefficient as a function of inlet design Mach no. for chin and aft entry inlets with ϕ = 160°.

perhaps M_{DES} = 5 would be a reasonable choice. However, this would require the inlet to operate significantly above its design Mach number, a factor that was not adequately addressed in the selection of the correlation for η_{KE} (Eq. 10). None of the data covered tests of inlets at M_0 considerably above their respective M_{DES}. Presumably, for the same M_1/M_0, η_{KE} would decrease for $M_{DES} > M_0$. Thus, M_{DES} = 6 was deemed the preferred choice. The choice of the larger A_4/A_2 was based on the slightly better average $C_{T_{N\,MAX}}$ at $\alpha = 0$.

Figure 11 shows corresponding C_{T_N} curves for chin and aft entry inlets all having a not atypical smile angle of 160°. Because of the previous arguments regarding inlet

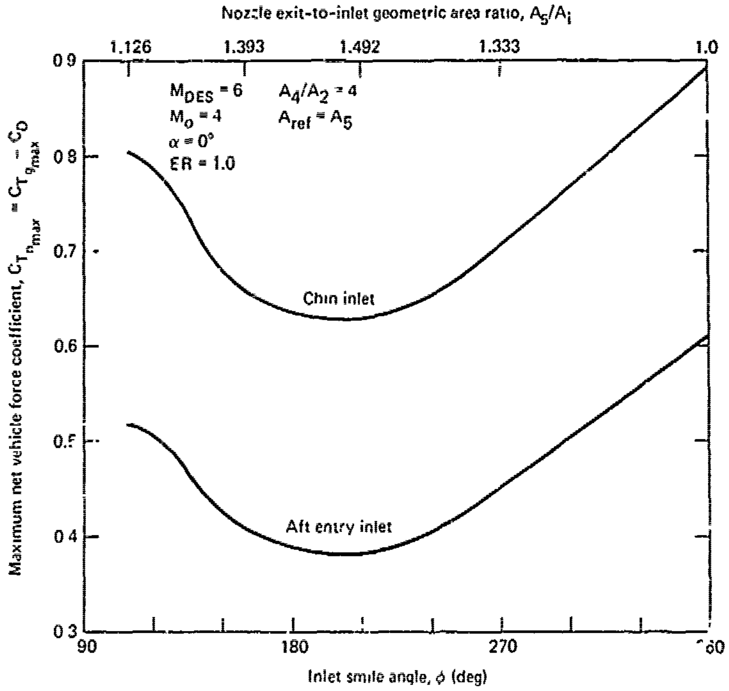

Fig 12 Maximum net force coefficient at $M_0 = 4$, as a function of smile angle for nose, chin and aft entry inlet designs with $M_{DES} = 6$.

operation at $M_0 > M_{DES}$, $M_{DES} < 6$ were not included in the aft entry summary. Results for other values of ϕ exhibit similar trends. The previously stated arguments for the nose entry used to select M_{DES} and A_4/A_2 are valid for the chin and aft inlets, so again M_{DES} = 6 and A_4/A_2 = 4 were chosen.

With M_{DES} and A_4/A_2 specified, it is now possible to compare the efficiency of engines having different types of inlets. To accomplish this, comparisons need to be made for cases where all of the engines produce the same net force. Figure 12 helps to serve in explaining the methodology used to make this comparison. Here, maximum net force coefficients (i.e., $M_0 = 4$, ER = 1, $\alpha = 0°$) are shown as a function of ϕ for engines all having $M_{DES} = 6$, $A_4/A_2 = 4$. The minima in the chin and aft entry curves are a direct consequence of the geometrical constraints on inlet size shown in Fig. 2. To enable comparison of engine efficiency at the same thrust level for all ϕ, C_{T_N} = 0.628 and 0.382 values were chosen. Thus, at the higher level, nose and all chin inlets can be compared and at the lower level, all three types can be compared. To reduce the $C_{T_{N\,MAX}}$ for $\phi \neq 209°$ engine designs, the engine inlet area is reduced holding A_5 constant. For example, for the nose inlet A_5/A_1 is increased from 1.0 to 1.53 to reduce C_{T_N} from 0.895 to 0.628. For $\phi <$ 360°, the reductions in A_1 are smaller since $C_{T_{N\,MAX}}$ are lower and the corresponding A_5/A_1, shown on the top scale in Fig. 12, are larger. An alternative method would be to reduce the engine ER, but this was not examined herein.

Figure 13 summarizes results for the chin and nose inlets at $M_0 = 4$, $\alpha = 0°$, $M_0 = 8$. $\alpha = 0°$ and $+5°$. Fuel flow is used as the index of efficiency. The $M_0 = 4$, $\alpha = 0°$ curve is for ER = 1 and thus is representative of efficiency during acceleration. The $M_0 = 8$, $\alpha = +5°$ curve shown in the middle figure is for $C_{T_N} = 0$ and thus is representative of cruise efficiency. For either case the nose inlet engine is more efficient than an engine with a chin inlet. If efficiency were the sole criteria for selection of ϕ, then a large smile angle would be the choice. However, as suggested by the sketches shown in Fig. 1, engines having ϕ greater than about 210° would not benefit from improved packaging efficiency relative to a nose inlet that has often been ascribed in other studies. In any event, the differences in efficiency between, say a $\phi = 180°$ chin and a nose inlet, are not profound, amounting to about 3% at $M_0 = 4$ and 9% at $M_0 = 8$. Maximum accelerative capability at $M_0 = 8$ is also slightly better for the nose inlet, as shown in the figure at the bottom. Had the basis for selecting the respective engine sizes been equal maximum thrust at $M_0 = 8$, there would be a greater difference in the relative efficiencies between the chin and nose inlets but the chin would have greater thrust potential at lower M_0. The general conclusion, however, is that on the basis of engine performance, the nose inlet would be preferred.

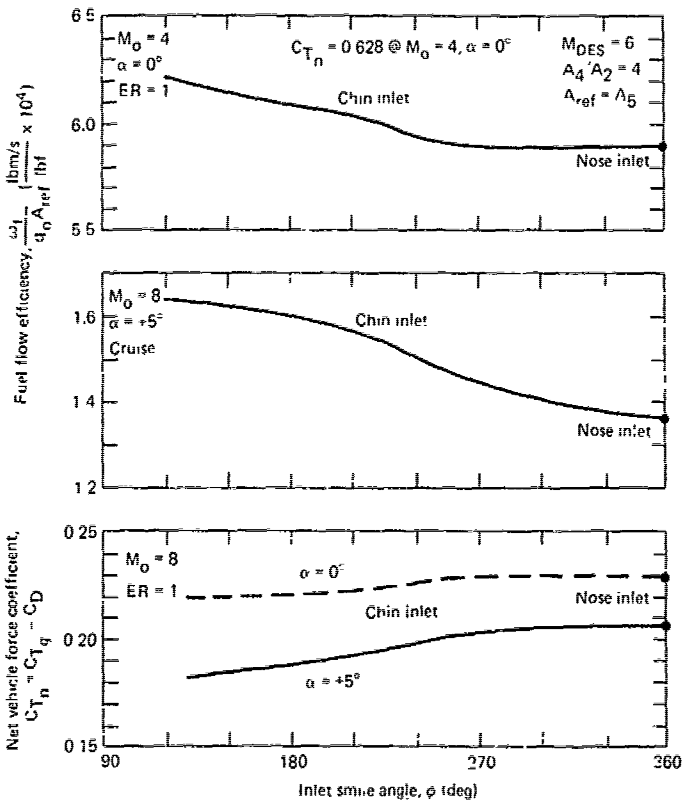

Fig. 13 Performance comparison of nose and chin inlet vehicle designs with $C_{T_{n_{max}}} = 0\ 628$ when $M_o = 4$, $\alpha = 0°$.

When the comparison is based on the lower value of C_{T_N} at $M_0 = 4$, $\alpha = 0°$ so as to include aft entry inlets, the arguments relative to the comparison of the chin and nose configurations are similar. On a fuel efficiency basis, the aft entry is poorer than the chin for the ϕ range of interest, as shown in Fig. 14. The curves relating to accelerative capability at $M_0 = 8$, shown in the bottom figure, exhibit trends for the chin and nose inlet similar to those for the engines designed for higher thrust. For the aft entry at $\alpha = 0°$, thrust levels are 60% to 70% of the corresponding chin inlet having the same ϕ. At first glance the curve for the aft inlet at $\alpha = 5°$ appears to be anomalous. In fact, the very large decreases in $_t$ with increasing ϕ and the significant differences relative to the chin inlet at the same ϕ are directly attributable to the far greater sensitivity in air capture of the aft inlet to change in α. For these conditions with smile angles less than about 220° the relative air capture of the aft inlet increases more rapidly with increasing α. For larger ϕ, the trend is reversed because the "shadowing" effect on the leeward side is more pronounced as the inlet is moved aft. In general, an engine with an aft inlet has less thrust potential and is less efficient than either a chin inlet or nose inlet engine.

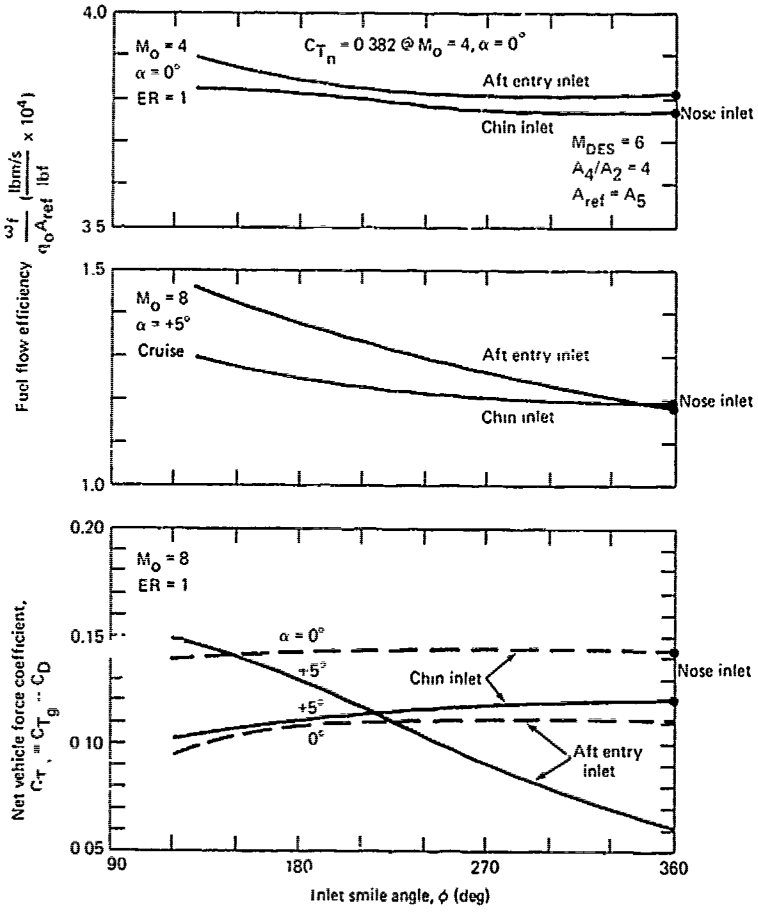

Fig. 14 Performance comparison of nose, chin and aft entry inlet vehicle designs with $C_{T_{n_{max}}} = 0.382$ when $M_0 = 4, \alpha = 0°$.

CONCLUSIONS AND RECOMMENDATIONS

The results of this study lead to the following conclusions and recommendations:

1. The net performance of nose inlet missile designs is somewhat better than comparable chin inlet designs when subjected to the same launcher cross-sectional area constraint. Aft entry inlet designs have substantially less thrust potential and lower efficiency than either the nose or chin designs;

2. A maximum inlet contraction ratio, $(A_0/A_i)_{MAX}$ exists, which is a function of the free stream Mach number. Further increases in A_0/A_i are not possible without causing inlet unstart. The overall maximum value is 8.5 at $M_0 = 7$. This conclusion is based on experimental results obtained primarily at angles-of-attack $\leq 3°$ and further testing is needed to substantiate the conclusion at the higher values of α;

3. The optimum inlet design Mach number falls in the middle of the desired flight Mach number range of operation, not near its upper limit. Consequently, future inlet experimentation should include tests at one and two Mach numbers above M_{DES};

4. The sensitivity of engine performance to yaw angle should be investigated. Chin or aft entry inlet missile designs require bank-to-turn steering which can introduce sideslip and the performance of both may be sensitive to yaw angle as well as angle-of-attack;

5. The maximum inlet capture area, A_i, is a function of smile angle in a given launcher constraint. The overall minimum occurs when $\phi = 208.6°$ for a box launcher and $\phi = 133.6°$ for a circular launcher. The maximum occurs when $\phi = 360°$ and $90°$; and

6. The choice of an optimum smile angle is not clear. A lower bound can be established when the radome size is defined. The optimum, however, would depend on a study in which internal packaging efficiency is included; such a study should be made.

REFERENCES

1. Waltrup, P.J., Anderson, G.Y., and Stull, F.D., "Supersonic Combustion Ramjet (Scramjet) Engine Development in the United States," Invited paper presented at the 3rd International Symposium on Air Breathing Engines, Munich, Germany, March 1976, JHU/APL Preprint.

2. Billig, F.S. and Dugger, G.L., "The Interaction of Shock Waves and Heat Addition in the Design of Supersonic Combustors," 12th Symposium (International) on Combustion, The Combustion Institute, Pittsburgh, PA., 19[illegible], pp. 1125-1134.

3. Moorhead, S.B., "The Latest in Ship Weapon Launchers - The Vertical Launching System," Naval Engineers Journal, April 1981, pp. 90-96.

4. Solomon, J.M., et al., "Inviscid Flowfield Calculations for Re-Entry Vehicles with Control Surfaces," AIAA Journal, Vol. [illegible], No. 12, Dec. 1977, pp. 1742-1749.

5. Billig, F.S., Orth, R.C., and Lasky, M., "Effects of Thermal Compression on the Performance Estimates of Hypersonic Ramjets," Journal of Spacecraft and Rockets, Vol. 5, No. 9, Sept. 1968, pp. 1076-1081.

6. Trexler, C.A., "Inlet Performance of the Integrated Langley Scramjet Module (Mach 2.3 to 7.6)," presented at the AIAA/SAE 11th Propulsion Conference, Anaheim, Cal., Sept. 29-Oct. 1, 1975, AIAA Preprint 75-1212.

7. Dunsworth, L.C. and Woodgrift, K.E., "Dual Mode Scramjet, Part I: Inlet Design and Performance Characteristics," The Marquardt Corp., AFAPLTR-67-132, Part I, December 1967.

8. Jilly, L.F. (Ed.), "Hypersonic Research Engine Project - Phase II: Aerothermodynamic Integration Model Development Final Technical Data Report," Garrett Airesearch Manufacturing Company of California, NASA-CR-132654, May 1975.

9. Waltrup, P.J., Billig, F.S., and Stockbridge, R.D., "A Procedure for Optimizing the Design of Scramjet Engines," invited paper presented at the AIAA/SAE 14th Joint Propulsion Conference, Las Vegas, NV., July 25-27, 1978, AIAA Preprint No. 78-1110; Also Journal of Spacecraft and Rockets, Vol. 16, No. 3, May-June 1979, pp. 163-172.

10. Waltrup, P.J., Billig, F.S., and Evans, M.C., "Critical Considerations in the Design of Supersonic Combustion Ramjet (Scramjet) Engines," presented at the AIAA/SAE/ASME 16th Joint Propulsion Conference, Hartford, Conn., June 30-July 2, 1980, AIAA Preprint 80-1284; Also Journal of Spacecraft and Rockets, Vol. 18, No. 4, pp. 350-356, July-August 1981.

11. Kutler, P., "Computation of Three-Dimensional, Inviscid Supersonic Flows," Lecture Notes in Physics #41, Springer-Verlag, 1974.

12. Henry, J.R. and Anderson, G.Y., "Design Considerations for the Airframe-Integrated Scramjet," 1st International Symposium on Air Breathing Engines, June 19-23, 1972, Marseille, France.

ACKNOWLEDGMENT

The authors extend their gratitude to Dr. M.D. Griffin for his efforts in developing and running the computer codes needed for the inviscid axisymmetric and three-dimensional inlet flowfield characterization. This work was supported by the U.S. Naval Sea Systems Command through Mr. J.W. Murrin (SEA-62R2) under contract N00024-81-C-5301.

APPENDIX

DETAILS OF INLET, ENGINE, DRAG, AERODYNAMIC AND VEHICLE PERFORMANCE

This Appendix contains descriptions of the procedures used to obtain inlet and engine internal performance, external aerodynamics and drags and the net force produced by the various missile designs. All of the working graphs and equations are presented along with specific exemplary cases for nose, chin and aft entry inlet missile designs.

SCRAMJET ENGINE CYCLE

Figure A-1 presents a schematic illustration of a typical supersonic combustion ramjet (scramjet engine) along with the station numbers used to subdivide the flow into regions of major interest - viz., the inlet, isolator air duct, fuel injector, combustor and nozzle. In the scramjet concept, the hypersonic speed, free stream air (station ⓪) is diffused to a lower supersonic speed (station ①) prior to entering the isolator air duct. An air duct is required to prevent the combustion induced shock system located at the entrance of the supersonic combustor (station ②) from adversely interacting with the inlet flowfield. Fuel is then injected either normally or at an oblique angle from the wall into the air stream at station ②. The fuel then burns in the supersonic combustor, (stations ② to ④) prior to expansion in the nozzle (stations ④ to ⑤).

The heart of the scramjet engine is the combustor which has the ability to operate over a wide range of flight conditions, e.g., M_0 = 4 to 8 at altitudes between sea-level and 30.5 km (100,000 ft) or higher. Figure A-2 is a schematic illustration that depicts the combustion process. Here, the flow entering the combustor is supersonic ($M_2 \geq 1$). Fuel is injected at station ② and the combination of the fuel injection and combustion processes produce a compression field depicted in Fig. A-2 as a single wave. Station ③ corresponds to conditions that would exist behind this single wave with upstream properties at station ②. Combustion occurs between stations ③ and ④ with the properties at station ④ being dependent on the properties at station ②, the combustor area ratio (A_4/A_2), the fuel properties and combustion efficiency (η_c), the combined total pressure losses due to the compression field, the heat addition process and wall skin friction (τ_w) and, finally, the wall heat transfer losses (Q_w). Since there is no throat at station ④, $M_4 \geq 1$.

The strength of the compression field (or wave) depicted in Fig. A-2 varies from a Mach wave, i.e., no shock, through the complete family of oblique shocks to a maximum corresponding to a normal shock (Ref. 2). For the cases of no shock or a normal shock, $A_3 = A_2$, but for oblique shocks, the flow is seperated and the effective cross-sectional area of the flow is smaller than the physical cross section of the combustor.

Because the combustion process is proceeded by a compression field of varying strength, the supersonic combustor has the unique ability to operate in both a supersonic and subsonic combustion mode, which is often referred to as dual-mode combustion. When M_2 is high, the strength of the compression field always corresponds to a maximum of an oblique shock wave over the entire fuel-air equivalence ratio (ER) range. In this case the flow in the combustor outside the viscous sublayer is entirely supersonic. However, for low values of M_2 and moderate to high values of ER, combustion is preceeded by the equivalent of a normal shock wave and the combustion process begins in a subsonic flow. However, even in this case, if $A_4/A_2 > 1$, the flow is reaccelerated through a thermal throat to a sonic or supersonic speed at station ④. This is referred to as the subsonic combustion mode. The limiting maximum effective ER ($ER_{eff} = ER \cdot \eta_c$) for a given M_0 (or M_2) corresponds to that which results in $M_4 = 1$. An example of these limits is given in Fig. 9 of the main text.

ENGINE CYCLE ANALYSIS

The cycle analysis used to determine engine performance is an integral approach developed over the past 12 years and is summarized in Refs. 2, 9 and 10. It permits solutions of the combustion process to be found without an a priori knowledge of the combustor area or wall static pressure distributions and is not limited to constant area, pressure or Mach number in the combustor (Ref. 2). Ref. 9 presents the methodology required for selecting the optimum inlet area contraction ratio (modified by the results of Figs. 6 and 7 in the main text), combustor area ratio and exit nozzle expansion ratio in accordance with prescribed engine design constraints and flight conditions. Additionally, Ref. 10 documents the sensitivity of the overall engine performance to inlet total pressure recovery (kinetic energy efficiency), isolator air duct and combustor length, fuel type, wall skin friction, nozzle efficiency and engine thermochemistry.

The results presented and assumptions used in Refs. 2, 9 and 10 are based on experimental data and analytical techniques developed from testing and analyzing scramjet engines and components over the past 20 years (see, e.g., Ref. 1). The veracity of the analysis for predicting scramjet engine performance has been established.

VEHICLE DESIGN CONSTRAINTS AND MISSION REQUIREMENTS

The current study was undertaken to develop the methodology needed to systematically determine engine sizing and integration requirements for hypersonic airbreathing missile applications. Three types of inlet configurations that have received considerable attention in the literature have been examined. As with any missile designs, certain launcher constraints and mission requirements must be met. Those chosen for this study are that the missile must fit within a square and be circular in cross section and that the missile must be capable of accelerating from Mach 4 to Mach 8 cruise speeds. The more detailed analysis was confined to a 50 x 50 cm (19.7 x 19.7 in.) x 400 cm (157.5 in.) box constraint.

The Mach 4 end-of-boost flight speed is a reasonable choice since the optimum two stage vehicle generally is obtained when the first stage accelerates the vehicle to approximately half its cruise speed. The vehicle length (L) to diameter (D) ratio of 8 that was selected is typical of high speed, airbreathing missile designs. Finally, a fixed geometry engine is assumed as it generally is preferred to minimize cost albeit with some loss in performance.

With the size of the missile thus constrained and the flight regime established, the remainder of this appendix will present detailed descriptions of the inlet and engine performance calculations and aerodynamics and drags used in this study as well as sample calculations of the results presented in the main text.

INLET PERFORMANCE

Inlet performance is a composite of three distinct parameters: air capture area ratio (A_o/A_1 - see Fig. A-1), kinetic energy efficiency (η_{KE}) or total pressure recovery and additive drag. The combination of A_o/A_1 and η_{KE} together with a specified inlet area contraction ratio (A_1/A_1) is sufficient to determine the global flow conditions at station ① for given conditions at station ⓪. These, in turn, are required to determine the global flow conditions throughout the remainder of the engine. Additive drag, on the other hand, is required to determine the net vehicle force. In the main text of this report, an empirical relation between η_{KE} and A_o/A_1 is established (Fig. 7). Since $A_o/A_1 = (A_1/A_1) \cdot (A_o/A_1)$, it oly remains to determine A_o/A_1 and the additi. drag coefficient ($C_{D_{add}}$) as a function of M_o, M_{DES} and angle-of-attack (α) to complete the characterization of the inlet.

The inlet air capture and additive drags were determined for the annular, chin and aft entry inlets depicted in Fig. 3 of the main text using a three-dimensional solution of the hyperbolic equations of motion. The analysis is very similar to that reported in, for example, Refs. 4 and 11, and codes of this type are now readily available.

The results of these computations are given in Figs. A-3 through A-16. Free stream Mach numbers of 3, 4, 5, 6, 7 and 5 were considered along with angles of attack of 0°, ±5° and ±10°. Figures A-3 through A-10 present A_o/A_1 and $C_{D_{add}}$ as a function of inlet smile angle (ϕ), M_o and angle of attack for the nose/chin inlets shown in Fig. 3 of the main text with M_{DES} = 4, 6, 7 and 8. Figures A-11 through A-15 present the corresponding results for the aft entry inlet depicted in Fig. 3(c) of the main text. Here, however, only inlet design Mach numbers of 6, 7 and 8 were considered. Note that the reference area is taken as the inlet geometric area (A_1) for a full circle ($\phi = 360°$) at zero angle of attack ($\alpha = 0°$). This permits direct comparison to be made between the various inlet designs at all values of ϕ, M_{des}, M_c and α.

Figures A-17 and A-18 present such comparisons and supplement those shown in Figs. 4 and 5 of the main text. Figure A-17 compares A_o/A_1 as a function of angle of attack for the nose and chin inlets for M_{des} = 6, 7 and 8 while Fig. A-18 compares A_o/A_1 of aft inlet designs with those of the nose and chin inlets for M_{des} = 6. The results in Fig. A-17 show that:

(1) There is a 20% to 25% decrease in air capture at all M_os and M_{DES} for the nose inlet designs ($\phi = 360°$) for angles of attack of ±10° compared with the air capture characteristics at $\alpha = 0°$;

(2) The loss in air capture at $M_o > M_{DES}$ and $\alpha = \pm 10^\circ$ of the nose inlets is eliminated by using a chin inlet with a smile angle of 270° or less; and

(3) For $M_o < M_{DES}$, $\alpha > 0^\circ$ and chin inlet designs with $\phi < 270^\circ$, the air capture increases with increasing and decreasing M_o over the zero angle of attack values. For example, for $M_{DES} = 6$, $M_o = 4$ and $\phi = 180^\circ$, the air capture at $\alpha = \pm 10^\circ$ is 28% higher than at $\alpha = 0^\circ$.

The results in Fig. A-18, on the other hand, show that the air capture ratio of the aft entry inlet is always less than that of the nose or chin inlet designs except for $M_o \geq M_{DES}$, $\alpha = \pm 10^\circ$ and $\phi = 90^\circ$ where the aft entry inlets air capture is 6% to 12% higher than for the chin.

The reason for these differences is that the bow shock of the aft entry design never intersects the cowl lip, even at angle-of-attack, except for the above mentioned cases. In addition, in a three-dimensional flow for $\phi < 360^\circ$ a lateral (non-axial) flow is established which permits a portion of the air to spill around the inlet which would not occur in an axisymmetric ot two-dimensional flow. Consequently, the air capture characteristics of the aft entry and, to some extent, the chin inlet are lower than would be expected for a comparable two-dimensional inlet design flying at angle-of-attack. Thus, whereas an aft entry inlet is a viable inlet design for a more nearly two dimension flow on a body at angle-of-attack, such as the NASA hypersonic engine (Ref. 12), it has less than desirable air capture characteristics for a hypersonic missile. This is especially so at low Mach numbers and low to moderate angle-of-attack.

ENGINE PERFORMANCE

The internal performance of a matrix of scramjet engines has been computed using the cycle analysis presented in Ref. 9. In order to make the results independent of a particular inlet design, however, requires that the results be compiled and presented as a function of the inlet contraction ratio (A_o/A_1) using the corresponding kinetic energy efficiency shown in Fig. 7 of the main text. Such computations have been made based on the following assumptions which are consistent with the norms established in Refs. 9 and 10:

(1) The combustor inlet area and diffuser exit area are equal, i.e., $A_1 = A_2$;

(2) The fuel is RJ-5 with $\eta_c = 100\%$. This assumption has been made to simplify the analysis. In an actual engine, RJ-5 is not sufficiently reactive to burn efficiently in the scramjet engine. Either the addition of 10 to 30% by weight of a highly reactive fuel (e.g., B_5H_9) or oxidizer pilot (e.g., ClF_3) are required to achieve high combustion efficiencies (Refs. 1 and 10). The properties of RJ-5 are as follows:

stoichiometry, f_s = 0.07284
heat of formation = 20 kcal/gm-mole
lower leading value = 9.97 kcal/gm
chemical formula = $C_{14}H_{18}$
molecular weight = 186.298
specific gravity = 1.07;

(3) The air consists of 0.75525 N_2, 0.23146 O_2 and 0.01325 A by weight;

(4) The combustor wall wetted-to-inlet area ratio (A_w/A_2) is 40.0;

(5) The inlet and combustor flows are in thermochemical equilibrium;

(6) Heat transfer through the walls of the combustor are negligible; and

(7) The nozzle exit stream thrust is based on an efficiency of 0.98 for an expansion that is one third of the way between frozen and equilibrium.

With these assumptions, a matrix of gross engine internal thrust coefficients (C_{T_g}) were computed for an altitude of 15.24 km (50,000 ft.) for effective contraction ratios of three to the maximum permitted (Fig. 7 of the main text), equivalence ratios of 0.25 to the maximum permitted for $M_4 \geq 1$ in 0.25 intervals, combustor area ratios (A_4/A_2) of 2, 3 and 4 and effective exit nozzle expansion ratios (A_5/A_0) of 1 to 8. Gross thrust coefficient in these cases is defined as

$$C_{T_g} = \left[\eta_n \cdot F_5 - F_0 - P_0 (A_5 - A_0)\right] / (q_o A_o) \qquad \text{(A-1)}$$

where F is the stream thrust. An altitude of 15.24 (50,000 ft.) was chosen for
8-20 simplicity. Although small variations in C_{T_g} will occur at other altitudes, the C_{T_g}s given are a good approximation for C_{T_g} all altitudes of interest.

The results are presented in Figs. A-19 through A-24 where C_{T_g} is given as a function of A_0/A_1 for $3 < M_0 < 8$, $0.25 < ER \leq 1.0$ or the maximum and $2 \leq A_4/A_2 \leq 5$ for each of the effective exit nozzle expansion ratios. The reference area (A_{ref}) in all cases is A_0. To use these curves for a particular inlet/engine design requires a knowledge of M_0, A_0/A_1 and A_i/A_1 of the inlet, A_4/A_2 and A_5/A_1. Then $A_c/A_1 = (A_i/A_1)$ (A_0/A_1), $A_5/A_0 = (A_5/A_1) \cdot (A_1/A_0)$ and C_{T_g} based on A_0 for the known M_0, A_4/A_2 and A_5/A_1 can be determined for each ER. To obtain C_{T_g} at values of ER, A_4/A_2, A_5/A_5 and M_0 other than those shown requires at least a three point interpolation.

AERODYNAMICS AND DRAGS

The final parameters needed before a complete vehicle performance estimate can be made, i.e., finding the net vehicle force coefficient (C_{T_N}) as a function of M_0, α and engine design, are the normal force coefficient per degree of angle-of-attack (C_N/α) and the zero lift external drag coefficients. For simplicity, a single curve for C_N/α has been assumed which is representative of those computed for other hypersonic missile designs. The relationship is

$$C_N/\alpha = 5.4 - 0.3M_0 \qquad \text{(A-2)}$$

where α is in radians. The reference area is a 50-cm (19.7-in.)-dia circle. Note that the functional dependence of C_N/α is linear with M_0. As such, its utility is limited to small angles-of-attack, i.e., $\alpha \leq \pm$ 10-15°.

The external drag coefficients needed are for the forebody, cowl and leading edge wave, the body friction and the tail wave and friction. The forebody (2.6:1 3/4 power nose) and cowl wave drag coefficients (C_{D_n}, $C_{D_{cw}}$) were computed using the same analytical procedures used to determine A_0/A_1 and $C_{D_{add}}$ for the inlets. A 6° cowl angle was assumed in computing $C_{D_{cw}}$. The cowl leading edge drag coefficient ($C_{D_{le}}$) was obtained assuming a leading edge diameter of 0.25 cm (0.1 in.). The body and tail friction drag coefficients (C_{D_f}, $C_{D_{tf}}$) were computed assuming a smooth, adiabatic wall with a fully developed turbulent boundary layer. The tail wave drag coefficient ($C_{D_{tw}}$) was obtained assuming a two-dimensional flow at the free stream conditions for over a 15° angle wedge with a 55° sweep angle, a total planform area of 2581 cm² (400 in²) and a thickness ratio of 5%. It should be noted that four control surfaces were assumed for the nose inlet vehicle designs assuming skid-to-turn maneuvers, and three surfaces for the chin and aft inlet design assuming back-to-turn maneuvers. The total tail planform area in both cases, however, is the same.

The resulting drag coefficients are shown in Figs. A-25 through A-30 as a function of free-stream Mach number. All are references to a 50-cm (19.7-in.)-dia-circle. Note that $C_{D_{le}}$ and $C_{D_{cw}}$ are also functions of M_{des}. For simplicity, C_{D_f} and $C_{D_{cw}}$ are given per unit body surface area and per unit projected frontal area, respectively, where the values of $C_{D_{cw}}$ are based on an A_3/A_1 of 2. This introduces less than a $\pm 2\%$ error in $C_{D_{cw}}$ for $1 \leq A_5/A_1 \leq 4$. Base drags are not included since it is assumed that the engine exit nozzle fills the maximum circle afforded by the launcher constraints.

SAMPLE CALCULATIONS OF NET VEHICLE FORCE COEFFICIENTS

With the inlet performance, engine performance and aerodynamics and drags established, it is now possible to present detailed examples of how the net force coefficients ($C_{T_N} = C_{T_g} - C_D$) at $M_0 = 4$ and 8 in the main text were generated. Specifically, the cases for which $C_{T_N} = 0.382$ at $M_0 = 4$, $\alpha = 0$ and $ER = 1$ (Fig. 12 of the main text) for the nose inlet and $\phi = 160°$ chin and aft entry inlets will be used as examples. Note that $M_{DES} = 6$ and $A_4/A_2 = 4.0$ in all three cases and that an iterative procedure is required to arrive at the A_5/A_1 needed to produce a $C_{T_N} = 0.382$ at $M_0 = 4$, $\alpha = 0$ and

ER = 1. The examples, however, only include the final computations.

To initiate these calculations requires that the inlet geometric area contraction ratio, A_i/A_1, be chosen such that it does not exceed the maximum contraction ratios, $(A_o/A_1)_{max}$, set forth in Fig. 7 of the main text. Since

$$A_i/A_1 = (A_o/A_1)_{max} / (A_o/A_i) \qquad \text{(A-3)}$$

and A_o/A_i varies with both M_c and α, bounds on both M_o and α need to be established before A_i/A_1 can be selected. The M_o bounds for the vehicle designs considered are $M_o = 4$ to 8. Also, missiles of this type generally follow a nearly zero lift trajectory during the initial stages of climb-out from $M_o = 4$ but require negative lift during the latter portion of the climb-out in order to level-off at the cruise altitude. This generally occurs at M_os > 6. Once at the cruise altitude, a positive α is required to maintain 1 "g" of lift. Consequently, $\alpha = 0^\circ$ at $M_o = 4$ and 5 and $\alpha = \pm 10^\circ$ at $M_o \geq 6$ have been assumed as the regions of principal interest. Higher α would normally occur in terminal maneuver at which time engine performance is relatively unimportant.

With these bounds, eq. (A-3) is then used to determine $A_i/A_1 = f(M_o, \alpha)$ using Fig. 7 for $(A_c/A_1)_{max}$ and Figs. A-5 and A-11, respectively, for A_o/A_i of the nose chin and aft entry inlets with $M_{DES} = 6$. The minimum of these values is then selected as the maximum A_i/A_1, $(A_i/A_1)_{max}$, for each inlet type. For the nose and $\phi = 160^\circ$ chin inlets, the minimum occurs at $M_o = 4$, $\alpha = 0^\circ$ and $(A_i/A_1)_{max} = 5.24/0.745 = 7.034$. For the $\phi = 160^\circ$ aft entry inlet, $(A_i/A_1)_{max} = 8.32/0.756 = 10.529$ which occurs at $M_o = 6$, $\alpha = +10^\circ$.

Had $\alpha = +10^\circ$ been the operating criteria at $M_o = 4$ and 5, then $(A_i/A_1)_{max}$ for the nose would still be 7.034 but that for the $\phi = 160^\circ$ chin inlet would be 5.413 which occurs at $M_o = 4$, $\alpha = +10^\circ$ and that for the ϕ aft entry inlet would be 7.686 which occurs at $M_o = 4$, $\alpha = +5^\circ$. A summary of these results for all values of ϕ is presented in Fig. A-31, where $(A_i/A_1)_{max}$ is given as a function of inlet smile angle using the two different bounds on α at $M_o = 4$ and 5.

With A_i/A_1 established for each design the remainder of the components of the net force coefficient are calculated as shown below:

Nose Inlet ($\phi = 360^\circ$)

In this case, the required A_5/A_i to achieve $C_{F_N} = 0.382$ for $M_o = 4$, ER = 1, and $\alpha = 0^\circ$ is 2.39. With A_5/A_i is 2.39, the areas needed to obtain the drag coefficients are:

$A_i = \pi(50)^2/4/2.39 = \underline{821.5\text{cm}^2\ (127.34\text{ in.}^2)}$

A_{cowl_x} = cowl area projected axially

$= A_5 - A_i$

$= \pi(50)^2/4 \cdot (1 - A_i/A_5) = 1141.9\text{cm}^2\ (177.0\text{ in.}^2)$

$A_{cowl\ lip}$ = cowl lip area

$= \pi D_{cowl} \cdot D_{lip}$

$= 2\pi\ (16.71)\ (0.254) = \underline{25.80\text{cm}^2\ (4.00\text{ in.}^2)}$

$L_{body} = 400 - L_{inlet}$

$L_{inlet} = r_{cowl}/\tan 16.61^\circ = 54.2\text{cm}\ (21.34\text{ in.})$

$L_{body} = 345.8\text{cm}\ (136.14\text{ in.})$

$L_{cowl} = (25 - r_{cowl})/\tan 6^\circ$

$= 84.0\text{cm}\ (33.07\text{ in.})$

8-32

$L_{cyl} = L_{body} - L_{cowl}$

$= 261.8\text{cm} \ (103.07 \text{ in.})$

A_{bw} = Body wetted area = $A_{\substack{cowl\\surf.}} + A_{\substack{cyl\\surf.}}$

$$A_{\substack{cowl\\surf.}} = \pi(r_{cowl} + 25)\left[L^2_{cowl} + (25 - r_{cowl})^2\right]^{1/2}$$

$= 10{,}925\text{cm}^2 \ (1993.3 \text{ in.}^2)$

$A_{\substack{cyl\\surf.}} = \pi D L_{cyl}$

$= 41{,}123\text{cm}^2 \ (6374.1 \text{ in.})^2$

$A_{bw} = \underline{52{,}048\text{cm}^2 \ (8067.4 \text{ in.}^2)}$

The zero left drag coefficients at $M_o = 4$ and $\alpha = 0^0$ referenced to A_5 are then:

$C_{D_{add}} = 0.248/2.39 \quad = 0{,}0104$ (Fig. A-6)

$C_{D_{cw}} = (1.590 \times 10^{-4})\ (177) \quad = 0.0281$ (Fig. A-26)

$C_{D_{le}} = (652 \times 10^{-3})\ (4.0) \quad = 0.0261$ (Fig. A-27)

$C_{D_f} = (3.53 \times 10^{-6})\ (8067.4) = 0.0285$ (Fig. A-28)

$C_{D_{t_w}} \quad = 0.0092$ (Fig. A-29)

$C_{D_{tf}} \quad = \underline{0.0030}$ (Fig. A-30)

C_D = total drag coeff. $= \boxed{0.1503}$

At $M_o = 8$ and $\alpha = +5^0$, the drag coefficients are:

$C_{D_{add}} \quad = 0$

$C_{D_{cw}} = (1.248 \times 10^{-4})\ (177) \quad = 0.0221$

$C_{D_{le}} = (3.88 \times 10^{-3})\ (40) \quad = 0.0155$

$C_{D_f} = (1.52 \times 10^{-6})\ (8067.4) = 0.0123$

$C_{D_{tw}} \quad = 0.0088$

$C_{D_{tf}} \quad = 0.0013$

$C_{D_\alpha} \quad = \underline{0.0228}$ (Eq. (A-2))

$C_D \quad = \boxed{0.0828}$

At $M_o = 8$ and $\alpha = 0^0$, $C_{D_\alpha} = 0$ and $C_{D_{add}} = 0$. Therefore,

$$C_D = 0.0828 - 0.0228 = \boxed{0.0600}$$

To obtain the gross engine thrust coefficients, C_{F_g}, the values of $A_o/A_1 = f(M_o, \alpha)$ are needed to obtain A_5/A_1 at each M_o and α. For $M_o = 4$, $\alpha = 0^0$ and $M_{DES} = 6$, $A_o/A_1 = 0.745$ (Fig. A-6). Therefore, from eq. (A-1) for $A_1/A_o = 7.034$, $A_o/A_1 = 5.24$. Also,

$$A_5/A_o = (A_5/A_1)\ /(A_o/A_1) = 2.39/0.745$$

$$= 3.208$$

To obtain C_{T_g} at $M_0 = 4$, $\alpha = 0°$ and ER = 1, Figs. A-19 through A-24 are entered using $A_0/A_1 = 5.24$ for $A_4/A_2 = 4$. The values of C_{T_g} corresponding to $A_0/A_1 = 5.24$ are divided by A_5/A_0 to reference them to A_5 and then plotted as a function of A_5/A_0 or A_5/A_1. This requires at least a three point interpolation scheme since the curves are not linear. The value of C_{T_g} corresponding to either $A_5/A_1 = 2.39$ or $A_5/A_0 = 3.208$ is then the actual C_{T_g} for the case being studied. For $M_0 = 4$, $\alpha = 0$ and ER = 1,

$C_{T_g} = 0.4372$

$C_D = \underline{0.1503}$

$C_{T_x} = \boxed{0.2869}$ $(M_0 = 4,\ \alpha = 0°,\ ER = 1)$

Fuel flow efficiency is then calculated from

$$\dot{w}_f/(q_0 A_5) = (ER)(f_s)/V_0 \cdot (A_0/A_1)(A_1/A_{ref}) \qquad \text{(A-8)}$$

At 15.24 km (50,000 ft.), $V_0 = 1180$ m/s (3872 ft/s) for $M_0 = 4$ and at ER = 1, $\dot{w}_f/(q_0 A_{ref}) = 3.773 \times 10^{-4}$ (lbm/s)/lbf.

At $M_0 = 8$, $\alpha = 0°$ and ER = 1, $A_0/A_1 < 1$. Therefore, $A_0/A_1 = 7.034$ and $A_5/A_0 = A_5/A_1 = 2.39$. Thus

$C_{T_g} = 0.2083$

$C_D = \underline{0.0640}$

$C_{T_x} = \boxed{0.1443}$ $(M_0 = 8,\ \alpha = 0°,\ ER = 1)$

At $M_0 = 8$, $\alpha = +5°$ and ER = 1, $A_0/A_1 > 1$, $A_0/A_1 = 7.034$ and $A_5/A_0 = A_5/A_1 = 2.39$. Consequently, C_{T_g} is the same as when $\alpha = 0°$. Then

$C_{T_g} = 0.2083$

$C_D = \underline{0.0808}$

and $C_{T_x} = \boxed{0.1275}$ $(M_0 = 8,\ \alpha = +5°,\ ER = 1)$

At $M_0 = 8$, $\alpha = +5°$ and ER = cruise ER (ER_c), $A_0/A_1 = 7.034$ and $A_5/A_0 = A_5/A_1 = 2.39$. However, in this case, $C_{T_g} \neq C_D$. Consequently C_{T_g} must be plotted as a function of A_5/A_1 for ER = 0.75, 0.5 and 0.25 and then the C_{T_g} corresponding to $A_5/A_1 = 2.39$ at each ER plotted as a function of ER. Then the cruise ER for $C_{T_g} = C_D$ at $A_5/A_1 = 2.39$ can be determined. In this case, $ER_c = 0.437$. Then the fuel flow efficiency can be determined from eq. (A-8) with $V_0 = 2360$ m/s (7744 ft/s). The value for $M_0 = 8$ cruise at $\alpha = +5°$ is 1.193×10^{-4} (lbm/s)/lbf.

Cone Inlet ($\theta = 360°$)

In this case, the required A_5/A_1 to achieve $C_{T_g} = 0.382$ at $M_0 = 4$ and $\alpha = 0°$ is 2.36 and A_0/A_1 is 7.034. The body areas needed to calculate the aero lift drag coefficients are:

$A_1 = \underline{830.8 \text{ cm}^2 \ (128.96 \text{ in.}^2)}$

$r_{c_{max}}$ = maximum cone radius $= r_1 \left[1 - 1.2/(A_0/A_1)\right]^{1/2}$

8-24 $r_i = \left[(A_i/\pi)\left(\frac{360}{160}\right)\right]^{1/2} = 24.41$cm (9.61 in.)

$r_{n_{max}} = (24.41)(0.4102) = 22.23$cm (8.75 in.)

Note that the factor $\left[1 - 1.2/(A_i/A_t)\right]^{1/2}$ requires the maximum nose radius to be small enough to permit the desired A_i/A_t to be achieved assuming a 20% internal contraction. Now,

A_{n_x} = projected nose area not included in A_i

$= \pi r_n^2 (200/360) = 863$ cm^2 (133.70 in^2)

$A_{cowl_x} = A_5 - A_{n_x} - A_i$

$= \pi(25)^2 - 863. - 832.$

$= 268.5$cm^2 (41.61 in.^{2})

$A_{cowl\ lip} = \left[2\pi r_i \left(\frac{160}{360}\right) + (r_i - r_n)\right](0.254)$

$= \underline{18.42\text{cm}^2\ (2.856\ \text{in.}^2)}$

l_n = nose length = (2.6) (2) (22.23)

= 115.6cm (45.51 in.)

A_{nw} = nose wetted area

$= (4/7)(\pi/2.6)\, l_n^2\, (200/360)$

$= 5126.0$ cm^2 (794.54 in.^{2})

l_i = 81.8cm (32.22 in.)

$A_{bw} = (400-81.8)(\pi)(50)\left(\frac{160}{360}\right) + (400-115.6)(\pi)(50)$ (200/360)

$= 47033$cm^2 (7290.2 in.^{2})

A_{tw} = total body wetted area

$= A_{nw} + A_{bw}$

$= \underline{52{,}159\text{cm}^2\ (8084.74\ \text{in.}^2)}$

The zero lift drag coefficients at $M_0 = 4$ and $\alpha = 0°$ referenced to A_5 are:

$C_{D_{add}} = .0248/2.36 = 0.0105$

$C_{D_{cw}} = (1.593 \times 10^{-4})(41.61) = 0.0066$

$C_{D_{lc}} = (6.52 \times 10^{-3})(2.856) = 0.0186$

$C_{D_n} = (.0757)(133.7/304.342) = 0.0333$ (Fig. A-25)

$C_{D_f} = (3.53 \times 10^{-6})(8084.74) = 0.0285$

$C_{D_{bw}} = 0.0092$

$C_{D_{br}} = \underline{0.0559}$

C_D = total drag coefficient = $\boxed{[illegible]}$

At $M_0 = 8$ and $\alpha = +5°$, the drag coefficients are:

$C_{D_{add}} = 0$

$C_{D_{cw}} = (1.248 \times 10^{-4})(41.61) = 0.0052$

$C_{D_{lc}} = (3.88 \times 10^{-3})(2.856) = 0.0111$

$C_{D_n} = (0.0638\ (133.7/304.342)$ $= 0.0280$

$C_{D_f} = (1.52 \times 10^{-6})\ (8054.74)$ $= 0.0121$

$C_{D_{tw}}$ $= 0.0088$

$C_{D_{tf}}$ $= 0.0013$

C_{D_α} $= \underline{0.0228}$

C_{D_a} $= \boxed{0.0895}$

At $M_o = 8$ and $\alpha = 0^\circ$, $C_{D_\alpha} = 0$ and $C_{D_{add}} = 0$. Therefore,

$$C_D = 0.0895 - 0.0228 \quad = \boxed{0.0667}$$

The same procedure used in obtaining C_{T_g} for the nose inlet is used to obtain C_{T_g} for the $\phi = 160^\circ$ chin. Here, however, A_o/A_1 at $M_o = 8$ and $\alpha = +5^\circ$ is 0.945 instead of 1.0. Consequently, the A_o/A_1 used to obtain C_{T_g} in this case is 6.647 instead of 7.034. The values of A_o/A_1 at $M_o = 4$, $\alpha = 0^\circ$ and $M_o = 8$, $\alpha = 0^\circ$ are the same as before. In addition, $A_5/A_1 = 2.36$ instead of 2.39. Thus, for $M_o = 4$, ER =1 and $\alpha = 0^\circ$, $A_5/A_o = 3.208$, $A_o/A_1 = 5.24$ and

$C_{T_g} = 0.4950$

$C_D = \underline{0.1097}$

$C_{T_N} = \boxed{0.3853}$

The corresponding fuel flow efficiency is 3.821×10^{-4} (lbm/s)/lbf. For $M_o = 8$, ER = 1 and $\alpha = +5^\circ$, $A_5/A_o = 2.497$, $A_o/A_1 = 6.647$ and

$C_{T_g} = 0.1963$

$C_D = \underline{0.0895}$

$C_{T_N} = \boxed{0.1068}$

For $M_o = 8$, ER = 1, and $\alpha = 0^\circ$, $A_5/A_o = A_5/A_o = 2.36$, $A_o/A_1 = 7.034$ and

$C_{T_g} = 0.1963$

$C_D = 0.0667$

$C_{T_N} = \boxed{0.1409}$

At cruise at $M_o = 8$ and $\alpha = +5^\circ$, $A_5/A_o = 2.497$, $A_o/A_1 = 6.647$ and $ER_c = 0.485$. The corresponding fuel flow efficiency is 1.267×10^{-4} (lbm/s)/lbf.

__Aft Entry Inlet ($\phi = 160^\circ$)__

In this design, the required A_5/A_1 to achieve $C_{T_N} = 0.382$ for $M_o = 4$, ER = 1 and $\alpha = 0^\circ$ is 1.48. A_1/A_1 in this case is 16.539. The body areas needed to calculate the zero lift drag coefficients are:

$A_1 = \underline{1327\text{cm}^2\ (205.68\ \text{in.}^2)}$

$$
\begin{aligned}
r_i &= 30.8\ (12.14\ \text{in.}) \\
r_{n_{max}} &= 30.8 \left[1 - (1.2/10.529)\right]^{1/2} \\
&= 29.0\text{cm}\ (11.42\ \text{in.})
\end{aligned}
$$

However, to be consistent with the inlet flowfields generated in Figs. A-11 and A-12, $r_i/r_n = 1.667$. Therefore

$$
\begin{aligned}
r_n &= 30.8/1.667 \\
r_n &= 18.48\text{cm}\ (7.27\ \text{in.}) \\
A_{nx} &= \pi(18.48)^2\ (200/360) \\
&= \underline{596.0\text{cm}^2\ (92.39\ \text{in.}^2)} \\
A_{cowl\ x} &= \pi(25)^2 - 1327 - 596.0 \\
&= \underline{40.5\text{cm}^2\ (628\ \text{in.}^2)} \\
A_{cowl\ lip} &= \left[2\pi\ (30.8)\ (160/360) + 2(30.8 - 18.48)\right](0.254) \\
&= \underline{28.40\text{cm}^2\ (4.40\ \text{in.}^2)} \\
L_n &= (2.6)\ (2)\ (18.48) \\
&= 96.1\text{cm}\ (37.83\ \text{in.}) \\
A_{nw} &= (4/7)\ (\pi/2.6)\ (96.1)^2\ (200/360) \\
&= 3542\ \text{cm}^2\ (549.0\ \text{in.}^2) \\
L_i &= \text{forebody cyl. length} = 10\,(18.48) - L_n \\
&= 88.7\text{cm}\ (34.92\ \text{in.}) \\
A_{bw} &= (400-184.8)\ (\pi)\ (50 + \\
&\quad (88.7)\ (2\pi)\ (18.48)\ \ 300/360) \\
&= 39{,}525\text{cm}^2\ (6126.4\ \text{in.}^2) \\
A_{tw} &= 39{,}525 + 3542 \\
&= \underline{43{,}067\text{cm}^2\ (6675)\ \text{in.}^2}
\end{aligned}
$$

The zero lift drag coefficients at $M_o = 4$ and $\alpha = 0^o$ referenced to A_5 are:

$$
\begin{aligned}
C_{D_{add}} &= (0.04)/1.48 && = 0.0270\ \ \text{(Fig. A-12)} \\
C_{D_{cw}} &= (1.617 \times 10^{-4}0\ (6.28) && = 0.0010 \\
C_{D_{le}} &= (6.32 \times 10^{-3})\ (4.40) && = 0.0278
\end{aligned}
$$

Note that a ΔM_o offset of -0.1 is used for the aft entry $C_{D_{cw}}$ and $C_{D_{le}}$ in Figs. A-26 and A-27. This is because the Mach number on the inlet's nose just prior to entering the second compression field is zero to 0.2. Mach numbers lower than M_o.

$$
\begin{aligned}
C_{D_n} &= (0.0757)\ (92.39/304.342) && = 0.0230 \\
C_{D_f} &= (3.53 \times 10^{-6})\ (6675) && = 0.0235 \\
C_{D_{tw}} & && = 0.0092 \\
C_{D_{tf}} & && = \underline{0.0030} \\
C_D &= \text{total drag coefficient} && = \boxed{0.1145}
\end{aligned}
$$

At $M_o = 8$ and $\alpha = +5^o$, the drag coefficients are:

$$C_{D_{add}} = (8.2 \times 10^{-3})\ (360/160)/1.48 \qquad = 0.0125$$

$$C_{D_{cw}} = (1.248 \times 10^{-4})\ (6.28) \qquad = 0.0008$$

$$C_{D_{\ell e}} = (3.88 \times 10^{-3})\ (4.40) \qquad = 0.0171$$

$$C_{D_n} = (0.0638)\ (92.39)/304.342) \qquad = 0.0194$$

$$C_{D_f} = (1.52 \times 10^{-6})\ (6675) \qquad = 0.0101$$

$$C_{D_{tw}} \qquad = 0.0088$$

$$C_{D_{tf}} \qquad = 0.0013$$

$$C_{D_\alpha} \qquad = \underline{0.0228}$$

$$C_D \qquad = \boxed{0.0928}$$

At $M_o = 8$ and $\alpha = 0^o$, $C_{D_\alpha} = 0$ but $C_{D_{add}} = (0.0168)/1.48 = 0.0114$.

Therefore,

$$C_D = 0.0928 - 0.0228 - 0.0125 + 0.0114 = 0.0689$$

Again, the same procedure as before is used to obtain the values of C_{T_g} corresponding to $A_5/A_1 = 1.48$. However, at $M_o = 4$, ER = 1 and $\alpha = 0^o$, $A_o/A_1 = 0.470$. Thus $A_o/A_1 = (10.529)\ (0.47) = 4.949$, $A_5/A_o = 3.149$ and

$$C_{T_g} = 0.4972$$

$$C_D = 0.1145$$

$$C_{T_N} = \boxed{0.3827}$$

For $M_o = 8$, ER = 1, and $\alpha = +5^o$, $A_o/A_1 = 0.762$, $A_o/A_1 = 8.023$, $A_5/A_o = 1.942$ and

$$C_{t_g} = 0.2290$$

$$C_D = 0.0928$$

$$C_{T_N} = \boxed{0.1362}$$

For $M_o = 8$, ER = 1, and $\alpha = 0^o$, $A_o/A_1 = 0.532$, $A_o/A_1 = 5.601$, $A_5/A_o = 2.782$ and

$$C_{T_g} = 0.1730$$

$$C_D = 0.0689$$

$$C_{T_N} = \boxed{0.1041}$$

At cruise at $M_o = 8$ and $\alpha = +5^o$, A_o/A_1, A_o/A_1 and A_5/A_o are the same as when ER = 1. In this case, $ER_c = 0.444$ and the fuel flow efficiency is 1.406×10^{-4} (lbm/s)/lbf.

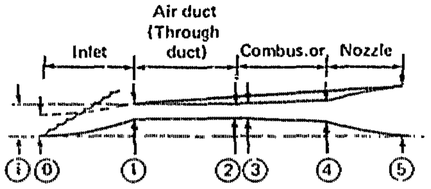
Inlet
Air duct (Through duct)
Combus.or
Nozzle
ⓘ
⓪
①
②
③
④
⑤

Fig. A-1 Schematic of typical scramjet engine.

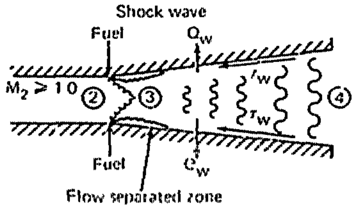
Shock wave
Fuel
Q_w
$M_2 \geq 1.0$
②
③
④
τ_w
Fuel
Q_w
Flow separated zone

Fig. A-2 Schematic of supersonic combustion process.

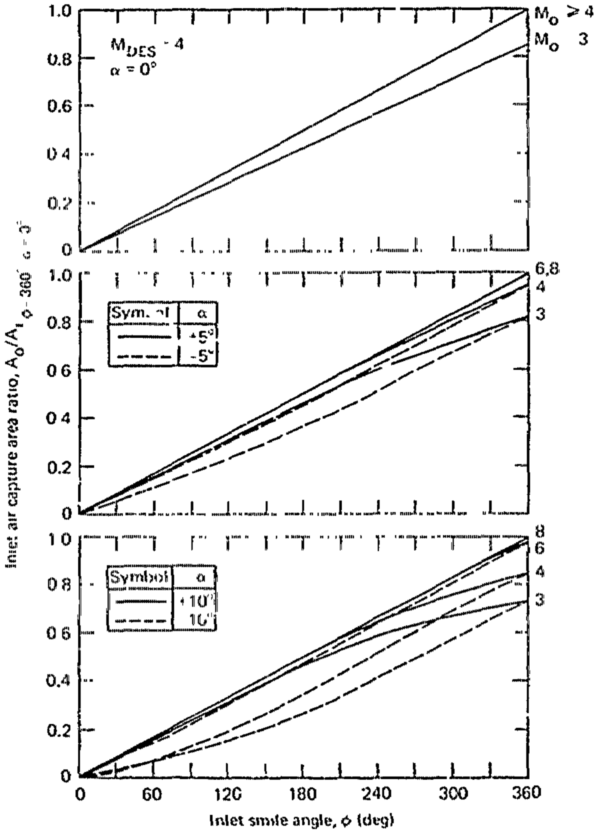

Fig. A-3 Air capture as a function of smile angle for 12.5° half-angle conical inlets with $M_{DES} = 4$

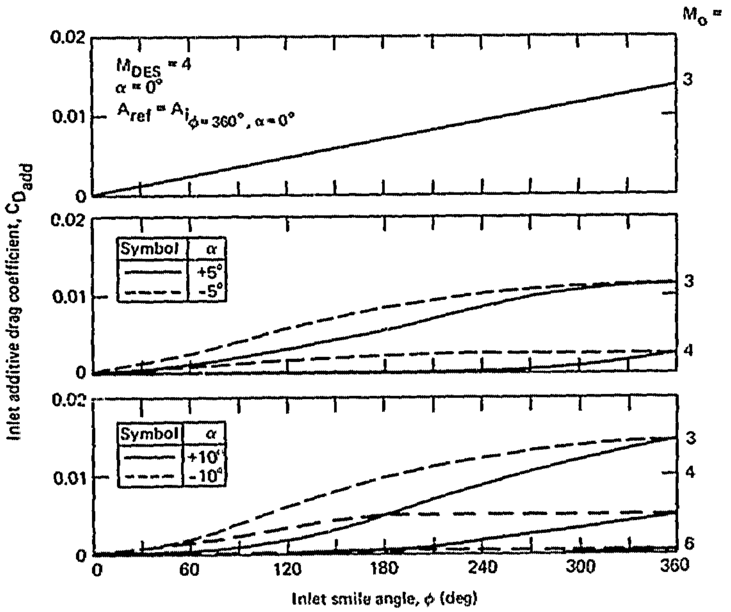

Fig. A-4 Additive drag as a function of smile angle for 12.5° half-angle conical inlets with M_{DES} = 4.

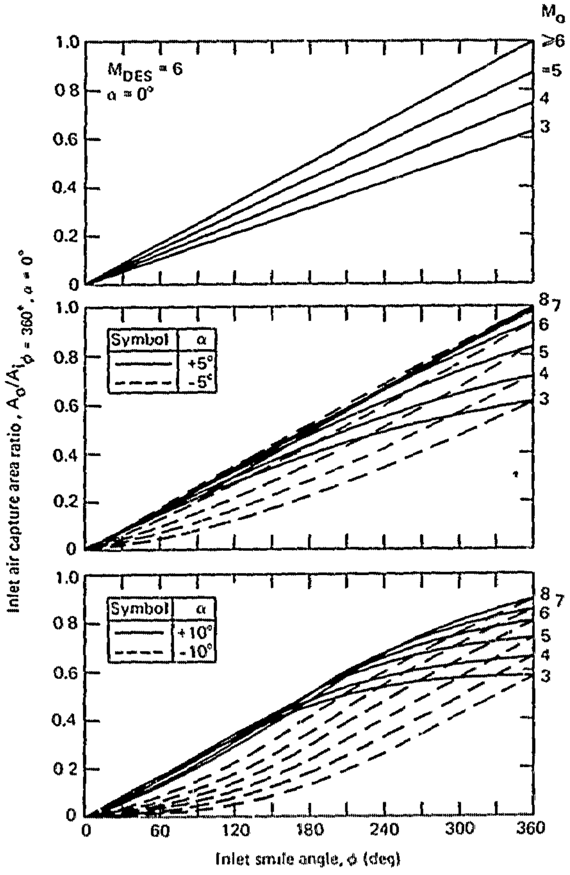

Fig. A-5 Air capture as a function of smile angle for 12.5° half-angle conical inlets with M_{DES} = 6.

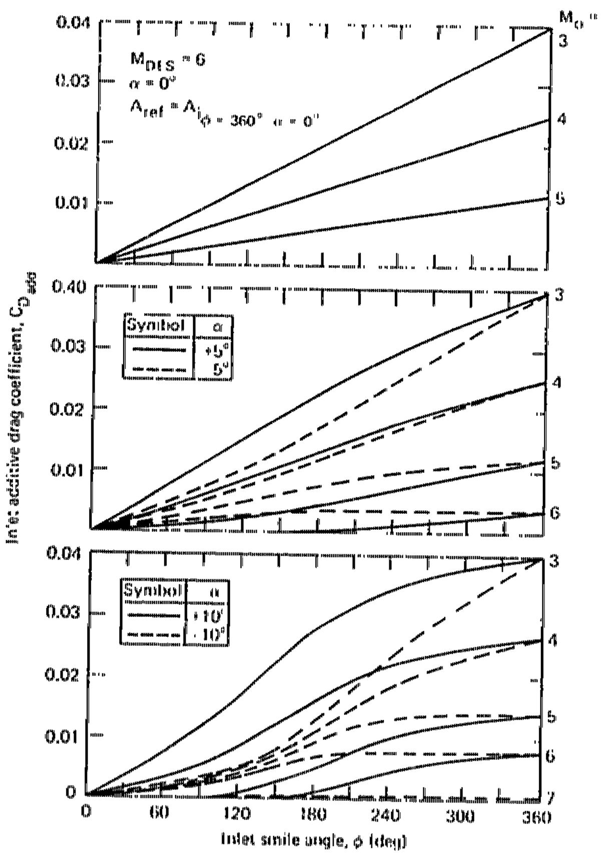

Fig. A-6 Additive drag as a function of smile angle for 12.5° half-angle conical inlets with M_{DES} = 6.

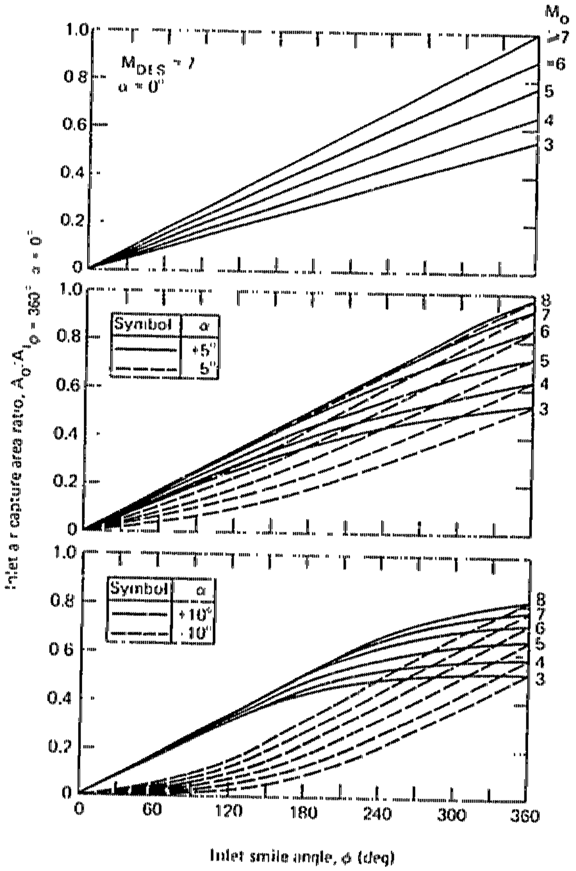

Fig. A-7 Air capture as a function of smile angle for 12.5° half-angle conical inlets with M_{DES} = 7.

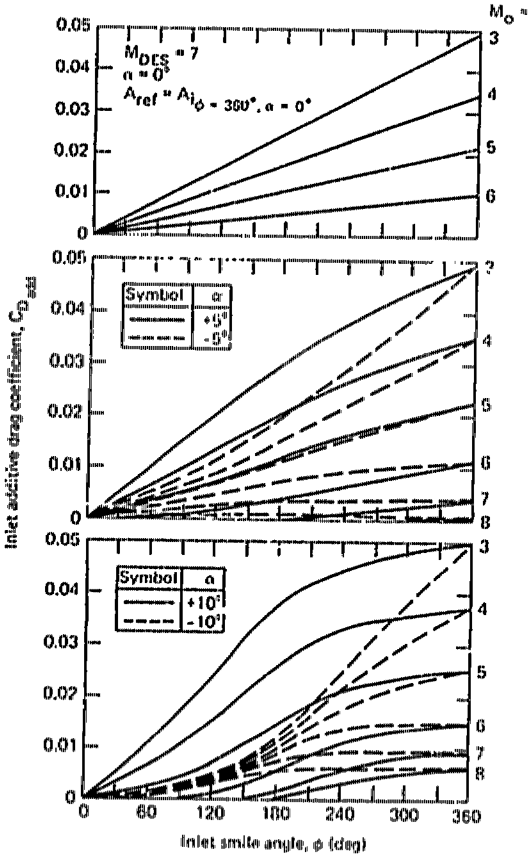

Fig. A-8 Additive drag as a function of smile angle for 12.5° half-angle conical inlets with $M_{DES} = 7$.

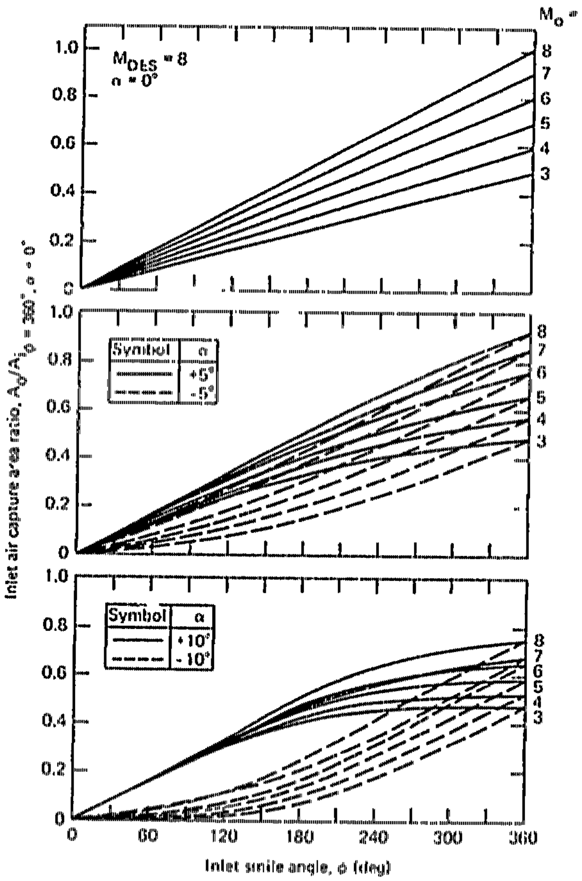

Fig. A-9 Air capture as a function of smile angle for 12.5° half-angle conical inlets with $M_{DES} = 8$.

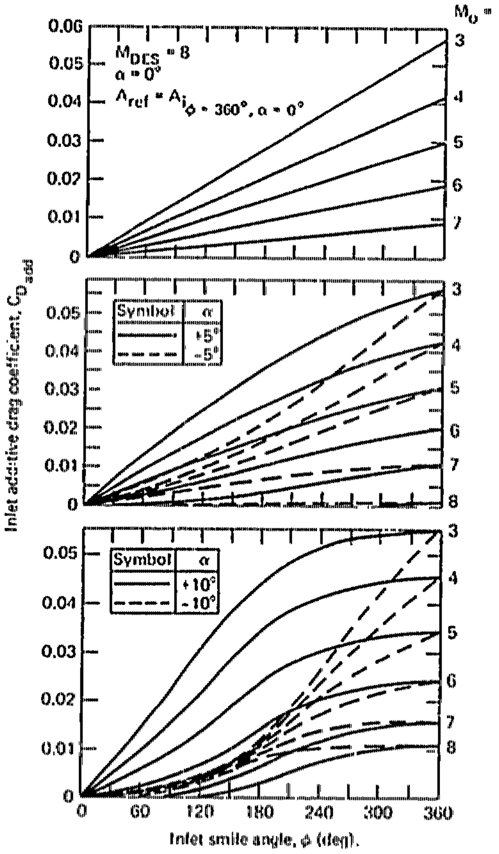

Fig. A-10 Additive drag as a function of smile angle for 12.5° half-angle conical inlets with $M_{DES} = 8$.

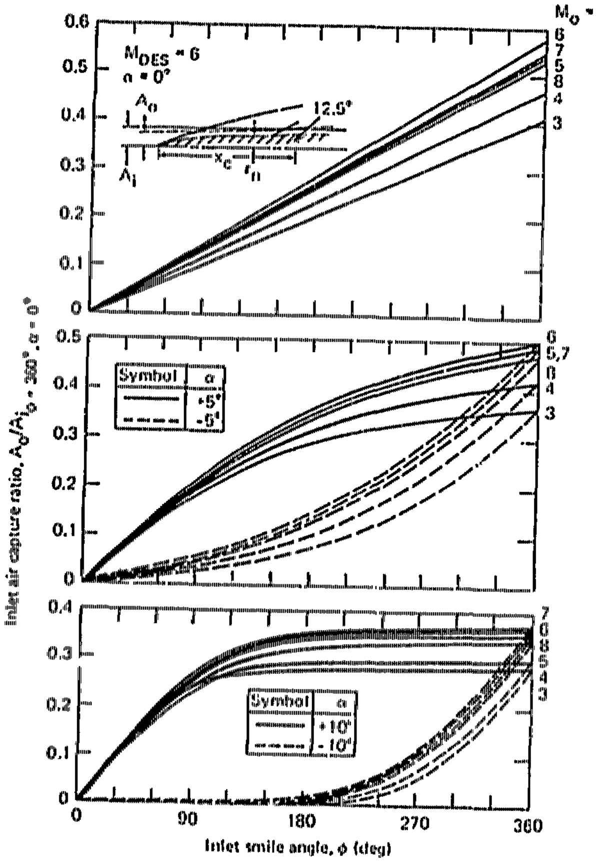

Fig. A-11 Air capture as a function of smile angle for aft entry inlets with 2.6:1 3/4 power noses, x_c/r_n = 10.0 and M_{DES} = 6.

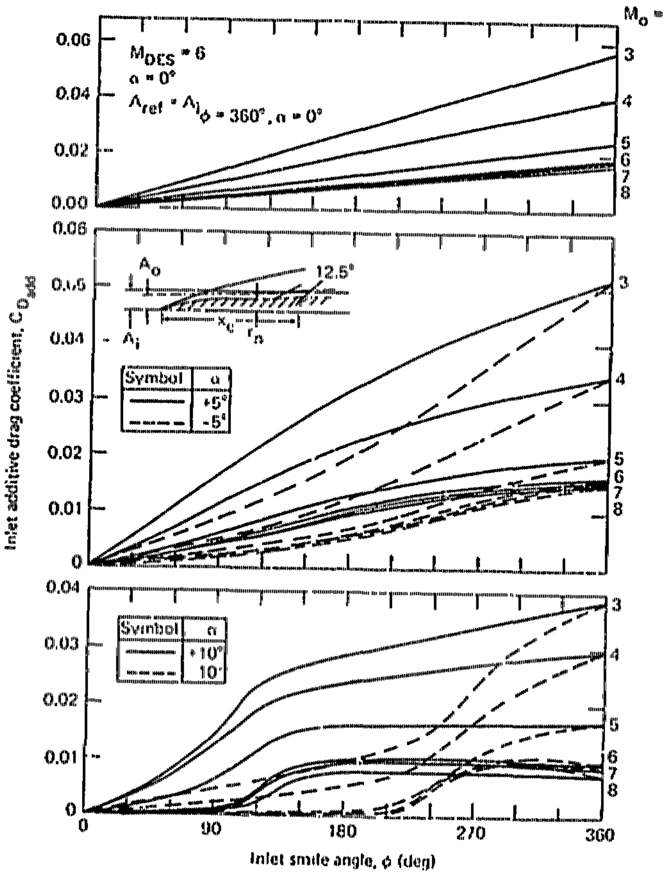

Fig. A-12 Additive drag as a function of smile angle for aft entry inlets with 2.6:1 3/4 power noses, x_c/r_n = 10.0 and M_{DES} = 6.

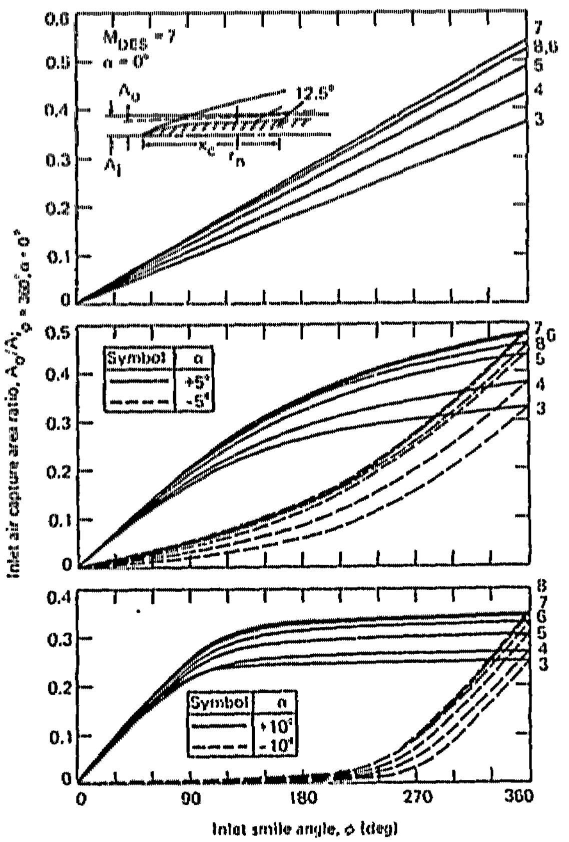

Fig. A-13 Air capture as a function of smile angle for aft entry inlets with 2.6:1 3/4 power noses, x_c/r_n = 10.0 and M_{DES} = 7.

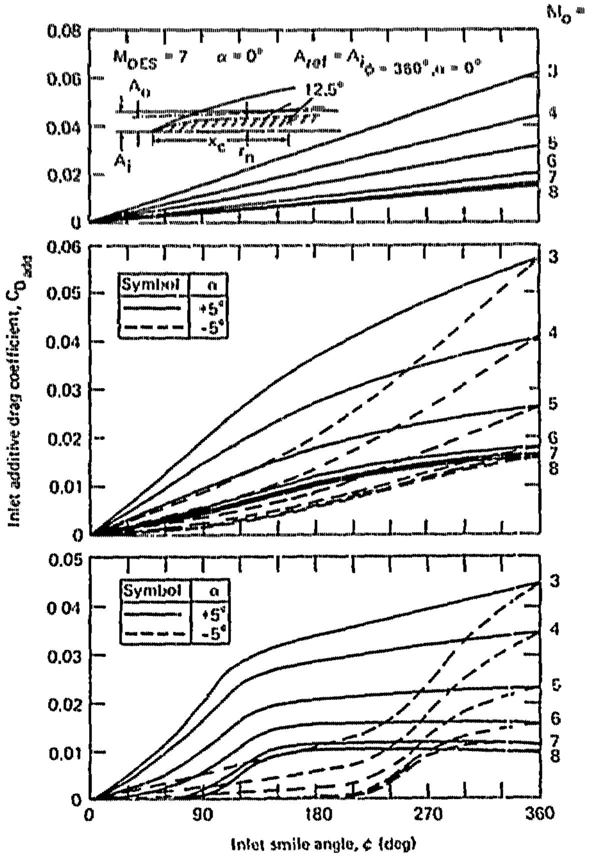

Fig. A-14 Additive drag as a function of smile angle for aft entry inlets with 2.6:1 3/4 power noses, x_c/r_n = 10.0 and M_{DES} = 7.

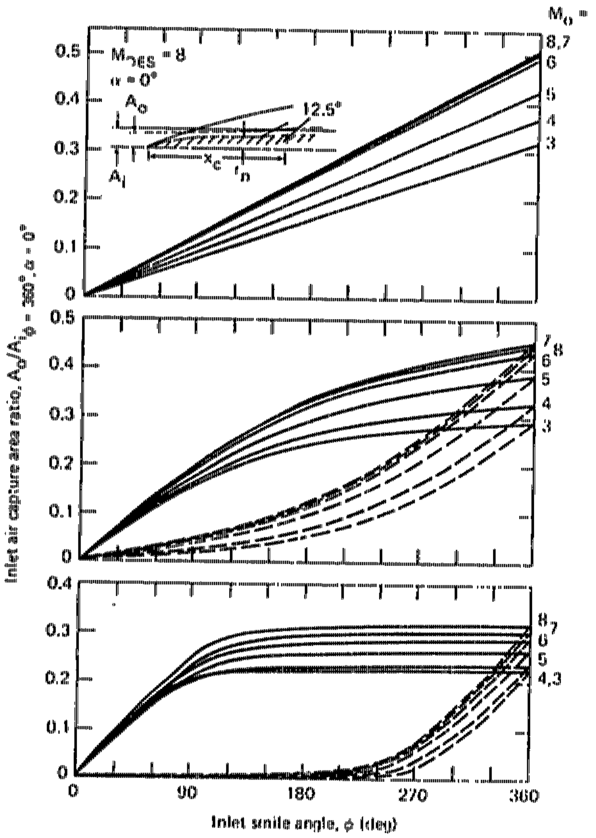

Fig. A-15 Air capture as a function of smile angle for aft entry inlets with 2.6:1 3/4 power noses, x_c/r_n = 10.0 and M_{DES} = 8.

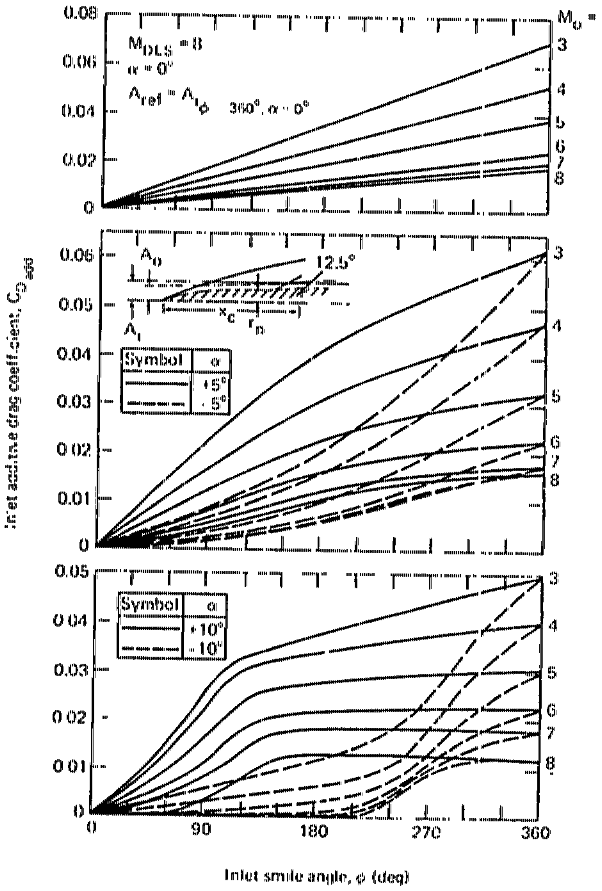

Fig. A-16 Additive drag as a function of smile angle for aft entry inlets with 2.6:1 3/4 power noses, x_c/r_n = 10.0 and M_{DES} = 8.

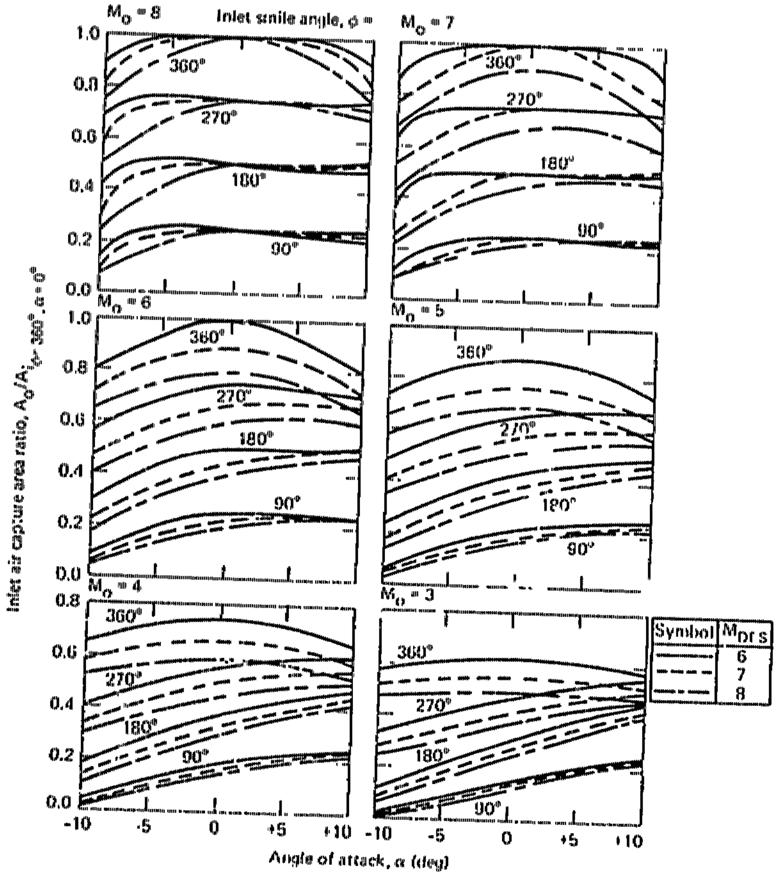

Fig. A-17 Air capture as a function of free stream and design mach number, angle of attack and smile angle for 12.5° conical forebody, nose/chin inlets.

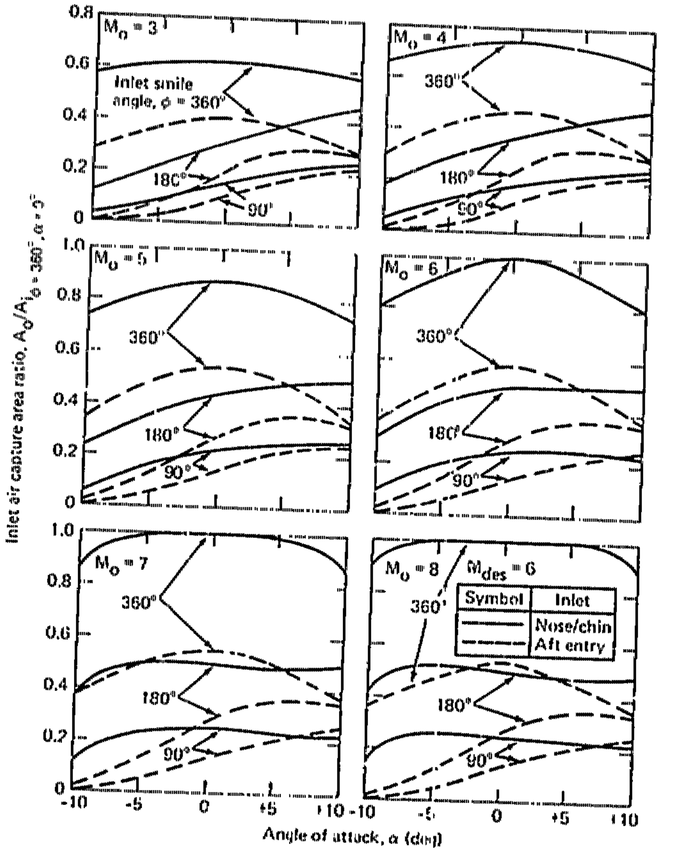

Fig. A-18 Comparison of air capture characteristics for nose/chin and aft entry inlets as a function of free stream mach number and angle of attack for an inlet design mach number of 6.

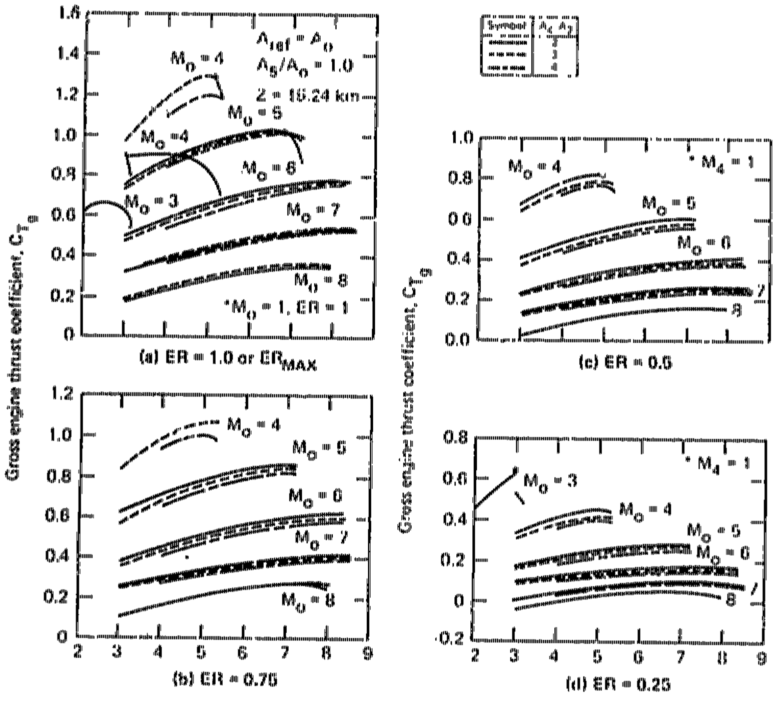

Fig. A-19 Gross engine thrust coefficient as a function of effective inlet contraction ratio for A_5/A_0 = 1.0.

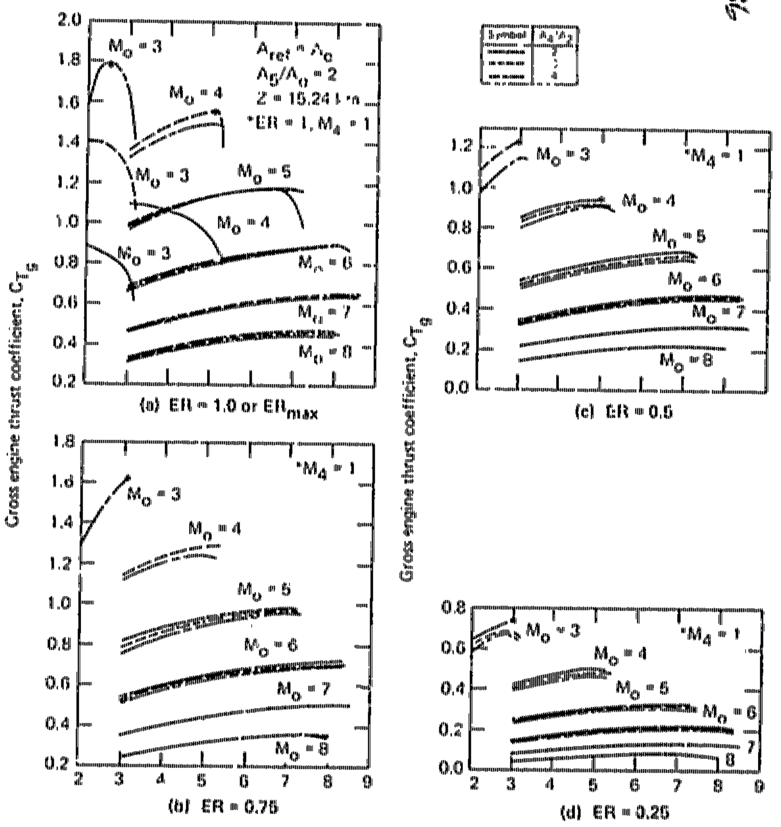

Fig. A-20 Gross engine thrust coefficient as a function of effective inlet contraction ratio for A_5/A_0 = 2.0.

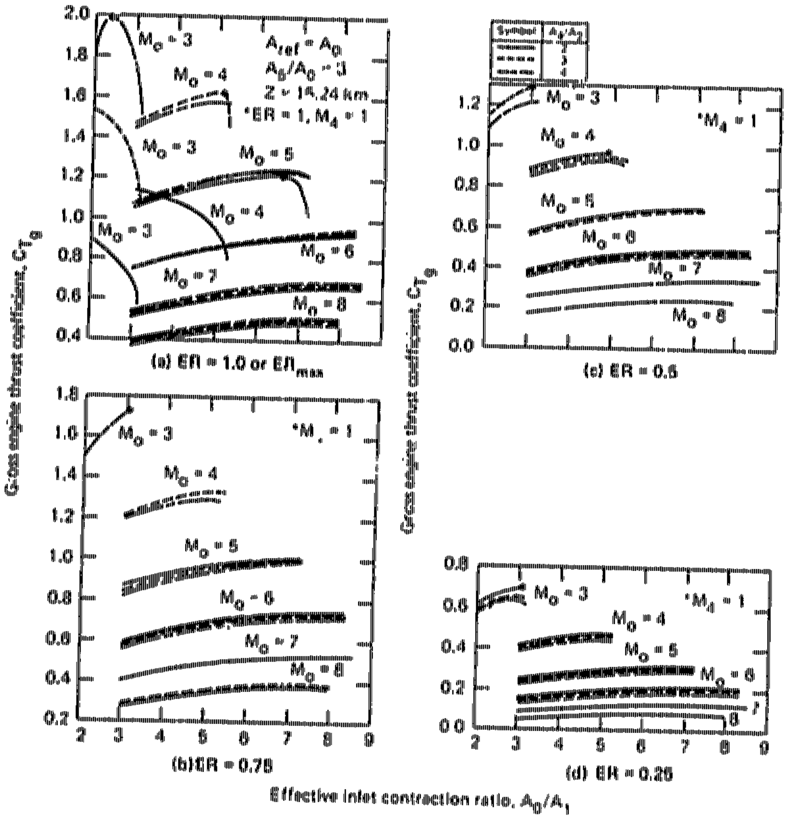

Fig. A-21 Gross engine thrust coefficient as a function of effective inlet contraction ratio for $A_8/A_0 = 3.0$.

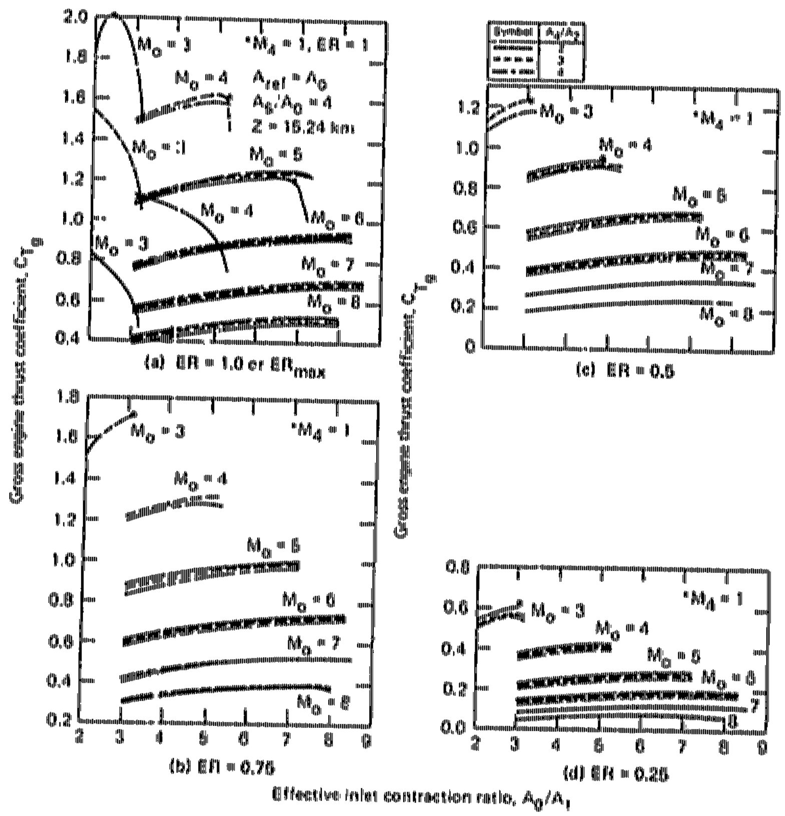

Fig. A-22 Gross engine thrust coefficient as a function of effective inlet contraction ratio for $A_8/A_0 = 4.0$.

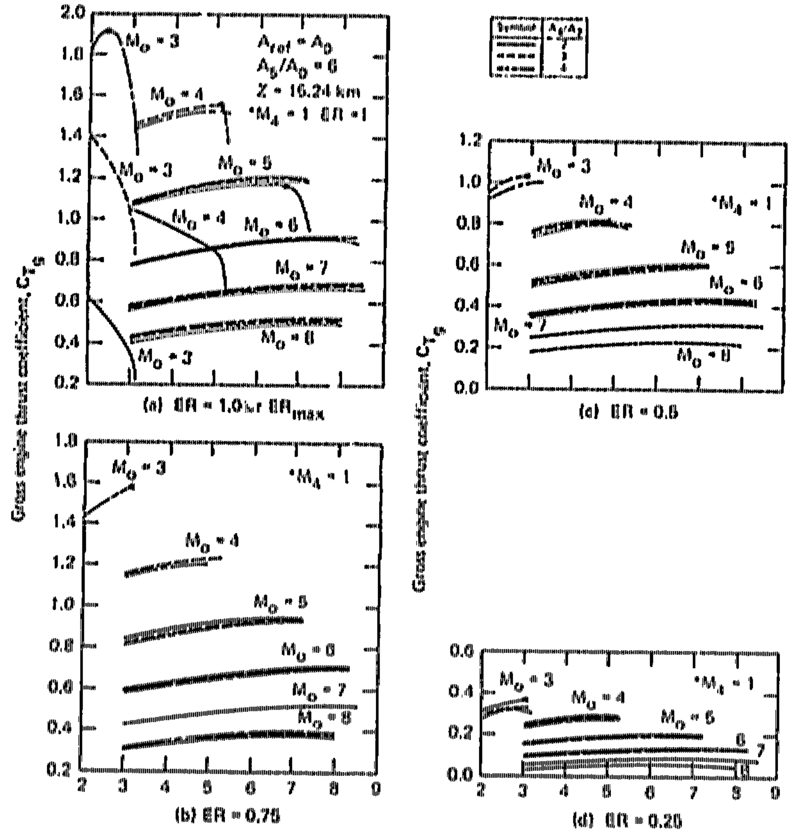

(a) ER = 1.0 or ER_{max}

(b) ER = 0.75

(c) ER = 0.5

(d) ER = 0.25

Effective inlet contraction ratio, A_0/A_1

Fig. A-23 Gross engine thrust coefficient as a function of effective inlet contraction ratio for A_6/A_0 = 6.0.

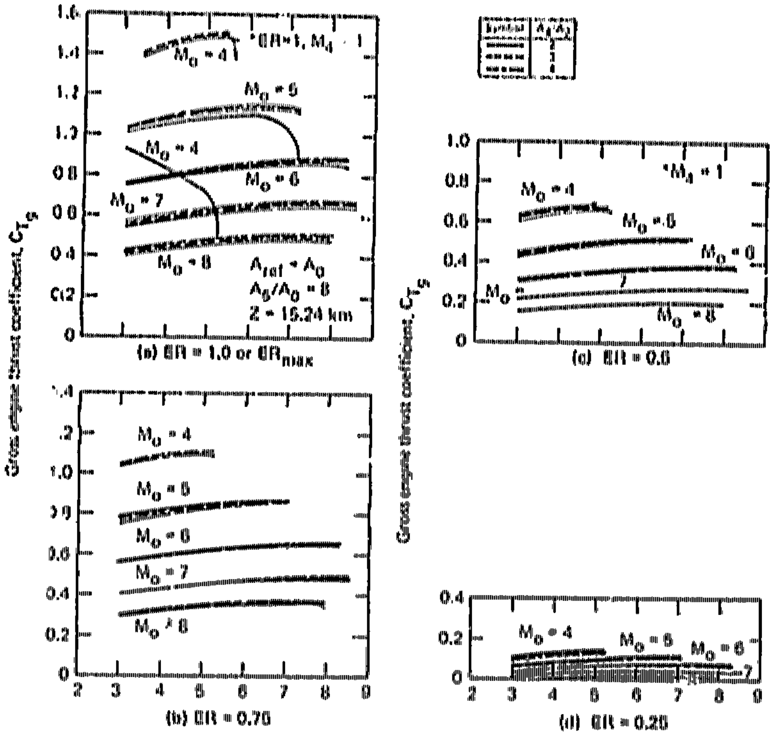

(a) ER = 1.0 or ER_{max}

(b) ER = 0.75

(c) ER = 0.5

(d) ER = 0.25

Effective inlet contraction ratio, A_0/A_1

Fig. A-24 Gross engine thrust coefficient as a function of effective inlet contraction ratio for A_6/A_0 = 8.0.

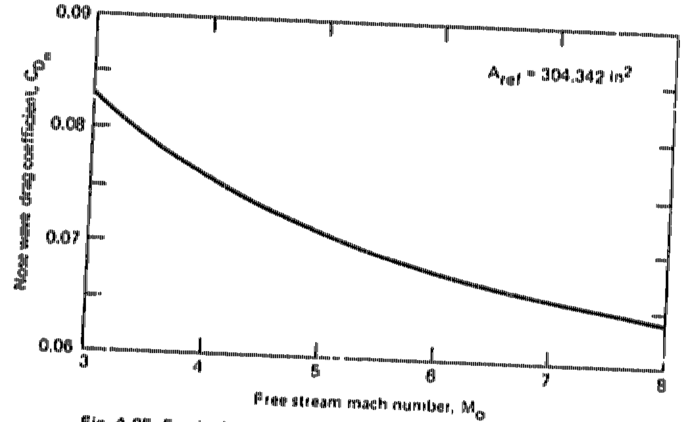

Fig. A-25 Forebody wave drag coefficient for 2.8:1 3/4 power nose.

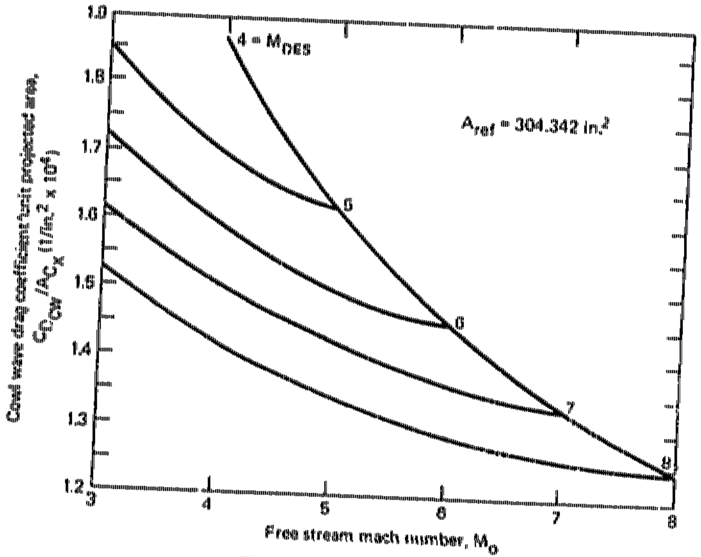

Fig. A-26 Cowl wave drag coefficient.

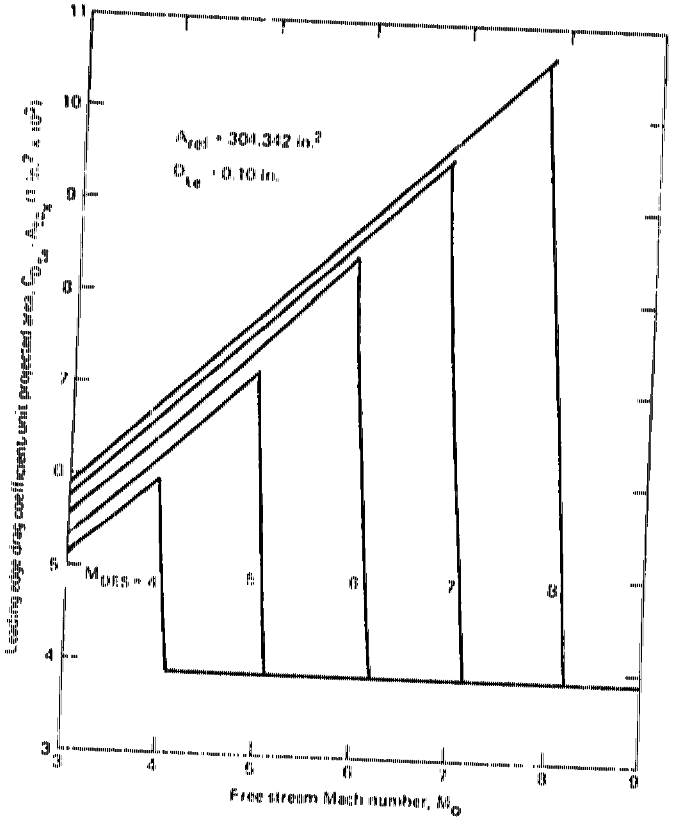

Fig. A-27 Cowl leading edge drag coefficient.

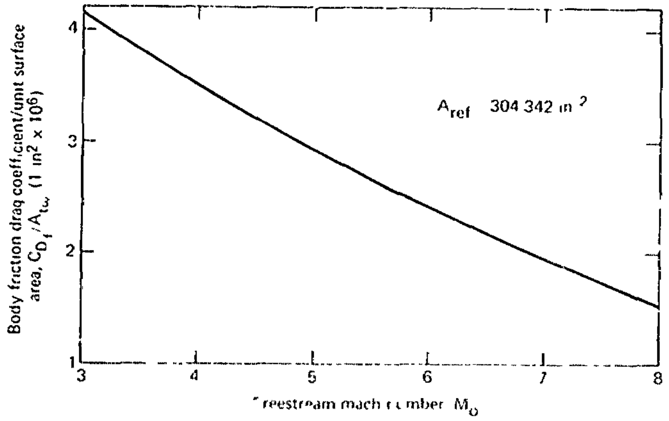

A-28 Body friction drag coefficient

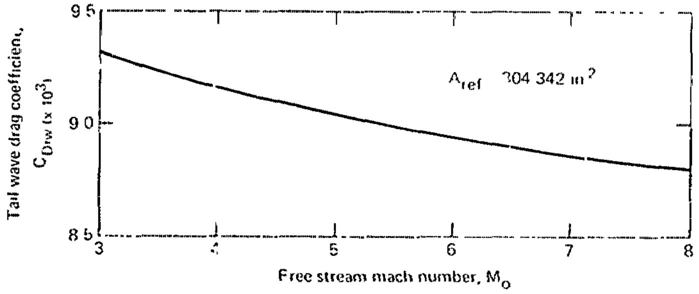

Fig A 29 Tail wave drag coefficient

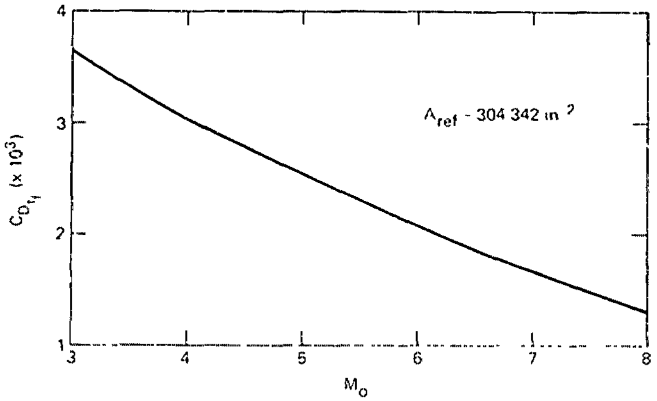

Fig A-30 Tail friction drag coefficient

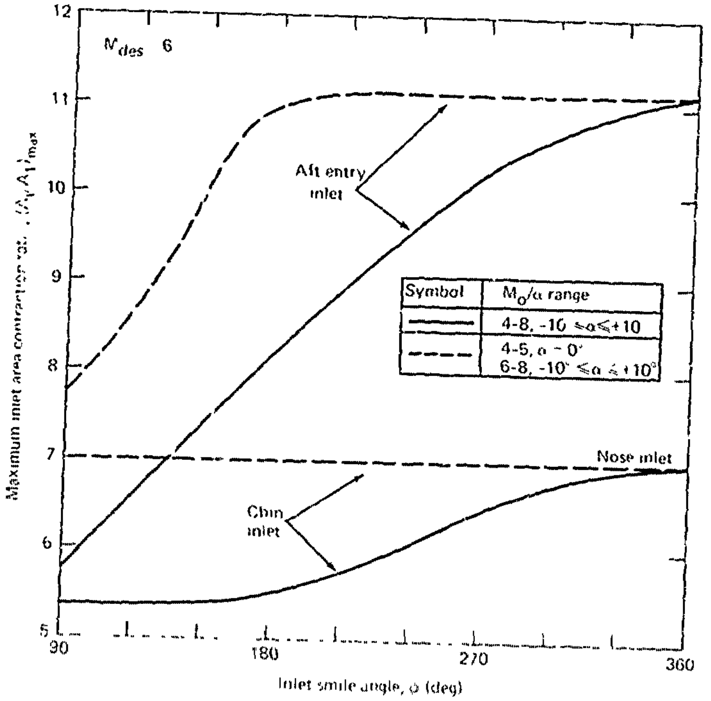

Fig. A-31 *Maximum inlet contraction area ratio as a function of smile angle for nose, chin and aft entry inlets with M_{des} = 6*

9-1

DESIGN CONSIDERATION AND ANALYTICAL COMPARISON OF DIFFERENT TYPES OF RAMJETS AND RAMROCKETS

by

Peter Benkmann[+)] and Peter A. Kramer[++)]
Institut für Raumfahrtantriebe
University of Stuttgart
Pfaffenwaldring 31
D 7000 Stuttgart 80
Germany

SUMMARY

Several types of ramjet and ramrocket (or ducted rocket) propulsion systems with hydrocarbon fuels for high sub- to supersonic missile application are theoretically analyzed and compared. Design considerations are discussed with respect to their performance impacts.

Fundamental physical connections as well as mission and internal design variables are investigated in order to give some insight into the ramjet`s and ramrocket`s performance and application potential. The results are presented in graphical form.

PREFACE

The results discussed below have been gained during an ongoing study under the sponsorship of the German Ministry of Defense in cooperation with the industry and the Deutsche Forschungs- und Versuchsanstalt für Luft- und Raumfahrt (DFVLR). The purpose is to support ongoing experimental and design work with theoretical analysis.

The high level of the Specific Impulse realized by ramjet systems can sometimes not be used because of the demand for higher thrust. Mostly the ramrocket can operate at the higher thrust level but at lower Specific Impulse than the ramjet. The design of an airbreathing missile depends not only on the demands on Specific Impulse and thrust, but also on the limitations of combustion pressure and temperature and the geometrical requirements. At a given situation of altitude and Mach number under the limitations and requirements mentioned above the choice of a sufficient operating system needs a detailed insight in the mutual dependance of the various parameters. Some theoretical layout of missile propulsion systems based on their behaviour is developed for some given criteria e.g. flight situation and geometry. Fig. 1 shows the cross-section stations of the ramjet and the ramrocket (ducted rocket).

1. METHOD OF ANALYSIS

A comprehensive computer program has been developed to calculate the aero-thermodynamic performance, i.e. the internal flow and thrust, of a broad variety of supersonic propulsion systems including ramjets and ramrockets resp. ducted rockets (1). This program has been originally targeted on an air breathing space transporter project (2,3). A derivative of this program is being used for missile propulsion as discussed here. Table 1 summarizes the most important simplifying assumptions for the cases presented here.

[+)] Dipl.-Ing., Project Engineer, [++)] Dipl.-Ing., Head Chemical Propulsion Group

Table 1: Analysis Methods and Simplifying Assumptions
General:
One-dimensional flow
No wall heattransfer
Design point and off-design point analysis
Internal thrust only, no external drag
Hot gas flow in chemical equilibrium except in nozzles

Specific Components:
Inlet diffuser performance according to AIA+) and
off-design correction according to Ref. 6
Combustion of all propellant combinations with
NASA SP-273 Program (Ref.7).
Fuel: Liquid Hydrocarbon, Oxidizer: Air, N_2O_4 resp. HNO_3
Mixing and combustion chambers with variable area and pressure
Nozzle flow with defined freezing point at the nozzle throat
Nozzle expansion to ambient pressure or to maximum engine
cross-section area

The comparisons given in this paper mainly show the two most important performance parameters:

1. The propellant Specific Impulse I_s as ratio of thrust to total propellant mass flow, including oxygen when a rocket-type combustion takes place.
2. The Thrust Density D_F as the ratio of thrust to maximum engine cross-section area.

Both parameters are equally applicable to all air breathing, rocket and combination propulsion systems without any limitations. The Thrust Density D_F is shown here rather than the more usual thrust coefficient $C_F = F/0{,}5\ \rho\ V^2 A$ which is less useful at varying and/or low speeds.

2. BEHAVIOUR OF A RAMJET WITH FIXED GEOMETRY AND TEMPERATURE LIMITATION AT CONSTANT ALTITUDE

For a high altitude missile with a ramjet propulsion system the correlations of fixed internal geometry and flight Mach number at constant altitude have been investigated theoretically and experimentally at the DFVLR at Braunschweig/Trauen (6). The goal of this study was to explore the whole range of physically existing solutions. Yet it turned out that the simple theoretical model in use sofar was not sufficient for that analysis. Therefore the program described above has been adapted. For constant altitude and variable flight Mach number mainly the internal geometry of the combuster and nozzle, i.e. combuster exit/entrance and nozzle throat/combuster exit, have been investigated as parameters. Additionally a combustion temperature limit had to be considered. Fig. 2 shows as an example the Specific Impulse versus flight Mach number with fixed geometry and/or limitation of the temperature at the exit of the combustion chamber. The variation of the flight Mach number results in a variation of fuel mass flow and Specific Impulse. Considering the line for a fixed cross-section area f_3=0.6, the Specific Impulse is rapidly descending from the beginning at Ma=2.75 (point A) to the end at Ma=4.5 (point D) with a slightly change of the bend of the curve. The temperatures are also varying and the dash-pointed part of the curve (point B to C) requires temperatures higher than the considered maximum of 2000 K. Another curve (dotted line) is plotted for a fixed temperature and therefore a varying cross-section area f_3. Here a maximum of I_s is found

+) Aircraft Industries Association (Refs. 4,5) at Ma=3.25. A third curve combines the limitations of the former two curves in the range from about Ma=3.5(point B)to Ma=4.4(point C), where at the former curves either the temperature was higher than the allowed maximum of 2000 K or the cross-section area at the throat was less than the fixed value of f_3=0.6. This combination of the two procedures with its limitations requires a diminution of the density of the inlet airflow. This can be realized by a supercritical operation of the inlet within a certain range which has still to be defined.

This third curve (solid line) fits the dash-pointed part of the curve with f_3=0.6 and variable temperature. For the curve from point A to D the behaviour of the total pressure at the end of the inlet diffusor and of the temperature at the ends of the inlet and the combustion chamber is shown in Fig. 3 and 4. At low Mach numbers, the critical cross-section area of the inlet diffusor is less than the cross-section area at the throat. Without any combustion one obtains thermal blocking at the throat (point A at Fig. 2).

Increasing the flight Mach number decreases the critical cross-section area of the inlet diffusor. So combustion cannot satisfy the fixed geometry requirement. This happens at about Ma=4. The total pressure curve with loss in Fig. 3 shows a maximum at about Ma=4. From Ma= 4 increasing the Mach number decreases the total pressure and increases the critical cross-section area of the inlet diffusor. The fuel mass flow decreases, temperatures decrease as in Fig. 4, passes the temperature limit (point C at Fig. 2), and finally no more combustion or fuel mass flow can take place at Ma=4.6. Here the critical cross section area becomes equal to that of the throat.

3. DESIGN PROCEDURE OF AN OPTIMUM RAMJET-ROCKET COMBINATION SYSTEM (DUCTED ROCKET) FOR A GIVEN FLIGHT SITUATION AND GIVEN BOUNDARY CONDITIONS

Specific Impulse I_S and Thrust Density D_F are the most important design-values of a ramjet engine beside its specific weight (weight per unit of thrust). Modern missile requirements tend towards high flight Mach numbers and long ranges. The pure ramjet does not necessarily fullfill the thrust requirements for high speed missiles at low altitudes. The combination with the rocket cycle can but does not always improve thrust with a penalty in I_S. To define the optimum propulsion system of this family the whole spectrum of the pure rocket over the ramjet-rockets to the pure ramjet has to be considered. For example a propulsion system of this type for a cheap target drone shall be designed for a sea level mission at Ma=2.5. Five different rocket gas generators have been combined with the ramjet cycle and plotted over a wide range of air/gas - mixture ratios in Fig. 5. In this case red fuming nitric acid has been used as the rocket gas-generator`s oxydizer. The rocket gas-generators have a range of mixture ratios from stoichiometric (curve 1) to extreme fuel-rich (curve 5). This leads to a ramjet afterburner from pure mixing without secondary combustion to nearly all-secondary combustion like in a pure ramjet.

The other three cases are located in between the extreme ones as true combination systems (ducted rockets). Fig. 5 shows the characteristic values I_S and D_F over the secondary (ramjet) mixture ratio as the independent variable and the primary (rocket gas generator) mixture ratio as parameter. Additionally the primary and secondary combustion temperatures have been introduced as boundary conditions.

These four diagrams can be used as a rapid graphical design method for ducted rockets. For the example discussed here an estimated drag coefficient for the given constant flight situation and the requirement to launch the missile out of an existing launch tube with a given cross-section area leads to a minimally required $D_{F_{min}}$ =1.9 x 10^5 N/m^2 (Diagram I).

All curves below $D_{F_{min}}$ do not fullfill the thrust requirement. The projection of the limiting points of the curves 1 to 5 into Diagram II cuts off all I_s curve pieces with insufficient thrust (dotted lines). In this case here the ramjet-like curve 5 gives the best values in I_s with sufficient D_F. Projecting the limiting points into the temperature diagrams III and IV connects the I_s and D_F curves with the related combustion temperatures. A chosen temperature limitation in the secondary combustor (ramjet) of 1000 K cuts off most of the solid lines in Diagram III. Only curve 1 (stoichiometric rocket gasgenerator) and curve 3 are left. A further temperature limitation of 2200 K in the primary combustor (rocket gas generator) finally leaves only curve 3 in Diagram IV with an OX/f = 2.47 ratio which fullfills all requirements. A ratio of a/f=28 leads to an optimal I_s value. This gives a relatively well defined set of preliminary design values for that engine. Yet in practice one would increase the limiting temperature in this case here in the secondary combustor to 1100 K in order to make use of the twofold I_s of curve 1 (ramjet-like system) compared to curve 3 (ducted rocket). This requirement is an additional result of that graphical short analysis.

4. BEHAVIOUR OF A RAMJET AT DIFFERENT FLIGHT SITUATIONS

Similar to the case of the chapter before a pure ramjet engine shall be designed for several different flight situations and for a pregiven minimal Thrust Density $D_{F_{min}}$. Considering four flight situations (altitude 0 km - Ma 1.9, alt. 3 km - Ma 1.8, alt. 6 km - Ma 1.7, alt. 10 km - Ma 1.6) there is a typical behaviour of D_F and I_s. The on-design behaviour is plotted in Fig. 6 and 7 with the according minimum thrust requirements.

The curves of the Specific Impulse for the four situations are overlapping. Only at high excess air the curves are spreading, where two opposite trends exist: higher altitude increases the Specific Impulse values, but lower Mach numbers decrease them. So with the given high Mach numbers at low altitudes no specific trend of the Specific Impulse values can be predicted. In addition at high excess air a maximum of the curve may exist. Yet the Specific Impulse at lower excess air, where the thrust requirements are fullfilled, is much lower.

As in the chapter before the basic design consideration has been made in the diagram for D_F (Fig. 6) rather than in the diagram for I_s (Fig. 7). High flight Mach numbers and low altitudes increase the D_F values. In addition to these flight situations excess air leads to a rapid increase of D_F. Flight situations with lower thrust values need much more fuel for the same increase of D_F. At the $D_{F_{min}}$ line the flight siuation with the highest altitude and the lowest Mach number requires stoichiometric combustion. At higher altitude and lower Mach numbers the $D_{F_{min}}$ requirements cannot be satisfied at all.

5. VARIATION OF SOME ENGINE PARAMETERS AT CONSTANT FLIGHT SITUATION

The examples discussed before of possible ramjet and ramrocket resp. ducted rocket designs show that the behaviour of the Specific Impulse and of the Thrust Density cannot be predicted by experience. This is due to the coupling of all effective parameters like pressure and mixture ratio in the primary rocket gas generator, cross-section area ratio and mixture ratio in the secondary ramjet combustor. Thus, decreasing D_F values are not coupled with increasing I_s values and vice versa. Generally, ramrocket resp. ducted rocket propulsion does not necessarily deliver higher D_F and lower I_s values than pure ramjet propulsion. For a flight situation like Mach=0.8 at sea level the four parameters just mentioned have been varied.

- Pressure in the rocket gas generator. This parameter has only a small influence on I_s and D_F. An increase of the pressure increases I_s and D_F slightly. The gradient is less at higher pressure. But, at this subsonic flight situation, a high pressure is essential for supersonic nozzle exhaust. The pure ramjet of course cannot run with supersonic exhaust at this subsonic flight situation.
- Mixture ratio in the rocket gas generator. Increasing mixture ratio decreases D_F slightly. I_s has a flat maximum at equivalence ratio=2. This relations are shown in Fig. 8 for fixed values of the other parameters. The maximum I_s occurs because of the optimum share at this case of chemical energy and kinetic energy from the rocket gas generator. The ramjet combustion chamber cross-section area ratio is $f_1=4$ and air/fuel ratio is $a/f=1$.
- Cross-section area ratio of the ramjet combustion chamber f_1. A small value of f_1 permits only little energy supply, e.g. values of $f_1=1$ are only applicable for those ramrocket (ducted rocket) propulsion systems with only little secondary combustion. On the other hand higher values of f_1 are only applicable with sufficient energy supply. In all considered variations of the parameters there is a maximum for I_s and D_F at $f_1=4$.
- Air/fuel mixture ratio at the ramjet combustor, shown in Fig. 9 and 10. For pure ramjets an increase of the air/fuel mixture ratio increases I_s. Under certain circumstances a maximum of I_s can occur. D_F decreases slightly. For ramrocket (ducted rocket) propulsion systems an increase of the air/fuel mixture ratio increases I_s. These values start at a higher level than the value of the pure ramjet, but are quite lower at higher air/fuel mixture ratios. The values for D_F are rather high at low air/fuel mixture ratios. They decrease rapidly with increasing air/fuel mixture ratios down to the lower level of the pure ramjet.

An additional variation of altitude and flight Mach number can considerably change these interactions. Also it can be seen, that even at this extreme low flight situation at Ma=0.8 for the use of a ramjet propulsion system, there are cases at which the operation of a pure ramjet can lead to better I_s and D_F values than competitive ramrockets. However supersonic exhaust at subsonic flight can generally not be obtained with the pure ramjet, but partly with the ramrocket.

6. OFF-DESIGN BEHAVIOUR

First I_s and D_F at on-design conditions and variable altitude are shown in Fig. 11. The relations are similar to those discussed in chapter 4 and shown in Fig. 6 and 7. However the flight Mach number is constant here. The parameter is the air/fuel mixture ratio. As can be expected the I_s values are higher and the D_F values are lower for the higher air/fuel mixture ratios. Therefore the maximum I_s values might not be useful because of the related low D_F values. The gradient of the D_F values is extreme at low air/fuel mixture ratios. At low air/fuel mixture ratios the I_s values are nearly constant. Fig. 11 shows purely on-design-values for I_s and D_F which generally decrease at off-design condition. The choice of the design-point has to consider this. Next Fig. 12 and 13 show the off-design behaviour for at two different design points with an individual internal geometry each:

- Design point at sea level, flight Mach number Ma=3, Mach number at the combustion chamber entrance =0.207, cross-section area ratio of the combustion chamber is $f_1=1.1544$ and cross-section area ratio of throat/combustion chamber exit $f_3=0.8$. The relatively high flight Mach number of 3 for the design point leads to sufficient values at lower off-design Mach numbers. The lower fuel supply in this case also lowers D_F. The I_s values even run through a maximum at about Mach=2. At the left end of the curve, the values for I_s and D_F might still be applicable.
- Design point at sea level, flight Mach number Ma=2, Mach number at the combustion

chamber entrance = 0.415, cross-section area ratio of the combustion chamber f_1=1, and cross-section area ratio of throat/combustion chamber exit f_3=0.8. The low on-design Mach number of 2 lowers the fuel supply, I_s and D_F rapidly at off-design conditions. No maximum exists for I_s. D_F is at an extreme low level. The possible fuel supply is much less than in the first case. A design point at the disadvantageous low flight Mach number of Ma=2 leads to a corresponding disadvantageous internal geometry which limits the fuel supply at lower off-design Mach numbers. Not discussed here are cases in which the off-design Mach numbers are higher than the on-design Mach number. These cases are presently under investigation and will be presented later. The results can be expected to be similar to these of chapter 2 where a fixed geometry with variable mixture-ratios and flight Mach numbers have been investigated.

7. CONCLUSION

Ramjet propulsion systems cannot be discussed with respect to their Specific Impulse only. Thrust per unit cross-section is an equally important qualification quantity which has an adverse slope with respect to mixture ratio. A further degree of freedom for design develops out of the integration of a rocket gas generator (ducted rocket). All internal design parameters (mixture ratios, geometries, pressures, temperature limitations) have to be thoroughfully weighted against each other. A variation of all important design parameters allow optimal use of the engine's capability. Prefixed parameters can restrict the performance drastically.

8. REFERENCES

(1) Peter A. Kramer, Rolf D. Bühler:
Integrated Turbo-Ramjet-Rocket Performance
Potential - Project ITUSTRA
3rd International Symposium on Air Breathing Engines,
München, Germany, March 7 - 12, 1976
ICAS - DGLR Paper No. 76 - 045

(2) Peter A. Kramer, Rolf D. Bühler:
Hybrid Rocket/Airbreathing Propulsion for Ballistic Space Transportation
Journal of Spacecraft and Rockets, Vol. 17, No. 4, July - Aug. 1980
AIAA Paper No. 79 - 7038 R

(3) Peter A. Kramer, Rolf D. Bühler:
Air Breathing Booster Stages for Space Transpoters Compared with Pure Rocket Systems
XXXth International Astronautical Congress,
München, Germany, Sept. 17 - 22, 1979
IAF Paper No. 79 - 09

(4) I.D.V. Faro:
Supersonic Inlets
AGARDograph No. 102, 1965

(5) Hans G. Münzberg:
Flugantriebe
Springer Verlag, Berlin, Heidelberg, New York, 1972, p. 157

(6) Egbert Riester:
Die Anwendung von Staustrahl-Raketen bei Flugkörpern in großen Höhen
Deutsche Froschungs- und Versuchsanstalt für Luft- und Raumfahrt,
Institut für Chemische Antriebe und Verfahrenstechnik,
Braunschweig, 1977, DLR-FB 77 - 47

(7) S. Gordon, B. J. McBride:
Computer Program for Calculation of Complex Chemical Equilibrium
Compositions, Rocket-Performance, Incident and Reflected Shocks
and Chapman-Jouget Detonations
NASA SP -273, 1971

ACKNOWLEDGEMENT

This work has been sponsored by the German Ministry of Defense, department RÜ Fo 4.

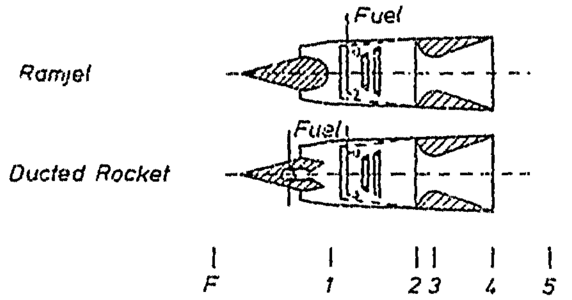
Fuel
Ramjet
Fuel
Ducted Rocket
F
1
2 3
4
5

Fig. 1 Stations of ramjet and ramrocket (ducted rocket)

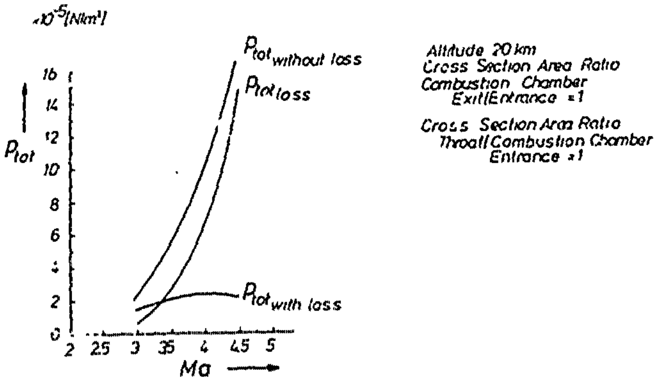

Fig. 3 Total Pressure at the end of the inlet diffusor

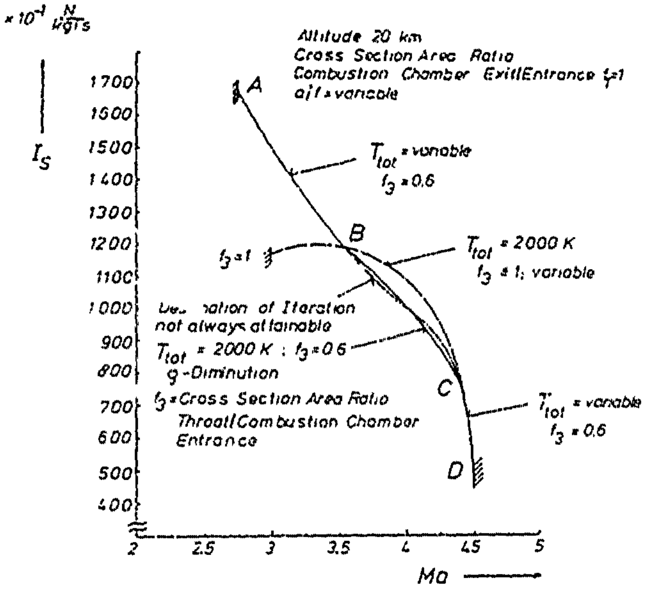

Fig. 2 Specific Impuls versus flight Mach number with fixed geometry, variable air/fuel mixture ratio, and/or limitation of the temperature

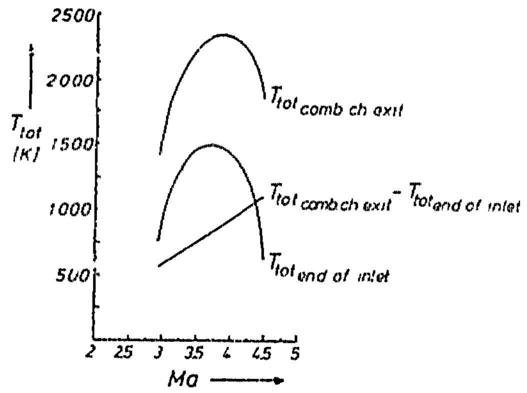

Fig. 4 Total temperatures at the ends of the inlet diffusor and the combustion chamber

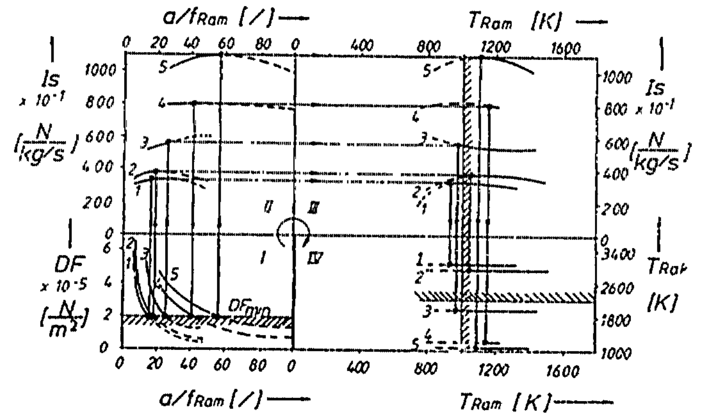

Fig. 5 Rapid graphical design method for ramjets and ducted rockets at a given flight situation.
Sea level altitude, Ma = 2.5.
Mixture ratios in the primary (rocket) combustor:

1 OX/f = 5.4 (stoich.)
2 OX/f = 4.2
3 OX/f = 2.47
4 OX/f = 1.2
5 OX/f = 0.6

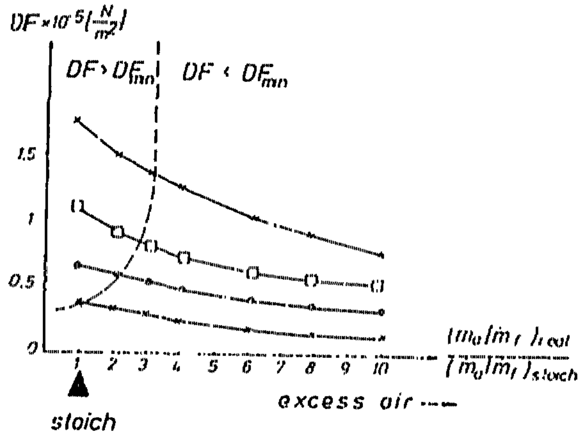

Fig. 6 Thrust Density of a pure ramjet versus fuel/air mixture ratio for several flight situations

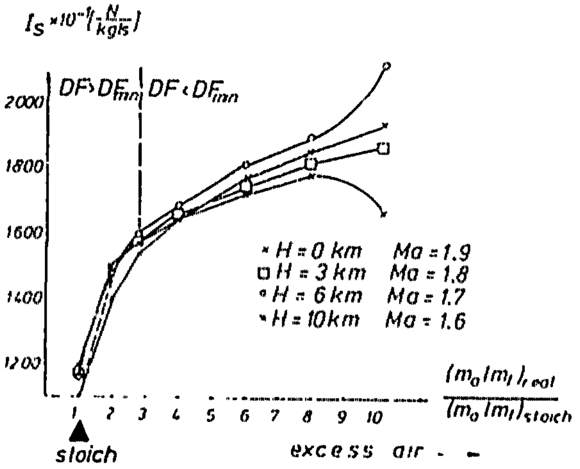

Fig. 7 Specific Impuls of a pure ramjet versus fuel/air mixture ratio for several flight situations

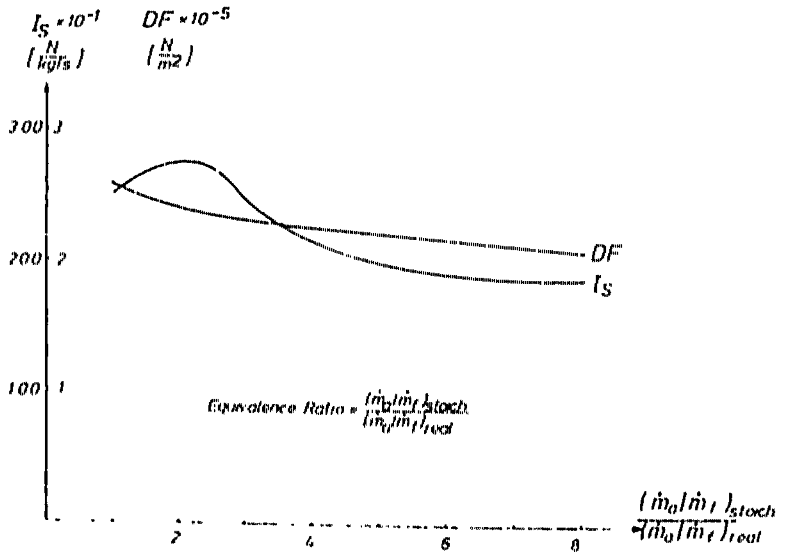

Fig. 8 Specific Impuls and Thrust Density versus ratio in the rocket gas generator of a ducted rocket.
Cross-section area ratio of the ramjet combustion chamber $f_1 = 4$, air/fuel mixture ratio at the ramjet combustor of 1
Propellant: RP-1, Oxidizer in the rocket gas generator: N_2O_4
Sea level altitude, Ma = 0.8

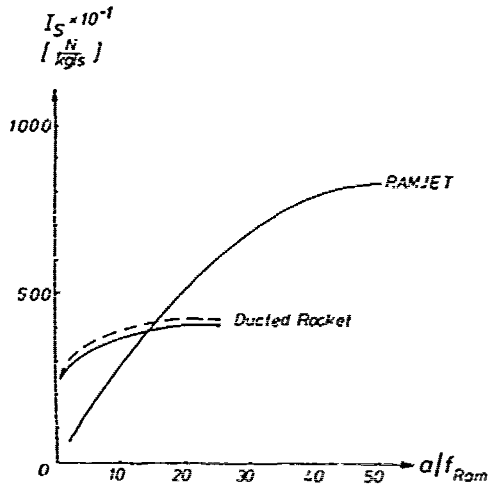

Fig. 9 Specific Impuls versus air/fuel mixture ratio at the secondary (ramjet) combustion chamber.

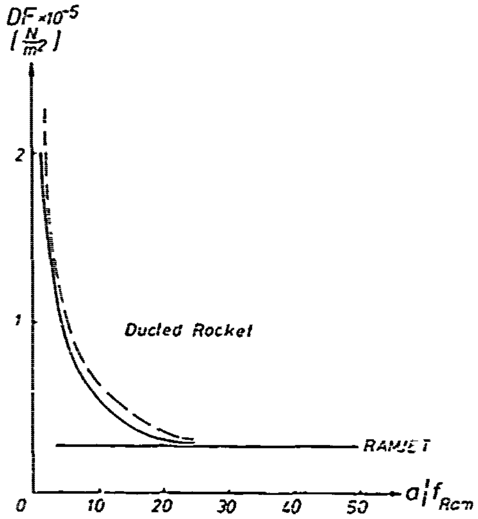

Fig. 10 Thrust Density versus air/fuel mixture ratio at the secondary (ramjet) combustion chamber.

Cross-section area ratio of the ramjet combustor exit/entrance f_1 = 4

Ducted rocket with equivalence ratios of 4 and 2 (dashed line),

oxidizer: N_2O_4

Sea level altitude, Ma = 0.8

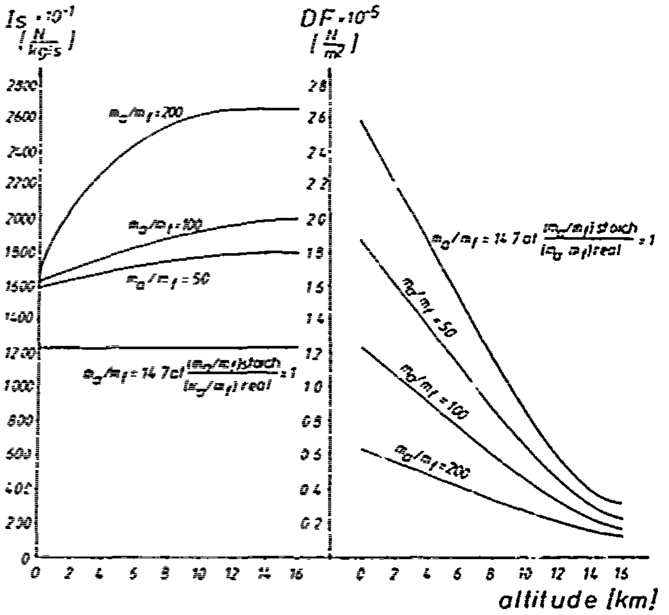

Fig. 11 Specific Impuls and Thrust Density versus altitude for various air/fuel mixture ratios. Ma = 2

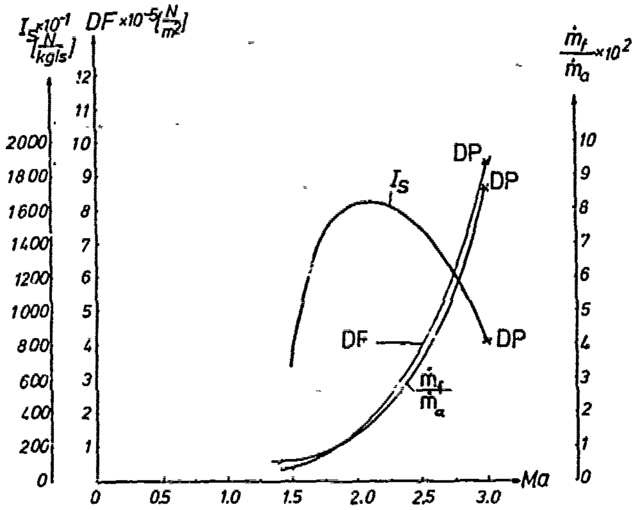

Fig. 12 Off-design performance:
Design point at Ma = 3, sea level altitude
Specific Impuls, Thrust Density and fuel/air
mixture ratio versus off-design flight Mach
number

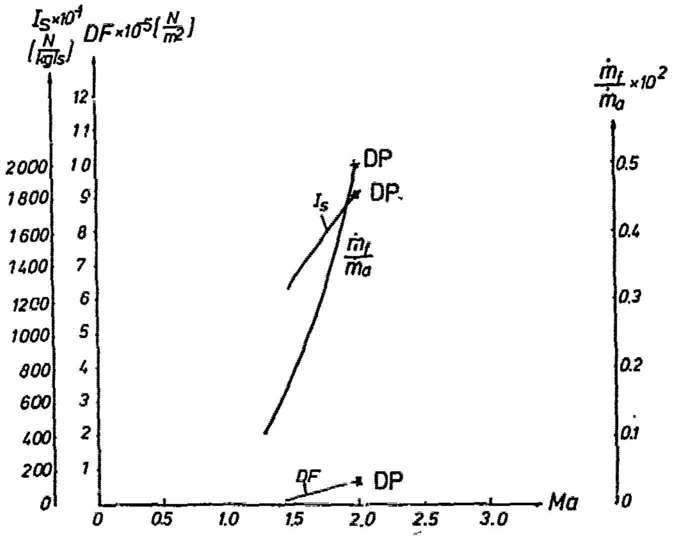

Fig. 13 Off-design performance:
Design point at Ma = 2, sea level altitude
Specific Impuls, Thrust Density and fuel/air
ratio versus off-design flight Mach number

DISCUSSION

R.Marguet

Quel est le domaine d'utilisation pour les cycles que vous envisagez?

Author's Reply

The applications are mainly for target drones and low altitude, high Mach number ramjets.

VALVELESS PULSEJETS AND ALLIED DEVICES FOR LOW THRUST, SUBSONIC, PROPULSION APPLICATIONS

10-1

J.A.C. Kentfield, Professor
Department of Mechanical Engineering
The University of Calgary, Calgary, Alberta
Canada
T2N 1N4

SUMMARY

A review is presented of predicted flight performances, based on well established static test-stand data, of current technology valveless pulsejets and comparisons are made with alternative forms of propulsion suitable for small, subsonic, vehicles. It is shown that valveless pulsejets have some performance advantages over other forms of propulsion for short-range missions requiring low thrust levels of less than about 600 Newtons (≈ 130 lbf). The advantages of valveless pulsejets in terms of simplicity when compared with other propulsion systems are also shown to be substantial.

Possible ways of improving pulsejet performance are discussed. The systems considered involve means for obtaining improved precombustion charge compression using twin alternately-firing pulsed combustors and more sophisticated units incorporating dynamic pressure-exchangers.

1. INTRODUCTION

Whilst the writer is of the opinion that the best and most generally useful application, in the field of flight propulsion, for valveless pulsed combustors lies in pressure-gain combustion systems for otherwise conventional gas turbine engines, there appears to be a potential for rather restrictive, and selective, applications in which pulsed combustors, or more specifically pulsejets, are used in their traditional role as thrust producers. The prime motivation for incorporating a pressure-gain combustor in a gas turbine is to generate an increase of stagnation pressure, across the combustion system, in addition to providing the temperature rise associated with the conventional steady flow combustor for which the pressure-gain combustor is substituted. It appears that Reynst was the first to suggest this application of valveless pulsed combustors (1). Recent work (2,3) has shown that a 6% stagnation pressure rise can be achieved at a stagnation temperature ratio of 2.5:1, under laboratory conditions, using a small [2.875 in (73 mm) combustion zone internal diameter] valveless pulsed combustor. There is a promise of greater pressure gains from larger units.

The use of a pulsejet as a thrust producer is in some respects a type of application which is easier to implement than a gas turbine pressure-gain combustor because the pulsejet does not have to be integrated with turbo-machinery. However, the desirability or otherwise of pulsejets as a propulsion device clearly depends upon their performance characteristics compared with those of alternative propulsion systems. The general proportions of a highly rated valveless pulsejet developed by the French company SNECMA and further improved by Lockwood (4) are shown in Fig. 1 (a). The device consists of a short inlet duct leading into a short, enlarged diameter, combustion zone connected at its far end to a long divergent tailpipe. A shorter multiple inlet version developed under the writer's direction appears in Fig. 1 (b). The essential philosophy of the multiple inlet concept is to reduce, in approximate proportion to the reduction of length, the time required for the mixing of air, fuel and residual products of combustion. This is accomplished by reducing the representative path length, proportional to the inlet diameter, which particles of air, fuel and residual products must traverse during the mixing process. This concept is described in more detail elsewhere (3,5).

An inherent problem when working with pulsed combustors, is that of predicting, and consequently obtaining a detailed understanding of, the non-steady flow events occurring internally. For highly rated pulsejets potentially suitable for propulsion application it is virtually essential to use a method-of-characteristics type theoretical treatment. However application of the method to pulsejets presents a number of problems associated, primarily, with the difficulty of modelling the combustion process in a satisfactory manner.

The performance prediction technique and other aspects of pulsejet design, operation and performance will now be considered.

2. THEORETICAL TREATMENT

The method-of-characteristics involves, in effect, solving simultaneously the equations for continuity, energy and momentum in a time dependent flow field. The appropriate differential equations are of the hyperbolic type. Details of the procedure can be found in many texts on compressible fluid flow.

The earliest solution obtained at The University of Calgary, due to Marzouk (6), was the result of a manual calculation for a cold-flow simulation of a very simple configuration featuring an inlet and outlet of uniform cross-sectional area. The solution, in the form of a wave diagram, was used to check a computerized representation of the cold flow model. The numerical technique employed for handling the forward (time) stepping procedure was that known as the Hartree backward difference technique. A description of the cold flow model, including the boundary conditions used, has been given by Marzouk (6).

The next step, in order to advance beyond a cold-flow model, was to model the combustion process itself and combine such a model with a hot-flow method-of-characteristics representation of the tailpipe and inlet flows. Attempts were made to represent the combustion process using various overall reaction rate type models but these did not yield realistic rates of pressure rise corresponding to those measured experimentally. Accordingly, it was finally decided to represent the combustion process by an empirical heat-release rate model the heat-release rate varying during the combustion process. A usable model of this type was derived by M. Rehman (7) and later incorporated in a hot-flow type method-of-characteristics computer programme by Cronje (8). In Cronje's model the heat released during the entire combustion process was made proportional to the mass of air inhaled into the combustion zone during the introduction process. A typical result, due to Cronje, for a configuration with a tapered inlet and tailpipe is shown in Fig. 2. The pressure-time trace of Fig. 2 agrees very closely both in magnitude and duration with experimentally obtained traces.

It can be said that further work is needed in order to model, correctly, the combustion process. A successful and generally applicable model of the combustion process should, ideally, then permit valveless pulsed combustors to be designed, and their geometry optimized, by use of numerical procedures only. Nevertheless, at this stage it appears, on the basis of Cronje's theoretical work (8), that the SNECMA/Lockwood configuration is an optimum one as attempts to evolve a configuration having a superior performance, by modifying the parameters defining the geometry of the numerical model were unsuccessful (6,8).

From the plot, on Fig. 2, of dimensionless velocity (local gas velocity divided by the acoustic velocity at ambient conditions) for the inlet flow it is apparent that a substantial backflow occurs, as indicated by the negative value of U, from the open end of the inlet. This, of course, gives rise to a transient reverse thrust unless this backflow is rectified, or redirected in a rearwards direction.

3. FLOW RECTIFICATION

There are at least three possible ways of handling the backflow from the inlet of a valveless pulsed combustor. One possibility is to use an intake flow passage offering a high resistance to backflow but a low resistance to inflow. Devices of this type, usually known as fluidic diodes, have the disadvantage of introducing strong irreversibilities into the flow system. Another, more attractive, possibility is to employ a rearward facing, inlet (or inlets). On the basis of flow visualisation evidence (2,9) this concept can result in poor mixing in the combustion zone when the inlets are attached to the same end wall of the combustion zone as the tailpipe. When this latter problem is avoided a very good performance can be obtained as evidenced by the SNECMA Ecrevisse (Crayfish) pulsejet unit although induction problems can arise if a suitable engine cowling is not used (10).

The third solution is to employ a flow rectifier, a "heavy current" fluidic device, which redirects rearwards backflow from a forward facing inlet whilst offering minimum interference to inflow. Two types of rectifier are shown; one is illustrated in Fig. 3, the other in Fig. 4. The earlier device, known as an auxiliary passage flow rectifier, shown in Fig. 3, relied upon a combination of Coanda effect and a gas curtain to deflect backflow (indicated by the arrows in the upper portion of Fig. 3) into a return bend. During induction flow passes more or less directly into the pulsed combustor (or pulsejet) intake as indicated in the lower portion of Fig. 3. The concept works, so far as can be established, perfectly in the sense that there is no backflow from the air inle . Simplified single outlet asymmetric versions of this device were also developed which were equally effective in inhibiting backflow from the air inlet.

Unfortunately the presence of a rectifier of the auxiliary passage type serves to reduce substantially the thrust producing performance of highly rated pulsed combustors to which it is fitted. It appears that this problem is due to the intimate coupling, within the rectifier, of the inflow and outflow passages.

Figure 4 shows the most successful of the rectifier concepts tried. This is, in essence, a venturi type non-steady flow thrust augmenter of the kind pioneered by SNECMA and Lockwood (11) but bent around into a U shape so that the backflow entrains air from the inlet into the convergent-divergent return bend (12,1). The virtues of this arrangement are that the return bend portion of the device is uncoupled from the pulsed combustor inlet and the additional air entrained actually results in a small thrust augmentation; the thrust increase more than offsets the losses due to turning the flow through 180°. As with the earlier device there was no detectable backflow from the inlet ports

Figure 5 shows the performances obtained by regulating the fuel inflow rate of a propane fuelled 2.875 in (73 mm) diameter SNECMA/Lockwood type pulsejet tested statically with two versions, an early and also a more advanced form, of the auxiliary passage flow rectifier shown in Fig. 3. Figure 5 also shows results obtained with the thrust augmenting type rectifier of Fig. 4. The result for the "no rectifier" case was achieved by simply adding the opposing thrusts, as measured using thrust plates, due to the tailpipe flow and backflow from the inlet. It should be noted that all the results shown in Fig. 5 were obtained at a test site located 3600 ft (1096 m) above sea level; the test results were not corrected to compensate for altitude.

4. FUEL SYSTEMS AND AUXILIARIES

Gaseous or liquid fuels are usually injected, under pressure, into either the inlet duct or the combustion zone of pulsejets from either a single injector or a series of injectors. A system of this type implies that either a pressure-pump is available or a pressurised fuel tank is employed. The latter arrangement has obvious advantages from the viewpoint of simplicity. The only other auxiliary equipment needed is an ignition system and an air jet to initiate flow through the combustor. Since both the ignition system and the air jet are used only at start-up they do not have to be carried in the flight vehicle.

Figure 6 shows a relatively sophisticated alternative fuel system, suitable for gasoline or kerosene type fuels, featuring a carburetor and hence not requiring a pressurised fuel tank. The system shown was actually designed for a high intensity hand held space-heater (14). The fuel is pumped from the tank to the carburetor by means of a pressure-pulse actuated diaphragm pump. The pressure pulses are derived from the pulsejet itself. The remaining items are not required once the engine has started and do not, therefore, have to be carried onboard the flight vehicle. A developed version of the system illustrated in Fig. 6 has now been operational for several years in connection with the space-heater application. The pulsejet unit of the space-heater is of the single inlet SNECMA/Lockwood type and has a combustion zone diameter of 3" (76 mm).

5. INFLUENCE OF PULSEJET SIZE ON SPECIFIC PERFORMANCE

During the course of the work reported here the writer became increasingly concerned about possible influences of unit size or scale (15). Normally, in order to avoid fuel handling and storage problems and also problems due to thermally overloading the laboratory environmental-control system, experiments were preferentially restricted to maximum thermal outputs in the region of 500 x 10³ Btu/h (≈ 150 kW). Outputs of this magnitude are achieved quite easily with highly rated valveless pulsejets of about 3 in (≈ 76 mm) diameter. Accordingly, a special study was carried out to establish the influences of scale on the specific performance of valveless pulsejets. The results of this study have been reported in full by A. Rehman (16).

The essential findings of the work directed at establishing the influence of size on the performance of pulsejets are displayed in Figs. 7 and 8. Figure 7 shows plots of specific thrust versus combustion zone diameter for three types of valveless pulsejet. The upper curve relates to units of the SNECMA/Lockwood type using propane fuel or gasoline fuel supplied under pressure. The intermediate curve is for SNECMA/Lockwood type pulsejets equipped with a carburetor in the inlet tract and fuelled by gasoline. The lowest curve applies to propane or butane fuelled pulsejets manufactured by the Thermo-Jet company. The information relating to these units was obtained from the literature (17). Information corresponding to that of Fig. 7, but relating to the specific fuel consumption of the units, is displayed in Fig. 8. The superficial implication of Figs. 7 and 8 is that the specific performance of most highly rated valveless pulsejets appears to increase with increasing combustion zone diameter. In fact an empirical relationship which serves to correlate the thrust performance appears in Fig. 7; θ of that relationship is the maximum specific thrust. More detailed consideration of the reasons for the observed behaviour indicate that the basic feature is that the relative significance of friction losses decreases with increasing Reynolds number. Less importantly, the relative significance of heat loss decreases with increasing combustor size. Hence, large valveless pulsejets tend to have better specific performances than small ones. The whole matter is discussed in much more detail elsewhere (3,16).

6. PERFORMANCE EXPECTATIONS

Based on data displayed in Figs. 7 and 8 augmented by additional information obtained from design [illegible]es, the characteristics are presented in Table 1 of a family of single inlet SNEC[illegible]wood type pulsejets equipped with flow rectifiers of the kind shown in Fig. 4. Th[illegible]ture and location of the shroud duct referred to in Table 1 are illustrated in Fig. 9.

Table 2 presents corresponding information to that of Table 1 but for shorter four-inlet type pulsejets. It is noteworthy that the specific weight of the four-inlet type actually exceeds that of the single inlet variety due to the lower specific thrust obtainable. It is probable that more than four inlets will be optimal for units larger than 3 in (76 mm) combustion zone diameter. Experiments show that 4 inlets is the maximum practical number for the 3 in (76 mm) diameter machine. Hypothesising with the number of inlets results in the information presented in Table 3. The latter table should be interpreted as conjecture somewhat guided by experiment.

The thrust-to-weight ratio quoted in the three tables are regarded as conservative and are representative of values which should be achievable with fairly long life units which may, for example, be suitable for, say, recoverable, and reusable, target drones. For some applications the great length of the single inlet concept may actually be advan-

10-4

TABLE 1

SINGLE-INLET TYPE PULSEJETS

DIMENSIONS		MAX. S.L.S. THRUST lb$_f$ (N)	S.F.C. AT MAX THRUST lb$_m$/lb$_f$h (kg/N.h)	MIN. S.F.C. lb$_m$/lb$_f$h (kg/N.h)	THRUST: WEIGHT RATIO (ESTIMATED)		MAX THRUST /$\frac{\pi}{4}$D² lb$_f$/in² (kn/m²)	MAX THRUST /L lb$_f$/ft (N/m)
COMBUSTOR INT. DIA D in (mm)	OVERALL LENGTH L in (mm)				WITH SHROUD DUCT	NO SHROUD DUCT		
3 (76)	54.5 (1385)	14.2 (63)	2.6 (0.265)	2.6 (0.265)	2.6	4.0	2.01 (13.82)	3.13 (45.8)
6 (152)	109.0 (2760)	82.0 (364)	2.1 (0.214)	2.1 (0.214)	3.6	5.7	2.91 (20.02)	9.03 (132.5)
9 (228)	163.5 (4140)	219.0 (970)	1.8 (0.184)	1.8 (0.184)	3.4	5.4	3.44 (23.70)	16.07 (235.0)

TABLE 2

FOUR-INLET PULSEJET CONFIGURATIONS

DIMENSIONS		MAX. S.L.S. THRUST lb$_f$ (N)	S.F.C. AT MAX THRUST lb$_m$/lb$_f$h (kg/N.h)	MIN. S.F.C. lb$_m$/lb$_f$h (kg/N.h)	THRUST: WEIGHT RATIO (ESTIMATED)		MAX THRUST /$\frac{\pi}{4}$D² lb$_f$/in² (kn/m²)	MAX THRUST /L lb$_f$/ft (N/m)
COMBUSTOR INT. DIA D in (mm)	OVERALL LENGTH L in (mm)				WITH SHROUD DUCT	NO SHROUD DUCT		
3 (76)	42.0 (1062)	9.5 (42.3)	2.2 (0.217)	1.8 (0.184)	2.0	2.8	1.34 (9.23)	2.71 (39.9)
6 (152)	84.0 (2130)	68.0 (303)	2.0 (0.204)	1.6 (0.163)	3.4	4.9	2.41 (16.60)	9.71 (142.3)
9 (228)	126.0 (3200)	171.0 (760)	1.7 (0.174)	1.4 (0.143)	3.1	4.4	2.69 (18.55)	16.29 (239.0)

TABLE 3

MULTIPLE-INLET PULSEJET CONFIGURATIONS

DIMENSIONS			MAX. S.L.S. THRUST lb$_f$ (N)	S.F.C. AT MAX THRUST lb$_m$/lb$_f$h (kg/N.h)	MIN. S.F.C. lb$_m$/lb$_f$h (kg/N.h)	THRUST: WEIGHT RATIO (ESTIMATED)		MAX THRUST /$\frac{\pi}{4}$D² lb$_f$/in² (kn/m²)	MAX THRUST /L lb$_f$/ft (N/m)
COMBUSTOR INT. DIA D & NO. OF INLETS		OVERALL LENGTH L							
in (mm)	NO. OF INLETS	in (mm)				WITH SHROUD DUCT	NO SHROUD DUCT		
3 (76)	4	42.0 (1062)	9.5 (42.3)	2.2 (0.217)	1.8 (0.184)	2.0	2.8	1.34 (9.23)	2.71 (39.9)
6 (152)	6	66.6 (1740)	68.0 (303)	2.0 (0.204)	1.6 (0.163)	4.8	6.6	2.41 (16.60)	11.90 (174.0)
9 (228)	8	89.1 (2260)	171.0 (760)	1.7 (0.174)	1.4 (0.143)	4.9	6.4	2.69 (18.55)	23.04 (326.0)

tageous if, for example, the pulsejet tailpipe is also used as a tail support structure in a very simple vehicle. The shroud duct should be useful in minimising side view radiation from the hot section of the engine. It may also be possible to achieve a useful measure of ramjet assistance, and drag reduction, under flight conditions.

7. COMPARISON WITH ALTERNATIVE PROPULSION PLANT

The single-inlet pulsejets of Table 1 have been compared with conventional gas-turbine turbojet and turbofan units. Data for the gas turbines were obtained from the literature (18). Turbojets and turbofans intended purely for lift purposes were omitted from the comparison although derivatives of these types intended for a thrust boosting function were included.

Figure 10 presents plots of thrust per unit frontal area versus sea level (static) thrust for static engine operation. It can be seen from this figure that pulsejets are only competitive for very low thrusts which are generally applicable to unmanned vehicles such as drones of various types. The corresponding specific fuel consumption relationship under static conditions is presented in Fig. 11. Here pulsejets are not really competitive although it will later be shown that forward flight can result in a significant reduction in the specific fuel consumption of carefully installed pulsejets. Nevertheless, the implication of Fig. 11, other considerations aside, is that if a pulsejet is selected preferentially it is only likely to be an acceptable unit for short range missions.

Figure 12 shows that the uninstalled thrust-to-weight ratio of valveless pulsejets appears to be quite competitive at very low thrust levels. It may be possible, with a more sophisticated, but probably more expensive, design approach than that selected by the writer to move the maxima of curves 2 and 3 further to the right.

An important characteristic of valveless pulsejets which is not apparent from any of three previous curves is simplicity and, as a consequence of this a potentially high reliability. Whilst highly rated valved pulsejets have earned a reputation for unreliability, due primarily to short flapper valve life, valveless pulsejets appear, on the basis of fairly extensive running experience, to be inherently reliable since, provided a pressurised fuel supply is used, there are no moving parts operating at engine frequency.

8. INFLUENCE OF FLIGHT MACH NUMBER

The influence of the flight Mach number on the performance of a pulsejet appears to depend very strongly on engine characteristics and the nature of the installation. Figure 13 shows the influence of flight Mach number on the net thrust and specific fuel consumption of a basic valveless pulsejet intended primarily for educational purposes. The unit, which is equipped with an auxiliary passage flow rectifier (Fig. 3) is "streamlined" only in the vicinity of the flow rectifier. The installation is thus of the simplest kind. Furthermore the engine, which is of 6 in (152 mm) combustion zone diameter, has a static thrust rating of only approximately 10% of that of the highly rated unit of equal diameter listed in Table 1. Hence it would be expected that the educational pulsejet would be relatively sensitive to drag and other influences of the free stream. The solid lines in Fig. 13 show the performance as measured under simulated flight conditions. The dotted curves were obtained as a result of attempting to correct for external drag and hence establish the true engine performance. The relatively significant increase in net thrust with flight speed is thought to be due to improved breathing due to forward speed. It seems reasonable to expect this effect to be less significant for more highly rated valveless pulsejets installed in such a simple way. The performance peak, apparent in Fig. 13, would, presumably, also occur at a higher subsonic Mach number with a more highly rated unit.

If Fig. 13 is regarded as one extreme featuring a very modestly rated unit installed in a very elementary way, Fig. 14 can be thought of as at the opposite end of the spectrum. These data, due to SNECMA (10), are for simulated flight up to a Mach number of 0.8 obtained with a very carefully packaged Écrevisse unit. A unit of this type was subsequently flown, in a drone type aircraft powered only by the pulsejet, at a Mach number of 0.85. The reasons for the large gains in performance at high subsonic Mach numbers apparent in Fig. 13 are presumably due to a combination of improved breathing, increased intake density, a bonus due to a subsonic ramjet effect superimposed on the pulsejet cycle. It is worth noting that the gains in performance presented in Fig. 14 are such as to make the Ecrevisse valveless pulsejet highly competitive, from a performance viewpoint, with many turbojets at high subsonic Mach numbers.

When a valveless pulsejet is to be considered as an alternative to a piston engine driving a conventional propeller for applications in relatively low speed vehicles the low weight but high fuel consumption of the pulsejet renders it competitive on a take-off weight basis, only for short flights of about 20 - 30 minutes duration. The influence on performance of altitude will not be considered here since this matter is handled relatively easily by conventional analytical techniques.

9. POTENTIAL FOR PERFORMANCE IMPROVEMENT

The writer, and other workers, have gathered fairly convincing, but somewhat circumstantial evidence which shows that, at the condition of the maximum fuel flow extinction point, highly rated valveless pulsejets appear to be operating with a mean fuel:air ratio in the combustion zone of only about 50% of the stoichiometric value. If a way could be found to approach, more closely, a stoichiometric mixture strength a substantial increase in thrust should be obtainable for a specified frontal area and structural weight.

Another means by which an improved performance should be attainable relates to increasing the normally rather minimal pre-combustion charge compression. A possible approach is to employ two valveless pulsejets each arranged to supercharge the other mutually. Such an arrangement is currently undergoing testing. Antiphase operation has been achieved successfully, with an accompanying reduction of noise, however, mutual supercharge has not yet been obtained. Figure 15 is a diagrammatic illustration of the twin-coupled unit together with a schematic of a simplified wave diagram showing the gas-dynamic principles involved.

Proceeding to a yet higher degree of complexity it may, in some circumstances, be worth advancing to a propulsion unit, also utilising non-steady compressible flow, based on the dynamic pressure-exchanger concept. Here a cellular rotor, with open ended passages, runs between two closely mounted end plates as shown in Fig. 16 (a). By providing such a machine with suitably arranged inlet and outlet ducts a jet propulsion type unit, with either combustion within the cells or in an external combustor, can be contrived. If such a machine were to be developed it would probably be of use only at low thrust levels below the range of normal, reasonably efficient, turbo machines. A pressure-exchanger thrust producer could almost certainly be arranged to have a specific fuel consumption significantly superior to that of a pulsejet. A low thrust per unit frontal area would probably render pressure-exchanger jet thrusters non-competitive with turbo-machinery for thrust levels for which turbojets and turbofans are normally used. Figure 16 (b) shows, diagrammatically, the construction of a typical pressure-exchanger. Further background material on dynamic pressure-exchangers, explaining the principles involved, is available (19).

10. CONCLUSIONS

Experimentally obtained static performances have been presented of representative current technology valveless pulsejets and the performances of these units have been compared with those of alternative propulsors. It is concluded that current technology valveless pulsejets are best suited, in the subsonic regime, to applications where low initial cost, simplicity and reliability are of dominant importance.

It is further concluded, from a performance viewpoint, that valveless pulsejets are most competitive with conventional propulsion systems for applications up to (static) thrust levels of about 130 lb_f (= 600 N). The shorter the duration of the mission the stronger becomes the case for selecting a valveless pulsejet in preference to an alternative air-breathing system. However, it should be remembered that other workers (SNECMA) have succeeded in achieving a performance at high subsonic Mach numbers comparable with that of many turbojets.

11. REFERENCES

1. Thring, M.W., editor, "Pulsating Combustion, the Collected Works of F.H. Reynst", Pergamon Press Ltd., London, 1961, Chapter I.

2. Kentfield, J.A.C., Rehman, M. and Marzouk, E.S., "A Simple Pressure Gain Combustor for Gas Turbines", American Society of Mechanical Engineers, Journal of Engineering for Power, Vol. 99, No. 2, April 1977, pp. 153-158.

3. Kentfield, J.A.C., Rehman, A. and Cronje, J., "The Performance of Pressure-Gain Combustors Without Moving Parts", American Institute of Aeronautics and Astronautics, Journal of Energy, Vol. 4, No. 2, March-April 1980, pp. 56-63.

4. Lockwood, R.M., "Summary Report on Investigation on Miniature Valveless Pulsejets", Report No. ARD-307, Hiller Aircraft Company, Palo Alto, Calif., 1962.

5. Kentfield, J.A.C., "Progress Towards a Pressure-Generating Combustion Chamber for Gas Turbines", Proceedings First International Symposium on Pulsating Combustion, (D.J. Brown, ed.), University of Sheffield, England, Paper No. 11, 1971.

6. Marzouk, E.S., "A Theoretical and Experimental Investigation of Pulsed Pressure-Gain Combustion", Ph.D. Dissertation, University of Calgary, Calgary, Alberta, Canada, 1974.

7. Rehman, M., "A Study of a Multiple-Inlet Valveless Pulsed Combustor", Ph.D. Dissertation, University of Calgary, Calgary, Alberta, Canada, 1976.

8. Cronje, J.S., "An Experimental and Theoretical Study, Including Frictional and Heat Transfer Effects, of Pulsed Pressure-Gain Combustion", Ph.D. Dissertation, University of Calgary, Calgary, Alberta, Canada, 1979.

9. Kentfield, J.A.C., "The Flow Rectifier, A Fluidic Alternative to the Pulsed Combustor Non-Return Valve", Paper No. 18, Proceedings (D.J. Brown, Editor), First International Symposium on Pulsating Combustion, University of Sheffield, Department of Chemical Engineering and Fuel Technology, 1971.

10. Marchal, R. and Servanty, P., "Note sur le Développement des Pulso-Réacteurs Sans Clapets", CR. ATMA, 1963, pp. 611-633.

11. Lockwood, R.M., "Interim Summary Report on Investigation of the Process of Energy Transfer From an Intermittent Jet to Secondary Fluid in an Ejector-Type Thrust Augmenter", Report No. ARD-286, Hiller Aircraft Company, Palo Alto, Calif., 1961.

10-7

12. Kentfield, J.A.C., Marzouk, E.S. and Rehman, M., "An Airbreathing Pressure-Gain Combustor Without Moving Parts", Paper No. 137, 15th International Symposium on Combustion, Tokyo, Japan, Combustion Institute, 1974 (only extended abstract published).

13. Marzouk, E.S. and Kentfield, J.A.C., "Pressure-Gain Combustion, A Means of Improving the Efficiency of Thermal Plant", Proceedings 9th Intersociety Energy Conversion Engineering Conference, (published by the A.S.M.E.), San Francisco, Aug. 1974, pp. 1125-1131.

14. Kentfield, J.A.C., "A New Light-Weight Warm-Air Blower for Rapidly Pre-Heating Cold-Soaked Equipment", Paper presented at A.S.M.E. Winter Annual Meeting, Atlanta, Georgia, Nov. 1977, A.S.M.E. Paper No. 77-WA/HT-20.

15. Kentfield, J.A.C., "Pulsed Combustion: Promising Areas for Further Research", Paper Presented at the Technical Meeting of the Combustion Institute, Canadian Section, Banff, Alberta, Canada, May 1977.

16. Rehman, A., "A Theoretical and Experimental Study of the Effect of Size on Liquid Fuelled Carburetted Valveless Pulsed Combustors", M.Sc. Dissertation, University of Calgary, Calgary, Alberta, Canada, 1978.

17. Taylor, J.W.R., "Jane's All the World's Aircraft 1974-75, Jane's Yearbooks, London, p. 771.

18. Sawyer, J.W., editor, "Sawyer's Gas Turbine Engineering Handbook", Gas Turbine Publications Inc., Stamford, Connecticut, U.S.A., 1972.

19. Azoury, P.H., "An Introduction to the Dynamic Pressure Exchanger", Proceedings, Institution of Mechanical Engineers, Vol. 180, Part 1, No. 18, pp. 451-480.

12. ACKNOWLEDGEMENTS

The author is grateful for financial support, for much of the work reported here, from the Natural Sciences and Engineering Research Council of Canada. The assistance was in the form of Operating Grant A7928.

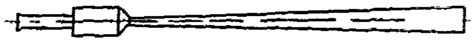

(a) SINGLE INLET AXI-SYMMETRIC CONFIGURATION

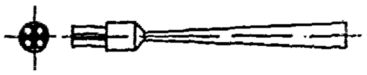

(b) SHORTENED MULTIPLE (FOUR) INLET CONFIGURATION

Fig. 1 Comparison of Proportions of Typical Single and Multiple-Inlet Valveless Pulsejets.

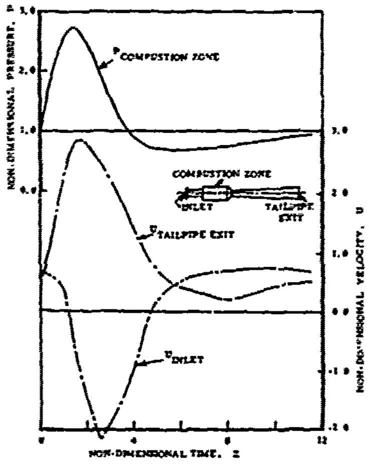

Fig. 2 Performance Prediction Using a Hot-Flow Numerical Model.

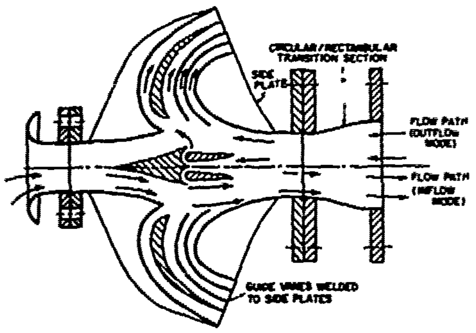
CIRCULAR/RECTANGULAR TRANSITION SECTION
SIDE PLATE
FLOW PATH (OUTFLOW MODE)
FLOW PATH (INFLOW MODE)
GUIDE VANES WELDED TO SIDE PLATES

Fig. 3 Symmetric Flow Rectifier of the Auxiliary Passage Type.

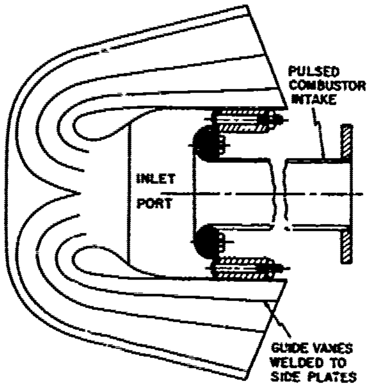

Fig. 4 Symmetric Flow Rectifier of the Thrust Augmenting Type.

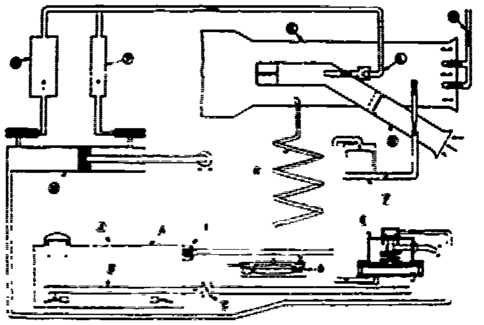

Fig. 6 A Non-Pressurised Gasoline or Kerosine Fuel System with Auxiliaries Used only when Starting.

A. Fuel tank
B. Fuel pipe with twin float-controlled valves
C. Fuel shut-off valve
D. Main fuel-pump (pressure actuated)
E. Starting fuel pump
F. Carburetor float chamber
G. Carburetor with non-return valve
H. Pipe with cooling coil
I. Fuel line pressure relief valve
J. Fuel tank vent
K. Pulsed combustor inlet
L. Starting-air jet in carburetor
M. Starting-air jets at combustor inlet
N. Double acting starting-air pump
O. Large-volume air reservoir (heater support-frame tubing)
P. Small-volume air reservoir

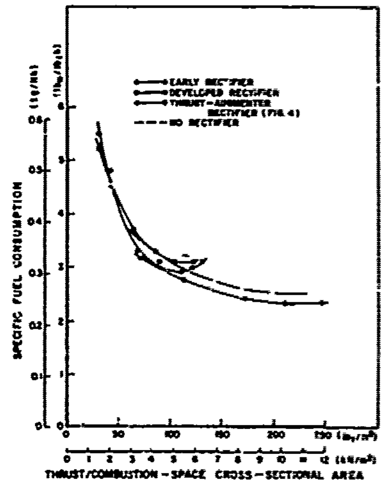

Fig. 5 Comparison of the Performances of a Single-Inlet Valveless Pulsejet Equipped with Various Flow Rectifiers.

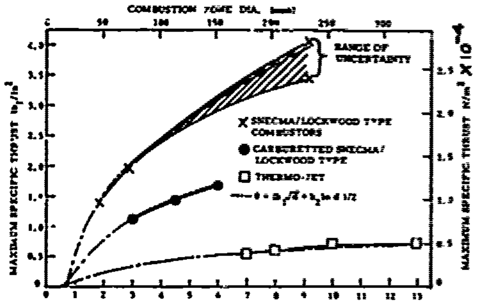

Fig. 7 Maximum Specific Thrust versus Combustion Zone Diameter for Valveless Pulsejets Operating at Sea Level Static Conditions.

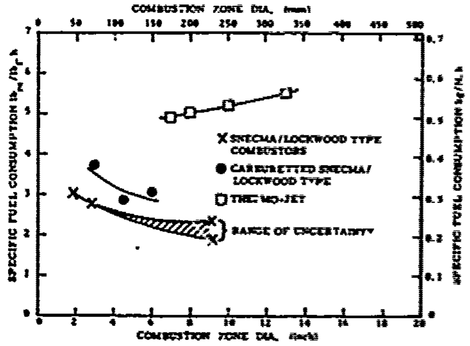

Fig. 8 Specific Fuel Consumption at Maximum Thrust versus Combustion Zone Diameter for Valveless Pulsejets Operating at Sea Level Static Conditions.

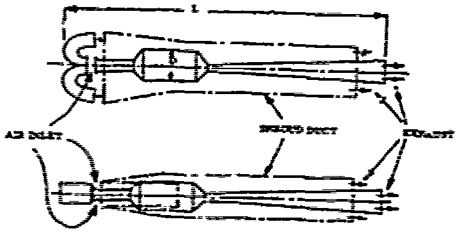

Fig. 9 Diagrammatic Illustration of a Single Inlet Valveless Pulsejet Equipped With a Flow Rectifier of the Type Shown in Fig. 4.

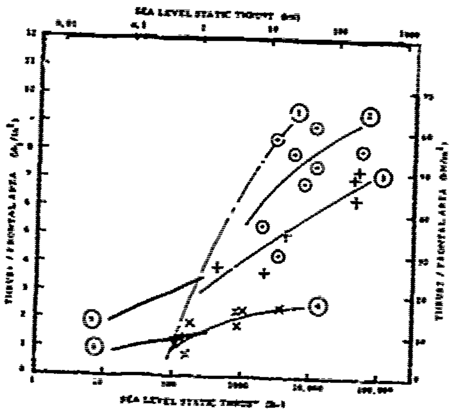

Fig. 10 Thrust per Unit Frontal Area versus Sea Level Static Thrust.

1. Gas turbine envelope curve
2. Pure jets with axial compressors ⊙
3. Best economy turbofans +
4. Pure jets with centrifugal compressors x
5. Valveless pulsejets (based on combustion zone diameter)
6. Valveless pulsejets (based on total frontal area)

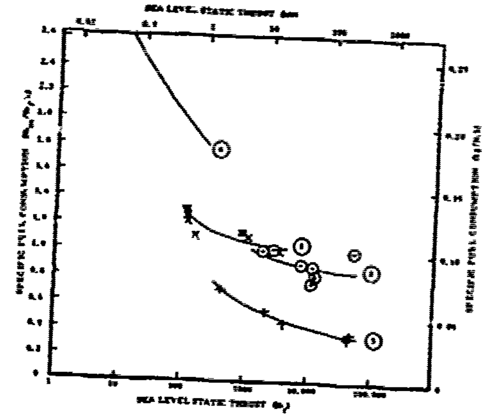

Fig. 11 Specific Fuel Consumption versus Sea Level Static Thrust

1. Pure jets with centrifugal compressors x
2. Pure jets with axial compressors ⊙
3. Best economy turbofans +
4. Valveless pulsejets

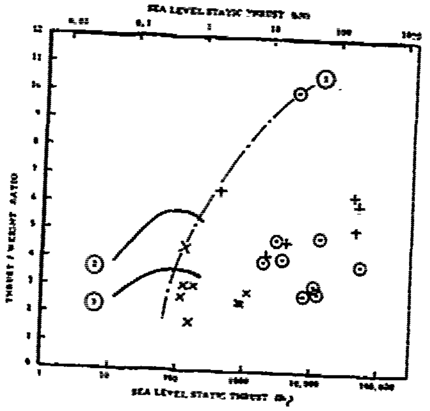

Fig. 12 Thrust-to-Weight Ratio versus Sea Level Static Thrust.

1. Gas turbine envelope curve
2. Valveless pulsejets without shroud duct
3. Valveless pulsejets with shroud duct

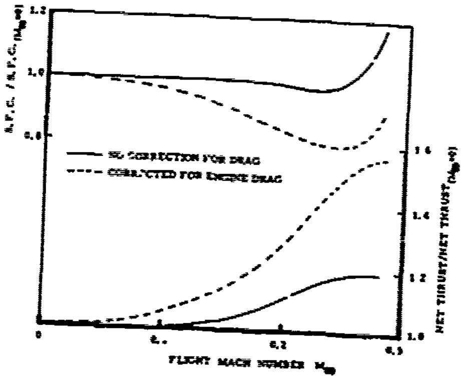

Fig. 13 Influence of Flight Mach Number on the Performance of a Modestly Rated Valveless Pulsejet Equipped with a Flow Rectifier of the Type Shown in Fig. 3.

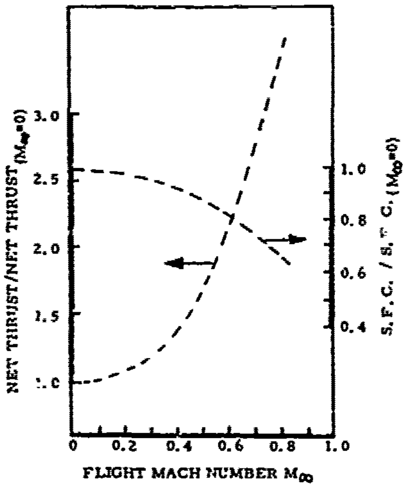

Fig. 14 Influence of Flight Mach Number on the Performance of a Carefully Installed SNECMA Écrevisse (Results due to SNECMA (10)).

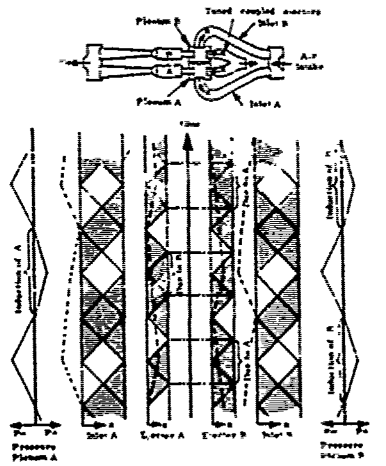
Plenum B
Tuned coupled ejectors
Inlet B
Air Intake
Plenum A
Inlet A
Time
Induction of A
Induction of B
Pressure Plenum A
Inlet A
Ejector A
Ejector B
Inlet B
Pressure Plenum B

Fig. 15 Twin Valveless Pulsejets Coupled Gasdynamically to Operate in Antiphase.

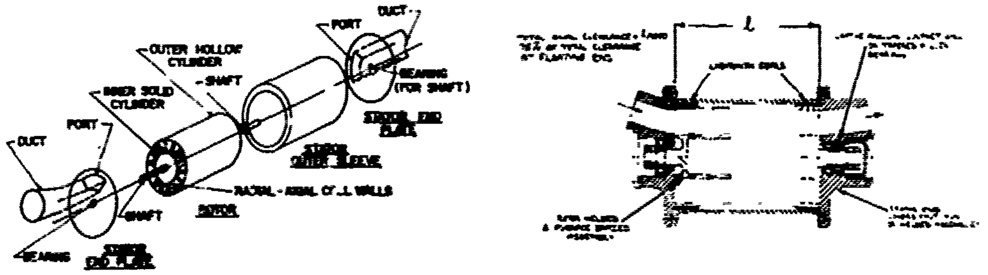
DUCT
PORT
OUTER HOLLOW CYLINDER
SHAFT
INNER SOLID CYLINDER
PORT
DUCT
BEARING (FOR SHAFT)
STATOR END PLATE
STATOR OUTER SLEEVE
RADIAL-AXIAL CELL WALLS
ROTOR
SHAFT
BEARING
STATOR END PLATE
l
LABYRINTH SEALS

(a)

(b)

Fig. 16 Basic Arrangment of a [illegible]amic Pressure-Exchanger.
a) Essential feature (diagrammatic)
b) Cross-section (diagrammatic)

DISCUSSION

B.Sobers

(a) Was the design model computerized?

(b) Was the model used to design the unit that was flight tested?

Author's Reply

(a) Yes, the design model, which is based on the method-of-characteristics as applied to one (space) dimensional time dependent compressible flow, was computerized. Brief details of the procedure, with mention of some of the restrictions, are given in Section 2 of the printed paper.

(b) The flight vehicle referred to in the paper (Section 8) was not due to the author. It was, in fact, a French prototype vehicle, using a valveless pulsejet, built some years ago by SNECMA. This work is described briefly in Reference 10 of the paper.

R.Marguet (in French)

What is the importance, from the viewpoint of military applications, of the acoustic characteristics of pulsejet propulsion?

Author's Reply

The application uppermost from the feasibility viewpoint is that of the propulsion of small, relatively low cost, target drones etc. For such applications the noise problem is not likely to be regarded as serious. If the device were to be used for active military purposes it may even be conceivable that the loud noise could be advantageous in helping to frustrate, whilst overflying enemy positions, oral communications etc. Certainly any activity requiring stealth is not a profitable field of applications for pulsejet powered vehicles.

MULTIPLE INTAKES FOR RAMROCKETS

by
E.-O. Krohn and K. Triesch
Deutsche Forschungs- und Versuchsanstalt
für Luft- und Raumfahrt e.V. (DFVLR)
Postfach 90 60 58
5000 Köln 90, Germany

SUMMARY

Several ramrocket missiles under development have a central combustion-chamber and more than one side-mounted intake - in general four. The junction of different inlet flows in a common chamber causes, in certain cases, flow instability and flow reversal in single ducts. The flow mechanism will be explained by examples. A computer program has been developed which calculates the overall performance of the system from single-inlet data. The results are compared with wind tunnel measurements. Methods for reducing the negative effects of combining multiple intakes with a common chamber are discussed.

SYMBOLS

A	area
d	diameter
h	diverter height
M	Machnumber
$\dot{m}$	mass flow
p	pressure
Re	Reynolds number
x	distance from body vertex
α	angle of attack
δ	boundary layer thickness
κ	ratio of specific heats
ϕ	angle of roll (def. Fig. 2)

SUBSCRIPTS

∞	free-stream condition
2	exit station of single inlets
3	mixing station
4	nozzle throat station
p	Pitot condition
RMS	root-mean-square value
t	total condition

1. INTRODUCTION

Modern air-launched ramjet-powered missiles have an integrated rocket-ramjet, for example, the very advanced "low volume ramjet (ALVRJ)". The booster, necessary to accelerate the missile to the ramjet's minimum operating speed, is installed within the ramjet combustion chamber in form of a solid propellant grain. After burnout of the booster air for ramjet operation is supplied through several (usually four) side-mounted inlets. Mixing of the individual airflows in the common chamber causes sudden changes in the performance of the inlets under certain conditions, especially during flight maneuvers. This may be accompanied by choked flow, reversed flow, and inlet buzz. The interference effects of multiple-inlet systems have been studied in close connection with ramjet missiles under development by MBB.

2. INLETS IN THE FLOWFIELD OF AN INCLINED MISSILE

To begin with, let us consider the flow conditions to which side-mounted inlets are subjected at angles of attack. The pitot-pressure distribution around an ogive-cylinder-body has been measured in the Mach number regime 1.5 to 2.5, at angles of attack up to 15°, and at different stations between 4 and 12 diameters behind the apex (Ref. 1). Figure 1 shows a selection of measured data at $M = 2.0$, for three angles of attack (5°, 10°, and 15°) and three longitudinal positions (4, 8 and 12 calibres). In the diagram lines of constant pitot-pressures (related to free stream pitot-pressure) have been plotted with a spacing of $\Delta p_p / p_{p\infty} = 0.1$ beginning with 0.9 at the outer field line. The measurements have been made with a pitot-rake fixed to the model and the values are therefore lower than normal shock values at high flow angles. Increasing the angle of attack increases the boundary layer thickness on the lee side of the body until a pair of vortices develops. At higher angles of attack the vortices separate from the body and the formation of a second pair of vortices begins. In the example, the pitot pressure drops as much as 60% of the free-stream value. Another very important factor affecting inlet performance is the flow angle relative to the inlet axis. Measurements of the flow angularity with 5-hole probes gave flow angles in the horizontal plane exceeding the angle of attack by 50%.

Figure 2 shows the pressure-recovery field of a half-axisymmetric inlet at a length station of $x/d = 9$ for various roll positions. At the top position of the inlet ($\phi = 0$), the pressure recovery decreases, even at small angles of attack, by an amount of about 13% due to boundary layer thickening. This value remains nearly constant at higher angles of attack because the vortices supply high energy air to the top region. Rotating the inlet into the immediate vortex area causes a steep decrease in pressure recovery to a minimum of less than 60%, in this example at $\alpha = 10°$. At higher angles of attack the vortex path moves above the inlet, and the pressure recovery increases. The inlet in side position ($\phi = 90°$) operates in a region of increased flow angle. In the example, this causes a decrease in pressure recovery with angle of attack (25% for $\alpha = 15^\circ$). A two-dimensional inlet with top-mounted ramp (like the Tornado inlet) would have a fundamentally different performance in this position: its pressure recovery would increase, the amount depending on the design. Finally, the inlet in bottom position has a pressure recovery nearly independent of the angle of attack. The maximum mass flow of an inlet shows, in the various roll positions, a dependence upon the angle of attack similar to the pressure recovery curve.

3. COUPLING OF INLETS

How does a system perform in which several inlets are connected with each other over a common combustion chamber? As long as the chamber pressure is so low that the inlet in the most unfavourable position still works in a supercritical mode, no problems will arise. This condition can - assuming a constant nozzle area - be practically achieved in two ways:

- The engine is designed for optimum inlet operation - meaning near the critical point - at cruise flight. In this case the fuel flow has to be reduced during flight maneuvers (liquid fuel) in order to maintain supercritical operation in all inlets. This, on the other hand means a loss of power just at the moment of increased thrust demand. This procedure is therefore only applicable for missiles with moderate maneuverability requirements.
- In the majority of cases the engine is designed for the critical maneuver case, keeping, in general, the fuel flow rate constant (solid fuel). Consequently, the inlets are oversized, resulting in increased external drag and higher supercritical normal-shock losses at cruise flight.

These considerations have raised the demand to optimize the inlets for cruising, and to allow subcritical operation during maneuvers. Initial wind tunnel tests with a 4-inlet system (Figure 3) revealed abrupt changes in pressure recovery and mass flow ratio in the subcritical regime even at zero angle of attack. In addition, a hysteresis was observed when reopening the nozzle. Analysis showed that throttling below critical operation brought only one inlet into the subcritical regime while the other three became more supercritical. With a total mass flow rate of 65% the summation of the individual mass flows requires reversed flow for the subcritical inlet with a rate of 35% of its supercritical mass flow. The consequences of throttling this inlet system into subcritical operation can be summarized as:

- Breakdown of mass flow by 30% results in loss of thrust and possible overheating of the combustion chamber
- Breakdown of pressure recovery increases the internal drag, causing loss of thrust.
- Reversed flow in one inlet causes steep increase in external drag.
- Buzz in the reversed-flow inlet transfers into the combustion chamber and possibly causes flame-out or mechanical destruction because of alternating overload.

For the investigation of multiple-inlet systems in the supersonic 60-cm DFVLR wind tunnel a model has been used (Figure 4), which enabled separate measurements of mass flow ratio and pressure recovery in the individual inlets by means of a quartered and calibrated Venturi-nozzle, and total measurements by a hydraulically actuated choked nozzle. Asymmetric inlet operation has already been observed with supersonic fighter aircraft having a twin-intake system and a single engine. This has been investigated by BEKE (Ref. 2) and MARTIN (Ref. 3) and related to missile propulsion by JELL (Ref. 4). The conditions leading to sudden changes in inlet performance are discussed with the help of Figure 5. Two assumptions are made:

- parallel entry of the flows into the mixing chamber. This is realized in the wind tunnel model,and
- constant static pressure in the entry plane. This assumption is so far realistic (Ref. 3) but errors are to be expected for strong reversed flows in single inlets.

Mass flow ratio and pressure recovery are related by the following linear expressions:

$$\frac{\dot{m}_3}{\dot{m}_\infty} = \frac{p_{t3}}{p_{t\infty}} \cdot \frac{A_4}{A_\infty} \cdot \frac{1}{M_\infty} \cdot \left(\frac{2+(\kappa-1)\, M_\infty^{\,2}}{\kappa+1}\right)^{\frac{\kappa+1}{2(\kappa-1)}} = \frac{p_{t3}}{p_{t\infty}} \cdot \frac{A_4}{A_\infty} \cdot f(M_\infty)$$

$$\frac{\dot{m}_3}{\dot{m}_\infty} = \frac{p_3}{p_{t\infty}} \cdot \frac{A_4}{A_\infty} \cdot f(M_\infty, M_3) \qquad \text{for static pressure}$$

That means: Operating points for constant nozzle areas are possible only on straight lines through zero. If for example "b" is the critical operation point, a single inlet could also operate subcritically at "c" or "d" with the same nozzle area. If the system is supplied by two inlets, one operating supercritically and the other subcritically, then the system operating point "c" is only possible with a combination of points "a" and "e". Accordingly, the following combination is obtained for a four-inlet system: three inlets operate at point "a" and one at point "f". Theoretically, a solution with two inlets each operating at "a" and "e" would be possible, but in pratice one inlet reaches the critical point first-either because of fabrication tolerances or because of disturbances in the entering flow. In this manner, the maximum slope of the subcritical branches of single inlets in a multiple-inlet system is obtained. Exceeding this slope causes the described unsteady performance.

These relatively simple relations were the basis for a FORTRAN-program (Ref. 5), which calculates the system performance from the knowledge of the single-inlet performances.

Two methods of solution have been investigated. In the first method, all possible combinations of the single inlet operating points were calculated. Then the solutions were arranged in order of the nozzle area, non-possible combinations eliminated, and one selected in case of several equivalent solutions. This method gave good results only for simple cases. With an increased number of points, the computing time and the necessary storage capacity became too large.

In the second method, the operating points are examined stepwise on all single-inlet performance lines. Only those solutions are allowed which give a steady decrease of the nozzle area A_4 when stepping through the regime from supercritical to subcritical operation, or a steady increase when going the other direction. The method will be explained by an example with two inlets. The static performance lines of the two inlets (Figure 6) are given by five points each (a...e, A...E) connected by straight lines. Four characteristic operating regimes can be distinguished:

- one supercritical with constant mass flow,
- one subcritical with falling pressure recovery, the slope is different for both inlets,
- one subcritical with slightly increasing pressure recovery, and
- one region without mass flow, representing the reversed flow regime in this simple example.

In the diagram showing the calculated performance of the system (Figure 7) the appropriate operating regions of the single inlets are marked, the first number denoting inlet I and the second inlet II. Starting with both inlets in supercritical mode, inlet II reaches its critical point first at "b". Since the slope of its subcritical branch is flatter than the limit, no unsteadiness is encountered and the inlet runs through regions 2, 3 and 4 while inlet I remains supercritical. After exceeding the critical point "B" of inlet I, the performance line falls continuously with inlet I operating along branch "2" and inlet II along branch "4". Reaching point "d" inlet II switches to branch "2" and inlet I to branch "4". This event is accompanied by irregular system performance and by a sudden change in external drag and longitudinal moments. After that the system performs smoothly again. A reopening of the nozzle causes no unsteadiness at this point and the performance follows a different path, so causing a hysteresis. At the end of line "31", inlet II operates in supercritical mode and inlet I at point "c". From here inlet I "jumps" into supercritical operation raising pressure and mass flow of the system by 30%. Irregularity can be avoided by increasing the Machnumber at station "2", because the slope of the subcritical branch of the static performance line is reduced by this means. This method is, in general, not practicable because of increased mixing losses.

A second example shows the attempt to calculate the case shown first (Figure 3). The measured performances of the four single inlets have been simplified for the calculation by straight line segments (Figure 8). The inlets showed considerable differences in their critical operating point which can be attributed to high fabrication tolerances. A common feature of all inlets was the absence of stable subcritical operation. After exceeding the critical point, the inlets ran into immediate buzz, and dropped in pressure recovery and mass flow by almost 40%. With the available missile model the performance lines could only be measured down to "zero" mass flow. The plotted reversed flow branch has been estimated from different test runs with large-scale inlets. In reversed flow, below a certain flow rate, the throat acts as a choked nozzle, and thus the operating points lie on a straight line through "zero". The low critical pressure recoveries are produced by model-dependent high subsonic losses (two 90° corners, Venturi nozzle, Carnot losses). Subcritical pressure recoveries below normal shock values are possible during buzz, since the operating mode in a buzz cycle varies between subcritical and highly supercritical operation with accordingly large shock losses. The result of the calculation (Figure 9) is not in complete agreement with the test results (Figure 3), but the tendencies are sufficiently predicted. The saw-tooth-like breaks at mass flow ratios 0.6 and 0.3 as well as the strong hysteresis between $\dot{m}_2/\dot{m}_\infty = 0.6$ and 1.0 are in good agreement. A closer analysis of the calculated data shows that first inlet II and then inlet III exceed the critical point and immediately go into reversed flow, and thus initiate the abrupt changes in performance. Inlets I and IV remain supercritical. This result agrees with the tests.

In the last example, the angle-of-attack performance of a 4-inlet system at Ma = 2.5 is investigated. The measured performances of a single inlet mounted on the side of a missile in various roll positions is shown in Figure 10. The inlet station was 7 diameters behind the body apex. The inlets were nearly free of buzz and had, in almost all cases, a steady transition from supercritical to subcritical operation. Evidently the most problematic position is that under 45° roll. An acceptable performance is obtained only up to about 4°. At higher angles pressure recovery and mass flow exhibit a rapid decrease because of the vortex influence. In the "x"-configuration two inlets in 45°-roll position are combined with two inlets in 135°-roll position which show a moderate angle-of attack sensitivity of less than 10%. A comparison between the computed (Figure 11) and the measured (Figure 12) performance of the total system shows good agreement. There is a surprisingly large region (shaded area) with at least one inlet with reversed flow. The calculation terminated here, since no data with reversed flow were available for the single inlets. A comparison with the single inlet performances shows clearly that the pressure recovery of the total system is determinded by the "worst" inlet. To improve the performance of this system the entering flow field had to be changed for the upper inlets. This would be possible by shifting the inlet plane forward, by influencing the vortex position with strakes, or by positioning the inlets between wings. In the "+"-configuration one inlet each in top and bottom position are combined with two side intakes (Figure 10). The performance data of the top inlet varies within a bandwidth of less than 10% up to 12° angle-of-attack, because the vortices by their rotation maintain a relatively good flow. The bottom inlet exhibits a considerable increase in pressure recovery and mass flow ratio. The side inlets show a strong angle-of-attack sensitivity because of the increased local flow angularity, and they are therefore decisive for the system performance. The calculated (Figure 13) and measured (Figure 14) performances are again in good agreement. In spite of the fact that there is reversed flow (through the side intakes) below 50% flow rate, the performance decrease at angle-of-attack is, however, considerably less than for the "x"-configuration. In addition the "+"-configuration has the potential for substantial improvements of the performance by use of inlets less sensitive to flow angularity.

4. MEANS FOR REDUCING THE COUPLING EFFECTS

It has been shown that the inlet flows in multiple inlet systems influence each other, if the pressure level in the combustion chamber rises above the critical value of one inlet. If the subcritical branch of this inlet exceeds a certain slope, abrupt changes in the total performance will be encountered. Essentially there are two reasons for a decreasing subcritical branch of the performance curve:

- A multi-shock inlet with internal compression, possibly with isentropic compression fields, and a weak terminal shock turns in subcritical operation into a condition with, in general, one oblique shock and one strong terminal shock, with accordingly higher total pressure losses. For missile application, simple inlets with low internal compression are commonly used; in these cases inlet buzz is the predominant reason.
- Buzz is, in the majority of cases, initiated by a shock-induced boundary layer separation on the ramp or centerbody, which starts a periodic oscillation of the terminal shock. This so-called DAILEY-instability (Ref. 6) can be suppressed by boundary layer suction, as demonstrated by HALL (Ref. 7), for example. Because of the thinner boundary layer, axisymmetric inlets need less bleed flow than two-dimensional intakes. During subcritical operation, the bleed flow increases rapidly behind the terminal shock, so that in axisymmetric inlets the flow capacity of the piping going through the spike reaches its limit very soon. Half-axisymmetric and two-dimensional inlets don't have this problem because the bleed air is dumped directly outside.

Figure 15 shows the performance of a half-axisymmetric inlet at $M = 2.5$ with and without bleed. The buzz-intensity (p_{RMS}/p_{t_∞}) is indicated by the vertical lines. Buzz could be suppressed nearly to zero mass flow, and the subcritical pressure recovery drop could be eliminated. The bleed rate was in the order of 1% to 2%. Stable flow is a prerequisite for allowing subcritical operation of an inlet system, and this for two reasons: avoidance of unsteady subcritical performance, and prevention of high alternating structural loads by pressure oscillation. During subcritical operation the performance of the engine is determined by the inlet with the lowest performance. This can, even for minor flight maneuvers, result in considerable power losses. So, a system with inlets in "x"-configuration will reach its operational limit at around 5° angle of attack (for $x/d = 8$). An improvement of the situation requires a deflexion of the vortex path. The situation with inlets in "+"-configuration is essentially better since no inlet is supplied by low-energy air. The system characteristic is primarily dependent upon the performance of the side mounted inlets under high flow angles. Here, two-dimensional inlets with the ramp tangential to the body show less sensitivity than axisymmetric types. However, these inlets can in bottom position, have a rapidly increasing mass flow with angle of attack and thereby force the other inlets into premature subcritical operation. The flow angle sensitivity of side-mounted half-axisymmetric inlets could be drastically improved by turning the spike into the flow direction (Figure 16). This was accomplished by a pneumatic selfcorrection system shown in the figure. The static pressures from both sides of the spike are fed into a pneumatic cylinder, which turns the movable part of the spike until pressure balance has been reached.

5. CONCLUDING REMARKS

Based on the results of this study, these conclusions can be made:

- The calculation of the performance of a multiple-inlet system from single-inlet data is in good agreement with measurements. Since the inlet in the most critical position governs the system performance, only its data need to be known exactly.
- Subcritical operation can be permitted to a certain extent when the inlets are free of buzz, which can be obtained by boundary layer bleed. Rapid changes in external drag and longitudinal moments must be taken into consideration.
- Inlet systems in "x"-configuration can operate properly only at small angles of attack up to the point at which vortex flow enters the upper inlets.
- Systems with "+"-configuration of inlets have a much better performance and can operate up to high angles of attack, if side intakes with low flow-angle sensitivity are used.

REFERENCES:

1. TRIESCH, K. — Influence of the Flowfield Around an Inclined Ogive-cylinder Body upon Supersonic Aft-intakes, in:"Contributions to Gasdynamics and Aerodynamics", pp. 61-78
ESA-TT 518 (1979)

2. BEKE, A. — Criteria for Initial Flow Reversal in Symmetrical Twin-Intake Air-induction Systems Operating at Supersonic Speeds,
NACA RM E55L02a (1955)

3. MARTIN, N.J.
HOLZHAUSER, C.A. — Analysis of Factors Influencing the Stability Characteristics of Symmetrical Twin-intake Air-induction Systems.
NACA TN 2049 (1950)

4. JELL, C.S. — Air Intake Aerodynamics and Operational and Installation Effects on Missile Powerplant Performance
AGARD LS-98 (1979)

5. TRIESCH, K.
KROHN, E.-O. — Berechnung von Drosselkurven eines Staustrahlantriebes mit einer Brennkammer und mehreren Überschalleinläufen
DFVLR-Bericht IB-251-80-K-1 (1980)

6. DAILEY, C.L. — Supersonic Diffuser Instability
Journal of the Aeronautical Sciences, Vol. 22, No. 11, (1955)

7. HALL, G.R. — A Criterion for Prediction of Airframe Integration Effects on Inlet Stability with Application to Advanced Fighter Aircraft
AGARD-CP-150 (1974)

12-6

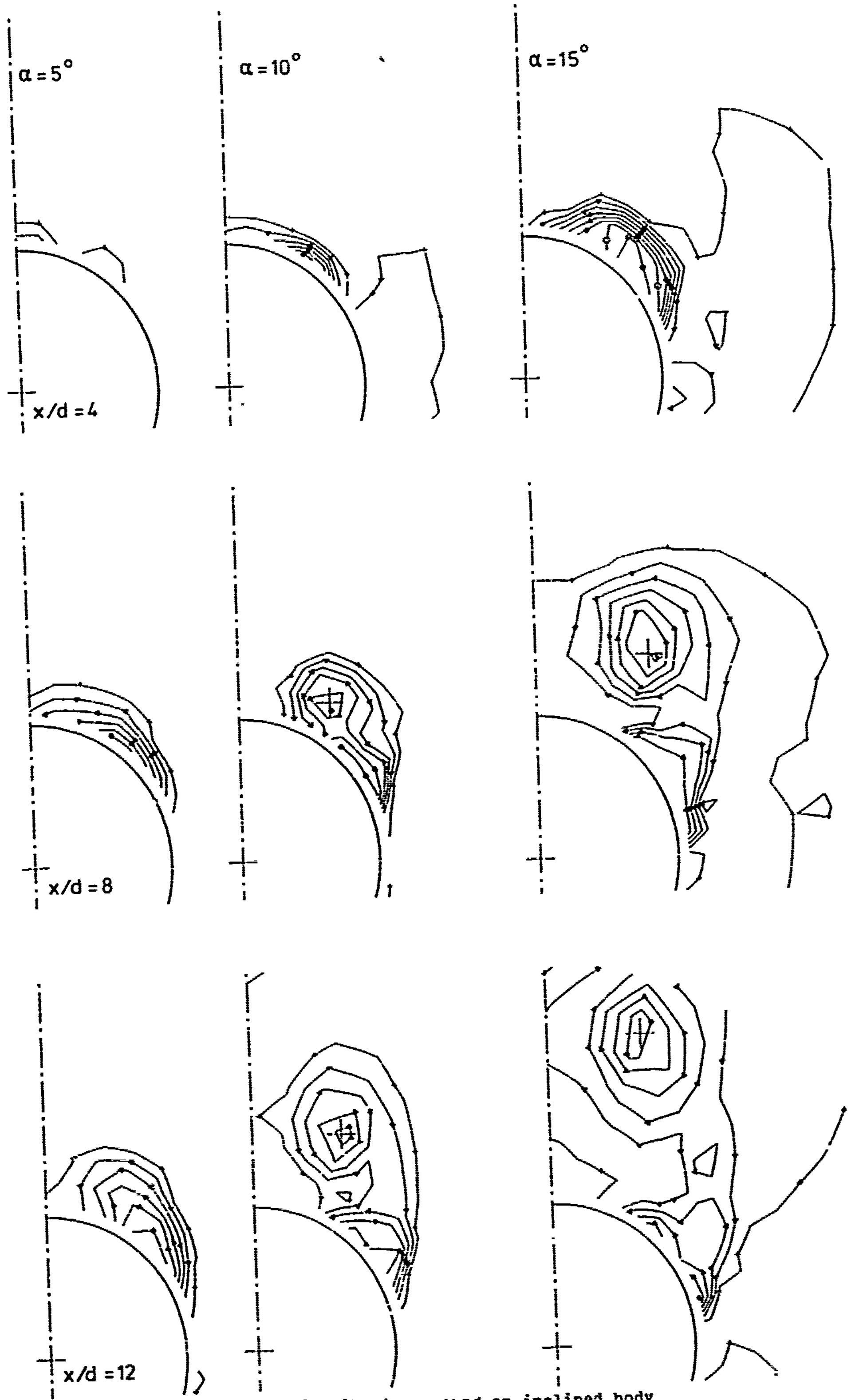

Fig. 1 Pitot-pressure distribution around an inclined body
$M = 2.0$, $Re = 3 \cdot 10^6 [m^{-1}]$, $d = 48.6 [mm]$

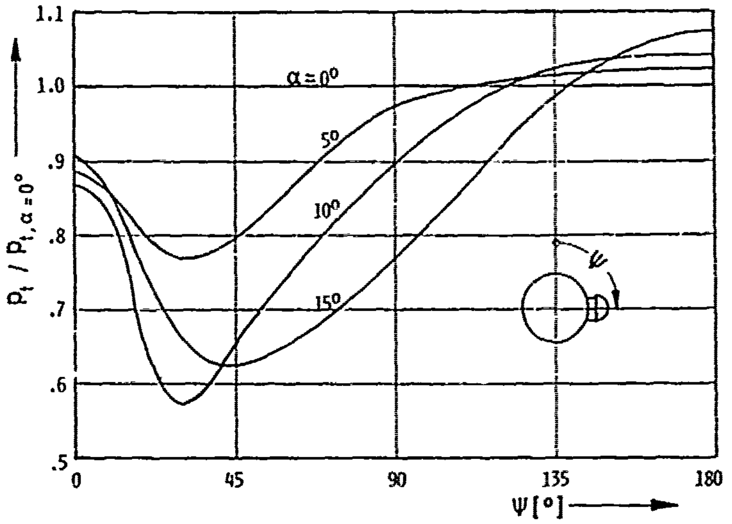

Fig. 2 Total-pressure recovery of a half-axisymmetric inlet
$M = 2.0$, $x/d = 9$, $h/\delta = 1.0$

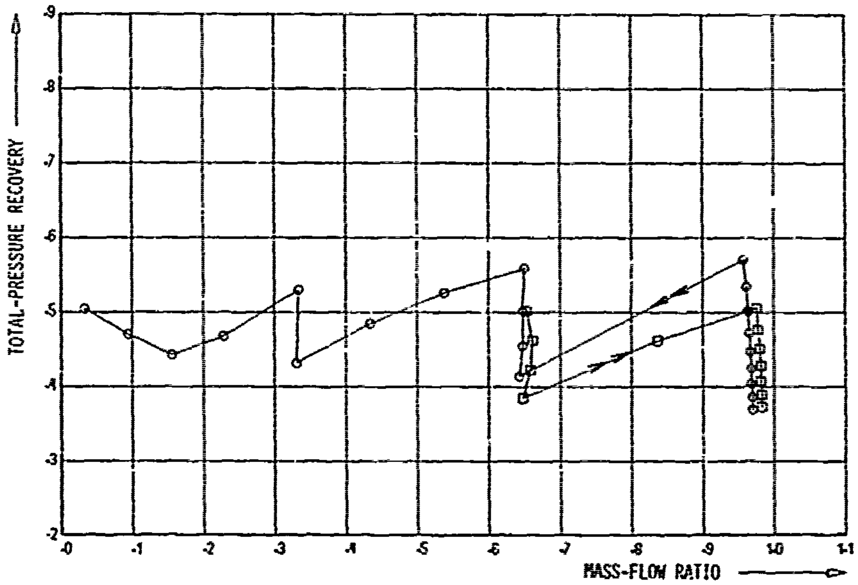

Fig. 3 Measured performance of a four-inlet system
$M = 2.5$, $\alpha = 0°$

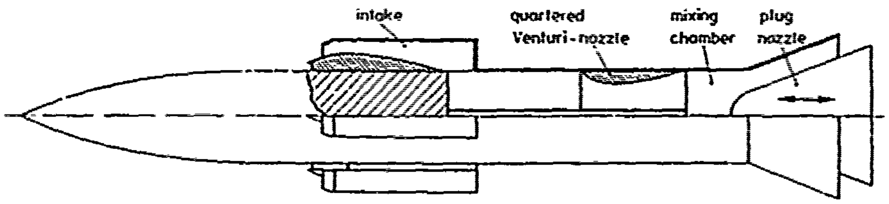
intake
quartered Venturi-nozzle
mixing chamber
plug nozzle

Fig. 4 Model for inlet testing

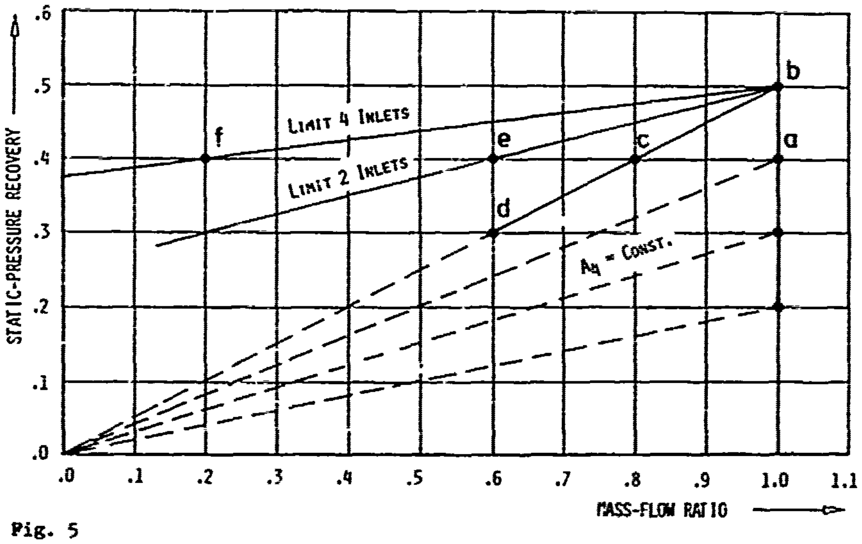

Fig. 5

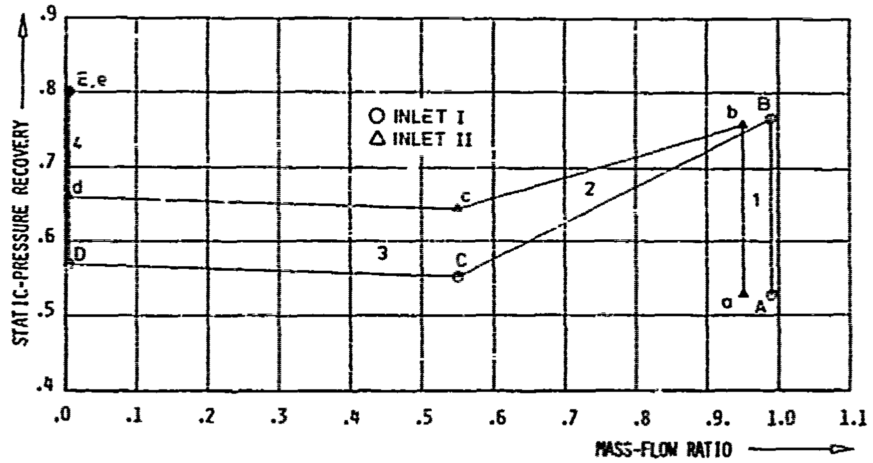

Fig. 6 Performance of two inlets

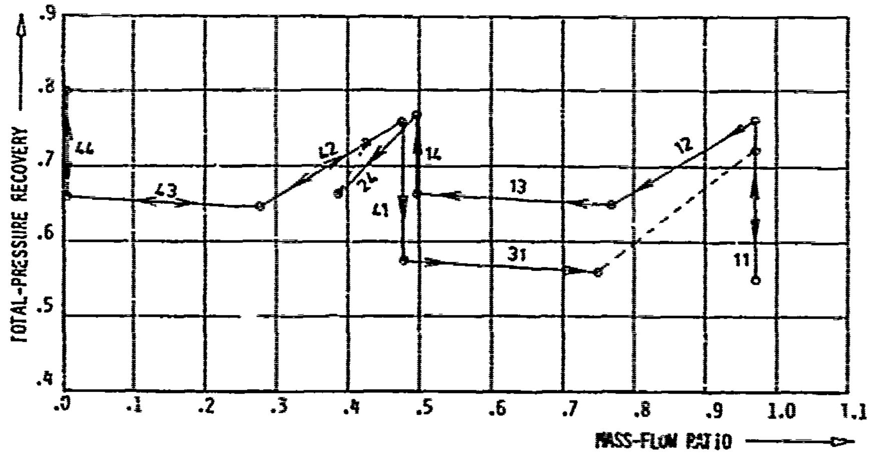

Fig. 7 Performance of twin-inlet system

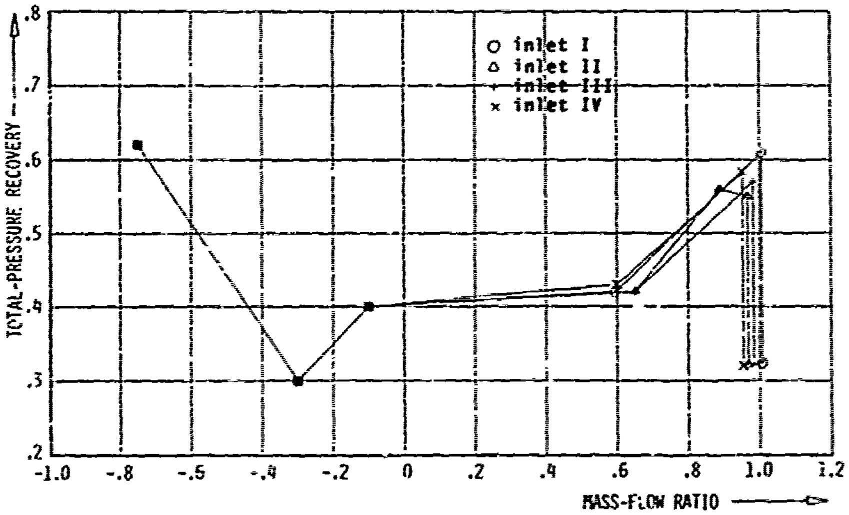

Fig. 8 Measured performance of four single inlets (simplified)
M = 2.5, α = 0°

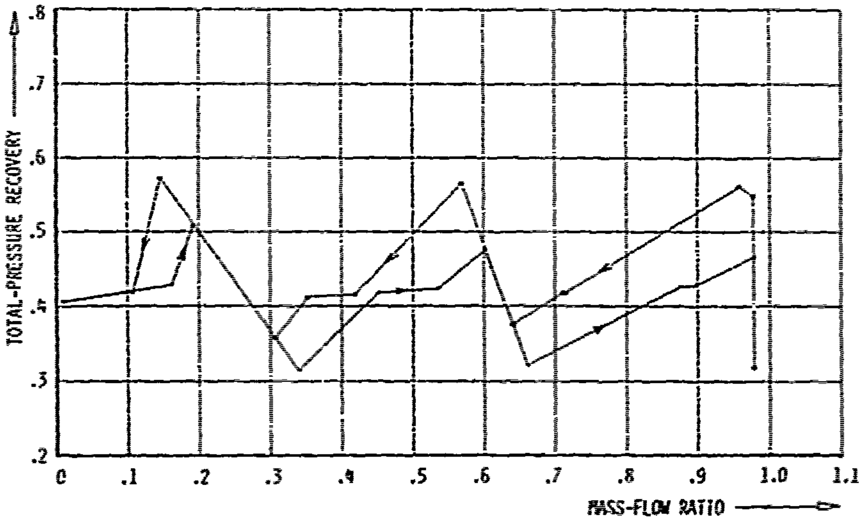

Fig. 9 Calculated performance of four-inlet system

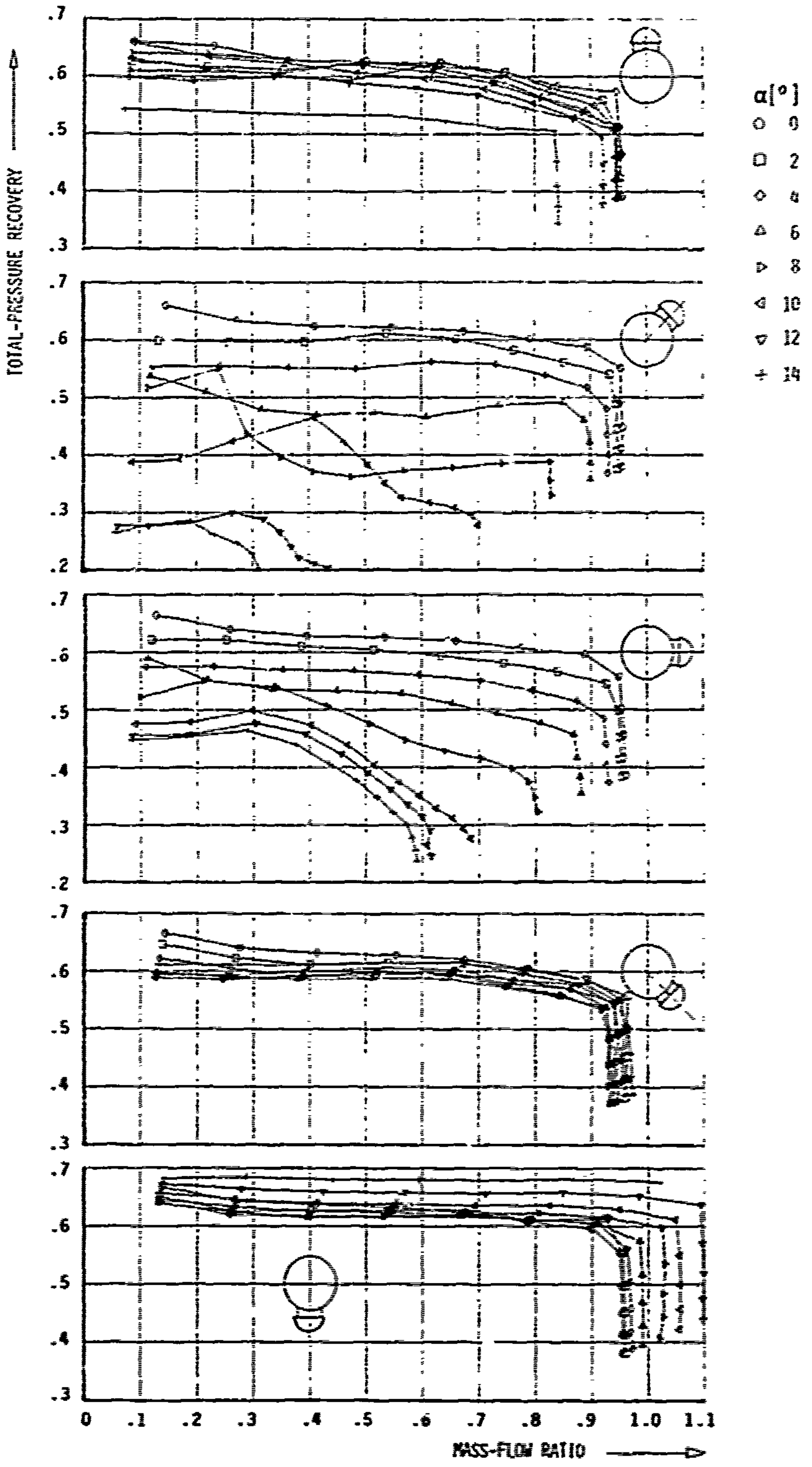

Fig. 10 Performance of a body-mounted inlet
$M = 2.5$, $x/d = 7$

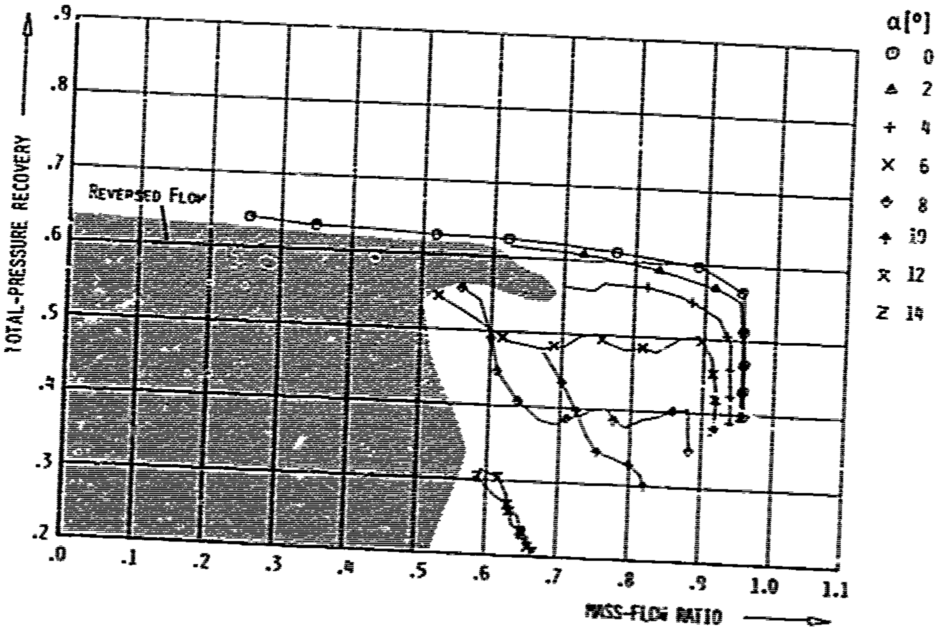

Fig. 11 Calculated performance of a four-inlet system
M = 2.5, X-configuration

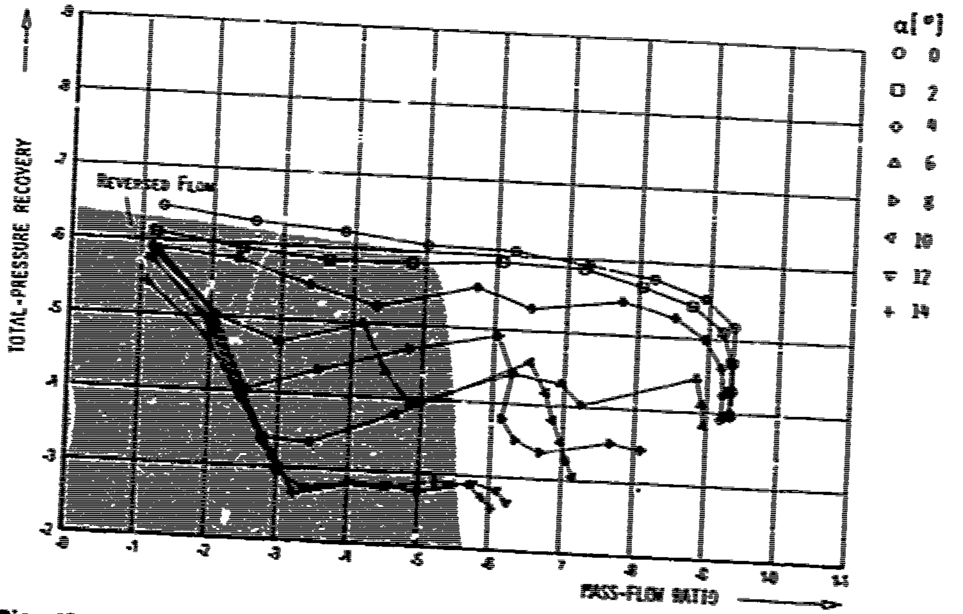

Fig. 12 Measured performance of a four-inlet system
M = 2.5, X-configuration

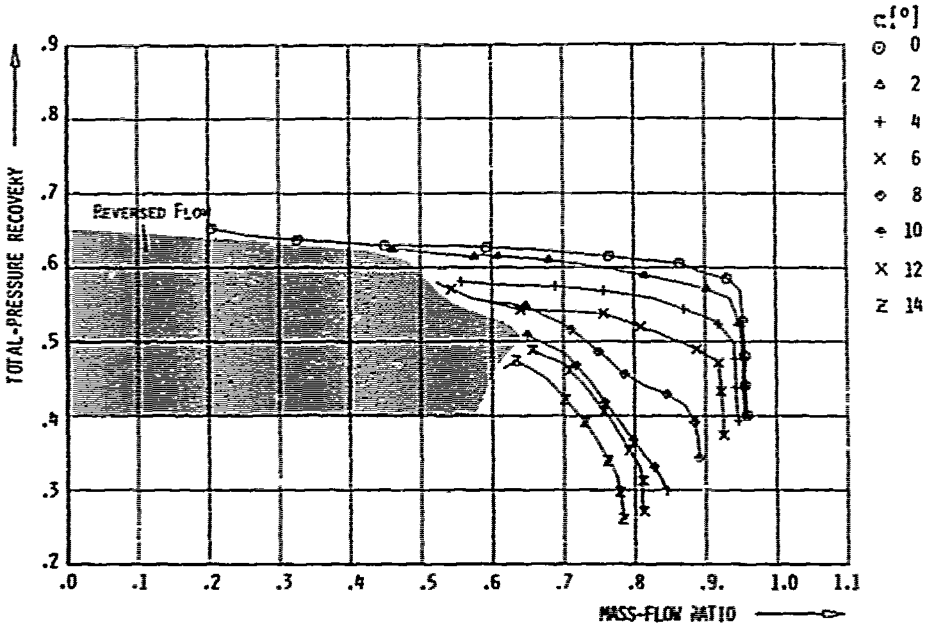

Fig. 13 Calculated performance of a four-inlet system
M = 2.5, +-configuration

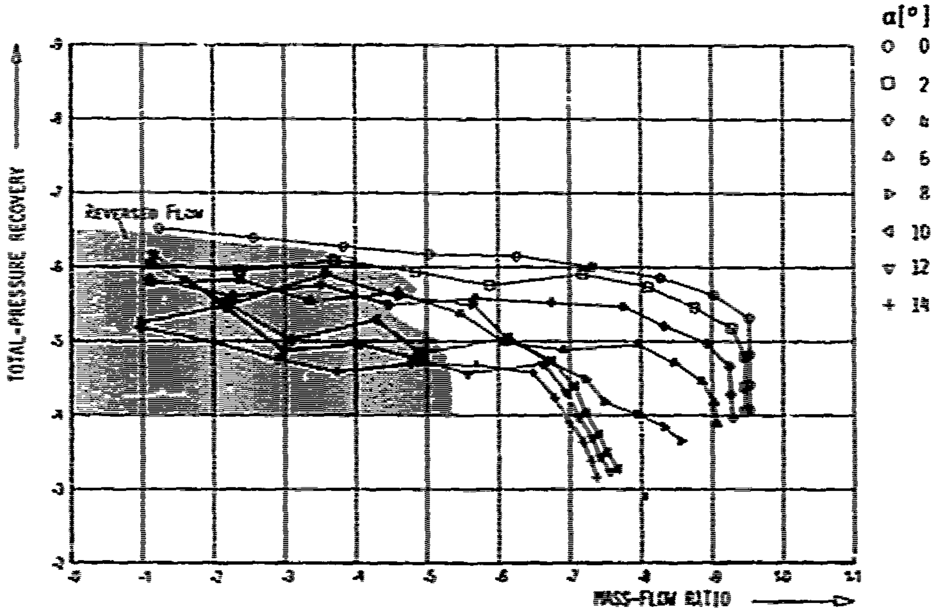

Fig. 14 Measured performance of a four-inlet system
M = 2.5, +-configuration

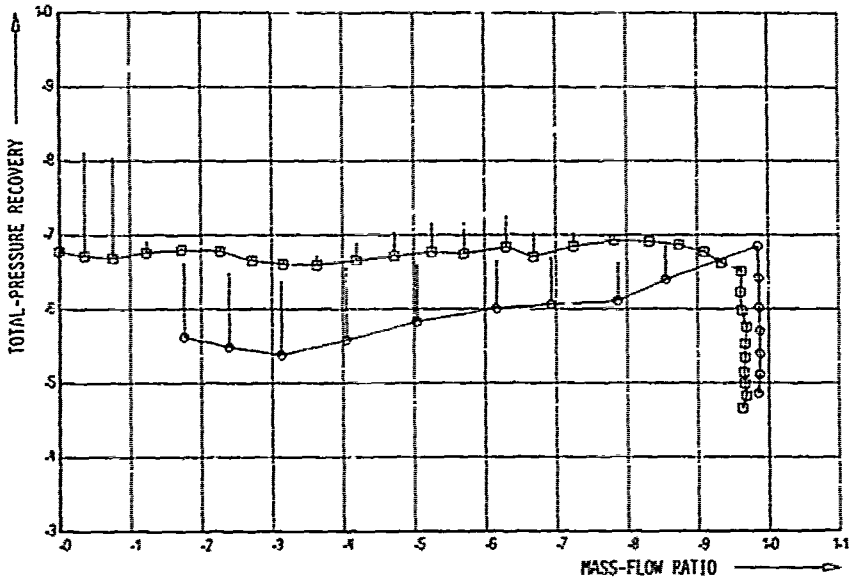

Fig. 15 Half-axisymmetric inlet with and without buzz-suppression
M = 2.5

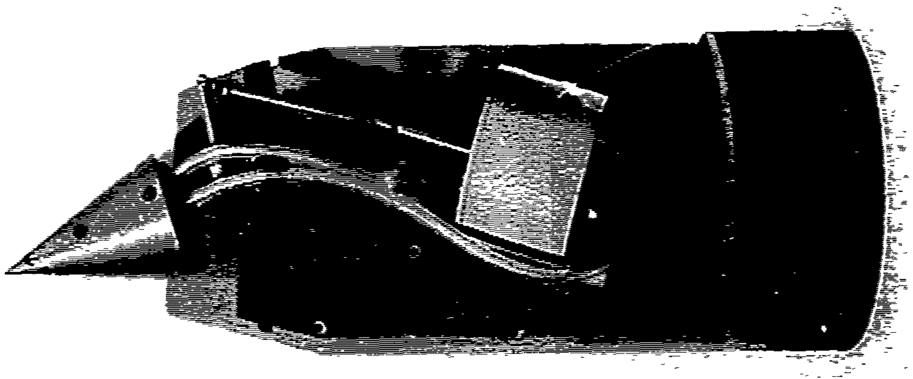

Fig. 16 Inlet with adjustable spike

DISCUSSION

E.Söffker

What was the basic difference between the intake system demonstrated first with the generally negative pressure recovery slope below the critical operation point into the subcritical region and the improved intake system?

Author's Reply

The intakes used in the first 4-inlet configuration (Figures 3 and 8) had no boundary layer bleed, whereas the intakes with improved performance in the later example did have bleed. The effect of bleed upon the inlet performance is shown in Figure 15.

One-Dimensional Non Linear Considerations on Supersonic Diffuser Buzz

Hermann-L. Weinreich
MBB Raumfahrt, Postfach 80 11 69, 8000 München 80

SUMMARY

This paper will deal with the fundamental aspects of supersonic intake buzz. A description of the basis phenomenon characteristics and a delimitation to other unsteady propulsion processes will be presented. A simplified intake propulsion stability analysis shows the possible influence of diffuser exit Mach number on the stability boundary in comparison to other well-known theories. Non linear example calculations using smooth intake pressure recovery curves can illustrate some experimentally observed buzz characteristics. The limits of the theoretical approach will be discussed, and the tendencies will be compared with experimental work.

LIST OF SYMBOLS

a	speed of sound	$t, \Delta t_c$	time, period of organ pipe type oscillation, eq. (3)
A	area	x	axial distance
L	length	$\varkappa$	ratio of specific heats
$\dot{m}$	mass flow	$\mu, \pi, \pi_0, \varrho, \varphi$	dimensionless perturbations of M, p, p_0, ϱ and $\dot{m}$, eq. (4)
M	Mach number	ϱ	density
p, p_0	pressure, total pressure	$\sigma, \sigma_{EI}, \sigma_{CI}$	slope of intake characteristic, eqs. (12,15,16)
q	factor regarding operation of entropy discontinuities, eq. (16)	$\mathfrak{M}$	ratio of total to static temperature, eq.(5)

Subscripts

$()$	no subscript indicates mean values of the internal flow or geometry
$()_\infty$	free stream condition
$\hat{()}$	perturbation due to entropy discontinuity. eqs. (7)
$()_{lin}$	result, valid only for small perturbations
$()_{I,N,T}$	inlet; nozzle, nozzle exit; inlet throat

1. INTRODUCTION

The first experimental investigations on multi-shock intakes for supersonic ram propulsion were performed by Ludwieg and Oswatitsch [1]. They used rotational intake models, where one or two oblique shocks were generated upstream the terminal shock with the aid of a centre body. The terminal shock stands in front of the intake cowl during subcritical operation. The capture mass flow therefore depends on the back pressure generated by the consumer (Fig. 1). During supercritical operation, the area of the swallowed stream tube does not depend on back pressure; in this case, the terminal shock stands within the intake diffuser.

During the tests of the multi-shock intake models, Oswatitsch found during supercritical operation an increase of the total pressure p_0 exceeding the Pitot pressure with a closing throttle (Fig. 2). During subcritical operation, a sudden unexpected pressure breakdown, in connection with a loud buzzing noise, was detected [1]. In spite of steady incident flow, periodic movements of the shock system, and associated pressure and mass flow pulsations, could be observed in nearly the entire subcritical regime [1]. The phenomenon was called buzz, due to the characteristic noise.

2. REMARKS ON THE EXPERIMENTAL EVIDENCE

The following statements on intake buzz are based on published papers, which have been collected during our own theoretical work on the problem [61, 63].

2.1 Presence of intake buzz

Even in the case of undisturbed axial supersonic indicent flow, buzz has been observed during subcritical operation in many types of intakes:

- Pitot intake [3, 4, 5, 52]
- external compression intake
  - axisymmetric intake [1, 12 - 23, 28, 29, 32 - 34, 37 - 41, 46 - 48]
  - half axisymmetric intake [59]; quarter axisymmetric intake [56]
  - rectangular (two dimensional) intake [26, 27, 42 - 45, 53 - 55, 57]
  - inverted rectangular intake [58]; external ramp intake [51]; scoop intake [8]
- mixed compression intake [24, 30, 50]
- internal compression intake [6]

The operation with the angle of attack, or with free stream distortions, may change the buzz boundaries. In this case, buzz could possibly already occur at subsonic incident flow conditions [51]. An increase in stable subcritical operation range, or a damping of buzz pressure pulsations, can be caused by shortening the tube between intake and nozzle [14, 15], or by the use of a turbo engine instead of a nozzle.

2.2 Importance of intake buzz for airbreathing missile propulsion

In comparison to aircraft propulsion, buzz is more difficult to prevent than with missiles, because of the following reasons:

- more limited measuring techniques
- in general, a fixed intake geometry
- greater limitations in engine regulations
- normally greater angles of incidence
- destabilizing interference effects between consumer and several intakes

To prevent buzz, it is therefore necessary

- o to choose a greater distance from the buzz boundary, however this having the disadvantage of increased supercritical total pressure losses, or
- o to accept the additional propulsion, and development costs needed for buzz-free intakes [59].

In addition, the consequences of intake buzzing are:

+ structural damage, due to peak-to-peak pressure pulsations of up to r than 0,5 $p_{o\infty}$
+ varying aerodynamic loads on the missile
+ risk of compressor stall
+ flameout with ramjets using fuels not self-igniting

In most cases (especially for supersonic sea skimmers) the consequences are more severe, due to the higher free stream total pressures.

3. FEATURES OF THE INTAKE BUZZ

Among the many observations conducted on the intake buzz, the descriptions given by Trimpi [14, 15], Dailey [18] and Stewart [38, 39, 40] show the greatest accuracy.

3.1 Simplified description of a buzz cycle using experimental observations [15] and theoretical considerations [61 - 63]

Start of cycle:

The terminal shock, standing in front of the intake cowl, will be forced upstream by upstream running compression waves. The associated mass flow reduction is propagated in form of a pressure lowering rarefaction wave into the intake. The causes for the movement of the shock system, the decrease in massflow, and the internal pressure breakdown may be as follows:

- the entrance of a vortex sheet (with a different total pressure on both sides) emanating from the shock intersection,under the cowl lip, called Ferri instability, was observed many times in connection with buzz [13 - 15, 25, 39 - 44, 45 - 48, 60].
- a shock induced boundary layer separation on the compression surface, which was termed Dailex instability, [14 - 20, 39 - 41, 46 - 48, 60].
- a local total pressure dip inside the free stream capture tube, increasing relatively with throttle ratio [51, 60].
- a certain decline of intake total pressure, with increasing throttle ratio (several general stability theories give different limits for the corresponding slope of the intake characteristics) [2, 7, 8, 21, 22, 35, 61].

The upstream shock movement continues until either, for relatively short intakes, a new highly subcritical quasisteady equilibriumstate (producing eventual backflow) will be reached, or for longer intakes, the shock will collide, during the upstream movement, with rarefaction waves returning from the nozzle, and generating a reduction in back pressure, in order that the shock can return into the intake.

The exhaust phase will be terminated even in the case of relatively short intakes, when the above-mentioned rarefaction wave, which starts the exhaust process, will return in the intake after reflection on the consumer. Supercritical pressure rise in the backfilling phase:

Due to the reduced back pressure, the terminal shock returns and enters again the intake diffuser (supercritical operation). The associated rise in mass flow propagates in form of a compression wave downstream to the consumer. There the wave will be reflected back to the intake, whereupon the terminal shock will be forced upstream. If the shock reaches now the instable position, a new buzz cycle will again be initiated. In such a case, we have a period, which is longer than the first mode period of a one sided closed organ pipe of equivalent length, only by the reaction time of the inlet and consumer.

In many cases, however,

- for slightly subcritical unstable throttling, or
- for a low level of Mach number in the tube between intake and nozzle,

the intensity of the possible supercritical internal compression waves is limited.Therefore a staged pressure rise and an elongated cycle period will result.

3.2 Definition of intake buzz, delimitation to other unsteady propulsion phenomena

Within the scope of this work, intake buzz should denote only such subcritical supersonic intake pulsations, where the period (longer than equivalent organ pipe period) is determined by the geometry of the connected consumer (tube and throttle, ram combustor, turbo-engine). Only in one case has a dominating buzz pulsation of higher organ pipe frequency been reported [12]. The total pressure amplitude during buzz can reach up to more than half of free stream total pressure and depends on intake geometry, internal Mach number level, and several other parameters.

Three other unsteady propulsion phenomena which partly come up in connection with buzz will only be briefly mentioned.

a. Sometimes a weak pressure pulsation connected with small motions of the terminal shock can be observed during subcritical phase of the buzz cycle [15, 18, 40], or before buzz is initiated [4, 59]. This phenomenon could be interpreted as an interaction between the befurcated part of the terminal shock and a local separation bubble [15], or as an interaction between terminal shock and external sonic line.

b. Unsteady total pressure profiles at the intake exit plane are also observed for highly supercritical intake operation. The unstable interaction of terminal shock and diffuser boundary layer appears to be the cause for the distortions.

c. During the cooperation between the supersonic intake and the turbo engine, it is also possible, that buzz can provoke compressor stall [64], and compressor stall can cause buzz.

4. UNSOLVED PROBLEMS AND A POSSIBILITY OF A NEW THEORETICAL APPROACH

During earlier work [61, 63], fifteen different theoretical explanations and descriptions of intake buzz have been discussed. These can be divided into two main groups:

- Theories which assume that the intake alone determines the stability behaviour: The theories presented by Ferri, Nucci [13] and Dailey [18] belong to this group. While the causes for the subcritical drop in efficiency presented in these papers have been confirmed by many other investigations, the explanation, that an intake buzz cycle is initiated by choking of the intake throat, due to vortex sheet ingestion [13], or boundary layer separation [18], has not been readily accepted [15 - 18, 25, 61, 63].

  Some other stability theories:

  - are correct only in cases, where the shock system breaks down at the stability boundary without reaction by the throttle (Pearce [35], Trimpi [15]),
  - seem to be oversimplified and not generally valid (Oswatitsch and Teipel [2], Hall [51], Billig [65])
  - are valid only for special cases of Ferri instability (Fisher, Neale, Brooks [41])
  - remain unexplained (Beastall [49]).
- Theories which assume that the stability behaviour is determined by interactions between intake and throttle:
  - For relatively short intakes, the theory by Mirels [7] appears to be accurate.
  - The famous Helmholtz-Resonator theory worked out by Sterbentz, Eward and Davids [21, 22] neglects the existence of internal pressure waves and was therefore not accepted [15, 61 - 63]. A similar theory was given by Fraiser [8].
  - The theory presented by Leynaert [36] could be useful in a case of a cooperation between a long slow acting intake and a short fast acting consumer.
  - The initial theory worked out by Stoolman [3] was later completed by Kowalewicz [5], Chang and Hsu [9, 10], Endwards [11] and extended by Hagashima et al [12]. The primary critisism of this theory is concerning the connection between disturbances ($\Delta p, \Delta M$) in the entrance area with the velocity of the terminal shock movement [61, 63]. According to [7, 61, 63], the disturbances depend primarily on the location of the terminal shock - the shock velocity can cause only additional effects of the order (diameter / L).
  - The different theories given by Hermann [24] and Fisher [42] exhibit experimental or theoretical contradictions.

The study of the existing literature shows the following unsolved questions:

Q1 Is it possible to describe the different buzz phenomena (Ferri, Dailey, Buffet [39 - 41], instability due to total pressure dip inside the capture stream tube) with the help of only one simplified global theory?

Q2 Will buzz be caused by non-linear intake behaviour alone, or arrise from the growing of weak interactions between intake and consumer?

Therefore the theoretical approach should have the following aims:

- An attempt should be made to include the different observed phenomena within a unified theory, which should be physically correct at least for a theoretical limiting case.
- Within the scope of question Q2, it should be examined to what extent the consumer has an influence on
  - the stability boundary, and
  - the pulsation cycle.

5. FORMATION OF A SIMPLIFIED THEORETICAL MODEL

The experience shows that buzz begins when the intake mass flow is throttled below a certain stability limit by the connected consumer, which can be a tube with throttle, a ram combustor, or a turbo engine. Using a turbo engine instead of a tube with throttle nozzle, an increased stability, due to additional damping, can result [28, 29, 50]. A ram combustor can produce additional damping or excitation for the intake nozzle interaction, depending on fuel properties, combustor geometry, or combustion behaviour.

Simplification 1:

The first step in the investigation of the intake consumer stability behaviour should therefore be limited to interactions between intake and nozzle alone.

In spite of simplification 1, the stability behaviour of an appropriate intake nozzle module (illustrated by Fig. 5) will be determined by at least 24 different parameters [61]. Most of these influential parameters describe the geometry of the intake. Therefore a general calculation of the unsteady intake flow, in regard to

- the shock boundary interactions (including separation effects),
- and vortex sheet and shear layers

without the use of doubtful approximations, seems hardly possible. On the other hand, the principle features of intake buzz are maintained with increasingduct length between intake and nozzle. This was demonstrated experimentally by Trimpi [14]. Therefore it seems to be apparent, that it is necessary to simplify the theoretical model in a radical manner, with the aid of

Simplification 2: $L_I <<< L$ (1)

Disregarding the high frequency oscillations mentioned in para. 3.2, this simplifying assumption means that the intake reaction time, following any disturbances, will be small compared with the propagation time of a pressure wave throughout the tube of length L. In the case of a relatively short intake, it is not necessary to pay particular attention to the dynamically stipulated deviations from the quasisteady intake behaviour. Thereforean especially simple calculation of the distortion process can be expected. As a result of a distortion by an upstreamtraveling wave, the intake will reach a new steady state in negligible time, where by a downstream traveling pressure wave and an entropy discontinuity will be generated. The intake throughflow will be mainly steady under the previously mentioned simplification. For the calculations, the complex intake behaviour can be therefore described by the quasisteady valid total pressure recovery characteristics. In general, nozzles are much shorter in comparison with intakes. Therefore the third approximation:

Simplification 3: $L_N <<< L$ (2)

will be physically more justified.

Wave nature of the internal distortions

The wave nature of the internal distortions, which was assumed by Mirels [7] who used the same simplifications, has been confirmed (especially for large L/L_I) by experimental work done by Trimpi [14, 15] and Stewart [39, 40].

In the case of a wave process, the boundary conditions at intake and nozzle correspond to those at opening and bottom of an organ pipe having one end open. The intake would represent a node, the nozzle an antinode of the pressure distribution. The period of a simple cycle would be determined by twice a pressure propagation through the tube moving back and forth:

$$\Delta t_c = \frac{4L}{a(1-M^2)} \qquad (3)$$

With sufficient throttling, nearly all buzz pulsation show indead a period comparable to Δtc. On the contrary, a necessary assumption for the application of the Helmholtz resonator model would be a much greater period.

Representation of the internal perturbation process

Two different mapping plots will be used to illustrate the internal flow process. The x, t-plane is used to illustrate the time-dependent wave propagation. The accompanying change in state may be depicted in the p_0, $\dot{m}$-plane. The total pressure characterizes the intake efficiency while the mass flow can be considered as a principle test variable.

6. INTERNAL FLOW CALCULATIONS USING SIMPLE WAVE THEORY

The pressure amplitude of the strongest internal waves during strongbuzzing does not exceed 30 percent. Therefore the internal wave processes can be approximately treated as isentropic:

Simplification 4:

The increase of entropy due to internal shock waves, which may be generated by converging compression waves is proportional to the third power of pressure amplitude and may be neglected.

In contrast, the entropy of the quasisteady intake exit air varies with intake exit total pressure, and that changes of entropy should be taken into account. Any change of intake total pressure will therefore, according to Fig. 7, generate an entropy discontinuity with separate regions of different entropy in the internal flow. The entropy discontinuities are special path lines and represent perturbations of density, temperature, Mach number, and $\dot{m}$ in a constant pressure region. Under the previously mentioned simplifications 2 and 3, the spatial extend of the simple compression waves generated by intake - or nozzle reactions are negligible small compared with L. Furthermore, the diverging rarefaction waves should also be depicted in a summation manner in the x,t plane according to Fig. 8.

Under the previously mentioned "simplification 4" (neglection of entropy increase due to the steepening of internal compression waves), all state variables in the constant state regions of the meshed network can be calculated step by step using the simple wave theory. Using the state characteristics for unsteady one dimentional flow [66 - 69], all state changes, due to simple pressure waves, or entropy discontinuities respectively, can be calculated in an easy manner.

With the abbreviations (4)

$$\pi \equiv \frac{\Delta p}{p} \qquad \pi_o \equiv \frac{\Delta p_o}{p_o} \qquad \varrho \equiv \frac{\Delta \rho}{\rho} \qquad \mu \equiv \frac{\Delta M}{M} \qquad \varphi \equiv \frac{\Delta \dot{m}}{\dot{m}} \qquad (4)$$

and using the state characteristics, in conjunction with the gasdynamic relations, the following relations for simple pressure waves may be obtained:

$$\Pi_0 = \frac{1 \mp M}{\mathfrak{M}}\,\pi \qquad \rho = \frac{1}{\varkappa}\,\pi \qquad \mu = \frac{\mp 1 - \frac{\varkappa-1}{2}M}{\varkappa M}\,\pi \qquad (5)$$

$$\varphi = \frac{M \mp 1}{\varkappa M}\,\pi \qquad \mathfrak{M} \equiv 1 + \frac{\varkappa-1}{2}M^2$$

or as a function of mass flow perturbating respectively:

$$\Pi_0 = \mp\frac{\varkappa M}{\mathfrak{M}}\,\varphi \qquad \rho = \frac{\mp M}{1 \mp M}\,\varphi \qquad \mu = \frac{1 \pm \frac{\varkappa-1}{2}M}{1 \mp M}\,\varphi \qquad \pi = \mp\frac{\varkappa M}{1 \mp M}\,\varphi \qquad (6)$$

Sign convention:

The upper sign always refers to changes of state due to upstream traveling waves, while the lower sign denotes changes due to waves traveling downstream.

The differential equations (5) can be integrated in closed form using the static pressure as an independent variable. This was one reason why the unusual p_0, p plane was used in earlier work [61 - 63], whereas in this study a graphical presentation of the internal changes in state will be given in the p_0, $\dot{m}$ plane. Using $\hat{\rho} = \hat{\varphi}$ to denote the intensity of a weak entropy discontinuity, the following relations can be obtained:

$$\hat{\Pi}_0 = \frac{\frac{\varkappa}{2}M^2}{\mathfrak{M}}\,\hat{\varphi} \qquad \hat{\rho} = \hat{\varphi} \qquad \hat{\mu} = \frac{1}{2}\,\hat{\varphi} \qquad \hat{\pi} = 0 \qquad (7)$$

With the aid of eqs. (5) - (7), all changes in state from one constant state region to the neighbouring can be calculated if the intensity and the type of the enclosed wave is known.

7. SOLUTION OF BASIC PROBLEMS

For the calculation of the state variables inside the meshed network, the magnitude of the individual waves is required. Therefore the changes of wave magnitude, due to fundamental unit processes, were determined using eqs.(5) - (7) with the respective boundary conditions:

o The intersection of simple pressure waves will not lead to a change of pressure amplitude within the scope of a theory of small amplitude.

o The intensity of an entropy discontinuity will not be changed by the intersection with a simple pressure wave. The amplitude of the incident pressure wave remains constant within the scope of an linear perturbation theory. The amplitude of the reflected pressure wave is proportional to the product of the amplitude of both incident waves and can be neglected withing the scope of a linear perturbation theory.

o In the case of a subsonic channel exit (characterized by M and M_N ,see Fig. 9), the exit boundary condition for simple wave reflection is the conservation of the ambient pressure p_∞ at the exit. For small perturbations one can find [61, 62]:

$$\left.\frac{\varphi_{32}}{\varphi_{21}}\right|_{lin} = \frac{(1-M_N^2)M - M_N^2(1-M)(1-\frac{\varkappa-1}{2}M)}{(1-M_N^2)M + M_N^2(1+M)(1+\frac{\varkappa-1}{2}M)} \qquad (8)$$

The following special cases are included:

- the closed end with M = 0, here the incident mass flow perturbation must be compensated: $\varphi_{32} = -\varphi_{21}$
- the open end with M_N = M: The resulting mass flow amplitude ratio (1-M)/(1+M) means, that the pressure pertubation vanishes: $\pi_{32} = -\pi_{21}$
- the critical (or supercritical) nozzle (M_N = 1): compared with the closed end, the loss in amplitude

$$\left.\frac{\varphi_{32}}{\varphi_{21}}\right|_{lin,\,M_N=1} = -\frac{(1-M)(1-\frac{\varkappa-1}{2}M)}{(1+M)(1+\frac{\varkappa-1}{2}M)} \qquad (9)$$

of the reflected wave increases with Mach number M.

o Equivalent to eq. (8), the interaction of an entropy discontinuity and a subsonic channel exit will lead to the following linear amplitude ratio:

$$\left.\frac{\varphi_{32}}{\hat{\varphi}_{21}}\right|_{lin} = \frac{\frac{1}{2}(M^2 - M_N^2)}{M + M_N^2(1+\frac{\varkappa-1}{2}M + \frac{\varkappa-1}{2}M^2)} \qquad (10)$$

According to eq. (8), this result is valid for nozzle and diffuser type exits respectively. While an entropy discontinuity (special path line) can never strike a closed end, the following special cases are included in eq. (10):

- the change of gas density at constant pressure can pass an open exit with M = M_N, without causing any wave reflection.
- the critical (or supercritical) nozzle will result in a pressure wave reflection of less than half the mass flow distortion φ_{32}:

$$\left.\frac{\varphi_{32}}{\hat{\varphi}_{21}}\right|_{lin,\,M_N=1} = -\frac{1-M}{2(1+\frac{\varkappa-1}{2}M)} \qquad (11)$$

13-6

- o In the case of simple wave reflection on an intake exit (Fig. 10), two boundary conditions had to be satisfied: Firstly, the pressure and mass flow perturbations of incident and reflected waves must be compatible with the intake characteristic. Secondly, the total pressure change due to the waves had to be in accordance with the total pressure recovery characteristic. If the intake characteristic curve is continuous in the considered operating point, the slope of the total pressure characteristic is given by σ,

$$\sigma = \frac{\Delta P_o}{P_o} \Big/ \frac{\Delta \dot{m}}{\dot{m}} \Big|_I \tag{12}$$

and the amplitude of the reflected waves can be obtained, after some manipulations,

$$\frac{\varphi_{32}}{\varphi_{21}}\Big|_{lin,I} = \frac{1 + \sigma\,\frac{1-(\varkappa-1)\Pi}{\varkappa\Pi}}{1 - \sigma\,\frac{1+(\varkappa-1)\Pi}{\varkappa\Pi}} \qquad \frac{\hat{\varphi}_{43}}{\varphi_{21}}\Big|_{lin,I} = \frac{2\,\frac{\varkappa-1}{\varkappa}\,\sigma}{1 - \sigma\,\frac{1+(\varkappa-1)\Pi}{\varkappa\Pi}} \tag{13}$$

The entropy discontinuity $\widehat{43}$ vanishes in the case of constant total pressure recovery ($\sigma = 0$), while the mass flow amplitude of the reflected wave φ_{32} equals φ_{21}. In this case, the intake is very similar to the open end of an organ pipe.

8. SUERSONIC DIFFUSER STABILITY WITH SMALL THROUGHFLOW PERTURBATIONS

The linear intake response, defined by eqs. (12) and (13), can also be obtained graphically by using the state characteristics (5) - (7). Therefore the unknown strength of the pressure wave 32 and the entropy discontinuity $\widehat{43}$ had to be iteratively brought in agreement with the intake characteristic in the two different state planes.

Semigraphical construction of the intake response (Fig. 11):

The intensity of the entropy discontinuity $\widehat{43}$ is both proportional to the total pressure change of the intake ($\hat{\pi}_{o43} + \pi_{o32} + \pi_{o21}$), and to the total pressure change of only the entropy discontinuity $\hat{\pi}_{o43}$. Therefore $\hat{\varphi}_{43}$ can be expressed as a function of $\pi_{o32} + \pi_{o21}$, as follows:

$$\hat{\varphi}_{43} = \frac{\varkappa-1}{\varkappa}\,\Pi\,(\pi_{o32} + \pi_{o21}) \tag{14}$$

Using eq (11), a semigraphical construction of the intake response in only one state plane (according to Fig. 11) is possible:

Starting from the indisturbed intake operating point 1, the mass flow may be reduced by φ_{21} by means of a small compression wave. Depending on the slope of the intake characteristic σ, the intake will respond in a different manner:

- In the case of supercritical operation without bleed ($\sigma = -\infty$), the incident mass flow reduction had to be compensated by the refelcted waves.
- In the case of $\sigma = 0$, no entropy discontinuity will be generated. The reflected pressure wave will double the incident mass flow reduction.
- The magnitude of the reflected pressure wave will increase with growing σ until an unlimited reaction will result within the scope of a linear perturbation theory, when the slope reaches the value of

$$\sigma_{AI} = \frac{\varkappa\Pi}{1+(\varkappa-1)\Pi} \tag{15}$$

The value σ_{AI} denotes the greatest possible slope of the intake characteristic, because at this operation point, the intake would react strongly, even by small perturbations without feed back from the consumer.

9. WEAK INTERACTIONS BETWEEN INTAKE AND SUPERCRITICAL NOZZLE

If friction between intake and nozzle can be neglected, then the intersection point of intake and nozzle characteristics represents the respective operating point of the intake. The question, whether such an operation point can represent stable interaction between intake and nozzle, can only be answered by the perturbation theory when the intake characteristic is differentiable in the neighbourhood of the operating point. This is not self-evident, because the boundary layer separation or vortex sheet ingestion would normally produce a discontinuity in the characteristic curve.

Under the assumption of supercritical nozzle pressure ratio, the nozzle characteristic will be a line with a slope of one in the π_o, φ plane. First of all, it should be examined whether stable interaction of intake and nozzle ceases at the top of the total pressure curve, as mentioned in [2]. Within the scope of the perturbation theory, the corresponding total pressure characteristic appears in form of a line of constant total pressure in the left side of Fig. 12. Assuming stable operation at time t_o, the nozzle discharge may be immediately reduced by φ_{21}. The resulting shift of the nozzle characteristic will cause a small compression wave to travel upstream. The total pressure rise π_{o21}, coupled with the mass flow reduction φ_{21}, depends on the internal flow Mach number in accordance with eq. 6.

The compression wave $\overline{21}$ will lead to an excessive total pressure at the intake exit. Therefore the intake will respond with a rarefaction wave $\overline{32}$, decreasing the mass flow, and pressure, down to the new intake operation point 3. No entropy discontinuity will be generated because the total intake pressure recovery did not change within the intake reaction (3' $\hat{=}$ 3). The mass flow 3 is now below the required nozzle throughflow. Consequently, the nozzle will react on the perturbation $\overline{32}$, and accelerate the gas with the aid of a rarefaction wave $\overline{43}$. Therefore, the intake will respond with an attenuated compression wave $\overline{54}$.

The pressure wave decays while oscillating between intake and nozzle and illustrates stable interaction of intake and nozzle at the peak of total pressure recovery. On the right side of Fig. 12, the analogous interference is treated for the case of positive slope of the intake characteristic. To obtain a clear picture of the main process, the paths and consecutive nozzle reactions of all the entropy discontinuity generated by intake reactions have been neglected. Within the scope of that simplification, a reduced attenuation of the wave cycle can be seen.

Looking for the boundary of stable interaction (using eqs. (6), (7), (9), (11), (12), (13)), it can be seen that in general, an undefinite number of weak secondary pressure waves are generated at the nozzle by entropy discontinuity reactions [61, 62]. For an undetermined number of special cases, it can be shown however [61, 62] that all the entropy discontinuities have a damping or excitingeffect on the formation of the main cycle. Fig. 13 shows the two most simple cases.

After some manipulations, the following boundary, for stable interaction of intake and supercritical nozzle, is obtained [61, 62]:

$$\sigma_{IS} = \frac{\varkappa M^2}{1+(\varkappa-1)M^2 - \frac{\varkappa-1}{\varkappa+1}(1-M^2)\{1+qM\}} \qquad q\begin{cases} 1 & \text{damping} \\ 0 & \\ -1 & \text{exiting} \end{cases}\text{effect on entrop. disc.} \tag{16}$$

The value of q depends on the mean effect of all entropy discontinuities on the formation of the main cycle.

10. COMPARISON OF DIFFERENT STABILITY THEORIES

Fig. 14 shows the influence of the mean internal flow Mach number M on

- the limit of absolute intake instability slope σ_{AI}
- the limit of intake nozzle interaction instability slope σ_{IS} - for the critical cases of maximum attenuation q = 1, indifferent effectioness, and maximum exitation by the entropy discontinuities.

Any change from the above assumptions (differentiable intake characteristic, length of intake and nozzle negligible compared to total length L, and for interaction stability boundary: a supercritical nozzle pressure ratio) can result in quite different stability boundaries:

+ Increasing the relative intake length, will cause a growing zone of wave dispersion at the intake and result in additional attenuation of the main cycle [61, 61]. Therefore, even with an intake greater than σ_{AI}, the intake flow may be stable.
+ The boundary of stable interaction can be changed if the consumer characteristic does not agree with the assumed supercritical nozzle.
+ A discontinuity within the intake characteristic, which immediately moves the slope from stable to unstable values, may not be observed because pulsations can start just at the discontinuity. Therefore, a measured slope of the intake characteristic at the origin of instability does not need to coincide with the interaction instability limit σ_{IS}.

The preceding stability statements can be compared with other well known theories under the above-mentioned simplifications (1) and (2):

o The result obtained by Mirels [7] is equivalent to eq. (6) under the additional assumption of small Mach number M, the entropy discontinuities being able to be neglected (q = 0) [63].
o The statement of Pearce [35] does not take the interactions with the consumer into account. The result would be comparable with eq (15).

The widely used Helmholtz resonator theory, proposed by Sterbentz, Eward, Davids [21 , 22], has been criticized extensively [14, 15]. The resulting instability slope limit is proportional to the relative length of the intake. In the case of a negligible relative intake length, the theory would state a stability limit of $\sigma = 0$, which was also stated by Oswatitsch and Teipel [2]. The Helmholtz resonator theory can not explain why sometimes (for higher internal Mach numbers and relatively long intakes) stable intake characteristics with large slopes can be observed.

11. STRONG INTERACTIONS BETWEEN INTAKE AND NOZZLE

The methods for the evaluation of small interactions between intake and nozzle, which was presented in chap. 7 to 10, can easily be extended for the investigation of strong nonlinear interaction processes. It can be seen that the intake characteristic is the source of principal nonlinearity. Using simplification 4 (chap. 4), the change in state, due to arbitrary simple wave, can be depicted in the p_0, p plane in closed form [61, 62], or can be integrated step by step in the $p_0, \dot{m}$ plane with respect to the parameter M.

In the case of a semigraphical construction (Fig. 15) of the intake response, the relation between the mass flow ratio of the entropy discontinuity, and the intensity of both pressure waves, becomes, according to eq. (14),

$$\frac{\hat{\dot{m}}_4}{\dot{m}_3} = \left\{1 + \mathfrak{M}_3\left[\left(\frac{p_{o3}}{p_{o2}}\,\frac{p_{o2}}{p_{o1}}\right)^{-\frac{\varkappa-1}{\varkappa}} - 1\right]\right\}^{-1} \tag{17}$$

Using eq. (17), the effect caused by the entropy discontinuity can be outlined in relation to the intensity of the reflected pressure wave $\overline{32}$. The example, illustrated in Fig. 15, shows the nonlinear intake response due to a mass flow reducing compression wave after a sudden reduction of the nozzle exit. The change in mass flow and total pressure caused by the entropy discontinuity is very small compared to the intensity of the pressure waves. Therefore, the investigation of the principle nonlinear interactions between intake and nozzle can be simplified by the omission of all entropy discontinuities. Such simplifications of typical nonlinear interactions are presented in the following figures:

Fig. 16 shows an isolated buzz cycle as the result of a sudden nozzle discharge throttling up to a value near to stability boundary. The strong rarefaction wave coming from the intake will be reflected from the nozzle. Due to the reduced back pressure, the terminal shock will return from the position in front of the cowl, and try to reach a supercritical state of equilibrium. The respective operating point 5 was attained by a simple downstream running pressure wave (and an associated entropy discontinuity) starting from the disturbed operating condition 4.

Within the scope of the simplifications 1 and 2, it is not necessary to pay particular attention to the different possible intermediate states during the unsteady change of intake operation. In the sequence, the intensity of the internal pressure waves running back and forth is attenuated because the new intersection of inlet and nozzle characteristic still represent a stable operation.

Fig. 17 shows a series of simple limiting cycles for various throttle ratings. They have a period corresponding to an organ pipe and are typical for intakes with a wide stable subcritical operating range. With closing throttle the total pressure amplitude grows, starting from a considerable high initial level, and goes through a maximum, the pulsation dies away when a second stable subcritical operating range is reached. In the illustrated example, the intake enters the reversed flow regime. The increasing intake total pressure with reversed flow has been observed experimentally [59] and correspondends with the transition of a nozzle characteristic.

Fig. 18 shows limiting cycles for an intake with a small stable subcritical operating range and a large amount of subsonic diffusion (small value of M). A throttle ratio just below the stability limit will produce a staged supercritical pressure rise and an appropriate elongated periodic cycle. With closing throttle, the number of supercritical interactions during the fill-up phase of the cycle is reduced since the amplitude of the pressure waves traveling down and back grow progressively. Finally, a limiting cycle with an organ pipe oscillation period will be reached.

An additional consideration of the effects caused by entropy discontinuities and internal wall friction can lead to the following results [61, 62]:

- Due to the impingement of entropy discontinuities on the nozzle, a large number of weak secondary pressure waves will be generated. If such a secondary wave, during buzz cycle, strikes the inlet, operating just near the stability limit, it can provoce the next cycle. Therefore, the cycle period can vary slightly. Even without regard of the intake and nozzle delay, the period does not need to be a multiple of half the organ pipe period.
- A local internal friction zone causes attenuation and stabilizing effects when it is concentrated at the intake exit. Total pressure losses, due to instrumentation at the intake exit, can therefore produce a too optimistic stability behaviour.

12. LIMITATIONS OF THE THEORETICAL MODEL AND COMPARISON OF THEORETICAL TRENDS WITH EXPERIMENTAL WORK

The principal simplification of the theoretical model, $L_I <<< L$ indicates a significant limitation:

Calculations of the transient behaviour, made for an intake with a long throat [61], showed that many interactions between the external shock system, and the internal diffuser can be required to obtain a new operating point after distortion. Remembering the high Mach number level inside the throat region and the resulting low propagation speed for the upstream traveling waves, a long reaction time is produced.

- Even in the case of a very long internal duct, a stabilizing and attenuating effect, caused by wave dispersion at the intake exit, can be expected. In comparison to the demonstrated example calculations, a smaller oscillation amplitude may result.
- In contrast to the simple theoretical model discussed, an intake of medium relative length will not reach a quasistationary operating point during a buzz cycle.
- In the case of similar length-of-intake and connected consumer, the dynamic behaviour of the intake may be slow compared with the consumer. In this case, a totally different theory has to take the dynamic behaviour of the intake flow into account while, in accordance with [36], a quasistationary consumer characteristic may be assumed.

In spite of the strong limitations, resulting from the principal assumptions, the presented simple model can explain in closed form different observed features of diffuser buzz using the associated intake characteristics:

1. By just crossing the stability boundary, large pulsations can be induced.
2. The building-up process will quickly lead to a limiting cycle. Even the first discernible cycle shows the typical shape of the following cycles.
3. The pressure amplitude, measured upstream the nozzle, grows in general with a closing throttle, starting from a considerable large initial value.
4. In the case of a wide stable subcritical operation range, as can be noticed occasionally for intakes exhibiting Ferri instability, a buzz period, comparable with the first mode period of an organ pipe, and nearly undependent from throttle ratio, can be found.
5. With a small subcritical operation range, buzz begins with a much longer period which will be shortened by increased throttling till finally a fundamental period will result.
6. Due to the disturbances always present in free stream, it is clear that by approaching the stability boundary, a growing number of isolated buzz cycles in irregular sequence can be noticed, especially in the case of intakes having a small subcritical operation range and a large amount of subsonic diffusion. This phenomenon is called buffet [39, 40].
7. The considerable differences of the stability behaviour of similar intakes may be explained by the strong effect of the small form differences in the pressure recovery characteristics.
8. Limited irregularities of the buzz cycle pattern can even result from only entropy discontinuities.
9. Examinations of the unsteady interaction between shock system and internal diffuser [61], showed an instantaneous decline of mass flow and Mach number in the throat of a subcritical operating intake, following the arrival of a compression wave at the intake exit.

The final question, as to how far the consumer influences the onset of buzz pulsations, may be answered by the following statements:

If the intake characteristic is differentiable in the neighbourhood of the stability boundary, then the consumer will have an influence on the stability behaviour. The stability boundary will be situated at such a throttle ratio, where exciting by the intake is compensated by the damping effect of the consumer.

When the stability boundary is crossed, a rapid buildup process of buzz pulsations may result from a marked curvature of the intake characteristic. So it may be possible that the stability boundary is determined by small linear intake consumer interactions, even in the case where the first discernible cycle shows the entire buzz pressure amplitude.

REFERENCES

[1] K. Oswatitsch, Der Druckwiedergewinn bei Geschossen mit Rückstoßantrieb bei hohen Oberschallgeschwindigkeiten, Forsch. u. Entwickl. des Heereswaffenamtes, Bericht-Nr. 1005 (1944), Nachdruck: DVL-Bericht-Nr. 49 1957/NACA TM 1140 1947

[2] K. Oswatitsch, I Teipel, Die Pulsationen von Stoßdiffusoren, ZAMP Vol, IXb. 1958, S. 462-477

[3] L. Stoolman, Investigation of an instability phenomena occuring in supersonic diffusors, Doctor of Phil. Thesis, C.I.T., Pasadena, Calif. 1953

[4] J. Nicolas, Etude expérimentale des écoulements pulsatoires dans une prise d'air supersonique, La Recherche Aeronautique No. 58, S. 23-28

[5] A. Kowalewicz, Stability analysis of a normal-shock diffusor, Archivum Mechaniki Stosowanej 5,16,1964 S, 1153-1184, February 1964

[6] H.R. Hunczak, E.J. Kremzier, Characteristics of perforated diffusers at free-stream Mach number 1.90 NACA RM E50 B02, May 1950

[7] H. Mirels, Acoustic analysis of ram-jet buzz, NACA TN 3574, 1955

[8] H.R. Fraiser, Supersonic inlet dynamics, J. of Aero/Space Sci. Vol. 27, S. 429-436, June 1960

[9] C.C. Chang, C.T. Hsu, Solution to Stoolmans external diffusion equation for instability of a normal shock inlet diffuser, Jet Propulsion Vol 28, No. 7, S. 457-460, July 1958

[10] C.C. Cang, C.T. Hsu, Aerodynamic instability of supersonic inlet diffusers A.R.S. Journal, Vol. 30, No. 6, S. 468-475, May 1960

[11] R.H. Edwards, Solution to the linearized quasi-stationary external diffuser equations, A.R.S. Journal Vol 29 No. 1 S. 54, January 1959

[12] T. Nagashima, T. Obokata, T. Asanuma, Experiment of supersonic air intake buzz, Institute of Space and Aero. Sci., University of Tokyo, Report No. 481, May 1972

[13] A. Ferri, L.M. Nucci, The origin of aerodynamic instability of supersonic inlets at subcritical conditions, NACA RM L50 K30, 1951

[14] R.L. Trimpi, An analysis of buzzing in supersonic ram jets by a modified one-dimensional nonstationary wave theory, NACA TN 3695, July 1956

[15] R.L. Trimpi, A theory for stability and buzz pulsation amplitude in ramjets and an experimental investigation including scale effects, NACA Report 1265, 1956

[16] R.L. Trimpi, Comments on supersonic diffuser instability, J. Aero.Sci. Vol. 23 No. 6 S. 611-612, 6.56

[17] R. L. Trimpi, Reply to further comments on supersonic diffuser instability, J.Aero.Sci. Vol. 24 No. 11 S. 845-846, Nov.1957

[18] C.L. Dailey, Supersonic diffuser instability, J.Aero.Sci. Vol. 22, No. 11, S. 733-749, Nov. 1955

[19] C.L. Dailey, Further comments on supersonic diffuser instability, J. Aero.Sci. Vol. 24, No. 1, S. 70-71, Jan 1957

[20] C.L. Dailey, Reply, J. Aero.Sci. Vol. 24, No. 11, S. 846, Nov. 1957

[21] W.H. Sterbentz, J.C. Evvard, Criterions for prediction and control of ramjet flow pulsations NACA TN 3506, Aug. 1955

[22] W.H. Sterbentz, J. Davids, Amplitude of supersonic diffuser flow pulsations, NACA TN 3572, Oct. 1955

[23] J. F. Connors, Effect on ramjet pressure pulsations on supersonic diffuser performance NACA RM E50 H22, Nov. 1950

[24] R. Hermann, Supersonic inlet diffusers and introduction to internal aerodynamics, Minneapolis-Honeywell Regulator Co. 1956

[25] D. D. Wyatt, A review of supersonic air intake problems, AGARDograph No. 27, Pergamon Press S.21-47; '58

[26] L.W. Gertsma, M.A. Beheim, Performance at Mach numbers 3.07, 1.89 and 0 of inlets designed for inlet engine matching up to Mach 3. NACA RM E58 B13, May 1958

[27] M.A. Beheim, L.W. Gertsma, Performance of variable two-dimensional inlet designed for engine inlet matching, I-Performance at design Mach number of 3.07, NACA RM E56 H23, Nov. 1956

[28] M.A. Beheim, S.W. Englert, Effects of a J-34 turbojet engine on supersonic diffuser performance, NACA RM E55 I21, Jan. 1956

[29] N.T. Musial, Comparison of effect of a turbojet engine and three cold flow configurations on the stability of a full-scale supersonic inlet, NACA, RM E56 K23, Jan 1957

[30] D.L. Motycka, J.B. Murphy, Experimental investigation of inlet-to-inlet shock interference, SAE National Aeronautic Meeting, Washington, D.C., April 12-15 1965

[31] G. Crispin, Einlaufdiffusoren für den Oberschallflug, DVL-Bericht Nr. 144, April 1961

[32] W. Trommsdorff, Versuche an einem fertigungsgünstigen Mehrstoßdiffusor bei Oberschallgeschwindigkeit DVL-Bericht Nr. 44, Sept, 1957

[33] W. Trommsdorff, Untersuchungen an Triebwerkseinläufen, DVL-Forschungsbericht 66-34, Mai 1966

[34] E. Söffker, Untersuchungen an einem Oberschalleinlaß-Diffusor mit stabilisierendem Ring, ZfW 8, Heft 2, S. 33-44, Febr. 1960

[35] R.B. Pearce, Causes and control of powerplant surge, Aviation Week, Vol. 52, No. 3 S21-25, Jan. 16,'50

[36] J. Leynaert, Pompage dans les entreés d'air supersoniques, ONERA TP866 ou l'Aeronautique et l'Astronautique, N22, 1970

[37] D.G. Stewart, Proposals for a further programme of intake instability research, ARL Techn.Memo 170, April 1957

[38] D. G. Stewart, Design of conical intakes for instability investigations, ARL. Techn.Memo. 179, Jan. 1958

[39] D.G. Stewart, Supersonic intake instability - the effect of design geometry on intakes of 25° cone semi-angle at M = 1.83, ARL Report M.E.104 Melbourne, Oct. 1962

[40] D.G. Stewart, Supersonic intake instability - further investigations of intakes of 25° cone semi-angle at Mach numbers up to 2.14 with and without boundary layer bleed, ARL Report M.E. 112, Melbourne, Jan, 1964

[41] D.G. Stewart, S.A. Fisher, Instability and turbulence in supersonic air intakes - the effects of free stream turbulence, Reynolds number and surface roughness on some axisymmetric intakes at M = 1,8 and 2.2, ARL Report M.E. 129 Melbourne, Nov. 1970

[42] S.A. Fisher, On the mechanism of supersonic intake instability with some thoughts for further work, ARL Note M.E. 313, Melbourne, March 1970

[43] S.A. Fisher, Tests at Mach 1.915 on an air intake proposed for Concorde, NGTE Report No. R290, 4/67

[44] S.A. Fisher, M.C. Neale, A.J. Brooks, On the subcritical stability of variable ramp intakes at Mach numbers around 2, NGTE Report No. R.311, Febr. 1970

[45] M.C. Neale, P.S. Lamb, Tests with a two-dimensional intake having all external compression and a design Mach number of 2, ARC, Current Papers No. 937, 1967

[46] E.L. Goldsmith, C.F. Griggs, The estimation of shock pressure recovery and external drag of conical centre-body intakes at supersonic speeds, ARC, R&M No. 3035, 1959

[47] C.F. Griggs, An investigation of two methods of suppressing shock oscillation ahead of conical centre body intakes, RAE, Techn.Note Aero. 2551, March 1958

[48] C.F. Griggs, E.L. Goldsmith, Shock oscillation ahead of centre-body intakes at supersonic speeds, RAE, Report Aero. 2477, Sept. 1952

[49] D. Beastall, Flow instability of centre-body diffusers at supersonic speeds, ARC, R&M No. 2933, 11/53

[50] R.G. Schweikardt, R.P. Grippe, A supersonic intake control system for the external compression mode, J. of Aircraft, Vol. 8, No. 12, S.995-1000, Dec, 1971

[51] G.R. Hall, A criterion for prediction of airframe integration effects on inlet stability with application to advanced fighter aircraft, AGARD-CP-150 Paper 2, Sept 1974

[52] J.E. Hawkins, YF-16 inlet design and performance, J. of Aircraft, Vol 13, No. 6, S.436-441, June 1976

[53] I.H. Retti, W.G.E. Lewis, Design and development of an air intake for a supersonic transport aircraft J. Of Aircraft Vol. 5, No. 6, S. 513-521, Nov.-Dec. 1968

[54] W.R. Haagenson, L.M. Randall, Inlet development for the B-1 strategic bomber, AIAA Paper No. 74-1064, Oct. 1974

[55] W.F. Imfeld, Development programme for the F-15 inlet, J.Of Aircraft Vol 13, No. 4, S.286-291, 4/76

[56] F.W. Burcham, D.L. Hughes, J.K. Holzman, Steady-state and dynamic pressure phenomena in the propulsion system of an F-111 Airplane, NASA TN D-7328, July 1973

[57] J. Peikert, Regelung von verstellbaren Oberschallufteinläufen, insbesondere zweidimensionalen Schrägstoßdiffusoren für Gasturbinenstrahltriebwerke zum Antrieb von Hochleistungsflugzeugen, Deutsches Patentamt, Auslegeschrift 25 45 019, 20.03.1980

[58] G. Laruell, Persönliche Mitteilung über das Stabilitätsverhalten der invertierten Rechteckeinläufe, ONERA, MATRA, Rolls-Royce, BAe, MBB-Intake Meeting Dez. 1979

[59] E.-O. Krohn, Persönliche Mitteilung über das Stabilitätsverhalten der halbrotationssymmetrischen Einlauf-Diffusoren. Diskussion: DFVLR-Köln, Institut für Experimentelle Strömungsmechanik/MBB 1979

[60] C.R. Dawson Supersonic diffuser instability, a summary and a bibliography of current literature, Aircraft Research Association, Bedford, Wind tunnel note, No. 47, June 1962

[61] H.-L. Weinreich, Eindimensionale Betrachtungen zum Stabilitätsverhalten von Einlaufdiffusoren für Überschall-Flugantriebe, Dissertation, TH-Darmstadt, 1979

[62] H.-L. Weinreich, Eine Untersuchung instationärer eindimensionaler Strömungsvorgänge, Institutsbericht, Fachgebiet Flugantriebe, THD 1978

[63] H.-L. Weinreich, Vergleichende Literaturdurchsicht zum Thema des Diffusorbrummens, Institutsbericht Fachgebiet Flugantriebe, THD 1978

[64] C.S. Ball, Air intake aerodynamics and operational and installation effects on missile powerplant performance, AGARD-VKI Lecture Series No. 98 Supplement, 12.-16.3.1979

[65] L. O. Billig, Automatic detection an suppression of inlet buzz in instrumentation for airbreathing propulsion, Proc. of the Symposium, MIT-press, S.453-460, 1974

[66] R. Sauer, Nichtstationäre Probleme der Gasdynamik, Springer Verlag 1966

[67] A.H. Shapiro, The dynamics and thermodynamics of compressible fluid flow, The Ronald Press 1954

[68] E. Becker, Gasdynamik, B.G. Teubner, Stuttgart 1966

[69] R. Courant, K.O. Friedrichs, Supersonic Flow and Shock Waves, Interscience Publishers, New York 1948

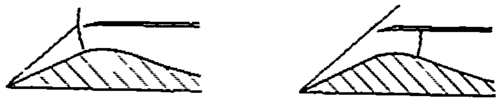

Fig. 1 Subcritical and supercritical intake operation

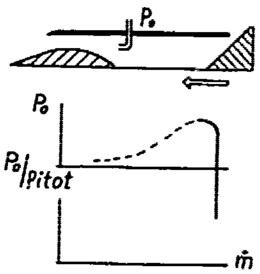

Fig 2 Typical total pressure recovery for an intake without internal contraction

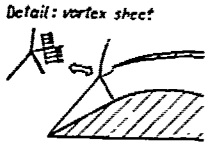

Fig. 3 Vortex sheet from shock intersection that triggers the Ferri instability

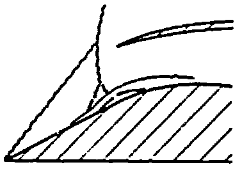

Fig. 4 Shock induced boundary layer separation which triggers the Dailey instability

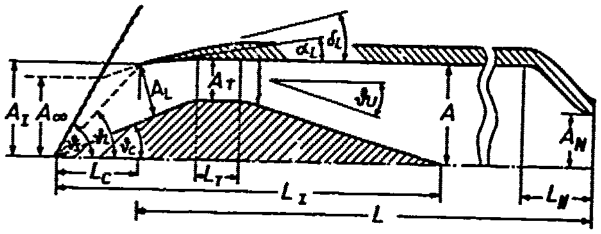

Fig. 5 Some geometric parameters influencing buzz in the case of a simple axisymmetric model

Fig. 6 Simple elongated model for stability analysis

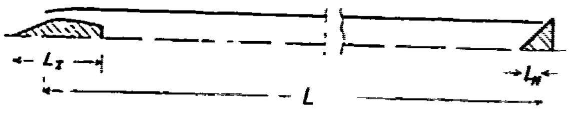

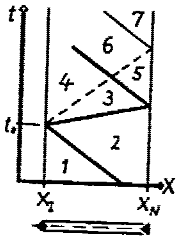

Fig. 7 Propagation of pressure waves and entropy discontinuities after a distortion of nozzle throughflow

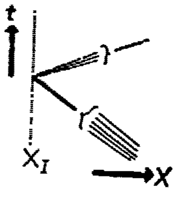

Fig. 8 Agglomaration of a diverging rarefaction wave

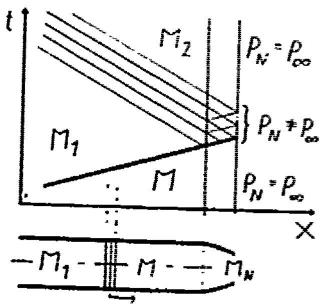

Fig. 9 Reflection of a pressure wave from an arbitrary open end of a tube

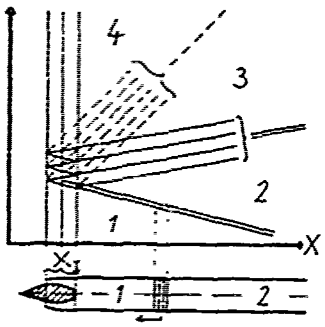
t
4
3
2
1
X
X_I
1
2

Fig. 11
Semi-graphical construction of the intake response for different slopes of the intake characteristic

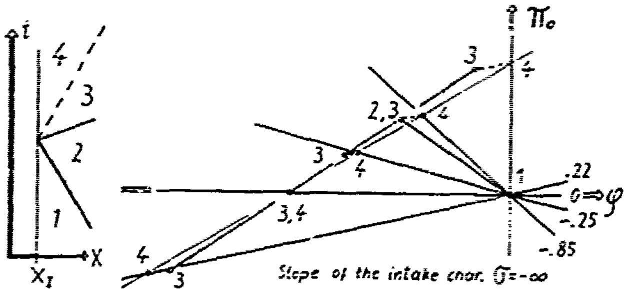
t
4
3
2
1
X
X_I
Π_o
3
4
2,3
4
3
4
3,4
4
3
1
.22
0⇒φ
-.25
-.85
Slope of the intake char. σ=-∞

Fig. 10
Reflection of a pressure wave $\overline{32}$ and an entropy discontinuity $\widehat{43}$ after distortion of the intake operating point 1

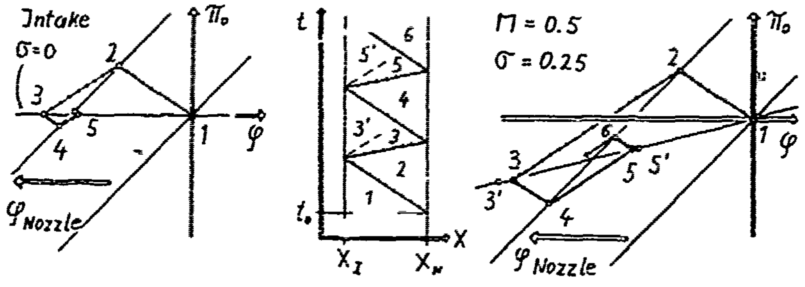
Intake
σ=0
Π_o
2
3
5
4
1
φ
φ_{Nozzle}
t
6
5'
5
4
3'
3
2
1
t_o
X_I
X_N
X
M = 0.5
σ = 0.25
Π_o
2
6
3
3'
5
5'
4
1
φ
φ_{Nozzle}

Fig. 12
Attenuation of a mass flow disturbance after a sudden discharge diminution

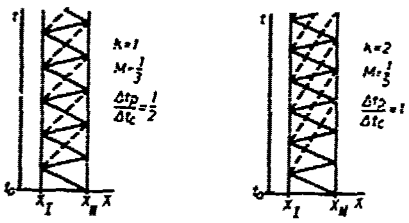
t
K=1
$M=\frac{1}{3}$
$\frac{\Delta t_p}{\Delta t_c}=\frac{1}{2}$
t_o
X_I
X_N
X
t
K=2
$M=\frac{1}{5}$
$\frac{\Delta t_p}{\Delta t_c}=1$
t_o
X_I
X_N
X

Fig. 13
Two most simple special cases:
K = 1: max. attenuation
K = 2: max. stimulation
due to entropy discontinuities

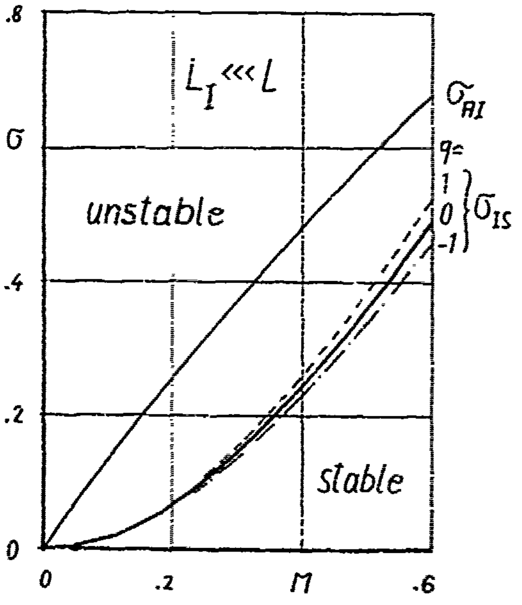

Fig. 14
Limit values for the slope σ of the intake characteristic (ass. $L_I \lll L$)
σ AI absolute stability boundary
σ IS stability boundary for interference with supercritical nozzle

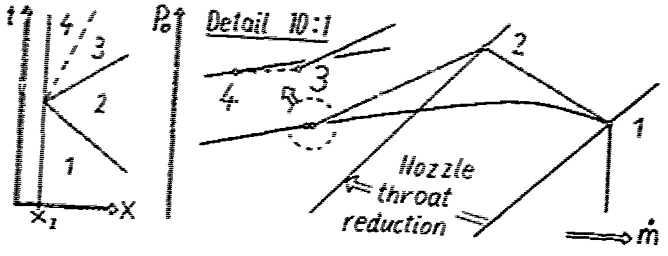
t
4
3
2
1
X_I
X
P_o
Detail 10:1
4
3
2
1
Nozzle throat reduction
ṁ

Fig. 15
Non linear intake response after sudden reduction of nozzle throat

Fig. 16
Isolated buzz cycle as a result of a too sudden nozzle discharge throttling up to a value near the stability boundary (simplified picture without entropy discontinuities)

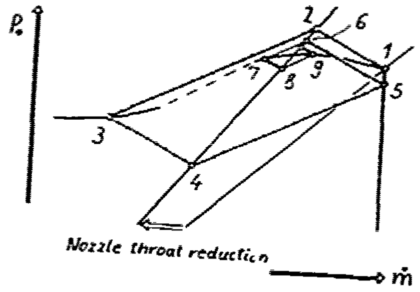
P_o
2
6
1
7
8
9
5
3
4
Nozzle throat reduction
ṁ

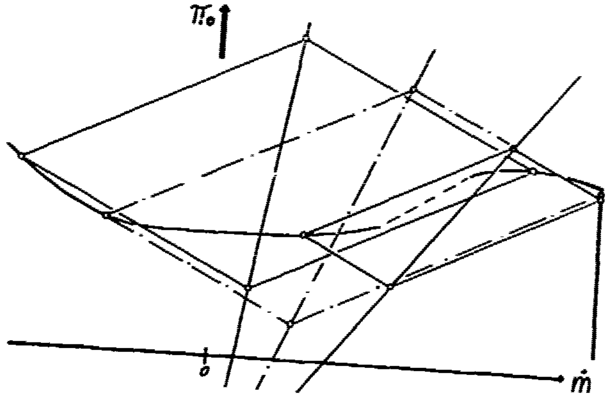

Fig. 17
Limiting cycles for different throttle ratings. Example of an intake with wide stable subcritical operation range

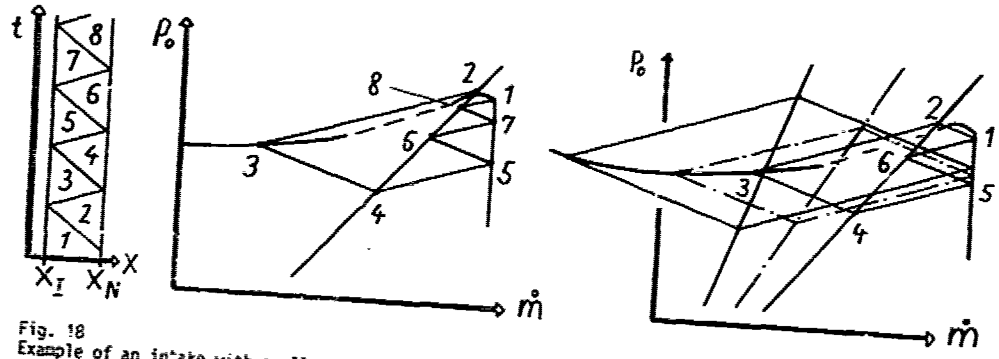
t
8
7
6
5
4
3
2
1
X_I
X_N
X
P_o
8
2
1
7
6
3
5
4
ṁ
P_o
2
1
6
3
5
4
ṁ

Fig. 18
Example of an intake with small stable subcritical operation range. Shortening of the recompression phase and approximation of an organ pipe type oscillation with increasing throttle ratings.

DISCUSSION

C.Limage

In recent experiments in the USA, it has been observed that the inlet instability has been driven by the ramjet combustion instability. Have you considered this type of interaction?

Author's Reply

The interference between inlet instability and combustion has been known for many years and have been reported, for instance, by Trimpi[14,15], Daily[18] and Sterbentz[21,22].

There also exists some theoretical approach for this problem (Mirels[7], Trimpi[14,15]).

Because the buzz phenomenon is not generally altered by the combustion process, it was decided to avoid the complication of calculating the wave dispersion and reflection by an internal combustion zone.

It seems to be possible that the theoretical method presented in References 61, 62 which include effects of internal area change and local friction could be extended for the consideration of the effects due to local heat addition.

H.Wittenberg:

In the last section of your paper, you have compared the results of your theory with experimental work in a qualitative way. Have you also made comparisons with experimental data quantitatively to investigate if your method can be used to predict the stability behavior of inlets?

Author's Reply

No, we are now just trying to make such comparisons with experimental work performed at the DFVLR by Mr Krohn. In my theoretical work which was performed at the technical university, I had no opportunity to make experimental measurements. I used for calculations one experimental pressure recovery characteristic which I found in the literature.

RANGE MAXIMIZATION METHOD FOR RAMJET POWERED MISSILES WITH FLIGHT PATH CONSTRAINTS

by

Ulrich M. Schöttle
Institut für Raumfahrtantriebe
University of Stuttgart
Pfaffenwaldring 31
D 7000 Stuttgart 80
Germany

SUMMARY

Mission performance of ramjet powered missiles is strongly influenced by the trajectory flown. The trajectory optimization problem considered is to obtain the control time histories (i.e. propellant flow rate and angle of attack) which maximize the range of ramjet powered supersonic missiles with preset initial and terminal flight conditions and operational constraints. The approach chosen employs a parametric control model to represent the infinite-dimensional controls by a finite set of parameters. The resulting suboptimal parameter optimization problem is solved by means of nonlinear programming methods. Operational constraints on the state variables are treated by the method of penalty functions. The presented method and numerical results refer to a fixed-geometry solid fuel integral rocket ramjet missile for air-to-surface or surface-to-surface missions. The numerical results demonstrate that continuous throttle capabilities increase range performance by about 5 to 11 percent when compared to more conventional throttle control.

1. INTRODUCTION

Ramjets are currently being considered as the primary propulsion candidate for a number of future atmospheric missiles as they offer the combined advantage of high specific impulse, high speed, continuous thrust and compactness (1). The integral rocket ramjet concept in its solid fuel ramjet version or solid ducted rocket version is of particular interest. The present paper addresses the problem of range maximization of an integral rocket ramjet missile and reports on application work which was performed in order to establish the performance capabilities, throttle requirements and parameter sensitivities of a given missile. The vehicle design and propulsion characteristics as well as the mission requirements were defined in previous industry studies and were prescribed (2). The mission of interest is schematically shown in Figure 1. We assume at the outset that the structure of the optimum trajectories consist of climb, cruise, descent and sea-skimming segments. Not shown in the sketch is the rocket boost phase which will accelerate the missile to ramjet ignition velocities. Only the ramjet powered flight will be considered. Mission objectives require trajectories below a prescribed maximum flight altitude in order to delay radar detection and a final weaving flight phase at sea-skimming altitudes. This type of maneuver will maximize the survivability of the missile against shipboard defense weapons. Ramjet trajectory problems have not received much attention in the control literature yet. This may be attributed, in part, to the fact that these works are rarely published beyond industrial reports for security reasons. Open-loop optimal trajectories for minimum fuel-to-climb, minimum time-to-climb and minimum time-to-intercept problems for an air-to-air liquid fuel ramjet-propelled missile are considered in (3). A separate important issue is the on-board implementation of the optimal control solution. This requires that the solution be found in a closed-loop form. The focus of the work (4) and (5) is mainly concerned with the derivation of such optimal control laws using singular perturbation theory.

Our goal is to obtain the optimal open-loop control program. The control problem is formulated by constructing a cost functional which penalizes violations of the inequality constraints. An efficient method to optimize complex atmospheric trajectories is to transform the continuous optimal control problem to one of parameter optimization. This technique has seen wide application to a great number of optimal control problems of varying complexity, (3), (7) to (13) and in our example proved to be less complex and difficult to solve than calculus of variation methods.

The remainder of this paper is organized as follows. In section 2 the optimization problem is stated. Then, in section 3, the numerical solution technique is described and in section 4 the missile simulation model is defined. The final section 5 presents some numerical results. The first examples concern level flight at sea-skimming altitude. Finally results for low-high-low flight profiles are obtained.

2. PROBLEM STATEMENT

The general nonlinear optimal control problem can be formulated as a problem of Bolza in the calculus of variations, i.e. extremize the performance index

$$J(\underline{u},\underline{\pi}) = \Phi\,[\underline{x}(t_f),\,\underline{\pi}] + \int_{t_o}^{t_f} L\,[\underline{x}(t),\,\underline{u}(t),\,\underline{\pi}]\,dt \qquad (1)$$

with respect to $\underline{u}(t)$ and $\underline{\pi}$, subject to the equations of motion

$$\dot{\underline{x}}(t) = \underline{f}(\underline{x},\underline{u},\underline{\pi}) \;,\quad \underline{x}(t_o) = \underline{x}_o \text{ specified} \qquad (2)$$

the boundary conditions

$$\underline{\psi}[\underline{x}(t_f),\underline{\pi}] = \underline{0} \qquad (3)$$

and inequality constraints

$$\underline{h}[\underline{x}(t_f),\underline{\pi}] \geq \underline{0} \qquad (4)$$

$$\underline{S}[\underline{x}(t),\underline{u}(t),\underline{\pi}] \geq \underline{0} \qquad (5)$$

In equations (1) to (5) $\underline{x}(t)$ represents the n-dimensional state vector, $\underline{u}(t)$ denotes the r-dimensional control vector, $\underline{\pi}$ represents a design parameter vector of dimension m_π, $\underline{\psi}$ is a q-dimensional vector function and Φ, L are scalar functions. The subscripts 'O' and 'f' refer to the initial and final values of the independent variable time 't', respectively. The initial time t_o corresponding to ramjet ignition is specified while t_f is free. Final time t_f is determined from the specified final mass which is used as stopping condition in the numerical algorithm.

$\underline{\psi}$ contains the specified values for terminal velocity v_f, flight path angle γ_f, altitude h_f and possibly lateral displacement y_f. The inequality constraints (4) and (5) result from structural limits, mission and propulsion requirements which bound the altitude-Mach number operational region and the controls. Specifically, it is required that recovery temperature $T_r(t) \leq T_{max}$, Mach number $M(t) \geq M_c(h,\mu)$, flight altitude $0<h(t) \leq h_{max}$, propellant flow rate $\mu_{min} \leq \mu_1 \leq \mu(t) \leq \mu_u \leq \mu_{max}$ with throttle ratio $\phi = \mu_u/\mu_1 \leq \phi_{max}$ and the resulting angle of attack $\varepsilon(t)=\sqrt{\alpha^2(t)+\beta^2(t)} \leq \varepsilon_{max}$ stay within pregiven limits.

Optimal control problems with constraints on the state and / or control are often solved by converting them to a sequence of unconstrained subproblems by means of penalty functions. These are added to the primary indicator of the system performance which in our case is the downrange coordinate $x(t_f)$. Thus, the functions Φ and L of equation (1) are augmented to include

$$\phi\,[\underline{x}(t_f),\underline{\pi}] = -\,x(t_f) + \sum_{i=1}^{q} \psi_i^2 \cdot P_i + \sum_{i=1}^{w} h_i^2 \cdot Q_i \tag{6}$$

and

$$L\,[\underline{x},\underline{u},\underline{\pi}] = \sum_{i=1}^{s} S_i^2 \; R_i \tag{7}$$

where

$$Q_i = \begin{cases} C_i > 0 & \text{if } h_i < 0 \\ 0 & \text{if } h_i \geq 0 \end{cases} \tag{8}$$

$$R_i = \begin{cases} K_i > 0 & \text{if } S_i < 0 \\ 0 & \text{if } S_i \geq 0 \end{cases} \tag{9}$$

P_i, Q_i (C_i) and R_i (K_i) represent coefficients penalizing violations of the different constraint conditions (3) to (5). The functional inequality constraints (7) are evaluated by integrating the constraint violations over the interval $[t_o, t_f]$ along with the numerical integration of equation (2). A sequence of optimal control problems with increasing penalty coefficients must be solved. In the limit, minimizing the augmented penalty function maximizes the range performance and drives the constraints into satisfaction. The derivation of necessary conditions for the optimal control problem stated above by means of the calculus of variations is straightforward and well documented in literature (6,7), and will not be repeated here. Some aspects of numerical solution techniques applied to the ramjet trajectory problem will be discussed in the next section.

3. SOLUTION METHODS

The most widely used iterative computational algorithms to determine optimal controls represent variations of either the gradient method or Newton's method in either function or Euclidean spaces and are local in nature.

Function Space Conjugate Gradient Method

In the beginning we sought the solution by use of a function space conjugate gradient (FCG) method (6,7). We used this technique successfully to obtain optimal controls for rocket ascent trajectory problems to near earth orbits. However, when applied to the ramjet trajectory problems the FCG method failed due to excessive computing time. This failure may be attributed, in part, to 1. the highly nonlinear characteristics of the missile and the ramjet propulsion system and 2. to the high number of equality and inequality constraints involved in our problem, which were handled by the method of penalty functions. During the iterative process the trajectory tended to leave the bounded altitude-Mach number region, for which valid ramjet propulsion data were available. Hence, comparatively high penalty coefficients had to be chosen already at the beginning in order to force the trajectory to stay within the limitations of the propulsion model. Adding penalty functions to the performance index containing periodically increased constants may change the original optimization problem to a large extent by creating narrow valleys in the state space resulting in extremely slow convergence. Therefore, the FCG method has been abandoned.

Parameter Optimization Methods

The appearance of efficient and robust algorithms to solve nonlinear programming problems (NLP) during the last decade has led to the replacement of the more complex calculus of variation methods by techniques which dicretize the problem in some way. Such an approach reduces the original continuous optimal control problem to one of finite-dimensional parameter optimization, i.e. NLP. The approximation of the original problem may parameterize the states as well as the controls (3, 13). The methods employed in the remainder of this study, however, parameterize only the controls. Parameter optimization methods and unresolved problems connected to it are surveyed by (8).

An obvious direct parameterization method is to represent the control vector function $\underline{u}$ (t) by an explicit function of a parameter vector $\underline{p} \epsilon E^m$ and thus control the trajectory by means of equation (2). Although it is natural to treat the controls as the independent variables and the states as the dependent variables in the systems equations (2) it is not essential to do so. In problems involving terminal state constraints and/or state inequality constraints it may be more convenient to treat some of the states as independent or nominal variables and to determine some or all control variables in terms of these independent variables through the state equations.

In our method of approach some control variables $u_i(t)$ are approximated by specifying

$$u_i(t) = T_i(\underline{p}_i, t) \qquad i = 1,2,\ldots, r_1 < r \tag{10}$$

where T_i are known functions of the m_i-dimensional parameter vector $\underline{p}_i$. The remaining $r-r_1$ control variables $u_{r1+1}, u_{r1+2}, \ldots, u_r$ will be uniquely determined in terms of a selected set of independent or nominal state variables. Similar to (10) a specific parameterization for these nominal state variables is adopted

$$x_j(t) = T_j(\underline{p}_j, t) \qquad j = 1,2,\ldots, r-r_1 \tag{11}$$

where each T_j is a known function of the m_j-dimensional parameter vector $\underline{p}_j$. The form of the parameterization (11) chosen should be consistent with the terminal conditions and the state inequality constraints of the problem. If the j state variables are enforced according equation (11), the control variables $u_{r1+1}, u_{r1+2}, \ldots, u_r$ are uniquely determined through the state equation (2). Unfortunately, in most cases these control variables cannot be determined explicitely in a straight-forward manner without having to integrate the differential state equation (2) numerically. To circumvent this difficulty we consider the variables x_j of (11) as nominal values for a pitch controller, which determines the controls $u_j(t)$ in such a way as to drive the current state variables to the nominal values of equation (11). Thus, the controls $u_{r1+1}, \ldots, u_r$ are defined by a control law

$$u_k(t) = T_k(\underline{p}'_k, x_k(t), t) = T_k(\underline{p}_k, t) \qquad k = 1,2,\ldots, r-r_1 \tag{12}$$

where T_k represents a specific relation of the nominal values $x_k(t)$ and the m_k-dimensional vector $\underline{p}_k$, which combines the parametervector $\underline{p}_j$ of eq. (11) and $\underline{p}'_k$. The control models utilized in different flight path segments are described in the next section.

Let $m = m_1 + m_2 + \ldots + m_r + m_\pi$ and define the m-dimensional parameter-vector $\underline{p}$ by $\underline{p}^T = [\underline{p}_1^T | \underline{p}_2^T | \ldots | \underline{p}_r^T | \underline{\pi}^T]$. For given initial values $\underline{x}$ (t_o) the dependent variables $\underline{x}$ can then be solved in terms of $\underline{p}$ by numerical integration of the differential state equation (2) in the interval $[t_o, t_f]$. The cost functional $J(\underline{u}, \underline{\pi})$ reduces to a function $z(\underline{p})$ and thus yields an ordinary minimization problem. This will be solved by a variable metric penalty function method employing either the Davidon-Fletcher-Powell (DFP) algorithm or the Broyden-Fletcher-Goldfarb-Shanno (BFGS) formula (10, 14). However, with respect to the boundary conditions (3) either penalty functions or projections may be employed. We found for our control problem that the DFP or BFGS algorithm coupled with a gradient projection technique for handling terminal state constraints offers computational advantages. Most trajectory optimization examples of section 5 were solved by an accelerated gradient projection scheme. In this case the penalty terms associated with the condition (3) are dropped from equation (6) and the parameter optimization problem may be stated as follows

$$\begin{array}{ll} \text{minimize} & z(\underline{p}) \\ \text{subject to the} & \\ \text{boundary condition} & \underline{g}(\underline{p}) = \underline{0} \end{array} \tag{13}$$

Note, that the differential constraints (2) do not enter into formulation (13) as they are solved by numerical integration.

The gradient projection algarithm (9) consists of a sequence of two-phase cycles, composed of one or more constraint restoration steps and one minimization step. Starting from an initial point $\underline{p}^o$ a varied point p^{k+1} is computed according

$$\underline{p}^{k+1} = \underline{p}^k + \alpha^k \cdot \underline{s}^k \tag{14}$$

where α^k represents the step length taken along the search direction $\underline{s}^k$ and the superscript indicates the iteration cycle. In the restoration phase the task to be accomplished by the parameter update scheme is to meet the desired end conditions within prescribed tolerances. The parameter set is updated using the displacement

$$\Delta\underline{p}^i = \alpha^i \cdot \underline{s}^i = -\alpha^i \cdot \underline{H}^i \cdot \underline{g}_p^i \, (\underline{g}_p^i \cdot \underline{H}^i \cdot \underline{g}_p^i)^{-1} \cdot \underline{g}^i \tag{15}$$

with a nominal value $\alpha^i = 1$, which may be reduced within $0.05 \leq \alpha \leq 1$ to enlarge the convergence region. In equation (15) $\underline{H}^i$ is a diagonal weighting matrix which attempts to normalize the effects of the various parameter and will be updated as described below. The notation $\underline{g}^i$ indicates $\underline{g}^i = \underline{g}(\underline{p}^i)$. The matrix $\underline{g}_p^i$ contains the partial derivatives of the constraints with respect to the parameters and $\underline{g}^i$ is the vector of constraint errors for the ith-iterate. The minimization step is accomplished along

$$\underline{s}^k = -\underline{H}^k \cdot \underline{F}_p^k \tag{16}$$

where F^k represents an augmented cost function

$$F^k = z^k + \underline{\lambda}^T \cdot \underline{g}^k \tag{17}$$

which adds the constraint errors $\underline{g}^k$ via a constant Lagrange multiplier

$$\underline{\lambda} = -(\underline{g}_p^k \, \underline{H}^k \, \underline{g}_p^k)^{-1} \cdot (\underline{g}_p^k)^T \cdot \underline{H}^k \, \underline{z}_p^k \tag{18}$$

to the original cost function $z(\underline{p})$.
The step lenght α^k is determined by a one-dimensional search

$$F(\underline{p}^k + \alpha^k \cdot \underline{s}^k) = \min_{\alpha} \; (F(\underline{p}^k + \alpha \cdot \underline{s}^k)) \tag{19}$$

using cubic interpolation to locate the scalar parameter α^k which yields the greatest cost decrease. This search is terminated prior to passing the minimum at α^k if either the parameter changes or the constraint errors exceed some prescribed bounds. In this case a new restoration cycle is initiated without modifying the matrix $\underline{H}$. Otherwise $\underline{H}$ is updated by use of quasi-Newton methods. These include the famous Davidon-Fletcher-Powell (DFP) and Broyden-Fletcher-Goldfarb-Shanno (BFGS) formulas (see for instance Ref. 14):

$$\begin{aligned} \underline{H}^{k+1} = {} & \gamma^k \cdot \underline{H}^k + \left[1 + \gamma^k \delta^k \cdot \frac{(\Delta\underline{F}_p^k)^T \, \underline{H}^k \, \Delta\underline{F}_p^k}{(\Delta\underline{p}^k)^T \, \Delta\underline{F}_p^k} \right] \frac{\Delta\underline{p}^k \, (\Delta\underline{p}^k)^T}{(\Delta\underline{p}^k)^T \, \Delta\underline{F}_p^k} \\ & - \gamma^k \cdot \frac{(1 - \delta^k)}{(\Delta\underline{F}_p^k)^T \underline{H}^k \Delta\underline{F}_p^k} \cdot \underline{H}^k \cdot \Delta\underline{F}_p^k \cdot (\Delta\underline{F}_p^k)^T \cdot \underline{H}^k \\ & - \frac{\gamma^k \cdot \delta^k}{(\Delta\underline{p}^k)^T \Delta\underline{F}_p^k} \cdot \left[(\Delta\underline{p}^k) \cdot (\Delta\underline{F}_p^k)^T \, \underline{H}^k + \underline{H}^k \cdot \Delta\underline{F}_p^k \, (\Delta\underline{p}^k)^T \right] \end{aligned} \tag{2o}$$

where $\gamma^k = 1 \, , \; \delta^k = 0$ for DFP method

$\gamma^k = 1 \, , \; \delta^k = 1$ for BFGS method

and $\Delta\underline{F}_p^k$ denotes

$$\Delta\underline{F}_p^k = \underline{F}_p(\underline{p}^{k+1}) - \underline{F}_p(\underline{p}^k)$$

and the subscipt p once again indicating partial differentiation with respect to $\underline{p}$.
The required partial derivatives with respect to $\underline{p}$ are computed numerically using either the method of forward finite differences

$$\frac{\partial z}{\partial p_j} = \frac{z^+ - z(p)}{\delta p_j} \quad , \quad \frac{\partial g_i}{\partial p_j} = \frac{g_i^+ - g_i(p)}{\delta p_j} \tag{21}$$

or central finite differences

$$\frac{\partial z}{\partial p_j} = \frac{z^+ - z^-}{2 \cdot \delta p_j} \quad , \quad \frac{\partial g_i}{\partial p_j} = \frac{g_i^+ - g_i^-}{2 \cdot \delta p_j} \tag{22}$$

where the notation $z^+ = z(p_1, \ldots, p_j + \delta p_j, \ldots, p_m)$ and $z^- = z(p_1, \ldots, p_j - \delta p_j, \ldots, p_m)$ is used. In the latter case a scheme suggested by Hull and Williamson(12) is employed to verify the magnitude of perturbation. However, the use of the central-difference formulas is avoided whenever possible to reduce the computational expenditure. In most examples the use of forward differences was appropriate. Another way of generating the partial derivatives is by the quadratures of the error of the optimality conditions (11). In (11) gradient generation by forward differences compare favorable with error-quadrature gradients.

4. SIMULATION MODEL

Dynamic Model

The flight of the missile is described by a set of seven differential equations written in a relative velocity coordinate system. This system has its orgin at the current position of missile's c.g. relative to an Earth-fixed nonrotating xyz-axes system and its axes are aligned as shown in Fig. 2. The equations of motion are as follows:

$$\begin{aligned}
\dot{v} &= \frac{1}{m}\,[F \cdot \cos\alpha \cdot \cos\beta - W] - g_o \cdot \sin\gamma \\
\dot{\gamma} &= \frac{1}{m \cdot v}\,[F \cdot \sin\alpha \qquad + A] - \frac{g_o}{v} \cdot \cos\gamma \\
\dot{\chi} &= \frac{1}{mv \cdot \cos\gamma} \cdot [F \cdot \cos\alpha \cdot \sin\beta + Q] \\
\dot{m} &= -\mu \\
\dot{x} &= v \cdot \cos\gamma \,.\, \cos\chi \\
\dot{y} &= v \cdot \cos\gamma \,.\, \sin\chi \\
\dot{h} &= v \cdot \sin\gamma
\end{aligned} \tag{23}$$

The associated elements of the state vector $\underline{x} = [v, \gamma, \chi, m, x, y, h]^T$ are the relative velocity magnitude v, the flight path angle γ, the relative azimuth χ, the mass and the coordinate of the missile point mass. g_o is the surface gravitational acceleration. The missile is controlled by the control vector $\underline{u}(t) = [\mu(t), \alpha(t), \beta(t)]^T$ whose components are propellant flow rate $\mu(t)$, angle of attack $\alpha(t)$ and sideslip angle $\beta(t)$. Structural limits, mission and propulsion requirements impose four operational constraints the violations of which are numerically integrated along (23).

$$\begin{aligned}
\dot{\zeta}_1 &= (T_r(t) - T_{max})^2 && \text{if } T_r(t) > T_{max} && \text{otherwise } \dot{\zeta}_1 = 0 \\
\dot{\zeta}_2 &= (M_c - M(t))^2 && \text{if } M_c > M(t) && \text{otherwise } \dot{\zeta}_2 = 0 \\
\dot{\zeta}_3 &= (h(t) - h_{max})^2 && \text{if } h(t) > h_{max} && \text{otherwise } \dot{\zeta}_3 = 0 \\
\dot{\zeta}_4 &= (h(t) - h^{\ 2} && \text{if } h(t) < h_o = 0 && \text{otherwise } \dot{\zeta}_4 = 0
\end{aligned} \tag{24}$$

with initial values $\zeta_i(t_o) = 0$ and required condition $\zeta_i(t_f) = 0$.

Aerodynamic and Propulsion Model

The aerodynamic and propulsive forces are obtained from the relationships

$$\begin{aligned} L &= C_L(\alpha,M)\cdot q\cdot S \\ D &= C_D(\alpha,M,h)\cdot q\cdot S \\ Q &= C_Q(\alpha,M)\cdot q\cdot S \\ F &= C_F(M,h,\mu)\cdot q\cdot S \end{aligned} \tag{25}$$

where q denotes the dynamic pressure $q = \frac{1}{2}\,\rho\,v^2$ and S is the reference area. Thrust F is considered to act along the vehicle body axis. The aero-thermodynamic heating load is described by the recovery temperature T_r which is given by the adiabatic equation

$$T_r = T\cdot(1 + \frac{\kappa-1}{2}\cdot M^2) \tag{26}$$

where T is the ambient temperature and κ is the specific heat ratio. The atmospheric properties, i.e. density ρ, temperature T, speed of sound a to define Mach number $M = v/a$, are derived from the 1962 US Standard Atmosphere model.

The aerodynamic data are given as drag polars and the dependence of the aerodynamic coefficients on angle of attack α and sideslip β is assumed linear at each Mach number, thus

$$\begin{aligned} C_L &= C_{L\alpha}(M)\cdot\alpha \\ C_D &= C_{D0}(M)\cdot(1+c\cdot h) + K(M)\cdot C_L^2 \\ C_Q &= C_{Q\beta}(M)\cdot\beta \end{aligned} \tag{27}$$

Since the missile is considered to be symmetric we assume $C_{Q\beta}(M) = C_{L\alpha}(M)$. The aerodynamic coefficients $C_{L\alpha}(M)$, $C_{D0}(M)$ and the induced drag constant K(M) are represented as tabular functions of M and are determined in dependence of the current Mach number by means of cubic spline interpolation. The thrust coefficient $C_F(M,h,\mu)$ is characterized by a strong sensitivity to the flight conditions M, h and to the propellant flow rate μ. It is also given in the form of tabular data. C_F is modelled for different values of μ = const. by bicubic spline functions and the dependence on $\mu(t)$ is determined by cubic interpolation between the several planes $C_F(M,h)|\,\mu$ = const .

The lower operational limit for the ramjet propulsion considered is given by the critical Mach number $M_c = M_c(h,\mu)$, which is also given in form of tabular data and modelled utilizing bicubic spline functions. With respect to the fuel flow rate μ the propulsion characteristics require $\mu(t)$ to obey $\mu_{min} \le \mu_1 \le \mu(t) \le \mu_u \le \mu_{max}$ with the additional restriction of $\phi = \mu_u/\mu_1 \le \phi_{max}$ for the throttle ratio ϕ.

Control Model

The trajectory is determined by three control variables: the mass flow rate $\mu(t)$, which implies thrust magnitude, the angle of attack $\alpha(t)$ and the sideslip angle $\beta(t)$. To formulate a trajectory optimization problem as a parameter optimization problem, the infinite-dimensional control must be represented by a finite set of parameters. There are several ways in which a parameter vector $\underline{p}$ can conveniently be chosen to approximate the continuous control $\underline{u}(t)$.

The time interval $[t_o, t_f]$ can be partitioned and the parameter of $\underline{p}$ can specify the magnitude of the control variables at specified points in time. Simple linear interpolation or cubic spline interpolation (11) can then be used to define the control variables at intermediate points in time. Alternatively, the parameters can be regarded as coefficients of some mathematical model, which may be either a function of time or a function of the current state. Both methods are employed in our control model.

Generally, we approximate the $\mu(t)$-control, i.e. propellant flow rate, by straight-line segments. In a limited number of examples cubic splines were used instead.

The angle of attack $\alpha(t)$-parameterization assumes constant flight path γ segments and

15-9 'cruise' phases at constant altitudes h, i.e. a flight profile as shown in Figure 1. The desired values of constant γ or h within path segments are considered as the nominal values for a simple pitch controller which defines $\alpha(t)$-control in a closed-loop form. During a climb or descent segment i the angle of attack is determined by

$$\alpha(t) = \alpha_{st}(t) - \alpha^{*} \left[\frac{\gamma(t) - \gamma_{ni}}{C_{\gamma i}} + \frac{\dot{\gamma}(t)}{C_{\dot{\gamma} i}}\right] \tag{28}$$

Within a constant altitude flight path segment α is calculated from

$$\alpha(t) = \alpha_{st}(t) - \alpha^{*} \left[\frac{h(t) - h_{nj}}{C_{hj}} + \frac{\gamma(t)}{C_{\gamma j}}\right] \tag{29}$$

In equations (28),(29) denote γ_{ni} and h_{nj} the desired values of flight path angle and flight altitude, C_{γ}, $C_{\dot{\gamma}}$, C_n represent weighting coefficients and α^{*} is a preset constant. Furthermore, α_{st} denotes the steady-state angle of attack

$$\alpha_{st} = \frac{m(t) \cdot g_o \cdot \cos \gamma_{ni}}{(F(t) + C_{L\alpha} \cdot q \cdot S)} \tag{30}$$

resulting from the second state equation (23) by setting $\dot{\gamma} = 0$ and $\sin \alpha = \alpha$. Note, that $\gamma_{ni} = 0$ for constant altitude flight phases. The bracket terms in equation (28) and (29) represent linear combinations of the error function and error rates of change. The α-control derived from (28) or (29) is restricted to $|\alpha(t)| \leq \varepsilon_{max}$ with ε_{max} a specified control bound.

At least four flight path segments are assumed: climb, constant altitude cruise, descent and constant altitude sea-skimming phase. The climb and descent phase may each be partioned in additional flight segments. However, only two constant altitude flight segments will be considered. In the constant altitude cruise leg the desired nominal altitude h_n is set equal to the specified maximal altitude h_{max} and in the sea-skimming phase the nominal value h_n is chosen to correspond to the specified terminal altitude h_f. As will become obvious from the next section, h_{max} represents the optimal cruise altitude for our trajectory problem.

The nominal values γ_{ni} as well as the weighting coefficients $C_{\gamma i}$, $C_{\dot{\gamma} i}$, C_{hi} for the pitch controller (28) or (29) of the different flight path segments i are collected in the parameter vector p to be optimized. Proper selection of the weighting constants will result in an optimal transient from the current states $\gamma(t)$ or $h(t)$ to the desired, nominal values.

The α-control model chosen represents an attempt to elliminate the explicit appearance of the final states h_f and γ_f in the boundary condition (3). Both are satisfied directly by the control (29). Furthermore, satisfaction of the path inequality constraints $h(t) \leq h_{max}$ and $h(t) > 0$ is achieved easily without the need of high penalty coefficients in the associated penalty functions. Hence, the numerical difficulties mentioned in section 3 regarding the use of penalty functions are kept to a minimum.

The sideslip angle is $\beta(t) = 0$ for all but the last path segment. In the final sea-skimming flight leg lateral maneuvering of the missile is accomplished by a bang-bang type β-control. The magnitude of $\beta(t)$ is numerically determined from the third state differential equation (23) for a specified lateral acceleration. A control constraint is imposed:

$$\beta(t) \leq \sqrt{\varepsilon_{max}^2 - \alpha^2(t)} \tag{31}$$

where $\alpha(t)$ results from equation (29). Hence, high lateral acceleration requirements resulting in higher β-angles will not be realizable.

The optimization technique determines the controls u(t) and $\alpha(t)$ in the sense of the above stated approximation. With this control model the resulting trajectory may not be optimal for the problem originally stated but should be very nearly so for most problems of interest.

5. NUMERICAL EXAMPLES

This section presents two examples illustrating the potential performance improvements that can result from the implementation of optimal controls. The first example considers a missile flight mission at sea-skimming altitudes and demonstrates the improvements gained by continuous throttle capabilities. The second example corresponds to a low-high-low mission profile. For all examples to be presented in this section the following remarks hold: all trajectory calculations were performed on a UNIVAC 1108 computer using double precision arithmetic. All simulated flights werde initiated at the same condition, which corresponds to ramjet ignition, and all had to meet the same boundary conditions v_f, γ_f and h_f. The trajectory calculations were terminated at depletion of a specified amount of fuel.

As mentioned above the first mission to be considered is one of level flight at low altitude and includes a final weaving flight path segment of prescribed length. The sea-skimming altitude, which is chosen equal to the terminal condition h_f, is maintained by $\alpha(t)$-controls determined from equation (29) the coefficients of which has been optimized in a separate calculation. Thus, only the fuel flow control $\eta(t)$ is to be optimized, since the sidslip angle β is determined by the requirement of a specific lateral acceleration. The boundary conditions $h_f = 10$ m and $\gamma_f = 0^\circ$ are satisfied directly by α-control (29). The remaining conditions to be met are the terminal velocity v_f, the required distance of weaving flight Δx_{wv} and flight path inequality constraints (24). Note, no condition on the lateral displacement is imposed since $y(t_f)$ is generally small. In the simplest case both v_f and Δx_{wv} could be satisfied (within numerical tolerances) by utilizing a control parameter consisting of just two parameters P2 : $p = [\eta, t_{wv}]^T$, i.e. constant fuel flow rate η and the initiation time t_{wv} of weaving flight. However, since there are two end conditions and only two control parameters there is no parameter left for optimization and thus the problem reduces to one of targeting. The specification of v_f and Δx_{wv} uniquely defines the two parameters mentioned which in our procedure are numerically determined by a (Newton-) restoration cycle (Section 3). As this special case P2 is of some practical interest some results are presented in Figures 3 to 5.

Figure 3 shows the effect of parameters η and t_{wv} on weaving flight distance for a specified final velocity v_f and different lateral accelerations a_1. For example, the choice of fuel flow $\eta(t) = 0.8 =$ const together with $t_{wv} = 0.62$ would yield a weaving distance of 2.1 while meeting the end condition v_f for a maneuvering acceleration of $a_1 = 2$. It is obvious from Figure 3 that for high maneuvering acceleration requirements $a_1 = 3$ and 4 only short weaving distances can be achieved even with full power setting. Furthermore, high lateral acceleration $a_1 = 4$ may not be maintained during the whole portion of weaving flight due to the associated rapid velocity decrease and due to the bounded sideslip angle $\beta(t)$ according equation (31). In Figure 3 the flight time t_f is also plotted; the differences of which for several accelerations a_1 are too small as to be shown in the graph.

The above discussion doesn't consider the constraint $T_r \leq T_{max}$ on the recovery temperature which, when imposed on the problem, renders many trajectories of Figure 3 unfeasible. This is evidenced by the velocity time profiles of Figure 4. This graph corresponds to a constant lateral maneuvering acceleration $a_1 = 2$ and considers the effect of different weaving flight distance requirements. If there is no weaving flight segment ($\Delta x_{wv} = 0$) the sea-skimming missile is continuously accelerated from the initial to the terminal velocity v_f by a constant power setting η. If weaving maneuvers are required $\Delta x_{wv} > 0$, the missile will be accelerated to a peak velocity at $t = t_{wv}$ well above the specified end condition

v_f and will be decelerated in the interval $t_{wv} \leq t \leq t_f$ of maneuvering flight to the prescribed terminal condition. The thrust associated with the specific fuel flow rate $\mu(t)$ = const required to meet both end conditions v_f and Δx_{wv} is not sufficient to cancel the increased drag during this flight phase. Thus, in order to meet increasing Δx_{wv} - requirements the missile has to be accelerated to higher velocities in the interval $t_o \leq t < t_{wv}$ if the terminal condition v_f is to be achieved. This is accomplished by utilizing higher fuel flow rates μ. However, this may result in a violation of the operational constraint $T_r < T_{max}$ (i.e. v_{max}) as is the case for the examples $\Delta x_{wv} = 2$ and $\Delta x_{wv} = 4$ shown in Figure 4. Hence, a constant power setting is not appropriate for medium to high Δx_{wv} - distance requirements and similarly for higher maneuvering accelerations a_1.

If the ramjet has some throttle capabilities it is reasonable to assume a constant fuel flow rate $\mu(t) = \mu_1$ during the first flight phase $t_o \leq t < t_{wv}$ and a different value $\mu(t) = \mu_2$ during the maneuvering interval $t_{wv} \leq t \leq t_f$. Such an example P3: $\underline{p} = [\mu_1, \mu_2, t_{wv}]^T$ is considered in Figure 5 and Figure 6 which correspond to a weaving distance $\Delta x_{wv} = 2$ and a lateral acceleration $a_1 = 2$. For comparison reasons the results of P2 as described above are included. In contrast to P2 the P3-control parameter model results in a velocity time profile which stays well below the v_{max} - limit and offers the added advantage of a range increase by 2.7 percent. Also shown in Figure 5 and Figure 6 are the results of a trajectory simulation assuming continuous throttle capabilities of the ramjet propulsion. This example P10: $\underline{p} = [\mu_1, \mu_2, \ldots, \mu_9, t_{wv}]^T$ uses ten parameters to be optimized and utilizes cubic spline functions to connect the discrete values μ_i as described in Figure 6. Regarding Figure 5 this continuous throttle control results in an initial velocity decrease to a value which is roughly maintained throughout the main portion of the first flight leg $t_o \leq t < t_{wv}$ and then is rapidly increased to a peak value at $t = t_{wv}$ required to reach the specified terminal velocity during the decelerating flight phase $t_{wv} \leq t \leq t_f$. It is evident from Figure 6 that the velocity $v(t)$ follows the v_{min} - boundary for some time and the "overshoot" - velocity is somewhat higher than for case P3. However, the peak velocity occurs only for a short period of time in contrast to the example P2 and P3, indicating that continuous throttling would be advantageous for higher Δx_{wv} and/or a_1 - requirements. A short violation of v_{max}, i.e. T_{max}, could possibly be tolerated. In addition the continuous fuel control of P10 results in a range benefit of 4.3 percent compared to the range performance achieved by constant power setting P2 (which may not be feasible!). For the P10 parameterization the fuel flow rises steadily to a maximum value (Figure 6) which is maintained during the weaving flight. The P3 control example utilizes the maximal possible propellant flow during this final flight segment.

In the remainder of this section we consider examples of low-high-low trajectories, i.e. the ramjet propelled missile is allowed to climb to a more efficient cruise altitude.

As stated in section 4 the climb and descent flight legs may be partitioned each into several subsegments of desired constant flight path angles. To this date at most three climb-subsegments and three descent-subsegments have been used and a maximum of 23 control parameters have been optimized which parameterize both fuel flow $\mu(t)$ and angle of attack α control. However, in order to reduce the computational expenditure necessary for sensitivity studies the dimension of the parameter vector $\underline{p}$ was reduced to 7 to 12 depending on mission requirements. In these examples the simplifying assumption of one climb segment and one descent segment was used. The weighting coefficients of the pitch control laws eq. (28) and (29) were chosen equal the corresponding optimized values of previous simulation runs and thus excluded from the parameter vector $\underline{p}$. Numerical comparisons indicate an accuracy loss of less than 0.4 percent of the simplified model for most missions of interest.

Figure 7 represents the time histories of flight altitude $h(t)$, velocity $v(t)$ and recovery temperature $T_r(t)$. This trajectory corresponds to mission requirements of $\Delta x_{wv} = 2$ weaving flight distance and lateral acceleration $a_1 = 2$. Regarding $h(t)$ optimal cruise occurs at the maximal allowed altitude. There is a small violation of the altitude constraint h_{max} at the beginning of the cruise segment. This violation could be cancelled at the expenditure of additional computing effort, however, it was considered to be tolerable. The velocity time history shows a continuous increase during the cruise phase, indicating that with the preset conditions no steady state is achievable. The magnitude of v(t) undergoes rapid changes during the descent and final skimming phase. It is noted from Figure 8 that fuel flow rate, i.e. thrust, is increased already during the descent phase. Thus, velocity is increased during the final portion of descent in order to cancel the deceleration of the weaving flight segment and to meet the boundary condition v_f. The recovery temperature increases accordingly and hits the T_{max} limit for a short time. Once again, this violation could be further decreased by additional computation but was considered acceptable. The corresponding controls are plotted in Figure 8. Considering the fuel flow control, which is parameterized by eight straight line segments, it is noted that fuel flow is steadily reduced during climb. This result is in contrast to the classical steady state performance analysis and to the findings of $^{(4)}$ where maximum throttle is found to be optimal using singular perturbation methods. In our example the utilization of maximum fuel flow results in a violation of the inflight constraint $M > M_c$ and hence is not feasible. It may be noted that the throttle ratio $\phi = \mu_c/\mu_1$ corresponds to the maximal allowed value of $\phi_{max} = 5$. This limit is not restrictive for flight examples requiring no weaving maneuvers. In such cases the maximal fuel flow rate, which occurs during the sea-skimming phase, is lower than in the example of Figure 8. Therefore somewhat lower fuel flow rates can be utilized during cruise. Numerical results for such flights show a steady, though small decrease of the optimal propellant flow rate during cruise at maximal possible altitude h_{max} reflecting decreasing angles of attack $\alpha(t)$.

Figures 9 to 11 show some results of sensitivity studies. Range performance is characterized by a strong sensitivity to maximal flight altitude h_{max}, to the distance of weaving flight Δx_{w} and to the maneuvering acceleration. In Figure 11 two simulation results are included (marked by triangles), which were obtained utilizing simplified fuel flow control while α-control remained unchanged. Both examples correspond to a maximal flight altitude 0.8, a maneuvering acceleration of 2 and a weaving distance of 2. The first example refers to a fuel flow rate which is linearly decreased during climb to the cruise fuel consumption rate μ. This optimal cruise value is maintained during cruise and descent phase. Maximal fuel flow is then used during the final maneuvering flight phase. This simplified μ-control results in a deterioration of the range performance by 6.9 percent. The second example marked in Figure 11 consumes fuel at a constant maximal rate during climb and utilizes an optimized fuel flow rate during cruise and descent and the maximal possible μ in the final flight path segment. This fuel control results in a violation of the Mach number condition $M \geq M_c$ and decreases flight range further to about 11.2 percent with respect to the range obtained by use of more complex fuel controls.

The numerical results show for same mission requirements almost identical fuel flow rates during cruise independent of the fuel control model used. This indicates that range improvements occur during transition phases in the climb and descent flight segments. Figure 12 considers flight range vs throttle ratio ϕ, which is an important aspect of the development of any missile propulsion system. For a maximal flight altitude 0.8 it is noted that an increase of throttle capabilities beyond a value of about 6 will not increase range performance. However, when mission requirements allow higher cruise altitudes increase of throttle ratio results in remarkable range improvements. The operational constraint $T_r \leq T_{max}$ requires throttle ratios greater than about 3.5 for the example considered.

6. CONCLUDING REMARKS

A range trajectory optimization problem for a ramjet powered missile is solved with a parameter optimization method. The trajectory consists of four distinct phases (climb, cruise, descent, weaving flight at sea-skimming altitudes). Penalty functions are employed on four state variable inequality constraints. Numerical simulation results are given for a range of different mission requirements. The results demonstrate the capability of the procedure to solve complex, realistic trajectory optimization problems. It is shown that depending on mission requirements continuous throttle capabilities of the ramjet propulsion system result in range improvements of about 5 to 11 percent when compared to more conventional fuel control. In addition, continuous throttling can prevent the missile from violating operational constraints.

7. ACKNOWLEDGEMENT

This paper is derived from a study sponsored by the Ministry of Defense, Federal Republic of Germany. Stimulating discussions with B. Crispin and W.D. Pohl of the Messerschmitt-Bölkow-Blohm GmbH. München, are gratefully acknowledged.

8. REFERENCES

(1) Thomas, A.N., "New-Generation Ramjets - A Promising Future", Astronautics and Aeronautics, June 1981

(2) Crispin, B. and Pohl, W.D., "Missile Characteristics and Mission Objectives", MBB-working data sheets, Oct. 1980

(3) Paris, S.W., Joosten, B.K. and Fink, L.E., "Application of an Advanced Trajectory Optimization Method to Ramjet Propelled Missiles", Optimal Control Applications and Methods, Vol. 1, 319 - 334 (1980)

(4) Glaros, L.N. and Crigler, S.W., "Real-Time Trajectory Control Using Augmented Energy Management", AIAA P-77-1052, Guidance and Control Conference, Hollywood, Fla., August 8 - 10, 1977

(5) Sridhar, B., "Trajectory Optimization of a Ramjet-Powered Missile Using Singular Perturbation Methods", 1978 Conference on Decision and Control, 17th, San Diego, Calif., Jan. 10 - 12 (1979)

(6) Hofer, E. and Lunderstädt, R., "Numerische Methoden der Optimierung", R. Oldenbourg Verlag, München, 1975

(7) Bryson, A.E. and Ho, Y.C., "Applied Optimal Control", Hemisphere Publishing Corporation, Washington, 1975

(8) Rauch, H. E., 'Problems and Techniques in Constrained Optimization", AIAA P-78-1408, AIAA/AAS Astrodynamics Conference, Palo Alto, Calif., August 7 - 9 (1978)

(9) Speyer, J.L., Kelley, H.J., Levine, N. and Denham, W.F., "Accelerated Gradient Projection Technique with Application to Rocket Trajectory Optimization", Automatica, Vol. 7, 37 - 43 (1971)

(10) Johnson, I.L., " The Davidon-Fletcher-Powell Penalty Function Method: A Generalized Iterative Technique for Solving Parameter Optimization Problems", NASA TN-D-8251, May 1976

(11) Kraft, D., "Finite-Difference Gradients Versus Error Quadrature Gradients in the Solution of Parameterized Optimal Control Problems", Optimal Control Applications and Methods, Vol. 2, 191 - 199 (1981)

(12) Hull, D.G. and Williamson, W.E., "Numerical Derivatives for Parameter Optimization", J. Guidance and Control, Vol. 2, 158 - 160 (1979)

(13) Hargraves, Ch., Johnson, F., Paris, St. and Rettie, I., "Numerical Computation of Optimal Evasive Maneuvers for a Realistically Modelled Airplane Pursued by a Missile with Proportional Guidance", AIAA P-79-1624, AIAA Atmospheric Flight Mechanics Conference, Boulder, Colorado, 6 - 8 August (1979)

(14) Jacobs, D. (Ed.), "The State of the Art in Numerical Analysis", Academic Press, 1977

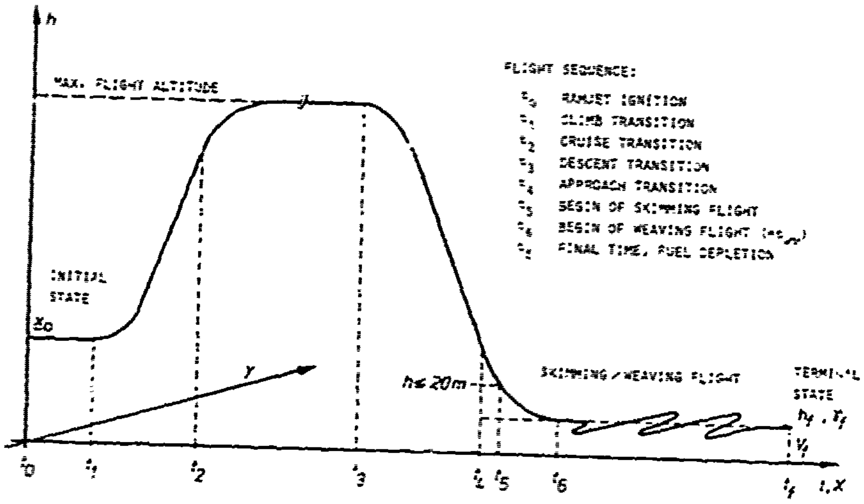
h
MAX. FLIGHT ALTITUDE
INITIAL STATE
$\underline{x}_0$
y
h≤ 20m
SKIMMING / WEAVING FLIGHT
TERMINAL STATE
h_f, γ_f
V_f
t_0
t_1
t_2
t_3
t_4
t_5
t_6
t_f
t, x
FLIGHT SEQUENCE:
t_0 RAMJET IGNITION
t_1 CLIMB TRANSITION
t_2 CRUISE TRANSITION
t_3 DESCENT TRANSITION
t_4 APPROACH TRANSITION
t_5 BEGIN OF SKIMMING FLIGHT
t_6 BEGIN OF WEAVING FLIGHT ($=t_{wv}$)
t_f FINAL TIME, FUEL DEPLETION

OPERATIONAL CONSTRAINTS

$T_r(t) \leq T_{max}$ STRUCTURAL LIMIT

$0 < h(t) \leq h_{max}$ MISSION REQUIREMENT

$x(t_f) - x(t_6) \geq \Delta x_{wv}$ " "

$M(t) \geq M_c(h, \mu)$ PROPULSION REQUIREMENT

FIGURE 1: MISSION PROFILE AND MISSION CONSTRAINTS

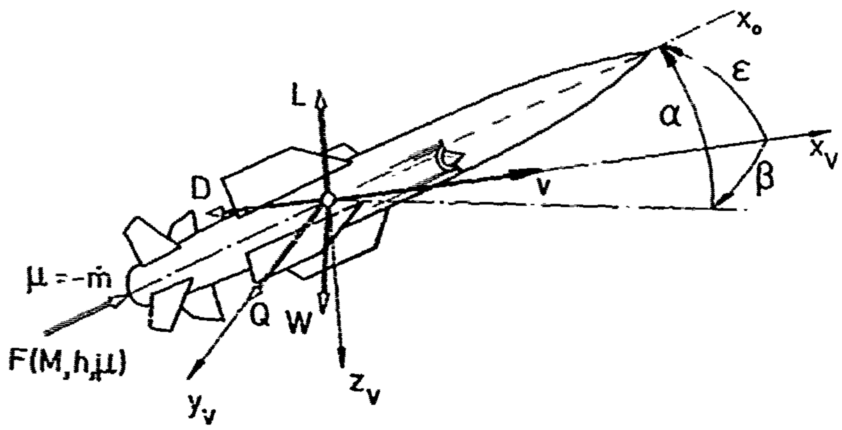
x_o
ε
α
x_v
β
L
D
V
μ = -ṁ
Q
W
F(M,h,μ)
y_v
z_v

CONTROL VECTOR

$\underline{U}(t) = \left[\mu(t), \alpha(t), \beta(t)\right]^T$

CONTROL BOUNDS

$\mu_{min} \leq \mu_l \leq \mu(t) \leq \mu_u \leq \mu_{max}$

$\varphi = \mu_u / \mu_l \leq \varphi_{max}$

$\varepsilon(t) = \sqrt{\alpha^2(t) + \beta^2(t)} \leq \varepsilon_{max}$

FIGURE 2: DEFINITION OF CONTROL VARIABLES AND FORCES

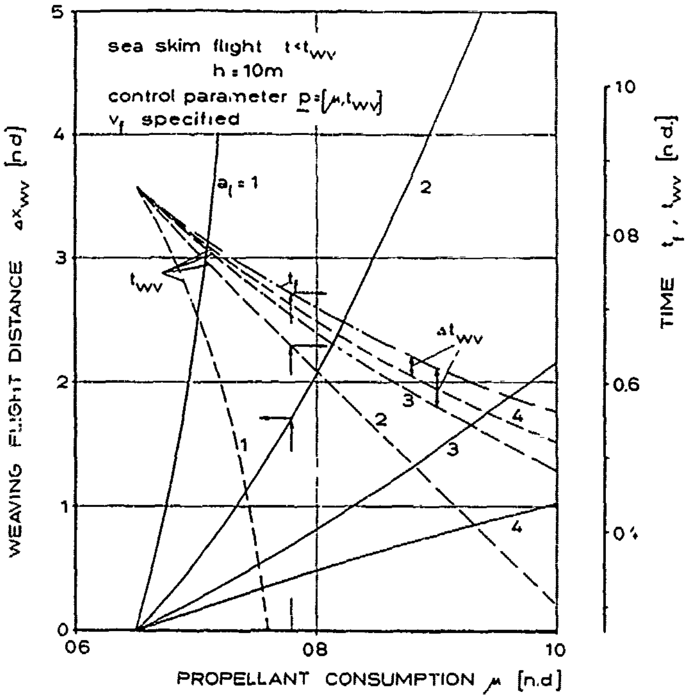

Figure 3: Effect of Control Parameters μ, t_{wv} on Weaving Flight Distance (Final Velocity v_f specified, Lateral Acceleration a_l varied)

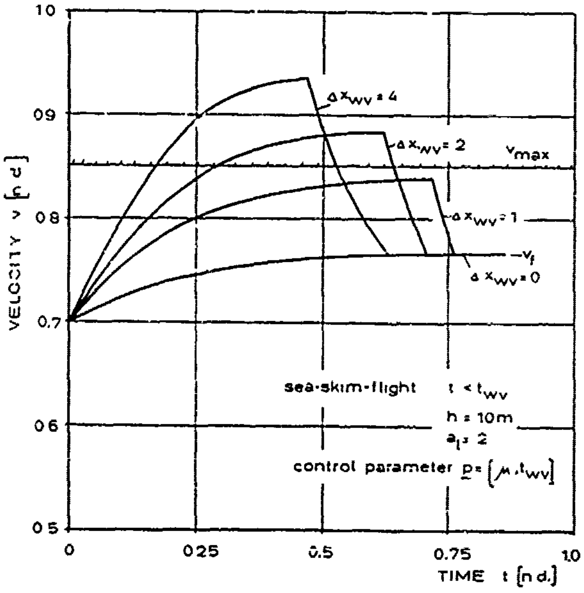

Figure 4: Velocity Time History in Dependence of Different Mission Requirements Δx_{wv} (v_f specified, level flight)

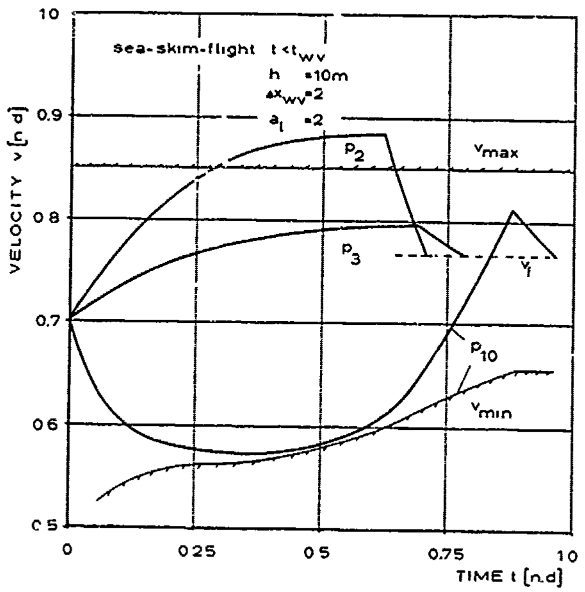

FIGURE 5: VELOCITY TIME HISTORY FOR THREE EXAMPLES OF FUEL FLOW CONTROL

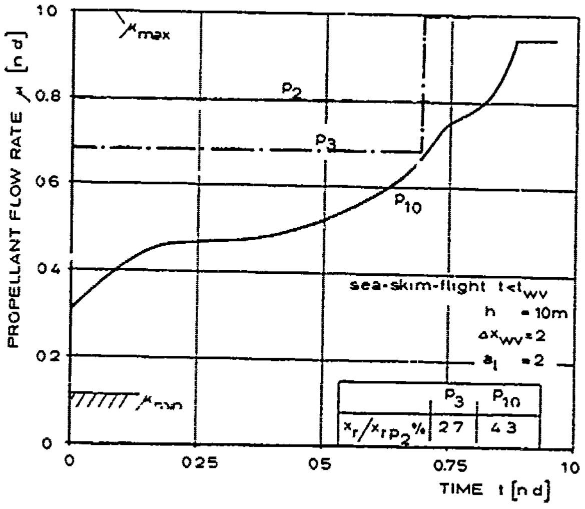

FIGURE 6: PROPELLANT FLOW RATE VS TIME FOR THREE EXAMPLES OF LEVEL FLIGHT

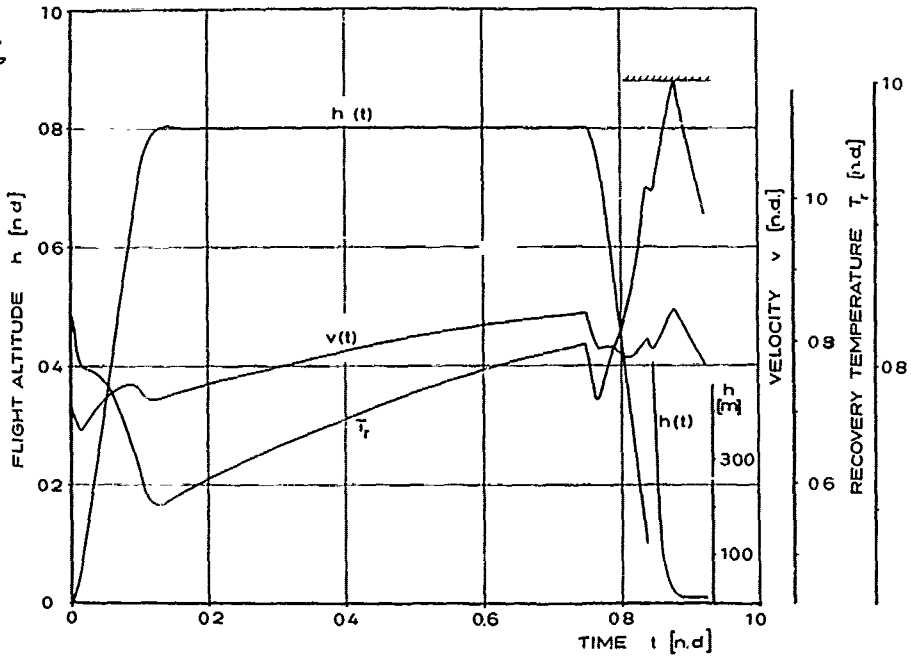

FIGURE 7: FLIGHT ALTITUDE, VELOCITY AND RECOVERY TEMPERATURE VS TIME

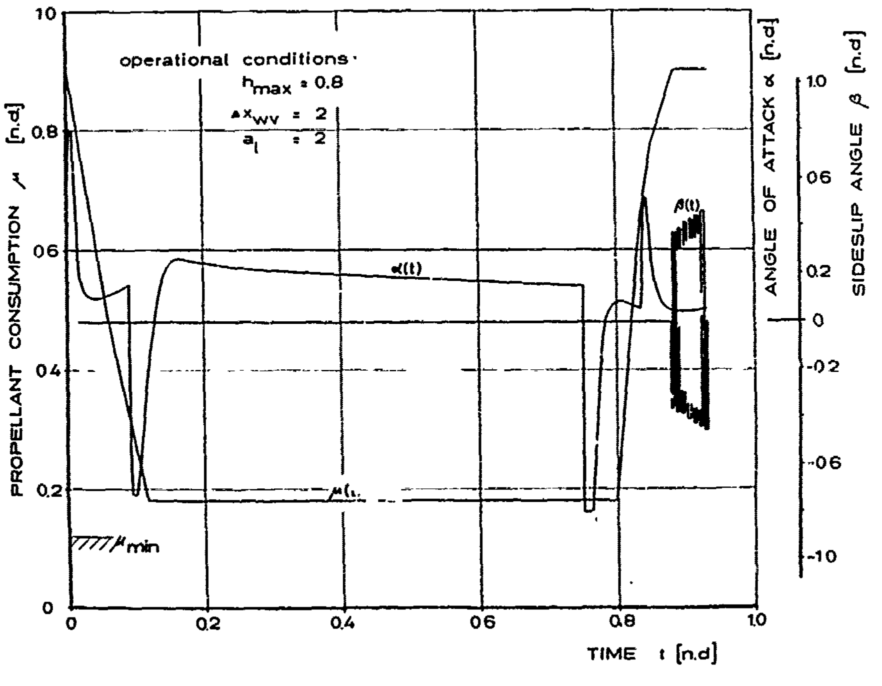

FIGURE 8: CONTROL VARIABLES AS FUNCTION OF TIME FOR FLIGHT EXAMPLE OF FIGURE 7

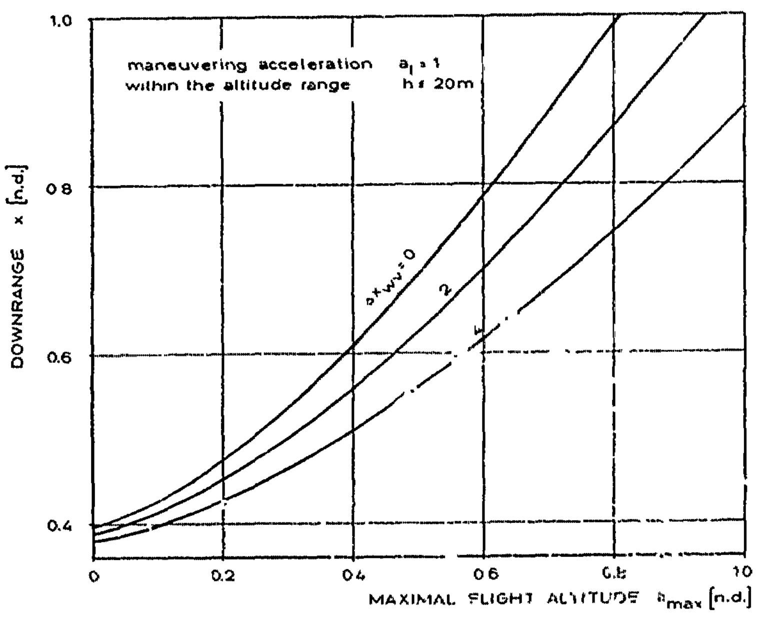

FIGURE 9: EFFECT OF ALTITUDE CONSTRAINT h_{max} ON RANGE PERFORMANCE

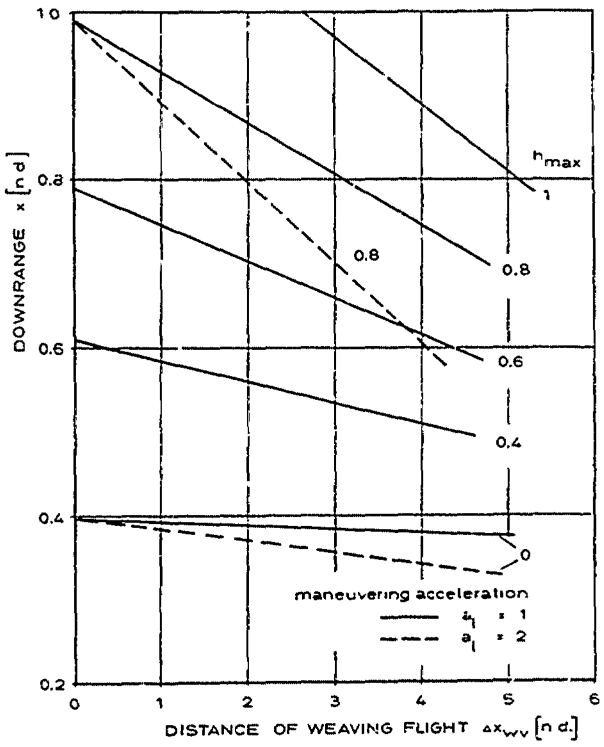

FIGURE 10: DOWNRANGE x IN DEPENDENCE OF WEAVING FLIGHT DISTANCE AND ALTITUDE CONSTRAINT

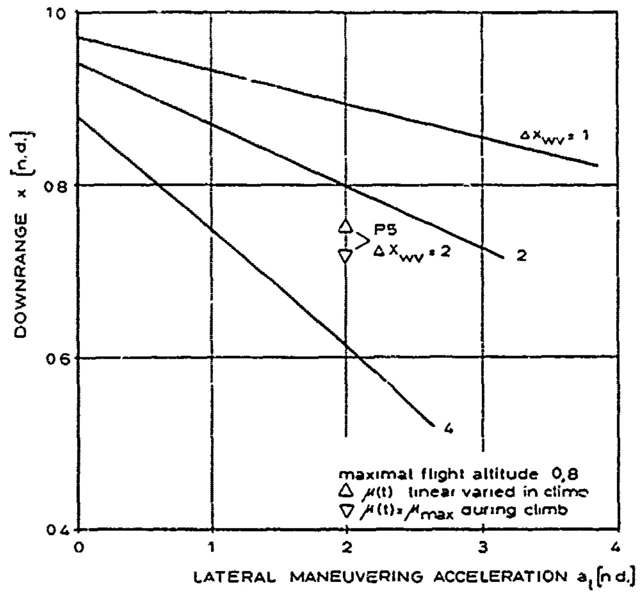

Figure 11: Range Performance vs Lateral Acceleration

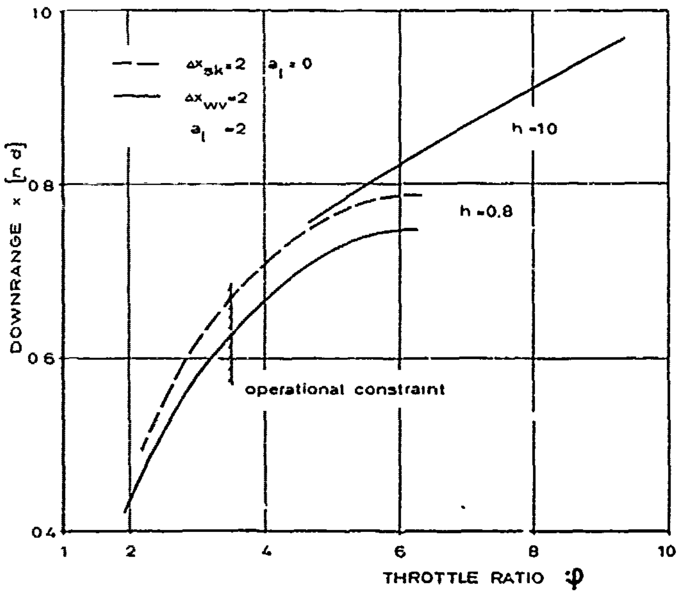

Figure 12: Effect of Throttle Ratio on Range Performance for low-high-low Flight Profiles with Cruise at Altitude h as noted

DISCUSSION

H.Wittenberg

The optimum control for maximum range, which you have shown in your examples, seems rather complicated to perform in actual flight. This is often the case for solutions, which are found by optimization theory. Have you compared your optimum range with the ranges which are obtained by simpler control functions, which approximate the ideal ones?

Author's Reply

Some examples of trajectory simulation results utilizing simple controls are given in the written paper. The simplified controls result in a range performance decrease of about 5 to 10 percent when compared to the optimal solution. However, the main advantage of the more complex control programs is seen in the fact that these controls can be adjusted such as to avoid violations of the operational constraints.

The problems of on board implementation of the control solution has not been considered.

T.Ballinger

Have you considered using your method with fewer constraints, particularly with regard to the altitude limits which seem a little low? If this were higher, would the throttle limits still be encountered? If such were the case, I wonder if you would encounter a more continuous control for both the angle of incidence and for the throttle?

Author's Reply

Both the altitude constraint and the throttle limits imposed on our problem are due to mission requirements and/or due to the characteristics of the propulsion system. We have considered higher altitude trajectories; however, the altitude had to be restricted to the range of available propulsion data, which is limited with respect to height.

Also, for a wide range of trajectory optimization problems, we have neglected the constraints on throttle ratio. Allowing higher altitudes and neglecting the propellant flow constraints would result in the same structure of the flight profile due to the control model chosen and hence would not change the characteristics of both the angle of attack and the throttle control.

Comment by R.Marguet (In French)

Application studies in France have shown that going to higher altitudes helps the optimization of range. The improvement in range at 20 to 22 kilometres is closer to 15% than 5%.

Author's Reply

Well, I think it doesn't make much difference whether I use trajectories for several maximum altitudes in the range between 10, 15 or 20 kilometres. It doesn't make any difference to the optimization effort. The reason why we constrained ourselves to this range is that we were considering ducted rocket ramjets with restricted throttle capabilities.

JET-AFTERBODY INTERFERENCE ON MISSILES IN SUPERSONIC FLOW x)

by

BERNHARD WAGNER
DORNIER GMBH
Postfach 1420
799 Friedrichshafen
West-Germany

SUMMARY:

For the axisymmetric base flow problem in presence of an exhaust jet a study is carried out taking into account essential physical parameters. Using the method of characteristics for the inviscid flow regions and Korst's treatment for the turbulent shear layers, the influence of the approaching boundary layers is introduced by the concepts of equivalent bleed and origin shift, and the ONERA angular criterion is used for the recompression process. With respect to the interferences in the confluence problem of internal and external shear layers special attention is given to the momentum terms in the ONERA criterion and a modification is performed in order to achieve agreement of both reattachment pressures at the confluence point. The investigations include separation from conical boattails by applying a simple separation criterion and extend to small angles of attack by computing the inviscid flow with the aid of a linearized characteristics method. Furthermore, for the axisymmetric case a first result is provided from numerical solutions of the full Navier-Stokes equations which are presently calculated in order to gain deeper insight into the flow structure.

1. INTRODUCTION

The importance of the base flow problem with respect to performance of missiles is obvious since a great part of the total drag might result from the afterbody if its design is not optimal. Therefore, the afterbody contains frequently a boattail for drag reduction (see e.g. /1/). But the increasing pressure on the surface of an axisymmetric afterbody when the diameter diminishes leads easily to separation. Once the flow is separated the stability is affected because the separation position moves asymmetric in consequence of a disturbance in the angle of attack. Additionally, in presence of an exhaust jet the separation regions may be largely extended due to high internal pressure resulting in loss of control if the control surfaces are covered by the separated flow.

In the past some authors developed prediction methods for this complicated flow problem in the axisymmetric case by use of a component model (see e.g. the survey paper /2/), based on the approach of a simple downstream facing step. The supersonic backstep problem can be calculated in the following way. For a trial value of the base pressure p_B, which is assumed to be constant in the stagnating separated regions, the inviscid boundaries of the base region are determined by the method of characteristics. Then a viscous shear layer is imposed on each boundary and the streamline discriminating between the external mass flow and the mass being reversed to the base region can be found. Finally a closure condition must be formulated for the reattachment process using the flow conditions on the discriminating streamline. By iterative improvement of the base pressure this condition is fulfilled and the solution is found. The first successful closure was accomplished in the theories of Korst /3/, Chapman /4/, and Kirk /5/. They assumed that the flow on the discriminating streamline stagnates at the reattachment point in an isentropic stagnation process and that the corresponding stagnation pressure is equal to the static pressure far downstream. While Korst predicted the base pressure satisfactorily for the case of turbulent shear layers without any account of an initial boundary layer at separation, Kirk has already introduced an approximation for this feature. Detailed analysis of experiments showed the quantitative success of the first approach of Korst having been due to the fact that two effects cancelled each other approximately, namely the neglect of the approaching boundary layer and an incomplete pressure recovery at reattachment /6/, /7/. This knowledge led to the construction of angular reattachment criteria which produce good results in connection with initial boundary layers.

The more complicated problem of a flow over an axisymmetric afterbody containing a centered propulsive jet has been treated by Addy /8/, who applied the ideas of Korst's restricted theory on the confluence of the two shear layers. But for good agreement with experiments it was necessary to modify the original recompression criterion by an empirical recompression coefficient depending on the ratio of nozzle radius to afterbody radius only. Further investigations for boattailed afterbodies led to modifications of this recompression coefficient introducing further parameters for such cases /9/. Since such a procedure cannot account for all physically important influences, especially not for a Reynolds number dependency, it led sometimes to still unsatisfactory flow predictions. Hence, it was decided at Dornier to introduce the boundary layer corrections in combination with the ONERA reattachment criterion into that method and to study the sensitivity of results to changes in uncertain empirical parameters or in differences concerning the treatment of the approaching boundary layer /10/. While this procedure corresponds in essence to the ONERA calculations for cylindrical afterbodies /11/, the addition of a first approximate account has been made for the interference between both shear layers during recompression. The present paper continues the previous investigations by additional discussions which are stimulated by an excellent survey paper given recently /2/.

---

x) This work has been supported by the German Ministry of Defense
under contract RüFo T/RF 42/80014/81413

If the external flow exhibits separation already on the boattail surface in consequence of high ratios of jet pressure to external pressure, a simple separation criterion has been included into the method /9/ extracted from many experiments on upstream facing steps /12/. Further evaluations of experiments indicated the importance of incipient separation effects /13/ and thus led to a modified version of the separation criterion which is presently used.

Only a few investigations are known which deal with angle of attack effects for afterbodies containing a propulsive jet (e.g. /14/, /15/). Restricted to small angles of attack for avoiding lee side vortices the separation line has been calculated in ref. 15 by neglecting the angle of attack influence on the inviscid external flow. Then, the variation of the separation position in circumferential direction followed solely from changes in the separation criterion due to corresponding changes in the boundary layer thickness known from the experiments /15/. In the present study the angle of attack influence on the external inviscid flow is added by linearizing the angle of attack effect with respect to the non-linear axisymmetric solution. This approach uses the well known linearized method of characteristics (see e.g. /16/) and is justified by restriction to sufficiently small incidence excluding the shedding of lee side vortices. Knowing the inviscid pressure and Mach number distribution and the three-dimensional boundary layer development, the base pressure and the separation point can be calculated for each meridian plane separately.

Since a base pressure calculation with the aid of the component model requires a lot of empirical parameters, which contain more or less uncertainties, the results are somewhat uncertain, too, if no further detailed experiments become available. Hence, the progress in numerical solutions of the Navier-Stokes equations suggests the use of these methods (e.g. /17/) in the present context in order to get further insight into the details of the flow structure. Although such numerical solutions may include some uncertainties, too, due to deficiencies in the knowledge about the turbulence structure in separated regions, this way is at present pursued at Dornier for the axisymmetric case and a first result is included in the paper.

2. COMPONENT APPROACH

2.1 External Inviscid Flow

Assuming homentropic flow and prescribing trial values for the base pressure p_B and the separation location the external inviscid flow in the axisymmetric case is computed with the aid of the method of characteristics for potential supersonic flow. Hence the separation shock (Fig. 1) is represented by an isentropic compression and lip shock effects cannot occur, which were supposed to cause considerable effects /18/ and could only be calculated by methods of characteristics for rotational flow. Correspondingly, also the inviscid internal jet flow is calculated, assuming it to be uniformly conical if not known otherwise. At the impingement point of both inviscid boundaries of the separated base region a system of two oblique shocks is presumed for determining static pressure and initial slipline direction behind the confluence point.

For cases with angle of attack additional characteristic equations have to be solved for the disturbances of Mach number and flow direction due to the incidence. Fortunately, the partial differential equation for the disturbance potential is linear and it exhibits the same characteristics in the physical space as the quasi-linear equation for the underlying axisymmetric case. Therefore, the numerical procedure is straightforward once the axisymmetric solution has been found in an iterative way. If the base pressure varies in circumferential direction, the parts of the inviscid flow fields which are influenced by p_B must be calculated separately for each meridian plane, the axisymmetric solution implicated. In applications of linearized characteristics methods discontinuities appear in the solutions when those characteristics are crossed which emanate from contour points of discontinuous curvature or discontinuous slope. Fortunately, the influence of these discontinuities concentrates on local zones while the global effects remain negligible. More details can be found in Ref. /19/.

2.2 Shear Layers

The method imposes two-dimensional shear layers on the three-dimensional inviscid boundaries assuming an asymptotic error function profile for the velocity distribution in the shear region. The local breadth of this layer depends on the distance of its origin and on the spread rate parameter, presently used in the form of Korst and Tripp /20/ as a pure function of Mach number M

$$\sigma = 12 + 2.758\,M\,. \qquad (1)$$

Since the experimental values for σ exhibit large scatter, the influence of that scatter has been studied in /10/. Because the pressure is presumed to be constant and identical with the base pressure across the shear layer, the density profile can be derived from the velocity distribution under the assumption of unity turbulent Prandtl number. This correlation follows from Crocco's relationship where non-isoenergetic cases are admitted with the stagnation temperatures in the external flow and in the separated base region being different /21/. Hence the principal treatment of hot exhaust jets is provided in the method /8/, but presently no use is made of this facility since the poor experimental information on those problems affects the reliability of corresponding predictions. The location of the velocity profile with respect to the inviscid boundary is found by fulfilling the momentum conservation law while the mass conservation fixes the position of the discriminating streamline already mentioned.

If an approaching boundary layer is present it undergoes a rapid expansion at the separation point or a rapid compression in case of a shock. This event can be calculated with sufficient accuracy by a simple formula of Nash /22/ for the change of the momentum thickness

$$\frac{\theta_2}{\theta_1} = \frac{\rho_{1a} u_{1a} M_{1a}}{\rho_{2a} u_{2a} M_{2a}} \qquad (2)$$

with the subscript a denoting the inviscid flow outside of the shear layer. Differences between eq.(2) and other treatments can be shown to have negligible influence on the base pressure. Introducing the initial disturbance by this layer and adding a bleed stream into the base region, the momentum and mass conservation laws yield that the position of the discriminating streamline and hence also the velocity on it depend only on a general bleed coefficient.

$$C_q = - \frac{\sigma}{L}\left(\frac{m}{\rho_a u_a} + \theta - \frac{i}{\rho_a u_a^2} \right) \qquad (3)$$

where m is the mass flow and i the momentum of the bleed stream. The length L consists of the length of the mixing layer from separation to impingement and, in addition, of a virtual upstream displacement of the shear layer origin due to the finite thickness of the initial layer. In that way eq. (3) contains the classical concepts of "equivalent bleed" and "origin shift" where the origin shift is presently carried out by the experimentally well proven procedure of ref. /23/. The present formulation of C_q (3) is slightly different to the original one of the ONERA (see /2/ or /24/) in order to make the recompression criterion formulas independent of σ (see /10/).

2.3 Recompression Criterion

Many efforts have been undertaken to model the recompression process properly /2/. From an engineering point of view the well established ONERA angular criterion is very convenient /6/ because it gives simple correlations and contains comprehensive empirical information. It is based on two experimentally evident facts for simple backsteps. Firstly, the recompression deflection angle for the restricted case of no bleed and no boundary layer $\overline{\psi}$ cannot be predicted theoretically but must be taken from experiments. For isoenergetic cases this limiting angle is a pure function of the outer flow Mach number shown in Fig. 2. It is very close to the corresponding angle calculated from Page's criterion /7/ in the important Mach number range ($2 \leq Ma \leq 4$), but differs essentially from Korst's restricted case. The limiting angle is well approximated by the hyperbola given also in fig. 2 /24/. Secondly, the changes of the actual recompression angle ψ as function of the general bleed coefficient C_q (3) are well predicted by the theory of Korst which gives an analytical expression for the gradient of ψ depending again on the Mach number alone for isoenergetic cases. Therefore, from the first two terms of a Taylor series expansion

$$\psi = \overline{\psi}(M_a) + C_q \left.\frac{\partial \psi}{\partial C_q}\right|_{C_q=0} \qquad (4)$$

the general bleed coefficient C_q can be calculated which states by eq. (3) a balancing condition between approaching boundary layer and base bleed. For a simple backstep the base pressure p_B is now iteratively improved until eq. (3) is fulfilled while for the two layer confluence problem eq. (3) gives an expression for the flux leaving each shear layer between the discriminating streamline and the streamline which separates the original external mass flux from the entrained mass, the so-called j-streamline.

Whereas this procedure signifies an independency of the reattachment pressure development in both shear layers except with the final pressures being equal, the treatment has been modified in Ref. /10/ with respect to the expected interference of both layers /10/. In reality already the pressures at the confluence point must be equal and that common pressure can be affected by the downstream flow conditions only in a very restricted manner /25/. Hence, instead of prescribing the reattachment by the inviscid flow direction behind the trailing shock system, the reattachment pressures - identical with the stagnation pressures on the discriminating streamlines - are required to be equal for both layers implying a curvature of the slipline between reattachment and final direction. The resulting reattachment direction accounts in a first approximate form for the interference between both reattachment processes in the confluence problem. This procedure is called "modified ONERA criterion" in the following.

2.4 Mass Balance and Final Solution

The sum of the entrained mass fluxes leaving both shear layers at the confluence point in addition to the original external and internal mass streams must be balanced by an eventually present base bleed

$$m_e + m_i = m_b. \qquad (5)$$

Also if no real base bleed m_b is present, eq. (5) permits in general a mass stream through the separated region from one shear layer to the other. The determination of m_e or m_i from eq. (3) requires therefore an estimation of the corresponding momentum term i. While this term has been neglected in /10/, it seems to be of relevance in the corresponding ONERA calculations /2/ and its effects are therefore investigated in some detail by the present study.

If both shear layers are treated independently the mass m and the momentum i can be taken from the outflow of each layer. This way is denoted by "momentum terms without interference" in the results presented.

However, in the important case of no base bleed also the bleed terms in eq. (3) for one of the shear layers can be understood as a result of the negative bleed due to the outflowing mass in the other layer. That method is presently characterized by "interference momentum terms" since it models an interference influence between both layers in addition to the mass flow interference (5).

Finally, in all cases the solution can be found by improving the base pressure until eq. (5) is fulfilled. In the non-isoenergetic case which means different stagnation temperatures in the external and internal inviscid flow the solution could be found by using an additional iteration loop in order to fulfill the energy balance for the base region. Although Addy's method provides this facility, no attempt has been made to compute those flows since the ONERA criterion has not been established for such cases and only few corresponding experiments are known.

2.5 Separation Criterion

Zukoski extracted from many experiments on upstream facing steps in supersonic turbulent flow the relation /12/

$$\frac{p}{p_1} = 1 + C\,M_1 \qquad (6)$$

where the subscript 1 denotes quantities immediately upstream of separation and p means a plateau pressure developed downstream in the separated zone or the final pressure immediately upstream of the step depending on the value of the constant C (0.365 or 0.5 respectively). But eq. (6) did not lead to generally good agreement with experiments and when recalculating C from experiments, a strong variation of this constant was found if the separation point moved within the rearward part of the afterbody /13/ as shown in Fig. 3. Since the values of C could approximately be reduced to a single curve if they are plotted against the distance from the base plane divided by the boundary layer thickness, these variations could be assigned to systematic incipient separation effects and could be approximated by the relation

$$C = C_0 \left(1 - e^{-\alpha \frac{s}{\delta}}\right) \qquad (7)$$

where s is the distance from the base, δ the boundary layer thickness and C_0 and α two constants which approximate the experimental findings best for the values 0.5 and 1 respectively (Fig. 3).

Since M_1 and p_1 in eq. (6) for an arbitrary position of the separation point are known from the inviscid solution, eqs. (6) and (7) relate the base pressure uniquely to the separation position. Hence, in the solution procedure the iterative change of the base pressure could easily be replaced by an iteration of the separation point without affecting the rest of the solution process.

3. RESULTS OF THE COMPONENT APPROACH

3.1 Cylindrical Afterbodies with Separation at the Base

Figures 4 and 5 contain comparisons of the theoretical base pressure plotted versus the ratio of nozzle exit p_j to external pressure p_∞ with FFA-experiments /13/ where the data of the nozzle boundary are unknown. The case of Fig. 4 was used in /10/ for comparison with all variants of the component model discussed in that paper. The best result was obtained by applying the modified ONERA recompression criterion in combination with the other components as indicated above. This result is represented by the solid line in Fig. 4. Changing over to the usual ONERA-criterion but including interference momentum terms (dashed line) leads to the deterioration of the predictions by a large amount in the directions of the original Korst criterion of isentropic recompression up to the final static pressure. However, introducing the momentum terms without regard to the interference (dashed-dotted line), being identical with the ONERA results given in /2/, the results achieved are for small pressure ratios similarly good as with the modified ONERA criterion while convergence failures occured for high pressure ratios just as in the Addy method which considerably underpredicts the base pressure. The convergence failures could be shown to be due to the fact that the necessary flow deflection in the external inviscid flow at impingement exceeds the maximum possible deflection angle in an oblique shock. Hence, this problem is probably related to the experimental observation of embedded normal shocks /15/ resulting in a flow pattern similar to the well-known Mach reflection.

Fig. 5 shows a further FFA-case having a higher external Mach number. Now only the momentum terms without interference are used and the conclusions are analogous to those for fig. 4. In addition, a result is presented for the modified ONERA-criterion including momentum terms which leads to a further improvement of the predictions. However, for high pressure ratios essential discrepancies still remain which can possibly be attributed to lip shock effects /18/ being not calculable with the present method because of the restriction to homentropic flow in the inviscid regions.

Fig. 6 depicts the comparions with an ONERA experiment for two different Mach numbers M_j in the nozzle exit which has a relatively small diameter /2/. Since the data of the nozzle boundary layers are known, they are introduced in the calculations. The ONERA-criterion including momentum terms without account for interference leads similarly as the ONERA theory /2/ to good agreement with the experimental values up to the high pressure ratios of the case $M_j = 2$ while the modified ONERA shows slightly higher deviations and the interference momentum terms cause large discrepancies. Fig. 7 again presents a comparison with an ONERA experiment which agreed excellently with the ONERA theoretical predictions /11/, the ONERA theory almost coinciding with the Addy-curve in Fig. 7. The present method overpredicts the base pressure somewhat, also if momentum terms without interference are used in the normal ONERA criterion. In order to give an impression how the very thin nozzle boundary layer, which is neglected in most investigations, affects the base pressure, corresponding results with and without internal boundary layer are given in Fig. 7. Although the internal boundary layer is about an order of magnitude thinner than the external one, it influences considerably the base pressure.(The complete experimental data for this configuration are known from private communication)

Summarizing these results it may be stated that the momentum terms in the recompression criterion are of obvious importance. But because of doubts on the correct way to introduce them a further uncertainty arises in the method in addition to those already discussed in /10/. Furthermore, the nozzle boundary layer appears to be always of reasonable influence also if it is extremely thin. Hence, in order to remove uncertainties from the prediction methods further thoroughly performed experiments are urgently needed which give detailed insight in the structure of the flow field for the two layer confluence problem. With regards to these aspects also numerical solutions of the full time averaged Navier-Stokes equations can be very helpful.

3.2 Results for Separation from Conical Boattails

According to Fig. 8 a good prediction of the separation point is achieved for all boattail angles β_e of the FFA-experiments /13/ in the rear part of the afterbody using the modifications of the separation criterion discussed above. But disagreement takes place in forward positions which is caused by the sensitivity of the separation criterion to small base pressure variations and by differences between theoretical and experimental pressure and Mach number distributions on the afterbody due to viscous effects at the body-boattail junction. The results of Fig. 8 are achieved using the empirical recompression coefficients for conical boattails /9/ which give especially good results for the FFA experiments. A change to the more physically based approach described in section 2 worsens the agreement between theory and experiment, again revealing the sensitivity of the separation point position to small changes in the base pressure.

Fig. 9 shows the corresponding results for the coefficient of the total afterbody drag C_{DB} plotted versus boattail angle β_e with the ratio of internal to external static pressure as parameter. The agreement with the experiments /13/ is good for small boattail angles and low pressure ratios where no separation or only incipient separation is present while the predictions become worse if extended separation regions occur.

In conclusion these results for boattail separation also establish the need for further detailed experiments and/or Navier-Stokes calculations in order to explore the sensitivities shown and to improve the reliability of the predictions.

3.3 Angle of Attack Results

First, for verification of the results from the linearized characteristics method a calculated boattail pressure distribution is compared with a corresponding experiment /14/ in Fig. 10. In three meridian planes which can be identified easily with the aid of the principal sketch given in this figure, the differences between the pressure coefficient of the angle of attack case and the corresponding axisymmetric case is depicted versus the distance from the body-boattail junction. The results show clearly the principal advantage of linearized characteristics method ("present method") compared with the usual linearization for supersonic flow ("linearized theory"), which means a linearization based on the undisturbed parallel flow. The present method represents much better the tendency of the measured pressures than the values from linearized theory which are constants in each meridian plane. Nevertheless, in the rear part of the afterbody the agreement becomes obviously poor because of boundary layer separation. But one must not be concerned on the following comparisons with FFA experiments from this point of view since the corresponding afterbodies extend only to one caliber behind the body-boattail junction. However, other discrepancies appeared in these measurements as already pointed out in Ref. /15/.

The boundary layer data needed for the separation prediction are taken from the experiments at angle of attack /15/ but these data are available only immediately upstream of the afterbody. Fig. 11 shows the calculated pressure distributions on an annular base of a conical afterbody compared with FFA-experiments /15/ for different ratios of jet pressure to external pressure. In general the experimental trend is approximated satisfactorily by the theory. For cases without separation on the boattail surface (p_j/p =1) the theoretical base pressure distribution compares well with the experimental pressure distribution at the end of the afterbody,and the agreement between theory and experiment is better by use of the empirical recompression coefficients /8/ than by use of the more physically based approach ("fundamental influence parameters"). This inaccuracy of the last mentioned and above discussed approach is probably due to the unknown changes of the boundary layer thickness over the boattail surface. For higher pressure ratios only the recompression coefficients are used because of the worse separation prediction by use of the more physically based approach as mentioned above. The predicted base pressure distribution exhibits little sensitivity to changes in the separation criterion as can be seen by comparison of the calculations using the real local pressures and Mach numbers with those based on the underlying axisymmetric data.

In contrast to the base pressure behavior the position of the separation line is considerably sensitive to such changes in the separation criterion (Fig. 12), especially in the forward part of the afterbody. Fig. 13 shows a comparison for the inclination of the plane going through the outermost leeside and windward side points with the measured inclination and with the simplified calculations by neglecting the deviations from the axisymmetric case in the external inviscid flow /15/. Obviously, the present method gives worse agreement for the higher pressure ratios but for a final judgement further details on the experimental separation line are needed.

In conclusion, for the angle of attack case the reliability of the predictions suffers even more than in the axisymmetric case from the lack of detailed experimental information. Navier-Stokes solutions could not yet be provided because of the high computational effort needed for fully three-dimensional calculations.

4. SOLUTIONS OF THE FULL NAVIER-STOKES EQUATIONS

Another approach to the afterbody problem is to solve numerically the time-dependent, compressible Navier-Stokes equations with time-averaged turbulence structure /26/. The planar two-dimensional computer program developed by S. Deiwert has been modified by J. L. Jacocks /17/ to enable computation of axisymmetric flow over nozzle afterbodies with either real or simulated plumes. The basic numerical algorithm is the explicit predictor-corrector scheme of MacCormack. Turbulence modelling is accomplished using the algebraic, two-layer eddy viscosity model of Baldwin and Lomax with a local modification as a function of vorticity described by Jacocks /17/. This method is presently being evaluated at Dornier and modified to account for the more recent schemes of Ref. /27/ and Ref. /28/.

The mesh generation is fully automatically based on a plume shape guess, the missile shape and an x-station prescription as a C-type mesh. Symmetry is ensured by mirror-image volumes at the centerline. The mesh consists of a fine mesh with a first cell size scaled with $1/\sqrt{Re}$ and totally 20 cells to represent the viscous dominated region and 15 cells for the outer mainly inviscid region. Fig. 14 depicts the mesh being used in the present example. Zero-slip conditions at solid surfaces are applied using the reflection principle on velocities, evaluation of the normal momentum equation for pressure, adiabatic wall conditions for internal energy, and the equation of state for density. Inflow boundary conditions are fixed in time at the initial free stream conditions as is the upper boundary condition. The outflow or downstream boundary condition is updated assuming zero gradients in the streamwise direction. For the supersonic real-plume calculation, the nozzle conditions are fixed to the initial supersonic jet conditions.

As indicated by fig. 14, the shear layer between jet plume and separated base region is not satisfactorily resolved in this preliminary test computation. Hence, no definite base pressure could be achieved and the calculated pressure exhibits considerable scatter immediately behind the base (fig. 15). The velocity profiles of the body boundary layer and the external shear layer (fig. 16) are well represented, but they are within the expected impingement region ($x/D \approx 9.3$) still far from the asymptotic form presumed in the component model. Therefore, this first result provides already a valuable insight into an aspect of the shear layer development which may cause considerable deviations from the component model assumptions. Further work will be done at Dornier in the near future in order to model properly also the second shear layer bounding the separated region.

5. CONCLUSIONS

The component approach in the present form allows to account for initial boundary layers and leads with the aid of the modified ONERA angular criterion to reasonable predictions of base pressures in spite of a few parameters and components remaining still somewhat uncertain. The separation point on boattail surfaces can be satisfactorily determined for the incipient separation range. For small angles of attack the calculated circumferential behavior of the base pressure is in agreement with experiments while the calculated separation lines seem to be less accurate. In order to improve the prediction method, additional detailed experiments are needed with respect to the confluence of two shear layers, to the separation on boattails, and to the angle of attack effects. Corresponding numerical solutions of the full Navier-Stokes equations can be very helpful, too, although then other uncertainties may arise from turbulence modelling in separated regions.

6. REFERENCES

/1/	WHITE, R.A.	Optimum afterbody considerations for supersonic flow with a centered propulsive nozzle including the effects of the flow separation. FFA TN AU-863, 1971
/2/	DÉLERY, J SIRIEIX, M	Ecoulements de culot. In: AGARD Lecture Series No. 98 "Missile Aerodynamics", 1979
/3/	KORST, H.H.	A theory for base pressure in transonic and supersonic flow. Journal of Applied Mechanics, Vol. 23, pp. 593-600, 1956
/4/	CHAPMAN, D.R. KUEHN, D.M. LARSON, H.K.	Investigation on separated flows in supersonic and subsonic streams with emphasis on the effect of transition. NACA Rep. 1356, 1958
/5/	KIRK, F.N.	An approximate theory of base pressure in two-dimensional flow at supersonic speeds. RAE-TN Aero 2377, 1959
/6/	CARRIÈRE, P. SIRIEIX, M.	Facteurs d'influence du recollement d'un écoulement supersonique. Proc. 10th Int. Cong. of Applied Mechanics, Stresa, Italy, 1960
/7/	PAGE, R.H. KESSLER, T.J. HILL, W.G.Jr.	Reattachment of two-dimensional supersonic turbulent flows. ASME-Paper 67-FE-20, 1967

/8/	ADDY, A.L. KORST, H.H. WHITE, R.A.	A study of flow separation in the base region and its effect during powered flight. AGARD CP-124, 1973
/9/	WHITE, R.A. ADDY, A.L. AGRELL,J.	An improved experimental-theoretical base pressure correlation for conical and cylindrical afterbodies with centered propulsive nozzle. Proc. 10th Int. Symposium on Space Technology and Science, Tokyo, Japan,1973
/10/	WAGNER, B. WHITE, R.A.	Supersonic base flow problem in presence of an exhaust jet. AIAA-Journal, Vol. 18, pp. 876-882, 1980
/11/	SIRIEIX, M. DÉLERY, J. MIRANDE, J.	Recherches expérimentales fondamentales sur les écoulements séparés et applications. ONERA TP No. 520, 1967
/12/	ZUKOSKI, E.E.	Turbulent boundary-layer separation in front of a forward facing step. AIAA-Journal 5, pp. 1746-1753, 1967
/13/	AGRELL, J. WHITE, R.A.	An experimental investigation of supersonic axisymmetric flow over boattails containing a centered propulsive jet. FFA TN AU-913, 1974
/14/	CORTRIGHT, E.M. SCHROEDER,A.H.	Investigation at Mach number 1.91 of side and base pressure distributions over conical boattails without and with jet flow issuing from base. NACA RM E51F26, 1951
/15/	WHITE, R.A. AGRELL, J.	Boattail and base pressure prediction including flow separation for afterbodies with a centered propulsive jet and supersonic external flow at small angles of attack. AIAA-paper 77-958, 1977
/16/	FERRI, A.	Linearized characteristics methods. In: Sears, W.R. (editor): General Theory of High Speed Aerodynamics, Princeton University Press, Princeton, N.J., pp. 557-568, 1954
/17/	JACOCKS, J.L.	Computation of axisymmetric separated nozzle-afterbody flow. AEDC-TR-79-71, 1980
/18/	KESSLER,T.J.	A theory for two-dimensional supersonic turbulent base flows. AIAA-Paper 69-68, 1969
/19/	WAGNER, B.	Auswirkung wichtiger physikalischer Einflußfaktoren auf die Strömung an zylindrischen und konischen Hecks mit Treibstrahl im Überschall. DORNIER FB 78/213, 1978
/20/	KORST,H.H. TRIPP, W.	The pressure on a blunt trailing edge separating two supersonic two-dimensional air streams of different Mach number and stagnation pressure but identical stagnation temperature. Proc. 5th Midwestern Conference on Fluid Mech., 1957
/21/	KORST, H.H. CHOW, W.L.	Non-isoenergetic turbulent ($P_{r_t}=1$) jet mixing between two compressible streams at constant pressure. NASA CR 419, 1966
/22/	NASH, J.F.	An analysis of two-dimensional turbulent base flow, including the effect of the approaching boundary layer. ARC R & M 3344, 1967
/23/	SIRIEIX, M. SOLIGNAC,J.L.	Contribution à l'ètude expérimentale de la couche de mèlange turbulent isobare d'un èculement supersonique. AGARD CP-4, 1966
/24/	SOLIGNAC,J.L. DELERY,J.	Contribution à l'ètude aerodynamique des systemes propulsifs à double flux. ONERA TP No. 1050, 1972
/25/	SIRIEIX,M. MIRANDE,J. DÉLERY,J.	Expèriences fondamentales sur le recollement turbulent d'un jet supersonique. AGARD CP-4, 1966
/26/	SCHMIDT,W.	Navier-Stokes-Untersuchungen an axisymmetrischen Flugkörper-Heckformen mit/ohne Treibstrahl. Presented at the 15th meeting of the DGLR-Ausschuß 281 "Flugkörper", DFVLR Cologne, March 1981.
/27/	JAMESON,A. SCHMIDT,W. TURKEL, E.	Numerical solutions of the Euler equations by finite volume methods using Runge-Kutta time-stepping schemes. AIAA-Paper 81-1259, 1981
/28/	MACCORMACK,R.W.	A numerical method for solving the equations of compressible viscous flow. AIAA-Paper 81-0110, 1981

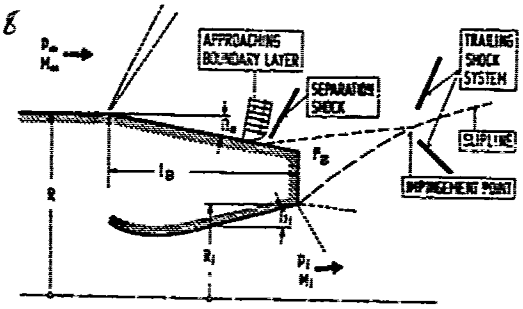
p_∞
M_∞
APPROACHING BOUNDARY LAYER
SEPARATION SHOCK
TRAILING SHOCK SYSTEM
SLIPLINE
IMPINGEMENT POINT
θ_e
l_B
p_B
R
R_i
θ_i
p_i
M_i

FIG. 1: Configuration and Nomenclature

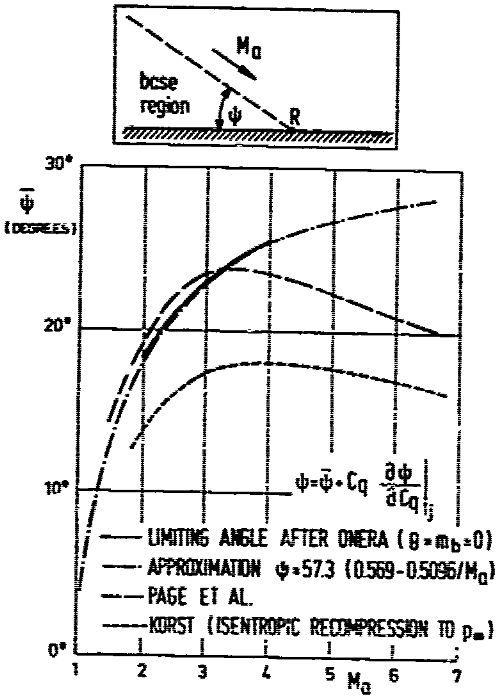

FIG. 2: Reattachment Deflection Angle (two-dimensional)

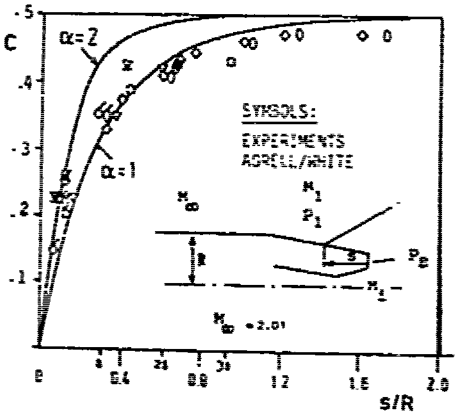

FIG. 3: Separation Criterion including Incipient Separation

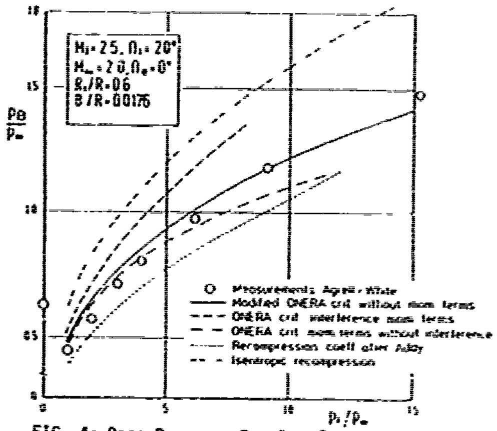

FIG. 4: Base Pressure Results for FFA Test Configuration

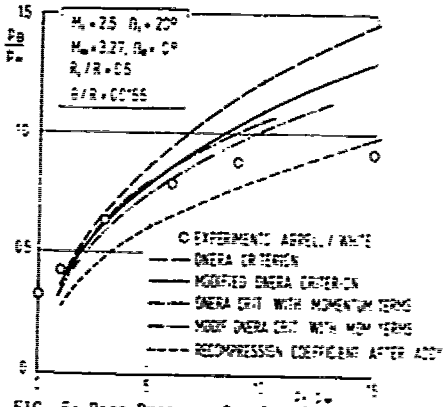

FIG. 5: Base Pressure Results for FFA Test Configuration

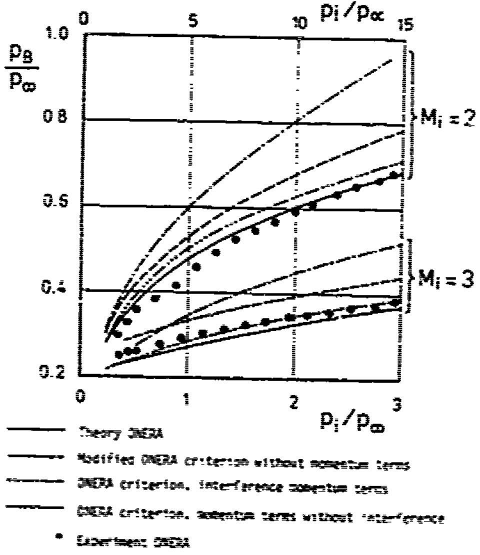

M_∞ = 1.97; θ_e = 0°; θ_i = 12°

R_i/R = 0.36; θ_e/R = 0.00945

θ_i/R = 0.0003 for M_i = 2

θ_i/R = 0.0005 for M_i = 3

FIG. 6: Base Pressure Results for ONERA Test Configuration

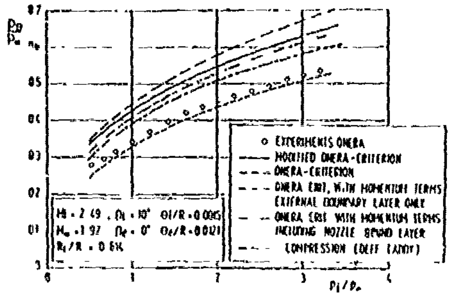

FIG. 7: Base Pressure Results for ONERA Test Configuration

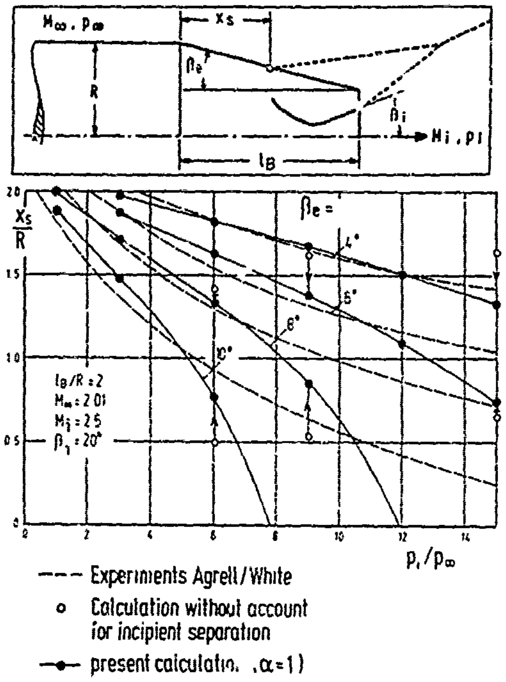

FIG. 8: Separation Point Position for Axisymmetric Flow over Conical Boattails

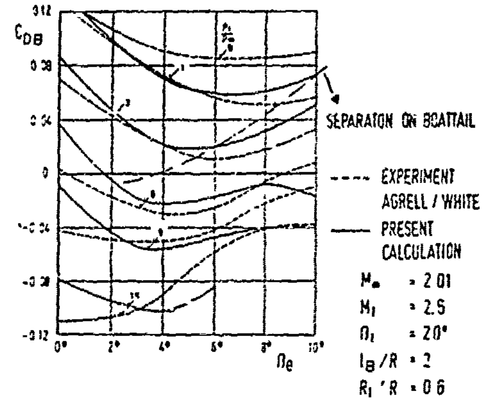

FIG.9: Total afterbody drag coeff':ient of conical boattails

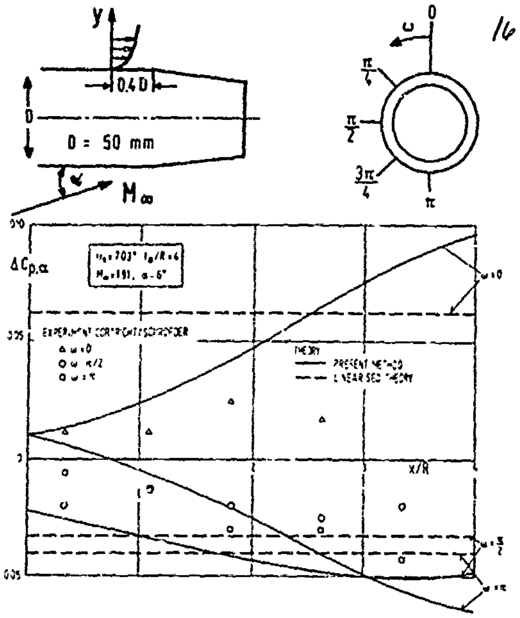

FIG.10: Pressure distribution due to angle of attack on a conical boattail

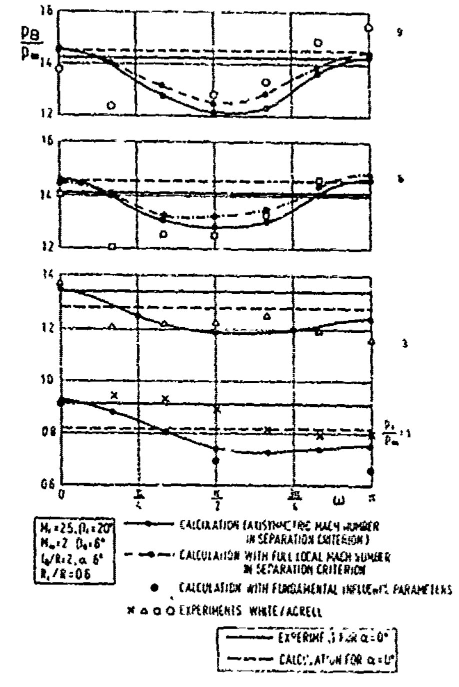

FIG.11: Base pressure distributions due to angle of attack

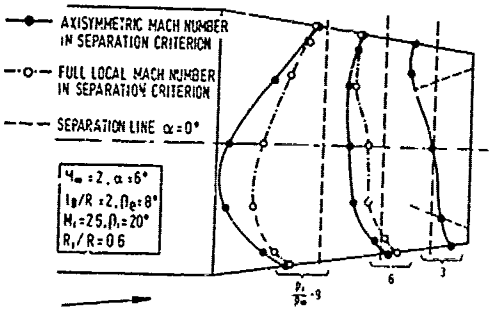

FIG.12: Calculated separation lines due to angle of attack

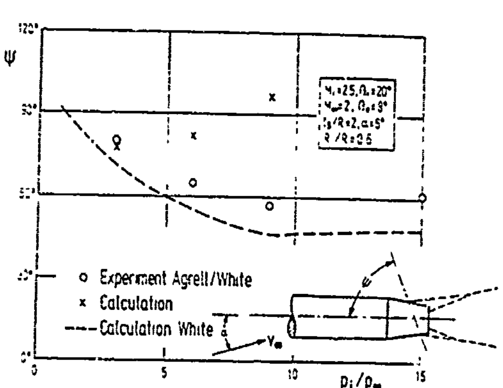

FIG.13: Angle between separation line and axis for a conical boattail at angle of attack

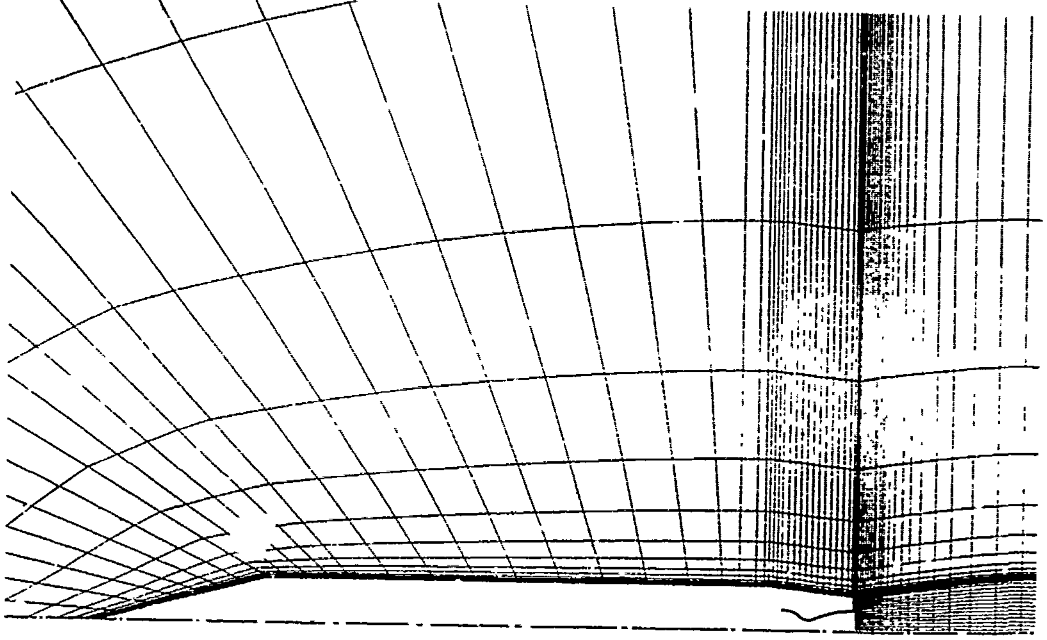

FIG.14: Computational mesh for Navier-Stokes solution

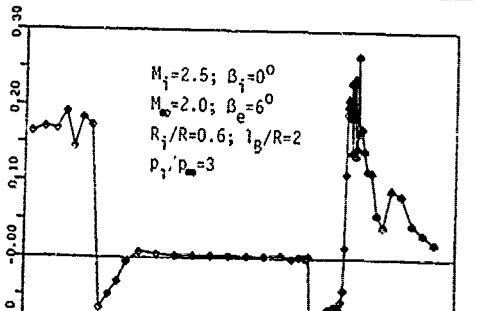

FIG.15: Pressure distribution on body and plume surface

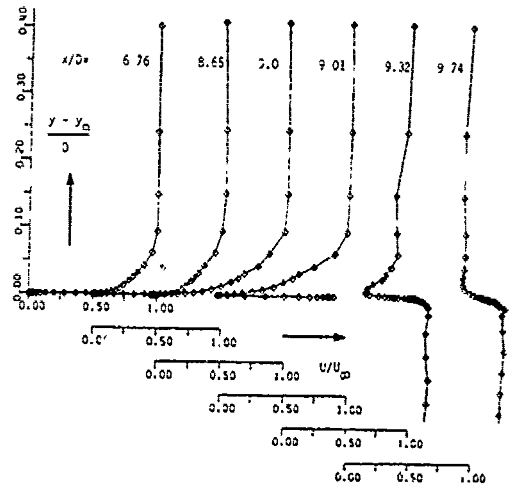

FIG.16: Velocity profiles for wall boundary layer and plume shear layer

DISCUSSION

T.Ballinger

Do you have an idea as to whether your method can be used with a hot jet efflux, and do you know of or plan to carry out any new experiments using a hot jet efflux?

Author's Reply

We do not intend to carry out such experiments, but we appreciate if research establishments would undertake detailed measurements on that subject. In principle, the method is capable to treat hot gas effects similarly as Addy's method. But at present, the ONERA recompression criterion accounts only for isoenergetic cases (equal stageration temperatures in the jet and in the external stream). Hence, we need further experimental information in order to make the predictions reliable for the case of hot jets.

J.Berard

L'auteur peut-il préciser si, à son avis, le modèle de culot qu'il a développé est capable de traiter le cas des jets réactifs? en particulier, dans le cas des moteurs-fusée à propergols solides, les gaz de combustion sont réducteurs, et la prédiction de la post-combustion est un problème important.

Author's Reply

I think that in principal, it could be introduced, but we don't know details of the hot gas effect on the recompression process.

BASE AND EXTERNAL BURNING FOR PROPULSION

by

Warren C. Strahle
Regents' Professor

and

James E. Hubbartt
Professor

School of Aerospace Engineering
Georgia Institute of Technology
Atlanta, GA 30332
USA

SUMMARY

Experimental studies are reported upon concerning base and external burning behind an axisymmetric bluff base body in Mach 3 flight. Pure hydrogen and hydrogen diluted with CO_2, He and N_2 were the fuels. A variety of base configurations were used and external burning used radial jet injection with both subsonic and supersonic jets. Some wind tunnel interference problems arose which limited consideration of the results to base pressure elevation to free stream static pressure. A maximum performance condition was identified as a line in I_{SP} - base pressure rise space which was achievable with all configurations and combinations of base and external burning. The major determinant of I_{SP} performance is the total heat dump rate into the wake, and only minor differences in performance result from configuration and fuel type details.

INTRODUCTION

There are several conceivable missions for bodies in supersonic flight where drag reduction would be beneficial. One method of achieving such drag modification is by external or base burning or a combination thereof. Various spurts of attention have been paid to these techniques, with the latest concerted effort having taken place recently.

In external burning the idea is to inject a fuel peripherally from a body in order to place it into the more-or-less inviscid stream external to the near wake. The compression waves from the combustion in the supersonic flow would then impinge on the largely subsonic near wake and elevate the base pressure. In pure base burning the injection takes place into the subsonic near wake and combustion elevates the base pressure by increasing the stagnation temperature of the dividing streamline. This in turn destroys the capability of the fluid to sustain a reattachment pressure rise and the base pressure tends toward the freestream static pressure. In pure external burning there is, in principle, no such constraint on the base pressure and levels above free stream static pressure could be expected.

Analysis(1) has revealed that with pure external burning the specific impulse performance is quite poor for large base pressure rises. This has been confirmed experimentally.(2) However, analysis(3) and experimentation(2,4) have determined that a) for low drag reduction pure base burning is efficient and b) the combination of base burning and external burning may be attractive for moderate drag reduction.

Through a sequence of programs, starting with cold flow manipulation of the near wake and progressing through burning tests, this laboratory has gathered substantial data on external/base burning phenomena. The purpose here is to draw this work together and attempt any generalizations which may be made.

TEST FACILITY

The blowdown-type test facility was designed to simulate the base flow for an axisymmetric body at Mach 3 with a bluff base. The Reynolds number, based on the base diameter is 3×10^6. The test section is shown in Fig. 1. The hollow cylindrical model is supported in the ducting upstream of the nozzle where the Mach number is 0.07. This virtually eliminates support effects. Gases for base injection and instrumentation leads are ducted into the model through the four support struts. Base pressure is evaluated as the average of five pressures measured on the base plane. The tunnel flow is not heated and the stagnation temperature drifts downward from about 483K to 453K during a typical run. Several pressures are measured on the model and tunnel surfaces to ascertain that flow conditions are repeated from test to test.

A computer based data acquisition ystem controls testing and data retreival.

From time-to-time a traversing probe is inserted into the wake to measure pitot and static pressures and stagnation temperature. This is especially crucial when wind tunnel interference effects are to be studied. In this regard, noting Fig. 1, any reflected wave from the base lip will reflect from the tunnel wall and reintersect the wake at 9.5 base radii downstream of the base. If the wake is not fully supersonic by this station, it is possible (and likely) that the base pressure will be altered by this interference effect.

The base configurations studied are shown in Figs. 2 and 3. With peripheral injection for external burning both supersonic and subsonic jets were used. Moreover, bases with and without a circumferential channel (for flameholding) were used. For pure base burning, a simple porous base plate was used. One other base plane, not shown, injected the hydrogen radially through a circumferential slot, since this was a configuration tested in Ref. (5) at Mach 2.14.

For foreign gas dilution of the hydrogen the facility is equipped to mix CO_2, He or N_2 with the H_2 upstream of the injection positions. This dilution was used to investigate the effect of injectant molecular weight and effective fuel heating value (h_{RP_f}).

RESULTS

The specific impulse (I_{SP}) is defined as the change in base pressure with and without injection times the base area divided by the injectant flow rate. That is, it is the drag change divided by fuel flow rate. The base pressure, p_b, and the free stream static pressure, p_1, are determinants of base drag. If $p_b \geq p_1$ base drag has been eliminated.

For pure base burning, cold H_2 injection, radial slot injection and subsonic radial jet injection the results are summarized in Fig. 4. These results are all for pure H_2. Except for the radial jet injection, a unique I_{SP} vs injection rate appears on Fig. 4. The injection parameter, I, is equal to the injectant flow rate divided by the free stream wind tunnel air mass flux through an equivalent base area. The slightly poorer performance shown by the radial jet injection is probably due to some axisymmetries, which are known to reduce performance.(6)

Perhaps a more illuminating way to present the data is on a plot of I_{SP} vs base force due to burning, as shown in Fig. 5. Here the maximum performance line of Fig. 4 becomes a straight line which has been placed in Fig. 5. On Fig. 5 have been shown only data with supersonic jet injection combined with base burning or for pure base burning. There is significant scatter on this figure; the lower performance points were visually identified with poor combustion with the radial jets. But the major point is the following: If everything is working well, it doesn't matter if pure base burning or a combination of external burning and base burning are used; the performance can achieve the maximum performance line if base force changes are less than or equal to the base drag. The efficiency is also impressive; 85% base drag reduction can be achieved at an I_{SP} of 4000 sec. This is comparable to ramjet efficiencies at these conditions and is achieved without inlet, combustion chamber or nozzle.

Three points lie to the right of the maximum performance line on Fig. 5, and they do so when attempting strong radial injection to increase the base force level (note the scale break on Fig. 5). High force levels were achieved here but probing of the wake indicates wind tunnel interference; the wake still contained subsonic portions of flow at 9.5 radii downstream of the base. Since base pressure on these runs was above free stream static, the wave emanating from the base lip is a compression wave and undoubtedly increased the base pressure upon reflection and intersection with the wake. Consequently, these points must be regarded as suspect. In this regard, Ref. (2) had a free jet boundary as the wave reflection surface and the opposite effect may have occurred, causing an underestimate of performance.

For the case of base pressure less than free stream static pressure, the wave emanating from the base lip is an expansion wave, and, if interference occurs, it is argued that performance is degraded. Hence, the results here are believed conservative at low base force levels.

Turning now to the effect of diluents, Fig. 6 presents the results at force levels corresponding to base drag reduction. It is found that by and large, if I_{SP} is scaled by the inverse of h_{RP_f}, the maximum performance line again represents all data. There is some scatter, especially at the mid-drag reduction point, but there is a remarkable collapse of the data. With dilution the molecular weight, density, flame temperature and turbulent mixing rates all must change. There is also a visible change in flame location. Nevertheless, the primary determinant of performance appears to be the total heat dump rate into the wake.

Temperature traverses on the wake centerline are shown in Fig. 7. It has always been found up to 3 radii downstream of the base that the mixture must be air-rich. Interestingly, the temperature differences with dilution cannot be accounted for by the dilution effect alone. The mixing rates must be altered to account for the differences in the temperature with the CO_2 dilution on Fig. 7.

Measuring temperature and pitot-static pressures on the wake centerline allows a Mach number estimate to be made, as shown in Fig. 8. Recall, if the Mach number does not exceed unity by 9.5 radii downstream interference is probably present, but the results should be conservative. On the basis of Fig. 8 it appears that the results presented are interference-free if the base drag reduction is less than 80% and $h_{RP_f} \leq 10{,}000$ Btu/lb.

CONCLUDING REMARKS

When operating at base force levels below those required to totally eliminate base drag, it appears that either base burning or combined external/base burning may be made to operate along a unique line in I_{SP} - base force space. This will occur for any fuel type if I_{SP} is scaled by the inverse of h_{RP_f}. At high base force levels the issue of performance and force level achievable is clouded by wind tunnel interference effects with all available data. Presuming these performance levels are of interest for some missions, it is imperative to design future high force level experiments in an interference-free environment.

REFERENCES

1. Mehta, G. K. and Strahle, W. C.,"Analysis of axially symmetric external burning propulsion for bluff-base bodies," AIAA Paper No 78-26, 1978.

2. Schadow, K. C. and Chieze, D. J., "Experimental investigation of combined base injection and external burning," AIAA Journal, 16, 1978, pp. 1084-1087.

3. Schetz, J. A., Billig, F. S. and Favin, S., "Approximate analysis of base drag reduction by base and/or external burning for axisymmetric supersonic bodies," AIAA Paper No. 80-1258, 1980.

4. Neale, D. H., Hubbartt, J. E. and Strahle, W. C., "Mach 3 hydrogen external/base burning," AIAA Paper No. 80-0280, 1980.

5. Townend, L. H. and Reid, J., "Some effects of stable combustion in wakes formed in a supersonic stream," Supersonic Flows, Chemical Processes and Radiative Transfer (eds. Olfe and Zahhay), Mac Millian, New York, 1964.

6. Neale, D. H., Hubbartt, J. E., Strahle, W. C., and Wilson, W. W., "Effects of External Compression on an Axisymmetric Turbulent Near Wake," AIAA Journal, 16, 1978, pp. 940-947.

ACKNOWLEDGEMENTS

This work was supported by the Air Force Office of Scientific Research under Contract No. F49620-78-C-0003. Dr. Leonard H. Caveny is the Program Monitor.

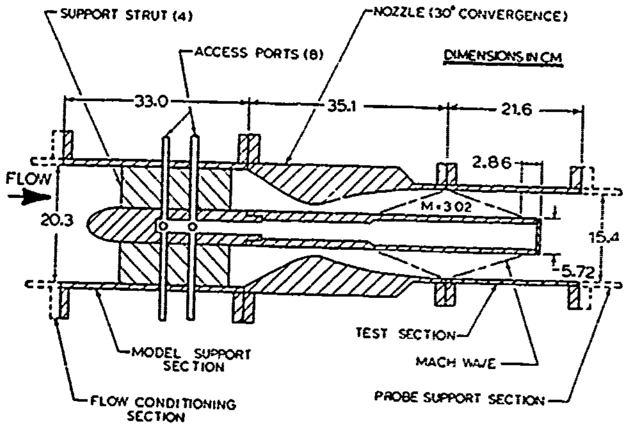
SUPPORT STRUT (4)
NOZZLE (30° CONVERGENCE)
ACCESS PORTS (8)
DIMENSIONS IN CM
33.0
35.1
21.6
2.86
FLOW
20.3
M=3.02
15.4
5.72
MODEL SUPPORT SECTION
TEST SECTION
MACH WAVE
FLOW CONDITIONING SECTION
PROBE SUPPORT SECTION

Figure 1. External/Base Burning Test Section Schematic.

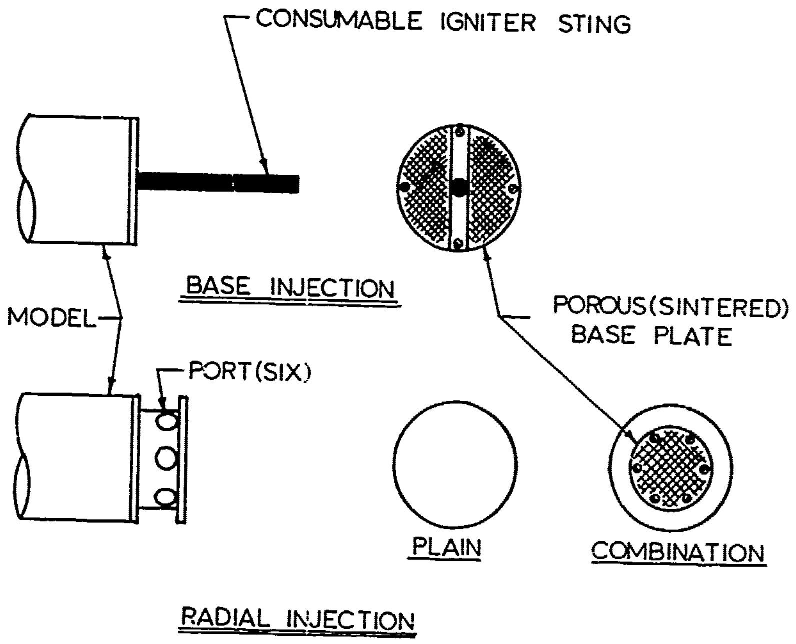
CONSUMABLE IGNITER STING
BASE INJECTION
MODEL
POROUS (SINTERED) BASE PLATE
PORT (SIX)
PLAIN
COMBINATION
RADIAL INJECTION

Figure 2. External/Base Burning Injection Configurations.

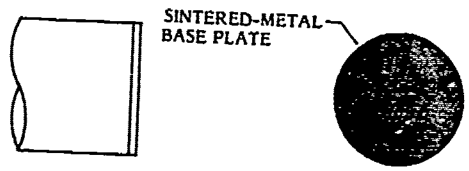
SINTERED-METAL BASE PLATE

BASE INJECTION

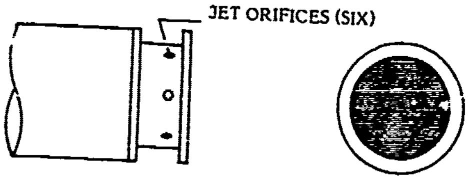
JET ORIFICES (SIX)

COMBINED BASE AND RADIAL INJECTION
CHANNEL FLAMEHOLDER

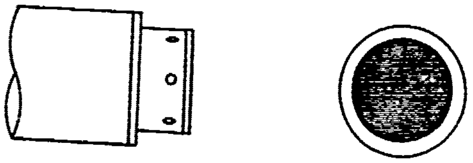

COMBINED BASE AND RADIAL INJECTION
STEP FLAMEHOLDER

Figure 3. External/Base Burning Injection Configurations.

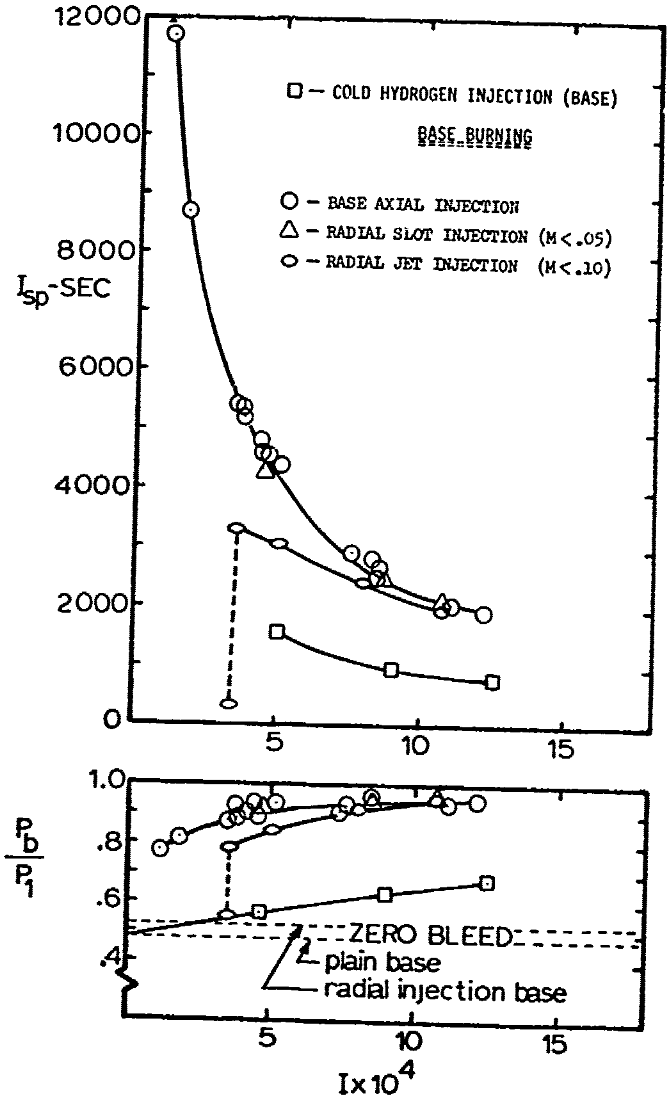

Figure 4. Specific Impulse and Base Pressure as a Function of Injectant Flow Rate.

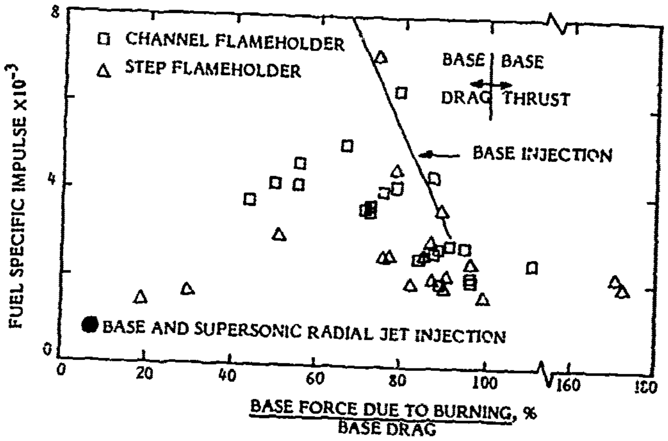

Figure 5. Specific Impulse vs. Base Pressure Rise.

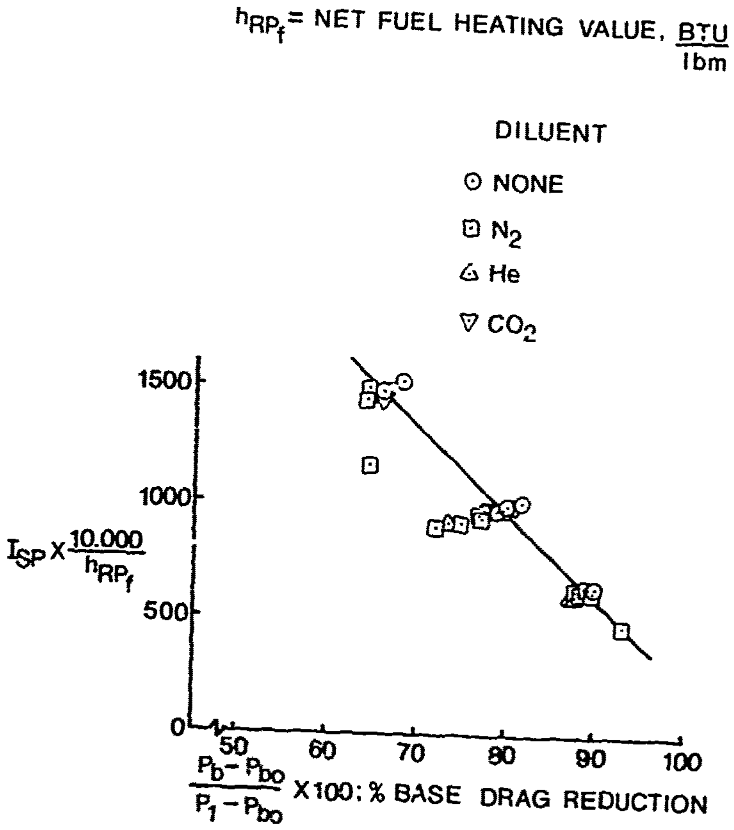

Figure 6. Diluent Effect on Performance.

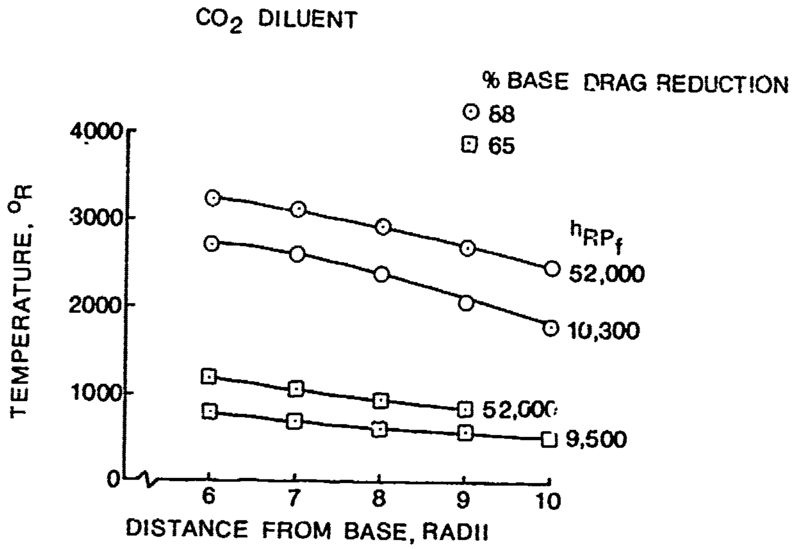

Figure 7. Wake Centerline Temperatures.

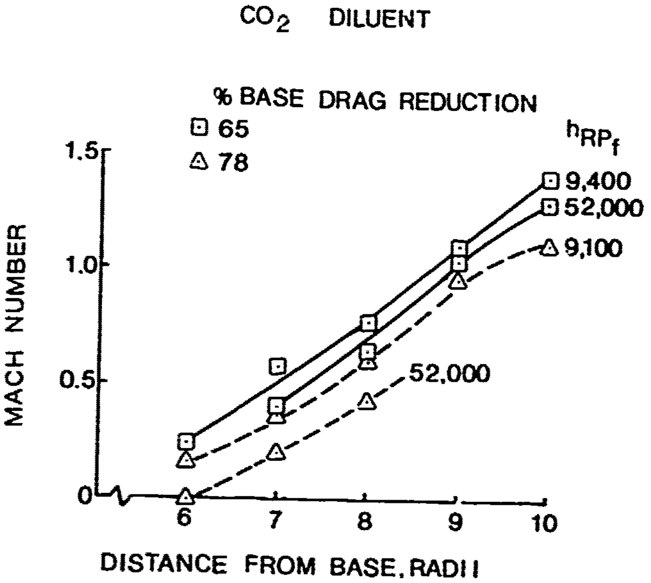

Figure 8. Centerline Mach Number vs. Distance from Base.

DISCUSSION

Comment by F.Stull

The slides shown do not match the preprint.

Author's Reply

While some of the slides do match, I have shown some later results than those in the preprint.

P.Choudhury

It seems that with "pre-burning", the peak temperature will move toward the body. In view of the superior drag reduction with "pre-burning", isn't the spatial rate of heat release rather than the total heat released more important for your correlation? Perhaps this will correlate both pre and after burning better.

Author's Reply

I am quite sure that is what is happening. We are getting combustion of hot gas injection, but it is altering the structure of the wake so that heat release occurs earlier.

R.Marguet

(a) Avez-vous fait des essais avec des combustibles solides appropriés, compte tenu des résultats avec ($H_2 + N_2 + O_2$). Combustibles spéciaux?

(b) Pensez-vous obtenir des pressions culot supérieures à la pression statique externe, en utilisant une combinaison d'injection latérale + centrale (avec des bonnes impulsion spécifiques)?

Author's Reply

(a) The reason that we diluted the hydrogen with the various dilutants was to simulate a solid propellant exhaust with lower heating value than pure hydrogen. We have been unable to find a solid propellant to put in the facility that will burn at the low pressure conditions without developing an actual rocket chamber to fire. So the answer is no, we have not done any solid propellant work. I would like to.

(b) The second question concerns lateral injection. In the supersonic case, we got very good performance, but the problem is the wind tunnel interference. I am positive that our wind tunnel had broken down when we got that impressive performance with both lateral injection and base injection.

When we inject laterally subsonically, we get exactly the same performance that we got from the base injection and could not raise the pressure above freestream static. But, we have been above freestream static pressure with the supersonic lateral injection.

P.Kramer

You mentioned an $I_{sp} \simeq 5000$ sec for that system, which has a lower pressure and a lower temperature in the combustor than a ramjet. Did you compare with the ramjet? How did you define I_{sp}?

Author's Reply

I_{sp} is defined as the change in base force level divided by total flow rate. At Mach 3 with the diluted fuel on the same basis that we computed the numbers, we get better I_{sp}'s than those of a ramjet. The trouble, of course, is that we can't get net thrust. The reason that the I_{sp} is better than a ramjet is that there is no inlet, which is a drag surface in a ramjet.

SERVICE EXPERIENCE WITH THREE GENERATIONS OF RAMJETS

BY: C F FLETCHER AND D R LANE
ROLLS-ROYCE LIMITED, PO BOX 3, FILTON, BRISTOL BS12 7QE

SUMMARY

Rolls-Royce has had the unique experience of developing three generations of ramjets for use in operational surface-to-air missiles, two with the RAF and one with the Royal Navy. Deployment overseas and in the forces of other nations has provided knowledge of operation and maintenance in tropical, arctic and marine environments. Rolls-Royce have made more ramjets than any other company in the West. The paper recounts the precautions taken during design to achieve reliability and a low level of maintenance effort. In the third generation, design has progressed to the establishment of 'wooden round' status for a factory filled liquid fuelled ramjet, with simple maintenance checks only at five year intervals. The reliability of the ramjet propulsion system in many practice firings of service maintained missiles by service crews is discussed and shown to compare well with that of rocket systems.

1 INTRODUCTION

The cautious approach by designers and development engineers of first generation ramjet propulsion systems for missiles implanted a belief, which to some extent still survives today, that ramjets are complicated and require extensive test and maintenance to ensure acceptable reliability in service. While it will remain a fact that ramjets of any type have a degree of complexity greater than that of a simple rocket, experience has shown that modern systems can be expected to have an equal reliability with similar in-service handling,ie no testing. This paper aims to show that with three generations of liquid fuelled ramjets, namely Thor for Bloodhound Mk1 and 2 and Odin for Sea Dart, the reliability 'track record' and the lessons learned have led to the understanding of the practicability of supersonic airbreathing propulsion without operational penalties. All three of these missiles were developed against very stringent requirements of performance and operating environment. Production programmes have involved approximately 5000 ramjets so far with that of Odin,for Sea Dart,continuing.

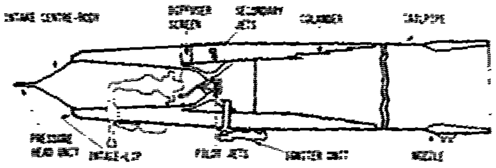

Figure 2 Thor Ramjet in Bloodhound Mk2

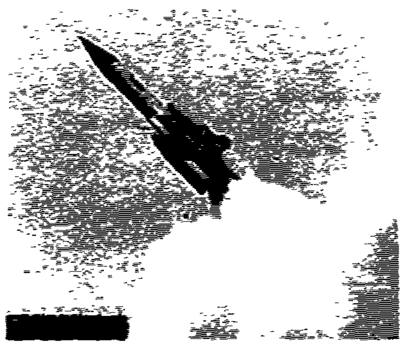

Figure 1 Bloodhound Mk2

2 BRIEF HISTORY OF BLOODHOUND AND SEA DART RAMJET PROPULSION UNITS

2.1 Bloodhound

During the late 1940's it was recognised that ramjet propulsion would be necessary to provide the range, speed, altitude capability and operational flexibility for the surface-to-air defence missiles being contemplated at that time. Following early successful flights of ramjet propelled test vehicles, project studies by the then Bristol Aeroplane Company and Ferranti led to the evolution of the Bloodhound land based anti-aircraft missile and the Thor series of ramjets to propel it. These were the first production ramjets in Europe to be offered for the propulsion of supersonic missiles. The Thor engine was designed as a pod unit for external mounting, and with this type of installation the ramjet receives a uniform flow of air and the hot tailpipe and exhaust nozzle can be adequately cooled by the external airflow. The twist and steer control method adopted for the missile imposed relatively modest incidence levels on the engine.

Development work started on the Thor 100 series engines, for Bloodhound Mk1, in 1952 with the Type Test in 1957. Some 300 to 400 missiles were fired during development, about half of which were used to investigate propulsion aspects. Although now obsolete it first entered service in 1959 with the RAF and subsequently with the Royal Australian Air Force and the Royal Swedish Air Force. Bloodhound Mk1 was followed in 1964 by the much improved Bloodhound Mk2, see Figure 1. The improvements in missile capability in terms of speed, altitude and range imposed changes on the propulsion system which led to the development of the Thor 200 series engines. Development work started in 1958 and the engine Type Test was completed in 1963. Only 40 development flights were carried out on this missile, of which 8 were specifically for propulsion investigations. This reduction, compared with Mk1, resulted both from the experience gained on Mk1 and from the major increase in the engine ground test capability provided by the then new High Altitude Test Plant at Rolls-Royce. This missile entered service in 1964 and is currently deployed with the RAF, the Swiss Government, and the Singapore Air Defence Command. It was also used at one time by the Swedish Air Force.

2.2 Thor Engine Design

Only the basic design features of the Bloodhound Mk2 propulsion system are considered here because those of Bloodhound Mk1 were generally similar.

Figure 2 illustrates the general arrangement of the Thor ramjet. It comprises a supersonic air intake and subsonic diffuser and a combustion system and exhaust nozzle as well as fuel system components. Combustion is initiated by two pyrotechnic igniters mounted externally on the engine. Auxiliary air intakes, which are mounted adjacent to the main intake of each engine, supply ram air to drive engine fuel and missile hydraulic pumps and these, together with the main intakes, are fitted with environmental protection covers on the launcher. Considerable testing was necessary during development to ensure that these covers were reliably ejected. The front cover is automatically blown off prior to launch by gas pressure generated within the engine by a pyrotechnic. The rear cover is removed when the missile moves off, by a lanyard attached to the launcher.

In the Bloodhound installation, where two podded engines are used, the fuel tanks, fuel turbopump, fuel control, thrust control and part of the metering system are mounted in the missile fuselage while the main secondary fuel throttle and distributor system are installed in the engine intake centrebody. The fuel system is hydromechanical with a Mach number control override to control missile speed. Undesirable intake operating conditions at high angles of incidence are prevented by a device which reduces fuel flow when pre-determined limits are exceeded by a free streaming cone in the missile nose. At launch the engine fuel system is already primed with fuel right up to a check valve situated in the air intake centrebody.

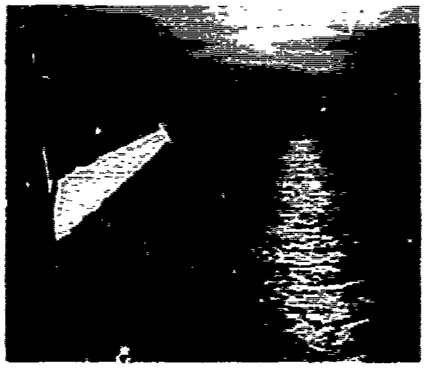

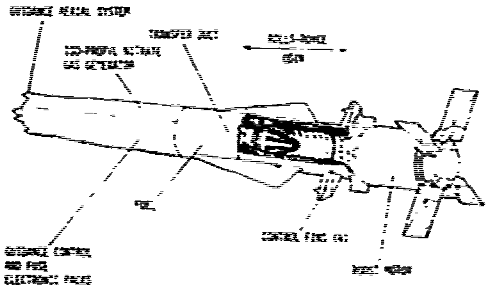

Figure 4 Sea Dart Boosted Missile

Figure 3 Sea Dart

2.3 Sea Dart

The Odin ramjet for the Sea Dart missile, Figure 3, was evolved from the requirements for a lightweight, compact medium range surface-to-air missile which was capable of being vertically stored in, and rapidly launched from, ships. The configuration selected involved the ramjet being built into the main airframe, as shown on Figure 4. The conical centrebody supersonic intake which contains equipment is mounted in the nose of the missile and, unlike Bloodhound, the missile is cartesian controlled and incidence levels can be relatively high. Downstream of the centrebody the subsonic air flow is transferred to a central cylindrical duct which is surrounded by missile equipment and the annular fuel tanks. Unlike Thor in Bloodhound, the buried installation of the ramjet combustor and exhaust nozzle within the missile rear airframe made an internal air cooling arrangement necessary.

Development work started on this engine in 1963 and Type Test was achieved in 1968. The number of development flights associated with this project was about 180 with 5 of these being nominated for early ramjet propulsion proving. Again the availability of the High Altitude Test Plant was fundamental in reducing the number of propulsion firings which were required. The Sea Dart missile entered service in 1975 and has been chosen by the Royal Navy as the main defence system for Type 42 destroyers and anti-submarine cruisers, and is also used by the Argentine Navy.

2.4 Odin Engine Design

The Odin engine comprises an air intake, transfer duct, combustor and exhaust nozzle as well as fuel system components. Combustion is initiated by a single pyrotechnic igniter. The principal items in the fuel system are a Fuel Air Ratio Control to meter fuel at the correct rate and a Thrust Control Unit to control missile speed in accordance with the measurement of air stagnation temperature. Unlike Bloodhound, the fuel tanks are factory filled and sealed off from the ramjet fuel system components by a stop valve until the boost motor has fired and the missile has left the ship. This is termed a 'dry' fuel system.

A chart showing the major milestone dates for the Thor and Odin engines, spanning almost 30 years, is given on Figure 5.

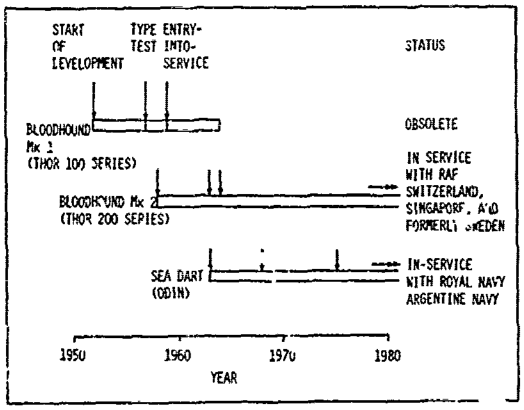

	APPROXIMATE NUMBER OF FIRINGS	PROPULSION SYSTEM RELIABILITY
BLOODHOUND Mk 2	100	100%
SEA DART	60	100%

Figure 6 Service Practice Firings Record of Service Maintained Missiles

Figure 5 Propulsion System Timescales

3 SERVICE FIRINGS RECORD

The results of these are summarised on Figure 6 and it is important to note that they relate to Service practice firings with standard Service maintained missiles of varying ages with either telemetry or with live warheads and fuses. They have covered all areas of the flight envelope. There have been no propulsion system failures out of nearly 100 Bloodhound Mk 2 firings, including one with a complete missile cold soak temperature down to -20°C. In addition, about 60 production Sea Dart missiles have been fired from ships with no propulsion problems. The 100% achieved reliabilities to date of these propulsion systems during Service firings exceeded those specified. It should be noted also that an equally high reliability standard was achieved in the later stages of R and D firings.

4 BLOODHOUND MK 2 OPERATIONAL REQUIREMENTS AFFECTING ENGINE DE

Missile requirements dictated that the Thor engine should be capable of operating up to high altitudes and at speeds between Mach 2 and Mach 2.6 with a maximum flight time in excess of 2 minutes. Furthermore the engine must be capable, with high reliability, of light-up and maximum thrust development within about 4 seconds of launch after long periods of exposure and, since this missile is land-based, the unprotected environment in which it may be deployed ranges from arctic to tropical conditions with very high humidity levels often being involved. In addition, the engine and its fuel system components are subject to high loads during boost acceleration and during manoeuvres in free flight and from vibration associated with flight and ground transportation. Light-up and operation in ambient temperatures associated with a land environment, ie -40°C to +52°C, at Sea Level, are required. These arduous operational requirements are summarised on Figure 7.

TYPE	LAND BASED, SURFACE-TO-AIR
SPEED RANGE	MACH 2 TO 2.6
ALTITUDE	SEA LEVEL TO HIGH
FLIGHT TIME	IN EXCESS OF 2 MINUTES
EXPOSURE (FOR LONG PERIODS)	WORLDWIDE
AIR TEMPERATURE RANGE AT SL	-40°C TO +52°C
MAX HUMIDITY	90 TO 95% AT 35°C
MAX LONGITUDINAL ACCELERATION	IN EXCESS OF 30G
NORMAL ACCELERATION	UP TO 16G
TRANSPORTATION	LAND, SEA, AIR

Figure 7 Bloodhound Mk2 Principal Operational Requirements

1 ENGINE PROTECTION COVER EJECTION

2 ENGINE LIGHT-UP RELIABILITY

3 SIMULATED LAUNCH TESTS

4 EXHAUSTIVE GROUND TESTING AT SIMULATED FLIGHT CONDITIONS

5 MECHANICAL INTEGRITY INVESTIGATIONS

6 DROP TESTS TO SIMULATE SHOCK LOADS

7 VIBRATION TESTING OF COMPONENTS

Figure 8 Thor in Bloodhound Mk2 Development Testing

5 THOR FOR BLOODHOUND Mk2 - DEVELOPMENT TESTING

Considering the stringent operational requirements of this missile, the high propulsion system reliability achieved in Service firings stems from careful design and the experience gained on Bloodhound Mk1 combined with the comprehensive engine ground test programme which was undertaken during development. Some of the more important aspects are summarised on Figure 8 and include:

a) Engine protection cover ejection, particularly under extreme icing conditions, see Figure 9.

b) Engine light-up reliability. A typical result is shown on Figure 10 where combustor rich and weak limits were determined over the range of flight speeds where light-up is required, to ensure that the run-up and starting characteristics of the fuel system are matched to these combustion requirements.

c) Launch and light-up demonstration on a real time transient facility at extreme ambient temperatures using flight standard fuelling systems.

d) Exhaustive ground testing at simulated flight conditions over the whole of the operational envelope of the missile. This includes combustion stability investigations as well as thrust and fuel consumption determination over the extremes of ambient temperature and at representative incidence levels.

e) Mechanical integrity tests on simulated 'worst case' trajectories.

f) Drop tests to simulate shock loads.

g) Vibration testing of components.

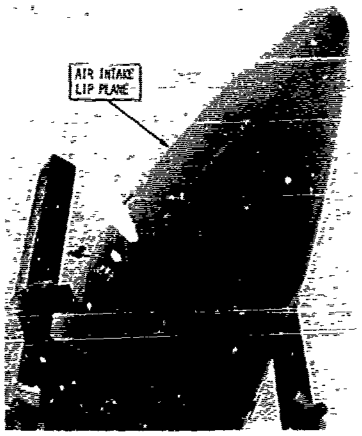

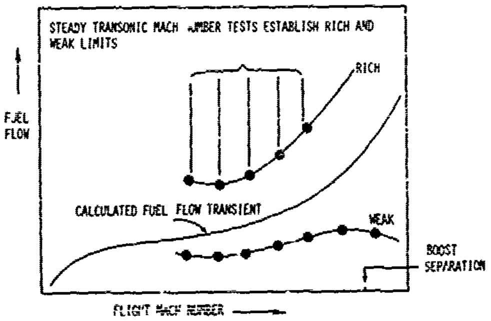

Figure 10 Engine Light-up Reliability Typical Ground Test Results

Figure 9 Bloodhound Mk2 Intake Cover Removal Simulation in Cold Conditions

6 SEA DART - OPERATIONAL REQUIREMENTS AFFECTING ENGINE DESIGN

To meet the missile requirements, the Odin engine has to operate between Mach 2 and Mach 3 and from Sea Level to medium/high altitudes to provide the propulsion for the interception of airborne threats to surface ships. In addition propulsion to fuel exhaustion in both the medium/high altitude role and the secondary anti-ship role is required. Again the engine must be capable, with high reliability, of light-up and maximum thrust production within 2 to 3 seconds of launch after long periods of storage with no pre-flight preparation or monitoring. The Royal Navy specification called for a very high propulsion system reliability (near 100%) in order to achieve the overall reliability requirements of the missile against a wide spectrum of targets.

TYPE	SHIP BASED, SURFACE-TO-AIR AND SURFACE-TO-SURFACE
SPEED RANGE	MACH 2 TO 3
ALTITUDE	SEA LEVEL TO MEDIUM/HIGH
EXPOSURE	MARINE; SHIPS MAGAZINE, LAUNCHER
AIR TEMPERATURE RANGE AT SL	-18°C TO +30°C
ENVIRONMENTAL TEMPERATURE	SHIPS MAGAZINE
MAX LONGITUDINAL ACCELERATION	IN EXCESS OF 30G
NORMAL ACCELERATION	UP TO 16G
TRANSPORTATION	LAND, SEA, AIR
SPECIAL REQUIREMENT	NO FUEL SPILLAGE

Figure 11 Sea Dart
Principal Operational Requirements

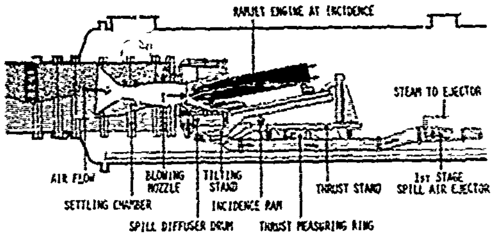

Figure 12 Diagram of Test Cell
- High Altitude Test Plant

Although the installed engine is normally stored within the controlled temperature and humidity environment of the ship's magazine, it is required to withstand the environment which would result from an air conditioning breakdown as well as the vibration levels associated with flight and transport in the ship or by air or on land. The very high boost acceleration and that associated with missile manoeuvre imposes high component loads which had to be taken into account in design. Additionally, during the short time the missile is on the launcher, the engine can be subjected to considerable water ingestion and salt spray. Light-up and operation in ambient temperatures associated with a marine environment, (ie -18°C to +30°C at sea level) are required. Because of the potential fire hazard on board ship as well as the possible contamination of electronic equipment, particularly in the buried engine Sea Dart configuration, leaks from the engine fuel system could not be tolerated under any circumstances. These requirements are summarised on Figure 11.

7 ODIN FOR SEA DART - DEVELOPMENT TESTING

The high propulsion system reliability achieved during Service firings can be attributed to experience gained from Bloodhound Mk1 and Mk2 and to the exhaustive engine and component test programme which was carried out during ground development. All engine 'hot' testing was carried out with the intake in a 'free jet' because Rolls-Royce experience shows this to be essential for the development of reliable ramjet engines and their fuel systems. A diagram of the test cell of the 'free jet' High Altitude Test Plant is shown on Figure 12, where full scale engine tests can be made over a wide range of flight conditions and incidence

1 ENGINE LIGHT-UP RELIABILITY
2 SIMULATED LAUNCH TESTS
3 EXHAUSTIVE GROUND TESTING AT SIMULATED FLIGHT CONDITIONS
4 MECHANICAL INTEGRITY INVESTIGATIONS
5 TETHERED FIRINGS
6 RAIN EROSION TESTS ON THE AIR INTAKE
7 DROP TESTS TO SIMULATE SHOCK LOADS
8 VIBRATION TESTING OF COMPONENTS
9 OPERATION WITH DIRTY FUEL

Figure 13 Odin in Sea Dart
Development Testing

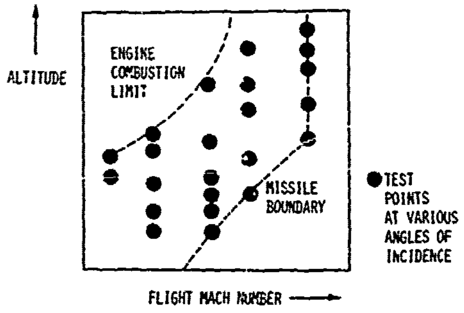

Figure 14 Odin Ramjet
Ground Test Envelope

angles. For Odin, major items in the development test programme are summarised on Figure 13 and include:

a) Engine light-up reliability investigations which were similar to those carried out on Thor.

b) Launch and light-up demonstration on a real time transient facility at extreme ambient temperatures.

c) Fuel control priming investigations using neutron radiography techniques.

d) Exhaustive ground testing at simulated flight conditions over the whole of the operational envelope of the missile and at incidence, as depicted on Figure 14. These tests included an investigation into the stability characteristics of the combustor, particularly at extreme altitudes, and thrust and fuel consumption measurements..

e) Mechanical integrity tests on simulated 'worst case' trajectories.

f) Tethered firings in which the complete missile and engine are 'flown' in a free jet facility to determine the vibration levels imposed on missile equipment by the engine. A test rig for this experiment is shown on Figure 15.

g) Rain erosion tests on the air intake.

h) Drop tests to simulate the shock loads which can result from depth charge action.

i) Vibration testing of components

j) Operation with dirty fuel

During production, manufacturing quality of the Odin is assured, as it was for Thor, by Production Quality Tests on engines selected at random at annual intervals. These tests, which are carried out on the High Altitude Test Plant facility, comprise:

- An engine thrust check at a specified flight condition
- A demonstration of the engine altitude capability at a specified flight speed
- A mechanical endurance test to a schedule which embraces the most arduous missile trajectories

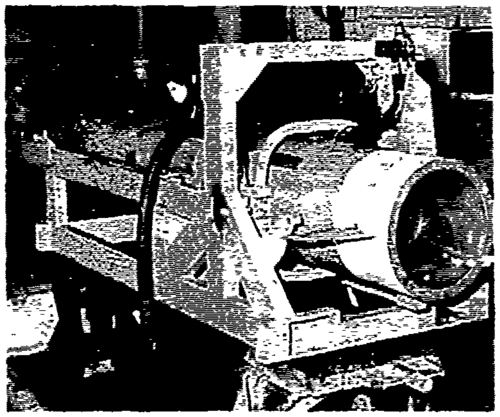

Figure 15 Sea Dart - Tethered Firing Trial

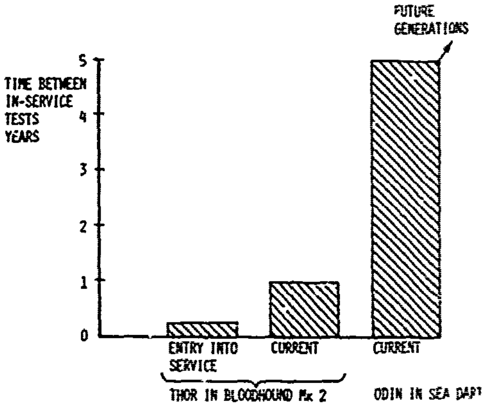

Figure 16 Thor and Odin Ramjets In-service Maintenance

8 PROGRESSION TOWARDS ZERO IN-SERVICE MAINTENANCE

8.1 General

The aim has always been that of achieving standards of maintenance equivalent to those of gun ammunition,ie no testing. In the days of Bloodhound Mk1 however it was necessary to establish the serviceability of the fuel system,at quarterly intervals,by running the turbopump in order to check the characteristics of the fuel flow controls and,in addition,careful priming of the fuel control was required to ensure a reliable light-up. Bloodhound Mk2 progressed to annual tests of the fuel system,and turbopump running was eliminated because the flow characteristics of the engine could be checked from an external fuel supply. In Sea Dart the fuel tanks are factory filled and only two components in the engine fuel system need be tested. Currently this occurs at 5 year intervals but clearance for a longer period is being sought. It is clear therefore that the reduction in maintenance complexity and the progressive increase in time between in-service tests over three generations (see Figure 16) gives confidence that no tests will be required in future generations of ramjet.

8.2 Thor Maintenance

A maintenance diagram is shown for Thor in Bloodhound Mk2 on Figure 17 which indicates the fuel system components which are tested. Connections for these are made via tapping points on the missile skin, thereby obviating any need to de-panel the missile. It has been predicted that the manpower requirement for the complete servicing of the ramjet propulsion system is about 1 man per 50 missiles. The estimated defect rate for the Thor engine, which has improved considerably over the years as a result of development and modification action, is as follows:

Defect Rate	One Defect Per
At entry into service	5.3 missile years
At present time (1981)	11.9 missile years

where Defect Rate is defined as:

$$\frac{\text{Number of missiles in service} \times \text{Number of years of survey}}{\text{Number of defects}}$$

The main problem areas have been concerned with the thrust control unit because of the extremely high degree of accuracy originally demanded to satisfy the performance requirements over the whole flight envelope. With today's knowledge some relaxation might be tolerated without having a significant effect on the overall system reliability.

The extended service life requirements of the Bloodhound system has led to the adoption of a reconditioning programme whereby engines are returned to the manufacturer after 10 years, and all rubber components including seals and diaphragms are replaced and fuel system items are reset and calibrated to be within the original manufacturing limits.

8.3 Odin Maintenance

Experience with Bloodhound showed that well designed ram-air fuel turbopumps could be relied on to perform instantly after many years of storage. For Odin, therefore, fuel system tests were simplified to those of the hydromechanical controls in isolation. To ensure freedom from contamination of missile equipment by kerosene, a procedure for the removal of these units for test was adopted which was readily accomplished with the 'dry' system described earlier. Priming and run-up of this 'dry' system was proved in many real-time launch simulations (including engine light-up) on ground tests in the High Altitude Test Plant. These tests included those with engines subjected to accelerated storage and

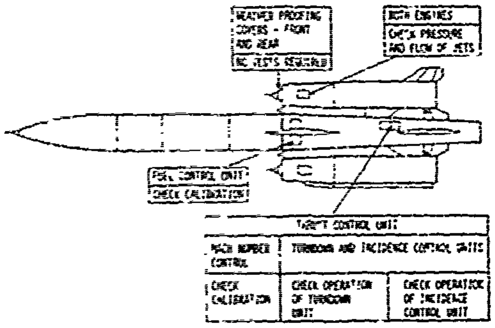
WEATHER PROOFING COVERS - FRONT AND REAR
NO TESTS REQUIRED
BOTH ENGINES
CHECK PRESSURE AND FLOW OF JETS
FUEL CONTROL UNIT
CHECK CALIBRATION
THRUST CONTROL UNIT
MACH NUMBER CONTROL
TURNDOWN AND INCIDENCE CONTROL UNITS
CHECK CALIBRATION
CHECK OPERATION OF TURNDOWN UNIT
CHECK OPERATION OF INCIDENCE CONTROL UNIT

Figure 17 Thor in Bloodhound Mk2 - Maintenance Features

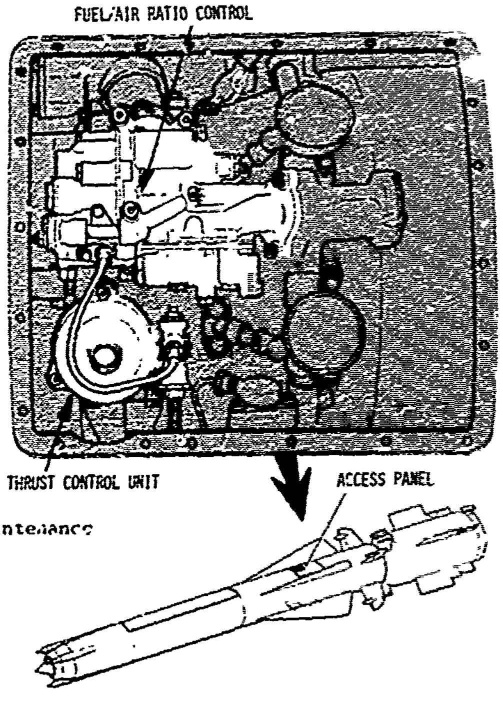
FUEL/AIR RATIO CONTROL
THRUST CONTROL UNIT
ACCESS PANEL

Figure 18 Drawing of Odin Maintenance Bay

extreme temperature conditions. The Fuel Air Ratio Control and Thrust Control units require relatively simple calibration testing every 5 years at a shore depot and removal of these is via the access panel on the missile,as shown on Figure 18. The decision to test these controls was taken in the absence of firm evidence of the effect on them of storage in the ship's magazine. Evidence is gradually being accumulated which is aimed at permitting the time between tests to be extended to 10 years. Eventually they may, in agreement with the Royal Navy, be dropped altogether. The reliability demonstrated with the twin pyrotechnic igniters of Thor and early Odin showed that a single igniter unit with a percussion initiating device would be satisfactory for Sea Dart in service. This unit requires no testing and currently has a life of 3 to 6 years, depending upon the environment.

The manpower requirement for the maintenance of Odin is about 1 man per 200 missiles. Using the same definition as for the Thor engine, analysis has shown that the Odin defect rate is 1 per 30 missile years. This improvement is a direct result of the lessons learned from Bloodhound and the generally more favourable environmental conditions enjoyed by Sea Dart.

1 EARLY UNDERSTANDING OF STORAGE/DEPLOYMENT ENVIRONMENTAL CONDITIONS

2 THE USE OF PROTECTION COVERS AND/OR PROTECTIVE VARNISH TO ELIMINATE ENVIRONMENTAL EFFECTS

3 THE AVOIDANCE OF ELECTROLYTIC ACTION BETWEEN METALS

4 THE ADOPTION OF A 'DRY' FUEL SYSTEM

5 FUEL SYSTEM MOVING PARTS POSITIONED SUCH AS TO REDUCE ACCELERATION EFFECTS

6 UTILISE BOOST ACCELERATION TO ASSIST FUEL SYSTEM PRIMING

7 ACCOUNT TAKEN OF GROUND TRANSPORT/HANDLING REQUIREMENTS

Figure 19 Lessons Learned to Ensure High Reliability

1 FUTURE MISSILE REQUIREMENTS MAY DEMAND MULTI LAUNCH PLATFORMS AND WORLD WIDE ENVIRONMENTAL CONDITIONS

2 EXPERIENCE FROM BLOODHOUND AND SEA DART PROPULSION SYSTEMS IS HIGHLY RELEVANT

3 FUTURE GENERATIONS OF RAMJET WILL HAVE HIGH RELIABILITY AND NO MAINTENANCE

Figure 20 For the Future

9 LESSONS LEARNED IN ACHIEVING HIGH RELIABILITY

The design task is to obtain instant readiness with trouble free operation and the correct performance levels after long periods of storage and ground handling. As a result of the experience gained from the Bloodhound and Sea Dart engine programmes,there has been a steady progression in the understanding of the key design areas and the precautions which are necessary to achieve high reliability and the elimination of in-service testing. These are summarised on Figure 19 and comprise:

a) The use of stainless steel where possible and protective dipped coatings where necessary to eliminate corrosion during long term service life in all environmental conditions.

b) The avoidance of electrolytic action between mating parts by careful matching of materials.

c) The adoption of a 'sealed' fuel system in which engine components remain dry until launch.

d) The use of sealed igniters.

e) The use of engine blanks while the missile is on the launcher to reduce environmental effects.

f) Seal materials selected for compatibility with operating temperatures and with liquid fuels in accordance with missile/engine life cycle requirements.

g) Moving parts in the fuel system positioned to reduce the effect of worst acceleration forces.

h) Utilise boost acceleration and fuel control position relative to the fuel tanks to assist the fuel system priming process.

i) Design for ground transportation/handling protection to prevent, for example, sensing probe damage and skin denting.

From the foregoing, it should be clear that the design and development of reliable ramjets depends critically on the early and precise statement of the missile long term storage and deployment environmental conditions.

10 FOR THE FUTURE

From the evidence shown here, future generations of liquid fuelled ramjet should enjoy the high reliability standards achieved with the Bloodhound and Sea Dart propulsion systems and require no maintenance testing. It is our opinion that design for launch from multiple platforms and other operational considerations exposed in recent NATO/NIAG studies should not invalidate the above claim. Of course, as shown, a carefully planned development programme will be necessary. The high reliability which has been demonstrated for the liquid fuelled ramjet also shows that the often claimed more simple alternative airbreathing propulsion systems, eg ram-rocket/ducted rocket and solid fuel ramjet, could have as good a reliability since there is nothing inherent in their overall concept which would pose widely different problems. These observations are summarised on Figure 20.

11 CONCLUSIONS (See Figure 21)

a) This paper has shown that the liquid fuelled ramjet has a comparable in-service reliability to that of the simple rocket, in spite of its greater complexity, while offering a wider operational capability. This has been achieved largely by careful attention to detail in design and exhaustive ground testing.

b) The experience gained on three generations of in-service ramjets designed for arduous missile trajectories and environmental conditions has led to the achievement of near 'wooden round' or 'sealed for life' status with simple maintenance checks currently only at 5 year intervals. This interval can be expected to be increased in the future.

c) It can be concluded that the ram-rocket/ducted rocket or solid fuel ramjet, which are generally claimed to be more simple in operation and development, could achieve similar reliability levels to those of the more versatile liquid fuelled ramjet.

d) The lessons learned from the Bloodhound and Sea Dart propulsion systems can be advantageously fed into design and development thinking for any future projects.

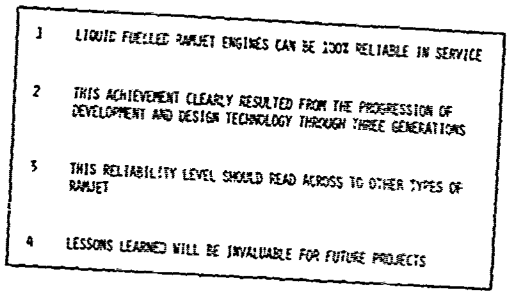

1 LIQUID FUELLED RAMJET ENGINES CAN BE 100% RELIABLE IN SERVICE

2 THIS ACHIEVEMENT CLEARLY RESULTED FROM THE PROGRESSION OF DEVELOPMENT AND DESIGN TECHNOLOGY THROUGH THREE GENERATIONS

3 THIS RELIABILITY LEVEL SHOULD READ ACROSS TO OTHER TYPES OF RAMJET

4 LESSONS LEARNED WILL BE INVALUABLE FOR FUTURE PROJECTS

Figure 21 Conclusions

EXPERIMENTAL INVESTIGATION OF A HYDROCARBON SOLID FUEL RAMJET

by

Dirk Meinköhn and Jürgen W. Bergmann
Deutsche Forschungs- und Versuchsanstalt für Luft- und Raumfahrt e.V. (DFVLR)
Institut für Chemische Antriebe und Verfahrenstechnik
D-7101 Hardthausen-Lampoldshausen (Germany)

Summary

A solid fuel ramjet motor was investigated in a connected-pipe air supply system under simulated in-flight operating condition. By taking into account diffuser losses based on empirical efficiencies, a set of states of the air upstream of the ramjet combustor was theoretically derived in order to simulate certain in-flight conditions of a ramjet-powered missile. The experimental investigation of internal ballistics, combustion efficiency and overall combustor performance covered a range of Mach-numbers between 1.5 and 3.0 for altitudes between sea-level and 6000 m. Polyethylene was chosen as hydrocarbon fuel in most of the tests. It was found that a suitable fuel regression can be established for varying performance requirements resulting from a particular ramjet mission, even by providing for trajectory dependent combustion efficiencies.

1. Introduction

Within the family of airbreathing engines, the solid fuel ramjet represents a design of utmost simplicity due to the lack of any moving parts (like valves, pumps, etc.). It consists basically of an air intake system, a thrust producing exhaust nozzle, and a combustor comprising the flameholding device, the ignitor, the combustion chamber containing the solid fuel, and the afterburn chamber for enhancement and completion of the combustion.

For all its apparent simplicity, the ramjet engine brings about particular difficulties in its operation, since the combustion processes strongly depend on the flight conditions. The operation of a solid fuel ramjet, in particular, depends on the interaction between the air intake system and the combustor, because the fuel regression as well as the mixing and burning of the propellants are governed by the physico-chemical laws of hybrid combustion.

It was our objective to investigate, as a first step, the combustion behavior in a model ramjet combustor for varied flight data (speed and altitude). The flight data were taken from certain points of a flight trajectory of a ramjet-propelled missile, which resulted from assumptions as to thrust and drag under the conditions of a preselected ramjet mission.

In order to work under realistic conditions for the upstream boundary of the combustor, the influence of a typical air intake system on the flight data was calculated for us by the Institut für Raumfahrtantriebe of Stuttgart University.

2. Proposed Mission for a Ramjet-Powered Missile

For a ramjet-powered missile, two types of missions may be considered. There is, in the first place, a mission with stationary cruising conditions, which is equivalent to fixed height of flight and fixed Mach-number. The other mission consists in providing post launch propulsion for some part or all of the flight trajectory of a small missile. The investigations presented in this paper are based on the latter type of mission, for which the solid fuel ramjet seems to be particularly suited. Starting from the requirements of distance to be covered by a given missile and provision of acceleration by the ramjet engine, the trajectory of the missile is characterized by the velocity requirements given in Fig.1 and by the requirements as to air mass flow and combustion pressure given in Fig.2. These requirements reflect the change in engine performance necessitated by the changing flight conditions. It was found that for the thrust requirement stoichiometric burning has to be assumed. The missile trajectory in terms of total pressure and total temperature of the air is given in Fig.3.

The solid fuel ramjet motor was then investigated with respect to the derived missile trajectory. This was done by selecting three points of the trajectory and carrying out motor tests under such stationary conditions as were required by these three points. It is our plan for the future to investigate a ramjet engine by continuous simulation of the complete trajectory.

3. Ramjet Motor Test Facility

The combustor tests were carried out on the connected-pipe test facility outlined in Fig.4. The air was supplied from a storage tank designed to hold 10 m^3 of air at a pressure of up to 180 bar. Via a series of controllable pressure regulators, the air pressure was reduced to a predetermined value, whereupon the cold air mass flow was measured with the help of a Fischer & Porter swirl flowmeter. It was then designed to achieve the necessary air temperature by passing the air flow through a heat reservoir consisting of two electric heat exchanger units of 7 kW each. After passage of a two-way valve, the air flow then was directed into the actual ramjet combustor. On entering the combustor, the state of the air flow is defined by a set of three parameters, namely the air mass flow, the total temperature, and the total pressure of the air. For a simulation of the selected conditions of the flight trajectory, these parameters were matched to the flight data which were modified by the calculated influence of the air intake system. It was, therefore, possible to simulate the ramjet operations in a connected-pipe system and the application of real diffusers was obviated.

The ramjet motor itself consisted of the flameholder, the ignitor, and a fuel block with a cylindrical combustion channel, an afterburner, and an exhaust nozzle. It was possible to test ramjet combustors up to Mach 2.5 at sea-level air conditions.

The aim of the investigation was

- to derive the fuel regression rate in its dependence on the air mass flux and the combustion chamber pressure for polyethylene, which was selected as reference fuel because of its clean combustion;
- to determine the combustion efficiencies;
- to investigate the effect of the combustion chamber geometry and the combustion time;
- to investigate different hydrocarbon fuels.

The hydrocarbon fuels under investigation - other than polyethylene (PE) - were polymethylmethacrylate (PMMA) and hydroxyterminated polybutadiene (HTPB). Depending on the initial state of the fuel (fluid, powder), the fuel blocks were prepared by casting or by compressing.

4. Combustion Efficiency and Fuel Regression

In consequence of the requirements of a selected flight situation, the following parameters had to attain given values:

total air inlet temperature	T_L	[K]
total air inlet pressure	P_{tot}	[bar]
or static combustion pressure	P_c	[bar]
air/fuel mass ratio	O/F	[-]
air mass flow	$\dot{m}_a$	[g/s]

By working with the combustion pressure P_c instead of the total air inlet pressure P_{tot} as a defining element for the state of the air flow, the influence of a particular flameholder was eliminated.

From the given values of $\dot{m}_a$ and O/F the mass flow $\dot{m}_f$ [g/s] is fully determined. The fuel mass flow $\dot{m}_f$, by itself, is a function of the fuel regression rate $\dot{r}$ [mm/s], the density of the fuel, and the size of the combustion channel surface, which is equivalent to the exposed fuel surface.

The regression rate $\dot{r}$ is one of the characteristic features of a fuel. It is a function of the oxidizer mass flux $\dot{M}_a$ [g/cm^2], the combustion pressure P_c and, to a lesser extent, of the oxidizer temperature T_L .

In view of the requirement as to $\dot{m}_f$ and also in view of a strong demand for volume restriction, the following lines of research were persued:

a) Investigation of the regression rate and the combustion efficiencies in their dependence on varying operating conditions for cast polyethylene fuel blocks, which were of one and the same geometry (essentially the combustion channel geometry and fuel block length).

fuel block length $L = 210$ mm

circular combustion channel cross-section

channel diameter $D = 60$ mm

b) Investigation of the regression rate of various hydrocarbon fuels, differing in composition, with various additives. For these tests, the fuel blocks were of the same size as with case (a). In order to facilitate the comparison, the motor tests were carried out under one and the same set of operating conditions.

c) Determination of the combustion efficiencies and the regression rates of a model combustor under the conditions equivalent to the selected flight situations. For these experiments, fuel blocks were made by compressing polyethylene powder. The combustion channel was cylindrical and the required O/F-values were attained by adjustment of the fuel block length L.

d) Search for a suitable combustion channel geometry with the aim to attain an acceptable length L of the fuel block. These experiments were carried out on fuel blocks obtained by compressing polyethylene powder. The fuel blocks were of a given length, with varying channel geometries.

5. Test Results

5.1 Regression Rates and Combustion Efficiency for Cast Polyethylene

For these tests, the geometry of the fuel block was kept unchanged. The total temperature of the incoming air was the same for all tests (280 K). The combustion time was kept at 60 s, if not otherwise explained.

Fig. 5 shows the influence of the combustion pressure and the air mass flow on the PE regression rate. One sees that for chamber pressures between 2 and 10 bar the pressure effect on fuel regression is not much lower than the one of the air flow. The influence of the air mass flux $\dot{M}_a$ on the regression rate is nearly the same for different chamber pressures, as Fig. 6 reveals. Using double-logarithmic coordinates to display $\bar{r}$ as a function of $\dot{M}_a$, the average slope can be found to lie around 0.36. Further analysis as to the pressure dependence finally brings about a power law approximation for the PE regression rate of the equation

$$\bar{r} = 0.0414 \cdot p_c^{0.3} \cdot \dot{M}_a^{0.36} \quad (1)$$

Fig. 7 shows how the approximation curve fits the experimental data.

The combustion efficiencies measured in these tests are displayed in Fig. 8. The diagram reveals - as expected - the strong influence of the chamber pressure on the efficiency of the combustion. Decreasing efficiencies for raising air mass flows - as can be extrapolated from the graph - are due to the fuel lean O/F ratios used in these tests.

In Figures 9 and 10, the combustion channel regression is depicted for varied combustion time t_B and for varied air mass flow.

5.2 Varied Hydrocarbon Fuel

In Table 1, the effect of varying hydrocarbon fuel is displayed. In these tests, fuel blocks of one and the same geometry were burned under the same set of conditions.

Fuel Composition		P_c	O/F	$\bar{r}$	$\bar{r}\cdot\rho$	
No.		[bar]		[mm/s]	[g/cm^{2}s]	
64	100% PE	4.13	54	0.111	0.0107	cast
004	100% PE	3.98	50	0.219	0.0185	compressed
111	75% PE, 25% HTPB	4.37	38	0.194	0.0167	compressed
117	35% PE, 65% HTPB	4.67	26	0.309	0.0290	cast
118	25% PE, 75% HTPB	4.75	23	0.344	0.0324	cast
109	100% HTPB	4.47	20	0.430	0.0402	cast
116	50% PMMA, 50% HTPB	4.47	26	0.289	0.0335	cast
115	25% PMMA, 75% HTPB	4.74	22	0.443	0.0434	compressed

Table 1 : Regression for Various Hydrocarbon Fuels

It appears from Table 1 that switching from cast to compressed polyethylene alone nearly results in a doubled regression rate. A further increase can be obtained by admixture of HTPB. Going over to a 100% HTPB fuel results in doubling the regression rate with respect to the compressed 100% PE fuel. As the heat of combustion is roughly the same for PE and for HTPB, it therefore seems to be possible to choose a fuel composition of PE and HTPB with any regression rate between 0.1 and 0.44 mm/s. For the higher percentage of HTPB, increasing soot formation has been observed, whereas for a 100% PE-fuel the combustion appears to be clean.

Taking PMMA instead of PE results in a visible increase in the soot production rates, but as PMMA possesses a heat of combustion which is roughly half the corresponding value of PE, the specific energy content of PMMA/HTPB-fuels is somewhat lower than that of the PE/HTPB-fuels.

5.3 Regression Rates and Combustion Efficiencies

In Table 2, a selection of flight conditions with resulting regression rates and combustion efficiencies are displayed.

The regression rate as a function of the altitude of flight for the three flight conditions which required stoichiometric burning (O/F = 16) is given in Fig. 11.

In-Flight Mach-Number	Altitude [m]	P_c [bar]	$\dot{m}_a$ [g/s]	O/F	$\bar{\dot{r}}$ [mm/s]	η_{c^*}
2.0	0	5.08	503	38	0.293	97.7
2.0	3000	3.62	360	37	0.226	96.9
2.0	5000	2.84	280	36	0.189	96.9
1.9	0	4.7	530	17.6	0.301	96.6
1.82	3000	3.38	340	16.4	0.154	96.8
1.7	6000	1.8	175	16.2	0.135	97.8

Table 2 : Regression Rate and Combustion Efficiency for Selected Flight Conditions

5.4 Combustion Channel Geometry

Fuel grains with circular cross-section were used for most of the experiments performed. The cylindrical combustion channel provides a relatively low fuel regression. The combustor length may be shortened or the fuel mass flow increased, if the fuel surface exposed to the combustion gases is enlarged. This can be done by using a star-shaped channel cross-section. A few test runs were performed to compare a star-shaped to a circular combustion channel. The circumference of the star used was so designed that it had nearly twice the circumference of the circle. The cross-sectional area of the duct, however, was kept unchanged. This, in consequence, insured an unchanged air mass flux as well as unchanged area ratios with respect to the flameholder and the exhaust nozzle. As was expected, the fuel regression increased proportional to the enlargement of the fuel surface. A doubled fuel regression was found for a doubled fuel surface.

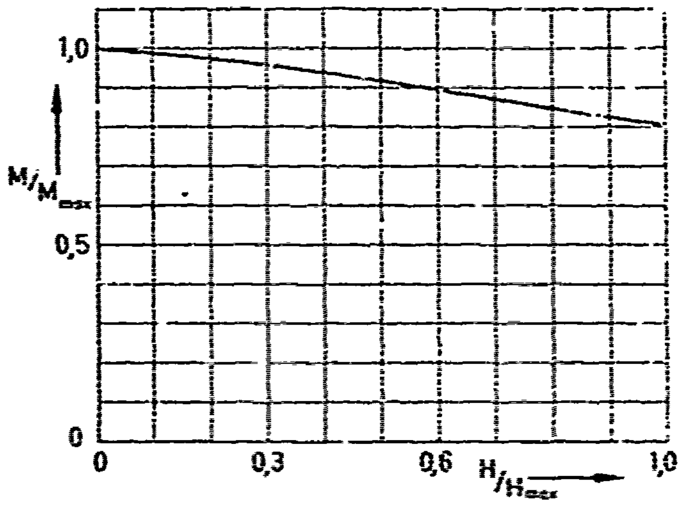

Fig. 1: Missile Velocity Requirements

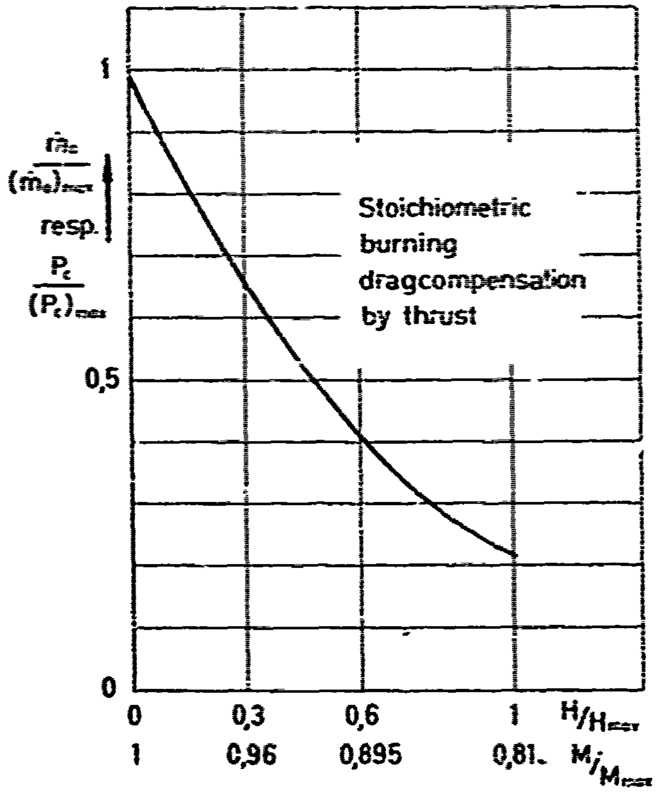

Fig. 2 : Air Massflow resp. Combustion Pressure Requirement.

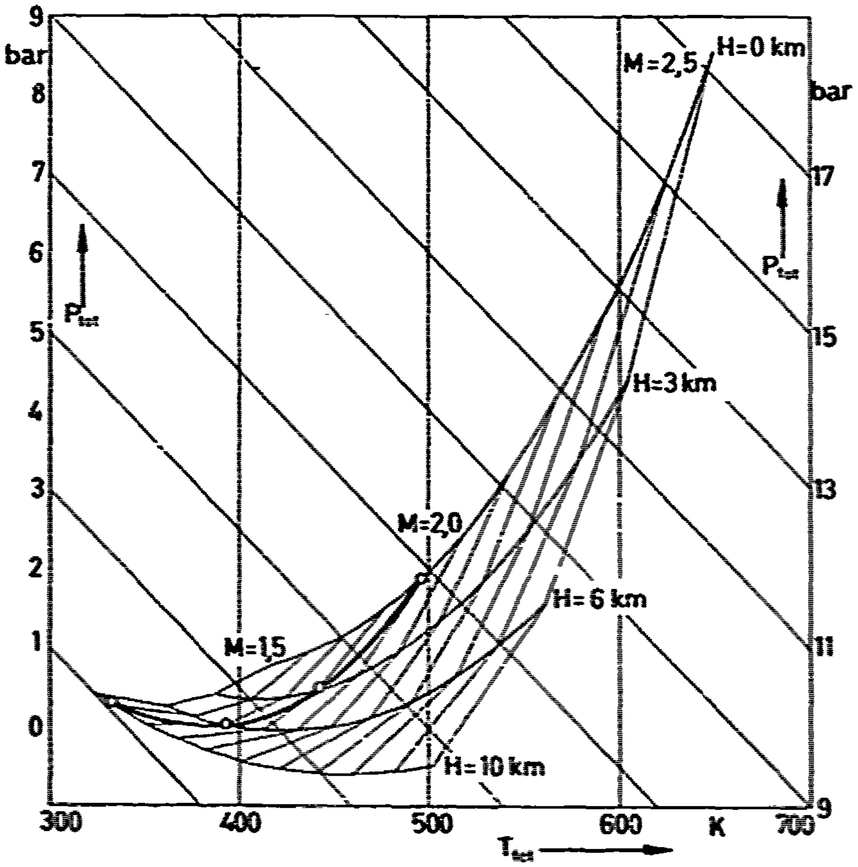

Fig. 3: Total Pressure and Total Temperature for Flight Data

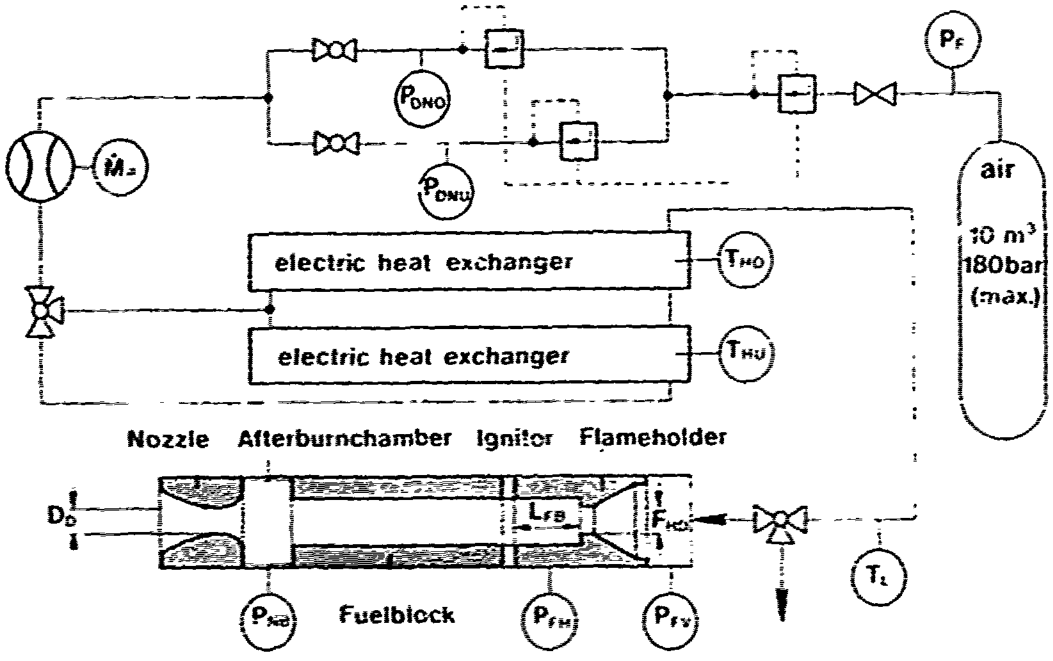
P_F
P_{DNO}
P_{DNU}
$\dot{M}_a$
air
10 m³
180bar
(max.)
electric heat exchanger
T_{HO}
electric heat exchanger
T_{HU}
Nozzle
Afterburnchamber
Ignitor
Flameholder
D_D
L_{FB}
F_{HO}
T_L
P_{NB}
Fuelblock
P_{FH}
P_{FV}

Fig. 4 Experimental Set-Up with Ramjet Motor

A09 6

DFVLR
EN-CA

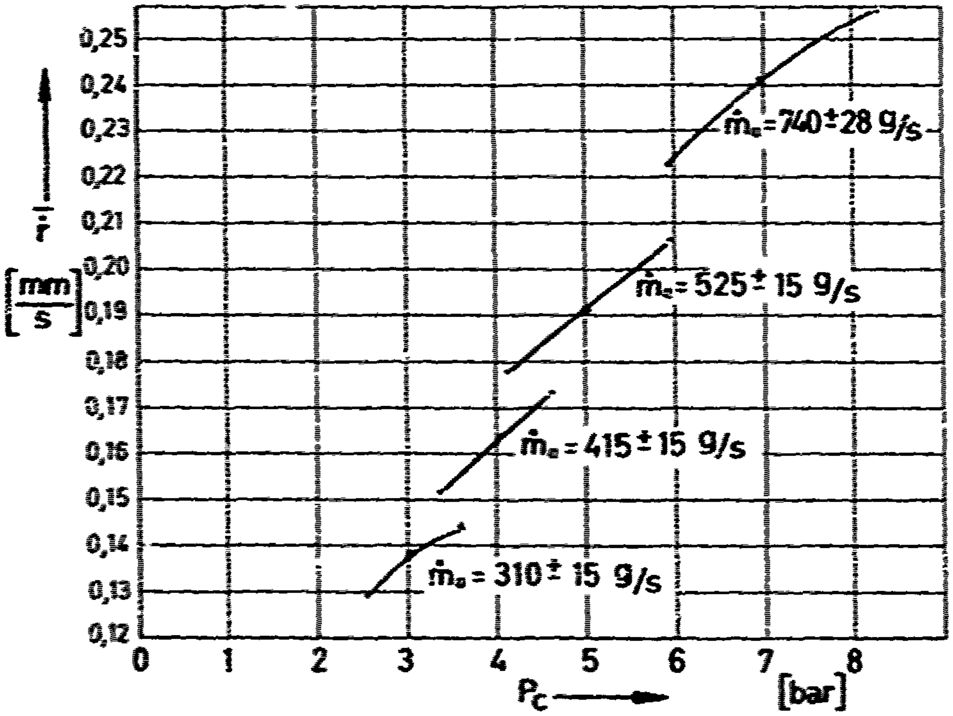

Fig. 5 : Regression Rate as a Function of Combustion Pressure

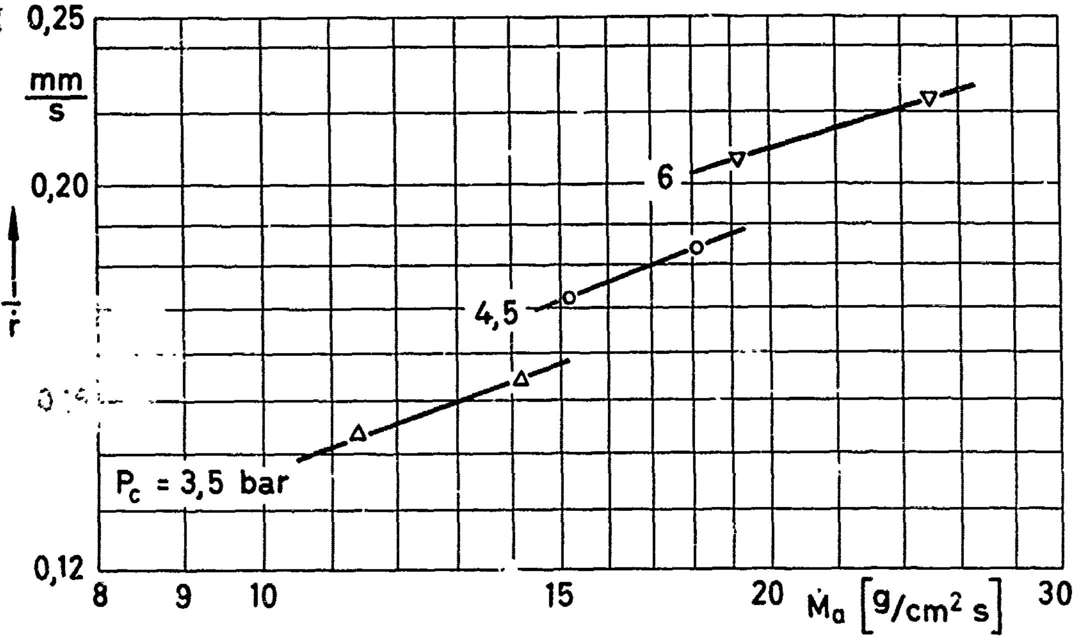

Fig. 6 : Regression Rate Dependence on Air Mass Flux and Pressure

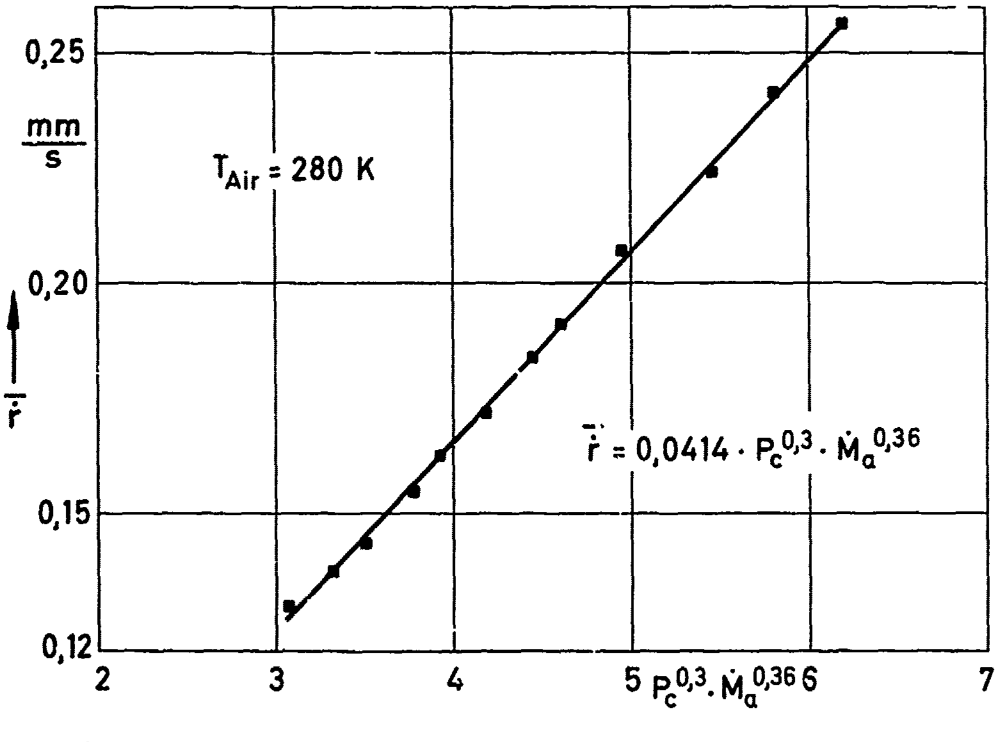

Fig. 7 : Regression Rate Power Low Approximation for Constant Air Temperature

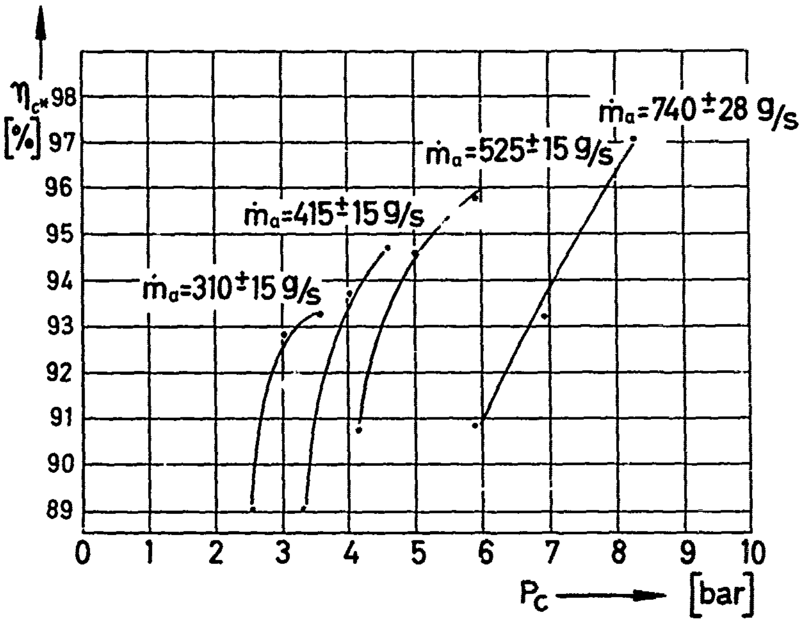

Fig. 8 : Combustion Efficiency as a Function of Combustion Pressure

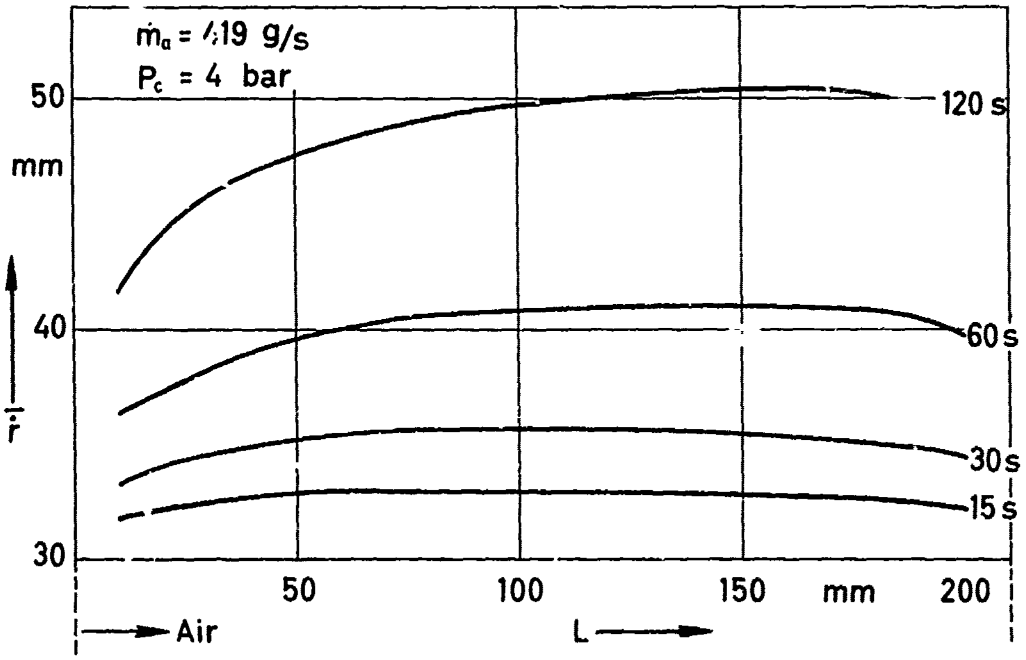

Fig. 9 : Combustion Channel Regression for Varied Combustion Time

21-10

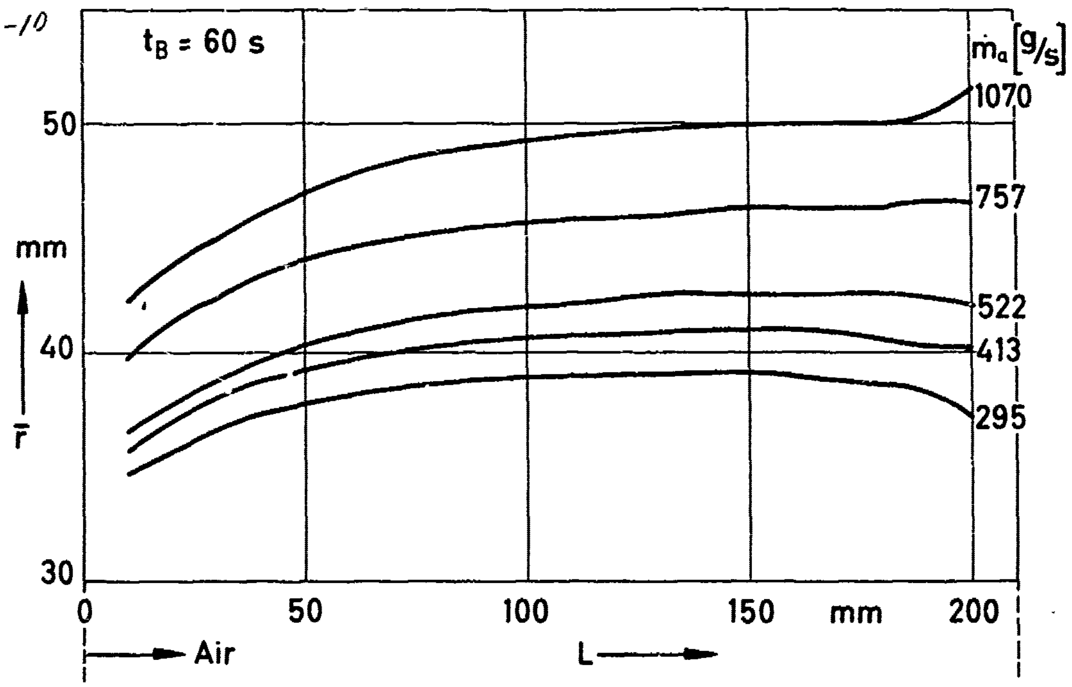

Fig. 10: Combustion Channel Regression for Varied Air Massflow

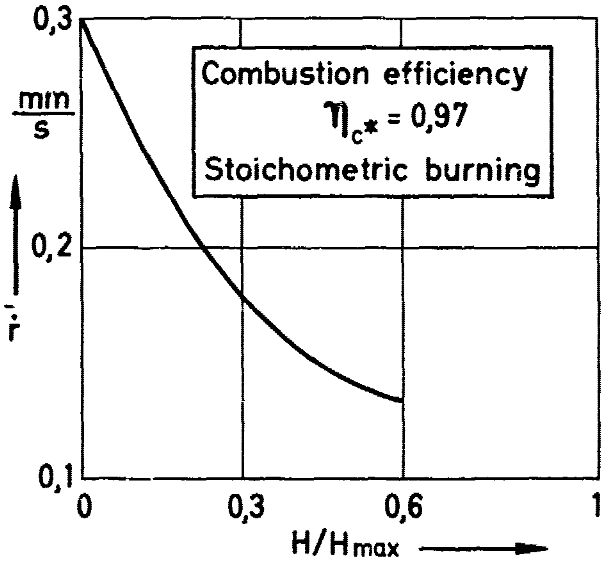

Fig. 11: Regression Rate for Selected Flight Situations

DISCUSSION

P.Korting

Did you observe during your experiments oscillatory combustion, and if so, what are the test conditions (chamber pressure, air flow) at which oscillatory combustion occurred?

Author's Reply

Oscillatory combustion has been observed, however, no unstable low frequency oscillations of large amplitudes.

P.Boszko

Did you have any problems obtaining ignition of the polyethylene charge? Did you use a conventional pyrotechnic composition?

Author's Reply

There were no problems at all in igniting the propellant. We used a conventional pyrotechnic device and therefore had no real ignition problem. The problems arose in initiating the igniting device. This is done electrically and sometimes the wires became disconnected.

P.Cazin

Pouvez-vous nous préciser si le taux de régression du combustible varie entre l'avant et l'arrière de la chambre de combustion.

Author's Reply

The local fuel regression is a function of air flow rate and combustion time. An example of the time dependence of local regression is given in Figure 9. An example of the dependence of local regression on air flow rate is given in Figure 10 of the paper. These two figures were not shown in my presentation of the paper.

B.Petit

Quels sont les nombres de Mach des écoulements aux différents endroits de la chambre de combustion (entrée, accroche-flamme, avant et arrière du chargement et en fin de chambre).

Author's Reply

Inlet: $M \leqslant .2$; Flameholder: $M \leqslant .7$; Combustor Chamber: $M \leqslant .5$; Afterburner Chamber: $M \leqslant .3$.

T.Myers

What was the L/D ratio of your secondary mixing chamber downstream of the fuel grain?

Author's Reply

Nearly one.

F.Culick

What were the amplitudes and frequencies of the oscillations?

Author's Reply

I can't remember, but I will personally give you that later on.

C.Ecary

What is the minimum pressure you experienced in the combustion chamber?

Author's Reply

Between approximately 2 and 15 bar. The lowest pressure was 1.8 bar.

BORON COMBUSTION IN DUCTED ROCKETS

by
Klaus C. Schadow
Naval Weapons Center
China Lake, California 93555, USA

SUMMARY

Two-dimensional, windowed combustor and water tunnel tests were performed to study the qualitative effect of inlet and combustor parameter on mixing and overall performance for solid boron propellant gas generator ramjets with two opposing 45° side air inlets. Highest combustion efficiencies were achieved at lowest air injection momentum (resulting in minimum mixing rates at the fuel/air intersection point) and lowest fuel injection momentum (resulting in highest gas-phase combustion temperatures during boron particle ignition because of fuel-rich plume ignition at the fuel injector). The decrease of the combustion efficiency with increasing air injection momentum may, in part, explain the observed combustion efficiency decrease with decreasing ramjet combustor pressure and increasing air-to-fuel ratio, which at constant air inlet geometry resulted in increasing air injection momentum. Tests with multiple fuel injectors showed that optimum plume ignition at the fuel injector was more difficult to achieve at decreasing fuel mass flow per fuel injector. The conclusions of this program are qualitative because of lack of detailed data, however, they provide insight into the importance of the combustor aerodynamics for achieving efficient boron combustion.

NOMENCLATURE

A	Area
a/f	Air-to-fuel ratio
c*	Characteristic velocity
l	Length
$\dot{m}v$	Momentum
$\dot{m}$	Mass flow
P	Pressure
V	Velocity
W	Width
α	Angle
η	Combustion efficiency
Δp	Pressure difference

Subscript

a	Air
a,w	Air simulated by water
CP	Combustion; gas generator
CS	Combustion; ramjet combustor
f	Fuel
f,w	Fuel simulated by water
t,M	Throat; primary motor
t,P	Throat; gas generator
5	Throat; ramjet combustor
Δc^*	Difference in characteristic velocity

INTRODUCTION

Efficient boron particle combustion in solid propellant gas generator ramjets (Fig. 1; (ducted rockets) depends on a number of coupled physical and chemical processes. These include turbulent mixing between the air and the gas generator plume, which contains boron particles and unreacted gaseous fuels, ignition/combustion of the gaseous fuels, and ignition/combustion of the boron particles.

The importance of the gaseous fuel combustion (gas-phase combustion) for boron particle ignition/combustion was studied by Schadow (Ref. 1-[illegible]) for coaxial mixing flow fields. It was shown that only as long as the gaseous fuels of the gas generator [illegible]de to react with the air before excessive mixing occurred, the resulting gas-phase combustion temperatures were above 1950K, and therefore high enough to free the boron particles from the inhibiting oxide layer.

These tests indicate that for achieving high boron combustion efficiency, in general, two requirements are demanded from the aerodynamics of the combustor: (1) to establish flow regions with near stoichiometric gaseous fuel/air mixture ratios and (2) to initiate gas-phase combustion in these mixing regions. The importance of these requirements for combustors with coaxial mixing has been well established and will be further illustrated in the following paragraph. In this paper, the insight into coaxial mixing will be used to interpret experiments which were performed to gain a qualitative understanding for non-coaxial mixing in combustors with side air inlets. Again, emphasis will be placed on the effect of the combustor aerodynamics on gas-phase ignition and overall performance.

For coaxial mixing, near stoichiometric mixture ratios with highest gas-phase combustion temperatures always exist in the extreme fore-end of the mixing region (Fig. 2, ref. 2). Therefore, for achieving high boron combustion efficiency, it is necessary to achieve gas-phase ignition at the gas generator nozzle (fuel injector). This was demonstrated in tests with solid boron propellants at low ramjet combustor pressure. For example, with supersonic gas generator exhaust velocity (fuel injection velocity) gas-phase ignition occurred several injector nozzle diameters downstream of the fuel injector after excess air mixing had taken place and the resulting gas-phase combustion temperatures were below the boron ignition temperature

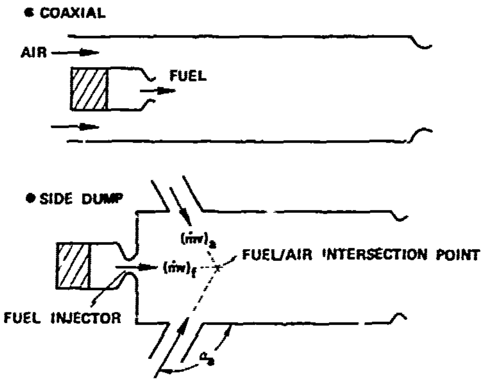

Figure 1. Gas Generator Ramjet.

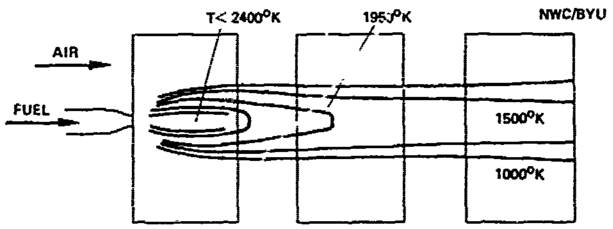

Figure 2. Theoretical Gas-Phase Combustion Temperatures (Boron Inert).

(< 1950K). As a result, the boron combustion efficiency was low. However, at subsonic fuel injection velocity, gas-phase ignition occurred at the fuel injector in the extreme fore-end of the mixing region where highest gas-phase combustion temperatures existed. As a result, boron combustion efficiency was high (Ref. 4). It must be emphasized that gas-phase ignition at the fuel injector has to be accomplished without increasing the mixing rate. If gas-phase ignition is achieved at the fuel injector with mixing or flameholding aids, the mixing rates may be too high and therefore flow regions with near stoichiometric mixture ratios might not exist and gas-phase combustion temperatures would be again too low (Ref. 4).

In general, coaxial mixing is most favorable to provide initially high gas-phase combustion temperatures for the boron particle ignition process because the air gradually mixes with the fuel. These favorable temperature conditions can be achieved independently of the fuel injection momentum and air injection momentum. On the other hand, coaxial mixing requires long combustor length and is not practical for many applications such as combustors with side mounted air inlets.

For combustors with side air inlets, mixing at the fuel/air intersection point (Fig. 1), in addition to plume ignition at the fuel injector, is critical. Therefore, in addition to the fuel injection velocity, which is critical for gas-phase ignition, the air and fuel momentum become important parameters. These parameters are critical for fuel penetration into the airstream and mixing rates at the fuel/air intersection point. Test conditions may exist, at which mixing rates and cooling rates at the fuel/air intersection point are too high, thus resulting in reduced fuel reaction rate.

To gain qualitative insight into non-coaxial mixing, experiments were performed at the Naval Weapons Center (NWC) using a two-dimensional (2D) windowed combustion chamber with two opposing side air inlets. The qualitative effects of combustor parameter such as fuel momentum $(\dot{m}v)_f$, air fuel injection velocity (v_f), air momentum $(\dot{m}v)_a$, and air inlet geometry on mixing/combustion and overall performance was studied by correlating mixing data from water tunnel tests with flame characteristics and combustion efficiency data from combustor tests. Experiments were made with non-metallized and boron-laden solid propellants. The majority of the water tunnel tests and the combustion tests using non-metallized propellants are published in Ref. 5. Highest combustion efficiencies in tests with an air injection angle of $\alpha_a = 90°$ were achieved at lowest experimental $(\dot{m}v)_f$ or v_f (to achieve plume ignition at the fuel injector) and lowest $(\dot{m}v)_a$ (to achieve good penetration of the reacting plume into the airstream).

In this paper, the 2D combustor tests with two opposing 45° side air inlets and solid boron propellants, as well as additional water tunnel tests, will be discussed. Specific objectives of the test program described in this paper were:

(1) to determine combustion efficiency as a function of independently varied v_f, $(\dot{m}v)_f$, $(\dot{m}v)_a$, and fuel injector numbers and as a function of air-to-fuel ratio and ramjet combustor pressure, which included the dependent variable of $(\dot{m}v)_a$;

(2) to describe flame characteristics in the windowed ramjet combustor as function of the same parameter, in particular to qualitatively assess the effect of position of plume ignition, which may occur at the fuel injector or may be delayed to the fuel/air intersection point, on overall performance;

(3) to describe water flow mixing characteristics in particular at the "fuel"/"air" intersection point as function of "fuel" and "air" injection momentum and "air" injection angle; and

(4) to provide qualitative insight into the effect of v_f, $(\dot{m}v)_f$ and $(\dot{m}v)_a$ on mixing and overall performance by correlating the results from water tunnel and windowed combustor tests.

The variation of the fuel injector number in the combustor tests was performed at constant overall propellant (fuel) mass flow, $\dot{m}_f$. Therefore, with increasing injector number, the $\dot{m}_f$ per injector was decreased. Experiments in Ref. 4 showed that optimum plume ignition at the fuel injector was more difficult to achieve with decreasing $\dot{m}_f$. This $\dot{m}_f$-scaling effect, which was related to the interaction between gaseous fuels and boron particles during plume ignition process, is not yet fully understood.

The 2D design of the water tunnel and combustor was chosen to simplify the flow field and to make the mixing/combustion more accessible for experimental observation. It must be realized, that the 2D flow field does not fully represent a 3D flow in an axisymmetric combustor with two opposing side air inlets.

EXPERIMENTAL SET-UP

Fig. 3 shows a schematic drawing of the laboratory combustor with solid propellant gas generator and windowed ramjet combustor with two opposing side air inlets. In the gas generator with a 45% weight boron-laden solid propellant, a two-throat arrangement was used to vary v_f at constant $\dot{m}_f$. Sonic and subsonic v_f were studied. The number of fuel injectors was varied from 1 to 2 and 3. Arrangement of the fuel injectors may be seen from Fig. 3. In the ramjet combustor, easy variation of the following air inlet geometries was achieved: axial position, L_{ax}; length, L_a; width, W_a; and angle, α_a. With the geometric air inlet changes, the air inlet Mach number varied between $0.05 < v_a < .68$.

During a typical test, the air mass flow, $\dot{m}_a$, was varied between about 2 and 4 lb/s with $\dot{m}_f$ constant at about 0.25 lb/s. Evaluation of the tests was performed at the lowest and highest air-to-fuel ratio, $a/f = \dot{m}_a/\dot{m}_f$, of about 8 and 20 corresponding to an equivalence ratio, ϕ, of about 1 and 0.4. The ramjet combustor pressure, P_{CS}, was varied between 25 and 92 psia by varying the ramjet combustor throat diameter D_S. With the changes of $\dot{m}_a$, P_{CS}, and the air inlet area, A_a, $(\dot{m}v)_a$ varied between 124 and 2980 lb ft/s^2, the fuel injector pressure ratio, P_{CP}/P_{CS}, between about 1 and 14.6, $(\dot{m}v)_f$ between 52 and 1250 lb ft/s^2, and the momentum ratio $(\dot{m}v)_a/(\dot{m}v)_f$, between .16 and 5.8. The $(\dot{m}v)_a$ is the product of the total $\dot{m}_a$ and v_a of one inlet, $(\dot{m}v)_f$ the product of both $\dot{m}_f$ and v_f of one injector. The detailed test conditions for each test may be seen from Table I, which gives a summary of the combustor tests.

Experimental methods consisted of gas generator and ramjet combustor pressure measurements, P_{CP} and P_{CS}, and high speed color photography of the flame in the ramjet combustor. For each test, the combustion efficiency, $\eta_{\Delta c}{}^{*2}$ (referred to η in the following) was calculated, which was based on the P_{CS} difference or characteristic velocity difference, Δc^*, with and without combustion. Because of the heavy hardware and relatively low $\dot{m}_f$, significant heat losses and therefore low calculated η even for efficient combustion must be expected.

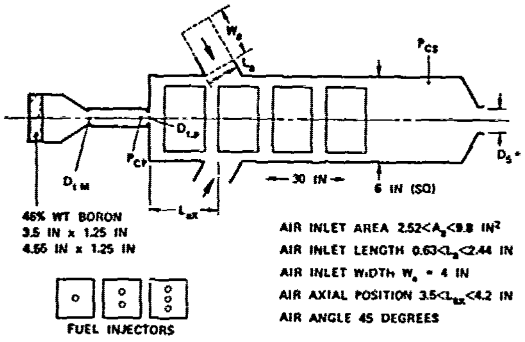

Figure 3. 2D Ramjet Combustor.

Fig. 4 shows a schematic drawing of the water flow tunnel. Aerated water was used to simulate the gas generator exhaust products ("fuel") and clear water to simualte the air. The geometric "air" inlet variables are shown in Fig. 4 and are summarized for each water tunnel test in Table II. "Air" and "fuel" momentum, $(\dot{m}v)_{a,w}$ and $(\dot{m}v)_{f,w}$, were varied by varying the pressure difference at the "air" inlet and "fuel" injector, $\Delta p_{a,w}$ and $\Delta p_{f,w}$.

TABLE I. Combustor Tests.

Test no.	Fuel injector number	$\frac{a}{f}$ —	$\frac{P_{CP}}{P_{CS}}$ —	$(\dot{m}v)_f$ $\frac{lb\ ft}{s^2}$	$(\dot{m}\ v)_a$ $\frac{lb\ ft}{s^2}$	$\frac{(\dot{m}v)_a}{(\dot{m}v)_f}$ —	$\frac{V_a}{M_a}$	P_{CS} psia
1a	1	13.0	6.2	756	138	0.18	0.052	55.7
b	1	18.1	4.9	813	242	0.30	0.057	81.1
2a	2	11.3	7.5	929	151	0.16	0.05[illegible]	54.5
b	2	15.9	5.7	947	247	0.26	0.0[illegible]	77.2
3a	3	17.0	5.3	551	153	0.28	0.058	49.9
b	3	17.0	5.4	862	244	0.28	0.059	76.6
4a	1	10.1	3.1	795	130	0.16	0.048	62.2
b	1	15.0	2.2	714	205	0.29	0.050	89.7
5a	2	10.7	2.7	674	125	0.19	0.048	59.4
b	2	15.0	2.1	633	216	0.34	0.052	86.6
6a	3	15.3	2.2	409	140	0.34	0.056	48.4
b	3	18.7	1.8	501	240	0.48	0.056	82.0
7a	1	13.9	~1	156	142	0.91	0.054	52.4
b	1	20.1	~1	127	246	1.92	0.059	76.5
8a	2	10.4	~1	123	125	1.02	0.047	61.2
b	2	14.6	~1	110	224	2.03	0.052	90.6
9a	3	13.0	~1	58	140	2.43	0.054	52.6
b	3	17.9	~1	52	241	4.63	0.058	78.1
10a	3	10.7	3.2	687	594	0.87	0.24	44.4
b	3	14.9	2.4	94	985	1.42	0.25	67.1
11a	1	12.6	~1	196	592	3.02	0.23	48.4
b	1	17.4	~1	186	1070	5.76	0.26	68.0
12a	2	9.5	3.1	802	515	0.64	0.20	54.0
b	2	12.8	2.4	836	859	1.02	0.21	83.6
13	2	18.0	~1	228	726	3.19	0.17	28.1
14	2	19.1	14.6	971	778	0.80	0.18	25.9
15	2	16.0	6.7	995	778	0.78	0.18	26.2
16	2	13.2	8.2	1220	2980	2.44	0.71	25.0
17	2	15.6	~1	315	2870	9.10	0.68	26.3
18a	2	6.9	4.2	1230	2410	0.20	0.092	63.1
b	2	9.8	3.2	1250	408	0.33	0.099	92.4
19a	1	17.4	~1	108	319	2.97	0.119	49.9
b	1	20.3	~1	127	508	4.01	0.12	78.1
20a	1	14.0	6.1	658	288	0.44	0.113	49.9
b	1	14.7	6.1	1027	497	0.49	0.119	77.5

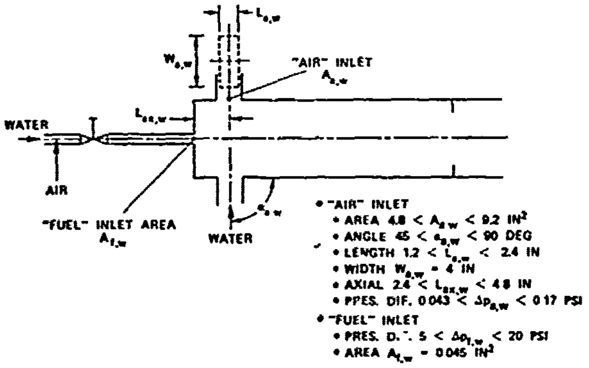
$L_{a,w}$
$W_{a,w}$
"AIR" INLET
$A_{a,w}$
WATER
$L_{ax,w}$
AIR
"FUEL" INLET AREA
$A_{f,w}$
WATER
$\alpha_{a,w}$
• "AIR" INLET
• AREA $4.8 < A_{a,w} < 9.2$ IN^2
• ANGLE $45 < \alpha_{a,w} < 90$ DEG
• LENGTH $1.2 < L_{a,w} < 2.4$ IN
• WIDTH $W_{a,w} = 4$ IN
• AXIAL $2.4 < L_{ax,w} < 4.8$ IN
• PRES. DIF. $0.043 < \Delta p_{a,w} < 0.17$ PSI
• "FUEL" INLET
• PRES. DIF. $5 < \Delta p_{f,w} < 20$ PSI
• AREA $A_{f,w} = 0.045$ IN^2

Figure 4. 2D Water Tunnel.

TABLE II. Water Tunnel Tests.

	$\alpha_{a,w}$ DEG	$L_{ax,w}$ IN	$L_{a,w}$ IN	$W_{a,w}$ IN	$A_{a,w}$ IN^2	$\Delta P_{a,w}$ PSI	$D_{f,w}$ IN	$A_{f,w}$ IN^2	$\Delta P_{f,w}$ PSI	$\frac{\dot{m}_{a,w}}{\dot{m}_{f,w}}$ —	$\frac{(\dot{m}v)_{a,w}}{(\dot{m}v)_{f,w}}$ —
1W	45	4.8	2.3	4	9.2	0.047	0.24	0.045	20	19.7	0.95
2W	45	5.5	1.2	4	4.8	0.172	0.24	0.045	20	19.7	1.82
3W	90	3.9	2.4	4	9.6	0.043	0.24	0.045	5	39.4	3.65
4W	60	2.4	2.3	4	9.2	0.047	0.24	0.045	5	39.4	3.82

The water flow characteristics were recorded with high speed and still photography. One example is shown in Fig. 5a. The significant aspects of the water flow field were emphasized in sketches as shown in Fig. 5b. In this paper, the varying flow characteristics will be described using such sketches.

To achieve proper flow simulation, similarities of geometry, Reynolds Number, $\dot{m}_a/\dot{m}_f$, and air-to-fuel momentum ratio, $(\dot{m}v)_a/(\dot{m}v)_f$, have to be maintained between water tunnel and combustor. Geometric similarity was achieved by using the same geometric dimensions (inlet and combustor) for both set-ups. The Reynolds number similarity was satisfactory with $Re = 0.5 \times 10^5$ in the water tunnel and $Re = 1.5 \times 10^5$ in the combustor. The "air"-to-"fuel" ratio in the water tunnel was varied between:

$$19.7 < \frac{\dot{m}_{a,w}}{\dot{m}_{f,w}} = \frac{2A_{a,w}\,\Delta p_{a,w}}{A_{f,w}\,\Delta p_{f,w}} < 39.4$$

which was in satisfactory agreement with the $\dot{m}_a/\dot{m}_f$ range in the combustor with

$$8 < \frac{\dot{m}_a}{\dot{m}_f} < 20$$

$A_{a,w}$ and $A_{f,w}$ are the "air" inlet and "fuel" injector areas. The "air"-to-"fuel" momentum ratio in the water tunnel was varied between

$$.95 < \frac{(\dot{m}v)_{a,w}}{(\dot{m}v)_{f,w}} = \frac{2A_{a,w}\,\Delta p_{a,w}}{A_{f,w}\,\Delta p_{f,w}} < 3.82$$

which was in satisfactory agreement with the $(\dot{m}v)_a/(\dot{m}v)_f$ range in the combustor with

$$.16 < \frac{(\dot{m}v)_a}{(\dot{m}v)_f} < 5.8$$

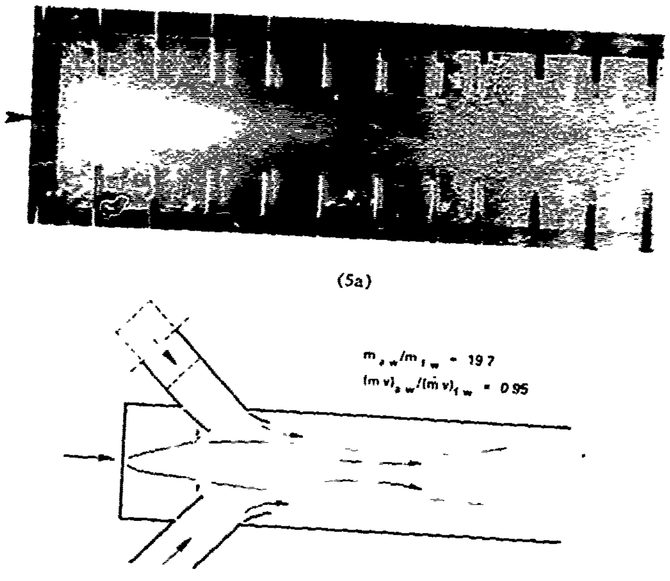

Figure 5. Water Flow Characteristics.

TEST RESULTS

22-6

Windowed Combustor Tests (Combustion Efficiency and Flame Characteristics)

Fig. 6 shows η for two P_{CS} levels. Generally, higher η was achieved at about 90 psia than 25 psia. It should be noted that with decreasing P_{CS}, $(\dot{m}v)_a$ increased from about 225 lb ft/s^2 to 750 lb ft/s^2 or v_a from 0.055 Ma to 0.18 Ma. The tests in Fig. 6 included a wide variation of $(\dot{m}v)_f$ which effect on η will be shown later.

Fig. 7 shows η for two a/f levels. Generally, higher η was achieved at about a/f ~ 11 than a/f ~ 16. It should be noted that with the increase in a/f, $(\dot{m}v)_a$ increased because of constant air inlet geometry.

Fig. 8 shows η as function of $(\dot{m}v)_a$ for wide ranges of P_{CS}, a/f, and $(\dot{m}v)_f$. All tests were made with one fuel injector. It may be seen that η generally decreased with increasing $(\dot{m}v)_a$.

Fig. 9 shows η as function of $(\dot{m}v)_a$ for all the tests conducted in this program. It may also be seen that η generally decreased with increasing $(\dot{m}v)_a$ despite the wide variation of P_{CS}, a/f, $(\dot{m}v)_f$, P_{CP}/P_{CS}, and fuel injector number.

Figs. 10 and 11 show η as function of $(\dot{m}v)_f$ and P_{CP}/P_{CS} for nearly constant $(\dot{m}v)_a$ of 130 lb ft/s^2. It may be seen that except for Test 2a, η was nearly independent of $(\dot{m}v)_f$ and P_{CP}/P_{CS} for this 45 to 65 psia P_{CS} range. The color movies showed that for all the tests except Test 2a in Figs. 11 and 12, plume ignition occurred at the fuel injector and good plume penetration into the airstream was achieved. In Test 2a, however, plume ignition did not occur at the fuel injector, but was delayed to the fuel/air intersection point. This delayed plume ignition may account for the lower η in Test 2a than Tests 1a and 4a at the same $(\dot{m}v)_f$. The delay in plume ignition in Test 2a may be the result of the combination of high $(\dot{m}v)_f$ or P_{CP}/P_{CS} and low $\dot{m}_f$ per one fuel injector.

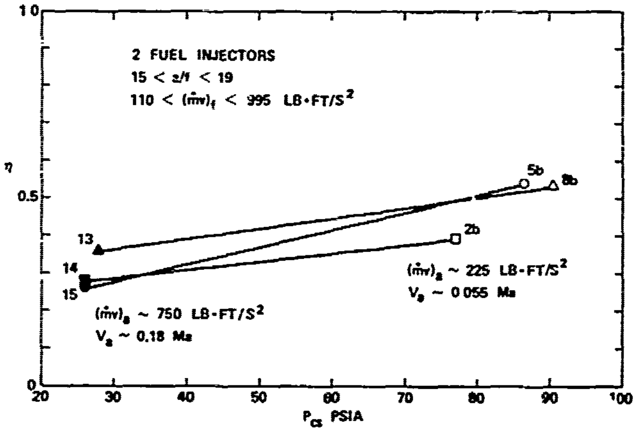

Figure 6. Combustion Efficiency vs. Ramjet Combustor Pressure.

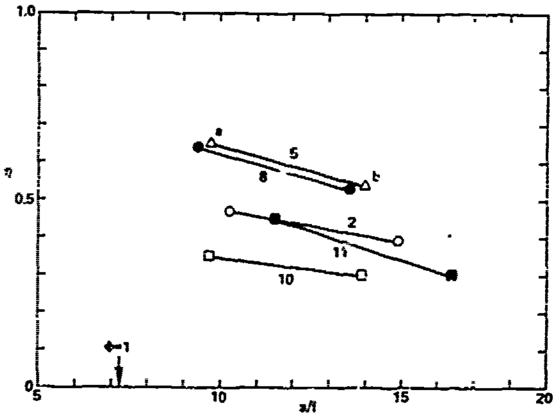

Figure 7. Combustion Efficiency vs. Air-to-Fuel Ratio.

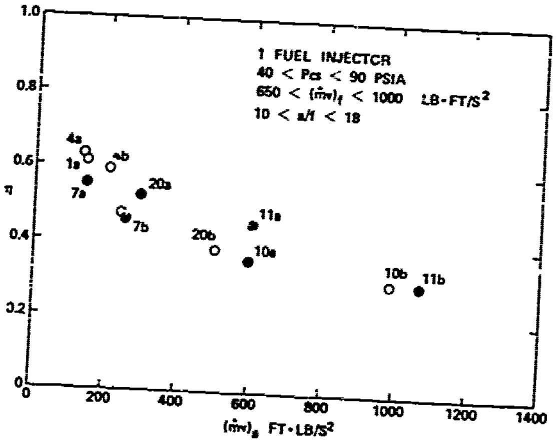

Figure 8. Combustion Efficiency vs. Air Injection Momentum (Selected Tests).

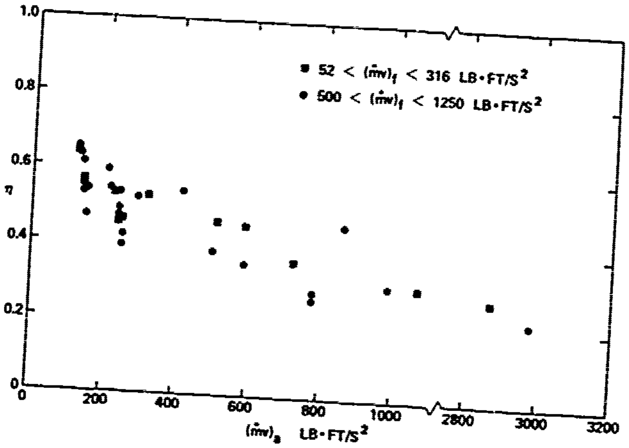

Figure 9. Combustion Efficiency vs. Air Injection Momentum (Combined Tests).

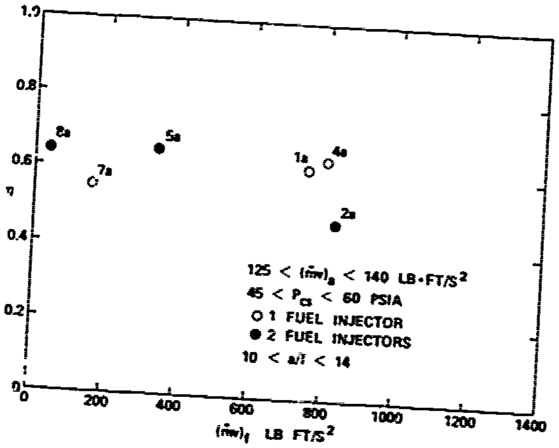

Figure 10. Combustion Efficiency vs. Fuel Injection Momentum (High Pressure).

22-8

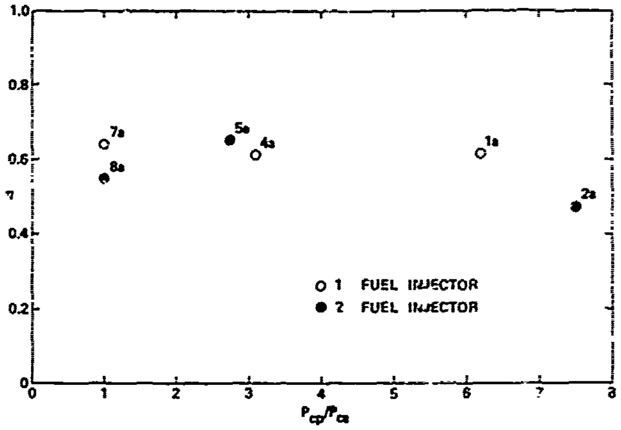

Figure 11. Combustion Efficiency vs. Fuel Injector Pressure Ratio.

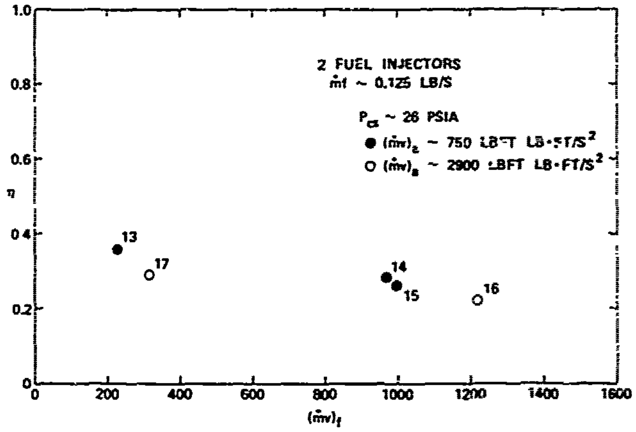

Figure 12. Combustion Efficiency vs. Fuel Injection Momentum (Low Pressure).

The effect of $(\dot{m}v)_f$ on η for $P_{CS} \sim 26$ psia may be seen in Fig. 12. The η decreased with increasing $(\dot{m}v)_f$. The color movies showed that plume ignition occurred at the fuel injector in Test 13 with low $(\dot{m}v)_f$, however, at the fuel/air intersection point for Tests 14 to 17 with high $(\dot{m}v)_f$. Good plume penetration into the air was achieved in all of the tests. The tests in Figs. 10 to 12 indicate that η was independent of $(\dot{m}v)_f$ or P_{CP}/P_{CS} as long as plume ignition was achieved at the fuel injector.

Fig. 13 shows η as function of $(\dot{m}v)_a/(\dot{m}v)_f$. The η generally decreased with increasing momentum ratio, which probably mainly reflects the effect of $(\dot{m}v)_a$ on η.

Fig. 14 shows the effect of fuel injector number for three P_{CP}/P_{CS} levels which corresponds to three $\dot{m}_f$ levels per fuel injector. It may be seen that, for P_{CP}/P_{CS} of about 1 and 2.5, η was not significantly effected by the fuel injector number. The color movies showed that in all of the tests at these P_{CP}/P_{CS}'s, plume ignition occurred at the fuel injector. At P_{CP}/P_{CS} of about 6.5, η decreased when the fuel injector number was increased from 1 to 2, and increased when the fuel injector number was increased from 2 to 3. Plume ignition occurred at the injector in Test 1a ($\dot{m}_f \sim 0.19$ lb/s per injector), however, at the fuel/air intersection point in Tests 2a ($\dot{m}_f \sim 0.11$ lb/s per injector) and 3a ($\dot{m}_f \sim 0.05$ lb/s per injector). A comparison of Tests 1a and 2a indicate that, at the same P_{CS}/P_{CP}, optimum plume ignition at the fuel injector was more difficult to achieve at decreasing $\dot{m}_f$ per injector and therefore η decreased. The η-increase for 2 to 3 fuel injectors was probably due to improved fuel/air mixing.

In summary, the results showed a strong effect of $(\dot{m}v)_a$ on η. In general, η decreased with increasing $(\dot{m}v)_a$ or increasing $(\dot{m}v)_a/(\dot{m}v)_f$. This result may, in part, explain the observed η-decrease with decreasing P_{CS} and increasing a/f which at constant air inlet area generally resulted in increasing $(\dot{m}v)_a$. It can be speculated that $(\dot{m}v)_a$ or $(\dot{m}v)_a/(\dot{m}v)_f$ have a strong effect on the mixing rate at the fuel/air intersection point, which was qualitatively studied in the water tunnel tests.

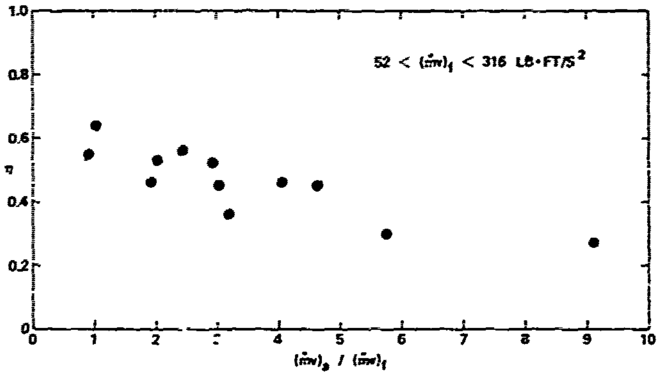

Figure 13. Combustion Efficiency vs. Air/Fuel Momentum Rates.

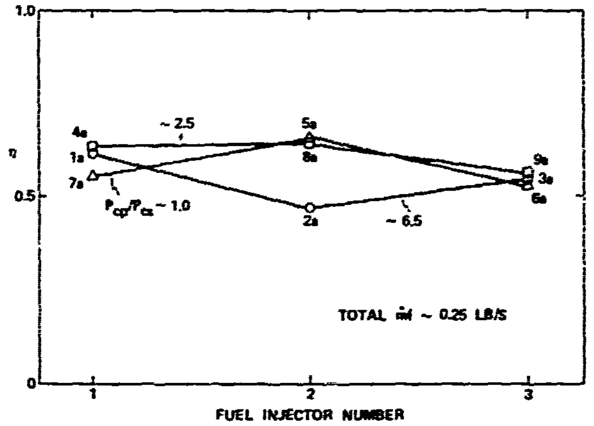

Figure 14. Combustion Efficiency vs. Fuel Injector Number.

The $(\dot{m}v)_f$ or P_{CP}/P_{CS} had no effect on η as long as plume ignition occurred at the fuel injector. The η decreased with increasing $(\dot{m}v)_f$ when plume ignition was delayed downstream to the fuel/air intersection point at low $\dot{m}_f$ or low P_{CS}.

The color movies indicated that good fuel penetration into the air was achieved independent of $(\dot{m}v)_f$. It appears that the 45% air injection angle was favorable to maintain good fuel penetration with decreasing $(\dot{m}v)_f$, which may also be seen from the following water tunnel test results.

Water Tunnel Tests

Figs. 15 and 16 show the effect of $(\dot{m}v)_{a,w}/(\dot{m}v)_{f,w}$ on the mixing characteristics, in particular, at the "fuel"/"air" intersection points. At $(\dot{m}v)_{a,w}/(\dot{m}v)_{f,w} = 0.95$ (Fig. 15), at which highest η was achieved in the combustor tests, mixing rates were visibly lower than at $(\dot{m}v)_{a,w}/(\dot{m}v)_{f,w} = 1.82$ (Fig. 16). The increase in mixing rates in the water tunnel tests with increasing $(\dot{m}v)_{a,w}/(\dot{m}v)_{f,w}$ may explain the observed η-decrease in the combustor tests with increasing $(\dot{m}v)_a$.

The effect of $\alpha_{a,w}$ on "fuel" penetration into the "air" for $(\dot{m}v)_{a,w}/(\dot{m}v)_{f,w} \sim 4$ is shown in Fig. 17. It may be seen, that at $\alpha_{a,w} = 90°$ significant amount of "fuel" was reflected from the "air" stream back into the plenum region. From here, it flowed downstream on both sides of the "air" inlet along the tunnel wall. These flow patterns indicate poor "fuel" penetration into the "air" stream at $\alpha_{a,w} = 90°$. At the same momentum ratio, "fuel" penetration was improved at $\alpha_{a,w} = 60\%$ and probably will be further improved at $\alpha_{a,w} = 45°$ which was not studied in the water tunnel.

32-10

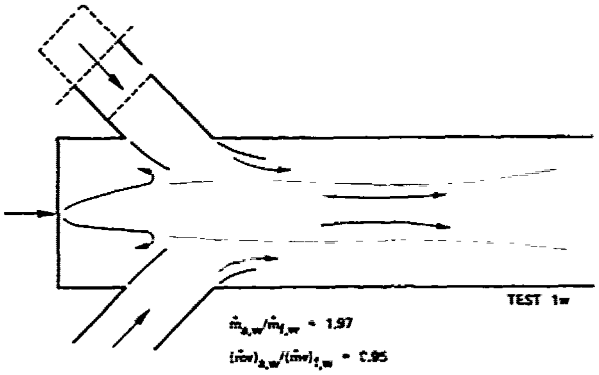
TEST 1w
$\dot{m}_{a,w}/\dot{m}_{f,w}$ = 1.97
$(\dot{m}v)_{a,w}/(\dot{m}v)_{f,w}$ = 0.95

Figure 15. Water Flow Characteristics at Low "Air" Injection Momentum.

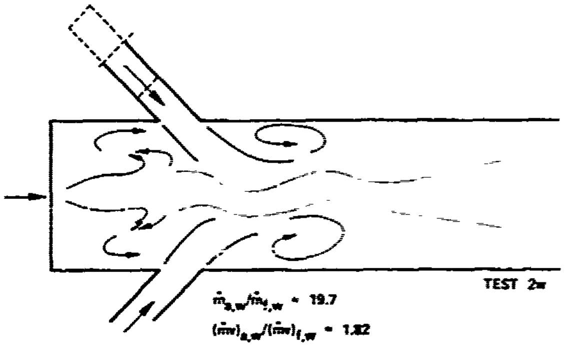
TEST 2w
$\dot{m}_{a,w}/\dot{m}_{f,w}$ = 19.7
$(\dot{m}v)_{a,w}/(\dot{m}v)_{f,w}$ = 1.82

Figure 16. Water Flow Characteristics at High "Air" Injection Momentum.

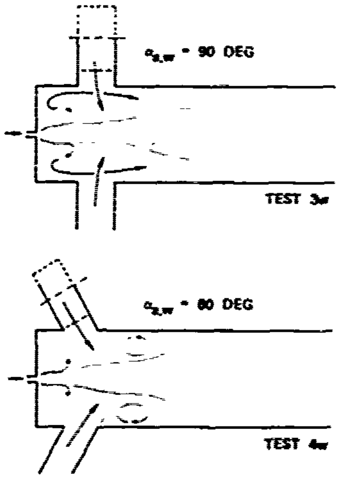
$\alpha_{a,w}$ = 90 DEG
TEST 3w
$\alpha_{a,w}$ = 60 DEG
TEST 4w

Figure 17. Water Flow Characteristics at Varying "Air" Injection Angle.

DISCUSSION

Efficient boron particle combustion depends on a number of interrelated combustor parameters. In the following, primarily the qualitative effect of $(\dot{m}v)_a$, $(\dot{m}v)_f$ and v_f (or P_{CP}/P_{CS}) on η will be discussed. Furthermore, the effect of fuel injector numbers will be considered which points out an $\dot{m}_f$ scaling effect on η. From the available test results, it is clear that only a qualitative assessment of the effect of each of the parameters on η can be made because of lack of detailed flow data. For the interpretation of the test results, the insight, which was previously gained into coaxial mixing, was helpful.

For the combustor with opposing side air inlets, $(\dot{m}v)_a$ appears to be the most critical parameter. The tests clearly showed that η decreased with increasing $(\dot{m}v)_a$. The water tunnel tests indicated that the η-decrease was caused by increasing mixing rates at the fuel/air intersection point which probably resulted in excess mixing or cooling in the reaction zone. Excess mixing is, in particular, critical for boron-laden fuels because the high mixing rates may prevent flow regions with high gas-phase combustion temperatures to be established which are required to free the boron particles from the oxide layer.

The demonstrated strong effect of $(\dot{m}v)_a$ on η may, in part, explain the η-decrease with increasing a/f and decreasing P_{CS} which at constant air inlet geometry resulted in increasing $(\dot{m}v)_a$. Although the η-dependence on a/f and P_{CS} cannot be explained by the effect of $(\dot{m}v)_a$ only, it seems clear that highest η at low P_{CS} and high a/f can be achieved at minimum $(\dot{m}v)_a$.

A strong effect also of $(\dot{m}v)_f$ on η was expected because it is critical for both fuel penetration into the air and plume ignition. However, the $(\dot{m}v)_f$ effect was less than anticipated because good fuel penetration was achieved even at the lowest $(\dot{m}v)_f$, and optimum plume ignition at the fuel injector was achieved over a wide range of test conditions as discussed in further detail in the following.

Good fuel penetration for all the tests was probably achieved due to $\alpha_a = 45°$. Water tunnel tests indicated that at this $\alpha_{a,w}$, even at lowest $(\dot{m}v)_{f,w}$, "fuel" penetrated into the "air" which was not the case for $\alpha_{a,w} = 90°$. In the combustion tests, no visible effect of $(\dot{m}v)_f$ on fuel penetration was noticed either; therefore it must be assumed that any significant effect of $(\dot{m}v)_f$ on η was mainly related to the effect of $(\dot{m}v)_f$ or v_f on plume ignition.

At low $(\dot{m}v)_f$ or subsonic v_f, plume ignition occurred at the fuel injector and highest η was achieved at all $(\dot{m}v)_a$ or P_{CS} levels. With plume ignition at the injector, probably highest gas-phase combustion temperatures were achieved as demonstrated for coaxial mixing in Ref. 4. With increasing $(\dot{m}v)_f$, the η remained constant when plume ignition was maintained at the optimum position at the fuel injector. This was the case for 45 psia $< P_{CS} <$ 65 psia with $\dot{m}_f > 0.25$ lb/s per fuel injector. The η decreased with increasing $(\dot{m}v)_f$, when the increase in $(\dot{m}v)_f$ resulted in delayed plume ignition at fuel/air intersection point. With this ignition delay, probably the plume combustion temperatures before fuel/air intersection were lower and the combustion during fuel/air intersection was more adversely effected by the high mixing rates. Decreasing η with increasing $(\dot{m}v)_f$ was observed at $P_{CS} \sim 25$ psia, and at 45 psia $< P_{CS} <$ 65 psia in tests with more than one fuel injector.

The observed plume ignition delay at low P_{CS} and high $(\dot{m}v)_f$ (or high v_f) is consistent with the coaxial mixing tests. It had been shown that the ignition delay, which is probably caused by long reaction rates and insufficient mixing on the molecular scale, resulted in low gas-phase combustion temperatures and low η.

The observed η-decrease at high $(\dot{m}v)_f$ and two or three fuel injectors point to the $\dot{m}_f$ scaling effect in plume combustion discussed earlier. The results of this program and of Ref. 4 indicate that plume ignition was more difficult to achieve at decreasing $\dot{m}_f$ and could therefore be more adversely effected by increasing $(\dot{m}v)_f$ or v_f. This $\dot{m}_f$ scaling effect, which in Ref. 4 was related to gaseous fuel/particle interaction during plume ignition, has to be considered when more than one fuel injector will be used. The $\dot{m}_f$ scaling effect is critical because the gain in improved mixing with multiple injectors may be offset by less than optimum plume ignition when $\dot{m}_f$ is decreased below a critical value.

CONCLUSION

For achieving high η in combustors with two 45° opposing side air inlets, the position of plume ignition and mixing rates at the fuel/air intersection point were critical. Highest η was achieved at lowest $(\dot{m}v)_f$ (resulting in plume ignition at the fuel injector and therefore in highest gaseous fuel combustion temperatures) and lowest $(\dot{m}v)_a$ (resulting in minimum mixing rates at the fuel/air intersection point). The strong effect of $(\dot{m}v)_a$ on η, may in part, explain the η-decrease with increasing a/f and decreasing P_{CS}, which at constant air inlet geometry resulted in increasing $(\dot{m}v)_a$. Tests with multiple fuel injectors showed that optimum plume ignition at the fuel injector was more difficult to achieve at decreasing $\dot{m}_f$ per injector.

The conclusions are qualitative because of lack of detailed flow data, however, they provide insight into the importance of the combustor aerodynamics for achieving efficient boron combustion.

REFERENCES

1. K. Schadow. "Boron Combustion Characteristics in Ducted Rockets," *Combustion Science Tech J., Vol. 5,* May 1972, pp. 107-117.

2. S. W. Abbott, L. D. Smoot, and K. Schadow. "Direct Mixing and Combustion Efficiency Measurements in Ducted, Particle-Laden Jets," *Amer Inst Aeronautics and Astronautics J, Vol 12, No. 3,* March 1974, pp. 275-282. AIAA, New York.

3. K. Schadow. "Study of Gas-Phase Reactions in Particle-Laden, Ducted Flows," *Amer Inst Aeronautics and Astronautics J, Vol II, No. 7,* July 1973, pp. 1042-1044. AIAA, New York.

4. K. Schadow. "Fuel-Rich, Particle-Laden Plume Combustion," *Amer Inst Aeronautics and Astronautics J, Vol 13, No. 12,* December 1975. AIAA, New York.

5. K. C. Schadow and D. J. Chieze. "Water-Tunnel and Windowed Combustor as Tools for Ducted Rocket Development," presented at the 1981 JANNAF Propulsion Meeting, New Orleans, Louisiana, May 1981, (publication UNCLASSIFIED.)

DISCUSSION

R.Lo

Wouldn't you consider average temperture in the mixing zone, boron particle size, and geometric considerations as more important parameters influencing combustion efficiency than air injection momentum?

Author's Reply

To achieve high boron combustion efficiency, high temperature zones downstream of the fuel injectors are essential to free the boron particles from their boron oxide layer. Air injection momentum (air injection velocity) is one of the major parameters determining the magnitude of the temperatures, and therefore, one of the major parameters affecting boron combustion efficiency. (Note: The following paper by Mr Besser also points out the importance of the air injection velocity.)

R.Lo

You showed us a slide where the ratio of the air momentum to fuel momentum varied from .5 to 2.5, and yet your flame pictures showed an optimum in-between these values.

Author's Reply

The flame photographs had no relationship to the test data I showed. They were only used as an example. These flame pictures were done with a non-metallized propellant that had no relationship to the combustion efficiency results in this presentation.

L.Nadaud

Quel est le pourcentage de bore et le pourcentage d'oxydant utilisés dans le propergol de votre générateur de bore.

Author's Reply

The detailed information I cannot give you, but the boron percentage was 46% by weight.

R.Monti

I think that all your data points out that the main parameter is the stay time of the boron particle at high temperature and so that would explain most of this data. The particle size distribution is also very important. Did you make any experiments of different particle size?

Author's Reply

The original particle size in the propellant is sub-micron. Of course, we don't know what agglomeration takes place in the gas generator and so we don't have detailed data on the effect of particle size.

RECHERCHE ET MISE AU POINT D'UN PROPERGOL SOLIDE POUR STATO-FUSEE

JL. BERARD - G. DORIATH - C. PERUT - DIRECTION TECHNIQUE AUTOPROPULSION
Centre de Recherches du Bouchet - B.P. N°2 - 91710 VERT LE PETIT - FRANCE

Des gaz réducteurs susceptibles d'alimenter le foyer d'une chambre statoréacteur peuvent être générés par un propergol sous oxygéné. La solution retenue en vue d'avoir une discrétion totale a été d'incorporer une faible quantité d'un oxydant organique dans un liant hydrocarboné. La composition portant le numéro de référence 1603 a été caractérisée des points de vue mise en oeuvre, propriétés mécaniques et balistiques. La répercution sur les paramètres balistiques de la granulométrie et du taux de la charge et de la nature du liant a été évaluée.

INTRODUCTION

Depuis le début des années 1970, la Société Nationale des Poudres et Explosifs (SNPE) en collaboration avec l'Office National d'Etudes et de Recherches Aérospatiales (ONERA), sous contrats de la Direction Technique des Engins (DTEN), a cherché à développer des propergols solides dont la combustion produisait des gaz réducteurs. Entre autres utilisations possibles, ceux-ci pouvaient servir de combustible pour la propulsion de statoréacteurs ne produisant pas de fumées. Nous nous proposons, dans le cadre de cet article de détailler la fabrication de ce type de propergols et de préciser leurs performances.

Cette nouvelle famille de propergols produisant des gaz réducteurs est la troisième d'une série de produits développés en France.

En effet, dans un premier temps la SNPE a mis au point des formulations à base d'un oxydant minéral et d'un liant hydrocarboné. Celles-ci découlaient de recherches exécutées dans les laboratoires de l'ONERA (3). Ce type de produits qui constituait la première génération, a subi avec succès des essais en vol de missile à carburant solide (1) (voir tableau 1).

La seconde génération, mise au point ultérieurement, était fondée sur l'utilisation du même oxydant dans un liant hydrocarboné densifié. L'augmentation de densité était compensée par une diminution de l'impulsion spécifique et de la chaleur de combustion dans l'air. En effet, la densification augmentait le taux de carbone au détriment du taux d'hydrogène. Cette seconde génération n'a subi jusqu'à présent que des essais en soufflerie.

Pour la troisième génération dont les propriétés d'un représentant vont être décrites, l'effort a porté plutôt sur l'augmentation de la chaleur de combustion dans l'air, sans modification de densité (voir tableau 1). Pour augmenter celle-ci, on s'est rapidement rendu compte que l'utilisation des oxydants minéraux classiques dans les propergols était insuffisante. Aussi divers oxydants organiques ont été alors testés. Ceux-ci donnent en général des performances supérieures car à l'état pur, ils brûlent plus facilement que les oxydants minéraux. Il faut donc des quantités plus faibles de ces produits énergétiques pour entretenir la pyrolyse du propergol.

Sur cette base, a été mise au point une série de propergols à vitesse de combustion et exposant de pression différents. Pour l'une des compositions les mieux connues, le gain de performance par rapport aux premières générations, c'est-à-dire la chaleur de combustion dans l'oxygène atteint 9 %.

I. EVALUATION DE LA COMPOSITION DE REFERENCE

Sous le nom de code 1603, a été figée une formulation de formule brute suivante (base 100 grammes):

$$C_{5.53} \quad H_{8.38} \quad O_{1.15} \quad N_{0.44} \quad P_{0.02}$$

Une telle formulation a une chaleur de combustion mesurée dans l'oxygène de 8020 cal/g et une masse volumique de 1060 kg/m^3.

I1. Température des gaz dans le générateur

Les codes de calculs habituels de prévision des performances théoriques des propergols, ne sont pas adaptés aux calculs de la température des gaz de pyrolyse des propergols froids. En effet, ils font l'hypothèse de l'équilibre chimique dans la chambre du générateur de gaz. Or la faible température de flamme conduit à une décomposition incomplète des liants. En particulier, les calculs font apparaitre des taux élevés de carbone solide (de l'ordre de 50 %). Or les analyses montrent la présence d'hydrocarbures légers et lourds. Par ailleurs, la composition exacte des produits de pyrolyse varie au cours du tir en fonction du temps de séjour dans le générateur de gaz (voir figure 5).

Par l'intermédiaire de thermocouples platine-platine rhodié on peut avoir accès à la température mesurée des gaz. Celle-ci s'établit à 920 K environ pour le propergol 1603.

12. Performances théoriques dans un statoréacteur

Pour évaluer les performances théoriques de ces propergols, il faut convenir de conditions de références pour le statoréacteur Dans les figures 1 et 2,on considère que celui-ci fonctionne à une pression de 0,57 MPa et que l'air est introduit dans des conditions d'altitude nulle et de Mach égal à 2. La figure 1 donne l'évolution de la température du foyer (Tc) et de l'impulsion spécifique (Is_{A+F}) ,par unité de poids du mélange air-réducteur,en fonction du rapport des débits d'air et de comburant (A/F). On voit que la température atteint 2600 K au voisinage du rapport stoechiométrique (9,8) et que l'impulsion culmine à 92 s.

La figure 2 décrit l'évolution en fonction du même rapport de l'impulsion ramenée au débit de carburant (Isp).

13. Mise en oeuvre du matériau

Sans détailler la composition exacte de la formulation 1603 qui est brevetée et classifiée, il est important d'indiquer quelques éléments fondamentaux : le taux de charges solides qui est incorporé au propergol est de moins de 30 % et le liant est à base d'une variété de polybutadiène, qui est un prépolymère relativement fluide. Aussi la pâte de propergol au malaxage est-elle peu visqueuse. Au viscosimètre BROOKFIELD, à un cycle par minute, celle-ci est de l'ordre de 2000 poises. La coulée du propergol même pour des formes de chargement tourmentées, est très aisée. La gravité seule permet de remplir les moules sans aucun artifice. Ceci contraste avec les difficultés de mise en oeuvre de propergols constitués de perchlorate d'ammonium (20-30 %)   de bore (35-45 %) et de réducteurs solides. Le dernier type de propergols est caractérisé par de fortes viscosités, car les granulométries de ces charges sont généralement voisines et fines. Seules les techniques d'injection et de compression permettent de réaliser des blocs et ceci dans des géométries simples, bloc à combustion frontale par exemple.

Après la coulée, la polymérisation du propergol est de 7 jours à 60°C.

14. Propriétés mécaniques et physiques

Les propriétés mécaniques du matériau ont été évaluées sur éprouvettes haltères à différentes vitesses de traction (R), entre 0,5 et 500 mm/mm (tableau 2) et dans la plage de température - 54, + 74°C. Le faible taux de charge en oxydant confère à ce produit de bonnes propriétés mécaniques. A 20°C, la charge à la rupture est de 7,9 bars et l'allongement maximal de 154 %. Ces valeurs sont respectivement égales à 32 bars et à 300 % pour - 54°C et à 5 bars et à 90 % pour 74 °C.

Les résultats de contraintes à la rupture sont représentés dans la figure n° 3 en réduisant les courbes par équivalence vitesse de traction-température.

Ces caractéristiques mécaniques rendent ce propergol particulièrement apte à l'utilisation en moulé-collé. Comme le niveau de vitesse de combustion impose une combustion radiale, et que le taux de résidus élevé interdit pratiquement une combustion frontale, seuls des blocs moulés-collés à combustion radiale sont donc possibles. En diamètre 300, un bloc de forme FINOCYLE durerait environ 200 secondes, ce qui correspond à une possibilité d'utilisation. Avec une forme étoilée en diamètre 200 mm, une durée de combustion de 40 secondes peut être également envisagée.

15. Caractéristiques de sécurité

Par rapport aux propergols classiques générant des gaz réducteurs, qui sont constitués d'un oxydant minéral (généralement le perchlorate d'ammonium) et d'un liant hydrocarboné, l'utilisation d'un oxydant organique à caractère explosif rend obligatoire une caractérisation fine de la sécurité d'utilisation.

Le tableau 3 fournit les valeurs de jugement habituelles dans ce domaine. La sensibilité amenée par l'utilisation de ces oxydants organiques reste voisine de celle des propergols à oxydants minéraux. Ils sont donc classés en 1-3.b (ONU).

16. Propriétés mécaniques des collages

Les qualités d'adhérence de la composition 1603 sur des liners et inhibiteurs de type PBCT, PBHT et PVC ont été évaluées en traction et en pelage. Les propriétés mécaniques sont très satisfaisantes notamment pour les liners de type PBHT. Par exemple, pour le liner PBHT/B, la charge à la rupture est de 5,4 bars. Cette valeur est très proche de la charge à la rupture de la composition 1603 qui est de 7 bars.

Toutes les ruptures des assemblages liner/1603 ont lieu de façon cohésive dans le propergol, ce qui confirme la qualité de ce collage, et l'aptitude de ces propergols à réaliser des blocs moulés-collés (tableau 3).

17. Evaluation de la vitesse de combustion en blocs

L'évaluation de la vitesse de combustion de cette composition a été effectuée entre 6 et 120 bars avec des blocs de 11 kg à canal central étoilé. La pression de chambre est réglée par un diaphragme en acier, ce qui permet d'éviter les dépôts. Le fonctionnement du moteur est stable dans le domaine de pression exploré. La vitesse de combustion est faible (0,92 mm/s à 50 bars). La courbe d'évolution de la vitesse en fonction de la pression confère au produit des possibilités importantes de modulation par modification au cours du tir de l'aire au col (figure 4). La vitesse de combustion passe de 0,5 mm/s à 10 bars à 1,6 mm/s à 120 bars. Le rapport de modulation est donc de 3,2 à 20°C entre ces pressions.

La combustion du produit laisse après tir un résidu charbonneux à l'intérieur de la chambre. Le pourcentage du résidu par rapport à la masse initiale de propergol n'est pas influencé par la température, la taille du chargement ou la pression de tir. Il est compris entre 10 et 14 %.

Le coefficient de température est de 0,55 % par degré. Ceci est une valeur relativement élevée, mais il est possible de réduire l'influence de ce paramètre par l'utilisation de la forte capacité de modulation.

18. Evaluation des rendements de combustion en chambre statoréacteur.

Le rendement de combustion en soufflerie a été évalué par l'ONERA dans une chambre de 200 mm de diamètre à 4 entrées d'air latérales en simulant une vitesse de vol de Mach 2 et une altitude de 1,5 km et par une société américaine ARC en chambre de 152 mm.

Dans le premier cas, le bloc générateur fonctionne à une pression moyenne de 32 bars et débite 0,280 kg/s pendant 47 s. Le débit d'air est de 7,2 kg/s. La richesse est de 0,38 (courbes de tir en figure n° 5). La chambre statoréacteur a parfaitement fonctionné, la perte de pression totale entre les manches à air et la fin de la chambre de combustion est de 14 %, le rendement de combustion défini comme étant le rapport entre le débit de gaz brûlé et le débit de gaz injecté est de 0,91.

La deuxième évaluation s'est déroulée dans le cadre d'un contrat de l'AFAPL. La SNPE a livré à ARC 10 chargements pour évaluation au banc et en chambre statoréacteur de 152 mm de diamètre. Cinq essais ont été réalisés avec succès dans cette dernière configuration. Les rendements de combustion sont très élevés (2).

19. Discrètion du jet du statoréacteur

Pour les propergols de la troisième génération, les produits de combustion des gaz de pyrolyse avec l'air sont essentiellement gazeux aux pressions et températures habituelles. En effet, ils sont constitués principalement d'azote et d'oxygène, et d'un peu de gaz carbonique et d'eau. En raison de l'efficacité de la combustion des gaz réducteurs, très peu d'hydrocarbures imbrûlés sortent de la chambre de combustion, et ils sont très dilués. Aussi la transparence du jet est, elle, très bonne, supérieure par exemple aux meilleurs propergols double base sans fumée. En effet, dans ce dernier cas, les additifs balistiques (sels de cuivre, de plomb) et la présence d'inhibiteur réduisent légèrement la transparence. Sous ce rapport, les formulations de ce type sont bien supérieures aux formulations au bore qui sont très indiscrètes.

2. RÉGLAGE DE LA VITESSE DE COMBUSTION

La composition dont les performances ont été décrites ci-dessus n'est que l'une des possibilités de réglage des propergols de troisième génération. En faisant varier divers paramètres, des variantes peuvent être atteintes.

21. Influence de la granulométrie de l'oxydant

L'utilisation d'une qualité plus grosse pour l'oxydant modifie profondément les qualités cinétiques du matériau (figure 6). La vitesse de combustion à 50 bars chute de 62 %. La sensibilité de la vitesse de combustion à la pression devient beaucoup plus faible. Le taux de résidu est légèrement supérieur à celui de la composition 1603. Il est compris entre 13 et 15 %. L'utilisation de variétés microniques de l'oxydant n entraîne pas de modification de la vitesse de combustion.

22. Influence du taux d'oxydant

La diminution de 22 % du taux de charge provoque une diminution importante de la vitesse de combustion. A 50 bars elle passe de 0,92 mm/s pour la composition nominale à 0,45 mm/s. La sensibilité en fonction de la pression n'est pas modifiée. Le taux de résidu n'est également pas affecté (figure n° 7). Comme on a remplacé l'oxydant organique,pour partie,par un liant de densité plus faible, la densité du propergol n'est plus que de 1,04.

En revanche, la diminution du taux en oxydant entraîne une augmentation du caractère réducteur des gaz générés. La chaleur de combustion dans l'oxygène devient égale à 8500 cal/g contre 8020 cal/g pour la composition 1603 nominale.

Si une diminution du taux de charge entraîne une diminution de la vitesse, une augmentation du taux de charge de 23 % entraîne une augmentation de 63 % de la vitesse de combustion. On voit ainsi que le type de formulation permet une variation de vitesse de combustion d'un facteur 3 environ.

23. Modification de la nature des liants

L'utilisation d'un liant polybutadiène modifié en remplacement du liant usuel entraîne, pour des taux de charge identiques, une modification assez sensible de l'évolution de la vitesse de combustion en fonction de la pression (figure 8). Cet effet est surtout notable à basse pression. Le taux de résidu est de 6 %, il est donc nettement plus faible que pour la composition 1603. Tous les autres paramètres (propriétés mécaniques, caractéristiques de sécurité) restent identiques.

3. CONCLUSIONS

L'intérêt de la composition 1603 réside dans sa forte chaleur de combustion dans l'oxygène par unité de masse, ses bonnes propriétés mécaniques, ses possibilités de modulation importantes et sa discrétion. Elle a toutefois une gamme de vitesse de combustion relativement peu étendue, une densité faible, un taux de résidu élevé, ces points peuvent constituer des handicaps pour certaines applications. Elle a déjà fait l'objet d'améliorations, en particulier, par diminution du taux de résidu. La composition ainsi améliorée entre dans un développement exploratoire actuellement en cours.

REFERENCES

(1) Pierre BERTON et Dominique [illegible]
Installations d'essais de stato-réacteur à l'ONERA
La recherche aérospatiale (1980) n° 4 p [illegible]-258

(2) B. David CORACKE
Third generation SNPE ducted rocket technology
1980 Janaf Propulsion Meeting Monterey, California 11-13 march 1980

(3) L. NADAUD, F. REYNAUD, A. MOUTET
Combustibles solides pour statoréacteurs
La recherche aérospatiale (1977) n° 1 p 31-38

TABLEAU 1

PERFORMANCES COMPAREES DES TROIS
GENERATIONS DE CARBURANTS SOLIDES POUR STATOREACTEUR

Produit	Référence composition centrale	Chaleur de combustion dans l'oxygène cal/g	Masse volumique kg/m^3
1ère génération	1601	7320	1100
2ème génération	1602	6920	1250
3ème génération	1603	8020	1060

TABLEAU 2

TRACTIONS A TEMPERATURE ET VITESSES VARIABLES DE LA COMPOSITION 1603

Température °C	Vitesse mm/mn	Propriétés mécaniques					Log a_t calculé sur Sm
		Sm bars	ε %	E bars	εm %	εr %	
+ 74	0,5	3,9	25	16	63	64	- 3,5
	5	-	-	-	-	-	
	50	5,0	29	17	89	90	
	500	5,8	32	18	101	103	
+ 60	0,5	4,0	28	14	67	68	- 2,8
	5	-	-	-	-	-	
	50	5,3	28	19	89	90	
	500	6,7	33	20	116	119	
+ 40	0,5	4,9	28	17	97	-	- 2
	5	5,3	32	17	91	-	
	50	6,1	33	18	108	109	
	500	7,9	38	21	142	146	
+ 20	0,5	6,5	27	24	125	125	0
	5	6,2	32	20	88	89	
	50	7,9	39	20	152	154	
	500	9,7	44	22	203	210	
- 10	0,5	9,1	49	20	240	243	+ 3,9
	5	13	67	20	302	304	
	50	10,4	57	18	177	-	
	500	15,8	44	36	323	388*	
- 40	0,5	22,1	84	28	297	301*	+ 8,8
	5	20,9	47	44	264	265*	
	50	26,7	57	47	270	329*	
	500	33,7	62	56	318	354*	
- 54	0,5	35,8	56	65	287	287*	+ 12
	5	35,7	61	59	300	300*	
	50	32,3	51	63	188	220*	
	500	62,2	75	84	311	337*	

Appareil Instron, Eprouvettes 1/2 Jannaf (longueur utile 50 mm)

* valeurs par défaut, l'éprouvette ne rompt pas à l'élongation maximum de la machine

TABLEAU 3

CARACTERISTIQUES DE SECURITE DE LA FORMULATION 1603

Epreuve	Appareil	Sensibilité	Observations
Sensibilité au choc	Julius Peters	50 Nm	très peu sensible
Sensibilité au frottement	Julius Peters	100 N	très peu sensible
Température d'auto-inflammation (5°C/mn)		280 °C	peu sensible
Aptitude à la détonation (Card Gap Test français)		150 cartes (~60 cartes US)	peu sensible
Sensibilité à la décharge électrique		pas d'inflammation à 726 mJ	peu sensible
Diamètre critique		40 mm	fort diamètre critique

TABLEAU 4

PROPRIETES MECANIQUES DES COLLAGES

Inhibiteur type	Mode de préparation	Traction R : 10 mm/mn (bars)	Pelage (daN/cm)
PBHT A	-	5,2	2,4
PBHT B	-	5,4	2,6
PBCT	-	3,3	1,6
PVC A	direct	4,8	-
PVC A	dégraissé et séché	5	1,0
PVC B	dégraissé et séché	5,5	-

FIGURE 1

EVOLUTION DE DIVERS PARAMETRES
EN FONCTION DU RAPPORT A/F

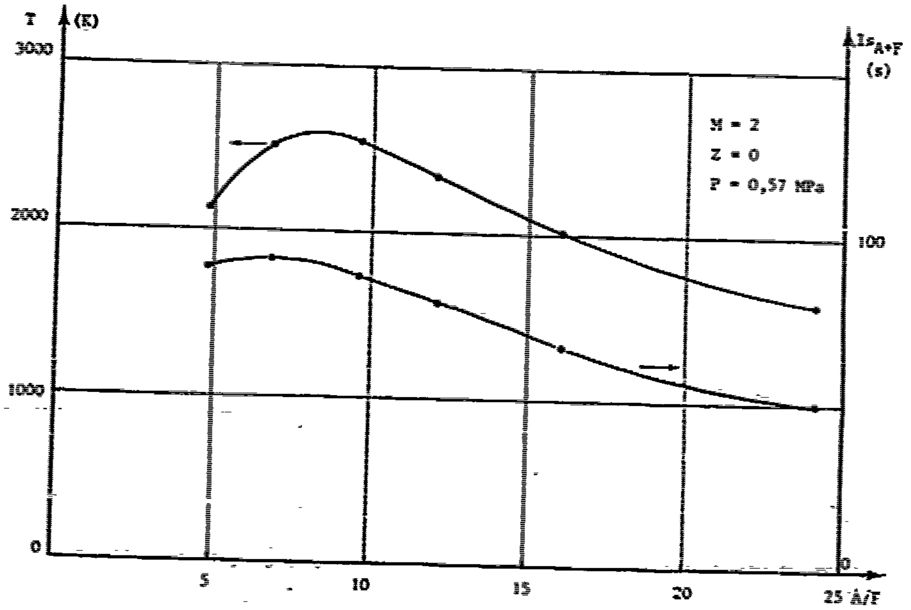

FIGURE 2
EVOLUTION DE L'IMPULSION SPECIFIQUE
PAR RAPPORT AU PROPERGOL EN FONCTION DE A/F

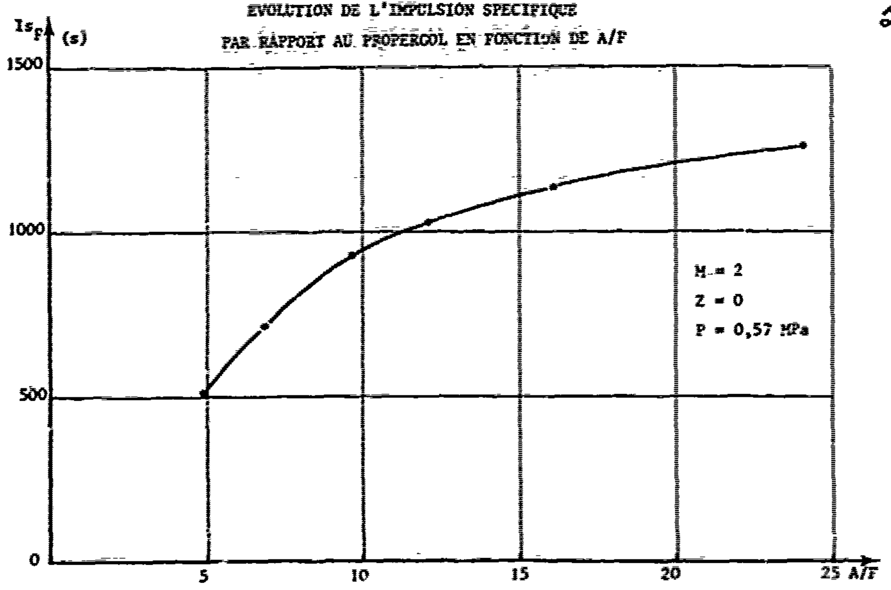

FIGURE 3
COURBE MAITRESSE Sm = f log 1/Ra$_t$

R = vitesse de traction mm/mn
a$_t$ facteur de translation

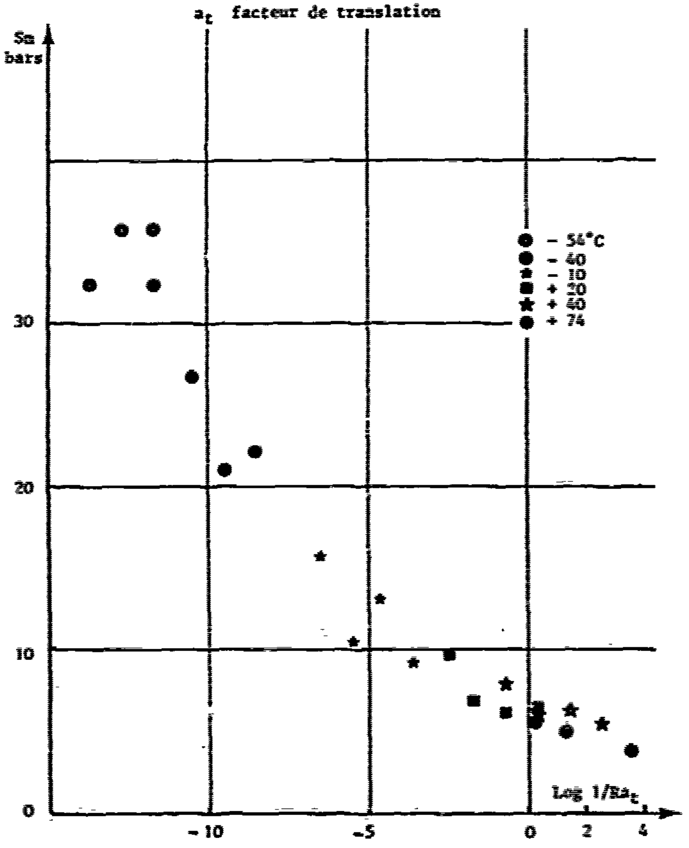

FIGURE 4

EVOLUTION DE LA VITESSE DE COMBUSTION
ET DU SERRAGE EN FONCTION DE LA PRESSION (COMPOSITION 1603)

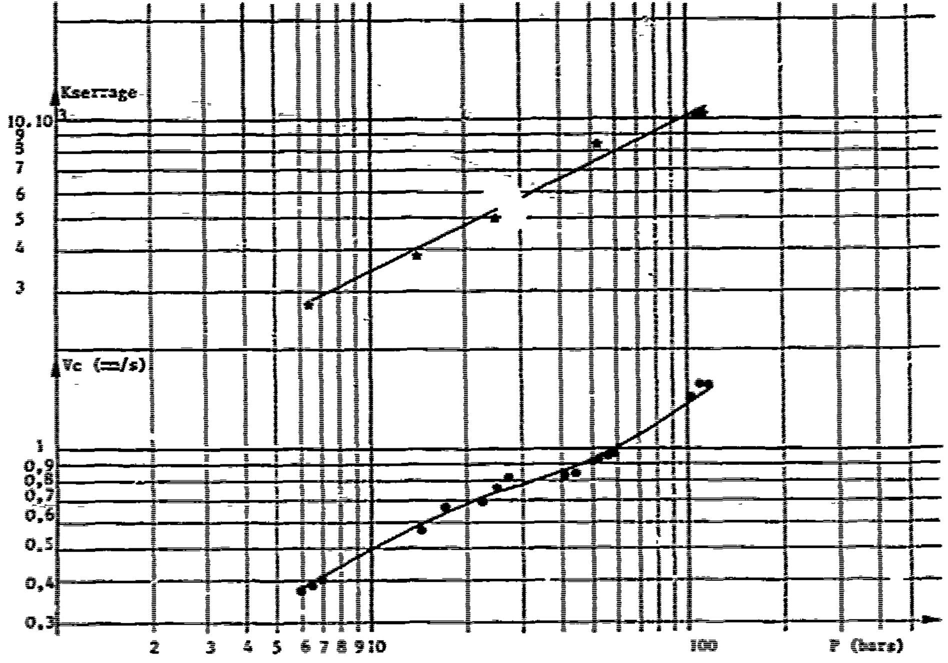

FIGURE 5

ESSAI EN CHAMBRE STATORÉACTEUR A L'ONERA

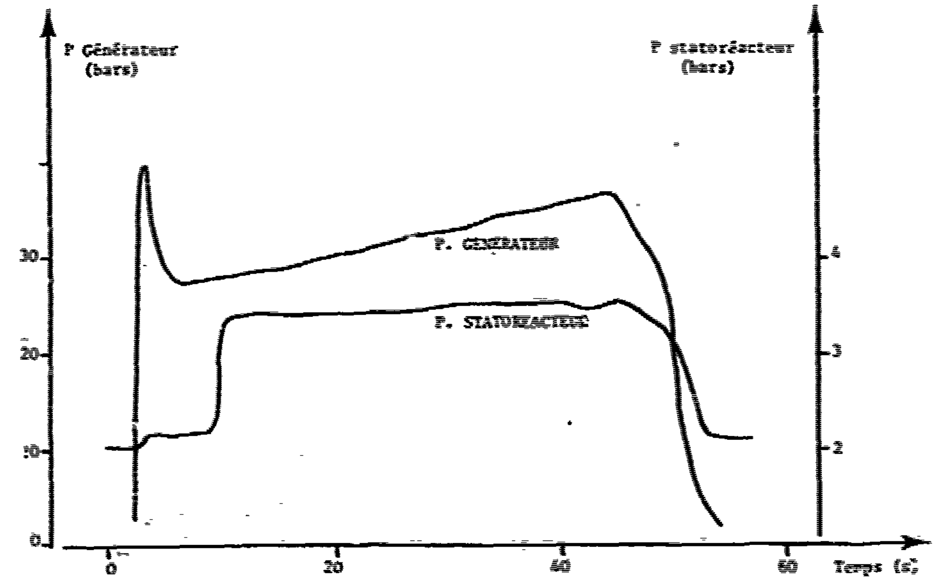

FIGURE 6

INFLUENCE DE LA GRANULOMETRIE DE L'OXYDANT SUR LA VITESSE DE COMBUSTION EN BLOCS

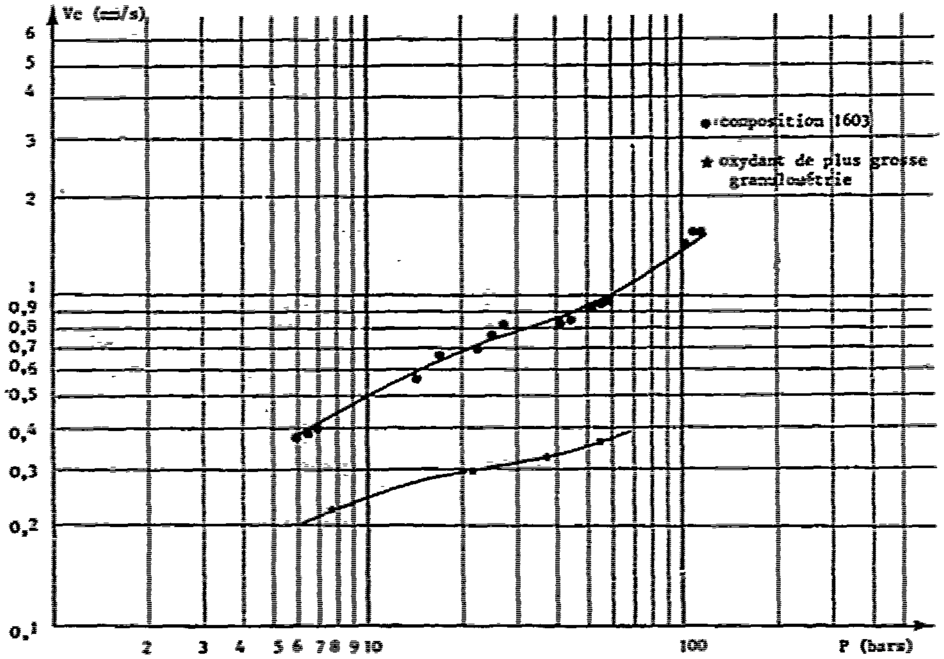

FIGURE 7

INFLUENCE DU TAUX DE CHARGE SUR LA VITESSE DE COMBUSTION EN BLOC

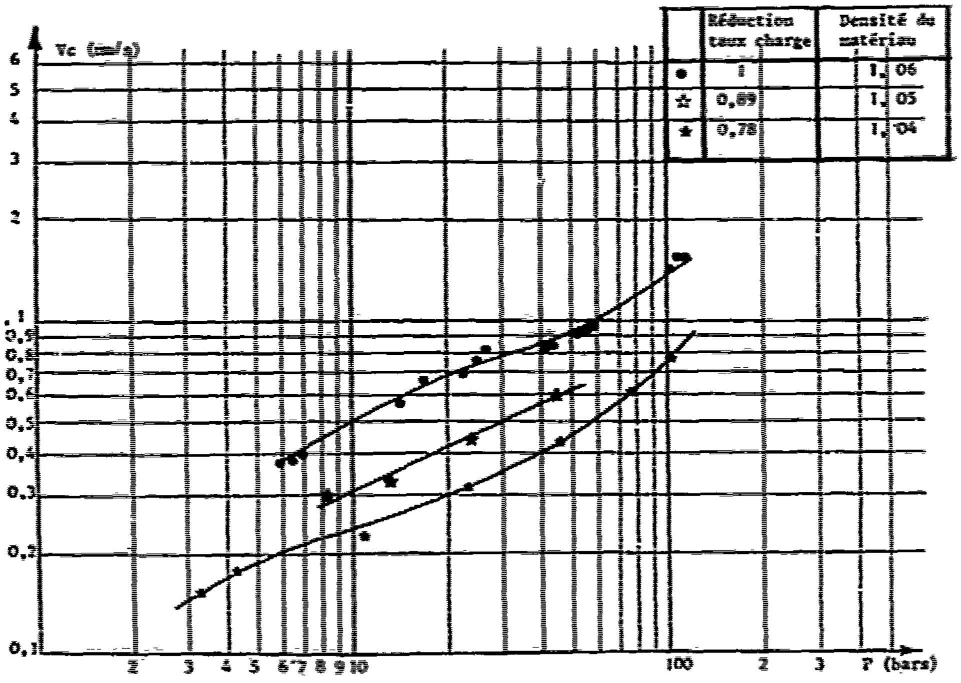

	Réduction taux charge	Densité du matériau
●	1	1,06
☆	0,89	1,05
★	0,78	1,04

FIGURE 8

INFLUENCE DE LA NATURE DU LIANT SUR LA VITESSE DE COMBUSTION

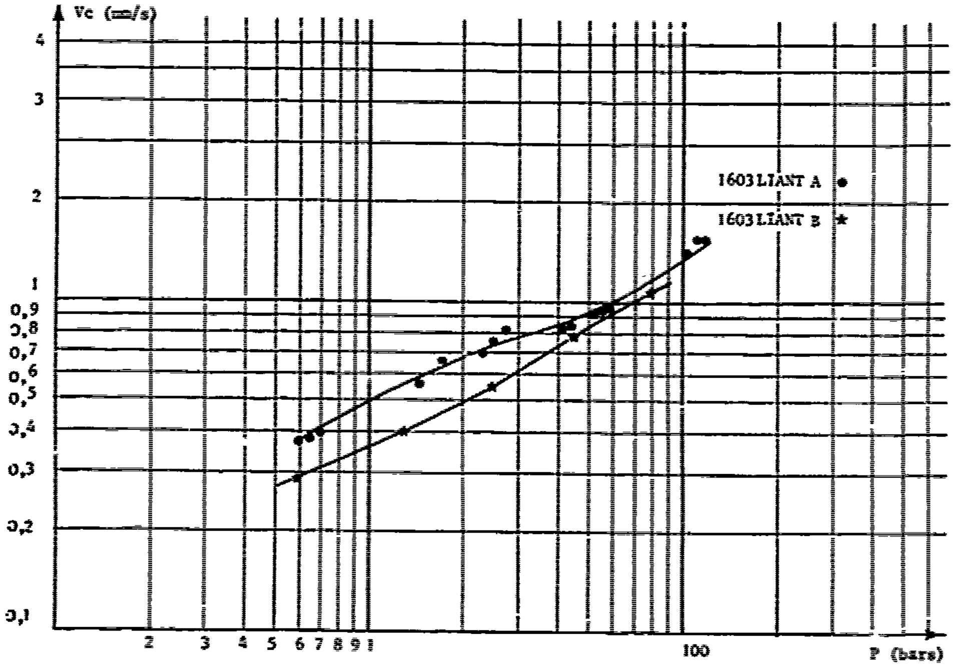

DISCUSSION

H.Besser

Concerning your viewgraph which showed ramcombustor evaluation of the propellant, a significant delay in ramjet ignition of about 5 to 8 seconds was noted. Can you comment on this?

Réponse d'Auteur (In French)

The sequence was delayed to simulate the booster.

DESIGN OF HYDROGEN FUELED RAMJETS AND RAMROCKETS

by

Dino Dini
Istituto di Macchine, Università di Pisa
Via Diotisalvi, 2
56100 Pisa, ITALY

SUMMARY

Problems arising from high energy fuels, particularly hydrogen, impose remarkable changes in interface components, geometry and control, of current ramjets and ramrockets design.
Starting from typical missions scenarios, advanced configurations are established for military applications. Variable geometry nozzles and combustion chambers are considered in the light of their combined effect with the intake, to give good performance and flexibility.
A numerical example of overall design is given for very high flight Mach numbers considering the problem arising from engine/airframe integration and cryogenic fuel storage. Particular attention is paid to features effecting installation of such engines in aircraft.

ROCKET ENGINES BURNING HYDROGEN AS FUEL

The idea of using oxygen and hydrogen as propellant is nothing new. It was put forward for the first time in 1 903, by a Russian mathematics, Ziolkowsky, and considered by Oberth in Germany almost at the same time.
It is surprising that the development of this propellant has been [illegible], starting only at the end of 1 958 when the Pratt and Whitney engine RL 10 was being perfecte[illegible] ay is attributable to the extreme properties of liquid hydrogen, its very low boiling point and very small specific mass, but now the great advance in space research has rendered high energy propellants more interesting.

Liquid hydrogen/liquid oxigen engine - Nowadays, it is a reusable high-performance rocket engine capable of various thrust levels. Ignited on the ground prior to launch, the cluster of three main engines operates in parallel with the solid rocket boosters during the initial ascent of the "Space Shuttle Transportation Systems". Each engine operates at a weight LO_2/LH_2 mixture ratio of 6 to 1 to produce a sea level thrust of 1 668 kN and a vacuum thrust of 2 091 kN (25% more than on the ground). The engines can be throttled over a thrust range of 65 to 109%, which provides for a high thrust level during lift-off and the initial ascent phase but allows thrust to be reduced to limit acceleration to 3 g's during the final ascent phase.
Each engine has fuel and oxidizer preburners that provide hydrogen-rich hot gases at approximately 1 030 K. These gases drive the fuel and oxidizer high-pressure turbopumps. The preburner gases pass through turbines and are directed through a hot-gas manifold to the main combustion chamber together with liquid oxygen and burn at approximately 3 590 K. The main chamber operating pressure at rated power level is approximately 20 700 kPa. The ratio of the area at the aft end of the combustion chamber to the throat area is 5 to 1. From this area, the nozzle assembly is designed for a 77.5 to 1 chamber expansion ratio for thrust efficiency at high altitudes.
The propellant feed system, figure 1, includes low and high pressure turbopumps for the liquid hydrogen fuel and liquid oxygen oxidizer. Each low-pressure fuel turbopump is an axial-flow pump driven by a two-stage turbine. It raises the pressure of the fluid being applied to the high-pressure fuel pump to prevent cavitation, normally operating at a speed of 14 000 rpm for increasing the pump pressure from 207 to 1 600 kPa. The turbine is driven by gaseous hydrogen at a nominal inlet pressure of 29 434 kPa.
The high-pressure fuel turbopump is a three-stage centrifugal pump driven directly by a two-stage turbine. The latter, in turn, is driven by hot gas supplied by the fuel preburner. This turbopump operates at a nominal speed of 35 000 rpm, increasing the pressure from 1 213 to 42 817 kPa. The nominal turbine inlet pressure and temperature are 35 605 kPa and 961 K, respectively.
The low pressure oxidizer turbopump is an axial flow pump that is driven by a six-stage turbine and powered by oxidizer propellant, to maintain sufficient inlet pressure to the high-pressure oxidizer pump, to prevent cavitation. Turbine-drive fluid at 30 944 kPa is provided from the high-pressure oxidizer pump discharge. The low pressure oxidizer pump nominally operates at a speed of 5 150 rpm, and increases the pump pressure from 690 to 2 881 kPa.
The high-pressure oxidizer turbopumps operate at a nominal speed of 29 057 rpm with a turbine inlet pressure and temperature [illegible] 34 046 kPa and 817 K, respectively. The pump pressure increase is from 2 482 to 31 937 kPa. The prebu[illegible] pump pressure increases from 30 592 to 52 642 kPa.

The high performances of this propellant are more or less evident from the high reaction temperature of the two costituents and expecially the small molecular mass of hydrogen.
The design of engines and launching rockets are greatly influenced by the very low temperature and small specific mass of liquid hydrogen. The mixture ratio is of special importance because there is no practical constraint on its selection; its value must be determined by an optimization study. The true significance of it can best be appreciated by the figure 2, which gives a comparison between tank sizes for three tanks containing the same propellant mass but for three different mixtures ratios.
The effect of combustion pressure is of course depending on weather a pressure-fed or pump-fed system is

used, but in both cases the use of higher pressures brings a performance advantage. The main reason for the performance advantage occurring from high combustion pressures lies in the ability to make use of nozzles of high expansion ratio.

A comparison of the theoretical maximum performance under the customary reference conditions (combustion pressure 6 890 kPa, expansion ratio 68, ambient pressure 101,3 kPa) gives:

- LO_2/LH_2: specific impulse, 391 s; combustion temperature, 3 000 K; weight mixture ratio, 4.0; bulk density, 2,746 kN/m^3;
- LO_2/kerosene: specific impulse, 300 s; combustion temperature, 3 700 K; weight mixture ratio, 2.6; bulk density, 10,003 kN/m^3;
- N_2O_4/N_2H_4: specific impulse, 292 s; combustion temperature, 3 300 K; weight mixture ratio 1.3; bulk density, 11,964 kN/m^3.

The small bulk density of the LO_2/LH_2 propellant renders necessary considerable tank volumes and structural loads which are still further increased by the strong thermal insulation required.
Liquid oxygen is 16 times denser than liquid hydrogen, hence the bulk density of the propellant varies considerably according to the mixture ratio; and optimization of this ratio requires careful study for each missile design.
Dependence of mean bulk density and vacuum specific impulse on mixture ratio is shown in figure 3, as comparison of liquid hydrogen with kerosene as rocket fuel, burned with liquid oxygen in each case.
Combustion pressure and mixture ratio depend on combustion chamber cooling. The best oxygen/fuel ratio regardless of engine cooling or vehicle design in respect to specific impulse is shown in figure 4; the optimum is somewhere around 4 to 1.

In calculating the tank volume, and the propellant quantities, corrections have to be made for the following factors: 5% of the tank volume for the vapour space above the contents; 1% of the initial contents for the residual liquids remaining at the end of burning period; residual propellant vapour at the end of the burning period; propellant lost by evaporation. Densities of propellant liquid and vapour in the saturated conditions are shown in the following table; the final column indicates the percentage residual vapour for tanks initially filled with 4 to 1 mass mixture ratio saturated liquid at a pressure of 100 kPa.

Pressure	Vapour,	(N/m^3)	Liquid,	(N/m^3)	%
(kPa)	GO_2	GH_2	LO_2	LH_2	Residual
100	43,44	12,36	11 199,2	693,33	0,7
200	84,34	24,61	10 826,5	661,95	1,3
300	125,50	35,99	10 551,9	637,43	1,9
500	196,13	60,80	10 149,9	594,28	3,2
800	318,72	101,99	9 747,8	532,50	5,2
1 000	397,17	140,23	9 502,6	479,55	6,9
1 315	505,04	293,22 Critical	9 179,0	293,22 Critical	12,1

Figure 5 shows how the specific theoretical vacuum impulse and the bulk density vary with the mixture ratio for a nozzle throat ratio of 40 (corresponding to an expansion ratio of the order of 500) and a combustion pressure of 3 500 kPa.
The power required for pumping is greater than with the standard liquid propellants Figure 6 shows the specific theoretical pumpability curve for the LO_2/LH_2 propellant as a function of mixture ratio for an engine working at a combustion pressure of the order of 3 500 kPa (fuel $\Delta p = 5\ 000$ kPa, oxidizer $\Delta p = 4\ 500$ kPa).

Liquid hydrogen/air engine - The propulsion system selected for this discussion consists of turbine engines for acceleration to Mach 3 to 4 range and convertible scramjets for the mission scenario. The turbine engines for the lower part of the boost speed range is based on the advanced state of turbojet development for the Mach 3 flight including the SST engine technology. Mach 3.5 and 4.0 capability with hydrogen fuel is highly desirable. The scramjet is the only air-breathing engine capable of operation from Mach 3.5 to the proposed mission flight speed. Technology evaluations at present time refer that the scramjet promises great potential, but that the feasibility of practical operation and performance remains to be shown by complete engine experiments.
The "dual-mode" NASA - Air Research Hypersonic Research Engine (HRE) is a small axisymmetric, variable geometry engine designed to perform from Mach 4 to 8. In the dual-mode principle, the location of the active fuel injector stages and the combustion move downstream to larger duct areas when the flight Mach number is decreasing. The key features of the concept are several stages of fuel injection in an expanding area combustor, which satisfy the basic aerothermodynamic geometry requirements for either sub or supersonic combustion.

One key to sustained hypersonic flight is an efficient airbreathing hydrogen - fueled engine. The integrated scramjet engine/airframe has been identified for military applications in the Mach 4 to 12 speed range. The hypersonic variable geometry propulsion system consists of multiple engine modules each with a forebody precompression inlet and plug nozzle exhausting. The axisymmetric multiple inlet scramjet modules efficiently capture forebody shock waves and compressed airflow. The plug nozzles serve to increase expansion area and allow the central body, figure 7, to be nearly stream aligned at the design Mach number for maximum installed thrust performance. The engines are designed to be integrated fully with a hypersonic airframe, accounting properly for all forces acting on the integrated vehicle.

The propulsion system requirements of the low range boost vehicle bring out the interest for the air augmented rocket. Suitable for high thrust and average specific impulse, such engine might be used at flight speed less than Mach 4.0, with variable geometry.
The air augmented rocket, for the propulsion of boost vehicles, is known as an engine which improves the propulsion efficiency of the rocket at low flight speeds, and which requires a smaller weight of manufactured structure than other airbreathing engines.
Simple engines with fixed geometry and variable airflow have realized at best about one third of the potential gain in specific impulse due to air augmentation. The failure to gain more is very largely due to the difficulty of arranging a fixed geometry which allows for expansion of the exhaust stream, after mixing is completed. With a fixed outer cowl, the specific impulse can be improved by arranging for the air intake diffuser to vary internally. A beneficial variation in air duct area might be arranged with comparatively simple moving parts operating in the cooler part of the engine. This has a double effect in improving performance; reduction in diffusor outlet area at high flight Mach number assists in intake matching.

SYSTEM CONCEPT

A satisfactory launch speed might rapidly be reached at low altitude by a turbo - ramjet - rocket multicycle missile.
Such kind of hybrid engine is enough flexible to meet a large variety of cruise conditions with speed quite higher than Mach 4. Like turbo-ramjet, this propulsion system, figure 7, is arranged with a lot of inlet and exhaust variable geometries.

A hydrogen - oxygen rocket combustion chamber is used to produce high pressure and temperature steam, for the count down and takeoff phase, during which the degree of super heat is controlled by the injection of suitable quantities of liquid water.
The steam flows directly to the nozzle assembly driving a high pressure turbine in a first stage of expansion, while useful energy for propulsion is realized in a central - body variable geometry plug nozzle.
The steam turbine is giving power to a cluster of multi - stage atmospheric air compressors accomodated into propulsive ducts around the turbo - rocket central body, for a sequence of operations going from cold to hot jets for take - off and acceleration phase.
The LH_2/LO_2 rocket and LH_2/air turbojet propulsion is followed by variable geometry LH_2/air ramjet and scramjet operation.

Application of current compressor technology to meet the higher core pressure ratios desired in advanced engines would result in a large number of stages and blades. To minimize weight, volume and stages, high tip speed and high blade loading for high stage pressure ratio are required. It is now possible to design compressors for an overall pressure ratio of 20 to 1 and only eight stages. To achieve this goal, the pressure ratio as high as 1.8 in the first stage is decreasing to 1.25 in the last one because of the increasing temperature. The first stage rotor has a design speed of 450 m/s. The hub - tip ratio ranges from 0.7 at the inlet to 0.95 at the outlet. A compression efficiency of 87 percent is obtainable.
A major objective of fan or compressor for a possible application as in figure 7 is to obtain high pressure ratio per stage with high efficiency. At 540 m/s tip speed, a stage pressure ratio of 2.2 has been already obtained with an acceptable efficiency of 82 percent, Ref. 1. We are confident that a higher level of efficiency in this high - speed range can be achieved by further improvement in blade design. With a two - stage fan, an overall pressure ratio of 2.8 and a peak efficiency at design speed of 85.5, were obtained.

Similarly, a higher core turbine inlet temperature is required for the application as in figure 7. Elevated temperatures and pressures for a short operation do not require, however, sophisticated cooling schemes to protect the blades.

Gaseous hydrogen GH_2 and oxygen GO_2 are directly aobtained by water electrolysis at the launch place. The most part of electrolytic cells are producing 0.2 Nm^3 of GH_2/kWh (0.0555 Nm^3/MJ) and 0.1 Nm^3 of GO_2/kWh (0.0277 Nm^3/MJ), i.e., respectively, with specific gravities 0.881 N/Nm^3 and 14.013 N/Nm^3, 0.04896 N/MJ and 0.38925 N/MJ. The weight mixture ratio for the combustion is becoming 0.38925/0.04896 = 7.95, corresponding, figure 3, about to the stoichiometric ratio, if all the electrolysis products are used.

The energy need for a modern electrolysis process may be at present time 14.65 MJ for producing 1 N of GH_2 and 7.95 N of GO_2. Liquefaction (L) may require 3.65 MJ per 1 N of LH_2 and 0.19 MJ per 7.95 N of LO_2. Therefore, the total energy need for production and liquefaction, at atmospheric pressure, of 1 N of LH_2 and 7.95 N of LO_2 is about 18.49 MJ, corresponding to 18.49/8.95 = 2.066 MJ per N of stoichiometric mixture LH_2 - LO_2.

The combustion temperature at a pressure (20 700 kPa) of the order of the main LH_2/LO_2 engines of the

"Space Shuttle" may be 3 500 K in the stoichiometric mixture ratio. The combustion product is of course water steam.
Such combustion temperature is obviously unacceptable for the turbine blades. Considering the short duration of the LH_2/LO_2 engine operation, a temperature of 2 000 K may be chosen. Pulverized water injection in the combustion chamber is used for decreasing temperature from 3 500 to 2 000 K.

In order to know approximately the water fraction β to be injected through the experimental values of the specific impulse given in figure 4, the following procedure is applied.
The initial entalpy i_1 (for: combustion pressure, p_1 = 20 700 kPa; specific heat ratio, n = 1,25; mixture ratio, O_2/H_2, 7.95; dissipation coefficient, μ = 0,95), respectively, for sea level (p_2 = 101,3 kPa), and 5 000 m altitude (p_2 = 53.9 kPa) at specific impulse (figure 4) 350 and 370 s, are

$$I_{sp} = w/g = \mu \sqrt{2\, i_1 \left(1 - (p_2/p_1)^{(n-1)/n}\right)}/g \qquad (1)$$

$$i_1 = 1{,}016 \text{ MJ/N} = 2\,381 \text{ kcal/kg} \quad \text{(sea level)}$$

$$i_1 = 1{,}069 \text{ MJ/N} = 2\,506 \text{ kcal/kg} \quad (5\,000 \text{ m})$$

corresponding to exhaust speeds

$$w = 3\,433 \text{ m/s} \qquad ; \qquad w = 3\,630 \text{ m/s}$$

The gradually injected water in the combustion chamber is increasing its entalpy from i_s = 0.0043 MJ/N (10 kcal/kg) to i_s = 0.612 MJ/N (1 435 kcal/kg, for T_s = 2 000 K and p_1 = 20 700 kPa).
Approximately, disregarding heat exchange dissipation effects, to be considered in the expansion efficiency, the fraction of the GH_2/GO_2 combustion products α, the injected water β, and the hydrogen $\gamma = \alpha/8.95$, it can be written, Ref. 3

$$\begin{aligned} \alpha &= i_s(1+\beta)/i_1 \\ \alpha + \beta &= 1 \end{aligned} \qquad (2)$$

from which

$$\beta = (i_1 - i_s)/(i_1 + i_s) \qquad (3)$$

We get, respectively for sea level and 5 000 m altitude

β = 0.248 α = 0.752 γ = 0.084 (sea level)

β = 0.272 α = 0.728 γ = 0.081 (5 000 m)

With a step by step procedure, from the ignition to the end of the acceleration phase, an optimized turbo/rocket - cold-hot turbo/fan propulsion system may be designed, to be followed by the variable geometry ramjet and scramjet operation.
The procedure is starting with the evaluation of the weight of LH_2, LO_2 and water, for the acceleration phase.
Establishing a mean value of the dissipation coefficient μ (taking into account of an approximated equivalence to the real hybrid engine used) and considering $i_1 = i_s$ in eq. 1, we get I_{sp} and w from eq. 1, from which the propellant weight flow G corresponding to the thrust T

$$G = g\, T/w \qquad (4)$$

to be used step by step. The propellant weight is obviously depending upon the acceleration phase duration.

In operation, hydrogen, oxygen and water, are supplied from turbopumps to the combustion chamber where steam is formed. The steam flows directly to the turbine and thence to the plug nozzle.

The expected overall efficiency of this hybrid boost engine is higher than rocket, because of quite less mean gas exhaust speed. The propellant consumption is reduced by the high propulsion efficiency of the turbofan operation.

The success of such boost engine combination is depending upon the real possibility of a large fraction of water injection into the combustion chamber, to have a high work tranfer from the turbine to the compressors.

A numerical approach may be obtained considering acceleration hybrid turbo - rocket as in figure 7 with $\mu = 0.6$ (taking into account che compressor work absorption for the engine equivalence), $i_1 = i_g = 0.612$ MJ/N, and $T = 100\,000$ N. We have from eq. 1

$$I_{sp} = 172 \text{ s} \qquad w = 1\,684 \text{ m/s} \quad \text{(sea level)}$$

$$I_{sp} = 177 \text{ s} \qquad w = 1\,735 \text{ m/s} \quad (5\,000 \text{ m})$$

and from eq. 4, for a 5 000 m ascent trajectory at a mean velocity $M = 2.0$, a mean weight flow during the time $\Delta t = 5\,000/2 \cdot 340 = 7{,}35$ s

$$C = 503 \text{ N/s}$$

So, with a propellant weight $C \cdot \Delta t = 3\,697$ N, we get, applying eqs. 2 and 3, storage weights and volumes

$$\beta_{av} \cdot 3\,697 = \text{(water)} = 961 \text{ N} = 961/g \cdot 1\,000 = 0.098 \text{ m}^3$$

$$\alpha_{av} \cdot 3\,697 = \text{(combustion products)} = 2\,736 \text{ N}$$

$$\gamma_{av} \cdot 3\,697 = \text{(hydrogen)} = 305 \text{ N} = 305/693.33 = 0.44 \text{ m}^3$$

$$2\,736 \cdot 7.95/8.95 = \text{(oxygen)} = 2\,431 \text{ N} = 2\,431/11\,199.2 = 0.217 \text{ m}^3$$

i.e., propellant and water for the hybrid acceleration engine require the volume equivalent to a circular cylinder 0.60 m and 2.67 m in diameter and length.

The advantages of the hydrogen fueled airbreathing ramjet and scramjet, for a flexible cruise flight to the target, are deriving from the higher energy per mass unit of on - board propellant. In fact, weight stoichiometric mixture ratio for air/hydrogen is $7.95 \cdot 100/23.14 = 34.356$. Air/hydrogen weight mixture ratio is ranging from 5 to 115, this meaning that a hydrogen fueled engine is very much flexible for speed variation during the cruise flight.

Compared to the acceleration phase, the on - board fuel volume for cruise is requiring quite less volume.

LH_2 AND LO_2 SUPPLY AND ON-BOARD STORAGE

Water electrolysis, by nuclear or solar energy, may be the primary candidate for gaseous hydrogen and oxygen production and derivery through pipelines to the missile launch place, where liquefaction plants are existing. Temperatures as low as 20 K (LH_2) and 90 K (LO_2) require vacuum - jacketed stainless steel pipe lines for transport from liquefaction plants to the missile launch site. The need to kip pipe lengths as short as possible is further emphasized in that each length is triplicated. Some of the liquid hydrogen changes to gaseous state during the fueling operation, and at any other time when the temperature and pressure exceed certain conditions. For reason of safety and fuel economics, the gaseous hydrogen must be collected and returned to the liquefaction plant through a second line. The third line provides redundancy and can be used either to deliver LH_2 or return GH_2

Flexible liquefaction plants produce LH_2 and LO_2 as much as it is used and to refill storage vessels.

Gaseous hydrogen and oxygen are piped from the water electrolyzers to or near the launch site, where electrical power is provided as needed for liquefaction.

The ground - to - missile connection is following a basic fueling concept: truck with dual vacuum jacketed flexible hoses manually connected between the hydrant pint and the single connection to the missile tanks.

Based on the largest demonstrated hydrogen liquefier capacity (6.2 N/s, 534 kN/day), it has been yet determined that a single plant having a capacity of 25.75 N/s is possible.

The technology required to build reliable fuel-cooled structures for the hostile environment within the engine has been developed.

Liquid hydrogen is stored in well insulated tanks, whose pressure is scheduled to minimize boil-off losses. When small amounts of hydrogen are vaporized by heat that does enter the tank, the gas is vented through a catalytic exhaust tube where the escaping hydrogen is flamelessy converted to water vapor. Several aluminum alloys and stainless steels are applied in lightweight structures for cryogenic liquids at extremely low temperatures, Ref. 2.

VARIABLE GEOMETRY IN MULTICYCLE ROCKET ENGINES

Significant changes to its thermodynamic cycle during the flight are required for the proposed missile propulsion systems, without incurring a performance and weight penalty which would cancel the value of variability.
The geared variable pitch fans of the boost engines claim variable final nozzles. The cycle variability provides adjustment of specific thrust, matching of fan and nozzle characteristics, and selection of fan-nozzle combination for optimum acceleration performances.

The operation of the variable-geometry axisymmetric ramjets over a broad flight speed cruise range is encountering combustor problems in a wide range of fuel air conditions.
Integrated engine/airframe performance is tied closely to the combined vehicle-engine design, so that it is necessary to conduct studies with particular vehicle designs. The scramjet concept could form a major experiment for the present composite vehicle.
The intake design must be a compromise approaching the optimum flow to the engine, with minimum efficiency loss and drag increase in the flight speed range, Ref. 4.

Detailed designs of the proposed turbo-ramjet-ramrocket have been carried out by the author. Their results are quite encouraging.

REFERENCES

|1| A.L. Morris and D.H. Sulam, "High Loading, 1 800 Ft/sec Tip Speed, Transonic Compressor Fan Stage" - 2: Final Report (PWA - 4 463, Pratt & Whitney Aircraft; NAS3 CR - 120991, 1 972.

|2| D. Dini, "Performance Characteristics of Turbo-Rockets and Turbo-Ramjets Using High Energy Fuel", AGARD Conference Proceedings No. 205, Paris, 6-9 September 1 976.

|3| D. Dini and P. Psarudakis, "Utilizzazione diretta dei prodotti della elettrolisi dell'acqua per turbogeneratore ad alto rendimento", 36° Congresso Nazionale ATI, Viareggio (Italy), 5-9 October 1 981.

|4| D. Dini and R. Lazzeretti, "Engine Intake Control Design for Advanced Fighter Aircraft", AGARD Conference Proceedings No. 274, Cologne, Germany, 1-2 October 1 979.

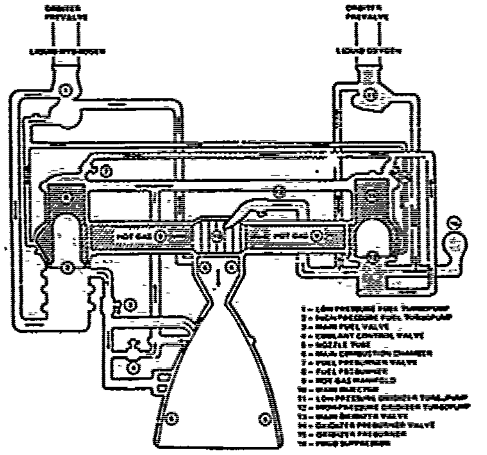
ORBITER PREVALVE
LIQUID HYDROGEN
ORBITER PREVALVE
LIQUID OXYGEN
HOT GAS
HOT GAS
1 - LOW PRESSURE FUEL TURBOPUMP
2 - HIGH PRESSURE FUEL TURBOPUMP
3 - MAIN FUEL VALVE
4 - COOLANT CONTROL VALVE
5 - NOZZLE TUBE
6 - MAIN COMBUSTION CHAMBER
7 - FUEL PREBURNER VALVE
8 - FUEL PREBURNER
9 - HOT GAS MANIFOLD
10 - MAIN INJECTOR
11 - LOW PRESSURE OXIDIZER TURBOPUMP
12 - HIGH PRESSURE OXIDIZER TURBOPUMP
13 - MAIN OXIDIZER VALVE
14 - OXIDIZER PREBURNER VALVE
15 - OXIDIZER PREBURNER
16 - POGO SUPPRESSOR

Fig. 1 - Propellant feed system for the Space Shuttle main engines.

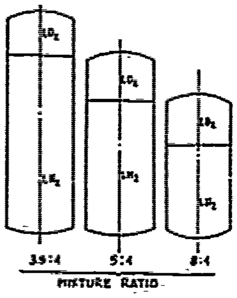
LO₂
LH₂
LO₂
LH₂
LO₂
LH₂
3.5:1
5:1
6:1
MIXTURE RATIO

Fig. 2 - Comparison between tank sizes for different mixture ratios.

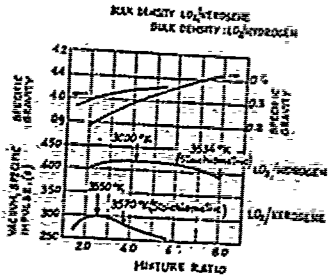

Fig. 3 - Dependence of mean bulk density and vacuum specific impulse on mixture ratio.

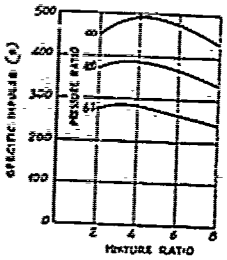

Fig. 4 - The best oxygen/fuel ratio in respect to specific impulse.

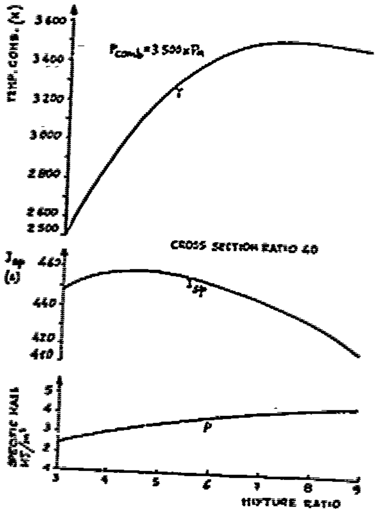

Fig. 5 - Performance of oxygen-hydrogen propellant as function of mixture ratios.

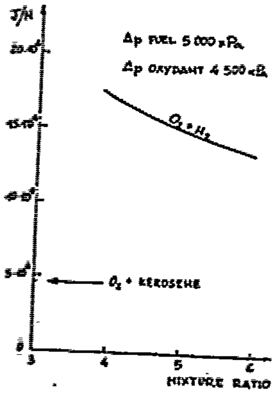

Fig. 6 - Comparison of specific pumping work of propellants.

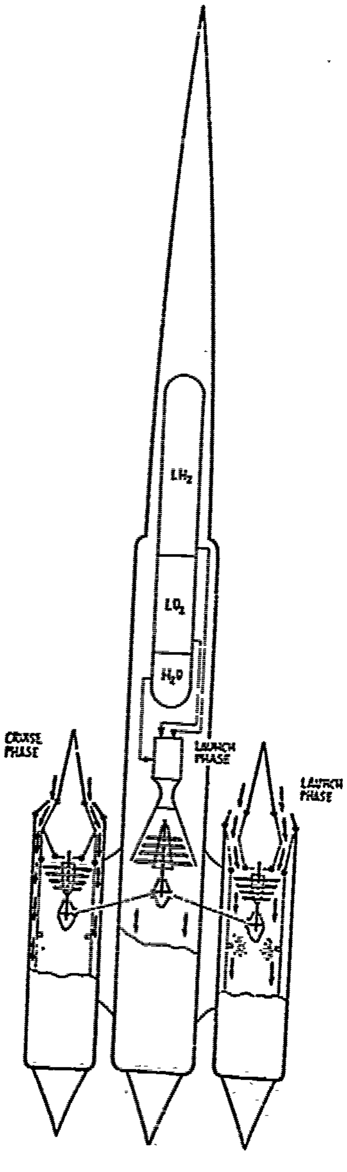
LH_2
LO_2
H_2O
CRUISE PHASE
LAUNCH PHASE
LAUNCH PHASE

Fig. 7 - Proposed hydrogen fueled turbo-ramjet-rocket.

DISCUSSION

R.Lo

I think Peter Kramer of the University of Stuttgart should comment on the overall idea of this type of turborocket ramjet. I would like to make a comment and ask a question concerning the injection of water into the hydrogen and oxygen rocket combustor. We are doing precisely this at my institute in DFVLR which we called a hydrogen-oxygen steam generator for push button demand electrical power generation. The problem of getting high droplet evaporation efficiency becomes more difficult as you try to inject water into very high temperature systems as you proposed. Any droplets remaining would damage the turborocket machinery which is in the wake of the steam generator. Why did you suggest 2000° K in your studies? Were you proposing to use ceramic blades or what?

Author's Reply

This idea came out of what you suggested as a stationary steam plant. A 2000° K temperature we can now potentially achieve with transpiration cooling of the blades for a short period of time. The problem is to inject water in a small volume. The problem is for a stationary power plant, but we may apply it to a rocket too.

P.Kramer

You wanted to reach Mach 3.7 within 7 seconds? What acceleration did you have?

Author's Reply

I don't know the number, but normally in designing a missile, the acceleration phase gives an altitude from 0 to 10,000 metres and takes about 40 seconds. In order to get there in 7 seconds, the acceleration would be too high.

Comment by P.Kramer

The turbomachinery will not survive.

Author's Reply

I took a temperature of 2000° K. This was used as a numerical example to put forth the idea. The 7 seconds is too high an acceleration.

P.Kramer

Did you compare it with a pure rocket booster instead of a turborocket booster? You know we are doing similar studies for Space Applications, and we found that the pure rocket booster balances out the weight disadvantages of the turborocket, so we came out with the same payload without the turborocket, but with the pure simple rocket. The turborocket saves fuel, but doesn't improve payload. That was our result.

Author's Reply

We need to study this more completely, but the main purpose of this kind of propulsion system is to improve the propellant efficiency. From a payload consideration, you are probably right.

27-1

THE ROLE OF LIQUID PHASE DROPLET DECOMPOSITION IN AN ADVANCED AIRBREATHING PROPULSION SYSTEM*

Melvin Gerstein and P. Roy Choudhury
Mechanical Engineering Department
University of Southern California
Los Angeles, California 90007

ABSTRACT

It has been observed that when a fuel droplet evaporates in a high pressure environment typical of an advanced ramjet the usual linear D^2 -t relationship does not hold. There is a strong evidence that at higher pressures, liquid phase decomposition is responsible for the sudden break in the relationship. The products of decomposition leave a tarry residue which is practically nonvolatile and burns only very slowly.

The present paper deals with the coupled effect of decomposition and evaporation of a typical fuel spray.

The results of this study show that droplet decomposition at higher pressure for both pure and commercial fuel blends has a significant influence on the combustion efficiency, carbon build-up on the walls of the combustion chamber and the possible formation of pollutants and particulate matter in the exhaust.

INTRODUCTION

Recent attempts to increase the combustion efficiency and performance of an advanced ramjet engine are primarily focused on the introduction of swirl in the flow field, use of better flame holders and various other novel design changes, such as the concept of vortex amplification by means of gas jets (Ref. 1). Although spray characteristics, evaporation and burning of fuel droplets are being investigated, the problem of possible liquid phase decomposition of the fuel has not received much attention. The existence of the liquid phase decomposition at higher pressures (Ref. 2) and its influence on the burner performance have been reported earlier by the authors (Ref. 3) using a single droplet as an example.

The coupled effect of evaporation and decomposition of a hexadecane spray with a realistic drop size distribution in a one dimensional flow field is reported in this paper. Results show that liquid phase decomposition at higher pressures might cause a substantial reduction of combustion efficiency of an advanced air breathing propulsion system.

ANALYSIS

In order to determine the effect of droplet decomposition and residue formation on the overall performance of a combustor the history of a hexadecane spray with a realistic drop size distribution has been chosen as an example. The fuel is assumed to be sprayed in a 600K, 4 atm. air stream travelling with a velocity of 50 m/s. The gas flow is assumed to be steady and one-dimensional with constant thermochemical properties. The distribution of drop size typical of an airblast atomizer was assumed to follow the data shown in Reference (4). The percent of the total population occupied by each subgroup with a given mean subgroup diameter is listed in Table 1. Hexadecane spray was assumed to follow this distribution.

TABLE 1

DISTRIBUTION OF MEAN SUBGROUP DIAMETERS

Percent Population	Mean Diameter of Subgroup (micron)	Percent Population	Mean Diameter of Subgroup (micron)
15	20	17	60
24	30	12	80
27	40	5	100

Coupled phenomena of evaporation/decomposition of the mean diameter of each subgroup were analyzed neglecting interparticular interaction between different subgroups. In other words, collision between droplets, shattering and their coalescence were ignored.

The following equations apply for the evaporation/decomposition of a droplet in a one-dimensional gas stream:

x-momentum:

$$\frac{du}{dt} = \frac{18\mu_g}{\rho_\ell} \frac{u_g - u}{D^2} \tag{1}$$

---

*Supported by an AFOSR Grant 77-3354

Droplet evaporation rate:

$$\frac{dD^2}{dt} = -\beta_o (1 + 0.3\, Re^{0.5} Pr^{0.3}) \qquad (2)$$

Rate of solid residue formation:

$$\frac{dC}{dt} = 4F\, (1-C)^2\, C_{s_o}\, \exp\, (-E/RT) - \frac{3}{2}\frac{C}{D^2}\frac{dD^2}{dt} \qquad (3)$$

Saturation temperature of an ideal mixture of a soluble residue and liquid fuel:

$$\frac{1}{T} = \frac{R}{h_{fg}}\, \ln \frac{2(1-C)}{(2-C)} + \frac{1}{T_s} \qquad (4)$$

where: C = concentration of the solid residue/density of pure solid residue
C_{s_o} = density of pure solid residue
D = droplet diameter
E = activation energy (40 kcal/gmole)
F = frequency factor
h_{fg} = enthalpy of evaporation
Pr = Prandtl number
R = gas constant
Re = Reynolds number $\rho_g\, (u_g - u)D/\mu_g$
T = droplet temperature
T_s = saturation temperature of the pure fuel
t = time
u = x component of droplet velocity
u_g = gas velocity
β_o = evaporation constant of the pure fuel
μ_g = viscosity coefficient of the gas
ρ_ℓ = density of the pure fuel

In deriving eqn. (1), Stokes' drag coefficient $C_D = 24/Re$ was assumed. The effect of flow was incorporated in eqn. (2) by using Ranz-Marshall correlation. Equations (3) and (4) are derived in Ref. (2) for a second order decomposition reaction leading to formation of residue which is soluble in the liquid fuel.

The following initial conditions were used for solving eqn. (1) through (4) simultaneously.

$$D(0) = D_o;\; u(0) = 0;\; C(0) = 0;\; T(0) = T_s \qquad (5)$$

When C approaches 1 the droplet consists only of nonvolatile residue and practically no liquid. At this point, evaporation ceases and $\frac{dD^2}{dt}$ approaches 0.

Since the residue burns extremely slowly, very little reduction in diameter is expected even when it enters the combustor.

Equations (1) through (4) with the initial conditions given by eqn. (5) are solved using a Fourth-Order Runge-Kutta scheme for coupled nonlinear ordinary differential equations (Ref. 5). Thermochemical properties of pure hexadecane were obtained from Ref. 6 and the value of evaporation constant $\beta_o = 3.5 \times 10^{-3}$ cm²/sec was estimated from the data of Ref. 7.

RESULTS AND DISCUSSION

Figure 1 shows the behavior of the mean diameter of each subgroup with time when the frequency factor F is assumed to be 10^{18} cm³/gmole-sec. At this value of F there is a strong coupling between evaporation and liquid-phase decomposition. The evaporation of the spray ceases 2 millisec after injection and the form of the initial distribution, now with smaller subgroup diameters remains virtually unchanged after that time. Figure 1 is basically the history of the distribution of droplet diameters if the same group of droplets are followed. Since droplets of different size are accelerated at different rates, the diameter distribution at a given geometric location will not be the same as that for the corresponding time. Figure 2 shows the distribution of the mean diameters of each subgroup at various physical locations. The spray ceases to evaporate only 1.5 cm downstream of the injection point. Once again the strong coupling for $F = 10^{18}$ is responsible for the behavior of the diameter distribution.

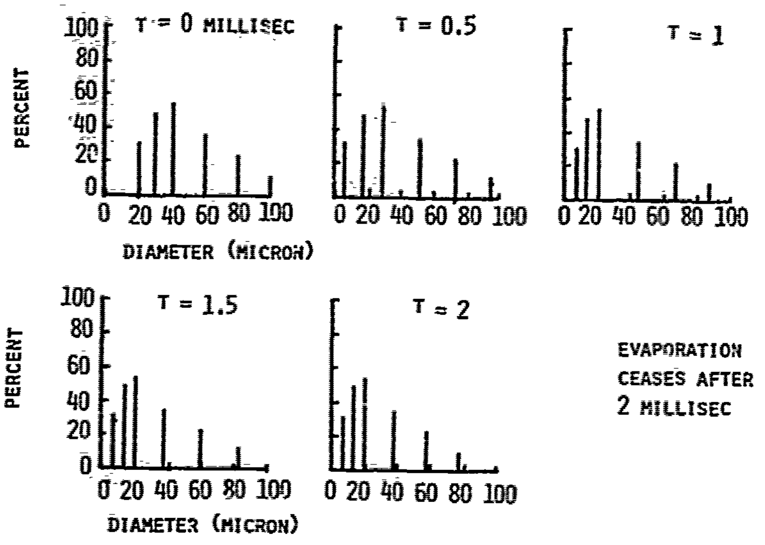

EVAPORATION
CEASES AFTER
2 MILLISEC

Figure 1. History of droplet distribution. Hexadecane spray 50 m/s, 600°K, 4 atm. air stream. $F=10^{18}$ cm^3/gmole-sec

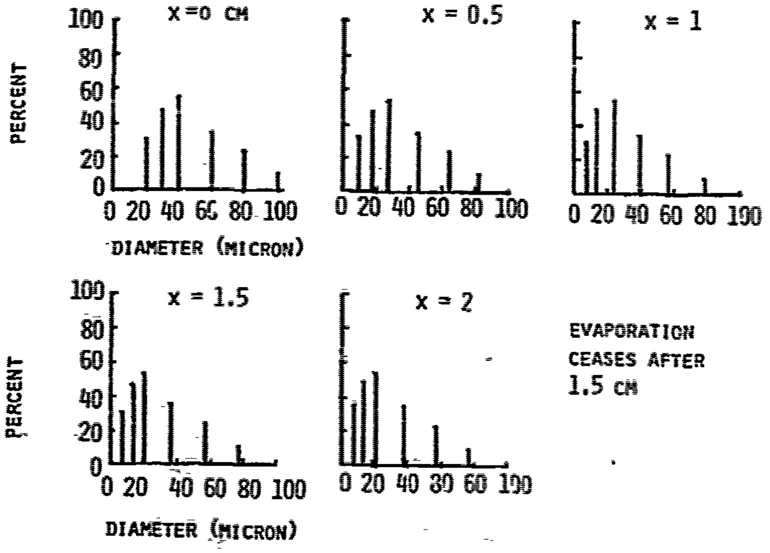

EVAPORATION
CEASES AFTER
1.5 CM

Figure 2. Behavior of hexadecane spray with distance 50 m/s, 600K, 4 atm air stream. $F=10^{18}$ cm^3/gmole-sec.

The details and the mechanism of the liquid-phase decomposition reaction are not known. But the importance of the process of decomposition is illustrated here by choosing two values of F. One causes a strong coupling between evaporation and decomposition and the other allows only a weaker coupling. A value of $F = 10^{15}$ cm3/gmole-sec is chosen for illustrating the second case. As mentioned previously, the decomposition chemistry is not known although pyrolysis studies of hydrocarbons have been the subject of research for many years. It is likely that the liquid phase decomposition processes leading to a char residue may resemble some of the gas phase reactions leading to smoke. The higher liquid density would tend to favor reactions depending on the fuel concentration. On the other hand, the relatively low liquid temperature compared to flame temperature would tend to rule out reactions of high activation energy. It is likely that atomized fuels contain dissolved air so that the influence of oxygen and the existence of oxidative cracking cannot be ignored.

In the work reported in Reference 2, a simple second order reaction was assumed to account for the formation of a solid residue.

$$\frac{dC_s}{dt} = k\, C_F^{\,2} \tag{6}$$

where $k = F \exp(-E/RT)$
C_F = fuel concentration
C_s = concentration of solid residue

It was further assumed that the solid was soluble in the fuel. Under these circumstances the vapor pressure of the fuel decreases with time as more and more solid is dissolved. The drop temperature increases leading to accelerated decomposition.

More recent work suggests that insoluble solids may form during the decomposition. Under these circumstances, the liquid temperature remains constant at T_s and the exponential nonlinearity of equation (3) does not exist.

Figure 3 shows the behavior of a 100 micron droplet for three different limiting cases. For the case of soluble residue, the residue formation is accelerated by the increase of mixture temperature indicated by eqn. (4). Because of the lower temperature the rate of formation of residue is smaller when the residue does not dissolve in the liquid fuel.

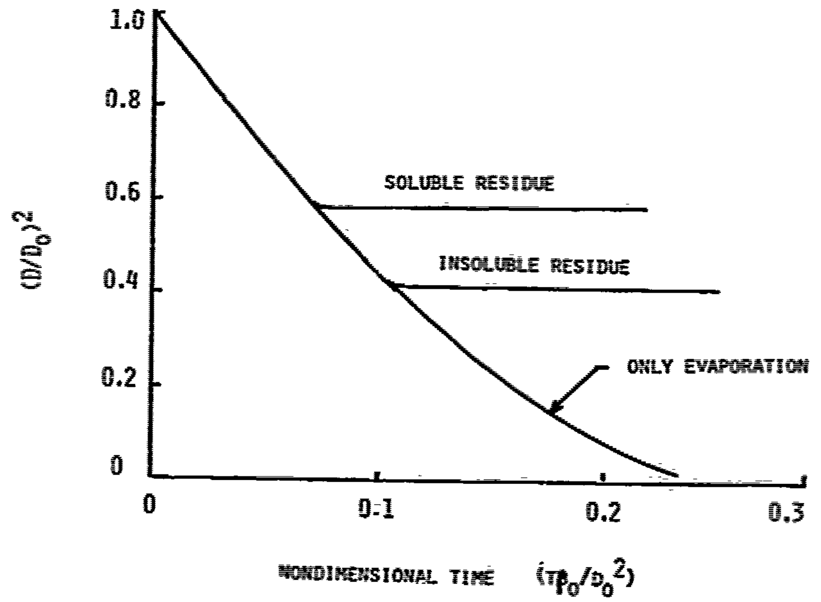

Figure 3. The effect of solubility of residue. 100 micron hexadecane droplet. 50 m/s, 600K, 4 atm air stream. $F=10^{18}$ cm3/gmole-sec.

For smaller characteristic times, the process of evaporation in the presence of forced convection is responsible for the reduction of droplet diameter. The overall behavior of the evaporating drop remains qualitatively the same but the particle growth would be slower for the insoluble char. Since the kinetics are not known, the break in the curve from liquid evaporation to char could still occur at roughly the same time period by adjusting the value of the reaction rateconstant, k. The behavior of the products of decomposition are now under study to evaluate the nature of the product by interrupting the evaporation process to look for soluble and insoluble products and to estimate a global reaction rate. The remainder of calculations in this paper have been made assuming a soluble product according to Reference 2.

Figures 4 and 5 show the distribution of diameters at various locations downstream of the injection point. These calculations are performed for F=10^{15}. At a distance of 5 cm, half of the original six subgroups has completely evaporated. Only one subgroup remains at 12 cm. Evaporation still continue at this point. Finally, the evaporation ceases completely at 14 cm and residues with a mean diameter of 6.7 micron remain in the flow field. Since most of the spray has already evaporated at this location, such a weak coupling is not expected to have a major impact on the performance of a ramjet combustor.

Although ramjets do not use pure hexadecane as fuel it is used here to illustrate a potential problem area which can have a major impact on the combustion efficiency, carbon deposit and particulate emission. Particulate emission as a source of pollution is not important in ramjets but depending upon the amount of emission it can reduce the combustion efficiency of a burner. Commercial fuel blends and future synthetic fuels such as shale oil are more susceptible to liquid-phase decomposition than pure fuels. Thus, the example of hexadecane shows a conservative estimate of the nature of the problem.

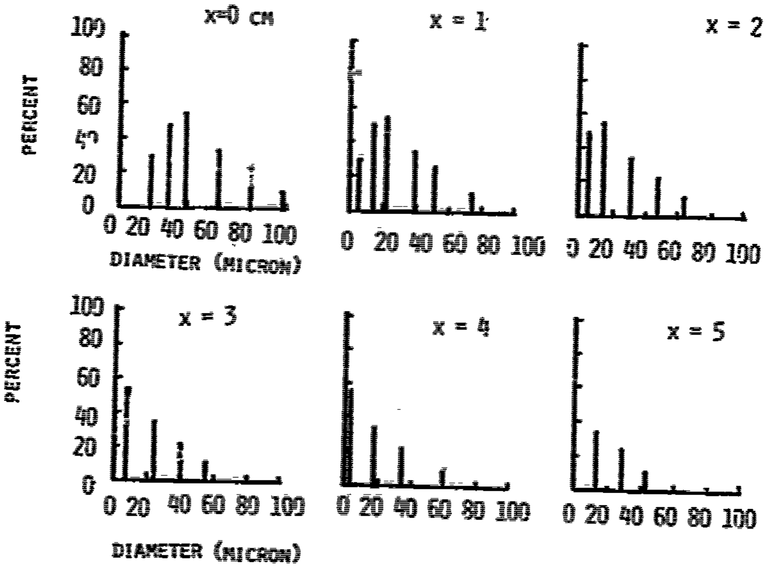

Figure 4. Diameter distribution of hexadecane spray at various locations. 50/ms, 600K, 4 atm air stream. F=10^{15} cm^3/gmole-sec.

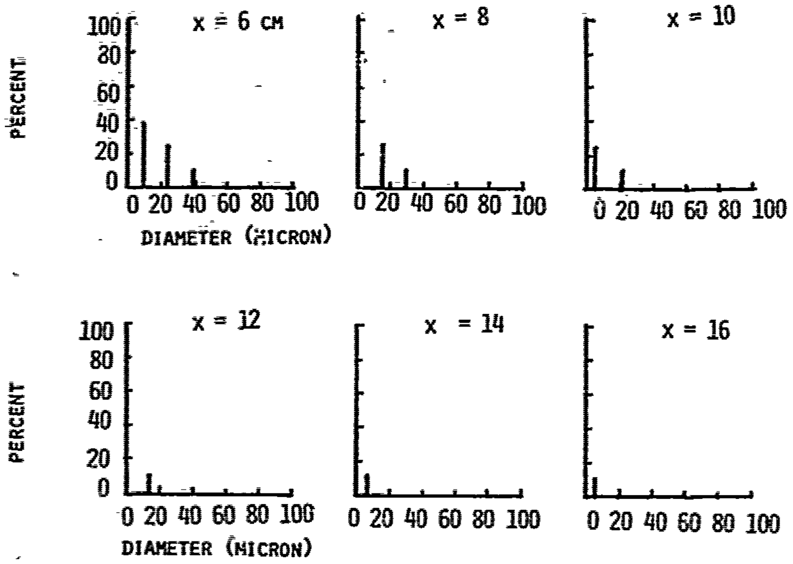

Figure 5. Diameter distribution of hexadecane spray at various locations. 50 m/s, 600K, 4 atm air stream. $F=10^{15}$ cm^3/gmole-sec.

The fluid mechanics has been simplified here by assuming a one-dimensional flow with constant gas properties. While this is not entirely correct in a ramjet environment, problems associated with liquid-phase decomposition are just as critical in a one-dimensional flow as in multidimensional flow systems. In a two-dimensional flow field and also with swirl the nonvolatile residue is expected to impinge on the walls of the chamber and cause deposits (Ref. 8). Residue particles which shatter at the wall on impact might contribute to the population of smaller particulate matter in the exhaust.

Figure 6 shows the percent of original mass of the spray that remains unevaporated at any given location downstream of the injection point. For the case of a strong coupling ($F=10^{18}$ cm^3/gmole-sec) roughly 34% of the original mass remains unevaporated. Thus, for this particular case the combustion efficiency might not exceed 66% because only 66% of the original mass of fuel is able to evaporate. The non-volatile residue particles burn very slowly. Reference 8 shows that for a typical burner with a given characteristic length, the reduction of diameter of these particles due to burning is not very significant.

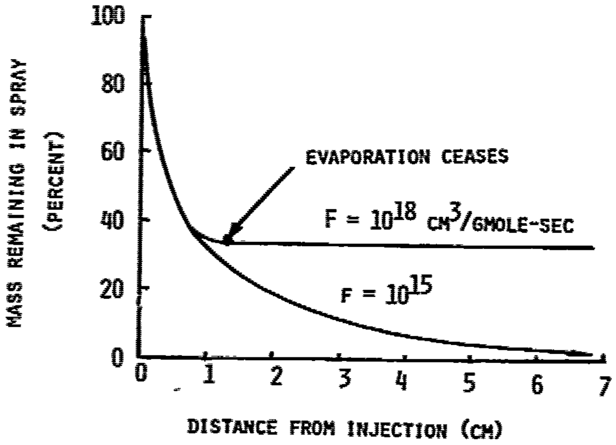

Figure 6. Mass remaining in hexadecane spray. 50 m/s, 600K, 4 atm air stream.

For the case of F=10^{15} cm^3/gmole-sec, the coupling between evaporation and decomposition is rather weak. The entire spray evaporates nearly completely before residues are formed. For this case, an ideal combustion efficiency of nearly 100% might be expected. Figure 7 is a plot of the possible ideal combustion efficiency based upon the amount of fuel actually evaporated. It is plotted from Fig. 6 and shows the combustion efficiency as a function of the characteristic length available for evaporation. When decomposition rate is faster than the evaporation rate, as in the case of F=10^{18}, an increase in the characteristic length would not change the burner performance significantly. The maximum possible combustion efficiency as a function of the frequency factor is shown in Fig. 8. It focuses attention on the importance of liquid phase decomposition in a burner with no restriction on the allowable characteristic length.

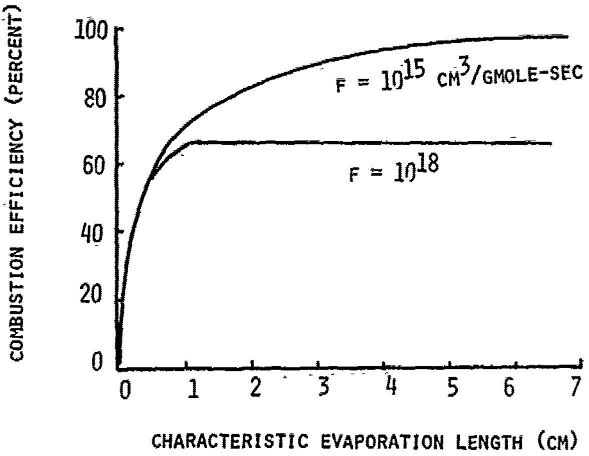

Figure 7. Combustion efficiency as a function of the characteristic evaporation length.

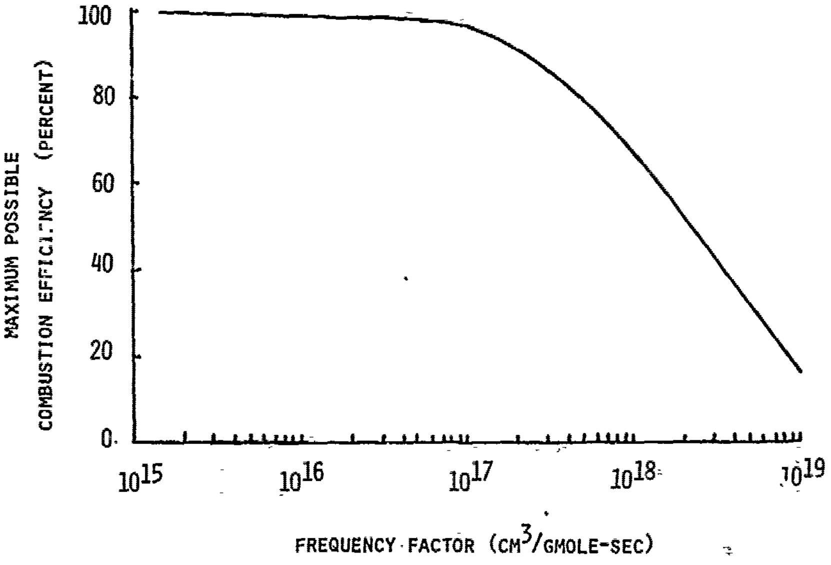

Figure 8. Maximum possible combustion efficiency with liquid phase decomposition.

REFERENCES

1. Choudhury, P. Roy, "Scaling and Performance of Dump Combustors with Transverse Gas Jets", AIAA Journal, Vol. 18, April 1980, pp. 450-454.

2. Farhangi, S., "Evaporation of Fuel Drops on a Hot Surface Considering Liquid Phase Decomposition," Ph.D. Dissertation, University of Southern California, Los Angeles, 1979.

3. Gerstein, M., and Choudhury, P.Roy, "Reduction of Combustion Efficiency Associated with Liquid Phase Drop Decomposition", 16th JANNAF Combustion Meeting, Naval Post-Graduate School, Monterey, Ca, Sept. 1979, Chemical Propulsion Information Agency Publication 308, Vol. II, Dec. 1979, pp. 557-568.

4. Lefebvre, Arthur H., "Airblast Atomization," Prog. Energy Combst. Sci, Vol. 6 pp. 233-261, (Fig. 34). Pergamon Press, 1980.

5. Carnahan, B., Luther, H.A., and Wilkes, J., "Applied Numerical Methods," John Wiley and Sons, 1969.

6. Obert, E.F., "Internal Combustion Engines and Air Pollution," Intext Educational Publishers, New York, 1968.

7. Mansour, M., "The Vaporization Behavior of a Fuel Drop on a Hot Surface," Ph.D. Dissertation, University of Southern California, Los Angeles, June 1977.

8. Gerstein, M. and Choudhury, P.Roy, "Liquid Phase Decomposition: A Possible Problem with Fuels in High Pressure Systems," Proceedings of the 1980 Heat Transfer and Fluid Mechanics Institute, Stanford University Press, pp. 79-91.

DISCUSSION

R.Monti

I think that the "sudden freezing" kind of model introduced by the authors is valuable and very proper as a first approach to the problem. However, I think that a more accurate model should take into account the thickness of the layer of decomposed liquid and relate it to the evaporation rate.

Author's Reply

The question raised by Professor Monti is very valid. Our model assumes that the entire droplet undergoes decomposition as a unit. There is no evidence that such a so called "sudden freezing" actually occurs. Preliminary observation shows that the droplet gradually becomes darker as the evaporation progresses. This might be due to a "surface effect" as Professor Monti suggests, or it might be due to uniformly distributed nuclei of insoluble residue species suspended in the liquid phase. At the present time. we are attempting to interrupt the evaporation process to determine the chemical composition as well as the nature of the products of decomposition. We are hoping that by the end of this academic year, we will be able to resolve whether a thin layer of decomposition product or a large number of dispersed insoluble nuclei exist. Only then a better and more appropriate model can be proposed.

The purpose of this paper was to point out the potential problem areas associated with droplet decomposition particularly for synthetic fuel and blended fuels. We thank Professor Monti for his kind words.

E.Warne

(a) Could the authors explain the apparent conflict between Figure 1 and Figure 2 in relation to the time to reach the cessation of evaporation. For example, 2 ms in Figure 1 and 0.4 ms in Figure 2 (2 cm at 50 m/s).

(b) What work was carried out to study heat transfer to the droplet since this is a vital component of the evaporation scene?

Author's Reply

(a) Actually, there isn't a conflict. The particles have zero initial velocity and they are accelerated to the gas velocity after a long period of time depending upon their diameter. After say 2 ms, they have not attained the gas velocity except, perhaps, the droplets with diameters under 5 microns. Also, the evaporation/decomposition rate is diameter dependent. The time and locations shown in Figures 1 and 2 appear to be consistent. Perhaps during my talk, I did not stress enough upon the momentum equation showing Stokes' drag and the velocity difference between the particles and gas.

(b) Detailed study of heat transfer to the droplet was carried out by Farhangi, a graduate student of USC. (Please see Reference in back of the paper.) In the present paper, the experimentally determined evaporation constant β_0 includes all the effect due to heat transfer. In order not to confuse the central issue of droplet decomposition, we have used the experimentally determined β_0 rather than the effect of conduction, convection and radiation heat transfer on the droplet. Thus, implicitly our study includes the effect of heat transfer.

COMBUSTOR MODELING FOR RAMJET DEVELOPMENT PROGRAMS

P. T. Harsha, R. B. Edelman, S. N. Schmotolocha* and R. J. Pederson*
Science Applications, Inc.
Combustion Science and Advanced Technology Department
21133 Victory Boulevard
Canoga Park, California 91303
US

SUMMARY

The development and application of a modular model for the prediction of the performance of sudden-expansion burners is described. This model is based on a concept in which the recirculation zone, treated as a stirred reactor, is coupled to a parabolic boundary layer formulation for the flow outside the recirculation zone. Hydrocarbon oxidation kinetics and turbulent kinetic energy turbulence models are included. In addition to the parabolic-flow and stirred reactor elements, a module representing the fuel injection process has been developed. Results of the application of the modular model to the analysis of cold-flow and reacting-flow dump combustor experimental data are described, and the use of the model as an interpretative tool in a recent ramjet combustor development program is outlined.

1. INTRODUCTION

Control of flame stabilization and flame propagation in a turbulent flow represents a key element in combustion chamber design. The placement and geometry of fuel injectors, flameholders, and air distribution ports are basic design parameters that govern the performance of a particular combustor. Therefore it is desirable to compute combustion chamber flowfields in order to understand the phenomena that occur in existing combustors and to predict the performance of new combustor concepts. Modeling can also be used to analyze the behavior of flameholders and fuel injectors under a variety of conditions. The insight gained through the use of these "unit" analyses can be of substantial use in the planning of a combustor test program and in the interpretation of combustor and combustor component test data. However, the computation of a generalized combustor flowfield is a formidable task, involving a number of complex coupled physical and chemical processes, which can include turbulent, recirculating flow, possibly with swirl, finite-rate chemical kinetics, and droplet evaporation and combustion. The obvious difficulties include not only the multitude of coupled mechanisms but also involve the typical disparity in characteristic length and time scales in combustion chamber flows. Despite these problems, considerable progress has been made in recent years in the development of calculation methods, using techniques for the solution of the elliptic governing equations and simpler yet physically perceptive "modular" modeling techniques.

A "unified" model of a combustion chamber flowfield in general requires the numerical solution of the elliptic form of the governing equations: Most practical combustion chamber flows involve large regions of recirculation in which axial diffusion is important. A considerable amount of research effort has been put into the development of numerical techniques for these problems, and successful comparison of calculation with experiment for recirculating flows with large heat release has been reported by Hutchinson, et al. [1] and by Abou Ellail, et al. [2], for example. Significantly, in both cases a careful adaptation of the numerical model to the specific experimental configuration was reported to be required, and in both of these papers it was noted that the details of the computation required careful handling to obtain the accuracy demonstrated. Furthermore, Abou Ellail, et al. [2] note that it is not possible to provide sufficient resolution in a detailed combustor flowfield computation to adequately describe processes, such as fuel injection, in which mixing initially occurs on a scale much smaller than that of the overall combustion chamber. Thus, while the development of numerical models capable of providing direct solution of the equations governing specific combustion chamber flowfields continues, a need exists for the development of physically perceptive yet mathematically simpler models. This requirement arises from the need to provide a model which allows reasonably rapid computation of a number of different, complex combustor geometries, and the need to develop models for those processes, such as fuel injection, which occur on scales smaller than can be adequately resolved in a detailed overall flowfield computation. The development of approximate methods - modular models - is a response to the requirements just outlined.

The basic interest in the application of approximate techniques is to avoid the complexities inherent in a direct calculation of a complex flowfield by making suitable assumptions that allow the flow to be computed using simpler approaches. Clearly the simplest possible procedure is to assume that the flowfield is effectively one-dimensional thus avoiding any necessity for definition or calculation of velocity or species profile effects. A somewhat more sophisticated approach is to assume that the combustor flowfield can be broken down into separate zones, each of which can be calculated individually in some detail, and then coupled together in some fashion to obtain an overall computational analog of the combustor flow. Such approaches are termed modular models, examples of which have been reported by Roberts, et al. [3] and Swithenbank, et al. [4]; the formulation described in this paper, while similar in that the overall combustor flowfield is broken down into computational subunits, provides far more detail than either of the former models.

---

* Formerly with Chemical Systems Division, United Technologies Corp., Sunnyvale, Calif.

In the present approach, the combustor flowfield, represented schematically in Figure 1, is broken down into three major components: a directed flow, which is treated as parabolic; a recirculation zone, assumed to be represented by well-stirred reactor(s); and a turbulent shear layer along the dividing streamline which separates the other two regions. The shear layer serves as the coupling region between the other two model components; fluxes of species and energy across this shear layer form the boundary conditions on the two computational regions. Finite-rate chemistry, based on the quasiglobal model [5] can be included in the formulations for both the directed flow and well-stirred reactor regions, although for the modular model calculations described in this report, the recirculation region well-stirred reactor formulation has been restricted to a global finite-rate chemistry model. The directed flow is assumed to be fully turbulent, with the turbulent viscosity defined by a two-equation turbulence model [6]. A key difference between this modular model and the models of Roberts, et al. [3] and Swithenbank, et al. [4] is the provision for the shear layer coupling region in the current model. Through the use of this element of the model, the division of the mass flux between the directed flow and the recirculation region is computed iteratively rather than specified empirically. Furthermore, the directed-flow region is computed in detail as a two-dimensional parabolic flowfield, rather than through a one-dimensional approximation, allowing the use of detailed computations of the mixing and chemical reactions in this region of the combustor.

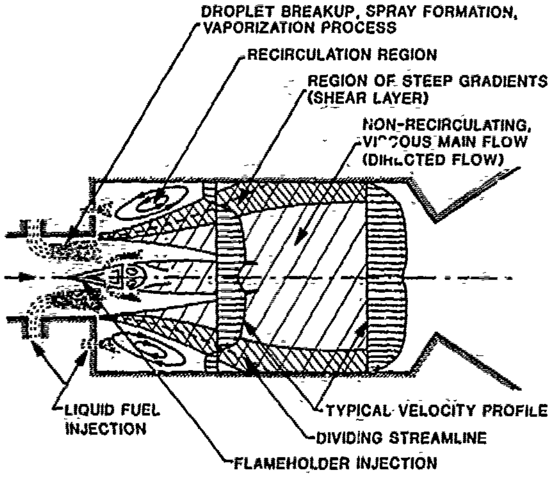
DROPLET BREAKUP, SPRAY FORMATION, VAPORIZATION PROCESS
RECIRCULATION REGION
REGION OF STEEP GRADIENTS (SHEAR LAYER)
NON-RECIRCULATING, VISCOUS MAIN FLOW (DIRECTED FLOW)
LIQUID FUEL INJECTION
TYPICAL VELOCITY PROFILE
DIVIDING STREAMLINE
FLAMEHOLDER INJECTION

FIGURE 1. Schematic of Sudden-Expansion (Dump) Burner

In this paper, the development of the modular model for a sudden-expansion combustor is described in detail. The model formulation, including the definition of coupling conditions and a description of the overall flowfield iteration procedure, is described in Section 2. Results of the application of the approach to the computation of a variety of sudden-expansion flowfields are described in Section 3; where the capabilities of this approach and current unified elliptic formulations overlap, such as in the computation of incompressible sudden-expansion flows, the results of the modular approach are compared with both available experimental data and unified model computational results. This is followed by a discussion of the use of the model as an interpretative tool in a current ramjet combustor development program. The description of this application focuses on the use of the model as a tool for the assessment of the causes of low performance encountered under some situations during the early phases of a combustor test program. This investigation led to recommendations and subsequent alterations in test variables, which resulted in improved performance in the second test phase. Overall conclusions reached from the work discussed in this paper are described in Section 5. The work described in this paper shows that there are considerable advantages to be gained from the use of analytical models as interpretative techniques and planning guides in conjunction with experimental combustor development programs.

2. MODULAR MODEL FORMULATION

The basic elements of the modular model formulation are a parabolic finite-difference computational technique [7], used for the directed-flow portion of the analysis, and a stirred reactor computation which represents large-scale recirculation regions. These elements, or modules, are coupled together through a simplified representation of the turbulent shear layer which exists between the directed flow and the recirculation region. In the modular approach, the shear layer representation is used to define the gradients in velocity, species, and enthalpy between the two regions of the flow, thus providing both the boundary conditions on the directed flow and the stirred reactor feed rates.

2.1 WELL-STIRRED REACTOR - THE RECIRCULATION ZONE MODEL

Flowfield regions in which intense backmixing occurs can approach the limit of complete mixing, and thus the well-stirred reactor concept is attractive for representing the recirculation regions in a sudden-expansion burner. For a well-stirred reactor, the equations describing the transport of energy and species reduce to the relations

Continuity

$$\dot{m}^I = \dot{m}^O = \dot{m} \tag{1}$$

Species

$$\frac{dM\alpha_i}{dt} = \dot{m}_i^I + V\dot{w}_i \tag{2}$$

Energy

$$h = \sum_i h_i\alpha_i = h^I + \dot{Q}/\dot{m} \tag{3}$$

where the superscripts I and O represent inflow to and outflow from the stirred reactor, M the mass contained within the stirred reactor, the α_i are the mass fractions of the i species in the reactor, $\dot{m}_i^I$ is the net inflow of species i, V is the reactor volume, $\dot{w}_i$ the volumetric production rate for species i due to chemical reaction, h the enthalpy, and $\dot{Q}$ the rate of heat addition to the reactor from its surroundings. Note that in this set of equations the species transport equation is written in non-steady form. This formulation has been adopted to facilitate solution of the stirred reactor governing equations with finite-rate chemical kinetics; the steady-state stirred reactor solution is obtained when $d\alpha_i/dt \to 0$.

Equations (1)-(3), along with expressions for the volumetric species production rates for the enthalpy as a function of species concentrations, and the equation of state, define the temperature and species concentrations in the stirred reactor, given the inflow rates for species and enthalpy. In the modular model, the net inflow of species and enthalpy can each be expressed as a line integral involving gradients evaluated along the dividing streamline, so that for the modular model the energy and species conservation equations for the stirred reactor can be written

Energy

$$-2\pi \int_0^s R_c(x)\rho\nu_T \sum \left[h_i^I(T^I)\,\frac{\partial\alpha_i^I}{\partial r}\right] ds + \dot{Q} - 2\pi \int_0^s R_c(x)\kappa\,\frac{\partial T}{\partial s}\,ds$$

$$= 2\pi \int_0^s R_c(x)\rho\nu_T \sum_i \left[h_i^O(T_R)\,\frac{\partial\alpha_i^O}{\partial r}\right] ds \tag{4}$$

where $R_c(x)$ represents the radial location of the dividing streamline, and

Species

$$\frac{d\alpha_i}{dt} = \frac{-2\pi}{\rho_c V}\int_0^s R_c(x)\left[\rho\nu_T\,\frac{\partial\alpha_i^I}{\partial r}\right] ds - \frac{2\pi}{\rho_c V}\int_0^s R_c(x)\left[\rho\nu_T\,\frac{\partial\alpha_i^O}{\partial r}\right] ds + \frac{\dot{w}_i}{\rho_c} \tag{5}$$

Here ρ_c represents a characteristic density of the stirred reactor region, and $\rho\nu_T$ a characteristic eddy diffusivity, evaluated from the outer flowfield solution in the region of the dividing streamline.

2.2 PARABOLIC MIXING: THE DIRECTED-FLOW MODEL

The second major element of the modular model for a sudden-expansion combustor is the formulation for the directed flow portion of the combustor flowfield. It is assumed that the boundary layer approximations apply to this part of the flowfield, so that the describing equations are parabolic. For a steady, axisymmetric flow these equations may be written:

Global Continuity

$$\frac{\partial r\rho u}{\partial x} + \frac{\partial r\rho v}{\partial r} = 0 \tag{6}$$

Species Diffusion for the ith Specie

$$\rho u \frac{\partial \alpha_i}{\partial x} + \rho v \frac{\partial \alpha_i}{\partial r} = \frac{1}{r} \frac{\partial}{\partial r} \left\{ r\rho \frac{\nu_T}{Sc} \left[\frac{\partial \alpha_i}{\partial r} \right] \right\} + \dot{w}_i \tag{7}$$

Momentum Equation

$$\rho u \frac{\partial u}{\partial x} + \rho v \frac{\partial u}{\partial r} = \frac{1}{r} \left\{ \frac{\partial}{\partial r} \left(r\rho\nu_T \frac{\partial u}{\partial r} \right) \right\} - \frac{\partial p}{\partial x} \tag{8}$$

and the

Energy Equation

$$\rho u \frac{\partial H}{\partial x} + \rho v \frac{\partial H}{\partial r} = \frac{1}{r} \frac{\partial}{\partial r} \left\{ \frac{r\rho\nu_T}{Pr} \left[\frac{\partial H}{\partial r} - \left(\frac{Pr}{Sc} - 1 \right) \sum_i h_i \frac{\partial \alpha_i}{\partial r} + (Pr - 1) \frac{\partial}{\partial r} \left(\frac{u^2}{2} \right) \right] \right\} \tag{9}$$

in which Pr and Sc represent the Prandtl and Schmidt numbers, respectively. These equations, along with expressions for the enthalpy

$$H = h + \frac{u^2}{2} \text{ and } h = \sum_i \alpha_i h_i(T) \tag{10}$$

and the equation of state

$$p = \rho RT \sum_i (\alpha_i / W_i) \tag{11}$$

can be solved, given an expression for the turbulent eddy viscosity $\mu_T = \rho\nu_T$. In the present formulation, this is defined by the two-equation turbulent kinetic energy model [6], in which transport equations are written for the turbulent kinetic energy, k, and its dissipation rate, ε. In boundary layer form, these equations can be written:

Turbulent Kinetic Energy

$$\rho u \frac{\partial k}{\partial x} + \rho v \frac{\partial k}{\partial r} = \frac{1}{r} \frac{\partial}{\partial r} \left(\frac{\mu_T r}{\sigma_k} \frac{\partial k}{\partial r} \right) + \mu_T \left(\frac{\partial u}{\partial r} \right)^2 - \rho\varepsilon \tag{12}$$

Turbulence Energy Dissipation

$$\rho u \frac{\partial \varepsilon}{\partial x} + \rho v \frac{\partial \varepsilon}{\partial r} = \frac{1}{r} \frac{\partial}{\partial r} \left(\frac{\mu_T r}{\sigma_\varepsilon} \frac{\partial \varepsilon}{\partial r} \right) + C_{E1} \frac{\varepsilon}{k} \mu_T \left(\frac{\partial u}{\partial r} \right)^2 - C_{E2} \rho \frac{\varepsilon^2}{k} \tag{13}$$

where $\mu_T = C_\mu \rho k^2/\varepsilon$. The turbulence energy dissipation rate, ε, can be related to a turbulent scale, ℓ_k, through the Kolmogorov hypothesis $\varepsilon \propto k^{3/2}/\ell_k$ so that the transport equation for turbulence energy dissipation can also be regarded as a description of the spatial variation of the turbulent length scale.

2.3 CHEMICAL KINETICS: THE QUASIGLOBAL MODEL

In both the stirred reactor and directed flow portions of the modular model volumetric chemical kinetic production rate terms appear in the species transport equations. These terms can be evaluated using a full hydrocarbon chemical kinetics scheme based on the quasiglobal kinetics model [5], which has as a key element a subglobal oxidation step

$$C_nH_m + \frac{n}{2} O_2 \rightarrow \frac{m}{2} H_2 + nCO \tag{14}$$

This reaction is unidirectional with an empirically determined rate (grams of fuel/cc/sec) given by

$$\frac{d[C]_{C_nH_m}}{dt} = A\, T^b\, P^{0.3}\, [C_nH_m]^{1/2}\, [O_2]\, \exp\,[-E/RT] \tag{15}$$

with the constants, A, b, and E/R defined in Table 1, where P must be given in atmospheres, T in degrees Kelvin and [] denotes molar concentration; coupled to this subglobal step are the intermediate reversible reactions also given in Table 1.

2.4 MODELS FOR THE FUEL INJECTION PROCESS

In addition to the basic components of a parabolic, directed flow analysis and a well-stirred reactor formulation, the modular concept can be extended to include other elements of the dump combustor flowfield, for example, the fuel injection process. The detail of the computation provided by the use of a parabolic directed flow analysis is the

TABLE 1. Extended C-H-O Chemical Kinetic Reaction Mechanism

$$k_f = AT^b \exp(-E/RT)$$

REACTION	A	b FORWARD	E/R
1) $C_nH_m + \frac{n}{2}O_2 \rightarrow \frac{m}{2}H_2 + nCO$	A. Long Chain 6.0×10^4 B. Cyclic 2.08×10^7	1 1	12.2×10^3 19.65×10^3
2) $CO + OH = H + CO_2$	5.6×10^{11}	0	0.543×10^3
3) $CO + O_2 = CO_2 + O$	3.0×10^{12}	0	25.0×10^3
4) $CO + O + M = CO_2 + M$	1.8×10^{19}	-1	2.0×10^3
5) $H_2 + O_2 = OH + OH$	1.7×10^{13}	0	24.7×10^3
6) $OH + H_2 = H_2O + H$	2.19×10^{13}	0	2.59×10^3
7) $OH + OH = O + H_2O$	5.75×10^{12}	0	0.393×10^3
8) $O + H_2 = H + OH$	1.74×10^{13}	0	4.75×10^3
9) $H + O_2 = O + OH$	2.24×10^{14}	0	8.45×10^3
10) $M + O + H = OH + M$	1.0×10^{16}	0	0
11) $M + O + O = O_2 + M$	9.38×10^{14}	0	0
12) $M + H + H = H_2 + M$	5.0×10^{15}	0	0
13) $M + H + OH = H_2O + M$	1.0×10^{17}	0	0
14) $O + N_2 = N + NO$	1.36×10^{14}	0	3.775×10^4
15) $N_2 + O_2 = N + NO_2$	2.7×10^{14}	-1	6.06×10^4
16) $N_2 + O_2 = NO + NO$	9.1×10^{24}	-2.5	6.46×10^4
17) $NO + NO = N + NO_2$	1.0×10^{10}	0	4.43×10^4
18) $NO + O = O_2 + N$	1.55×10^9	1	1.945×10^4
19) $M + NO = O + N + M$	2.27×10^{17}	-0.5	7.49×10^4
20) $M + NO_2 = O + NO + M$	1.1×10^{16}	0	3.30×10^4
21) $M + NO_2 = O_2 + N + M$	6.0×10^{14}	-1.5	5.26×10^4
22) $NO + O_2 = NO_2 + O$	1.0×10^{12}	0	2.29×10^4
23) $N + OH = NO + H$	4.0×10^{13}	0	0
24) $H + NO_2 = NO + OH$	3.0×10^{13}	0	0
25) $CO_2 + N = CO + NO$	2.0×10^{11}	-1/2	4.0×10^3
26) $CO + NO_2 = CO_2 + NO$	2.0×10^{11}	-1/2	2.5×10^3

Reverse reaction rate k_r is obtained from k_f and the equilibrium constant K_c

key feature of the modular model that allows the inclusion of a fuel injection module. This is particularly true in the case of liquid fuel injection, for at the fuel/air ratios appropriate for ramjet combustor operation, the liquid fuel streams initially occupy a very small portion of the overall combustor cross-sectional area. The liquid fuel injection model makes use of a combination of empirical information and turbulent mixing calculations. For example, the fuel jet penetration from the wall is computed through the use of an empirical penetration correlation [8], using a breakup time correlation [9] to estimate the downstream distance at which penetration is to be computed. That is, it is assumed that the fuel jet has turned parallel to the airflow at the axial position at which the initial fuel jet has broken up into droplets, as given by the breakup time correlation and the local airflow velocity.

Since the basic modular model formulation involves an axisymmetric flowfield, individual fuel jets cannot be resolved, and it is assumed that the liquid fuel spray forms an annulus whose cross-sectional area may either be specified or computed based on an assumed fuel spray bulk velocity. A bulk spray evaporation correlation is then used to compute the fuel vaporization rate; this correlation [10] is a function of the initial velocity and temperature difference between the fuel spray and the surrounding air stream. Spreading of the fuel jet is computed through use of a turbulent mixing hypothesis as for the mixing process in the remainder of the parabolic flow. Figure 2 shows the results of a computation of the fuel injection process for three fuel injectors, located in the combustor inlet wall, along the centerline, and in a midstream position. Shown are the computed contours of the fuel mass fraction, α_F, with the vapor-phase fuel shown as the solid line and the liquid-phase fuel as the dotted line, as a function of both axial and radial position in the combustor inlet. For these calculations the air inlet velocity was approximately 700 ft/sec at a temperature of 1600°K; the overall fuel/air equivalence ratio was 0.6. The results shown in Figure 2 provide a good example of the detail of the fuel injection process available through use of this aspect of modular modeling.

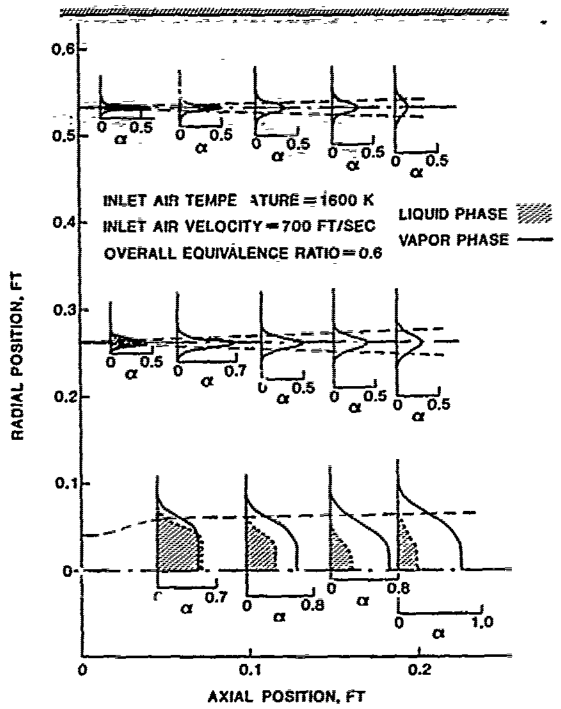

FIGURE 2. Predicted Fuel Mass Fraction Distributions for Simultaneous Injection at Three Radial Locations

2.5 COUPLING RELATIONS AND ITERATION PROCEDURE

The overall logic of the calculation procedure is shown schematically in Figure 3. Inlet conditions can be defined upstream or downstream of the fuel injection station as required; if liquid fuel injection is specified, the penetration and spreading of the liquid fuel jets are computed as described in the preceding section. The computation proceeds to the dump plane in the sudden-expansion combustor, at which point the dependent variables in the flowfield are stored for later use in the recirculation zone iteration procedure.

An initial state for the stirred reactor must be specified in order to begin the iteration procedure. This state is reasonably arbitrary, except that a reacted temperature level must be specified. The shape of the dividing streamline separating the directed flow and the recirculation zone must also be specified, along with the shear stress level, expressed as a "skin friction" coefficient. The initial stirred reactor state, in conjunction with a model for the shear layer between the recirculation zone and the directed flow then defines the boundary conditions for the parabolic directed flow calculation. Directed flow computations are carried out to the axial station at which the end of the recirculation zone has been defined; as part of these computations the diffusive flux of species and energy across the dividing streamline is computed. These fluxes then define a new set of stirred reactor "feed rates", i.e., species and energy fluxes into the recirculation zone region. Convergence of the procedure is defined by the change in the stirred reactor feed rates from iteration to iteration; each species and the energy flux must change less then 0.1% before the convergence criteria are satisfied. If they are not, the species and energy fluxes, and the overall diffusive mass flux and physical recirculation zone volume are used to compute a new stirred reactor state. The pressure required for this computation is taken to be the arithmetic average of the pressures computed as part of the directed flow solution at the beginning and end of the recirculation region. The new stirred reactor state is then used to define new directed flow boundary conditions, and the computation is restarted from the dump station. When convergence is achieved, typically in 3-5 iterations, the combustor calculation is continued to the specified combustor exit station.

In describing the coupling between the stirred reactor and directed flow elements of the model, it is useful, for clarity, to consider a simplified formulation for the stirred reactor, using a global finite-rate kinetics model. In this model, the fuel consumption rate is given by the expression

$$\frac{dC_F}{dt} = -C_F C_{O_2}^{3/2} A \exp(-B/RT) \qquad (16)$$

where the C's have the units (moles/cc/sec), T is in °K, and R is in kcal/mole °K; $A = 3.80 \times 10^{15}$ and $B = 15,600$. Performing the manipulations necessary to recast Eq.(16) in terms of mass fractions, and substituting into Eq.(2), results in a set of simultaneous equations for the active species of the form:

$$\frac{dM\alpha_{O_2}}{dt} = \dot{m}^I_{O_2} - W_{O_2}\alpha_F\alpha_{O_2}^{3/2} V\theta(T) \tag{17}$$

$$\frac{dM\alpha_F}{dt} = \dot{m}^I_p - W_F \frac{\alpha_F\alpha_{O_2}^{3/2}}{(n + m/4)} V\theta(T) \tag{18}$$

$$\frac{dM\alpha_{CO_2}}{dt} = \dot{m}^I_{CO_2} - W_{CO_2}\left(\frac{n}{n + m/4}\right)\alpha_F\alpha_{O_2}^{3/2} V\theta(T) \tag{19}$$

$$\frac{dM\alpha_{H_2O}}{dt} = \dot{m}^I_{H_2O} + W_{H_2O}\left(\frac{m/2}{n + m/4}\right)\alpha_F\alpha_{O_2}^{3/2} V\theta(T) \tag{20}$$

$$\frac{dM\alpha_{N_2}}{dt} = \dot{m}^I_{N_2} \tag{21}$$

where n and m are the carbon and hydrogen atoms in the general fuel molecule C_nH_m, the W's are the molecular weights of the species, and

$$\theta(T) = \rho^{3/2} A \exp(-B/RT)/W_F W_{O_2}^{3/2} \tag{22}$$

Given the specification of the $\dot{m}^I_i$, Eqs.(17-21), along with the perfect gas equation of state and Eq.(3) are solved to obtain the new steady-state values of the active species, i.e., the values obtained when $dM\alpha_i/dt \rightarrow 0$.

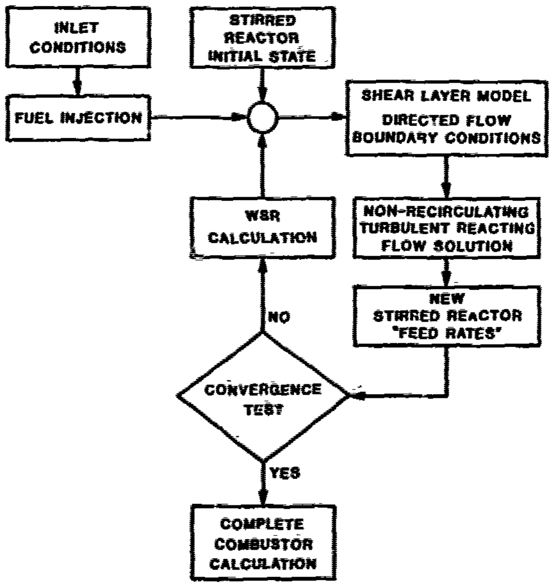
INLET CONDITIONS
STIRRED REACTOR INITIAL STATE
FUEL INJECTION
SHEAR LAYER MODEL DIRECTED FLOW BOUNDARY CONDITIONS
WSR CALCULATION
NON-RECIRCULATING TURBULENT REACTING FLOW SOLUTION
NEW STIRRED REACTOR "FEED RATES"
NO
CONVERGENCE TEST
YES
COMPLETE COMBUSTOR CALCULATION

FIGURE 3. Modular Model Calculation Logic

A key element in the modular formulation is the model for the shear layer between the recirculation zone and the directed flow. It is the computation in this region that provides the boundary conditions for the parabolic directed flow calculation; through the gradients in energy and species mass fractions computed from the directed flow solution, the influx rates $\dot{m}^I_i$ in Eqs.(17-21) and the energy flux h^I in Eq.(3) are evaluated. The shear layer region is computed in a simplified form: It is assumed that the shear layer can be modeled as a region $\ell(x)$ across which all dependent variables (i.e., velocity, temperature, and species mass fractions) vary linearly. It is further assumed that the shear layer width itself is specifiable by a linear growth law,

$$\ell = ax + b \tag{23}$$

99-8 in which a and b are constants. The constant b can be related to the initial boundary layer thickness at the expansion plane, while the constant a can be related to empirical expressions for shear layer growth rate. For self-similar shear layers, the constant a can be related to the shear stress level at some characteristic point in the shear layer. However, for reacting sudden-expansion burner flows self-similar shear layer concepts do not apply and the dividing streamline shear stress is, in the modular model, independently specifiable.

As shown in Figure 4, the dividing streamline shape $R_c(x)$ is specified: This specification also defines the dividing streamline stream function value ψ_w. Along $\psi = \psi_w$, the turbulent shear stress is specified through the use of an input "skin friction coefficient":

$$C_{FW} = \tau_w / \frac{1}{2}\bar{\rho}\bar{U}^2 \tag{24}$$

where $\bar{\rho}$ and $\bar{U}$ are evaluated as the average of their values along the flowfield centerline and along the streamline $\psi = \psi_p$. As noted above, temperature and species mass fractions are assumed to vary linearly across the shear layer. If ψ_p is defined as the streamline immediately "outside" the recirculation region (i.e., within the directed flow) and ψ_r is a (an imaginary) streamline immediately "inside" the recirculation zone, then, for species i

$$\left.\frac{\partial \alpha_i}{\partial r}\right)_w = \frac{\alpha_{ip} - \alpha_{ir}}{\ell(x)} \tag{25}$$

and for temperature

$$\left.\frac{\partial T}{\partial r}\right)_w = \frac{T_p - T_r}{\ell(x)} \tag{26}$$

where α_{ir} and T_r are the values of the species mass fractions and temperature obtained from the stirred reactor solution.

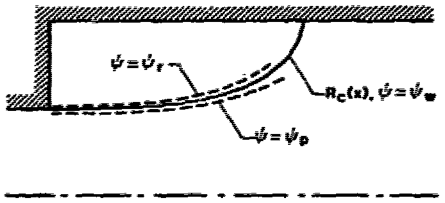

FIGURE 4. Dividing Streamline Definition Sketch

The boundary conditions at $\psi = \psi_w$ established by Eqs. (24-26) define, through the parabolic solution, effective gradients which can be used to define the influx into the stirred reactor. For example,

$$\dot{m}_i^I = 2\pi\int_0^L -\rho\,\frac{\nu_T}{Sc}\,\frac{\partial \alpha_i}{\partial r}\,R_c(x)dx \tag{27}$$

where L is the distance measured along the dividing streamline and ν_T the turbulent diffusivity for momentum; Sc is the Schmidt number. In discretized stream function coordinates, using the transformation $\rho u r dr = \psi d\psi$, Eq. (27) can be rewritten as

$$\dot{m}_i^I = \frac{-\pi}{Sc}\int_0^L \frac{d}{\Delta\psi}\left(\alpha_i^r - \alpha_i^p\right) R_c(x)dx \tag{28}$$

where $d \equiv \rho u r^2 \mu_T/\psi$. Defining

$$\bar{\alpha}_i^p = \int_0^L \frac{d}{\Delta\psi}\,\alpha_i^p\,R_c(x)dx \Bigg/ \int_0^L \frac{d}{\Delta\psi}\,R_c(x)dx \tag{29}$$

and noting that, by definition, α_i^r is constant,

$$\dot{m}_i^I = \frac{-\pi}{Sc}\int_0^L \frac{d}{\Delta\psi}\,R_c(x)dx\left\{\alpha_i^r - \bar{\alpha}_i^p\right\} = \dot{m}_D^I\left(\alpha_i^r - \bar{\alpha}_i^p\right) \tag{30}$$

Substituting Eq. (30) into Eq. (2), and taking $d(M\alpha_i)/dt = 0$, results in the working form of the well-stirred reactor species equation used in the modular model. A similar development can be followed for the energy flux term h^I in Eq. (3). 99-9

With the describing equations derived, the iteration procedure involved in the modular model can be restated. Given the conditions in the directed flow at the start of the recirculation zone, either by calculations begun upstream of the dump station or as input conditions, and given initial guesses for the recirculation zone state, α_i^r and T^r, as well as the geometric variables $R_c(x)$ and a and b in the shear layer width expression, and the "skin friction coefficient" C_{FW}, the parabolic calculation proceeds to the end of the recirculation zone, using Eqs. (25) and (26) as boundary conditions. When the end of the recirculation zone is reached, $\bar{\alpha}_i^p$, $\bar{h}^p$, and $\dot{m}_D^i$ are evaluated, and these quantities are used, along with an input specification of Q, to compute a new stirred reactor state from Eqs. (17-22). The process is repeated until changes smaller than 0.10% are observed in $\bar{\alpha}_i^p$ and $\bar{h}^p$, after which the remainder of the combustor calculation is carried out.

Boundary conditions for the turbulent kinetic energy, k, and the turbulent kinetic energy dissipation rate, ε, are established in the same manner as described for the mean total energy and species equations. Thus, values are assumed for the turbulent kinetic energy and its dissipation rate for the stirred reactor region, k_r and ε_r, respectively, and the gradients in k and ε along the dividing streamline are established from the relations

$$\left.\frac{\partial k}{\partial r}\right)_w = \frac{k_p - k_r}{\ell(x)} \tag{31}$$

$$\left.\frac{\partial \varepsilon}{\partial r}\right)_w = \frac{\varepsilon_p - \varepsilon_r}{\ell(x)} \tag{32}$$

As is evident from this discussion, a number of parameters must be specified, either empirically or through comparison of model predictions with experiment, for a modular model computation to proceed. These include the size and shape of the recirculation zone, the coefficients a and b in Eq. (23), the recirculation zone values of k and ε, and the dividing streamline skin friction coefficient C_{FW}. While this is a fairly lengthy list of coefficients, and is in addition to the inlet and wall boundary conditions that must be specified in any formulation, experience has shown that good results can be achieved using a reasonably limited range of values of these coefficients. For example, both the size and shape of the recirculation zone can be adequately specified as functions of the dump combustor geometry, and it has been found that the shear layer initial thickness, spread rate, and shear stress distribution along the dividing streamline have a marked effect on the static pressure distribution computed for the combustor. This suggests that an outer iteration loop can be used to adjust the computation for a specific combustor geometry through matching of the computed static pressure profile with experimental data for that geometry, and this technique has been successfully used to match computed and experimental distributions of static pressure for both cold flow and reacting flow. The modular approach is not a generalized predictive tool in the sense that it can be relied upon in the absence of experimental data; instead, the model is one which, given a limited amount of available data, can be used to predict and interpret the phenomena occurring within the combustor under test, and to provide a means for scaling test results to cover a more general range of interest to the combustor designer.

3. APPLICATION OF MODULAR MODELING TO SUDDEN-EXPANSION FLOWFIELDS

In order to demonstrate the application of the modular model to the analysis and interpretation of sudden-expansion flowfield data, calculations of a variety of different sudden-expansion flows have been carried out. These flowfields include incompressible and compressible nonreacting flows and premixed reacting flows; in the latter case, both one-step global and the full quasiglobal chemical kinetics models have been used. Although there are a number of empirical coefficients in the model, these computations illustrate that coefficient values can be selected based on one set of data, and in large part, used for the computation of different flowfields. Where changes in coefficients are required the differences in each case can be related to physical differences in the flowfields in different configurations.

3.1 COLD FLOW APPLICATIONS

Validation and demonstration of the modular model requires detailed data for the sudden-expansion configuration of interest. One such source of detailed data is the work reported by Chaturvedi [11] for an essentially incompressible sudden-expansion flowfield. The sudden-expansion configuration investigated by Chaturvedi involved an area ratio of 4.0 with an inlet Reynolds number (based on inlet diameter) of 2×10^5. The inlet velocity was thus of the order of 100 ft/sec. A variety of expansion angles were studied, varying from 15° to 90°; the 90° expansion angle case is of the most interest in this model validation work. Chaturvedi's apparatus had an L/D of 25 based on the inlet diameter (L/D = 13 based on "combustor" diameter) and was aspirated by a centrifugal pump and butterfly valve assembly at the downstream end; the inlet was a bellmouth intake directly coupled to the expansion section. Because of the differences in Chaturvedi's experimental apparatus relative to a typical sudden-expansion combustor configuration, which include the lack of an exhaust nozzle section, the greater mixing chamber length relative to a typical ramjet combustion chamber, and the lack of an inlet section, the modeling assumptions necessary to match the modular model predictions with these data are not necessarily appropriate for a ramjet combustor. However, Chaturvedi's data, which include axial and radial profiles of mean velocity, axial and radial turbulent intensity components, and total pressure, are detailed enough to provide a critical test of modeling capability.

The parameters, in addition to wall boundary conditions and inlet conditions, that must be specified for a modular computation include: recirculation zone size and shape, shear layer initial thickness and growth rate, dividing streamline shear stress coefficient, recirculation zone turbulent kinetic energy level, and recirculation zone turbulent dissipation length scale. Initial work [12] had established, for typical sudden-expansion ramjet combustors, that the dividing streamline shape was well represented by a parabolic arc arranged such that at the step, $dr/dx = 0$, and which intercepts the wall at a distance 9.2 step heights from the inlet. This recirculation zone length correlation was based on Drewry's results [13]. This work also showed that the dividing streamline shear stress coefficient had a strong effect on the predicted static pressure distribution, while the turbulent kinetic energy dissipation rate length scale assumed for the recirculation zone had a strong effect on the rate of transport into and out of the recirculation region. The shear layer initial thickness and rate of growth had little overall effect, over the range considered in the earlier work.

Although Chaturvedi's data show a reattachment point at 9.2 step heights from the inlet and indicate an essentially parabolic recirculation zone shape, comparison of the predictions of the model with the data for static pressure and centerline velocity showed that these data could not be reproduced with the parabolic recirculation zone boundary that had been used. Instead, an extended recirculation zone shape had to be adopted. Figure 5 illustrates the experimentally determined recirculation zone shape, and the parabolic and modified recirculation zone shapes adopted for the computation. Note that when the extended shape is used, the effective recirculation zone length for purposes of computing the stirred reactor volume is kept at the 1.61 ft distance indicated by the data; thus the extension represents an approximate model of a region over which the displacement effect of the shear layer bounding the dividing streamline relaxes to that of a wall boundary layer. A detailed description of the evaluation of the remaining model parameters for this flowfield is given elsewhere [14]. It is important to note that the adjustment of the model parameters carried out for this case was done with reference to the wall static pressure and centerline velocity measurements: The detailed profile data were not used in the modeling iteration.

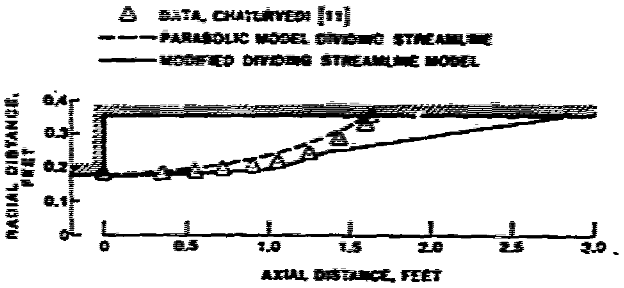

FIGURE 5. Comparison of Assumed Dividing Streamline Shapes With Chaturvedi Data [11].

The incompressible sudden-expansion represents a configuration for which the computational capabilities of the modular and unified models overlap, so that for this flowfield a comparison of results obtained using both types of model is of considerable interest. To provide this comparison, calculations of the Chaturvedi sudden-expansion flowfield were carried out using an elliptic code developed from the Imperial College primitive variables formulation. The inlet conditions and turbulence modeling used for the elliptic calculation were identical to that used in the modular approac . Thus, for both sets of calculations, the initial velocity was taken to be uniform across the inlet, the initial turbulent kinetic energy level was $10^{-4}U_0^2$, based on Chaturvedi's data, and the initial turbulence energy dissipation rate was obtained from $\epsilon = 1.6 k^{1.5}/\ell_k$ with $\ell_k = 0.1 r_0$. A standard set of two-equation model coefficients have been used for all of the flowfield computations reported in this paper; thus: $C_\mu = 0.09$; $C_{\epsilon 1} = 1.40$; $C_{\epsilon 2} = 1.95$; $\sigma_k = 1.00$; $\sigma_\epsilon = 1.22$. Wall boundary conditions for the elliptic computations were defined using a "wall-function" technique and the downstream boundary condition was obtained through use of a zero axial gradient hypothesis for all dependent variables. The unified model calculation used a 100 x 25 (x-r) grid to minimize numerical diffusion problems, and was continued for 1200 iterations to obtain a "mass imbalance" convergence criterion of less than 0.01%.

Comparisons of radial velocity profiles obtained through use of the unified model with those obtained from the modular calculation and with Chaturvedi's [11] experimental data are shown in Figures 6 and 7. It is evident from these figures that the unified model predicts a greater mixing rate and shorter recirculation zone length than the data indicate; however, no effort was made to optimize the unified model calculations for these data (through, for example, modifications to the wall boundary conditions used in the computation). It is interesting to note that for X/D = 2 and X/D = 4, the unified model velocity profile shape predictions are similar to those the modular model produces, up to the dividing streamline. The modular model, of course, provides no detail within the recirculation region. Also of interest is the steepening of the velocity profile in the near wall region between X/D = 6 and X/D = 8 that is predicted by both models, Figure 7. This provides further evidence that the shear layer relaxation region hypothesized to exist in the modular model formulation of the flowfield is in fact a feature of this flow. Radial turbulent kinetic energy profiles for X/D = 6 are shown in Figure 8. Although the elliptic model produces a slightly lower level of turbulent kinetic energy than does the modular approach, both calculations are in reasonably good agreement with the data. These comparisons indicate that for this configuration, the modular approach is capable of providing predictions of the details of the flowfield that are in agreement with both the experimental data and with predictions obtained from unified techniques. Furthermore, they provide evidence that the shear layer and recirculation zone models included in the modular approach are adequate representations of both of these regions.

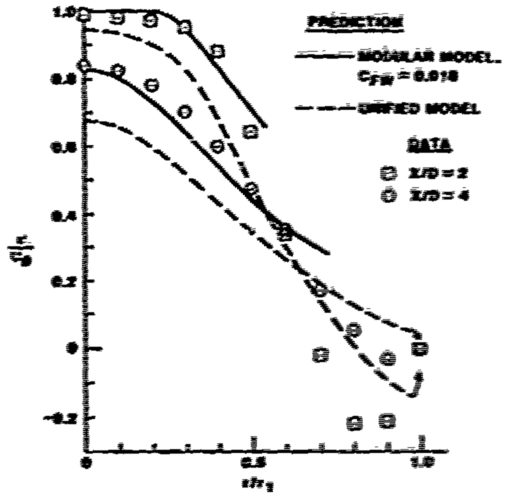

FIGURE 6. Comparison of Velocity Profiles Predicted by Modular and Unified Models With Chaturvedi Data [11]

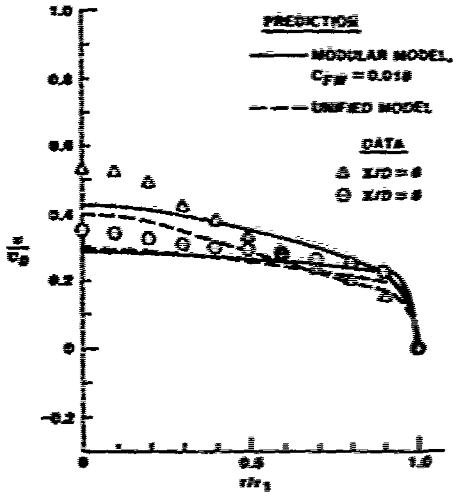

FIGURE 7. Comparison of Velocity Profiles Predicted by Modular and Unified Models With Chaturvedi Data [11]

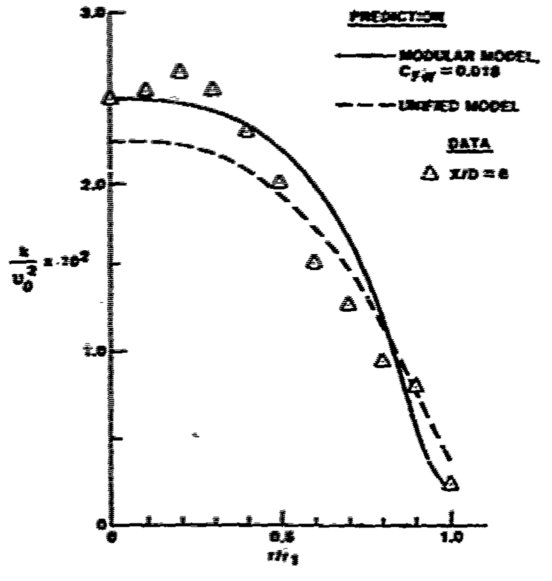

FIGURE 8. Comparison of Turbulent Kinetic Energy Profiles Predicted by Modular and Unified Models With Data of Chaturvedi [11]

3.2 REACTING FLOW APPLICATIONS

69-12

The configuration described by Craig, et al. [15] is, while a sudden-expansion, considerably different from that studied by Chaturvedi [11]. The basic configuration studied involved a combustor L/D of 3, a dump area ratio A_3/A_2 of 2.25, and an exit nozzle area ratio $A_2/A_3 = 0.40$. Thus it is considerably shorter than Chaturvedi's apparatus and incorporates an exit nozzle contraction which was not used in Chaturvedi's work. Both of these differences can be expected to have substantial effects on the overall flowfield development. Cold flow and reacting flow experimental results are reported for this sudden-expansion configuration. In the modular model computations, the cold flow data were used to evaluate the model coefficient values for the specific configuration, and computations of a premixed dump combustor at a fuel/air ratio of 0.053 were then carried out using these coefficient values for comparison with the data presented in Ref. 15. In the experiments, the fuel used was JP-4 which was represented in the computations by propane. Both a simple one-step global finite-rate chemistry model and the full hydrocarbon oxidation kinetics as represented by the quasiglobal model were used to represent the chemical kinetics processes in the directed flow. The global model was used for the recirculation zone in all cases. Propane was chosen to represent the fuel because previous studies with propane had resulted in the development of a one-step finite-rate kinetics model that represented fairly accurately the ignition delay for propane-air (although not the overall reaction time) over a range of conditions of interest in this work. Initial conditions included an inlet total temperature of 554°K and an inlet static pressure of 1.83 atm. With a mass flow rate of 1.57 kg/sec, the inlet velocity and static temperature were 159 m/sec and 543°K, respectively; the inlet Mach number was 0.351. Initial turbulent kinetic energy and dissipation rate values were established in the same manner as for the cold flow calculations, and the geometry of the combustor and recirculation zone was the same as in the cold flow calculations.

Both combustion efficiency and wall static pressure distribution data are available for this configuration, and the results of the modular model calculation of these quantities are shown in comparison with the experimental data in Figure 9. The combustion efficiency was computed from the mass-average temperature at each axial location in the calculation, using the JANNAF temperature-rise combustion efficiency definition [16]. For these data, T_{T5}(ideal) = 2178°K. Note that in these comparisons, data points are shown for the fuel/air ratio 0.053 value at which the computations were carried out. These data points were obtained from plots of combustion efficiency vs. fuel/air ratio presented in Ref. 15 for three different values of combustor L/D. The band shown for each data point represents the range of observed combustion efficiencies as a function of fuel/air ratio and is a better indication of the overall trend of the combustion efficiency vs. length data than are the individual data points themselves. Some caution is advised in interpreting the combustion efficiency comparison shown in Figure 9 since three different combustor configurations were involved in obtaining the data. Thus the relationship between recirculation zone length and combustor length is different for each of the three combustors tested. On the other hand, the static pressure data (for two fuel/air ratios which bracket the fuel/air ratio used in the computation) and the predictions are both for a combustor L/D of 3.0.

A point that should be noted in reviewing the results presented in Figure 9 is that the level of agreement with the data obtained was arrived at by increasing the kinetic energy level in the recirculation zone substantially over the levels found to be appropriate for the cold flow cases already discussed. One possible physical cause for this increased turbulent energy level in the recirculation region is the large-scale oscillation of the recirculation zone that has been observed in a variety of reacting, recirculating flowfields [17]. While the fluctuations that such oscillations produce are not strictly turbulence, two factors combine to suggest that they can be interpreted in the context of an analytical flow model as increased turbulent intensity levels in the recirculation zone. One is that the oscillations enhance the rate of mixing in the recirculation region and in the shear layer bounding it, and the second is that some of the energy in these oscillations can be expected to provide a source of turbulence energy. For all other factors equal, the increase in turbulent kinetic energy in the model recirculation zone, while not increasing the mixing rate within that region, does increase the effective viscosity along the dividing streamline, and thus the rate of transport across the shear layer. It also changes, both directly and indirectly through the transport mechanism, the rate of transport of turbulent kinetic energy to the recirculation zone. Thus the increased turbulent energy level in the recirculation zone required to achieve good agreement with the available data for the Craig, et al. premixed combustor appears to be plausible on physical grounds.

While these results indicate a good overall level of agreement with experimental data for a premixed combustor, the nonpremixed case involving liquid fuel injection is of considerably greater practical interest. To test the applicability of the modular approach (which, as noted in Section 2, incorporates a semi-empirical model for liquid fuel injection) to the analysis of nonpremixed ramjet combustor flowfield, the experimental configuration tested by Schmotolocha and Economos [18] was selected. For these experiments an area ratio $A_3/A_2 = 9$ combustor was used, with liquid JP-4 injected perpendicularly from the inlet walls through an equally-spaced ring of orifices located 6 in. upstream of the dump plane. The inlet air Mach number for this combustor was 0.49 and the global fuel/air equivalence ratio was 0.63. Since the experiments involved a heavy wall combustor, and the code is presently limited to either adiabatic or isothermal wall boundary conditions, the effects of heat loss to the walls on the predicted temperature-rise combustion efficiency were approximated by using a lower air temperature value measured at the exit of the combustor during isothermal testing in place of the actual inlet air temperature. As in the premixed combustor investigation, the reaction rate for the JP-4 fuel was modeled using a global expression derived for propane. However, for these calculations the thermodynamic coefficients and molecular weight of the fuel were those appropriate for JP-4.

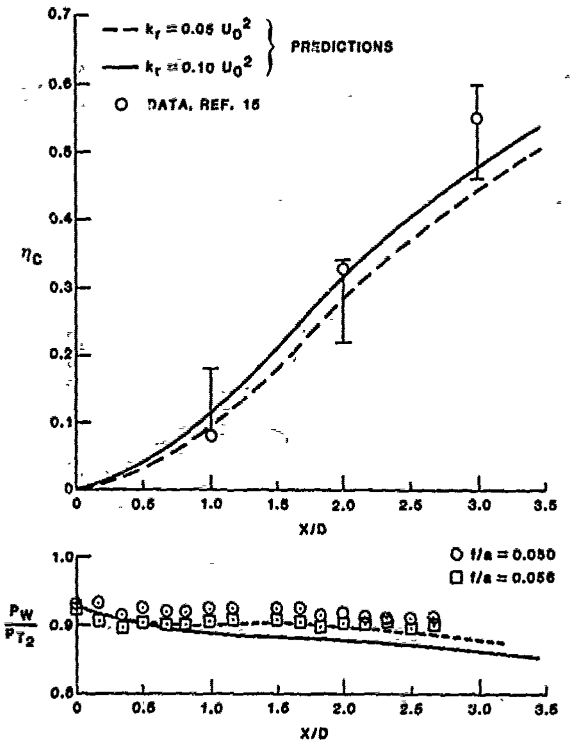

FIGURE 9. Comparison of Predicted and Measured Combustion Efficiency and Wall Static Pressure Distributions, Premixed Sudden-Expansion Combustor, Global Finite-Rate Chemistry Model.

Model coefficients were taken to be those established from the modeling of the premixed dump combustor described earlier in this section, despite the large difference in dump area ratio between the combustor used by Craig, et al. [15] and the present combustor. Results of these computations are shown in Figure 10. In the lower part of Figure 10, the computed combustion temperature distribution is shown. Coalescence of the isotherms along the recirculation zone boundary reflects the highly turbulent shear layer region. The predicted equivalence ratio in the recirculation zone, ϕ_{RZ}, is 1.87, as compared to a measured value of 1.70, for the globally fuel-lean overall equivalence ratio of $\phi_o = 0.63$. Note that the vaporization process resulting from liquid fuel injection into the 1110°R airstream effectively reduces the heterogeneous mixture temperature levels, as shown by the presence of a 1000°R isotherm. A comparison of predicted and measured radial temperature profiles is provided at the combustor exit plane. As expected, the measured temperature near the wall is lower than theoretical due to local heat loss. In the region near the centerline the local temperature is substantially underpredicted, which could result from deficiencies inherent in the turbulence modeling or in the global finite-rate chemical kinetics model (which substantially overpredicts the required reaction time compared to a more complete chemical kinetics formulation), or both. However, the mass flow in this region is small relative to the overall combustor mass flow, so that overall combustion efficiency, which is based on mass-averaged temperatures, is well represented. This is shown in the upper part of Figure 10; the two experimental points represent combustion efficiency obtained from exit species distributions and from exit total temperature.

These results show that the modular model approach can provide good overall predictions of combustor performance parameters and a substantial level of detail for the processes occurring within the combustor. The major value of the modular approach, however, is not the prediction of combustor performance, but the use of the model as a tool to interpret combustor test data. In the next section, an example of this use is outlined.

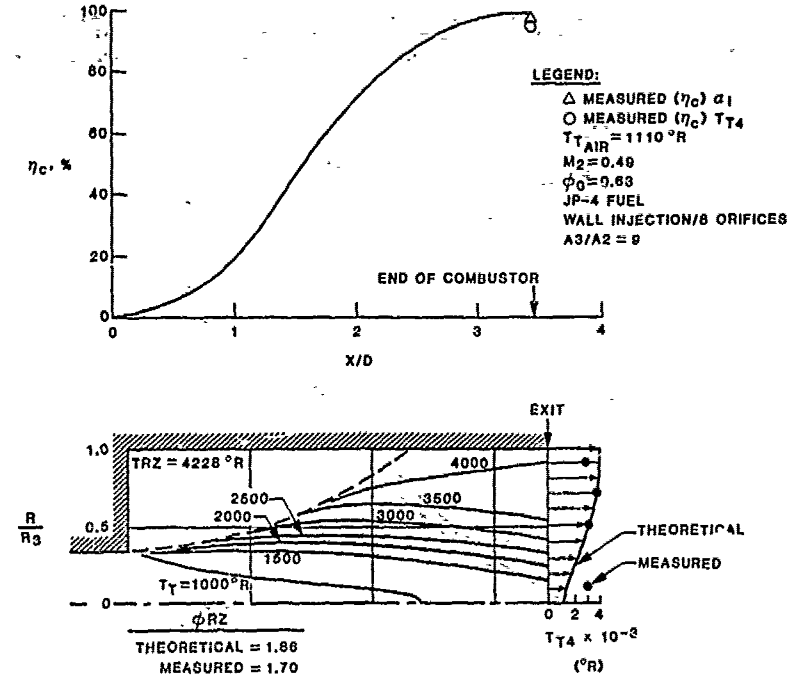

FIGURE 10. Comparison of Modular Model Prediction With Measured Dump Combustor Performance, Liquid Fuel Injection. Data From Ref. 18.

4. APPLICATION OF MODULAR MODELING FOR RAMJET PERFORMANCE DIAGNOSTICS

One of the most important determinants of liquid fueled ramjet performance is the fuel distribution at the combustor entrance. For the sudden-expansion liquid fueled ramjet, the interaction between the inlet fuel distribution and recirculation zone state is a further important consideration. A variety of observations have shown that for wall injection of the fuel, the recirculation zone equivalence ratio is generally more fuel-rich than the overall (global) equivalence ratio. This is demonstrated by the data of Schmotolocha and Economos [18], which was obtained for three different inlet conditions and at two different locations of the fuel injection orifices upstream of the dump plane. Indeed, the measurements described in Ref. 18 indicate that for overall equivalence ratios greater than 0.2, the equivalence ratio in the recirculation region is always greater than unity. These data are shown in Figure 11 in which the results of a modular model computation at one overall equivalence ratio are also shown: The agreement between the experimental results and the computation is reasonably good.

In the experiments described in Ref. 18 plain orifice fuel injection was used. For plain orifices, fuel penetration characteristics are reasonably well documented, and the empirical penetration correlation used in the model is based on data for plain orifices. However, plain orifices are not widely used in ramjet design because of their poor turndown characteristics which result in the need for several sets of orifices to obtain a wide ramjet operating range. The most commonly used fuel injector in liquid fuel ramjet applications is the poppet injector, which has a much broader turndown range than does a plain orifice. However, penetration characteristics from poppet injectors under ramjet operating conditions are not well documented. Indeed, there exists one investigation of poppet (and other nozzle) penetration characteristics under ramjet operating conditions in which it was observed that the penetration from poppets is essentially nil [19]. While other results indicate that penetration characteristics similar to orifice injection can be obtained using poppets, it remains clear that the penetration characteristics of poppets are not as well known as for plain orifices.

At one operating condition, which involves a relatively high inlet temperature, low ramjet combustor performance was observed in a recent test program: At this one condition performance was considerably lower than at other test conditions. Review of the available results suggested that fuel distribution effects were a possible cause, and in particular that at the operating condition in question the fuel penetration from the wall-mounted poppet fuel injectors may have been negligible. To investigate this possibility, and to study the effects of fuel distribution on combustion performance, a series of parametric modular model computations was carried out.

29-15

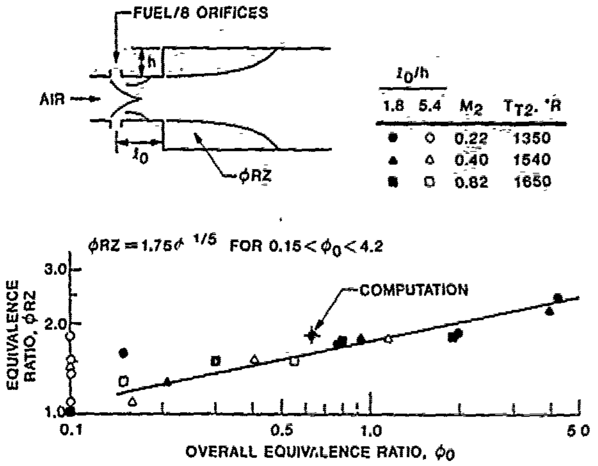

FIGURE 11. Fuel Concentration in Recirculation Zone. Data From Ref. 18.

In the modular approach, fuel injection is modeled using an empirical correlation for penetration and a breakup time correlation. The latter correlation defines the downstream position at which the penetration is computed; from this point the fuel spray is assumed to vaporize at a rate given by a bulk spray vaporization correlation. After injection, the fuel is assumed to reside in an annular region at the position specified by the penetration correlation, and spreading of this annulus is computed using a turbulent mixing model. For the conditions of interest in the parametric study, vaporization occurs rapidly, so that the parameter to be varied was the fuel penetration height. Figure 12 shows the predicted recirculation zone equivalence ratio as a function of fuel penetration height obtained from the parametric study. Of particular interest is the result for near-zero penetration height, $\ell/r_o \approx 0$. Under this condition, for a global equivalence ratio of unity, the predicted recirculation zone fuel/air ratio is extremely fuel-rich, with $\phi_{RZ} = 4.5$. This high value of equivalence ratio produces a substantially cooler recirculation region than would be obtained for conditions nearer stoichiometric, and this in turn leads to reduced flame propagation rates and lower overall combustion efficiency in the combustor. Evaluation of the effect of the rich fuel/air ratio in the recirculation zone on overall performance is, however, complicated by difficulties that are encountered in modeling chemical kinetics in very fuel-rich regions.

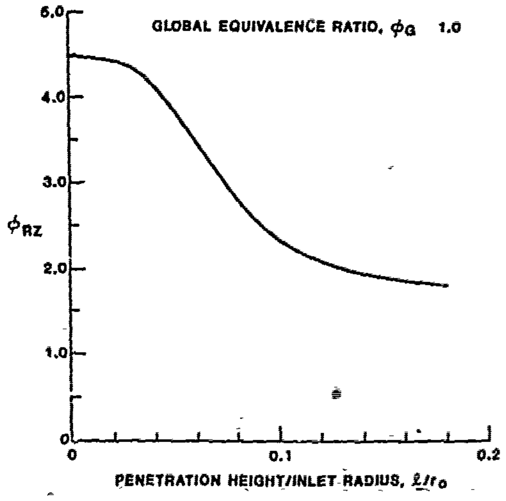

FIGURE 12. Recirculation Zone Equivalence Ratio as a Function of Penetration Height.

There is no currently available finite-rate chemical kinetics model which can provide adequate results for complex hydrocarbon fuels under fuel-rich conditions, at temperatures at which the effects of dissociation manifest themselves. The modular model formulation used for the computations described in this paper includes as options either a one-step

29-16

finite-rate model or the quasiglobal kinetics model. In the former case, the products of combustion are the fully-reacted species H_2O and CO_2, so that the effects of dissociation are ignored, and the overall reaction rate is underpredicted. The quasiglobal model used in the modular formulation is valid for complex hydrocarbon fuels and includes the effects of dissociation, but is not appropriate for equivalence ratios much above stoichiometric. Other models have been proposed for fuel-rich conditions, such as the four-step model of Dryer and Glassman [20], but this model ignores dissociation effects. Thus it is difficult to obtain reliable estimates for the chemical kinetic rates that pertain in combustors in which significant regions of the flowfield are highly fuel-rich. This difficulty is reflected in the performance results shown in Figure 13. While the trend of combustion efficiency as a function of fuel penetration distance obtained through the use of the one-step global kinetics model is as expected, the magnitude of the overall change is relatively small and probably incorrect. The reason that the magnitude of these results can be expected to be incorrect is that the global finite-rate model can be expected to significantly overpredict the recirculation zone temperature for fuel-rich conditions, since the only effect of fuel-rich operation that this model recognizes is a dilution of the products of combustion with excess fuel for $\phi >> 1$. With this model, the reaction rate is linear with respect to fuel concentration, whereas evidence exists that for fuel-rich conditions reaction rates do not continue to increase with fuel concentration, and, as noted earlier, dissociation effects are also ignored.

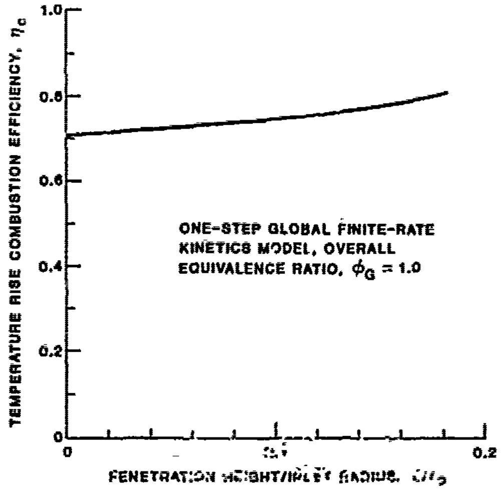

FIGURE 13. Predicted Overall Combustion Efficiency as a Function of Fuel Penetration Height.

Nevertheless these results indicate that for the conditions considered, low values of fuel penetration distance are directly coupled to reductions in overall combustor performance. Since further development testing using fuel injection schemes designed to increase fuel penetration resulted in significant performance improvements, it can be considered that the trends demonstrated by this modeling effort have been experimentally verified.

5. CONCLUSIONS

The problems encountered in the development of advanced ramjet combustors, which include flame stabilization, flame propagation, and spray combustion phenomena, all involve a strong coupling between fluid mechanics and chemical kinetics. Because of this strong coupling, analytical combustor models are required to sort out the various mechanisms that contribute to overall performance. The ability to compute, in some detail, combustion chamber flowfields is necessary in order to understand the phenomena that occur in existing combustors and to estimate the performance characteristics of new combustor concepts.

In response to the needs just outlined, a detailed model of the sudden-expansion liquid-fueled ramjet combustor has been developed. This model makes use of the modular concept, in which the overall combustor flowfield is broken down into a number of regions, each of which is analyzed in detail using a technique suitable for the specific part of the flowfield. These analytical subelements, or modules, are then coupled together iteratively, through their boundary conditions. The examples given in this paper have shown that this approach can yield good agreement with experimental data for a variety of configurations, and that the model provides a useful tool for the analysis and interpretation of ramjet combustor test data, as well as a technique useful for scaling and for the parametric analysis of ramjet design features.

Because the modular model depends on the existence of sufficient experimental data to provide a means of establishing the values of its adjustable parameters, it is not an analytical method that can be relied upon in the total absence of experimental data. However, it has been shown by the examples in this paper that the experimental data required to adjust the coefficients in the modeling is both minimal and easily obtained: For the axisymmetric sudden-expansion configuration wall static pressure distributions provide a suitable comparison. Moreover, for the complex interactions involved in a ramburner flowfield no currently existing analytical model can be considered to be truly predictive. For example, the accurate prediction of the recirculation zone length in a sudden-expansion configuration is a well-known problem in the application of elliptic solution techniques. In the modular approach, this length is specified as part of the model definition, using empirical relations that have been verified for a variety of different configurations and flow conditions. The modular approach can also easily incorporate considerably more detail than is feasible with current elliptic solution techniques, particularly with respect to finite-rate chemical kinetics and heterogeneous transport processes. The method outlined in this paper thus provides a powerful technique for the analysis of ramburner combustion processes.

REFERENCES

1. Hutchinson, P., Khalil, E. E., and Whitelaw, J. H., "Measurement and Calculation of Furnace-Flow Properties," Journal of Energy, Vol 1, No. 4, July-August 1977, pp. 212-219.

2. Abou Ellail, M. M. M., Gosman, A. D., Lockwood, F. C., and Megahead, I. E. A., "Description and Validation of a Three-Dimensional Procedure for Combustion Chamber Flows," Report FS/77/27, Imperial College, October 1977.

3. Roberts, R. A., Aceto, L. D., Kollrack, R., Teixeira, D. P., and Bonnell, J. M., "An Analytical Model for Nitric Oxide Formation in a Gas Turbine Combustor," AIAA Journal, Vol. 10, No. 6, June 1972, pp. 820-826.

4. Swithenbank, J., Poll, I., Vincent, M. W., and Wright, D. D., "Combustion Design Fundamentals," Fourteenth Symposium (International) on Combustion, The Combustion Institute, Pittsburgh, 1973, pp. 627-636.

5. Edelman, R. B. and Fortune, O., "A Quasi-Global Chemical Kinetic Model for the Finite Rate Combustion of Hydrocarbon Fuels," AIAA Paper 69-86, 1969.

6. Launder, B. E., Morse, A., Rodi, W., and Spalding, D. B., "Prediction of Free Shear Flows - A Comparison of the Performance of Six Turbulence Models," Free Turbulent Shear Flows, Vol I, Conference Proceedings, NASA Report No. SP-321, 1973, pp. 463-519.

7. Boccio, J. L., Weilerstein, G., and Edelman, R. B., "A Mathematical Model for Jet Engine Combustor Pollutant Emissions," NASA CR-121208, GASL TR-781, General Applied Science Laboratories, 1973.

8. Catton, I., Hill, D. E., and McRae, R. D., "Study of Liquid Jet Penetration in a Hypersonic Stream," AIAA Journal, Vol. 6, No. 11, November 1977, pp. 2084-2089.

9. Clark, B., "Break-up of a Liquid Jet in a Transverse Flow of Gas," NASA TN-D-2424, August 1964.

10. Ingebo, R. and Foster, H., "Drop Size Distribution for Cross-Current Break-up of Liquid Jets in Air Stream," NASA TN-4087, October 1957.

11. Chaturvedi, M. C., "Flow Characteristics of Axisymmetric Expansions," Journal of the Hydraulics Division, Proceedings of the American Society of Civil Engineers, Vol. 89, No. HY3, May 1963, pp. 61-92.

12. Harsha, P. T. and Edelman, R. B., "Application of Modular Modeling to Ramjet Performance Prediction," AIAA Paper 78-944, Fourteenth Joint Propulsion Conference, Las Vegas, Nevada, July 25-27, 1978.

13. Drewry, James E., "Characterization of Sudden-Expansion Dump Combustor Flowfields," AFAPL-TR-76-52, Air Force Aero Propulsion Laboratory, July 1976.

14. Harsha, P. T. and Edelman, R. B., "Mixing and Combustion in High Speed Air Flows," AFOSR TR 80-1005, SAI-80-020-CP, Science Applications, Inc., Canoga Park, CA, July 1980.

15. Craig, R. R., Drewry, J. E., and Stull, F. D., "Coaxial Dump Combustor Investigation," AIAA Paper 78-1107, AIAA/SAE 14th Joint Propulsion Conference, July 25-27, 1978.

16. Airbreathing Combustor Development Committee, "Recommended Ramburner Test Reporting Standards," CPIA Publication 276, Chemical Propulsion Information Agency, March 1976.

17. Edelman, R. B. and Harsha, P. T., "Laminar and Turbulent Gas Dynamics in Combustors-Current Status," Progress in Energy and Combustion Science, Vol. 4, No. 1, 1978, pp. 1-62.

18. Schmotolocha, S. N. and Economos, C., "An Experimental Combustion and Flame Stabilization Study of Dump Burners," AFOSR-TR-75-1446, September 1975.

19. Rosfjord, T. J., "Experimental Investigation of Fuel Sprays Formed by Ramburner Injectors," 1979 JANNAF Propulsion Meeting, Vol. 2, CPIA Pub. 300, 1979, pp. 585-607.

20. Hautman, D. J., Dryer, F. L., Schug, K. P., and Glassman, I., "A Multistep Overall Kinetic Mechanism for the Oxidation of Hydrocarbons," Presented at 1980 Technical Meeting, Eastern Section, The Combustion Institute, November 12-14, 1980.

ACKNOWLEDGEMENT

Research partially supported by Air Force Office of Scientific Research under Contract F49620-80-C-0082 under the direction of Dr. B. T. Wolfson and by Air Force Aeropropulsion Laboratory under Contract F33615-77-C-2062, John Smith, technical monitor.

DISCUSSION

L.Glasspoole

How long do your computer calculations take?

Author's Reply

The computation time depends primarily on the complexity of the chemistry model used in the computation. When a one-step global finite-rate model is used, a complete combustor computation requires 4–5 minutes on a CDC 7600 computer; this involves typically five iterations of the overall procedure. When the quasi-global detailed kinetics model is used, typical computation times are of the order of 15 minutes on a CDC 7600.

THE MATHEMATICAL MODELLING OF AIR-AUGMENTED ROCKET COMBUSTORS: A PROGRESS REPORT

J.C.P. Birchley
L.T. Glasspoole
A.S. Wilson
Procurement Executive, Ministry of Defence
Propellants, Explosives and Rocket Motor Establishment
Westcott, Aylesbury, Buckinghamshire HP18 0NZ

The theoretical bases for the calculation of axisymmetric and three-dimensional ducted flows are set out and suitable solution procedures are outlined. Progress is illustrated by presentation of results from examples of axisymmetric ducted flow calculations and directions for future work are indicated.

Nomenclature

a_{ij} (j = -4, -3, ..., 4)	Coefficients of polynomial defining specific heat of i'th species.
a_ϕ, b_ϕ, c_ϕ	Constants in wall boundary condition for ϕ .
A_j	Constant factor in expression for forward rate coefficient - equation 17.
C_p	Specific heat of i'th species.
C_D	Empirical constant relating effective eddy viscosity to turbulent kinetic energy and its dissipation rate - equation 10.
C_1, C_2	Empirical constants in transport equation for eddy energy dissipation rate - equation 12.
diag.	Coefficient in equation 31 relating corrections for velocity and pressure.
E_j	Activation energy for forward rate coefficient of j'th reaction - equation 17.
F_i	Mass fraction of i'th species.
G_i, G	Gibb's free energy of i'th species and for mixture.
ΔG_j	Gibb's free energy change per unit of j'th reaction.
h_i, h	Thermal component of enthalpy of i'th species, and of mixture.
H	Total enthalpy.
k	Turbulent kinetic energy $\frac{1}{2}(u'^2 + v'^2 + w'^2)$ where u', v', w' are the fluctuating components of velocity.
k_{fj}, k_{bj}	Forward and backward reaction rate coefficients for j'th reaction.
K_{cj}	Equilibrium coefficient for j'th reaction.
L	Length of parallel part of combustor.
n_j	Temperature exponent in expression for rate coefficient of j'th reaction - equation 21.
M	Molecular weight of mixture.
M_i	Molecular weight of i'th species.
m_i	Chemical species i .
N	Conversion factor for chemical reaction rate (= 6.023×10^{20}).
NR	Number of reactions.
NS	Number of chemical species.
N1, N2, N3	Number of grid points in (x,r,θ) directions, respectively.
p	Pressure.
p'	Modified pressure (see Table 1).
r	Radial coordinate.
r_d	Duct radius.
R	Universal gas constant.

S_i, S	Entropy of i'th species, and of mixture.
S_ϕ	Source term for solution variable ϕ .
T	Temperature.
u	Axial component of velocity.
v	Radial component of velocity.
w	Transverse component of velocity.
$\dot{w}_i$	Rate of mass production of i'th species.
x	Axial coordinate.
α_{uj}, β_{ij}	Number of molecules of species i taking part in one unit of the j'th reaction, as reactants and products, respectively.
δx, δr, $\delta\theta$	Increment in grid coordinates x, r, θ.
ε	Turbulent energy dissipation rate.
θ	Transverse coordinate.
μ	Effective eddy viscosity.
ρ	Mass density.
σ_H, σ_k, σ_m, σ_ε, σ_ϕ	Turbulent exchange coefficients for enthalpy, turbulent kinetic energy, species, turbulent energy dissipation rate, and ϕ , respectively.
ϕ	General flow property.
Φ	Effective viscous dissipation rate.
Subscripts	
P	Value at inlet port or primary nozzle exit.
Superscripts	
(C)	Value at centreline.
$*$	Approximate value of flow variable (ρ, p, u, v, w) before correcting for overall mass continuity.

INTRODUCTION

The successful design of an air-augmented rocket vehicle encompasses a number of complex problems. The one which is addressed here is that of assessing the performance of the secondary combustion chamber. The design and realistic testing of such a unit may be expected to be a difficult, time-consuming and expensive exercise, involving as it does the provision of flight test or flight simulation facilities. Such a programme of work was considerably beyond the limit of current funding. Instead a modest theoretical investigation was initiated, aimed at gaining insight into the problems of combustor ignition and permitting trends in combustor behaviour to be established. It was decided that the investigation would proceed on two fronts. Firstly, use was to be made of existing expertise and techniques to develop a computer code to calculate axisymmetric, non-recirculatory, ducted flow. This computer code was to be an extension of the capabilities of existing free-flow computation techniques, the hope being that significant progress could be attained for a comparatively small expenditure of effort. Secondly, and with a longer time-scale, work was to be initiated on a computer code designed to calculate three-dimensional ducted flow, with due allowance for flow asymmetry and recirculation. The latter emphasis is necessary to enable the effects of, e.g. flight angle-of-attack and inlet geometry to be accounted for. This paper reports progress on these topics.

NUMERICAL MODELLING OF FLOWS

In carrying out a mainly theoretical study of flows with combustion the overall flow behaviour may be ascertained by examining the behaviour of such features as the values of velocity, pressure, temperature and chemical composition at points throughout the flow. In addition the way in which the (steady state) flow develops as it passes through the flow region is influenced by the processes of mixing, so that the turbulent characteristics of the flow must also be considered. The behaviour of properties such as these may be described by a set of simultaneous partial differential equations, together with additional relations for the state variables. Further expressions for the rates of production of various quantities are required, for example the production of chemical species may be determined from the law of mass action applied to a suitably chosen chemical scheme, utilizing appropriate thermodynamic and reaction rate data. Formulation of the flow behaviour in this way permits the problem to be cast into a tractable mathematical form. Transformation of the differential equations into finite difference forms makes it possible to approximate the relationships between the continuously varying flow properties by discrete values defined at a finite number of points within the flow region. When expressed in this way the problem is ideally suited to efficient solution by digitial computer, and details of how this approach has been followed for axisymmetric and three-dimensional flows are given below. Only after completion of this process may practically interesting quantities (e.g. thrust) be derived.

AXISYMMETRIC FLOW

A simple geometry was assumed for the axisymmetric flow study (Fig. 1). The air stream was assumed to be parallel and uniform at the duct inlet, while the primary nozzle wall was assumed to taper to infinitesimal thickness at its lip, thus avoiding problems of both flow asymmetry and recirculation. Wall boundary layers upstream of the duct inlet plane were neglected. The flow was permitted to be subsonic/subsonic (outer/inner streams, respectively), subsonic/supersonic or supersonic/supersonic, but the problems of calculating choked subsonic flow were essentially deferred by limiting consideration to a parallel-sided duct for this initial stage of the investigation.

Governing equations

The equations governing the flow include those of conservation of axial momentum, energy and chemical species, written in familiar boundary layer form,

(a) conservation of axial momentum,

$$\rho u \frac{\partial u}{\partial x} + \rho v \frac{\partial u}{\partial r} = \frac{1}{r}\frac{\partial}{\partial r}\left(r \mu \frac{\partial u}{\partial r} \right) - \frac{\partial p}{\partial x} \quad ; \tag{1}$$

(b) conservation of total enthalpy

$$\rho u \frac{\partial H}{\partial x} + \rho v \frac{\partial H}{\partial r} = \frac{1}{r}\frac{\partial}{\partial r}\left\{ \frac{r\mu}{\sigma_H}\left[\frac{\partial H}{\partial r} + \sum_i \left(\frac{\sigma_H}{\sigma_{m_i}} - 1 \right) h_i \frac{\partial F_i}{\partial r} + \left(\sigma_H - 1 \right) \frac{\partial(\frac{1}{2}u^2)}{\partial r} + \left(\frac{\sigma_H}{\sigma_k} - 1 \right) \frac{\partial k}{\partial r} \right] \right\} \quad ; \tag{2}$$

(c) conservation of chemical species,

$$\rho u \frac{\partial F_i}{\partial x} + \rho v \frac{\partial F_i}{\partial r} = \frac{1}{r}\frac{\partial}{\partial r}\left(\frac{r\mu}{\sigma_{m_i}} \frac{\partial F_i}{\partial r} \right) + \dot{w}_i \quad . \tag{3}$$

Here x , r are the axial and radial co-ordinates, respectively, u and v are axial and radial components, respectively, of the velocity, ρ is the density, p the pressure, H the total enthalpy and F_i , $\dot{w}_i$ are, respectively, the mass fraction and rate of formation of the i'th chemical species. In addition σ_H is the turbulent exchange coefficient ratio for enthalpy, σ_{m_i} the turbulent exchange coefficient ratio of mass for species i , while μ is the effective eddy viscosity, k is the kinetic energy of turbulence ($= \frac{1}{2}(u'^2 + v'^2)$ where u' , v' are turbulent fluctuations of the velocity components) and σ_k the turbulent exchange coefficient ratio for k . The last three terms on the right of equation (2) represent differential turbulent diffusion with respect to total enthalpy of chemical species, mean flow kinetic energy and turbulent kinetic energy, respectively. In this work it was assumed that the turbulent exchange coefficient for mass (turbulent Schmidt number) had the same value for each chemical species and that this was the same as the value of the turbulent exchange coefficient for enthalpy (turbulent Prandtl number), i.e. that the turbulent Lewis number was unity.

Radial pressure variations in the flow field were accommodated by way of an approximate form of the radial momentum equation,

$$\rho u \frac{\partial v}{\partial x} = - \frac{\partial p}{\partial r} \quad , \tag{4}$$

and consideration of local continuity, as outlined in Ref. 1, together with a global continuity statement,

$$\int_0^{r_d} \rho u r dr = \text{constant} \quad , \tag{5}$$

where r_d is the duct radius.

The temperature, T , and the total enthalpy are related via the equation

$$H = h + \tfrac{1}{2}u^2 + k \quad , \tag{6}$$

where h ($\equiv h(T)$) is the mixture enthalpy per unit mass, given by

$$h = \sum_i h_i F_i \quad . \tag{7}$$

The local gas density may then be recovered from the ideal gas equation of state

$$p = \frac{R}{M} \rho T \quad , \tag{8}$$

where R is the universal gas constant and M the mean molecular weight. M is defined by the relation

30-4

$$M = \left[\sum_i \left(\frac{F_i}{M_i}\right)\right]^{-1} . \qquad (9)$$

where M_i is the molecular weight of the i'th chemical species.

Turbulent flow modelling

Closure of the flow equations (1-3) is achieved by writing the turbulent eddy viscosity coefficient, μ, as a function of the turbulent kinetic energy, k, and the eddy energy dissipation rate, ε, in the form

$$\mu = C_D \rho K^2 \varepsilon^{-1} , \qquad (10)$$

where C_D is an empirical constant. The description of the turbulent behaviour of the flow is completed by way of two additional transport equations for k and ε

$$\rho u \frac{\partial k}{\partial r} + \rho v \frac{\partial k}{\partial r} = \frac{1}{r}\frac{\partial}{\partial r}\left(\frac{r\mu}{\sigma_k}\frac{\partial k}{\partial r}\right) + \mu\left(\frac{\partial u}{\partial r}\right)^2 - \rho\varepsilon ; \qquad (11)$$

$$\rho u \frac{\partial \varepsilon}{\partial x} + \rho v \frac{\partial \varepsilon}{\partial r} = \frac{1}{r}\frac{\partial}{\partial r}\left(\frac{r\mu}{\sigma_\varepsilon}\frac{\partial \varepsilon}{\partial r}\right) + C_1 \frac{\varepsilon}{k} \mu\left(\frac{\partial u}{\partial r}\right)^2 - C_2 \rho \frac{\varepsilon}{k} . \qquad (12)$$

In equation 12 σ_ε is the turbulent exchange coefficient ratio for ε, while C_1 and C_2 are empirical constants. Equations 10-12 comprise one of several well-established "two-equation" turbulence models (see, e.g. Ref. 2), this version being chosen since it has been successfully employed in similar flows[1].

Thermodynamics and chemical reactions

The thermodynamic properties of the flow are calculated by defining the thermodynamic behaviour of the constituent chemical species and evaluating mean flow properties from a knowledge of the local chemical composition. For each chemical species the thermodynamic quantities enthalpy h_i, entropy S_i, and Gibbs free energy G_i are given by

$$h_i = \int_{T_o}^{T} Cp_i(T')dT' + h_i(T_o) , \qquad (13)$$

$$S_i = \int_{T_o}^{T} \frac{Cp_i(T')dT'}{T'} + S_i(T_o) , \qquad (14)$$

$$G_i = h_i - T S_i , \qquad (15)$$

where the specific heats are calculated from the ninth order polynomial

$$Cp_i = \sum_{j=-4}^{4} a_{ij} T^j . \qquad (16)$$

The Gibbs free energy change ΔG_j per unit of the j'th reaction is computed from equation 15, and this yields the equilibrium constant K_{cj} via the partition equation

$$\ln K_{cj} = -\Delta G_j/RT + \sum_{i=1}^{NS} (\alpha_{ij}-\beta_{ij}) \ln (RT) , \qquad (17)$$

where α_{ij}, β_{ij} are the stoichiometric coefficients in the reaction scheme represented by

$$\sum_{\ell=1}^{NS} \alpha_{\ell j} m_\ell \underset{k_{bj}}{\overset{k_{fj}}{\rightleftharpoons}} \sum_{\ell=1}^{NS} \beta_{\ell j} m_\ell , \quad (j = 1 \leq \ell \leq NR) . \qquad (18)$$

The net reaction rate for the j'th reaction is given by the law of mass action as

$$R_j = k_{fj} N^{\sum_\ell \alpha_{\ell j}-1} \prod \left(\frac{F_\ell \rho}{M_\ell}\right)^{\alpha_{\ell j}} - k_{bj} N^{\sum_\ell \beta_{\ell j}-1} \prod \left(\frac{F_\ell \rho}{M_\ell}\right)^{\beta_{\ell j}} , \tag{19}$$

and the rate of production of the i'th species is

$$\dot{w}_i = M_i \sum_{j=1}^{NR} (\beta_{ij} - \alpha_{ij}) R_j . \tag{20}$$

In equation (19) the reaction rate R_j is given in kmole m^{-3} s^{-1} if the rate coefficients k_{fj}, k_{bj} are in the ml-molecule-second units, density is in kg m^{-3} and $N = 6.023 \times 10^{20}$. The forward rate coefficients may be written in Arrhenius form:

$$k_{fj} = A_j T^{n_j} \exp(-E_j/T) . \tag{21}$$

and the equilibrium relation

$$k_{bj} = k_{fj}/K_{cj} . \tag{22}$$

permits the backward rate coefficient to be evaluated.

Boundary conditions

The flow boundary conditions are readily specified at the duct axis where, because of the assumed symmetry of the flow, it is sufficient to ensure that

$$\frac{\partial \phi}{\partial r} = 0 \quad \text{at} \quad r = 0 , \tag{23}$$

where ϕ represents any property of the flow. At the duct wall the values of the components of velocity were set to zero, as were the values of k and ε. The behaviour of these quantities and effective values of the turbulent eddy viscosity coefficient in the near-wall region were determined by the procedures of Refs 3 and 4, while for temperature and enthalpy the computer program was equipped with the option of calculating either adiabatic or constant heat flux conditions^3. In this investigation the duct wall was also considered to be non-porous and chemically inactive.

Initial conditions and solution procedure

A calculation may be started from any plane normal to the duct axis across which the radial profile of each variable is known. In the present work the duct "inlet" plane was arbitrarily but conveniently defined as that plane containing the primary nozzle exit. Simple but effective techniques are available for estimating the primary nozzle exit conditions (e.g. Ref. 5), while details of the air stream may be determined from a knowledge of likely flight conditions.

The solution procedure is a well-established marching implicit integration technique, closely based on that described in Ref. 3. Comprehensive details of the finite-differencing methods and the mathematical approach to the solution, as well as a wealth of hints and advice, are contained therein and further explanation will not be given here.

3-D FLOWS

Considerable understanding of, and some worthwhile quantitative information about air-augmented rocket combustors can be obtained from a consideration of axisymmetric ducted flows. However, in a real missile, constraints on the size and shape of the combustor are likely to be limiting factors in the design of the propulsion unit, and hence it is important that the best use is made of the space available. It is unlikely that space utilisation can be optimised without considering a fairly wide range of inlet configurations and flight conditions, and the way in which such factors affect the rate of mixing and the extent of any recirculation zones. Such conditions, coupled with the comparatively low cost of numerical modelling vis-a-vis a hardware development programme, made it attractive to extend the present investigation to consider three-dimensional aspects of the flow.

In the same way that finite difference techniques have been used to model axisymmetric, recirculating reacting flows, e.g. Ref. 1, 3-D flows may also be treated. The configuration under investigation involves one or more streams of hot, fuel-rich exhaust flowing from a primary chamber into a cylindrical secondary combustor into which air is ducted by means of a number of inlet ports, (see e.g. Fig. 2). The chamber is assumed to possess a plane of symmetry. In view of the complex nature of the coupling between the chamber conditions and those external to it, it has been decided, for the time being at least, to restrict attention to the secondary chamber. Conditions are specified at all the inlet ports, and at the primary orifice, and the condition of zero streamwise diffusion is imposed at the start of the expansion nozzle.

Governing equations

In cylindrical polar coordinates (x,r,θ) the transport of any scalar quantity ϕ can be expressed as follows:

$$\rho\left\{u\frac{\partial\phi}{\partial x}+v\frac{\partial\phi}{\partial r}+\frac{w}{r}\frac{\partial\phi}{\partial\theta}\right\}=\frac{\partial}{\partial x}\left(\frac{\mu}{\sigma_\phi}\frac{\partial\phi}{\partial x}\right)+\frac{1}{r}\frac{\partial}{\partial r}\left(r\frac{\mu}{\sigma_\phi}\frac{\partial\phi}{\partial r}\right)+\frac{1}{r^2}\frac{\partial}{\partial\theta}\left(\frac{\mu}{\sigma_\phi}\frac{\partial\phi}{\partial\theta}\right)+S_\phi\ . \tag{24}$$

where ρ is the mass density, (u,v,w) are the velocity components; μ is the turbulent viscosity, and σ_ϕ is the exchange coefficient ratio (Prandtl number) for the quantity ϕ. The source term S_ϕ is a function of the field variables and is evaluated according to Table 1. The quantities which satisfy equation (24) are the velocity components (u,v,w), the turbulence kinetic energy k, the turbulence energy dissipation rate ε, the total enthalpy H, and the species mass fractions F_i, $i=1\ldots NS$. The turbulent viscosity is given by equation 10, while the state variables of pressure p, density ρ and temperature T are determined from equations 7, 8 and the continuity equation

$$\frac{\partial}{\partial x}(\rho u)+\frac{1}{r}\frac{\partial}{\partial r}(r\rho v)+\frac{1}{r}\frac{\partial}{\partial\theta}(\rho w)=0\ . \tag{25}$$

Boundary conditions

1 Surface $\theta=0,\pi$.

With the assumption of symmetry about this plane, we have

$$\frac{\partial\phi}{\partial\theta}=0\ ,\quad \theta=0,\pi\ . \tag{26}$$

2 Centreline $r=0$.

Due to the three-dimensional nature of the flow, the boundary is significant only in that the (r,θ) co-ordinates are singular. The conditions are provided by the equations themselves, in which we set

$$\left.\begin{aligned}\frac{\partial^2\phi}{\partial r^2}^{(C)}&=4\left(\frac{1}{N_2}\sum_{i_2=1}^{N_2}\phi(\delta r_1\ ,\theta_{i2}\ ,x)-\phi^{(C)}(x)\right)\Big/\delta r_1^{\,2}\ ,\\ \frac{\partial\phi}{\partial r}^{(C)}&=\Big\{\phi(\delta r_1\ ,0\ ,x)-\phi(\delta r_1\ ,\pi\ ,x)\Big\}\Big/2\delta r_1\ ,\\ \text{and}\quad\frac{\partial\phi}{\partial\theta}^{(C)}&=\frac{\partial^2\phi}{\partial\theta^2}^{(C)}=0\ .\end{aligned}\right\} \tag{27}$$

where the superscript (C) refers to the value at $r=0$, δr_1 is the first radial increment, and there are N_2 grid planes with θ = constant.

3 Wall boundaries at r, $x=0$.

At the wall, either a logarithmic wall function, as presented in Ref. 4, is used to simulate the profile, or a condition of the form

$$a_\phi\frac{\partial\phi}{\partial n}+b_\phi\phi=c_\phi\ . \tag{28}$$

is used, where a_ϕ, b_ϕ, c_ϕ are constants.

4 Inlet ports and fuel orifice at r, $x=0$.

The condition $\phi=\phi_{p_i}$ is specified for each variable at each inlet.

5 Downstream condition

With the assumption that there is negligible diffusion in the axial direction, the condition

$$\frac{\partial^2\phi}{\partial x^2}=0\ . \tag{29}$$

is used.

Solution procedure

In view of the coupled, non-linear nature of the differential equations 24, 25, and relations 6-10, 13-22, we adopt an iterative procedure to determine the solution, similar to that described in Ref. 1. The method is briefly summarised as follows.

1) With initial estimates for the field variables, equation 24 is solved for (u,v,w) in turn. This is done by discretizing the equation and boundary conditions, and solving the resulting hepta-diagonal matrix equation. It is not necessary to obtain the exact solution to this, and an approximate method such as three alternating direction applications of the tridiagonal matrix algorithm is probably sufficient. This can be repeated if necessary. The solution thus obtained is, however, based on the estimated density and pressure fields ρ^*, p^*, say, and we write the solutions as (u^*, v^*, w^*).

2) We note that $\underline{u}^*$ does not satisfy equation 25 so we introduce the correction terms Δp, $\Delta\rho$, $\Delta\underline{u}$ so that

$$p = p^* + \Delta p \quad , \quad \rho = \rho^* + \Delta\rho \quad , \quad \underline{u} = \underline{u}^* + \Delta\underline{u} \quad . \tag{30}$$

Equation 8 is then used to eliminate ρ from equation 25. If the resulting equation, with p and $\underline{u}$ substituted from equation 30, is linearised with respect to Δp and $\Delta\underline{u}$, it is possible, by setting

$$\Delta\underline{u} = -\frac{1}{(\mathrm{diag})}\,\mathrm{grad}\,(\Delta p) \quad . \tag{31}$$

where (diag) is the diagonal coefficient in the matrix equation, to obtain an equation of the form of equation 24 for Δp. The boundary condition

$$\frac{\partial}{\partial n}(\Delta p) = 0 \quad . \tag{32}$$

is then used, and the pressure, density and velocity fields are updated.

3) Equation 24 is solved as in 1) above for k and ϵ in turn, and the eddy viscosity μ is recalculated using equation 10.

4) The enthalpy $\bar{H}$ is then calculated, from which the temperature is extracted, by means of equations 6, 7, 13 and 16.

5) The equations for the mass fractions F_i are solved for each species, and also for element concentration. The F_i are then adjusted to comply with element conservation, and with the constraint

$$\sum_{i=1}^{NS} F_i = 1 \quad .$$

6) The temperature is recalculated as before, and the molecular weight is evaluated by means of equation 9.

7) The above procedure is repeated until a converged solution is obtained, or until it is apparent that the process will not converge.

At each stage in the calculation, the latest available estimates are used for p, $\underline{u}$, T, μ, ρ, and for the evaluation of S_ϕ. After each stage, the maximum change in the solution for ϕ is monitored. Quantities which are hardly changing are then recalculated less frequently. In addition, some or all of the variables are under-relaxed when these are updated.

RESULTS

At this interim point of the investigation it has not proved possible to show any results from the three-dimensional flow computer program since it is not yet at a sufficiently advanced stage of development. However, the results of calculations of some examples of axisymmetric flows are presented below.

The first of these examples, chosen to enable comparisons to be made with previously published results[5], represents a small scale duct in which an outer stream of heated air mixes with a coaxial inner stream of heated hydrogen. Both streams are supersonic and the scale of the duct is such that little chemical reaction is expected to occur within the length of duct considered because of the short time involved (≈ 10 μs). For this reason the calculation is essentially an exercise in computing details of the pressure field and the flow was accordingly treated as chemically inert to reduce computing costs. Details of the input conditions are given in Table 2, while Table 3 lists values of the turbulence model constants. The results of the calculation are illustrated by Figs 3 and 4. In Fig. 3 the centreline pressure, normalized by the duct wall pressure, is plotted against downstream distance and compared with results from Ref. 6: agreement is reasonably satisfactory. Fig. 4 is an isometric plot of the whole pressure field and shows the disposition of the various shock and expansion waves occurring in the flow. It should be noted that the "shock-capturing" nature of the treatment of pressure waves used in the present analysis results in considerable "smearing" of the shock structure, but it is hoped that this treatment will be sufficiently accurate for present purposes.

The second example is again a wholly supersonic flow, but of a more representative scale and with a realistic primary flow composition. The outer flow is assumed to be an undiffused Mach 4 airstream. Details of the input conditions are given in Table 4: turbulence model constants are again as listed in Table 3. Two calculations were made with this flow geometry, with and without chemical reaction, to illustrate the effect of combustion of the flow. The reaction mechanism used for the reacting case is shown in Table 5, values of the rate coefficients being taken from Ref. 7 (thermodynamic data in all cases considered here were derived from the JANAF Thermochemical Tables, Ref. 8.). The results of these calculations are shown as isometric diagrams of pressure (Figs 5 and 8 for the reacting and inert flows respectively) and temperature (Figs 6 and 9). The shock pattern apparent in the pressure diagrams is illustrated schematically in plan form in Fig. 7. Comparison of the temperature fields, with and without reaction, shows that ignition of the flow in this case occurs downstream of the intersection of the outer shock after reflection from the duct wall.

CONCLUDING REMARKS

Considerable progress has been made towards the capability to calculate ducted rocket flows, as the illustrative examples testify. However, this success is as yet limited to flows with axial symmetry, which do not undergo choking, and, moreover, has not been achieved without difficulty. Early stages in the investigation were marked by problems of stability of the calculation procedure, associated particularly with the prediction of pressure. These difficulties have not been entirely eradicated and further investigation will be necessary. Flows which undergo choking, either physically or because of thermal effects, present a special problem for the axisymmetric flow program. The marching integration technique is intrinsically unsuited to the analysis of such flows, in which conditions at a downstream station control the upstream flow, unless some form of iterative adjustment of, e.g., the initial mass flow can be carried out (as is done for example in nozzle flow calculations, see Ref. 5). This aspect of the problem will require further work.

As far as the three-dimensional analysis is concerned, a major factor likely to influence the effectiveness of such a treatment applied to the secondary combustion chamber flow is the computational effort required. Since the treatment is not only over a three-dimensional field but also iterative by nature (to account for flow recirculation for example) not only will the required computer storage be large, the many grid points involved also imply a larger number of individual computations per iteration, resulting in a computing task of considerable magnitude. Emphasis has to date been aimed at assembling a technique which provides physically realistic answers: future work will need to concentrate on computing efficiency while maintaining physical realism if this approach is to be practically useful.

Finally, both the axisymmetric and the three-dimensional treatments are theoretical, with limited input of data from real devices. If this type of approach is to be of practical use in either a design or assessment context it will need to be carefully tested and proven against suitably designed experiments before its reliability can be assumed.

REFERENCES

1 Jensen, D.E., Spalding, D.B., Tatchell, D.G., and Wilson, A.S., "Computation of structures of flames with recirculating flow and radial pressure gradients", Combustion and Flame, 34, 309-326 (1979)

2 Launder, B.E., and Spalding, D.B., "Mathematical models of turbulence", Academic Press, London and New York, 1972

3 Patankar, S.V., and Spalding, D.B., "Heat and mass transfer in boundary layers (2nd edition)", Intext Books, London, 1970

4 Gibson, M.M., and Spalding, D.B., "Application of the k-w model of turbulence to boundary layers with streamwise pressure gradients, large temperature variations and transpiration cooling", Imperial College, London, Mechanical Engineering Department Report EHT/TN/A/32 (1971)

5 Wilson, A.S., "A user's guide to computer programs for the calculation of conditions in flames and rocket nozzles", Unpublished MOD(PE) Report (1972)

6 Kurkov, A.P., "Mixing of supersonic jets including the effects of transverse pressure gradient using difference methods", NASA Technical Note TN D-6592 (1971)

7 Jensen, D.E., and Jones, G.A., "Reaction rate coefficients for flame calculations", Combustion and Flame, 32, 1-34 (1978)

8 Stull, D.R., and Prophet, H. (Eds.), "JANAF Thermochemical Tables, 2nd Edn.", National Bureau of Standards (Washington, DC). NBS-NSRDS No. 37 (1971)

TABLE 1

Source terms for three-dimensional transport equations

ϕ	$S\phi$
u	$\frac{-\partial p'}{\partial x} + \frac{\partial}{\partial x}\left(\mu \frac{\partial u}{\partial x}\right) + \frac{1}{r}\frac{\partial}{\partial r}\left(r\mu \frac{\partial v}{\partial x}\right) + \frac{1}{r}\frac{\partial}{\partial \theta}\left(\mu \frac{\partial w}{\partial x}\right)$
v	$\frac{-\partial p'}{\partial r} + \frac{\rho w^2}{r} + \frac{1}{r}\frac{\partial}{\partial r}\left[r\mu \frac{\partial v}{\partial r}\right] - \frac{2\mu v}{r^2} + \frac{\partial}{\partial \theta}\left(\mu \frac{\partial}{\partial r}\left(\frac{w}{r}\right)\right) + \frac{\partial}{\partial x}\left(\mu \frac{\partial u}{\partial x}\right) - \frac{2\mu}{r^2}\frac{\partial w}{\partial \theta}$
w	$\frac{-1}{r}\frac{\partial p'}{\partial \theta} - \frac{\rho v w}{r} + \frac{1}{r^2}\frac{\partial}{\partial \theta}\left(\mu \frac{\partial w}{\partial \theta}\right) - \frac{1}{r^2}\frac{\partial}{\partial r}(r\mu)w + \frac{1}{r^2}\frac{\partial}{\partial r}\left(r\mu \frac{\partial v}{\partial \theta}\right) + \frac{1}{r}\frac{\partial}{\partial x}\left(\mu \frac{\partial u}{\partial \theta}\right) + \frac{2}{r^2}\frac{\partial}{\partial \theta}(\mu v)$
k	$\Phi - \rho\varepsilon$
ε	$(C_1\Phi - C_2\rho\varepsilon)\,\varepsilon/k$
H	$\left\{\frac{\partial}{\partial x}\left(\mu \frac{\partial}{\partial x}\right) + \frac{1}{r}\frac{\partial}{\partial r}\left(r\mu \frac{\partial}{\partial r}\right) + \frac{1}{r^2}\frac{\partial}{\partial \theta}\left(\mu \frac{\partial}{\partial \theta}\right)\right\} \left\{(1 - \frac{1}{\sigma_H})\left(\frac{u^2 + v^2 + w^2}{2}\right) + \left(\frac{1}{\sigma_k} - \frac{1}{\sigma_H}\right) K\right\}$
	$+ \sum_{i=1}^{N^c}\left\{\frac{\partial}{\partial x}\left(\mu h_i \frac{\partial}{\partial x}\right) + \frac{1}{r}\frac{\partial}{\partial r}\left(r\mu h_i \frac{\partial}{\partial r}\right) + \frac{1}{r^2}\frac{\partial}{\partial \theta}\left(\mu h_i \frac{\partial}{\partial \theta}\right)\right\}\left\{\left(\frac{1}{\sigma_{mi}} - \frac{1}{\sigma_H}\right) F_i\right\}$
F_i	$\dot{w}_i$

where $p' = p + \frac{2}{3}\mu\left(\frac{\partial u}{\partial x} + \frac{1}{r}\frac{\partial}{\partial r}(rv) + \frac{1}{r}\frac{\partial w}{\partial \theta}\right)$

and

$$\Phi = \mu\left\{2\left[\left(\frac{\partial u}{\partial x}\right)^2 + \left(\frac{\partial v}{\partial r}\right)^2 + \left(\frac{1}{r}\frac{\partial w}{\partial \theta}\right)^2\right] + \left(\frac{1}{r}\frac{\partial v}{\partial \theta} + \frac{\partial w}{\partial r}\right)^2 \right.$$

$$+ \left(\frac{\partial w}{\partial x} + \frac{1}{r}\frac{\partial u}{\partial \theta}\right)^2 + \left(\frac{\partial u}{\partial r} + \frac{\partial v}{\partial x}\right)^2 - \frac{2w}{r^2}\frac{\partial v}{\partial \theta}$$

$$\left. - \frac{2w}{r}\frac{\partial w}{\partial_r} + \frac{4v}{r^2}\frac{\partial w}{\partial \theta} + \frac{2v^2 + w^2}{r^2}\right\} .$$

TABLE 2

Input conditions for example 1

	Primary nozzle	Air stream
Radius, m	1.0×10^{-3}	3.76×10^{-3}
Velocity, ms^{-1}	5012	2548
Pressure, Nm^{-2}	5.066×10^{5}	2.533×10^{5}
Temperature, K	1100	1500
Chemical species concentrations (mole fraction)		
N_2	0.0	0.7856
H_2	1.0	0.0
CO_2	0.0	3.27×10^{-4}
H_2O	0.0	6.95×10^{-3}
O_2	0.0	0.2071

TABLE 3

Turbulence model constants

C_D	0.09	σ_H	1.0
C_1	1.62	σ_m	1.0
C_2	1.92	σ_k	1.0
		σ_ε	1.3

TABLE 4

Input conditions for example 2

	Primary nozzle	Air stream
Radius, m	0.01	0.0376
Velocity, ms^{-1}	2500	1400
Pressure, Nm^{-2}	5.066×10^{5}	1.013×10^{5}
Temperature, K	1500	300
Chemical species concentrations (mole fraction)		
N_2	0.1083	0.7856
H_2	0.1904	0.0
CO	0.4385	0.0
CO_2	0.0893	3.27×10^{-4}
H_2O	0.1734	6.95×10^{-3}
O_2	1.322×10^{-9}	0.2071
H	1.013×10^{-4}	0.0
OH	1.014×10^{-7}	0.0
O	5.710×10^{-11}	0.0
HO_2	1.000×10^{-9}	0.0

TABLE 5

Chemical reaction scheme

Reaction	Forward rate coefficient[a]
$O + O + M = O_2 + M$	$3 \times 10^{-34}\ \exp(900/T)$
$O + H + M = OH + M$	$1 \times 10^{-29}\ T^{-1}$
$H + H + M = H_2 + M$	$3 \times 10^{-30}\ T^{-1}$
$H + OH + M = H_2O + M$	$1 \times 10^{-25}\ T^{-2}$
$CO + O + M = CO_2 + M$	$7 \times 10^{-33}\ \exp(-2200/T)$
$OH + H_2 = H_2O + H$	$1.9 \times 10^{-15}\ T^{1.3}\ \exp(-1825/T)$
$O + H_2 = OH + H$	$3 \times 10^{-14}\ T\ \exp(-4480/T)$
$H + O_2 = OH + O$	$2.4 \times 10^{-10}\ \exp(-8250/T)$
$CO + OH = CO_2 + H$	$2.8 \times 10^{-17}\ T^{1.3}\ \exp(330/T)$
$OH + OH = H_2O + O$	$1 \times 10^{-11}\ \exp(-550/T)$
$CO + O_2 = CO_2 + O$	$4.2 \times 10^{-12}\ \exp(-24000/T)$
$H + O_2 + M = HO_2 + M$	$2 \times 10^{-32}\ \exp(500/T)$
$H + HO_2 = OH + OH$	$4 \times 10^{-10}\ \exp(-950/T)$
$H + HO_2 = H_2 + O_2$	$4 \times 10^{-11}\ \exp(-350/T)$
$H_2 + HO_2 = H_2O + OH$	$1 \times 10^{-12}\ \exp(-9400/T)$
$CO + HO_2 = CO_2 + OH$	$2.5 \times 10^{-10}\ \exp(-11900/T)$
$O + HO_2 = OH + O_2$	$8 \times 10^{-11}\ \exp(-500/T)$
$OH + HO_2 = O_2 + H_2O$	5×10^{-11}

(a) rate coefficients in molecule-ml-second units

Copyright © Controller HMSO, London, 1981

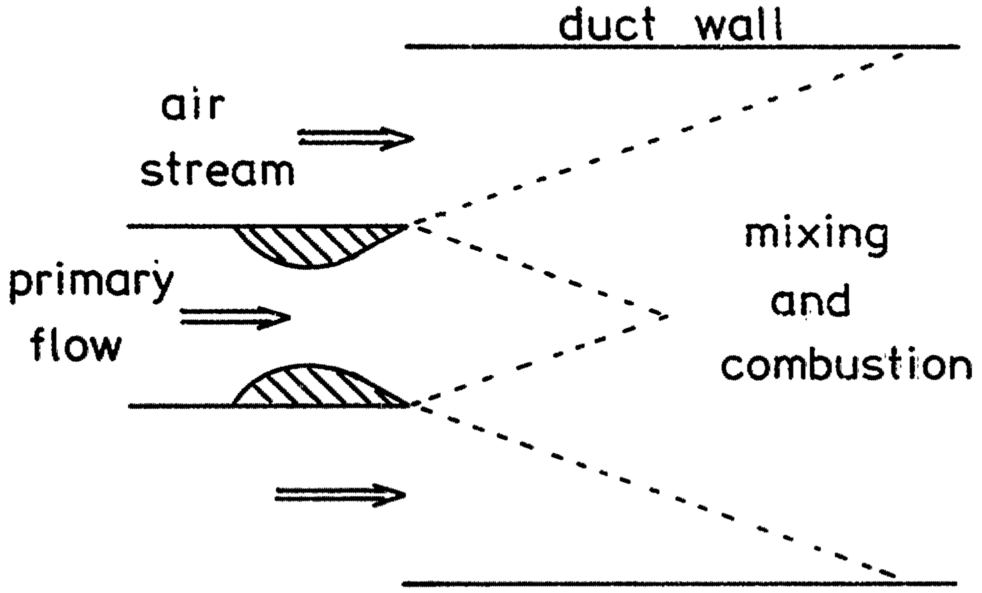
duct wall
air
stream
primary
flow
mixing
and
combustion

Fig. 1 Axisymmetric flow geometry

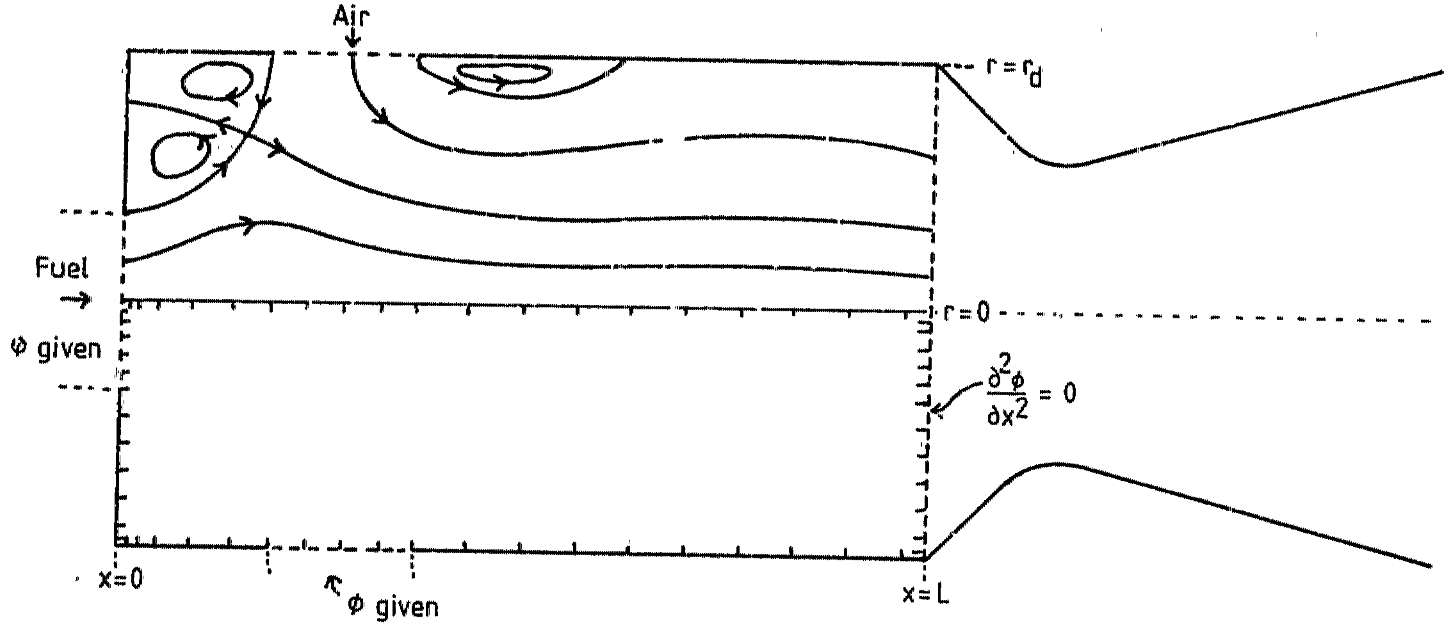
Air
$r = r_d$
Fuel
ϕ given
$r=0$
$\frac{\partial^2 \phi}{\partial x^2} = 0$
$x=0$
ϕ given
$x=L$

Fig. 2 Typical three-dimensional flow geometry, indicating example inlet configuration, computation grid and streamlines

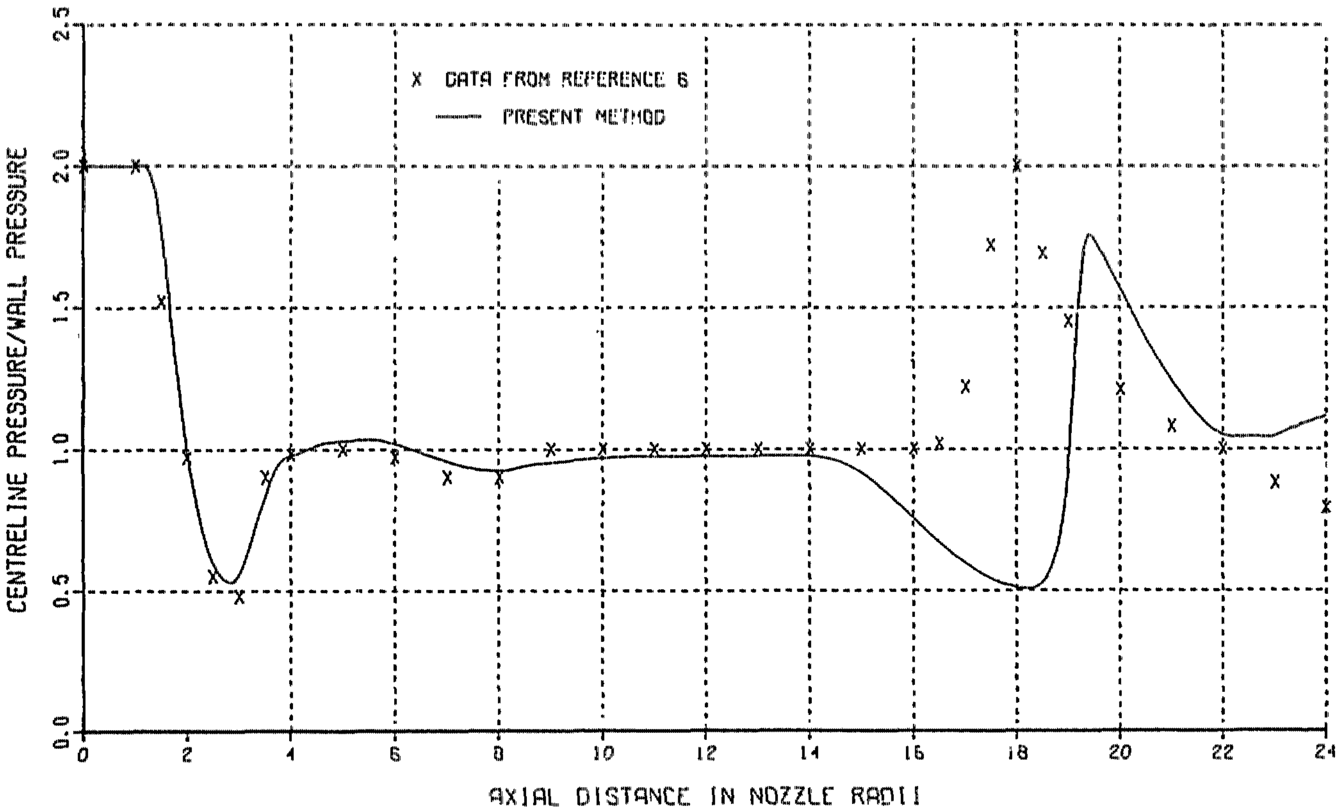

FIG.3 SUPERSONIC DUCTED FLOW - COAXIAL JETS WITHOUT CHEMICAL REACTION
CENTRELINE PROFILE OF NORMALISED STATIC PRESSURE

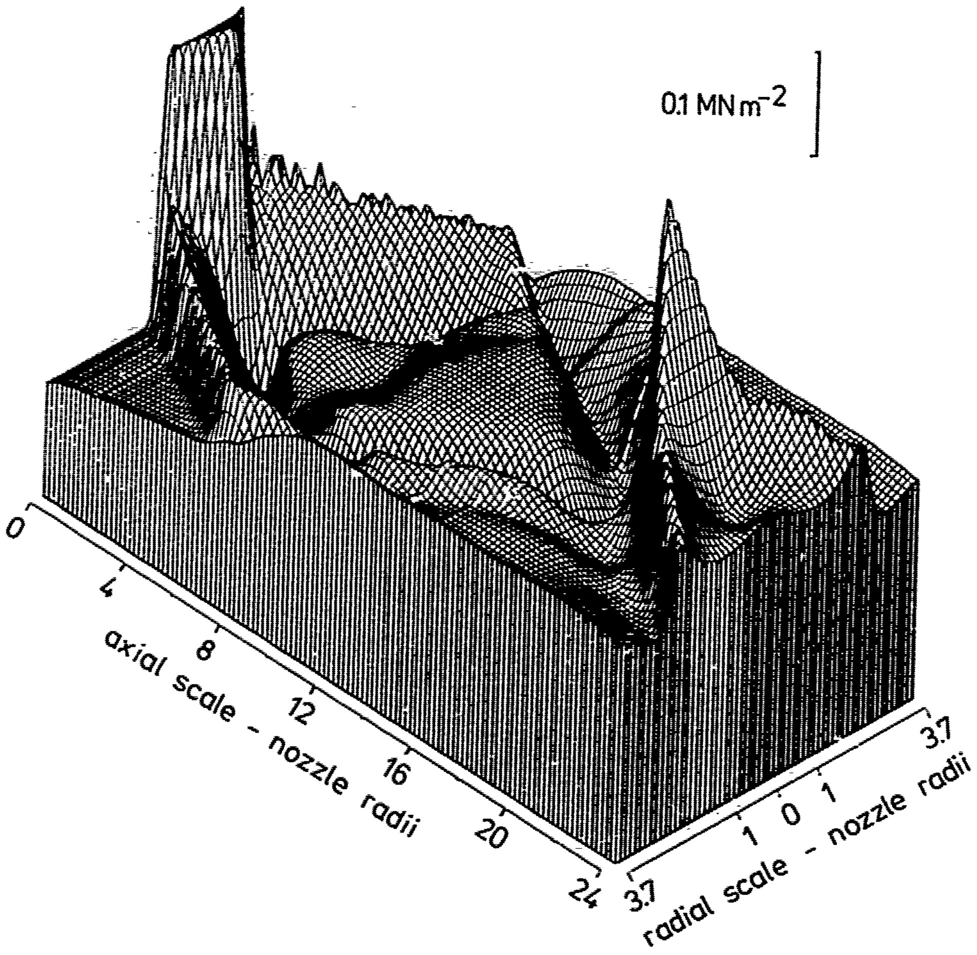

Fig.4 Isometric diagram of pressure field of small-scale ducted inert coaxial jets

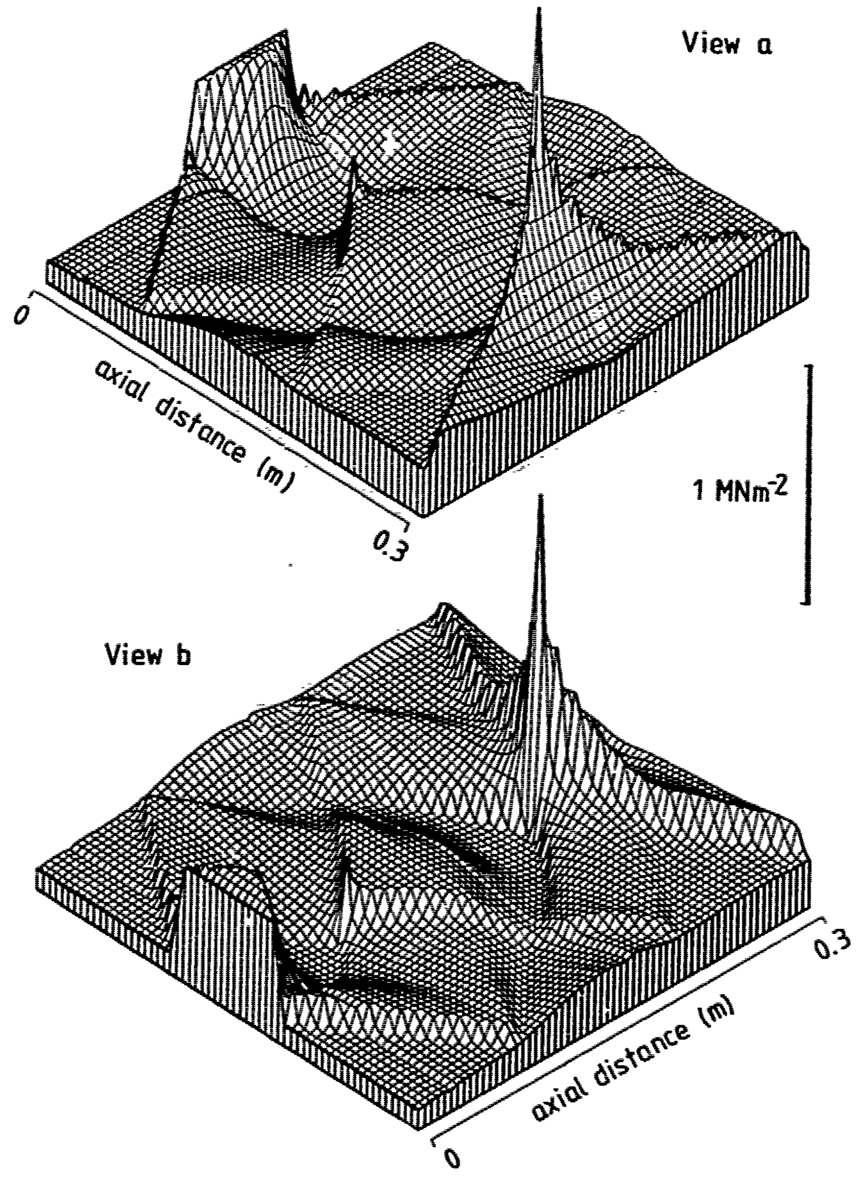

Fig. 5 Isometric diagrams of example case pressure field

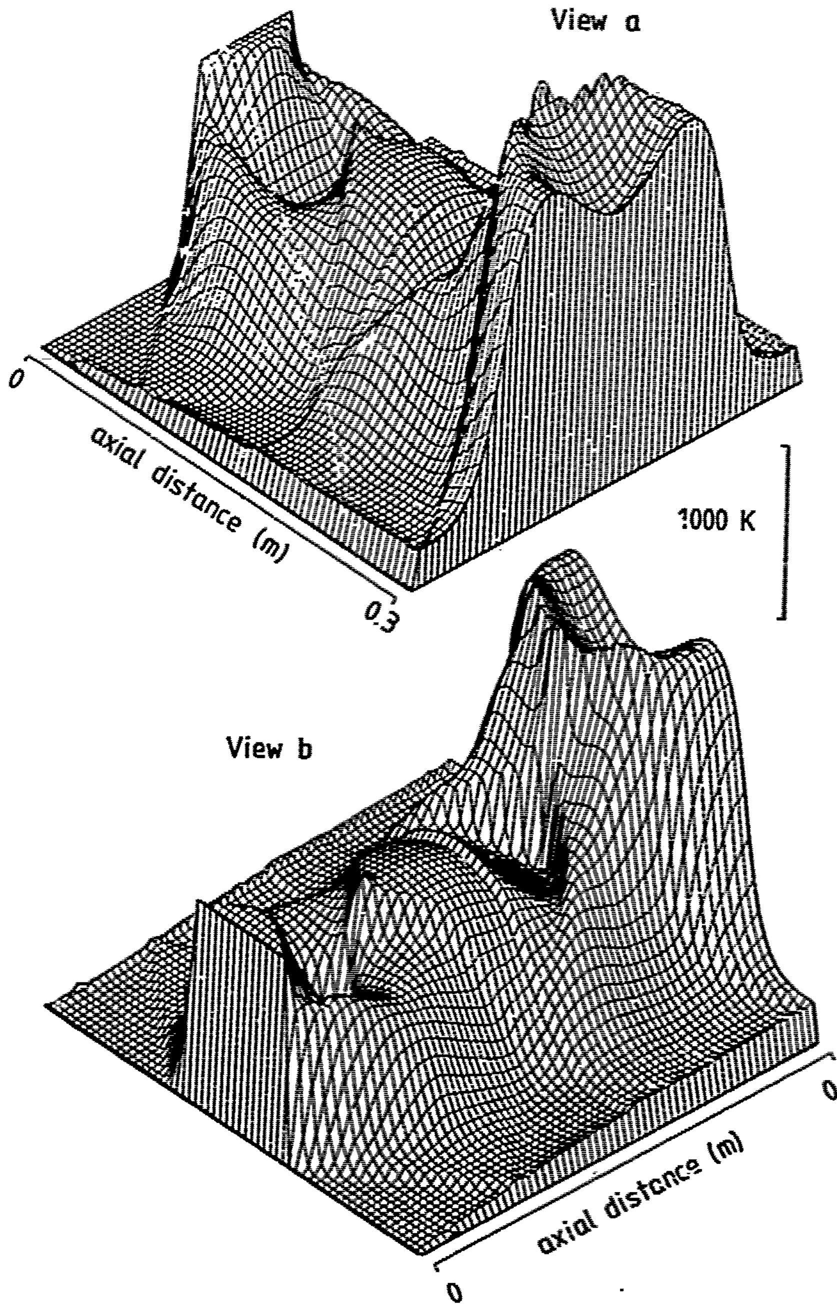

Fig. 6 Isometric diagrams of example case temperature field

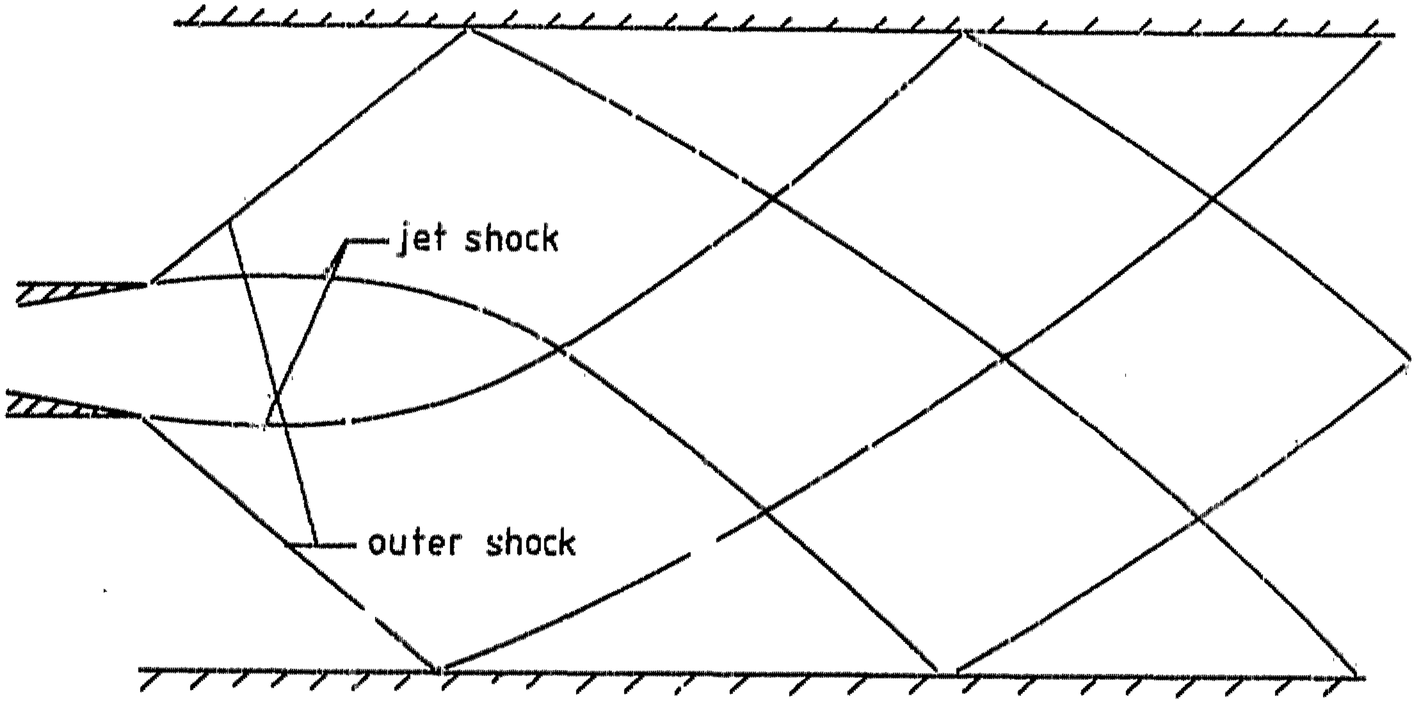
jet shock
outer shock

Fig. 7 Diagram illustrating plan of shock pattern for example case

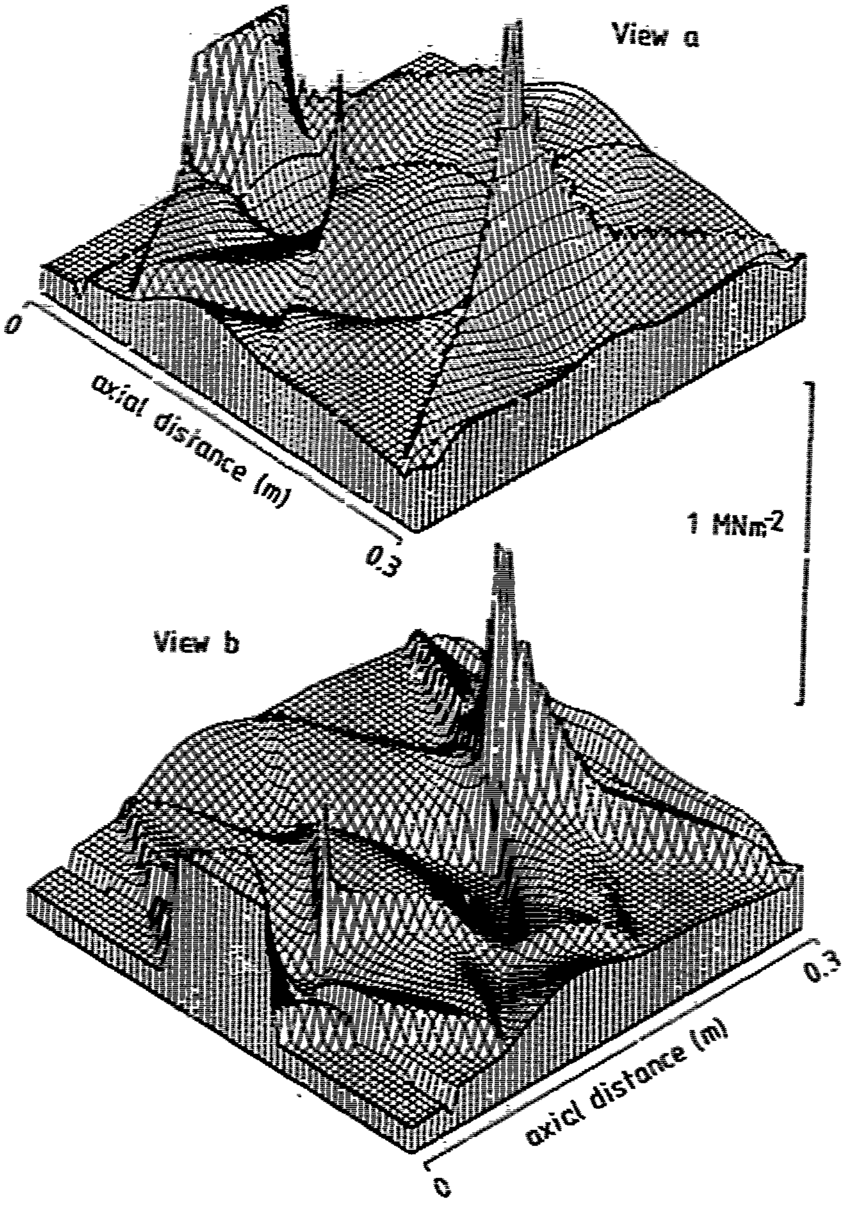

Fig. 8 Isometric diagrams of pressure field – example case without chemical reactions

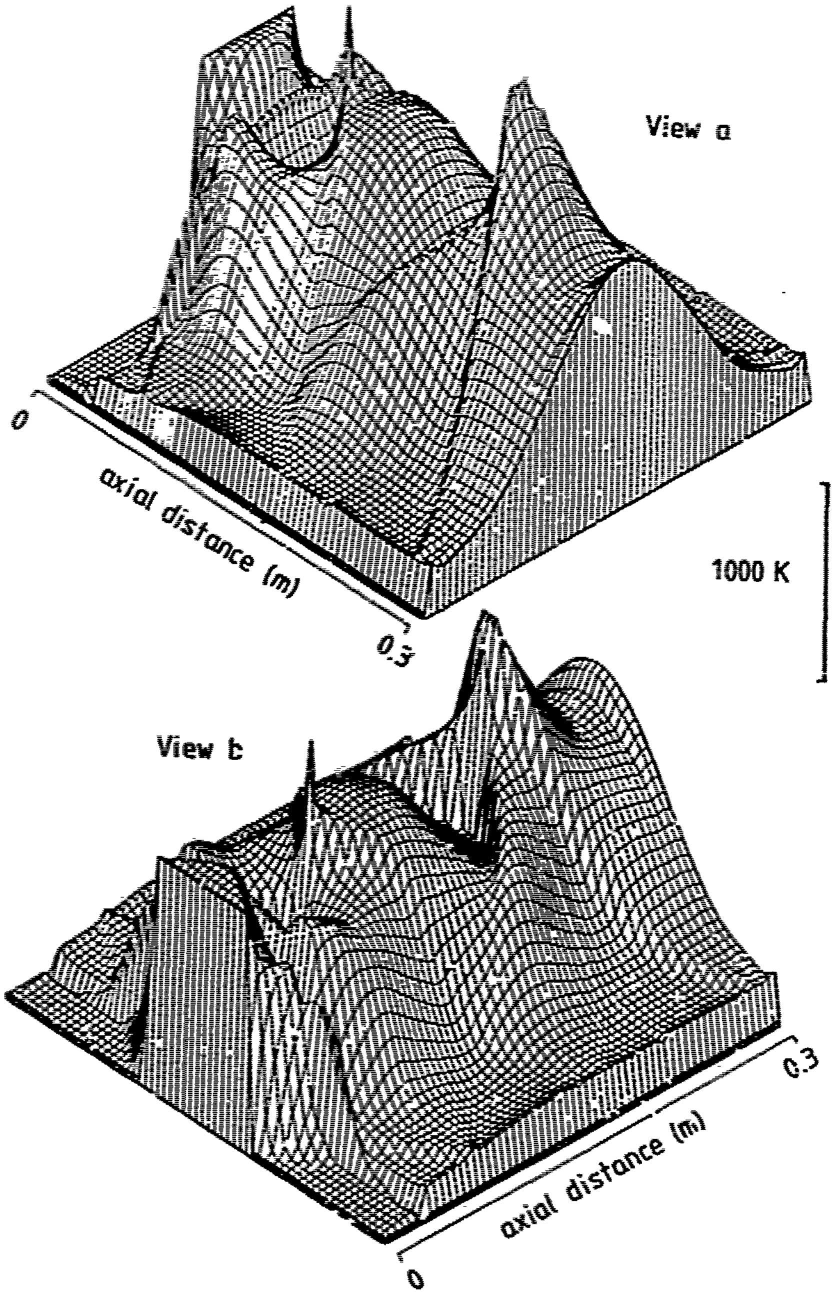

Fig.9 Isometric diagrams of temperature field - example case without chemical reactions

COMBUSTOR MODELLING STUDIES FOR RAMJETS

P. Roy, A.F. Schlader and J. Odgers
Department of Mechanical Engineering
Universite Laval
Quebec, CANADA, G1K 7P4

ABSTRACT

Using premixed propane-air within a baffle-stabilised, ceramic-lined combustor, detailed measurements were made of the gas composition at several stations downstream of the recirculation zone. The test rig was operated at atmospheric conditions over a range of equivalence ratios from ϕ = 0,70 to 1,82. The test results were then analysed and a simple three-equation model was developed to describe the composition and temperature profiles.

Further tests were then made to verify the model, some of which were with steam injection. The model was found to be satisfactory for all conditions examined.

NOMENCLATURE

A	Collision frequency factor	$(L/mol)^{n-1}/s$
fC_3H_8, fCO_2, fCO, fH_2, fH_2O	Molar fractions	
$d/d\tau$	Time derivative	
E	Activation energy	cal/g mol
n	Order of reaction	
P	Pressure	atm
R	Universal gas constant for use with P/RT R = 0,08206 -E/RT R = 1,986	 atm L/(mol K) cal/(mol K)
T	Temperature	K
X	Distance from primary baffle to any point downstream	m
α	Partial order of reaction	
ε	Partial order of reaction	
ϕ	Equivalence ratio	

Subscripts

1	Refers to reaction rate	$-3dfC_3H_8/d\tau$
2	Refers to reaction rate	$dfCO_2/d\tau$
3	Refers to reaction rate	$dfH_2O/d\tau$

1. INTRODUCTION

In its broadest sense a ram-jet combustor may be likened to an uncooled version of a gas turbine primary zone operating at a somewhat higher velocity. Thus it would seem possible that a suitable hydrocarbon combustion model developed for the one, would be applicable to the other.

This present work describes such a model. In order to minimise mixing effects, a premixed, prevaporised propane-air system was used and the analysis was restricted to points downstream of the combustor recirculation zone. To minimise heat losses, the entire combustor was ceramic lined and the recirculation zone was defined by the space between a primary baffle (80% blockage) and a downstream secondary baffle (20% blockage).

The use of a baffled recirculation zone and the absence of both film cooling and dilution air resembles, in general, the character of a ram-jet. On the other hand, the system might be said to be representative of an isolated primary zone of a gas-turbine combustor.

Because of its pre-mixed nature it may not be unreasonable to presume that the system is reaction rate controlled - a fact to a large degree substantiated by the uniformity of gas analysis noted in the subsequent experiments. Both temperature and species measurements were derived from gas analyses carried out at a series of planes downstream from the combustor. These values were then used to derive the simple combustion model which was later substantiated by additional tests, both with and without, steam injection.

2 TEST RIG AND INSTRUMENTATION

The test rig is very similar to that described in detail in [1]* and [2]. A schematic is given in Fig. 1. Separately metered air and fuel are premixed upstream of the inlet baffle to the combustor. The fuel injector was a simple cylindrical distributor, 0,75 m upstream of the combustor baffle, fitted with injection holes normal to the air stream (32 holes of 1,3 mm diameter). At all conditions great care was taken to ensure that the propane was injected in the gaseous phase thereby obviating the need for any evaporation time.

To ascertain the degree of pre-mix, carbon dioxide (selected because of its density similarity to propane) was injected into the air stream and the mixture strength was determined by sampling at numerous points (30) at the combustor inlet in the plane of the primary baffle. These results indicated that no single value differed from more than ±2,7% from the mean value. This was considered satisfactory.

---

* Numbers in [] are listed in the table of References.

TEST RIG

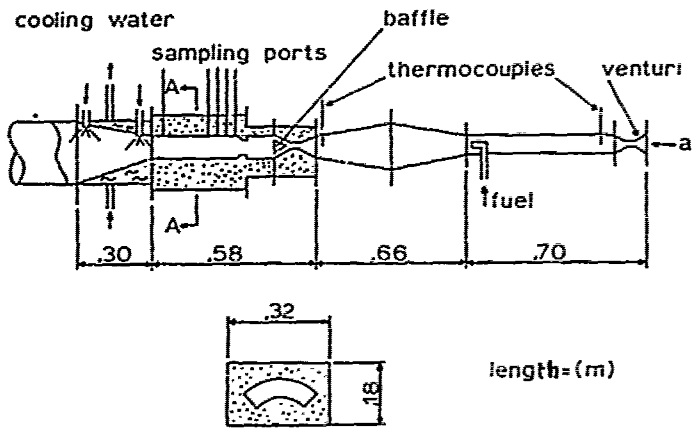

section "A-A" FIG.1

The combustor itself was a 90° sector of an annular chamber (hydraulic diam. = 0,127 m) being totally lined with ceramic and having a recirculation zone stabilised with both a primary and secondary baffle. Downstream of the recirculation zone was another refractory-lined sector containing the sampling ports which were situated at distances of 129 mm, 163 mm, 214 mm, 262 mm and 379 mm from the primary baffle. Air velocities were selected so as to give residence times commensurate with those which obtain within ram-jet and gas-turbine combustors (i.e. 2-8 ms).

The experiments covered the following range of inlet variables -

T_3	inlet temperature:	ambient (recorded)	$\emptyset$	equivalence ratio	0,697 - 1,32	
P_3	inlet pressure:	ambient (recorded)	t_c	'cold' residence time	18-30	ms
$\dot{m}_a$	air mass flow:	0,18 - 0,30 kg/s	t_h	'hot' residence time	5,35-8,39	ms
$\dot{m}_f$	fuel mass flow	0,01 - 0,02 kg/s	u_g	'cold' gas velocities	12,6-21	m/s

The cold residence times were calculated at inlet conditions based upon the diameter and mean velocity within the recirculation zone. Hot residence times were based upon the mean velocities obtained at the inlet and any of the various planes of measurement.

Gas analyses were withdrawn from one or other of the five planes mentioned above. Three samplers were used in any one plane and each sampler was fitted with 3 sampling ports. All the samples were combined prior to analysis to give a representative mean analysis for any given plane. The occasional independent check substantiated the validity of this technique. The samplers were water cooled, (the outlet temperature from the sampler was still sufficiently high to prevent water condensation, T_{outlet} = 100°C) and the line from the samplers was steam-traced up to the entry to the gas analysis apparatus. This latter was a double instrument, prepared for rapid gas chromatography. Determinations were made of C_3H_8(FID), CO_2, CO, H_2, O_2 & N_2. As a check on the accuracy of the sample, comparison was made of the derived value of equivalence ratio and that based on the air and fuel metering. The maximum difference between the two values for any test was 3% which is well within the normally accepted value of ±5,0%.

Heat losses from the system were assessed by measurement of the temperature of the outer metal liner supporting the ceramic. In no case did the heat loss exceed 0.62%. This was considered to be sufficiently low so as not to merit correction.

NO_x measurements are not included. The few measurements which were made showed them to be in substantial agreement with the empirical predictions of Lipfert [3] and Kretschmer et al. [4]. NO_x was deliberately not considered for the model since (a) the intention was to keep the 'combustion' as simple as possible and (b) predictions using the empirical techniques of [3] and [4] appear to be quite satisfactory for NO_x determination at the exhaust.

3. DESCRIPTION OF THE MODEL

The present trend in modelling hydrocarbon combustion is to use a multi-kinetic scheme involving numerous reactions. However, such schemes usually assume that the first phase of the combustion process is the breakdown of the hydrocarbon into carbon monoxide and hydrogen, or alternatively, to carbon monoxide and water. The first stage (i.e. hydrocarbon breakdown) is assumed to be either infinitely fast or dependent upon an empirical (experimentally) determined rate step assuming a single reaction (an assumption which is totally at variance with theory and justified only be expedience). Having attained the end of this first stage, a multi-step reaction is assumed for the combustion of the carbon monoxide and, if necessary, hydrogen. Equations are generally included to enable the formation of NO_x to be calculated. Typical examples are given in [5 to 12]. A possible exception to the assumption of the hydrocarbon breakdown mechanism is methane which could be treated as a multi-reaction scheme involving the initial breakdown. An alternative to the above complex modelling is the simple, convenient, one-step reaction mechanism (so-called global reaction) as portrayed by several workers [13 to 16]. One justifiable objection to this simple approach is that it does not enable the pollutants to be separately assessed (i.e. CO and UBHC).

The present model represents a compromise between these two types. The reaction is represented as a three step mechanism using propane as fuel -

$$C_3H_8 + 3{,}5\ O_2 \longrightarrow 3\ CO + 4\ H_2 \qquad (1)$$

$$3\ CO + 1{,}5\ O_2 \longrightarrow 3\ CO_2 \qquad (2)$$

$$4\ H_2 + 2\ O_2 \longrightarrow 4\ H_2O \qquad (3)$$

$$\underline{C_3H_8 + 5\ O_2 \longrightarrow 3\ CO_2 + 4\ H_2O} \qquad (1)+(2)+(3)$$

This mechanism includes a limited oxidation rate of the fuel, since it is active throughout the flame, and is represented by the following three rate equations:

$$-dfC_3H_8/d\tau = A_1(P/RT)^{n_1-1} .\ fC_3H_8^{\,n_1-\alpha_1} .\ fO_2^{\,\alpha_1}\ e^{-E_1/RT} \qquad (4)$$

$$dfCO_2/d\tau = A_2(P/RT)^{n_2-1} .\ fCO^{\,n_2-(\alpha_2+\varepsilon_2)} .\ fO_2^{\,\alpha_2} .\ fH_2O^{\,\varepsilon_2}\ e^{-E_2/RT} \qquad (5)$$

$$dfH_2O/d\tau = A_3(P/RT)^{n_3-1} .\ fH_2^{\,n_3-\alpha_3} .\ fO_2^{\,\alpha_3}\ e^{-E_3/RT} \qquad (6)$$

The second equation was proposed by Hottel [17] to describe his results for a stirred reactor.

The results from the present series of experiments were employed to determine values of the various constants for Eqns. (4) to (6). If the three equations are valid, then at any plane within the combustor, it should be possible to specify the amounts of C_3H_8, CO_2, CO, H_2, O_2, H_2O, and N_2.

In order to derive the values of the various paramaters, test results were selected that had a common equivalence ratio (Ø) within a narrow margin of fluctuation. Four groups of these results have been formed on the lean side and three on the rich, with the following mean Ø values (Table I). The results in these groups are mean values for a range of tests in which Ø varied very slightly (±0,01).

Table I

Mean Ø Values of Experimental Results Which Were Used for Model

Ø ≤ 1	Ø > 1
0,701	1,09
0,855	1,21
0,914	1,32
0,987	

To facilitate the computation of the parameters, the gas constituents appearing in the three rate equations have been expressed as functions of temperature by a best-fit equation for each Ø of table I. The same method was also used to represent the experimental values of the rates, but adding one more step of calculation. For exemple, the rate of CO_2, i.e. $dfCO_2/d\tau$, is obtained by forming the derivative $dfCO_2/dT$ from the equation representing CO_2 vs. T, and then multiplying it with the derivative dT/τ obtained from the equation representing T vs. τ. This gives then the following rates:

$$dfCO_2/d\tau = dfCO_2/dT \quad dT/d\tau \qquad (7)$$

$$dfC_3H_8/d\tau = dfC_3H_8/dT \quad dT/d\tau \qquad (8)$$

$$dfH_2O/d\tau = dfH_2O/dT \quad dT/d\tau \qquad (9)$$

The derivative $dT/d\tau$ is common to all three of [illegible] ove equations. Thus the rates, molar fractions, temperature and pressure in equati[illegible]), (5) and (6) were known from the experimental results. The values of the parameters [illegible] ese equations were then obtained by isolating one parameter on the left side of one of these equations, and taking for the remaining parameters on the other side, values given in the literature for the first trial [17 to 20]. These are given in Table II. Then, the isolated parameter with its calculated value was shifted to the right side of the equation and another parameter was transferred to the left. This cyclic procedure was repeated for all parameters until the rates expressed by the equations (4), (5) and (6) matched the values derived from the experimental results.

Since the variables (rate, molar fractions, pressure and temperature in equations (4), (5) and (6) covered a wide range of flame temperature and Ø, it was possible to demonstrate by the above calculations that the parameters A and E, are functions of T only whereas the parameters n, α and ε depend upon T and to a somewhat lesser degree upon Ø. The hypothesis of variable orders of reactions and variable activation energy E was put forward and discussed by Levy and Weinberg [21]. This, however, is not considered in the global reaction mechanism where a slow rate-determining step is assumed to dominate the mechanism [22]. The results obtained here confirmed this hypothesis, and polynomial functions of T and to a lesser degree of Ø have been used to represent the parameters (A, n, α, ε, E) in equations (4), (5) and (6). For the parameters the following expressions were obtained.

Table II

Data taken from Literature and Used to Asses the Values of the Parameters Used in the Solution of Eqns. (4), (5) & (6)

Source		Parameter Values		
		A $(L/mol)^{n-1}/s$	n	E (cal/mol)
Hottel et al [17]	$f'CO_2$	$2{,}9 \times 10^{10}$	1,75	-15,000
Avery et al [19]	$f'C_3H_8$	$5{,}4 \times 10^{13}$	2,0	-21,000
Kretschmer et al [20]	$f'C_3H_8$	Variable as function of ϕ	Weak 2ϕ Rich $\frac{2}{\phi}$	Variable as function of ϕ

Lean side: $\phi \leq 1$

$A_1 = \exp\,[9{,}80282 + 0{,}0177138\,T - 2{,}46812 \times 10^{-5}\,T^2 + 1{,}46127 \times 10^{-8}\,T^3 - 2{,}82414 \times 10^{-12}\,T^4]$

$E_1 = 2{,}29232 \times 10^4 - 43{,}8464\,T + 0{,}0263129\,T^2$

$n_1 = 2{,}49825 - 0{,}210153\,\phi - 6{,}07512 \times 10^{-4}\,T$

$\alpha_1 = 0{,}431636 + 4{,}38222 \times 10^{-5}\,T$

$A_2 = \exp\,[12{,}82 - 6{,}4667 \times 10^{-4}\,T + 2{,}2667 \times 10^{-6}\,T^2]$

$E_2 = 1{,}2358 \times 10^4 - 10{,}59\,T + 9{,}2262 \times 10^{-3}\,T^2$

$n_2 = 0{,}7962 + 0{,}05558\,\phi + 5{,}374 \times 10^{-4}\,T - 3{,}949 \times 10^{-8}\,T^2$

$\alpha_2 = -0{,}2387 + 0{,}9157\,\phi - 4{,}415 \times 10^{-4}\,T + 1{,}858 \times 10^{-7}\,T^2$

$\varepsilon_2 = -0{,}4133 - 0{,}4789\,\phi + 2{,}004 \times 10^{-3}\,T - 7{,}813 \times 10^{-7}\,T^2$

$A_3 = \exp[-14{,}7894 + 6{,}11699 \times 10^{-2}\,T - 5{,}20148 \times 10^{-5}T^2 + 2{,}40499 \times 10^{-8}T^3 - 4{,}25903 \times 10^{-12}\,T^4]$

$E_3 = 1{,}62708 \times 10^4 - 21{,}8015\,T + 1{,}34966 \times 10^{-2}\,T^2 + 2{,}22496 \times 10^{-7}\,T^3$

$n_3 = -0{,}120686 + 0{,}0413256\,\phi + 1{,}79418 \times 10^{-3}\,T - 4{,}00207 \times 10^{-7}\,T^2$

$\alpha_3 = 1{,}24458 - 0{,}0475454\,\phi - 1{,}0372 \times 10^{-3}\,T + 3{,}67014 \times 10^{-7}\,T^2$

Rich Side: $\phi > 1$

$A_1 = \exp\,[23{,}2993 - 0{,}0208873\,T + 1{,}51196 \times 10^{-5}\,T^2 - 2{,}29646 \times 10^{-9}\,T^3]$

$E_1 = 5{,}321 \times 10^4 - 99{,}2928\,T + 0{,}0772317\,T^2 - 1{,}64845 \times 10^{-5}\,T^3$

$n_1 = 0{,}262345 + 0{,}686424\,\phi + 9{,}67385 \times 10^{-4}\,T - 2{,}83092 \times 10^{-4}\,\phi\,T$

$\alpha_1 = -6{,}26856 + 3{,}21021\,\phi + 9{,}52742 \times 10^{-3}\,T - 4{,}80779 \times 10^{-3}\,\phi\,T + 7{,}09639 \times 10^{-2}\,\phi^2$
$\qquad - 2{,}08734 \times 10^{-6}\,T^2 + 6{,}72829 \times 10^{-7}\,\phi^2\,T^2$

$A_2 = \exp\,[24{,}615 - 0{,}0139356\,T + 1{,}01772 \times 10^{-5}\,T^2 - 1{,}49559 \times 10^{-9}\,T^3]$

$E_2 = 1{,}43248 \times 10^4 - 14{,}9636\,T +$ [illegible]$142349\,T^2 + 9{,}57874 \times 10^{-7}\,T^3$

$n_2 = 1{,}8463 - 0{,}464621\,\phi + 0{,}327879\,\phi^2 - 0{,}000561141\,T + 1{,}34725 \times 10^{-7}\,T^2 + 4{,}86453 \times 10^{-4}\phi\,T$
$\qquad - 6{,}16589 \times 10^{-8}\,\phi^2\,T^2$

$\alpha_2 = 7{,}904 - 14{,}8385\,\phi + 7{,}56984\,\phi^2 + 0{,}0047155\,T - 6{,}03403 \times 10^{-7}\,T^2 - 0{,}00476403\,\phi\,T$
$\qquad + 7{,}02645 \times 10^{-7}\,\phi^2\,T^2$

$\varepsilon_2 = -34{,}5125 + 45{,}7687\,\phi - 13{,}449\,\phi^2 + 0{,}0210546\,T - 3{,}36879 \times 10^{-6}\,T^2 - 0{,}0179327\,\phi\,T$
$\qquad + 2{,}3543 \times 10^{-6}\,\phi^2\,T^2$

$A_3 = \exp\,[37{,}9777 - 0{,}0494814\,T + 3{,}47914 \times 10^{-5}\,T^2 - 7{,}04779 \times 10^{-9}\,T^3]$

$E_3 = 5{,}05266 \times 10^4 - 91{,}892\,T + 0{,}071018\,T^2 - 1{,}48654 \times 10^{-5}\,T^3$

$n_3 = 0{,}0435549 + 0{,}405397\,\phi + 4{,}12306 \times 10^{-4}\,T + 1{,}96293 \times 10^{-4}\,\phi\,T$

$\alpha_3 = 5{,}05741 - 7{,}74854\,\phi - 3{,}69989 \times 10^{-3}\,T + 5{,}2833 \times 10^{-3}\,\phi\,T + 1{,}85779\,\phi^2$
$\qquad + 5{,}5344 \times 10^{-7}\,T^2 - 8{,}77687 \times 10^{-7}\,\phi^2\,T^2$

By analysing the foregoing expressions obtained for the parameters, one sees that two sets of equations are required to cover the range of reaction conditions investigated (Table I), - one set for the lean side, i.e. $\phi \leq 1$ and one set for the rich side, i.e. $\phi > 1$. This has also been reported by other workers [20].

The parameters (A, n, α, ε, E) have the following numerical values for the given values of ϕ and T.

Table III

Variation of the parameters with ϕ and T

ϕ	,8			1,0			1,2		
T[K]	1200	1600	2000	1200	1600	2000	1200	1600	2000
A_1	$3x10^6$	$12,1x10^6$	$81,9x10^6$	$3x10^6$	$12,1x10^6$	$81,9x10^6$	$4,14x10^6$	$21,4x10^6$	$1,83x10^{10}$
E_1	8198	20130	40482	8198	20130	40482	16800	24500	31700
n_1	1,60	1,36	1,12	1,56	1,32	1,07	1,31	1,57	1,82
α_1	0,48	0,50	0,52	0,48	0,50	0,52	0,57	0,82	0,71
A_2	$4,45x10^6$	$43,5x10^6$	$8,78x10^8$	$4,45x10^6$	$43,5x10^6$	$8,78x10^8$	$4,68x10^8$	$4,58x10^9$	$1,17x10^{11}$
E_2	12900	19000	28100	12900	19000	28100	18522	30748	49000
n_2	1,43	1,6	1,76	1,44	1,61	1,77	1,85	1,91	1,99
α_2	0,23	0,26	0,35	0,41	0,45	0,54	0,38	0,44	0,63
ε_2	0,48	0,41	0,09	0,39	0,31	-0,01	0,52	0,35	0,20
A_3	$13,8x10^6$	$8,17x10^8$	$2,05x10^{10}$	$13,8x10^6$	$8,17x10^8$	$2,05x10^{10}$	$14,96x10^6$	$17,96x10^7$	$2,93x10^9$
E_3	9929	16850	28430	9929	16850	28430	16835	24417	31891
n_3	1,49	1,85	1,9	1,46	1,73	1,87	1,31	1,57	1,83
α_3	0,49	0,49	0,60	0,48	0,48	0,59	0,58	0,84	0,87

Inspection of the numerical results in Table III confirms the previous statement that the parameters n, α and ε depend for the most part on T and to a lesser degree on ϕ. The values given in Table III seem to be within the range of those found by other workers [17, 20, 21]. However, the value of ε_2 seems to be too small at high temperature. The order of reaction n_1 shows a decrease as T increases, which is contrary to what one might expect. The values of n are derived from experimental results, and no physical explanation for this phenomenon can be given at this time. In fact, all the values of the parameters were derived from best-fit equations, and must be considered more as working tools rather than being necessarily representative of the real phenomena. However, the strong influence of temperature in these parameters has certainly a fundamental explanation which may be close to that given by Levy and Weinberg [21]. They postulated that global mechanisms are valid only at temperatures close to the maximum heat release rates and above. At lower temperatures it is almost certain that radicals assume an important role. The values noted for the experimentally determined parameters probably reflect this latter influence.

To determine the composition and temperature profiles with the proposed model, a numerical (simultaneous) integration of Eqns. (4, 5 & 6) is required. This integration was rather complex and the convergence problems were dealt with by the law of propagation of errors [23]. For most experiments, the observed temperatures were over 1000 K and for this reason no attempt was made to develop the model below this temperature. Therefore, it was assumed that between the inlet and the position marking 1000 K (as predicted by the model) the temperature rise would be linear. The final step of the integration procedure was determined by the position at which the CO_2 concentration corresponded to the theoretical, adiabatic, dissociated flame temperature. This latter value was computed using the data given in [24].

Altogether 10 steps of integration were used to cover the range of CO_2 obtained for a particular condition. The program for the integration of the rate equations consisted of calculating the residence time, the distance, the flame temperature by enthalpy balance, and the composition (CO_2, CO, H_2, O_2, N_2, H_2O, Ar, C_3H_8) for a given increase of CO_2 up to its maximum value. The rate equations gave the values of CO_2, H_2O and C_3H_8; the remaining components being defined by mass balance.

4. EXPERIMENTAL POINTS AND DERIVED PARAMETERS

The data reported here are representative and illustrate typical results obtained from a much larger amount of work [2]. A single experiment consisted of operating the rig at a given condition long enough for gas samples to be obtained from each of the five planes downstream of the recirculation zone. For each such experiment, fuel and air-mass flows were determined, as also inlet temperatures and pressures, humidity, external wall temperatures, static and total pressures.

To establish the correlation parameters, 17 experiments were made. These are tabulated below (Table IV). In addition to these tests, a further 18 experiments were performed at various conditions. A major objective of the thesis [2], from which this work is cited, was to investigate the effects of steam injection upon premixed combustion. Many, but not all, of these later [18] experiments concerned steam addition, and the model was used to make predictions.

Figure 2 gives an example of a weak mixture test (expt. No. 1) which was used to establish the parameters of Table III. The scatter of the model prediction lines is due to the averaging of values taken from all the experiments Nos. 1-17. Figure 3 illustrates the results for a rich mixture (expt. No. 15). The remaining data exhibited similar scatter.

Table IV

Conditions of Experiments Used for Obtaining Calibration Parameters*

Exp. No.	Ø	$\dot{m}_a$ kg/s	$\dot{m}_f$ kg/s	P_3 kPa	T_3 K	Exp. No.	Ø	$\dot{m}_a$ kg/s	$\dot{m}_f$ kg/s	P_3 kPa	T_3 K
1	0,697	0,218	$9,73 \times 10^{-3}$	103	312	10	0,967	0,274	$1,76 \times 10^{-2}$	103	298
2	0,705	0,284	$1,28 \times 10^{-2}$	103	311	11	0,979	0,269	$1,67 \times 10^{-2}$	102	311
3	0,839	0,293	$1,57 \times 10^{-2}$	103	313	12	1,016	0,180	$1,14 \times 10^{-2}$	103	309
4	0,852	0,177	$9,68 \times 10^{-3}$	103	311	13	1,102	0,238	$1,63 \times 10^{-2}$	102	306
5	0,852	0,229	$1,24 \times 10^{-2}$	103	305	14	1,077	0,175	1.23×10^{-2}	103	310
6	0,877	0,271	$1,51 \times 10^{-2}$	103	293	15	1,205	0,181	$1,39 \times 10^{-2}$	103	309
7	0,890	0,237	$1,36 \times 10^{-2}$	102	306	16	1,216	0,216	$1,70 \times 10^{-2}$	103	311
8	0,919	0,292	$1,71 \times 10^{-2}$	103	305	17	1,317	0,178	$1,49 \times 10^{-2}$	103	310
9	0,934	0,178	$1,06 \times 10^{-2}$	102	305						

*Full details of these tests are given in [2].

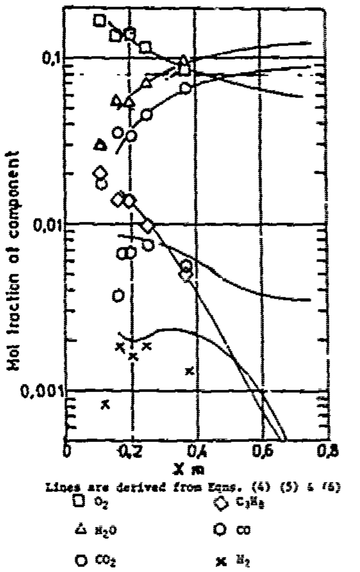

Fig. 2: Data Used to Establish Correlation Parameters at Ø = 0,70

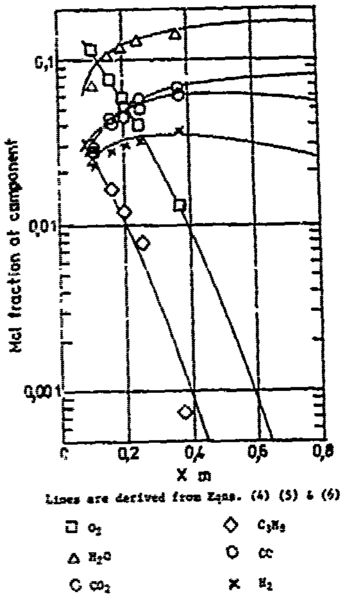

Fig. 3: Data Used to Establish Correlation Parameters at Ø = 1,21

From Figs. 2 and 3 it will be seen that for the major constituents (CO_2, H_2O, O_2) of the analysis, the agreement between the model and the experimental points is quite good. Additionally, the final point of the integration of the model (for each of the major constituents) lies close to the equilibrium value. The minor constituents (CO, H_2, C_3H_8) are perhaps not quite so satisfactory but are still considered to be acceptable.

In addition to composition, the model also predicts the temperature at any plane and for three conditions (Expts. Nos. 1, 12 & 15), Fig. 4 gives a comparison between experimental results and computed temperatures from the gas analysis. The model follows very closely the experimental values and comes close to the equilibrium temperature at the final point of integration (Maximum difference is about 40 K considering all Expts. No. 1-17) showed similar behaviour to Figs. 2-4.

At this point it was considered that all the parameters of the model had been established and that it was ready for application.

5. MODEL PREDICTIONS

Prior to the steam investigation experiments were made, using air, to test the efficacy of prediction. A typical set of predictions and measured values is illustrated in Figs. 5 & 6. In general the agreement is good and similar remarks apply as given in Para. 4.

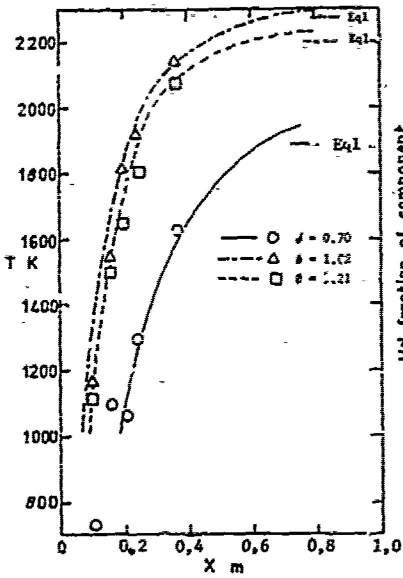

Fig. 4: Temperature Predictions

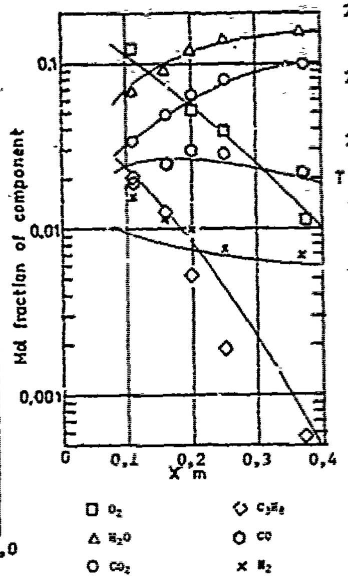

Fig. 5: Predicted and Experimental Results ∮ = 0,99

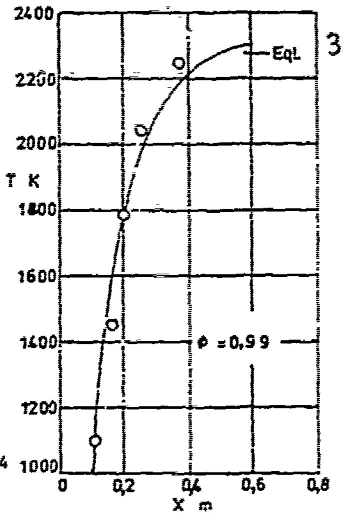

Fig. 6: Predicted and Experimental Values of Temperature

A more severe test of the model was obtained by testing it outside of the range of conditions for which it was derived. This was achieved by injecting steam at an upstream position such that the gases entering the combustor were fully premixed air, propane and steam. Predictions were then made and these are compared with the experimental results in Figs. 7 & 8. Also, for comparison, are the results of a test which used air. Both tests were operated at a nominal value of ∮ = 0,90. Actually, values of ∮ = 0,91 and ∮ = 0,89 were obtained respectively for the "with steam" and "without steam" tests. The quantity of steam injected was defined in terms of the fuel mass flow as $\dot{m}_{steam}/\dot{m}_{fuel} = 0,532$

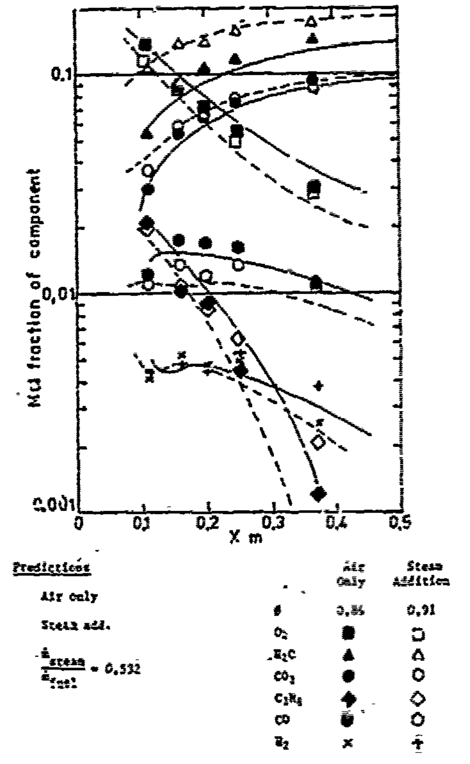

Fig. 7: Comparison of Experiments and Model Predictions for Tests With and Without Steam Injection

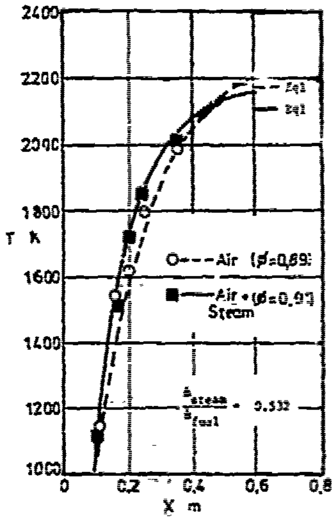

Fig. 8: Comparison of Experiments and Model Predictions for Tests With and Without Steam Injection

It will be seen that (Fig. 7) the component predictions are acceptably good both for the propane/air and propane/air/steam. The differences between the two tests are also predicted quite quantitatively. Because the unburned components are quite small, the effects are not so obvious in terms of temperature (Fig. 8). In this latter case the measured temperatures, although in reasonable agreement with the model predictions, do not illustrate the differences suggested by the predictions.

These results (plus those of the 15 remaining tests) confirm the validity of the model within this geometry. The effects of steam on combustion, both from the viewpoint of combustion analysis and model prediction/analysis will be presented elsewhere. Suffice to say that the prediction scatter is very similar to that illustrated here.

6. GENERAL DISCUSSION OF THE MODEL

The present model represents a compromise between the simple one-step 'global' reaction model and the complex multi-equation kinetic schemes. It predicts all the stable substances found in hydrocarbon/air mixtures with the exception of NO_x. This latter may be estimated independently by one or more of the empirical methods suggested earlier [3 or 4] or by other published techniques. The accuracy of prediction within the limits of the experimental conditions investigated is very satisfactory, both in terms of components and temperature.

Because of its relative simplicity, the computing time is small (in comparison with many kinetic schemes) and it offers potential for combining with a suitable mixing model.

There is a disadvantage in the requirement of a separate series of reaction parameters for rich and weak mixtures, but this has been found to be necessary for many other correlations, both of the simple and complex types.

Like most other correlation formulae, the validity is always in some doubt due to the limited experimental data. In particular, it would be nice to test the data at pressures and inlet temperatures other than atmospheric. Unfortunately this is not possible with the existing test facilities.

An attractive possibility would be to attempt to apply the model to predict the performance of a pre-mixed, pre-vaporised gas turbine combustor. Unfortunately, to date, the published information has been insufficient to enable predictions to be made.

Ram-jet combustors also offer attractive possibilities for this type of model since there is neither film-cooling or dilution problems. The semi-prevaporisation/premix of a ram-jet may make the model directly applicable. In the present work the results have been presented in terms of a distance function, X, but it may well be more satisfactory to express the results in terms of residence times.

7. CONCLUSIONS

1. A three-step model has been proposed to describe the combustion with a fully premixed propane/air system. Some 510 different experimental results were used to define the model.
2. After the above derivation, the model was used to predict a further 540 experimental points comprising propane burning in air or air + steam. The predictions are in sensible agreement with the experimental values even though those conditions having steam addition are outside the frame of the model calibration.
3. The model is capable of predicting CO_2, H_2O, CO, H_2, C_3H_8, O_2, N_2 and Ar.
4. There is potential application for the model both in the field of ram-jets and the gas turbine.

8. ACKNOWLEDGEMENTS

The financial assistance of the Canadian Natural Sciences and Engineering Research Council is gratefully acknowledged.

REFERENCES

1. Roy, P., Schlader, A.F., & Odgers, J., "Premixed Combustion in a Baffle Combustor and the Effect of Steam Injection", J. of Engineering for Power, pp. 387-393, Oct. 1974.
2. Roy, P., "Modelage et Etude de la Combustion prémélangée avec et sans Injection de Vapeur:, Thèse présentée à l'Ecole des gradués de l'Université Laval pour l'obtention du grade 'philosophiae doctor', 1980.
3. Lipfert, F.W., "Correlation of Gas Turbine Emission Data", ASME Paper No. 72-GT-60.
4. Kretschmer, D., & Odgers, J., "Modelling of Combustors: The Effects of Ambient Condition: upon Performance", ASME Paper No. 73-WA/GT-6.
5. Edelman, R.B. & Fortune, O., "A Quasi-Global Chemical Kinetic Model for the Finite Rate Combustion of Hydrocarbon Fuels", AIAA, Paper 69-86, 1969.

6. Mellor, A.M., Bilger, R.W., Shisler, R.A. & Tuttle, J.H., "Emissions from Aircraft Fuel Nozzle Flames", Report No. PURDU-CL-75-04, July 1975.

7. Pratt, D.T., "Calculation of Chemically Reacting Flows with Complex Chemistry", in Studies in Convection, Vol. 2, B.E. Launder, Ed., Academic Press, 1977.

8. Pratt, D.T., Wormeck, J.J., "CRECK - A Computer Program for Calculation of Combustion Reaction Equilibrium and Kinetics in Laminar or Turbulent Flows", Washington State University Report WSU-ME-TEL-76-1, 1976.

9. Spalding, D.B., & Serag-Eldin, M.A., "Prediction of the Flow and Combustion Processes in a Three-Dimensional Combustion Chamber", ISABE, Munich, March 1976, 489.

10. Edelman, R., & Economos, C., "A Mathematical Model for Jet Engine Combustor Pollutant Emissions", AIAA/SAE, 7th Propulsion Joint Speciallist Conference, Paper No. 71-714, June 1971.

11. D'Souza, M.V., & Karim, G.A., "An Analytical Study of Methane Oxidation in a Steady - Flow Reactor", Comb. Science & Tech., 3, 1971, p. 83.

12. Kollrack, R. & Aceto, L.D., "Recirculation Effects in Gas Turbine Combustors", 95th Winter Annual Meeting of the ASME, Paper No. 74-WA/GT-3, Nov. 18, 1974.

13. Longwell, J.P., & Weiss, M.A., "High Temperature Reaction Rates in Hydrocarbon Combustion", I. & E.C., 47, No. 8, p. 1634.

14. Avery, W.H., & Hart, R.W., "Combustor Performance with Instantaneous Mixing", I. & E.C., 45, No. 8, 1953, p. 1934.

15. Essenhigh, R., "An Introduction to Stirred Reactor Theory Applied to Design of Combustors, Combustion Technology", Pennsylvania, State University, Some Modern Developments, 1973.

16. Kretschmer, D., & Odgers, J., "Modelling of Gas Turbine Combustors - A Convenient Reaction Rate Equation", ASME, J. Eng. for Power, July 1972, p. 173.

17. Hottel, H.C. et al, Tenth Symposium (International) on Combustion, p. 111, The Combustion Institute, 1965.

18. Kozlov, G.I., Seventh Symposium (International) on Combustion, p. 142, The Combustion Institute, 1958.

19. Avery, W.N., and Hart, R.W., Ind. Eng. Chem., Vol. 45, p. 1634, 1953.

20. Kretschmer, D., and Odgers, J., Journal of Engineering for Power, ASME, p. 173, July 1972.

21. Levy, A., and Weinberg, F.J., Combustion and Flame, Vol. 3, p. 229, 1959.

22. Fristrom, R.M., and Westenberg, A.A., Flame-Structure, p. 326, McGraw-Hill, 1965.

23. Weinberg, F.J., Proc. Roy. Soc., 241, p. 132, 1957.

24. JANAF Thermochemical Tables, 2nd Edition, N.B.S., U.S. Dept. of Commerce, June 1971.

DISCUSSION

R.Monti

I wonder if the very large variation of the "constants" A_i, E_i, with temperatures up to 3–4 order of magnitude for A_i, does not make your model questionable.

Author's Reply

I do not think the model is questionable within its constraints. Variations of E, A and n have been noted by various workers other than ourselves. An example is cited in the text (Ref.12). I believe that it might stem from representing a multitude of reactions by a single "global" reaction. The one-equation model (Ref.16) also has a variable E and a, but this equation has had a very widespread application to a large number of experimental conditions and types of combustion equipment. Also, I believe that Essenhigh accepts this concept. For this reason, I do not think that the model is questionable from this viewpoint. It is certainly an empirical model with pseudo-constants, but that does not necessarily make it unreliable as a tool.

J.Winter

What do you anticipate will be the effect of inlet temperature and pressure on the "constants" derived for the model?

Author's Reply

It is difficult to answer this question without the experimental data. However, if I had to make a prognostication of the effects of inlet temperature and pressure, I would utilize the corrections suggested for our earlier one-step equation. These may be found in References 16 and 20. The basis for this thought would be the similarities of the form of the present equations to the older one. I would again stress that it is only a suggestion and experimental confirmation would be required to give a measure of confidence.

NATIONAL DISTRIBUTION CENTRES FOR UNCLASSIFIED AGARD PUBLICATIONS

Unclassified AGARD publications are distributed to NATO Member Nations through the unclassified National Distribution Centres listed below

BELGIUM
Coordonnateur AGARD – VSL
Etat-Major de la Force Aérienne
Quartier Reine Elisabeth
Rue d'Evere, 1140 Bruxelles

CANADA
Defence Science Information Services
Department of National Defence
Ottawa, Ontario K1A OK2

DENMARK
Danish Defence Research Board
Østerbrogades Kaserne
Copenhagen Ø

FRANCE
O.N.E.R.A. (Direction)
29 Avenue de la Division Leclerc
92320 Châtillon sous Bagneux

GERMANY
Fachinformationszentrum Energie,
Physik, Mathematik GmbH
Kernforschungszentrum
D-7514 Eggenstein-Leopoldshafen 2

GREECE
Hellenic Air Force General Staff
Research and Development Directorate
Holargos, Athens

ICELAND
Director of Aviation
c/o Flugrad
Reykjavik

ITALY
Aeronautica Militare
Ufficio del Delegato Nazionale all'AGARD
3, Piazzale Adenauer
Roma/EUR

LUXEMBOURG
See Belgium

NETHERLANDS
Netherlands Delegation to AGARD
National Aerospace Laboratory, NLR
P.O. Box 126
2600 A.C. Delft

NORWAY
Norwegian Defence Research Establishment
Main Library
P.O. Box 25
N-2007 Kjeller

PORTUGAL
Direcção do Serviço de Material
da Forca Aerea
Rua da Escola Politécnica 42
Lisboa
Attn: AGARD National Delegate

TURKEY
Department of Research and Development (ARGE)
Ministry of National Defence, Ankara

UNITED KINGDOM
Defence Research Information Centre
Station Square House
St. Mary Cray
Orpington, Kent BR5 3RE

UNITED STATES
National Aeronautics and Space Administration (NASA)
Langley Field, Virginia 23365
Attn: Report Distribution and Storage Unit

If copies of the original publication are not available at these centres, the following may be purchased from:

Microfiche or Photocopy	*Microfiche*	*Microfiche*
National Technical	ESRO/ELDO Space	Ministry of Technology
Information Service (NTIS)	Documentation Service	Reports Centre
5285 Port Royal Road	European Space	Station Square House
Springfield	Research Organization	St. Mary Cray
Virginia 22151, USA	114, Avenue de Neuilly	Orpington, Kent BR5 3RE
	92, Neuilly-sur-Seine, France	England

The request for microfiche or photocopy of an AGARD document should include the AGARD serial number, title, author or editor, and publication date. Requests to CFSTI should include the NASA accession report number.

Full bibliographical references and abstracts of the newly issued AGARD publications are given in the following bi-monthly abstract journals with indexes:

Scientific and Technical Aerospace Reports (STAR)
published by NASA,
Scientific and Technical Information Facility,
P.O. Box 33, College Park,
Maryland 20740, USA

United States Government Research and Development
Report Index (USGDRI), published by the Clearinghouse
for Federal Scientific and Technical Information,
Springfield, Virginia 22151, USA

ISBN 92-835-0312-X

Printed by Technical Editing and Reproduction Ltd
Harford House, 7-9 Charlotte St, London, W1P 1HD

31-11

B 206
4

AGARD
NATO OTAN
7 RUE ANCELLE · 92200 NEUILLY-SUR-SEINE
FRANCE
Telephone 745.08.10 · Telex 610176

DISTRIBUTION OF UNCLASSIFIED AGARD PUBLICATIONS

AGARD does NOT hold stocks of AGARD publications at the above address for general distribution. Initial distribution of AGARD publications is made to AGARD Member Nations through the following National Distribution Centres. Further copies are sometimes available from these Centres, but if not may be purchased in Microfiche or Photocopy form from the Purchase Agencies listed below.

NATIONAL DISTRIBUTION CENTRES

BELGIUM
Coordonnateur AGARD – VSL
Etat-Major de la Force Aérienne
Quartier Reine Elisabeth
Rue d'Evere, 1140 Bruxelles

CANADA
Defence Science Information Services
Department of National Defence
Ottawa, Ontario K1A 0K2

DENMARK
Danish Defence Research Board
Osterbrogades Kaserne
Copenhagen Ø

FRANCE
O.N.E.R.A. (Direction)
29 Avenue de la Division Leclerc
92320 Châtillon sous Bagneux

GERMANY
Fachinformationszentrum Energie,
Physik, Mathematik GmbH
Kernforschungszentrum
D-7514 Eggenstein-Leopoldshafen 2

GREECE
Hellenic Air Force General Staff
Research and Development Directorate
Holargos, Athens

ICELAND
Director of Aviation
c/o Flugrad
Reykjavik

ITALY
Aeronautica Militare
Ufficio del Delegato Nazionale all'AGARD
3, Piazzale Adenauer
Roma/EUR

LUXEMBOURG
See Belgium

NETHERLANDS
Netherlands Delegation to AGARD
National Aerospace Laboratory, NLR
P.O. Box 126
2600 A.C. Delft

NORWAY
Norwegian Defence Research Establishment
Main Library
P.O. Box 25
N-2007 Kjeller

PORTUGAL
Direcção do Serviço de Material
da Forca Aerea
Rua da Escola Politecnica 42
Lisboa
Attn: AGARD National Delegate

TURKEY
Department of Research and Development (ARGE)
Ministry of National Defence, Ankara

UNITED KINGDOM
Defence Research Information Centre
Station Square House
St. Mary Cray
Orpington, Kent BR5 3RE

UNITED STATES
National Aeronautics and Space Administration (NASA)
Langley Field, Virginia 23365
Attn: Report Distribution and Storage Unit

THE UNITED STATES NATIONAL DISTRIBUTION CENTRE (NASA) DOES NOT HOLD STOCKS OF AGARD PUBLICATIONS, AND APPLICATIONS FOR COPIES SHOULD BE MADE DIRECT TO THE NATIONAL TECHNICAL INFORMATION SERVICE (NTIS) AT THE ADDRESS BELOW.

PURCHASE AGENCIES

Microfiche or Photocopy
National Technical
Information Service (NTIS)
5285 Port Royal Road
Springfield
Virginia 22161, USA

Microfiche
Space Documentation Service
European Space Agency
10, rue Mario Nikis
75015 Paris, France

Microfiche or Photocopy
British Library Lending
Division
Boston Spa, Wetherby
West Yorkshire LS23 7BQ
England

Requests for microfiche or photocopies of AGARD documents should include the AGARD serial number, title, author or editor, and publication date. Requests to NTIS should include the NASA accession report number. Full bibliographical references and abstracts of AGARD publications are given in the following journals:

Scientific and Technical Aerospace Reports (STAR)
published by NASA Scientific and Technical
Information Facility
Post Office Box 8757
Baltimore/Washington International Airport
Maryland 21240; USA

Government Reports Announcements (GRA)
published by the National Technical
Information Services, Springfield
Virginia 22161, USA

Printed by Technical Editing and Reproduction Ltd
Harford House, 7–9 Charlotte St, London W1P 1HD

ISBN 92-835-0312-X